JPL Publication 04-6

Proceedings of the 12th JPL Airborne Earth Science Workshop

Robert O. Green
Editor
Jet Propulsion Laboratory
California Institute of Technology

National Aeronautics and Space Administration

Jet Propulsion Laboratory
California Institute of Technology
Pasadena, California

December 2003

This publication was prepared at the Jet Propulsion Laboratory, California Institute of Technology, under a contract with the National Aeronautics and Space Administration.

Contents

Introduction 1

EO-1 Hyperion Measures Canopy Drought Stress in Amazônia
G. P. Asner, D. Nepstad, G. Cardinot, P. Moutinho, T. Harris, and D. Ray 3

Retrieval of Marine Water Constituents Using Atmospherically Corrected AVIRIS Hyperspectral Data
S. Bagheri and S. Peters 11

AmeriSat–Requirements Analysis for a Hyperspectral Land Remote Sensor Constellation for Energy Exploration
R. Beck 17

Assessment of Soil Erosion Potential in Semi-Arid Soils using Hyperspectral Technology
E. Ben-Dor, N. Goldshalager, O. Braun, B. Kindel, A.F.H.Goetz, D. Bonfil, M. Agassi, Y. Binyaminy, and A. Karnieli 27

Assessment of Hyperion for Characterizing Mangrove Communities
M. Demuro and L. Chisholm 39

Endmember Selection for Multiple Endmember Spectral Mixture Analysis
P. E. Dennison and D. A. Roberts 49

Using AVIRIS Data to Map and Characterize Subaerially and Subaqueously Erupted Basaltic Volcanic Tephras: The Challenge of Mapping Low-Albedo Materials
W. H. Farrand 55

Unsupervised Change Detection for Hyperspectral Images
M. Frank and M. Canty 63

Relative Performance of HATCH and Three Other Techniques for Atmospheric Correction of Hyperion and AVIRIS Data
A. F. H. Goetz, B. Kindel, M. Ferri, and E. Gutmann 73

Forest Information Products from AVIRIS and Hyperion
D. G. Goodenough, H. Chen, A. Dyk, T. Han, S. McDonald, M. Murdoch, K. O. Niemann, J. Pearlman, and C. West 83

Applying Tafkaa for Atmospheric Correction of AVIRIS over Coral Ecosystems in the Hawai'ian Islands
J. A. Goodman, M. J. Montes and S. L. Ustin 91

Monitoring the On-Orbit Spectral Calibration of the New Millennium EO-1 Hyperion Imaging Spectrometer
R. O. Green 97

Inflight Calibration Experiment Results for AVIRIS on May 6, 2002 at Rogers Dry Lake, California
R. O. Green and B. Pavri 109

Using AVIRIS in the NASA BAA Project to Evaluate the Impact of Natural Acid Drainage on Colorado Watersheds
P. L. Hauff, D. W. Coulter, D. C. Peters, M. A. Sares, E. C. Prosh, F. B. Henderson III, and D. Bird 121

Use of EO-1 Hyperion Data for Inter-Sensor: Calibration of Vegetation Indices
A. Huete, T. Miura, H.-J. Kim, H. Yoshioka 131

Hyperspectral Detection of Forest Fuel Attributes as Input to Farsite Fire Model in the Front Range of Colorado
G. J. Jia, I. C. Burke, and S. A. Hall 139

Mineral Mapping with AVIRIS and EO-1 Hyperion
F. A. Kruse 149

Preliminary Results—Hyperspectral Mapping of Coral Reef Systems Using EO-1 Hyperion, Buck Island, U.S. Virgin Islands
F. A. Kruse 157

Hyperion Studies of Crop Stress in Mexico
D. B. Lobell and G. P. Asner 175

Measuring Trace Gases in Plumes from Hyperspectral Remotely Sensed Data
R. Marion, R. Michel, and C. Faye 181

Ecosystem Impacts of Woody Encroachment in Texas: A Spatial Analysis Using AVIRIS
R. E. Martin and G. P. Asner 191

Atmospheric Correction of Spectral Imagery: Evaluation of the FLAASH Algorithm with AVIRIS Data
M. W. Matthew, S. M. Adler-Golden, A. Berk, G. Felde, G. P. Anderson, D. Gorodetsky, S. Paswaters, and M. Shippert 199

Discrimination and Biophysical Characterization of Brazilian Cerrado Physiognomies with EO-1 Hyperspectral Hyperion
T. Miura, A. R. Huete, L. G. Ferreira, and E. E. Sano 207

Analysis of AVIRIS Data from LEO-15 using Tafkaa Atmospheric Correction
M. J. Montes, B.-C. Gao, C. O. Davis, and M. Moline 213

Methods for Detecting Anomalies in AVIRIS Imagery
B. S. Penn and M. W. Wolboldt 219

The Use of AVIRIS Imagery to Assess Clay Mineralogy and Debris-Flow Potential in Cataract Canyon, Utah: A Preliminary Report
L. Rudd and E. Merényi 231

A Subpixel Target Detection Technique Based on the Invariance Approach
J. R. Schott, K. Lee, R. Raqueno, G. Hoffmann, and G. Healey 241

Volcanic CO_2 Abundance of Kilauea Plume Retrieved by Means of AVIRIS Data
C. Spinetti, V. Carrere, M.F. Buongiorno and D. Pieri 251

AVIRIS and Archaeology in Southern Arizona
D. A. White 259

Estimating Surface Soil Moisture in Simulated AVIRIS Spectra
M. L. Whiting, L. Li and S. L. Ustin 269

Introduction

This publication contains the proceedings of the JPL Airborne Earth Science Workshop—a forum held to report science research and applications results with spectral images measured by the NASA Airborne Visible/Infrared Imaging Spectrometer (AVIRIS). These papers were presented at the Jet Propulsion Laboratory from February 25–28, 2003.

EO-1 HYPERION MEASURES CANOPY DROUGHT STRESS IN AMAZÔNIA

Gregory P. Asner,[1] Daniel Nepstad,[2,3] Gina Cardinot,[2]
Paulo Moutinho,[2] Thomas Harris,[1] David Ray[3]

1. Introduction

Amazon moist tropical forests account for about 70–80 Pg (70–80 x 10^{15} g) of the world's terrestrial carbon stocks and roughly 4–6 Pg (~10%) of the annual net primary productivity (NPP). Because of the large carbon pools and fluxes in this region, much attention has focused on the effects of land use on Amazon forest cover and carbon storage, and on the potential feedbacks to regional and global climate (Shukla et al. 1990). The role of climate in modulating interannual variability of Amazon forest phenology and NPP has received little attention until recently (Tian et al. 1998, Asner et al. 2000), yet this variation may be significant from both climatological and ecological perspectives. Large uncertainties persist regarding spatial and temporal patterns of biosphere-atmosphere carbon exchange, and these uncertainties impede global analyses of CO_2 sources and sinks, and thus changes in climate forcing (Ciais et al. 1995). Climate-driven phenology and NPP variability in the Amazon also has important implications for basin hydrology, river biology and biogeochemistry, trace gas fluxes, and spatial and temporal patterns of land-use change.

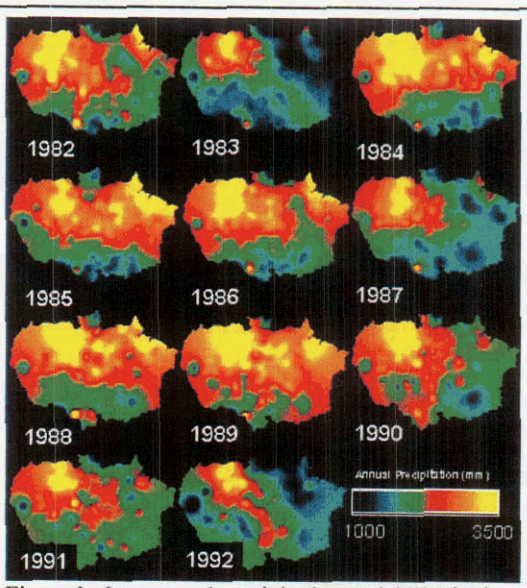

Figure 1. Interannual precipitation variability in the Amazon basin. ENSO periods (1983, 1987, 1991-1992) can be linked to decreased rainfall, especially in the southeast region of the basin (Asner et al. 2000)

There is now increasing focus on the effects of the El Niño-Southern Oscillation (ENSO), which is known to decrease rainfall in the Amazon basin (Marengo 1992). For example, the 1983, 1987, and 1991/92 ENSO events varied in strength, but all resulted in anomalously low precipitation throughout much of the region (Figure 1). Because the factors controlling forest phenology and productivity throughout the tropics are not well known, independent observations are needed to evaluate estimates of a biological response to climate variation.

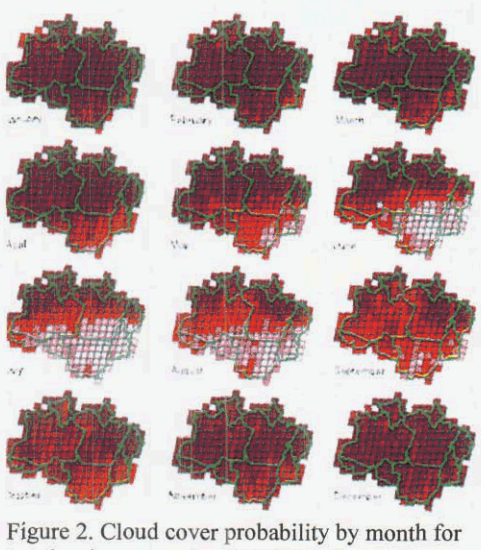
Figure 2. Cloud cover probability by month for Landsat imagery of the Brazilian Amazon (Asner 2001). Whiter indicates fewer clouds.

Whereas annual variations in rainfall are starting to be understood in the Amazon Basin, seasonal variations are not well known. There is a pronounced dry season that extends from June to November throughout the eastern and central Amazon, but spatial variation in the strength of this dry season remains poorly quantified. Phenological losses of canopy foliage are reduced during the dry season through forest deep root access to soil water reserves (Nepstad et al. 1994). Nonetheless, field measurements do show that Amazon forest canopies respond to seasonal dry periods, with litterfall increases of 10–35% and decreases of total leaf area index (LAI) of up to 30% (Asner et al. 2000, Nepstad et al. 2002). Cloud cover information from more than 54,000 Landsat images of the Brazilian Amazon yielded a spatial proxy for seasonal rainfall patterns in the Amazon, as shown in Figure 2.

[1] Carnegie Institution of Washington, Stanford California
[2] Instituto de Pesquisa Ambiental da Amazônia, Bélem, Brazil
[3] The Woods Hole Research Center, Woods Hole, Massachusetts

The central, south and southeast portions of the Amazon Basin experience a period of decreased cloud cover and precipitation from June through November.

There are likely important effects of seasonal and interannual rainfall variation on forest leaf area index, canopy water stress, productivity and regional carbon cycling in the Amazon. While both ground and spaceborne studies of precipitation continue to improve, there has been almost no progress made in observing forest canopy responses to rainfall variability in the humid tropics. This shortfall stems from the large stature of the vegetation and great spatial extent of tropical forests, both of which strongly impede field studies of forest responses to water availability. Those few studies employing satellite measures of canopy responses to seasonal and interannual drought (e.g., Bohlman et al. 1998, Asner et al. 2000) have been limited by the spectral resolution and sampling available from Landsat and AVHRR sensors.

We report on a study combining the first landscape-level, managed drought experiment in Amazon tropical forest with the first spaceborne imaging spectrometer observations of this experimental area. Using extensive field data on rainfall inputs, soil water content, and both leaf and canopy responses, we test the hypothesis that spectroscopic signatures unique to hyperspectral observations can be used to quantify relative differences in canopy stress resulting from water availability.

2. Study Region and Areas

The experiment was located in Brazil's Tapajós National Forest, in east-central Amazonia (2.897° S, 54.952°W; Figure 3). This forest receives 600–3000 mm of rain each year, with a mean of 2000 mm; it experiences severe drought during El Niño events (Figure 1). The forest is situated on a flat terrace of Tertiary sediments capped by the Belterra Clay Formation, and is approximately 90 m above the water level of the Tapajós River, located 10 km to the west. The Oxisol soil (Haplustox) is dominated by kaolinite clay minerals and is free of hardpan or iron oxide concretions in the upper 12 m. The water table is located at ~100 m depth.

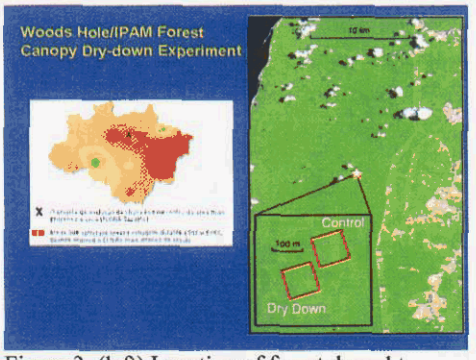

Figure 3. (left) Location of forest drought experiment in the central Brazilian Amazon. (right) Landsat image of forest drought experiment and control area, located within the Tapajos National Forest.

We selected two floristically and structurally similar, one-ha (100 x 100 m) plots from an initial survey of 20 hectares of forest. We encountered 182 and 203 species represented by individuals with diameter at breast height (1.3 m, dbh) of at least 10 cm (trees) and 5 cm (lianas) in the treatment and control plots, respectively. The plots shared 54 tree species in common with at least 2 individuals per plot, therefore allowing us to compare responses to the experimental treatment within the same species. The plots also had similar physiognomy, with the exception of a 600-m^2 treefall gap on the edge of the control plot. The forest surrounding the plots had emergent trees up to 55 m in height, with continuous canopy varying in height from 18 to 40 m. The study plots were placed in areas where most of the canopy was <30 m high to facilitate access to the tree crowns. Above-ground biomass of trees =10 cm dbh and lianas =5 cm basal diameter at the beginning of the experiment was 291 and 305 Mg ha-1 in the treatment and control plots, respectively.

At their closest points, the plots were 25 m apart. Four wooden towers (13-30 m in height) and 80-100 m of catwalk (8-12 m height) provided access to the canopy in each of the 1-ha plots. Soil shafts (12-m deep, with 2.1 x 0.8 m openings, n=3 per plot and n=5 as of April 9, 2001), with a wooden infrastructure, provided belowground access. Sampling grids with 10-m distances between points were established with 10 x 10 points inside of each plot and a perimeter of sampling points outside of each plot, for a total of 12 x 12 = 144 points. These grids were used for measurements of surface soil water content, leaf area index, canopy openness, and other measures. A 1- to 1.7-m deep trench was excavated around the treatment plot to reduce the potential for lateral movement of soil water from the surrounding forest into the plot, and to provide a conduit for water excluded from the plot. A similar trench was excavated around the control plot to avoid the confounding of throughfall exclusion and trenching effects. As with many large-scale ecosystem manipulations, this experiment was prohibitively large and expensive to permit replication.

Throughfall was partially excluded from the treatment plot during the rainy season of 2000, from late January through early August, and during the rainy season of 2001, from early January through late May, using 5,660 panels made of clear, PAR-transmitting greenhouse plastic mounted on wooden frames. The panels were removed during the dry season to reduce their influence on the forest floor through shading and heating. The panels

increased forest floor temperature by no more than 0.3°C. While they were in place, the panels were flipped on their sides every two to three days to transfer accumulated litter onto the forest floor. Each 3 x 0.5 m panel drained into a plastic-lined, wooden gutter (30 cm wide) that carried the water into the trench, which was also lined with plastic. Water flowed by gravity from the perimeter trench into a deeper drainage ditch (1.7–2.3 m depth), which extended 220 m away from the plot into a small valley. The panels and gutters covered only ~75% of the forest floor, because openings we left around tree stems. We did not exclude stemflow from the plot. Estimates of daily rainfall were made with two wedge-shaped rain gauges located in the center of an 80-m wide clearing 500 m from the experimental plots. Trampling of the forest floor was reduced in the experimental plots by directing foot traffic onto wooden walkways. Despite this precaution, 17% of the treatment plot and 15% of the control plot had visible signs of foot traffic as of January, 2001 (based on three, randomly-placed, 100-m transects across each plot). Forest floor damage in the treatment plot was greater than in the control plot because of the installation of panels and gutters. However, the control plot suffered similar forest floor damage because measurements of canopy cover, leaf area index, litterfall, and throughfall within the sampling grid required ground access; elevated drainage gutters provided access to the grid in the treatment plot.

3. Field Sampling

The amount of throughfall excluded by the panels was calculated for each exclusion period as the increase in soil water content in the control plot minus the increase in soil water content in the treatment plot, plus the difference between deep seepage of soil water (below 11 m depth) in the control and treatment plots. Deep seepage was estimated as evapotranspiration minus rainfall minus the increase in soil water content for a given time interval. Evapotranspiration was assumed to be 4 mm per day, based on published estimates for Amazon forest ET during the wet season. Drought affects forests primarily through its effects on soil moisture. Previous studies have found that forests in seasonally-dry Amazonia absorb soil water from depths of 8 m and more during periods of severe drought (Nepstad et al. 1994). We therefore monitored volumetric soil water content (cm^3 water cm^{-3} soil) to 11 m depth in both the treatment and control plots.

We measured soil water using Time Domain Reflectometry (TDR) to a soil depth of 30 cm. The pre-dawn leaf water potential of mature trees was measured at approximately 2-wk intervals during the dry seasons and at longer time intervals during the wet seasons to provide a measure of canopy drought stress. Six tree species common to both forest plots were studied, with three individuals per species in each plot, and four leaves sampled per individual. Leaves were clipped before sunrise, and stored in plastic bags on ice until water potential was measured using a pressure chamber. Measurements were always completed within one hour of clipping.

We measured leaf area index (LAI) before and during the throughfall exclusion treatment at each of the grid sampling points using LICOR LAI-2000 Plant Canopy Analyzers. One instrument was placed above the canopy on a tower to measure incoming radiation with no canopy influence; the other instrument was used for the understory measurement, made with the same directional orientation as the above-canopy instrument. The instruments were inter-calibrated above the canopy at the beginning of each set of measurements. Measurements were made under conditions of diffuse skylight. LAI calculations were made using the inner three quantum sensor rings to minimize the overlap among measurements made in adjacent grid points.

4. Spaceborne Imaging Spectroscopy

Earth Observing-1 (EO-1) Hyperion imaging spectrometer data were collected over the experimental sites in July and November 2001, corresponding with the early and late parts of the dry season. Details of the mission are available on the EO-1 internet website at: http://eo1.gsfc.nasa.gov. The imagery was delivered in L1A calibrated radiance format from NASA Goddard Space Flight Center (GSFC), Greenbelt, Maryland. Three calibration steps were applied to the radiance as suggested by GSFC: (1) a pixel shift was applied to samples 129–256 in the shortwave-infrared (SWIR) wavelength region to co-register this portion of the data with the visible and near-infrared (NIR) observations; (2) the visible and NIR bands were multiplied by a scale factor of 1.08, and the SWIR bands were multiplied by a scale factor of 1.18; and (3) the wavelength values were increased by 2 nm for all bands. These steps were necessary to bring the data set up to the currently available calibration level. The Hyperion data were then spectrally and spatially subset. The zero-value visible bands 1–4 and SWIR bands 226–242 and the overlapping bands 58–78 were removed, resulting in a 200 band subset.

Apparent surface reflectance was estimated from the Hyperion radiance data using the ACORN atmospheric correction algorithm (AIG-LLC, Boulder, Colorado). ACORN uses the 1.14 μm water vapor feature to compute atmospheric water vapor thickness. The water vapor bands near 1.4 and 1.8 μm were then removed. The

resulting reflectance spectra still contained some anomalies; however, no ground calibration was applied since the noise was not systematic.

The two calibrated spectral reflectance cubes were geo-located using differentially-corrected GPS data points collected throughout the area. Owing to the fact that all calibration steps, including atmospheric correction, are not perfect, and given our interest in isolating relatively small differences in canopy reflectance between the two sites, we employed a comparative analysis of the sites by ratioing spectral signatures. Since the two sites were close together spatially, site-based ratioing of the results eliminated the contribution of atmospheric differences to the multi-date comparison of sites.

5. Spectroscopic Indices

Imaging spectroscopy offers a unique set of observations – and thus tools – to analyze the molecular absorption and scattering features of materials. Traditional multi-spectral observations, such as from Landsat, SPOT, AVHRR and MODIS sensors, provide a subset of the capabilities provided by hyperspectral imagers. Although imaging spectroscopy affords the means to analyze full spectral features of materials, many vegetation indices have been developed to condense and simplify the analysis of high-dimensional spectral data while also attempting to maximize the information content of the indices. The normalized difference vegetation index (NDVI) is a prime example. The NDVI is the normalized difference of reflectance at red (~680 nm) and near-infrared (~750–850 nm) wavelengths (= [NIR-RED]/[NIR+RED]). The NDVI is sensitive to canopy greenness, fractional photosynthetic radiation absorption (fPAR) and canopy leaf area. It is available from nearly all multi-spectral sensors. However, the NDVI is also known to become insensitive, or to saturate, in canopies with leaf area indices (LAI) greater than about three or four (Choudhury 1987, and many others).

Novel vegetation indices have been developed using imaging spectrometers. These indices are derived from a variety of spectral channels, often using observations from very narrow wavelength regions of the spectrum. Because leaf pigments absorb photons at visible wavelengths (400-690 nm), whereas water absorbs in near-IR (750–1300 nm) and shortwave-IR (1500–2500 nm) regions, a narrow and contiguous sampling of the spectrum at these wavelengths allows the development highly sensitive indices. The following are a few indices that have proven useful to understanding the spatial and temporal dynamics of vegetation:

Table 1. Five narrowband vegetation indices available for analysis from the EO-1 Hyperion spaceborne imaging spectrometer.

Index	Index Name	Equation	Reference
NDVI	Normalized Difference Vegetation Index	(R800-R680)/(R800+R680)	Choudhury (1987)
SR	Simple Ratio	R800/R680	Sellers (1985)
NDWI	Normalized Difference Water Index	(R857-R1241)/(R857+R1241)	Gao (1996)
PRI	Photochemical Reflectance Index	(R531-R570)/(R531+R570)	Gamon et al. (1992)
ARI	Anthocyanin Reflectance Index	(1/R550) – (1/R700)	Gitelson et al. (2001)

The simple ratio (SR) is one of the oldest vegetation indices. Like the NDVI, it is sensitive to canopy greenness, fPAR and leaf area. The normalized difference water index (NDWI) was designed for sensitivity to canopy water content (Gao 1996). Two pigment-related indices unique to imaging spectroscopy are the photochemical reflectance index (PRI; Gamon et al. 1992) and anthocyanin reflectance index (ARI; Gitelson et al. 2001). The PRI has been used to study changes in xanthophyll cycle pigments, providing a means to estimate photosynthetic light-use efficiency (LUE). Anthocyanins are water soluble pigments that cause the red coloration of plant tissues. These red pigments are expressed differentially by species and within species, with observed variations resulting from leaf aging, stress and nutrient status.

We used the EO-1 Hyperion spectrometer observations to calculate these five narrow-band vegetation indices. We ratioed the sites to look for differences that might be the result of precipitation throughfall exclusion in the Amazon forest dry-down experiment.

6. Results and Discussion

Differences in plant available water (PAW) in the soils of the drydown and control forest areas were pronounced (Figure 4). In comparison to the control area, PAW was 54% and 56% lower in the drydown site in July and November, respectively. Decreasing PAW followed the well-known monthly pattern of decreasing rainfall during the dry season (June–December), but the precipitation throughfall exclusion greatly enhanced the effect of seasonal drought on the drydown forest area (Figure 4).

The average canopy reflectance spectra from EO-1 Hyperion of the dry-down and control areas are shown in Figure 5. A zoom graph of the visible (500–700 nm) spectral range and the spectral bands used to create the narrow-band vegetation indices is also provided. Visible reflectances were higher and near-IR reflectances were lower in the early dry-season (July) in comparison to the late dry-season (November). These differences between imaging dates likely resulted from changes in upper-canopy architecture, canopy water content, and LAI; however, a precise cause for this observed change is not clear. It is also possible that these general differences in the visible and near-IR spectral regions are due to atmospheric effects.

Both canopies maintained LAI values in July and November, and these LAI values were well into the saturation zone for both the NDVI and SR (Figures 6). The LAI of the control area actually increased from July to November, while it decreased slightly in the drydown site. Leaf water of the drydown and control canopies was also similar in July and November (Figure 6).

Despite the similarity of LAI and leaf water within each site at the beginning and end of the dry season, there were substantial differences between the two sites on each imaging date. The drydown site had an average LAI value that was 8% and 19% lower than the control area in July and November, respectively (Figure 6). While leaf water was nearly the same in the drydown and control sites in July, the drydown area was nearly 30% lower in leaf water at the end of the dry season (November).

Another important biophysical difference between the drydown and control areas was found in the specific leaf area (SLA) values of species common to both sites. SLA is the leaf area per unit mass, which is a good inter-species indicator of leaf thickness. SLA values were nearly twice a high among species in the control than in the drydown forest areas (Figure 7). This finding indicated that the vegetation responded to persistent drought by developing leaves of greater thickness, which reduced transpiration and increased leaf longevity.

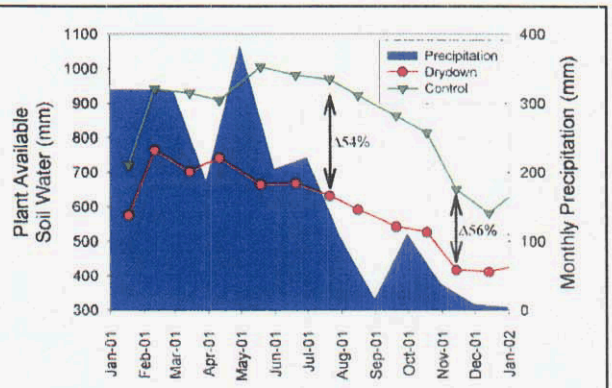

Figure 4. Monthly plant available soil water (mm) and precipitation for the period January 2001–2002. EO-1 Hyperion acquisition dates are shown in black arrows.

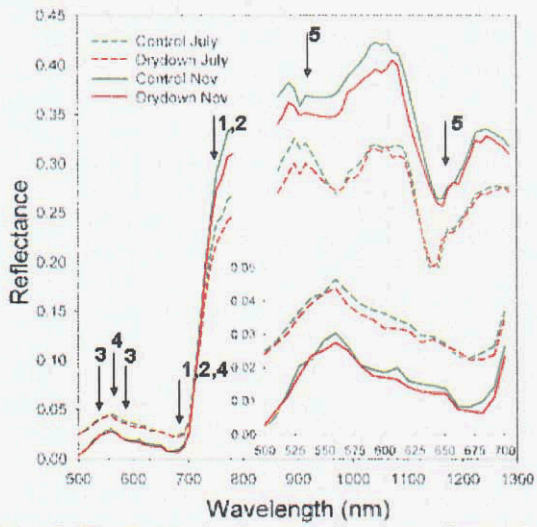

Figure 5. Hyperspectral reflectance signatures of control and drydown sites in the Central Amazon, acquired in July and November 2001 by EO-1 Hyperion. Numbers show spectral bands used to calculate the (1) NDVI, (2) SR, (3) PRI, (4) ARI, and (5) NDWI.

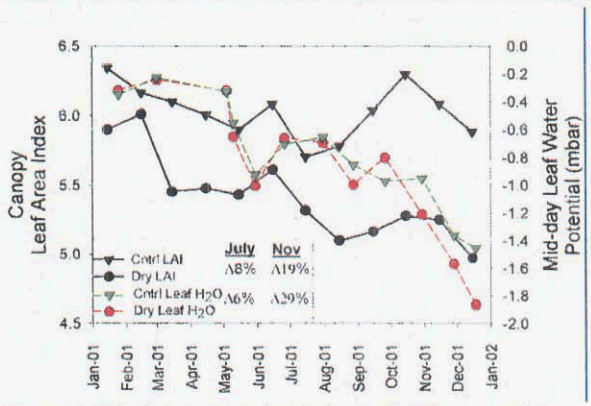

Figure 6. Monthly LAI and mid-day leaf water potential from January 2001-2002 for the control and drydown experimental areas. Percentage differences in LAI and leaf water at each Hyperion observation date are shown in the legend.

A summary of all major leaf and canopy properties for the drydown and control forest areas in July and November 2001 is provided in Table 1. In July at the beginning of the dry season, plant available soil water and leaf water potential were both high in the control area but decreased to moderate levels by the end of the dry season in November. During both imaging periods, LAI and leaf thickness (1/SLA) were very high and low, respectively, in the control area.

In contrast to the control area, the drydown forest site had moderate plant available soil water and high leaf water in July. Both of these properties decreased dramatically to low levels by November. Meanwhile, both LAI and leaf thickness (1/SLA) remained high at the beginning and end of the dry season in 2001 (Table 2).

These differences between drydown and control forest areas, at the start and end of the dry season, had differential effects on the hyperspectral narrowband indices derived from the EO-1 Hyperion imagery (Figure 8). Interestingly, the ratio of NDVI and SR values for the drydown and control areas remained nearly constant at 1.0 in both July and November. This indicated no measurable NDVI or SR response of the drought either at the beginning or end of the dry season. This result is not surprising, given that the NDVI and SR saturate at LAI values in the three to four range. This result suggests that multi-spectral sensors, such at Landsat or AVHRR, cannot detect changes in canopy "greenness" as provided by the NDVI or SR for drought conditions in Amazon humid tropical forests.

In contrast to the traditional NDVI and SR indices, the canopy water index (NDWI) was highly sensitive to drought conditions (Figure 8). The ratio of drydown:control area NDWI was nearly 1.0 (no difference) at the beginning of the dry season (July) but decreased substantially to about 0.25 by the end of the dry season in November.

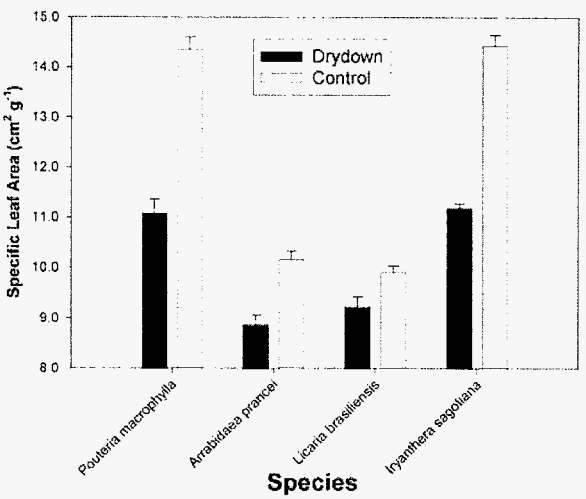

Figure 7. Specific leaf area – a measure of leaf thickness – for four species common to the drydown and control forest areas.

Canopy Properties and Changes During Dry Season

Control Forest	*July*	*November*
Plant-avail Water	High	Moderate
Leaf Water	High	Moderate
LAI	Very High	Very High
Leaf Thickness	Low	Low
Drydown Forest		
Plant-avail Water	Moderate	Low
Leaf Water	High	Low
LAI	High	High
Leaf Thickness	High	High

Table 2. Summary of leaf and canopy properties in the control and drydown forest areas in July and November 2001.

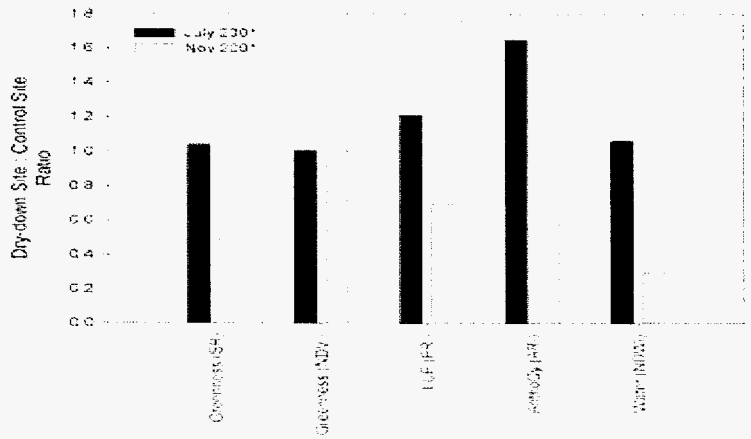

Figure 8. Ratio of narrowband vegetation indices for drydown vs. control areas, derived from EO-1 Hyperion in July and November, 2001.

This result suggests that the NDWI is sensitive to canopy foliage area and water content at high values obtained by tropical forests. This also indicates that the effects of the precipitation throughfall exclusion were best observed at the end of the dry season, when the affects of drought are at maximum. These effects were most evident in the plant available soil water, leaf water and leaf thickness data obtained in the field (Table 2).

Light-use efficiency (LUE), or the amount of carbon uptake by vegetation per unit energy absorption, is a critically important determinant of net primary production in ecosystems (Field et al. 1995). Hyperion observations indicated about a 20% higher and a 20% lower LUE in the drydown area in July and November, respectively (Figure 8). It is difficult to ascertain the cause of increased LUE in the drought-stressed forest at the beginning of the dry season. It is possible that this site had a flush of new foliage prior to the July image, a potential response to foliage loss in the previous dry season. This hypothesis is supported by the concomitant observation of 60% higher anthocyanin levels (ARI; Table 1) in the drydown site at the beginning of the dry season. Anthocyanin, or leaf redness, is a general indicator of newly-formed foliage prior to the full development of chlorophyll pigments that changes the leaf color to green. The much lower LUE in the drydown (vs. control) by the end of the dry season is more understandable, as the drought site had much less leaf water at this time of the year. A simultaneous indicator of anthocyanin levels (ARI) showed 40% lower values in the drydown as compared to the control area in November.

7. Conclusions

The results presented in this communication indicate that narrowband vegetation indices available from the spaceborne imaging spectrometer, EO-1 Hyperion, can be used to monitor drought impacts on humid tropical forests. The first-ever measurements of soil and plant water stress at the landscape scale were combined with the first-ever spaceborne imaging spectrometer observations to test the sensitivity of these hyperspectral indices. We found that:

a. Drought stress in the central Amazon is most evident in decreased plant available soil water, leaf water potential, and specific leaf area.
b. Narrowband NDVI and SR observations are insensitive to changes in leaf area index and canopy water content in humid tropical forests.
c. Narrowband canopy water observations (NDWI) are highly sensitive the changes in canopy leaf area and water content in humid tropical forests.
d. Narrowband pigment indices related to light-use efficiency and anthocyanin levels indicate the onset of stress effects caused by chronic water stress.

These preliminary findings strongly suggest that only narrowband, hyperspectral observations can be used to detect canopy drought stress in humid tropical forests such as in the central Amazon Basin. Additional spaceborne imaging spectrometer observations are critically needed to continue this assessment in other forest types and climatic conditions.

8. Acknowledgements

This work was supported by NASA NIP grant NAG5-8709, NASA New Millenium (EO-1) Program grant NCC5-481, and the National Science Foundation.

9. References

Asner, G.P., Cloud cover in Landsat observations of the Brazilian Amazon, *International Journal of Remote Sensing*, 22, 3855–3862, 2001.

Asner, G.P., A.R. Townsend, and B.H. Braswell, Satellite observation of El Niño effects on Amazon forest phenology and productivity, *Geophysical Research Letters*, 27, 981–984, 2000.

Bohlman, S.A., J.B. Adams, D.L. Peterson, Seasonal foliage changes in the Eastern Amazon Basin detected from Landsat Thematic Mapper satellite images, *Biotropica*, 30, 376–393, 1998.

Choudhury, B.J., Relationships between vegetation indices, radiation absorption and net photosynthesis evaluated by a sensitivity analysis, *Remote Sensing of Environment*, 22, 209–233, 1987.

Ciais, P., et al., A large northern hemisphere CO_2 sink indicated by the $^{13}C/^{12}C$ ratio of atmospheric CO_2, *Science*, 269, 1098–1102, 1995.

Field, C.B., et al., Global net primary production: combining ecology and remote sensing, *Remote Sensing of Environment*, 51, 74–88, 1995.

Gamon, J.A., J. Penuelas, and C.B. Field, A narrow-waveband spectral index that tracks diurnal changes in photosynthetic efficiency, *Remote Sensing of Environment*, 41, 35–44, 1992.

Gao, B.-C., and A.F.H. Goetz, Retrieval of equivalent water thickness and information related to biochemical components of vegetation canopies from AVIRIS data, *Remote Sensing of Environment*, 52, 155–162, 1995.

Gitelson, A.A., M.N. Merzlyak, and O.B. Chivkunova, Optical properties and nondestructive estimation of anthocyanin content in plant leaves, *Photochemistry and Photobiology*, 74, 38–45, 2001.

Marengo, J.A., Interannual variability of surface climate in the Amazon basin, *International Journal of Climatology*, 12, 853–863, 1992.

Nepstad, D., et al., The role of deep roots in the hydrological and carbon cycles of Amazonian forests and pastures, *Nature*, 372, 666–669, 1994.

Nepstad, D., et al. The effects of partial throughfall exclusion on canopy processes, aboveground production, and biogeochemistry of an Amazon forest, *Journal of Geophysical Research*, 2002.

Sellers, P.J. Canopy reflectance, photosynthesis, and transpiration, *International Journal of Remote Sensing*, 6, 1335–1372, 1985.

Shukla, J., et al., Amazon deforestation and climate change, *Science*, 247, 1322-1325, 1990.

Tian, H., et al., Effect of interannual climate variability on carbon storage in Amazonian ecosystems, *Nature*, 396, 664–667, 1998.

Retrieval of Marine Water Constituents Using Atmospherically Corrected AVIRIS Hyperspectral Data

Sima Bagheri[1] and Steef Peters[2]

1. INTRODUCTION

This paper reports on the validation of bio-optical models in estuarine and nearshore (case 2) waters of New Jersey-New York to retrieve accurate water-leaving radiance spectra and chlorophyll concentration from the Airborne Visibile/Infrared Imaging Spectrometer (AVIRIS) imaging spectrometer data. MODTRAN-4 was applied to remove the effects of the atmosphere so as to infer the water-leaving radiance. The study area - Hudson/Raritan of New York and New Jersey (Figure 1) is an extremely complex estuarine system where tidal and wind-driven currents are modified by freshwater discharges from the Hudson, Raritan, Hackensack, and Passaic rivers. Over the last century, the estuarine water quality has degraded in part due to eutrophication, which has disrupted the pre-existing natural balance, resulting in phytoplankton blooms of both increased frequency and intensity, increasing oxygen demand, and leading to episodes of hypoxia. As the end result, a thematic map of chlorophyll-a concentration was generated using an atmospherically corrected AVIRIS ratio image. This thematic map serves as an indication of phytoplankton concentration. Such maps are important input into the geographic information system (GIS) for use as a management tool for monitoring water resources.

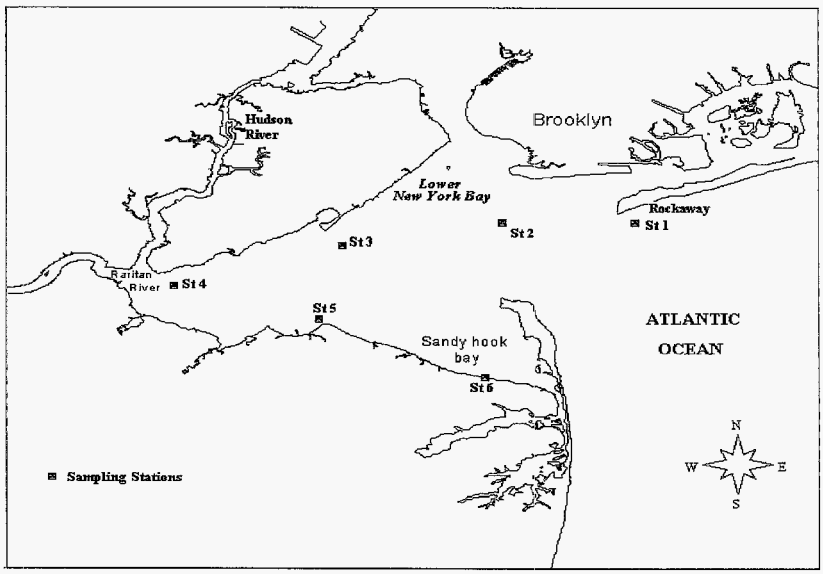

Figure 1. Map of the study area with the locations of sampling stations

2. MATERIALS AND METHODS

The research was based on imaging spectrometer data from AVIRIS, field spectroradiometer, and water samplings. Based on these measurements optical water quality models are constructed linking the water constituent concentrations to (i) the inherent optical properties (IOP), using the specific inherent optical properties (SIOP), and (ii) to the subsurface (ir) radiance reflectance (Bagheri and Dekker, 1999, and Bagheri et al., 2000 and 2001. A simple optical water quality model was calibrated on measurements of optical water constituent concentrations and inherent optical properties and used to simulate subsurface irradiance reflectance (or water leaving radiance). The following is a brief description of the field/laboratory method used to establish the IOPs of the estuary for retrieval of water quality concentrations from the AVIRIS data:

A) Upwelling and downwelling radiances/irradiances (E_u and E_d) were measured using the OL754 field spectroradiometers. The goal was to parameterize the bio-optical model relating the CDOM, TSM and algal

[1] New Jersey Institute of Technology
[2] Vrije Universiteit, The Netherlands

pigment concentrations, to the light absorption and scattering and to the water leaving radiance, through direct and laboratory based optical measurements. In short, the link between remotely sensed upwelling radiance and underwater inherent optical properties is made through subsurface irradiance reflectance R(0-).

B) To estimate optically-important water quality parameters coincident with the R(0-)measurements, samples (0.2 to 0.5 m depth) were taken for laboratory analysis. Standard procedures (Rijkeboer et al., 1998) were used to determine concentrations of total chlorophyll-a (TCHL) defined as the sum of chlorophyll-a and phaeopigment (to index phytoplankton abundance) and total suspended matter (TSM). TCHL and TSM were determined according to the Dutch standard methods NEN 6520 (1981) and NEN 6484 (1982) respectively. TCHL varied between 22 mg m^{-3} and 46 mg m^{-3} indicating that sampling did not coincide with any major phytoplankton bloom. Likewise, TSM (7-11 g m^{-3}) was not remarkably high nor low for this time of year. Phytoplankton species were also identified and enumerated in the samples for inclusion in the library spectra of the estuary.

C) The two IOPs measured directly were spectral absorption (a) and spectral beam attenuation (c), using an Ocean Optics-2000. (Note: Use of this device for measuring IOPs is experimental and has not been referenced in the published literature.)

Spectral scattering (b) was then deduced via subtraction of a from c (b=c-a).

A simple optical water quality model based on the work of Gordon (1975) was calibrated for measurements of optical water constituent concentrations and inherent optical properties and used to simulate subsurface irradiance reflectance (or water leaving radiance).

$$R(0-) = r\,(b_b/(a+b_b)) \tag{1}$$

Where
a is the total absorption coefficient, b_b is the backscatter coefficient
r is a factor based on the geometry of incoming light and volume scattering in the water.

The water constituents are expressed in their specific (per unit measurement) absorption and backscattering coefficients:

$$a = a_W + a^*_{TSM}TSM + a^*_{ph}CHL + a^*_{CDOM}CDOM_{440} \tag{2}$$
$$b_b = b_{bW} + b_{TSM}TSM$$

The asterisks denote that a and b_b are specific inherent optical properties (SIOP), i.e. per unit concentration denoted by the subscript.

The inversion of such a model (using semi-analytical algorithms) can be used to characterize the estuarine waters in terms of chlorophyll concentration, colored dissolved organic matter and total suspended matter from the observed spectra. Validation of the concentration estimates by optical means and the AVIRIS atmospheric correction is based on in situ measurements of spectra and concentrations.

3. SIMULATION MODELING AND RETRIEVAL TECHNIQUE

The AVIRIS images the earth's surface in 224 spectral bands approximately 10 nm wide covering 400-2500nm. AVIRIS records the integrated effects of the solar source, the atmosphere and the targeted surface. To compensate for the atmospheric effects, an atmospheric and air-water interface correction algorithm based on MODTRAN-4 was utilized. MODTRAN is a radiative transfer model developed by US Air Force Geophysical Laboratory which describes the radiative transfer process in the entire system from the solar source to the remote sensor via the hydrosols. A quantitative treatment of radiative transfer and atmospheric correction is the only way to achieve accurate (multi/hyperspectral) water leaving radiance measurements from satellite and airborne observations and to obtain accurate estimates of concentrations of optical water constituents. The input atmospheric parameters used in MODTRAN-4 were as follows:

Horizontal visibility = 20 km	Midlattitude summer atmosphere urban (5km) aerosol model
Solar zenith angle=55	Solar azimuth angle=83
Modtran 16 streams mode	O_3 scaling factor = 2.0

The above parameters were applied to the spectra where in situ measurements were collected during the course of the project (1999-2001). MODTRAN was able to bring the envelope of AVIRIS spectra reasonably close to

simulated spectra but the results dictated the reconstruction of the "true" values of the band ratio image (702/675) based on chlorophyll field observation and measured SIOP (Figure 2). Results of Modtran are summarized as follows:

1) There is considerable spectral noise
2) There are significant deviations in bands 675 and 702 nm
3) There are unexplained large differences in the blue and NIR

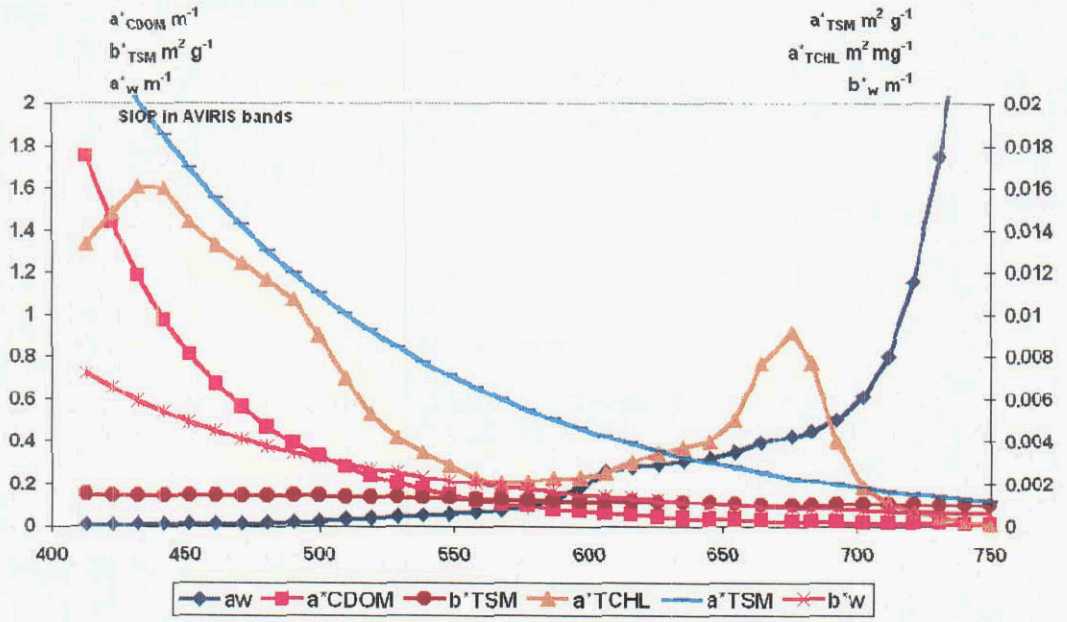

Figure 2. Measured SIOP were input into the forward Gordon model to simulate spectra at the Keyport Harbor (St5) and Traid Bridge (St4) locations for comparison with AVIRIS spectra.

A semi-analytical CHL algorithm was applied to obtain a reasonable estimate of the spatial distribution of CHL concentration (Figure 3). Atmospherically corrected ratio image of the AVIRIS was generated as a thematic map to represent the spatial distribution of CHL concentration as indication of phytoplankton concentration (Figure 4). The following is a summary of the procedures applied:

1) A CHL algorithm was fitted on simulated spectra
2) The ratio image (702/675 nm); based on atmospherically corrected AVIRIS bands) was scaled between reasonable values based on a priori knowledge of possible CHL concentrations sampled at Keyport Harbor (St5) and Traid Bridge (St4) sampling locations
3) The CHL algorithm was applied to the scaled ratio image to obtain the spatial distribution of CHL concentration

The simulation modeling demonstrates the value of AVIRIS observations. The result of the analysis as shown in Figure 3 can be summarized as follows:

1) Spectra below 500 nm are uncorrectable and unreliable.
2) The envelope of the spectra is quit irregular, indicating that there remains a substantial amount of sunglint within the AVIRIS data.
3) The irregularity of the spectra is such that the balance between 670 and 700 nm observations seems to be affected, making CHL determinations based on ratios difficult.
4) The general shape of the envelope and the range of values seem to be realistic for 500 and 750 nm. Although normally the spectral maximum is observed around 550 nm, but in this case it is shifted to the right.

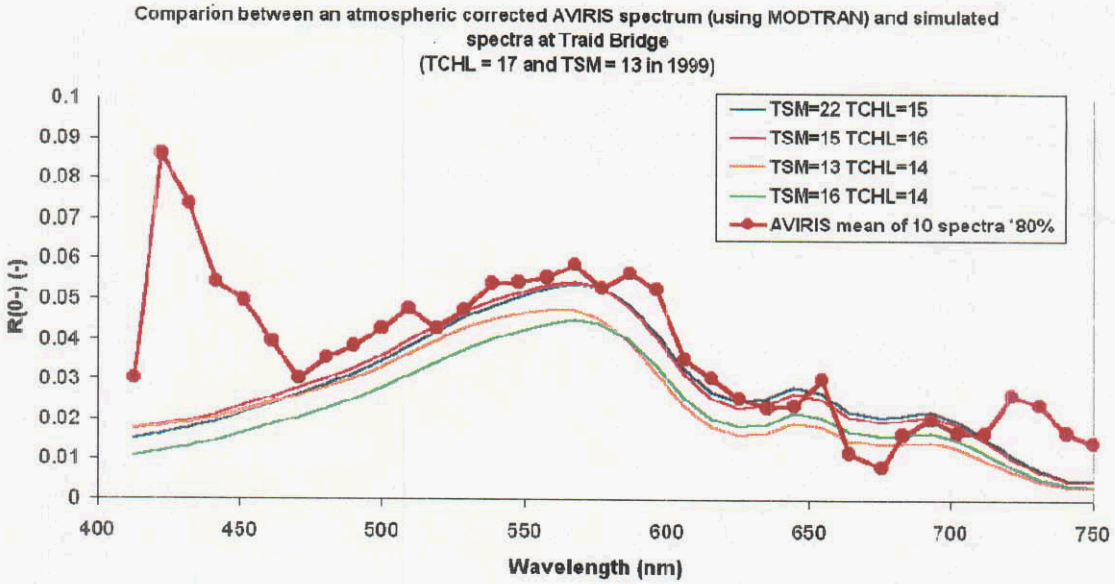

Figure 3. The AVIRIS spectrum after atmospheric correction was scaled down with 20%. (Note: The scaling difference may be due to many reasons, primarily due to the time difference between the measurements)

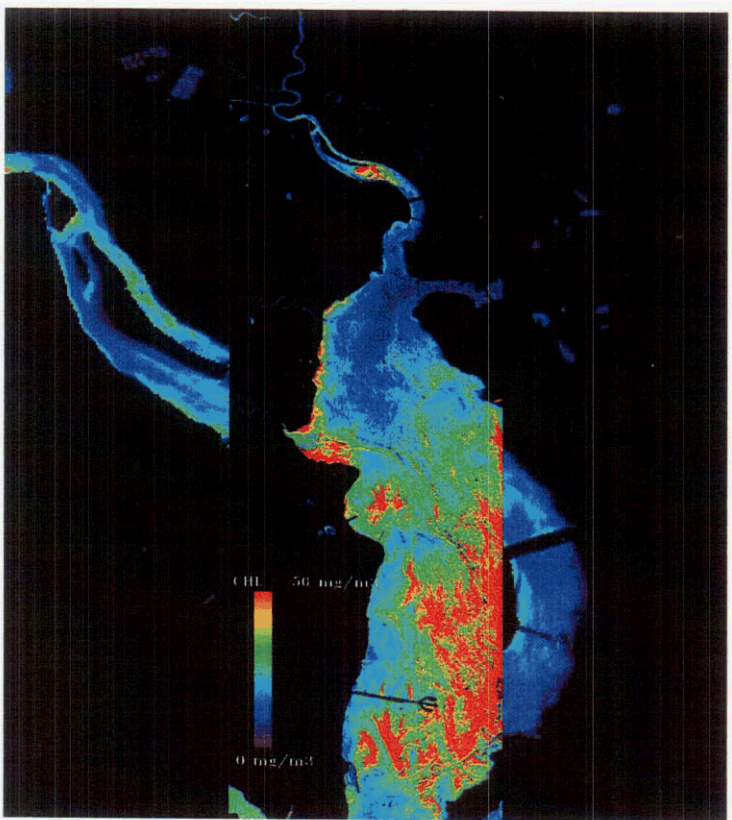

Figure 4. Bloom-like structure up the Raritan River as depicted in AVIRIS atmospherically corrected ratio image (702/675)

4. CONCLUSION

In our approach IOP of water constituents were used to model the reflectance. A reasonable fit was found between modeled and measured R(0-) using the optical model and RT code.

We conclude that the AVIRIS spectral data provides the opportunity to distinguish the atmospheric effect from the marine water effect to set the estimated turbidity for CHL concentration retrieval. Development of a robust algorithm for simultaneous retrieval of atmospheric aerosol optical properties, CHL, CDOM and TSM is a very challenging task. Nevertheless, such an algorithm is needed to make progress in this area. The model for the coupled atmosphere-marine water provides the link between the spectra measured by the AVIRIS spectrometers and the in situ measurements of spectral irradiances in the water.

5. ACKNOWLEDGEMENT

This project was funded by the National Science Foundation (BES-9806982). Support of the NASA Headquarters and the AVIRIS Experiment Team is greatly appreciated.

6. REFERENCES

Bagheri, S., and Dekker A. Nearshore Water Quality Assessment Using Bio-Optical Modeling and Retrieval Techniques, NASA and AVIRIS'99 Geoscience Workshop, JPL Publication 99-17, Jet Propulsion Laboratory, Pasadena, California, February 8–12,1999.

Bagheri, S, Rijkeboer M, Pasterkamp R, and Dekker A. Comparison of the Field Spectroradiometers in preparation for Optical Modeling, Proceedings of the Ninth Airborne Earth Science Workshop, JPL Publication 00-18, Jet Propulsion Laboratory, Pasadena, California, February 23–27, 2000.

Bagheri, S. Stamnes, K and Li, W. Application of Radiative Transfer Theory to Atmospheric Correction of AVIRIS Data, Proceedings of the Tenth Airborne Earth Science Workshop, JPL Publication 02-1, 2001.

Gordon, H. R., O. B. Brown and M. M. Jacobs, 1975. Computed Relationships between Inherent and Apparent Optical Properties of a Flat Homogeneous Ocean. Appl. Optics, 14:417–427.

NEN 6484 (1982) Water: Determination of the content of not dissolved material and its ignition residue. Nederlands Normalisatie instituut, Delft, The Netherlands (in Dutch).

NEN 6520 (1981) Water: Spectrophotometric determination of chlorophyll a content, Nederlands Normalisatie instituut, Delft, The Netherlands (in Dutch).

Rijkeboer, M, Dekker, A.G., and Hoogenboom, H.J., 1998, Reflectance spectra with associated water quality parameters measured in Dutch waters (Speclib-TK-database). Institute for Environmental Studies, E98/12, The Netherlands.

AmeriSat - Requirements Analysis for a Hyperspectral Land Remote Sensor Constellation for Energy Exploration

Specifications for a Complete, Routine, and Operational Hyperspectral Geological Survey of the United States and Miscellaneous Regions at 1:24,000 as part of the USGS National Map

Richard Beck, Department of Geography
University of Cincinnati, Cincinnati, Ohio 45221
richard.beck@uc.edu

Introduction

The physical and economic well being of the United States of America depends upon a stable and affordable supply of abundant energy. Energy security for the United State of America will continue to depend primarily on fossil and nuclear fuels for the next few decades at a minimum. Efficient and successful exploration for new sources of energy requires precise and consistent geological surveys. Despite years of global exploration activity, much of the world and indeed even the United States has *not* been geologically surveyed at a scale appropriate for energy exploration, environmental hazard analysis, environmental protection or land use planning.

Need for a Precise U.S. Geological Survey at 1:24,000 as part of the USGS National Map and Gateway to the Earth

Energy exploration requires a precise, consistent and accessible U.S. Geological Survey at 1:24,000. For example, although the basic unit of geological analysis, the formation (a significant layer or body of rock), is defined as being mapable at a scale of 1:24,000, less than a tenth of the more than 55,000 1:24,000 scale USGS topographic quadrangles have ever been mapped geologically and these maps are inconsistent at best. This is especially ironic given that almost all other U.S. Geological Survey location data are available in the form of high-quality 1:24,000 scale quadrangles (Figure 1).

Energy exploration takes place on a scale of tens of meters, not kilometers and depends on precise moderate resolution spatial information to make certain that exploration roads are constructed safely and responsibly and so that seismic crews can negotiate proposed seismic lines with a minimum of environmental impact. Similarly, seismic shot points are surveyed to meter-scale precision and exploration wells costing upwards of $10 million each must be located precisely relative to geologic structure, land ownership, elevation and location. This is especially true in the case of directional drilling and detailed three-dimensional seismic surveys. Hard and soft rock mining operations require similar precision for sampling and successful recovery of ore and fossil fuels as well as the safety of the miners.

Figure 1. Simplified outline map derived from one of the few existing 1:24,000 U.S. Geological Survey geological quadrangle maps. Subsequent figures show this outline map superimposed upon Landsat, ASTER and AVIRIS imagery for comparison.

Land Remote Sensor Comparison for the 1:24,000 U.S. Geological Survey

As part of the specification development process for a land remote sensing system for the 1:24,000 geological survey necessary for more efficient energy and mineral exploration, we compared the effectiveness of historical, current and proposed multispectral and hyperspectral imaging instruments capable of remotely sensing the visible, near-infrared, short-wave infrared, and thermal-infrared regions of the electromagnetic spectrum (Table 1). This spectral versatility is necessary to differentiate and to identify the geological formations to be surveyed in a semi-automated manner (Dwyer et al., 1995).

We chose a test site in an area known to produce petroleum, coal, oil shale and uranium. These were the same test site considerations identified by Bailey et al. (1984) in their comparison of the Landsat Multispectral scanner (MSS) and Thematic Mapper (T.M.) instruments flown on Landsats 1 through 5. Their results will not be repeated here although we have chosen the same primary test site on the western edge of Dinosaur National Monument to facilitate comparison of historical, current and proposed land remote sensing systems for geological surveys. We begin with an evaluation of the suitability of the Landsat satellites for geological surveys at 1:24,000 before considering two alternatives (ASTER and ALI/HYPERION) as prototypes for the next-generation of geological survey satellites. We then propose specifications for a new series of next generation land remote sensing satellites for the USGS named AmeriSat.

Table 1. Current satellites capable of remotely sensing the complete VIS/NIR/SWIR/MIR/TIR spectrum necessary for geological surveys.

Spacecraft/Instrument	Landsat-7 / ETM+	EO-1/ALI	EO-1/Hyperion (AVIRIS prototype used for this study)	Terra/ASTER	AmeriSat Constellation
					(ALI+ / Hyperion+)
Spectral Range	0.4-2.4 10.7-12.7 microns	0.4-2.4 microns	0.4-2.5 microns	0.5-0.9 1.6-2.4 8.1-11.7 microns	0.4-2.5 microns
Panchromatic Bands	1	1	0	0	1/1
Visible Bands	3	6	60	2	6/35
Near Infrared Bands	1	2	60	2 (stereo)	3/35
Short Wave Infrared	1	1	60	1	1/172
Middle Infrared Bands	1	1	60	5	1
Thermal Band	1	0	0	5	1
Spatial Resolution	15, 30, 60 m	10, 30 m	30 m	15, 30, 60 m	30 m/15 m
Swath Width	185 km	37 km	7.5 km	60 km	185/30 km
Spectral Coverage	Discrete	Discrete	Continuous	Discrete	Both
Pan Band Resolution	15 m	10 m	N/A	N/A	10 m
Stereo	no	no	no	yes	yes
Number of Bands	7	10	220	14	10 and 220
Number of Spacecraft	1	1	1	1	4-6
Temporal Resolution	16 days	16 days	16 days	16 days	4-8 days
	(8 days with Landsat-5)				
Source: NASA EO-1 briefing materials					

Summary of Current Satellites Capable of Remotely Sensing Visible/NIR/SWIR/MIR/TIR Electromagnetic Radiation (Satellites Good for Geologic Surveys)

Natural materials exhibit a very broad "rainbow" of "color". Only a very narrow slice of this rainbow is visible to human beings. A series of civilian (USGS/NASA) satellites has been designed to view an increasingly complete spectrum in steadily narrower slices of the "rainbow" known as bands and in steadily increasing spatial detail. Table 1 summarizes current satellites that are capable of remotely sensing throughout the visible (VIS), near infrared (NIR), short wave infrared (SWIR), Middle Infrared (MIR), and Thermal Infrared (TIR) part of the electromagnetic spectrum. These satellites are capable of seeing all of the parts of the electromagnetic spectrum necessary to differentiate geologic formations in the case of multispectral (less than 100 bands) satellites and even to identify the types of minerals in the geologic formations in the case of hyperspectral (generally greater than 100 bands spaced closely enough to create spectra from images) satellites.

These space-borne imaging instruments (or air-borne prototypes of very recent and proposed space-borne systems) were compared with each other as well as historical systems to gauge their effectiveness with regard to improving the efficiency of resource exploration and management at 1:24,000. As one might expect, this comparison

demonstrated that improved spectral resolution (finer slices of the rainbow) and improved spatial resolution (the ability to see smaller objects) resulted in progressively more useful imagery for energy exploration.

Landsat MSS Series

The first series of geological survey satellites, the Landsat multispectral scanner (MSS) satellites were crude but provided regional imagery of some use in energy exploration (4 bands at 80 meter resolution). These satellites could miss whole football fields and yet they provided the first views of the earth from space for most geologists, researchers and the public. Research with these images did contribute greatly to the development of plate tectonic theory and suggested improvements for future satellites for resource exploration. Examples of MSS imagery over the Dinosaur Quarry Quadrangle test site used here are available in Bailey and Anderson (1982) and Bailey et al., (1982, 1984).

Landsat TM Series

The second series, the Landsat thematic mapper (TM) satellites, provided much more complete coverage of the spectrum and moderately useful spatial detail (5 and 1 bands at 30 and 120 meters respectively) (Figures 2 and 3). While this series could have been quite useful to regional resource exploration (e.g., Beck et al., 1995)

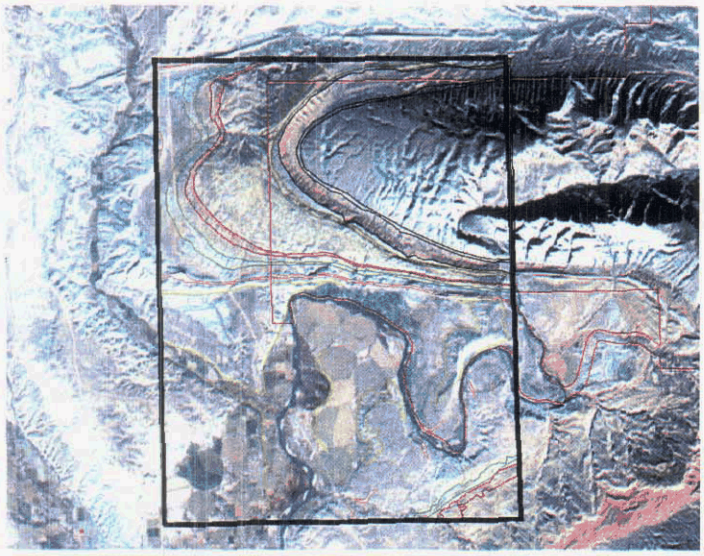

Figure 2. Simplified outline map derived from one of the few existing 1:24,000 U.S. Geological Survey geological quadrangle maps superimposed upon a Landsat-7 ETM+ visible image. The image quality is good but not sufficient for energy exploration.

Landsat ETM+ Series

Although the Landsat system is absolutely crucial with regard to maintaining the continuity of our record of global change and to support regional early warning systems with regard to food supplies, the rate of deforestation, outbreaks of plant diseases, drought, and land use change, its technology is more than two decades old and the 5 band, 30 meter multispectral data it produces are not sufficiently detailed for practical geological surveys at the 1:24,000 scale.

ASTER on TERRA

The advanced spaceborne thermal emission and reflection radiometer (ASTER) is a Japanese/U.S. instrument on a Japanese satellite that has many improvements over the U.S. Landsat ETM+ series of satellites but has several features that limit its use for energy exploration. While ASTER has a greater number of bands with greater radiometric sensitivity than Landsat, ASTER's bands do not have the same spatial resolution throughout the visible and infrared parts of the spectrum. This requires the geologist to artificially coarsen the visible bands or to artificially resample the infrared bands before statistical processing. Both processes result in fuzzy images (Figure 4) of dubious statistical validity.

ASTER's (as well as Landsat's) spatial resolution is too coarse to be of extensive use in petroleum exploration (Figures 2, 3, and 4). This is because most geological surveys are the starting point for subsurface seismic interpretation and the choice of locations for exploration wells. Petroleum geologists typically record the geologic formation at each shot point (small wells filled with lots of dynamite) along a seismic survey line in areas of good geologic exposure (where you can see the rocks at the surface). These shot points or VIBROSEIS stations (places where heavy trucks shake the ground) are typically spaced every 25 meters along a seismic line to create the artificial seismic waves later recorded by microphones.

The seismic wave arrival time patterns are interpreted with the aid of surface geology to tell geophysicists the type of rock and the expected speed of the seismic waves. They then use this time and speed information to calculate the depth of the various rock units and their structure beneath the ground surface with the help of powerful computers. Meanwhile, the geologists also collect samples to determine the likelihood of a source of petroleum, the likelihood of a porous and permeable reservoir, the likelihood of a seal to trap the petroleum beneath the surface, and measure

the angle of the layers (if any) at the surface to provide a series of known starting points for subsurface interpretation. These data points are then used to locate the contacts between geologic units with a spatial precision of approximately 5 to 15 meters at a scale of 1:24,000.

Given the 25 meter spacing of seismic survey points and the need to locate geologic contacts with a precision of 5 to 15 meters at 1:24,000, *the ideal satellite for geological surveys would have a spatial resolution of at least 15 meters* (a four-fold increase in data density over 30 meter data) or finer. This requirement for 15 meter spatial precision means that the 30 and 60 meter spatial resolution of the short wave infrared and thermal bands of the ASTER instrument are too coarse for geological surveys of use to day-to-day petroleum exploration. Despite these limitations, some ASTER data will undoubtedly be used for regional exploration projects given the lack of more suitable alternatives.

The public domain ASTER data are interesting scientifically because of their ability to differentiate (but usually not identify) more rock types than Landsat-7. The ASTER data will have enormous educational and research value for many decades into the future.

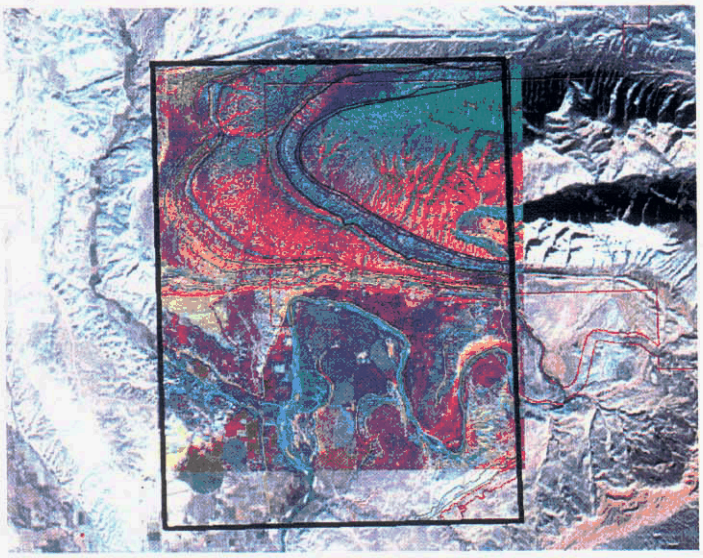

Figure 3. Simplified outline map derived from one of the few existing 1:24,000 U.S. Geological Survey geological quadrangle maps superimposed upon a Landsat-7 ETM+ principal components image. The image quality and differentiation of many of the geologic formations are fair to good but not sufficient for energy exploration. Several formations were missed by this 30 meter image.

ALI on EO-1

The Advanced Land Imager (ALI) on the Earth Observing (EO-1) satellite represents a new generation of technology designed to provide scientific continuity with the Landsat TM and ETM+ series of satellites. It promises to be more useful for regional geological surveys than Landsat ETM+ given the addition of four more 30 meter visible and near infrared bands and a 10 meter panchromatic band to assist with geometric registration. *The most valuable feature of ALI is that all of the multispectral bands have the same spatial resolution.* This is the ideal case for the statistical extraction of the maximum amount of spectral information. ALI does lack the thermal bands carried by the Landsat TM, Landsat ETM+ and ASTER satellites. Although the thermal band is of great value scientifically, it is rarely used in petroleum exploration.

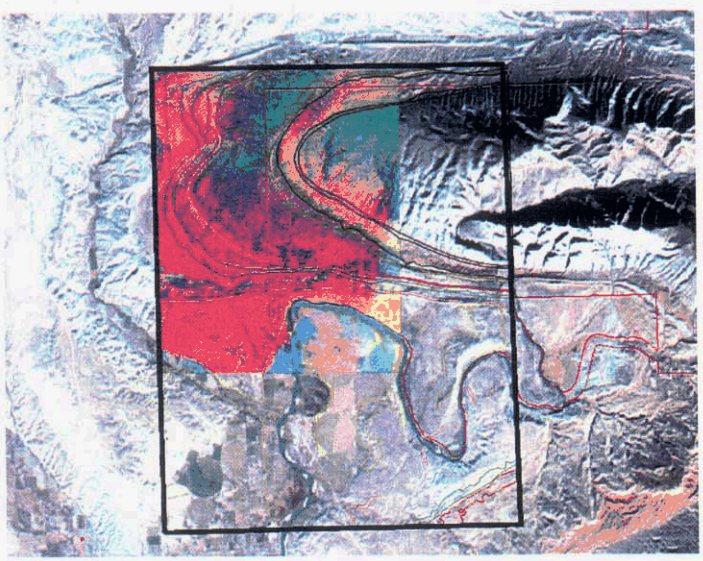

Figure 4. Simplified outline map derived from one of the few existing 1:24,000 U.S. Geological Survey geological quadrangle maps superimposed upon an ASTER principal components image. The image quality is poor because not all of ASTER's bands have the same spatial resolution. Its differentiation of the geologic formations is fair to good but far from sufficient for energy exploration. Many formations were missed by this 15/30 meter image.

Multiple thermal bands do have the ability to differentiate rock types however and at least one thermal band at the same resolution as the VIS, SWIR and MIR bands would be useful. ALI data for the Utah test site only recently became available. ALI is better than Landsat ETM+ and ASTER in terms of signal-to-noise ratio. It will be very useful for regional geologic reconnaissance but its 30 meter resolution is too coarse for 1:24,000 scale geological surveys.

Similarly, *ALI's discrete spectral coverage (limited number of widely spaced bands) prevents the use of USGS-developed automated mineral identification and mapping software* (http://speclab.cr.usgs.gov) to create the "first draft" of each quadrangle before field checking and refinement.

As will be shown below, hyperspectral 15 meter spatial resolution satellite image data, while not ideal for very detailed geological mapping, are a powerful tool that will usually be adequate for rapid geological surveys at the 1:24,000 scale (Figure 5). This spatial resolution represents a good compromise between our needs for economic/environmental security as well as defense/intelligence security.

Hyperion on EO-1 and its AVIRIS "Proxy"

Hyperion is a hyperspectral sensor that records a continuous series of 220 very narrow bands from the visible throughout the short wave infrared part of the electromagnetic spectrum (wavelengths of 0.4–2.5 microns). This is an extremely important feature for rapid semi-automated geological surveys for energy at 1:24,000 scale (Dwyer et al., 1995). This is because the USGS has developed software that compares the amount of "light" reflected from the earth's surface in each one of these bands to laboratory measurements of a wide variety of minerals (as well as plants). Each mineral has a unique signature that can be used to identify it from space (Clark, 1999; Clark and Rousch, 1984; Clark et al., 1993; Gaffey et al., 1993; Salisbury, 1993; Swayze et al., 2000).

The USGS software looks at each pixel in the image and its spectrum of "light" (Clark and Swayze, 1995; Dwyer et al., 1995). It then compares this spectrum of "light" with USGS digital libraries of mineral spectra to identify the minerals in each pixel before mapping them. These computer generated first drafts of geologic maps can then be field checked by geologists who examine the nature of the contacts between the geologic formations before completing the maps.

While actually identifying the minerals in each formation from the satellite is the optimum case, the large amount of spectral information recorded by hyperspectral instruments can be distilled statistically to differentiate rock types on the ground with extraordinary effectiveness far beyond that of the human eye. These distilled statistical images can be created within a few minutes on a modern laptop computer. The geologist then simply traverses each quadrangle and assigns an identity to each of the geologic formations imaged without having to follow every contact on foot.

Hyperion data for the test site have only recently become available. Therefore this study began with AVIRIS data as a proxy for Hyperion. A simple comparison of Hyperion vs. AVIRIS has been added to the end of this study accordingly. The conclusion is that AVIRIS was a reasonable proxy for Hyperion but that future hyperspectral satellites should be designed to imitate AVIRIS as much as possible given its higher spatial resolution and higher signal-to-noise ratio. An example of one of these statistically distilled hyperspectral images from AVIRIS recorded from an ER-2 aircraft (a forward principal components analysis) over the Utah test site is shown in Figure 5. The continuous spectral coverage and 20 meter spatial resolution of this early proxy for Hyperion demonstrates extraordinary improvement in the ability to differentiate (and identify) geologic formations.

Experience with the 15 meter panchromatic band on Landsat-7 (most if its bands have 30 meter resolution) indicates that 15 meter resolution is necessary to confidently differentiate sampling

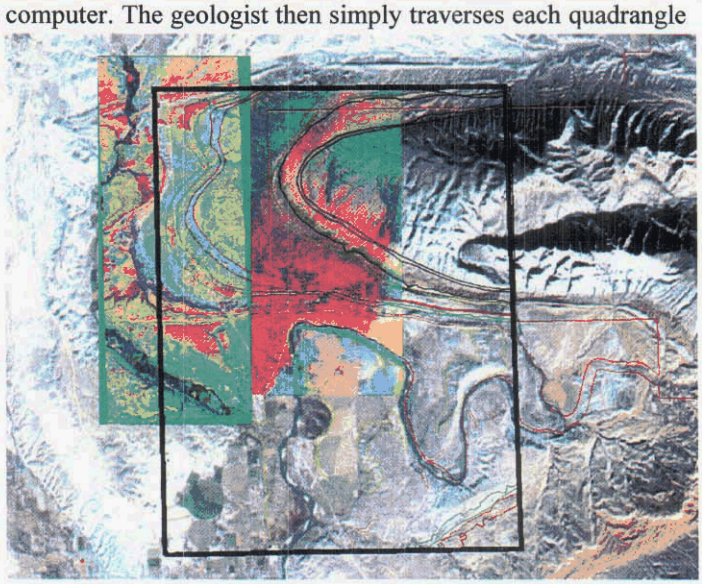

Figure 5. Simplified outline map derived from one of the few existing 1:24,000 U.S. Geological Survey geological quadrangle maps superimposed upon an AVIRIS hyperspectral principal components image. The image quality is good to excellent because all of the AVIRIS bands have the same spatial resolution. Its differentiation of the geologic formations is good to excellent. Nearly all of the geologic formations were found by this 20 meter spatial resolution image. The precision with which these formations and their boundaries are located is a little too coarse for petroleum exploration.

sites at the 1:24,000 scale. As noted above in our discussion of energy exploration activities, 15 meters is probably the coarsest practical spatial resolution. To demonstrate this, we scanned one of the few (paper) 1:24,000 geological quadrangles available and, subsampled it to 15 meter spatial resolution before geometrically warping it to match our test satellite and aircraft imagery (Figure 6). As the reader can see, some of the detail has been lost but most of the key features are still visible.

The example shown in Figure 7 indicates that the current experimental Hyperion instrument must be upgraded to 15 meter spatial resolution for geological surveys useful to energy exploration. Our experience with 15 meter panchromatic data at 1:24,000 indicates that this is adequate and represents a four-fold (2 squared) increase in data density. All of these demonstration data were imported into an ArcView geographic information system to carefully verify the conclusions stated above (Figures 1–5).

Lithologic Identification vs. Discrimination - Utah "Whole Rock" spectral mapping with Hyperion and AVIRIS.

Hyperspectral data allow the identification as well as exceptional discrimination of even similar lithologies for geologic mapping for energy exploration.

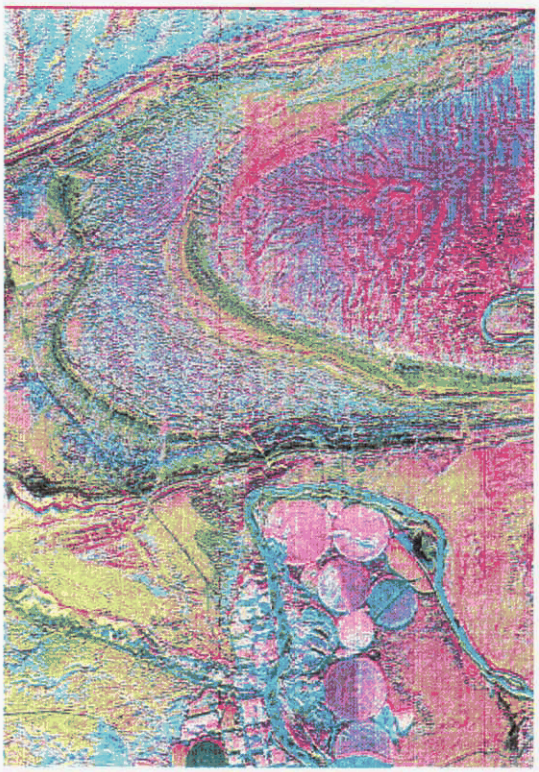

Figure 6. Advanced Land Imager (ALI) forward principal components of nine multispectral bands. The image differentiates most of the formations mapped by the USGS but does not allow for the direct spectral identification of lithology. Future systems would also benefit from higher spatial resolution on the order of 15 meters.

Figure 7 (left). Atmospherically corrected Hyperion spectral angle map (SAM) of the same area showing pixels similar to the whole rock spectrum shown in Figure 8.

The 160 bands result in a relatively complete spectrum for every pixel in the image above. Spectra measured in the field or in the laboratory from field samples (Figure 8) can then be compared to each pixel in the image across all of the bands to see if they are similar to a user defined similarity index such as a user defined spectral angle threshold. Pixels passing the similarity test are then shown as white pixels on an output image. The following image is a map of occurrences of pixels relatively similar to the field spectrum shown below.

Examples of similarly processed AVIRIS hyperspectral data for (nearly) the same area are shown below (Figure 9). The reader will see that the "whole rock" spectra (as opposed to spectra from spectral libraries of individual minerals) help make up for the relatively low signal-to-noise ratio and larger pixel size in Hyperion relative to AVIRIS.

Nonetheless, the higher spatial resolution and higher signal-to-noise ratio of AVIRIS allow the precise mapping of strata with outcrop widths on the order of a single pixel with amazing continuity as in the spectral angle mapper result in Figure 9.

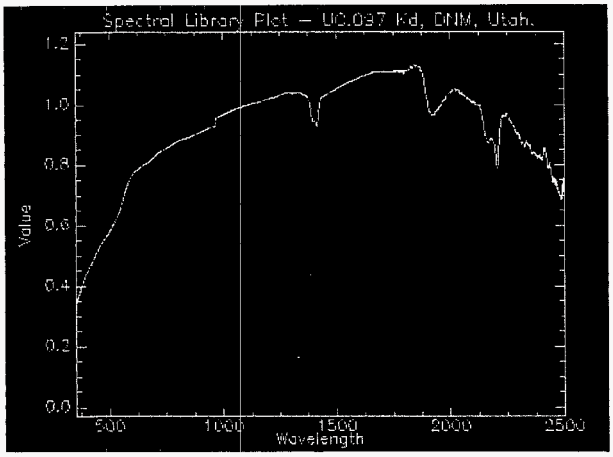

Figure 8. "Whole Rock" spectrum UC.097 (White sandstone from a dipslope of the Cretaceous, Dakota Formation characterized by hoodoo weathering and a good kaolinite doublet in the SWIR.

Pixels passing the similarity test are then shown as white pixels on an output image. Figure 9 is a map of occurrences of AVIRIS pixels similar to the sample reference spectrum in Figure 8. The results are more precise than those of Hyperion, presumably due to its higher signal-to-noise ratio and smaller pixel size. Future hyperspectral satellites should attempt to simulate AVIRIS to the extent possible. Spatial resolutions finer than 15 meters would be useful for energy exploration.

As a further guarantee of defense/intelligence security, all 15 meter hyperspectral imagery purchased from commercial suppliers by the U.S. government should be in the care of the USGS. This will provide U.S. government key control of the data stream and allow selective black outs of sensitive areas while meeting the genuine need for affordable, high-quality satellite imagery for energy exploration and U.S. economic-environmental security.

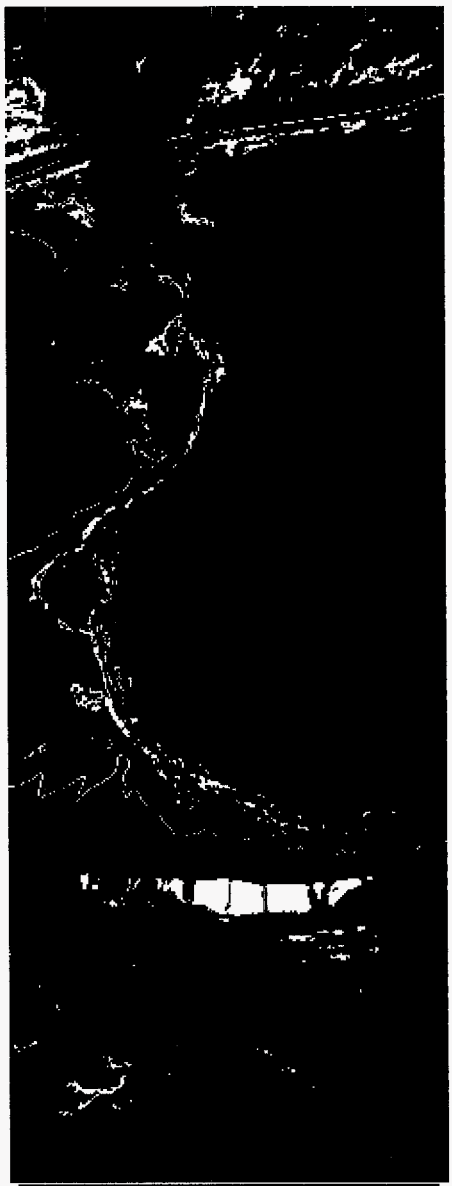

Figure 9. Atmospherically corrected AVIRIS spectral angle map (SAM) of the same area showing pixels similar to the whole rock spectrum shown in Figure 8.

Conclusion - AmeriSat

The 1:24,000 scale United States geological survey needs to be completed in order to ensure the economic security of the United States in the 21st century. A new series of land remote sensing satellites meeting the following specifications must be constructed, launched *and used* to meet this need. We refer to this constellation of U.S. geological survey satellites as AmeriSat. Most of the satellite technology necessary to complete the 1:24,000 U.S. geological survey already exists. Satellite systems capable of accelerating the survey to completion in less than two decades must meet the following requirements:

1. Continuity with the Landsat series (ALI with stereo and a thermal band).
2. 15 meter hyperspectral coverage of the 0.4 to 2.5 micron wavelength region.
3. A minimum swath width of 30 km to minimize seams within quadrangles.
4. Free automated data delivery via FTP, or at cost of media (relative to the cost of the satellites).
5. Off-nadir pointing capability for emergency response.
6. A constellation of four identical satellites, with a fifth on orbit spare satellite in constant reserve. There are 55,000 quadrangles to cover and the earth is frequently cloudy. This constellation and its ground systems will be approximately 70 percent of the cost of the AmeriSat system.

7. A partnership with academia, industry and the public from the beginning. The USGS does not have enough people to get the job done. This partnership should be budgeted at 10% as well.
8. USGS quality control of all geological quadrangle maps to guarantee consistency and availability in GeoTiff (loss-less raster) and ArcView shape files (as separations similar to those in USGS DLGs). This will also probably cost around 10% of the total project.

A summary of AmeriSat's general specifications is listed in Table 2.

Cost

We estimate that the project will cost approximately $250M/year for the next 20 years. Satellite hardware and ground station construction costs will probably consume 70% of these funds during years 1–4 and again during years 10–14, assuming a 6–8 year lifespan for each satellite. Funding will be focused on applications during non-construction years.

Table 2. Summary of AmeriSat specifications.

Features	Specifications
Spectral Range	0.4-2.5 microns
Panchromatic Bands	1/1
Visible Bands	6/35
Near Infrared Bands	3/35
Short Wave Infrared	1/172
Middle Infrared Bands	1/1
Thermal Band	1
Spatial Resolution	30 m/15 m
Swath Width	185/30 km
Spectral Coverage	Both
Pan Band Resolution	10 m
Stereo	yes
Number of Bands	10 and 220
Number of Spacecraft	4-6
Temporal Resolution	4-8 days
Emergency Pointing Capability	(similar to Hyperion on EO-1)

References

Bailey, G.B., and Anderson, P., 1982, Applications of LANDSAT imagery to problems of petroleum exploration in Quaidam Basin, China, American Association of Petroleum Geologists Bulletin, v. 66, no. 9, p. 1348-1354.

Bailey, G.B., Dwyer, J.L., Francica, J.R., and Feng, M.S., 1982, Extraction of geologic information from Landsat MSS and thematic mapper simulator data for the Uinta and Piceance Basins, Utah and Colorado, in Proceedings of International Symposium on Remote Sensing of Environment, Second Thematic Conference: "Remote Sensing for Exploration Geology", Ft. Worth, Texas, December 6-10, 1982, p. 43-70.

Bailey, G.B., Dwyer, J.L., Francica, J.R., and Feng, M.S., 1984, Update on the use of remote sensing in oil and gas exploration, in Symposium Unconventional Methods in Exploration for Petroleum and Natural Gas, 3rd, Dallas, Texas, 1982, Proceedings: Dallas, Southern Methodist University press, p.231-253.

Bailey, K., Beck, R.A., Frohn, R., Krute, R., Pleva, D., Plumer, D., Price, M., Ramos, C., South, R., and 2001, *Native American Remote Sensing Distance Education Prototype (NARSDEP),* Photogrammetric Engineering and Remote Sensing, v. 67, no. 2, p. 193-198.

Beck, R.A., Burbank, D.W., Sercombe, W.J., Riley, G. W., Barndt, J.K., Berry, J. R., Afzal, J., Khan, A.M., Jurgen, H., Metje, J., Cheema, A., Shafique, N.A., Lawrence, R. D., and Khan, M. A., 1995, *Stratigraphic evidence for an early collision between northwest India and Asia*, Nature, v. 373, p.55-58.

Clark, R.N., and Roush, T.L., 1984, Reflectance spectroscopy: Quantitative analysis techniques for remote sensing applications, J. Geophys. Res., 89, 6329-6340.

Clark, R.N., G.A. Swayze, A. Gallagher, T.V.V. King, and W.M. Calvin, 1993, The U. S. Geological Survey, Digital Spectral Library: Version 1: 0.2 to 3.0 m, U.S. Geological Survey, Open File Report 93-592, 1326 pages.

Clark, R.N. and Swayze, G.A., 1995, Mapping Minerals, Amorphous Materials, Environmental Materials, Vegetation, Water, Ice and Snow, and Other Materials: The USGS Tricorder Algorithm. Summaries of the Fifth Annual JPL Airborne Earth Science Workshop, January 23- 26, R.O. Green, Ed., JPL Publication 95-1, p. 39-40.

Clark, R.N., 1999, Spectroscopy of Rock and Minerals, and Principles of Spectroscopy, http://speclab.cr.usgs.gov/PAPERS.refl-mrs/refl4.html

Dwyer, J.L., Kruse, F.A., and Lefkoff, A.B., 1995, Effects of Empirical Versus Model Based Reflectance Calibration on Automated Analysis of Imaging Spectrometer Data: A Case Study from the Drum Mountains, Utah, Photogrammetric Engineering and Remote Sensing, v. 61, no. 10, p. 1247-1254.

Gaffey, S.J., L.A. McFadden, D. Nash, and C.M. Pieters, 1993, Ultraviolet, Visible, and Near-infrared Reflectance Spectroscopy: Laboratory spectra of Geologic Materials, in Remote Geochemical Analysis: Elemental and Mineralogical Composition (C. M. Pieters, and P.A.J. Englert, eds.), Cambridge University Press, Cambridge, 43-78.

Salisbury, J.W., 1993, Mid-infrared spectroscopy: Laboratory data, in Remote Geochemical Analysis: Elemental and Mineralogical Composition (C. M. Pieters, and P.A.J. Englert, eds.), Cambridge University Press, Cambridge, 79-98.

Swayze, G.A., Clark, R.N., Goetz, A.F.H., Livo, K.E., and Sutley, S.S., 2000, AVIRIS 1998 Low Altitude Versus High Altitude Comparison Over Cuprite, Nevada, http://speclab.cr.usgs.gov/cuprite98-low/cuplow+high.html

Assessment of Soil Erosion Potential in Semi-Arid Soils Using Hyperspectral Technology

E. Ben-Dor,[1,4] N. Goldshalager,[2] O. Braun,[3] B. Kindel,[4] A.F.H. Goetz,[4] D. Bonfil,[5] M. Agassi,[2] Y. Binyaminy,[2] and A. Karnieli[6]

[1]Department of Geography and Human Environment, Tel-Aviv University, Israel
[2]Soil Erosion Research Station, Soil Conservation and Drainage Division, Ministry of Agriculture, Israel
[3]Bar-Kal Systems Engineering, Ltd., Netania, Israel
[4]Center for the Study of Earth from Space, Cooperative Institute for Research in Environment Sciences (CIRES), University of Colorado, Boulder, Colorado
[5]Gilat Experimental Station, Ministry of Agriculture, Israel
[6]The Remote Sensing Laboratory, Jacob Blaustein Institute for Desert Research, Ben Gurion University of the Negev, Israel

INTRODUCTION

Soil erosion by water runoff is a matter of great concern in both bare and agricultural lands. This process may lead to significant effects, such as water lost to the soil profile, decline in soil fertility and productivity, and increased peak stream flow, as well as associated floods. The main cause of the runoff from rain and overhead irrigation water is the structural crust that develops over bare soils during rainfall or irrigation events that significantly reduces the soils' infiltration rate. The hydraulic conductivity of this crust is a few orders of magnitude lower than that of the underlying soil (e.g., McIntyre, 1958; Morin and Benyamini, 1977). Whenever the hydraulic conductivity of the crust is lower than the rainfall intensity, ponding, runoff and soil erosion will occur.

Most of the available methods for assessing the physical crust status use disturbed soil samples that do not represent exact field conditions (Keren and Singer, 1989, 1991) or use simulation techniques that cannot mirror exact field conditions (Agassi and Bradford, 1999). Consequently, mapping and predicting soil structural crust processes are of great interest and importance to soil scientists and farmers. Apparently, crust potential mapping is not a straightforward problem, and to the best of our knowledge, this technique has never been conducted.

Recent studies by Goldshalager et al. (2001, 2002) and Ben-Dor et al. (2003), showed significant relationship existed between selected wavelengths readings and infiltration rates, when measured under controlled laboratory conditions. Further, they were able to create a spectral library that contains spectra of three soils from Israel, in varying rain energies and crust position, and to show that a different correlation existed for each soil.

Because significant spectral changes occur within the soil surface as a result of raindrop impact (see Goldshalager et al., 2002), it is assumed that the hyperspectral technology will enable capturing of spatial variation within a rain-affected field and will provide a real-time spatial overview of soil crust related properties (such as soil erosion and infiltration). The purpose of this study is to examine the feasibility of hyperspectral technology together with careful

laboratory and field measurements in order to identify soil properties that are related to the structural crust formation and status over agricultural soils in Israel.

MATERIALS AND METHODS

The area selected for this study is located in the Negev area of southern Israel in the fields of the Experimental Farm Station of Gilat. The soils in this area are Loamy Loess and defined as Loess by the local Israeli definition system (Dan and Raz, 1970) and calcic haploxeralf according to the USDA definition (Soil Survey Staff, 1975). The mechanical composition is 28% clay, 47% silt and 25% sand and the mineralogy of the soil, estimated by XRD is: ~14% montmorillonite, ~50% kaolinite, ~27% illite and ~17% calcite. The area is relatively dry, having annual precipitation of about 200 mm concentrated mostly during December through April.

The Flight Campaign

The airborne sensor selected for this study is the Airborne Image Spectrometer for Applications (AISA) (Mäkisara et al., 1993). The AISA is a programmed computable push broom airborne imaging spectrometer with wavelength range between 400 and 900 nm. The size of the CCD detector array is 384 by 286 pixels and the spectral bandwidth is >1.5 nm (max. 186 channels) which can be summed up to 9.6 nm. The swath width is 384 pixels and the IFOV is 1 mrad, enabling a pixel size of 1 meter from 1000 meter altitude where the FOV is 22°. The integration (exposure) time is 4 ms, and the pixel data is digitized to 12 bits. On March 24, 2001, the AISA sensor was mounted onboard a twin engine piper Aztec aircraft and flown over the study area in altitude of 3000 meter (providing about 3 meter pixel size and 1.2 km swath) with 30 spectral bands (421–888 nm) characterized by Full Width Half Max (FWHM) ranging from 1.55 to 1.71 nm. The signal-to-noise ratio of the sensor over a 50% albedo target provides reasonable values ranging around a value of 90 (maximum 125 minimum 20). The raw data was radiometerically converted into radiance using laboratory calibration file provided by the SpecIm© company which were collected prior to the flight. The radiance data were corrected into reflectance units using an ACORN code (Atmospheric CoRrection Now, ACORN, 2001) polished by ground reflectance spectra of 4 soil samples that were taken during the overpass on the ground.

Laboratory Study

Rain Simulator

Soils were collected from a nearby field, brought to the laboratory, air-dried and then, passed through a 4-mm sieve. Two experiments (several months apart) using two batches of soils were employed to determine the relationship between the spectroscopy and the infiltration rate of the soil in the laboratory. The soils in each experiment were identically packed into 30 x 50-cm perforated soil boxes, 4 cm deep, over a layer of 6 cm coarse sand. Four runs (two for each experiment) were employed. For each run, the boxes were placed on a soil box carousel, 5 boxes per run, at a 5% slope, and were subjected to a simulated rainstorm, using distilled water (Morin et al., 1967). In each experiment, at first run, the simulated rainstorm provided a fog type rain (no energy), having intensity similar to the infiltration rate of the soil. The storm lasted until the measured rate of percolation (in this case also infiltration) reached that of the measured simulated rainstorm intensity. Then the rainfall was stopped and the soil boxes were left to rest until drainage ceased from all the boxes. One soil box was randomly taken out and photographed. At this stage the rainfall energy was changed to ~22.3 joule mm^{-1} m^{-2}. The carousel was rotated again with four of the remaining soil boxes, which were subjected to

rainstorm intensity approximately similar to the initial infiltration rates of the soil. At first the storm lasted until ~3.5 mm of rainfall had been applied (equal to ~70–80 joule) during which time the infiltration rate was continuously measured. Then one box was randomly removed and photographed. This procedure was repeated several times until ~89 mm of rainfall was accumulated (see Table 1 for more details). After the rainstorm was stopped, the soil boxes were oven-dried for 48 h. at 35°C and then for a week at room temperature. In Table 1 also given are the equivalent infiltration rate measured for each rainstorm event, the accumulated rain amount and its corresponding energy are presented. Fifteen to twenty soil samples were taken from each box for spectral reflectance measurements in the laboratory without disturbing the soil crust. These measurements were carried out, using ASD spectrometer with a portable light source that measured a soil sample under a constant halogen illumination and reflectance geometry conditions across the VIS-NIR-SWIR region (0.4–2.4 μm). The reflectance of the soil samples was measured against Halon, and the final spectrum of each measurement was presented relative to this reference. An average spectrum for every rain treatment was calculated, using the samples taken from each soil box. The spectra were stored and later processed to analyze the spectral-infiltration relationship. In several locations around the study areas, samples were collected from the surface (the upper 1 cm), covering an area of about 5 m^2, brought to the laboratory and analyzed for $CaCO_3$.

Table 1: Infiltration rate and rain storm energy for each treatment used in the crust simulator experiment.

Accumulated Rain Energy (Joule)	Infiltration Rate (mm/Joule)	Rain Accumulation (mm)
0	44	0
0	48	0
71	32	3.2
80	37	3.6
109	28.5	4.9
145	24	6.5
160	35	7.1
216	21	9.7
280	30	12.5
290	17	13
400	25	17.8
506	11.5	22.7
560	17.5	25
613	11.5	27.5
800	12	35.6
1012	7	45.4
1270	7	57
1842	3.5	82.6
1985	4.6	89

Field Measurements

During the overpass, soil samples were collected around the area from several targets to enable rectifying the radiometric measurements into relative reflectance. Four controlling soil plots, within the agricultural areas field of Gilat farm, were selected to study the crust spectral response

from the air. The plots were characterized by a noticeable crust that formed during rainstorm events that lasted two months (100 mm). Each plot was divided into two subplots: 1) the "non crust" plot, composed of bare soil, with the thin crust broken by a gentle plowing of the upper soil layer 24 hours before the flight, and 2) "crusted" plot, composed of crust soils (formed by natural rain) with noticeable crust occurrences. The last rain event in the area (affecting the "crusted" plots) was reported in March 10, 2001 (2 mm) suggesting that the soil maintained a basic hygroscopic moisture capacity which was measured to be around 4%.

Results and Discussion

Figure 1 provides a gray scale subset image that sampled from the entire flight line image and covers the study area. Also overlain in this image are selected controlled plots and the exact locations of the soil sampling for the $CaCO_3$ determination. The study area is rather flat, characterized with vegetation (beans, barely and wheat) side by side to the bare soil plots (with and without organic residual). The soil plots are marked on the image (1–4) to draw the attention for further discussion. From looking on the image it is noticeable, that albedo variation occurred within these selected plots (1-4) as well as within other areas along the image. One of the basic factors that control soil brightness in an arid environment is the $CaCO_3$ content. Basically, this component can be assessed from hyperspectral technology, simply by using the strong absorption feature at 2330 nm (Gaffey, 1986). However, as the AISA sensor does not cover the SWIR region, this information cannot be extracted from the current data base and hence cannot confirm or reject the above brightness assumption. To check this, we used the 18 soil samples (randomly sampled) and their $CaCO_3$ content measured in the laboratory. Plotting the $CaCO_3$ content versus the albedo parameter of each ground target (calculated from the area under the spectral curve between 489 to 888 nm) shows no correlation between the two (Figure 2). This suggests that the albedo tone variation may have emerged from another source and probably from the physical crust formation.

Figure 3 presents a ground overview of one of the field plot (Plot-3 in Figure 1) after breaking the soil crust with a discus (non-crusted) at 24 hours before the flight, whereas some small-crusted areas can be visible at the edge of this plot. The photo also shows a close Nadir view from 80 cm. It is evident that by naked eyes, a soil color changes from bright to dark tones is visible within the soils based on their crusting position.

Extracting the spectra of each plot (calculated from an average of about 40 pixels) showed that the spectral base line (and hence the soil albedo) is higher in the crusted soils than in the non-crusted soils. Figure 4 provided the spectral reflectance of the selected plots, with and without the crust layer. The crust plots are higher in about 3-6% (reflectance units) or about 30% (in relative values) than the non crusted plots.

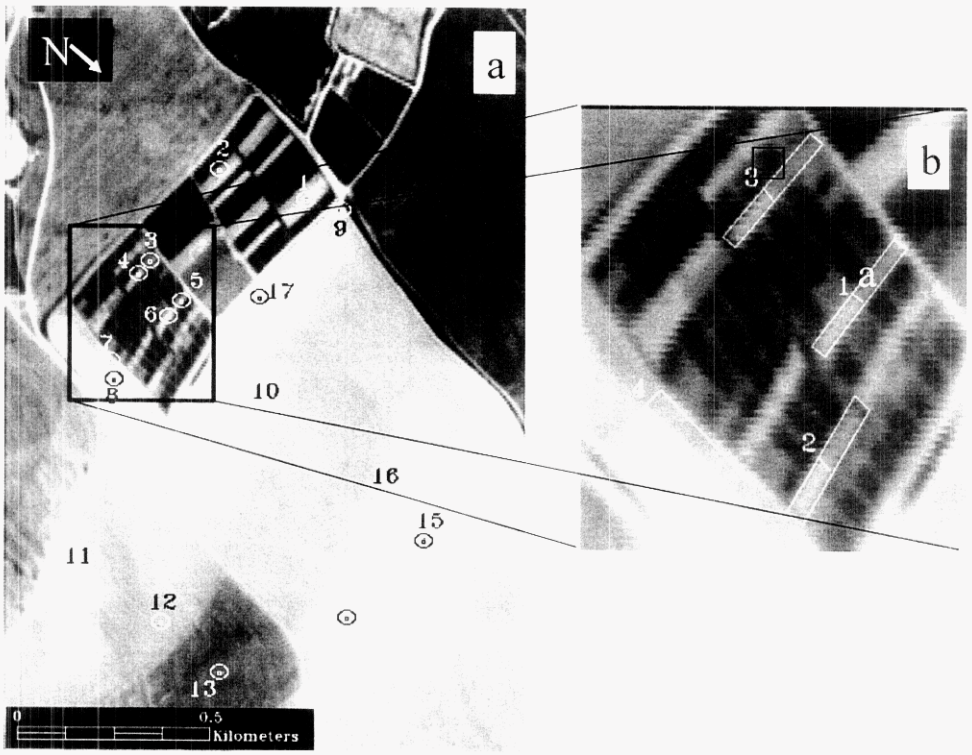

Figure 1: The study area on a grayscale image (band 14, 576 nm): (a) the position of the controlled plots (crusted and non-crusted) and (b) the ground soil sample (for $CaCO_3$ content analysis) overlain.

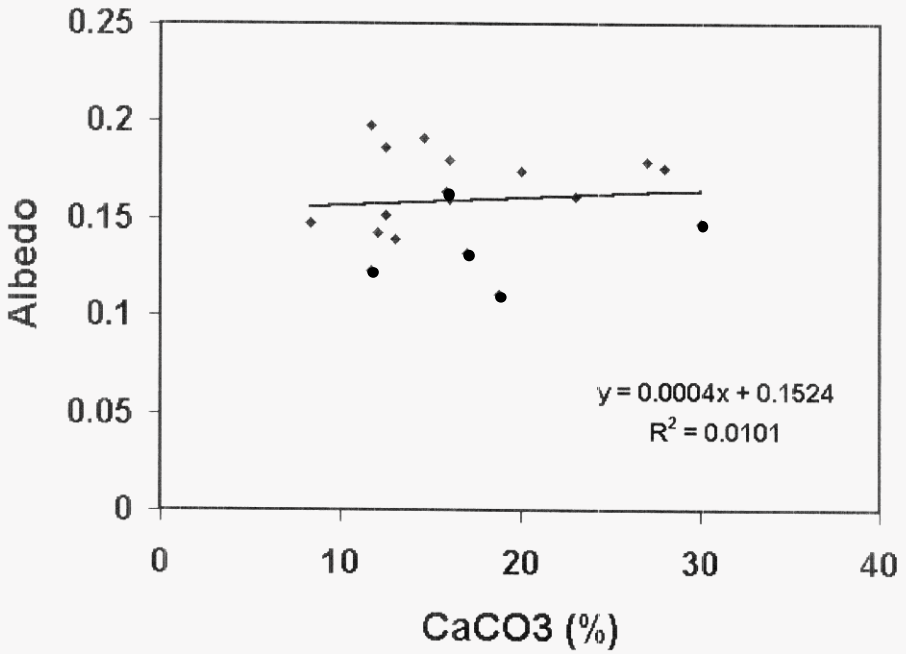

Figure 2: The relationship between the $CaCO_3$ content versus the albedo (the area under the spectral curve between 489 to 888 nm) of the samples shown in Figure 3.

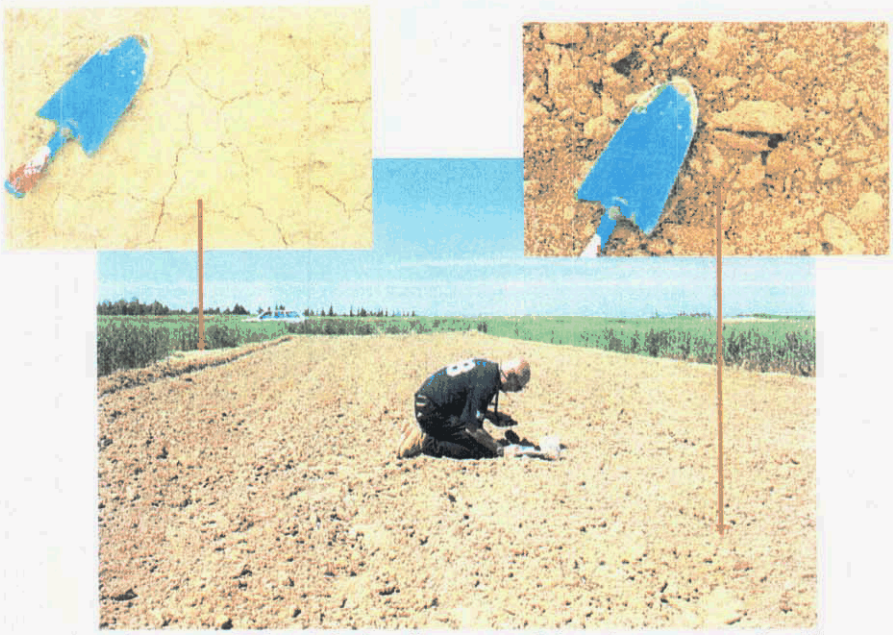

Figure 3: An overview image of Plot 3 in its discus position (non-crusted). Also provided are two enlargement images showing the crusted (a) and non-crusted (b) soils from a distance of 80 cm.

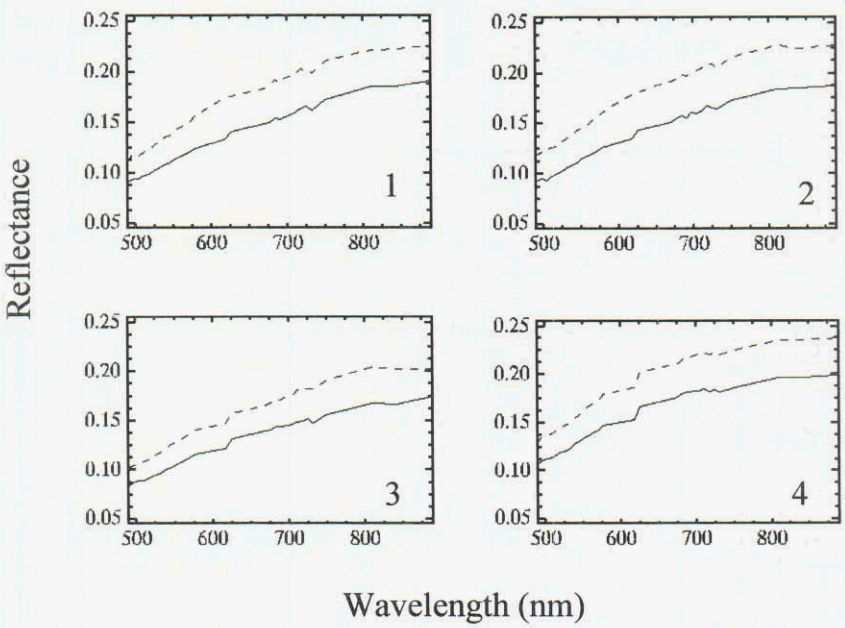

Figure 4: The reflectance spectra of the controlled plots in both crusted and non-crusted position. Dot lines represent the crusted soil (light tones in Figure 1) and solid line the non-crusted soil (dark tones in Figure 1).

Figure 5 provides an overview of the soil in the laboratory tray after applying rainstorm at energies of 613 and 1842 joule/m^2 (taken from the first experiment). Also presented is the bulk soil with no rain energy (non-crusted soil). It is well observed from this figure that albedo changes occur in the direction just as observed in the field: in the high raindrop energy—the soil

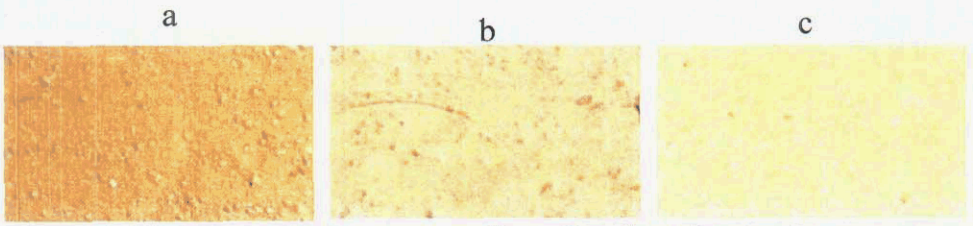

Figure 5: Three images showing the crust position after the rain simulator treatments in three different rain energies: (a) 0, (b) 613 joule m^2, and (c)1842 joule m^2.

are brighter, whereas in the low (or no) raindrop energy—the soils are darker. The spectra of all treatments are given in Figure 6 (a,b). As well seen, a noticeable spectral sequence occurs, going from a low raindrop energy (low crusted) to a high raindrop energy (highly crusted) rain. These values are equivalent to high and low infiltration rates respectively, as measured simultaneously during the rainstorm event and are given in Table 1. The overall reflectance changes in the laboratory were found to be similar to what were found in the image: 3% in the lower energies and 8% in the highest energies levels. As seen, the shape of the spectra is constant with rain energy (no new spectral features or slope changes occurs when going from one rain energy to another) where the only significant spectral change is the reflectance offset. It is interesting to note that Goldshalager et al., 2001 have found that in the SWIR region, not only albedo changes are noticeable, but also changes in the spectral features positions and intensity occurs. This is based mainly on the specific spectral information of OH in clay minerals across the SWIR region, which is not active in the current AISA VIS-NIR spectral region.

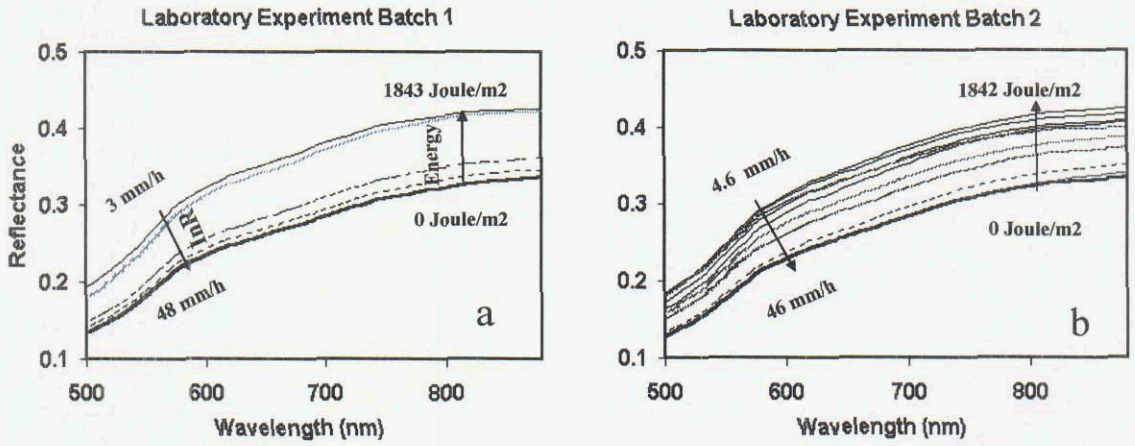

Figure 6: The laboratory spectra of the crusted soil after applying different rain energies to the soils (a represent the first experiment and b represent the second experiment taken in few months apart).

Although the VIS region is less informative than the SWIR region, the albedo changes observed in the laboratory treatments suggest that quantitative relationship between spectral parameters and the crusting phenomenon may be possible. To quanitively assess this relationship, we calculated the Normalized Spectral Area (NSA), which is the area under the ratio curve (generated by using a crusted soil (test) spectrum against standard non crusted soil spectrum

(reference)). The ratio spectra are given Figure 7(a,b) and show that the ratio spectra increased as the rain energy increased and the infiltration rate decreased. Plotting the area under the ratio curve (NSA) against the infiltration rates is given in Figure 8. A significant relationship between the two parameters (infiltration rate versus the NSA) was obtained (r2= 0.83). In order to apply the NSA model to the field data, the reflectance image data were processed as the laboratory spectral data. In this regard, we selected a polygon from a selected "non-crusted" sub plot of plot-3 (see Figure 1) and used it as a reference in which every pixel in question may be calculated for its NSA. In order to apply the calibration equation obtained in the laboratory for the entire area, all non-soil pixels were masked out and then the model was applied on a (soil) pixel by pixel basis. The result is an image given in Figure 9 with a color ramp representing the "Infiltration Rate" (InR) values. In the processed image, several areas holding high and low InR values can be seen. The low InR area (marked as A on the image) is a plowed (dry) field, which exhibits NSA values within the detection limit of the InR calibration curve. Based on the NSA values of this soil, it is assumed that the current plot is holding a good (non) crust condition in which the soil infiltration potential is high and the erosion risk is minimal. The high InR areas (marked as B, C and D) are holding InR values that are outside the calibration range. Area B represents a dirt road enriched with high $CaCO_3$ content (27%) lime which is relatively higher than the average $CaCO_3$ content of the entire population that stands on 13.8% (SD 5%). Area C also consists of high $CaCO_3$ content (30%) and thus are not suspected to be crusted under the current analysis where area D consists of $CaCO_3$ content of 14.6%; and hence represents a significant crusted area. Another factor inherent in the calibration results is the soil moisture status (wet or dry) that also can change the soil color tones. This parameter can as well as the $CaCO_3$ features can be masked out by using the SWIR region, and hence by AVIRIS, but not with the current AISA sensor. More study in this direction has to be applied to make the crust mapping more accurate and totally independent of field information. Using the AVIRIS sensor in this direction, may be a step forward to achieve this aim. The spectral information suggests that there is a significant potential to do so under more complex soils systems.

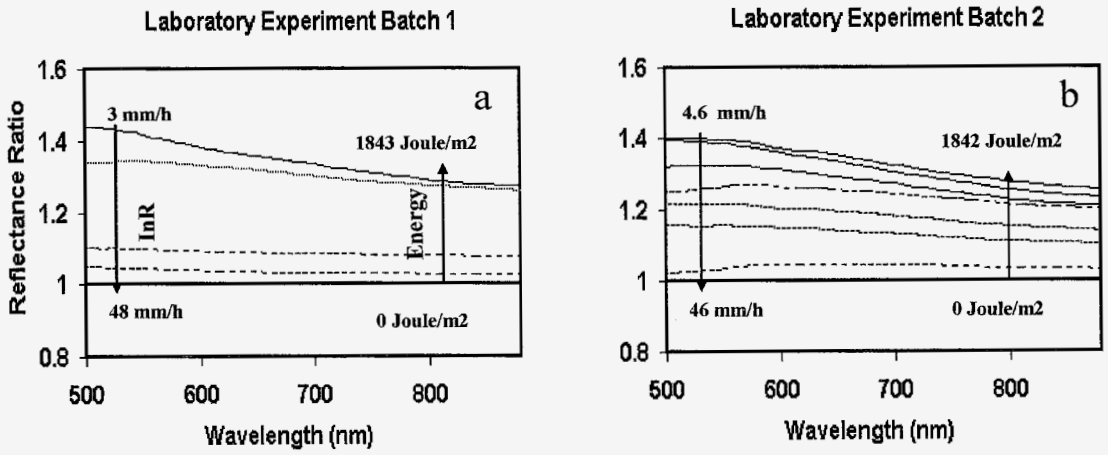

Figure 7: The ratio spectra of the laboratory treatment shown in Figure 8. Each spectrum composed of the reflectance at every rain energy treatment against the reflectance at 0 energy level.

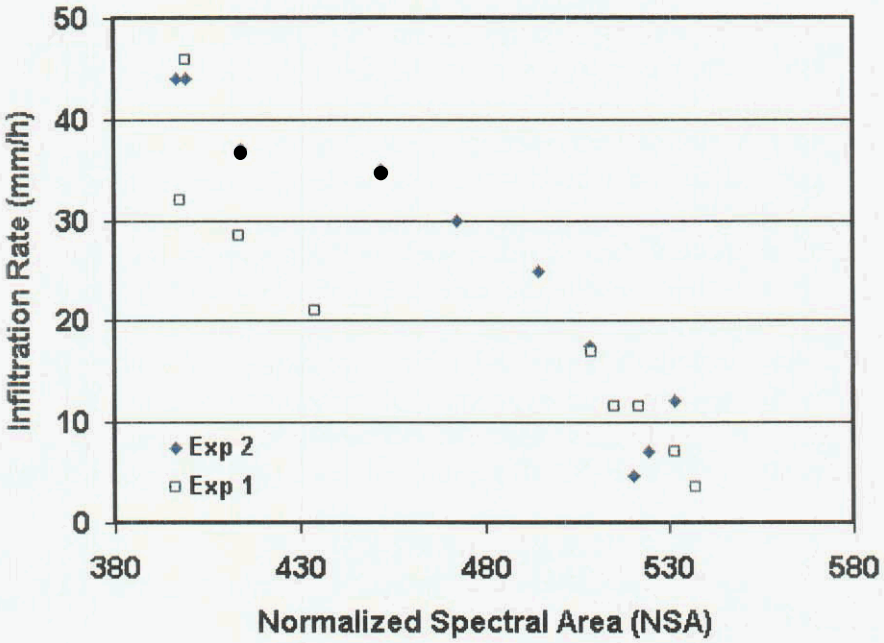

Figure 8: The relationship between the infiltration rate (InR) and the Normalized Spectral Area (NSA) using the laboratory information obtained by the two experiments.

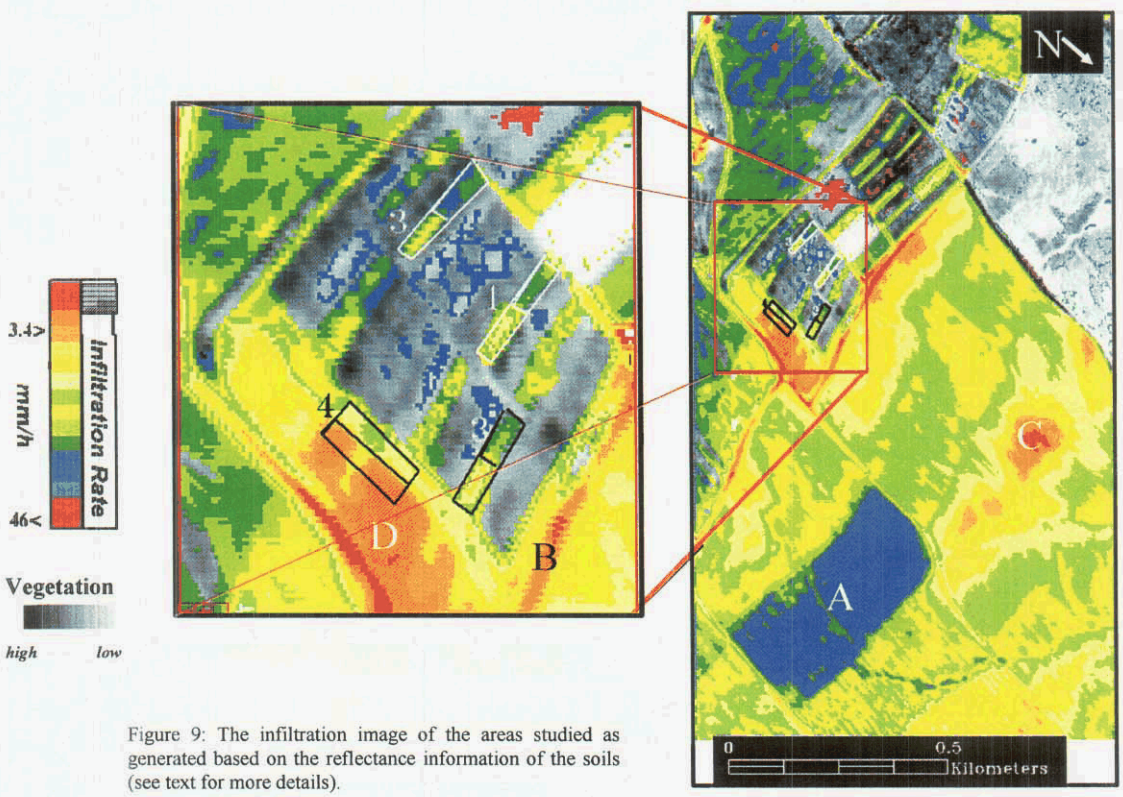

Figure 9: The infiltration image of the areas studied as generated based on the reflectance information of the soils (see text for more details).

SUMMARY AND CONCLUSIONS

The main conclusion of this study is that reflectance properties of Loess crusted soils have a systematic relationship with the crust status. In the soil examined, the albedo parameters across the entire VIS-NIR region hold a significant correlation with raindrop energy, and particularly with infiltration rate. A normalized spectral curve, using a non-crusted soil spectrum as a reference, was suggested to use whereas the area under the ratio curve, suggested to be the parameter for the soil albedo. Doing so enables the utilization of the laboratory spectral relationship with other spectral data sources, such as the hyperspectral sensors introduces. The spectral variation in the field within the selected plots vary within the confident range the laboratory experiment provided. The soils' pixel-by-pixel calculation of the InR shows a reasonable picture for the selected area and their surroundings. We hope that more ideas and thoughts on how to further apply the hyperspectral technology further in this direction will be presented by more other investigators. The AVIRIS sensor in this regard may play an important role as it covers the entire VIS-NIR-SWIR region and has a relatively good signal to noise ratio.

ACKNOWLEDGMENT

This study was conducted under a CIRES fellowship foundation program at Center for the Study of Earth from Space (CSES) University of Colorado at Boulder.

REFERENCES

ACORN, 2001. Atmospheric Correction Now, Analytical Imaging and Geophysics LLC Version 3.12.

Agassi, M., and J. M. Bradford, 1999. "Methodologies for interrill, soil erosion studies." *Soil & Tillage Research* 49: 277–287.

Ben-Dor, E., N. Goldshalager, M. Benyamini, and D. G. Blumberg, 2003. The Spectral Reflectance properties of Soil's structural crust in the SWIR spectral region (1.2–2.5μm), *Soil Science Society of American Journal* 67:289–299.

Dan, Y., and Z. Raz, 1970. *Soil Association Map of Israel.* Volcani Institute for Agriculture Research, Israel (in Hebrew).

Gaffey, S. Y., 1986. "Spectral reflectance of carbonate minerals in the visible and in near infrared (0.35–2.55 μm): calcite, aragonite and dolomite." *American Minerals* 71: 151–162.

Goldshalager, N., E. Ben-Dor, Y. Benyamini, D. Blumberg, and M. Agassi, 2001. "The spectral reflectance of soil's structural crust in the SWIR region 1.2–2.5 μm." *Terra Nova* 7:23–55.

Goldshalager N., E. Ben-Dor, Y. Benyamini, M. Agassi, and D. Blumberg, 2002. Soil Crusting and Infiltration Processes as Monitored by Soil Reflectance Spectroscopy in the SWIR region, *Remote Sensing of Environment Journal (in press).*

Keren, R., and M. J. Singer, 1989. "Effects of low electrolyte concentration on hydraulic conductivity of clay-sand-hydroxypolymer systems," *Soil Science Society of America Journal* 53: 349–355.

Keren, R., and M. J. Singer, 1991. "Hydroxy-aluminum's effects on permeability of clay-sand mixtures," *Soil Science Society of America Journal* 55: 61–65.

Mäkisara, K., M. Meinander, M. Rantasuo, J. Okkonen, M. Aikio, K. Sipola, P. Pylkkö, and B. Braam, 1993. "Airborne imaging spectrometer for applications (AISA)," in *International Geosciences and Remote Sensing Symposium Digest*, (Tokyo, Japan), pp. 479–481.

McIntyre, D. S., 1958. "Permeability measurement of soil crusts formed by raindrop impact," *Soil Science* 85: 185–189.

Morin, J., and Y. Benyamini, 1977. "Rainfall infiltration into bare soil," *Water Resour. Res.* 13(13): 813–817.

Morin, J., D. Goldberg, and I. Singer, 1967. "Rainfall simulator with rotating disk," *Trans American Society of Agriculture Engineering* 10: 74–79.

Soil Survey Staff, 1975. *Soil Taxonomy: A Basic System of Soil Classification for Making and Interpreting Soil Surveys*, Handbook, U.S. Dept. Agriculture, 436.

ASSESSMENT OF HYPERION FOR CHARACTERIZING MANGROVE COMMUNITIES

Martina Demuro and Laurie Chisholm[1]

1 Introduction

Mapping the distribution of species and vegetation types in coastal wetlands has become important because of the need for wetland inventories and their biodiversity (Finlayson *et al.,* 1999; Phinn and Finlayson, 1999). Vegetation is also regarded as a bio-indicator of site conditions and it is therefore important to understand changes in its distribution and the process acting upon it (Küchler, 1988; Blasco *et al.*, 1996; Muller, 1997; Klemas, 2001). Mapping methods need to be efficient and cost effective (Mumby *et al.*, 1999) with satellite remote sensing systems having been used extensively for mapping the distribution of vegetation types in coastal wetlands and other environments (Gross *et al.*, 1989; Phinn *et al.*, 1999). The detection of vegetation types will depend directly on the sampling unit used by the sensor (pixel) and the area imaged. The signal recorded for each pixel is composed of a mixture of components that characterize each community, including the species, canopy openness, height and substrate. Broad-band multispectral imagery is usually analyzed using methods that classify whole pixels using limited spectral information (Vane and Goetz, 1993), which do not account for the problem of mixed pixels. The discrimination of vegetation types using satellite-borne sensors is usually based on the structure (height, openness) and broad vegetation categories (such as woody, perennial, evergreen) (Lewis, 1999; Holmgren and Thuresson, 1998). A common criticism of satellite remote sensing is its inability to define features of interest that are related to ecological processes because of the crude spectral and spatial dimensions of the images (Rougharden *et al.,* 1991; Holmgren and Thuresson, 1998). Advantages of higher spectral resolution imagery include the acquisition of detailed spectral information of the features on the ground (Ustin *et al.,* 1991) and the possibility of image analysis procedures that aim to detect target spectra at a sub-pixel level (Curran, 1994; Clark, 1999; Mustard and Sunshine, 1999). Airborne hyperspectral data have been used to detect minerals and plant biochemicals that have distinct absorption features (Curran, 1994; Serrano *et al.,* 2002) and species distribution (Dehaan and Taylor, 2002; Parker Williams and Hunt Jr., 2002). EO-1 Hyperion is the first satellite-borne hyperspectral sensor to orbit the Earth, capable of recording spectral information superior to previous satellite sensors. Hyperion differs from previous satellite sensors in that it records radiance in many narrow contiguous bands spanning the visible to the near infrared portion of the spectrum. Hyperion has a spatial resolution of 30 meters and records radiance in 220 bands spanning from the blue at 450 nm to the middle infrared at 2500 nm. Each band has a width of approximately 10 nm.

1.1 Objectives

This study aims to assess Hyperion for its ability to discriminate vegetation types based on species composition. The study focuses on the vegetation of coastal wetlands, namely temperate mangrove, saltmarsh and casuarinas forests. To the authors' knowledge there are currently no studies that have tried Hyperion imagery for mapping mangrove species diversity and saltmarsh vegetation as yet.

2 Study Site

The study was conducted in the Minnamurra River estuary, New South Wales. The study area is located approximately between S 34□36' and 34□37' and between E 150□50' and E 150□51'. The estuary sub-catchment area where this study is based is approximately 10 km^2 (Figure 2.1). The estuary is in an advanced stage of infilling and the river follows a meandering channel characterized by three bends flowing around three sand deposits (Carne, 1991). The Minnamurra River estuary has been listed as a nationally important wetland in Australia because "it is a good example of a wetland type occurring within a biogeographic region in Australia" and because "the wetland supports native plant or animal taxa or communities which are considered endangered or vulnerable at the national level" (Environment Australia 2001).

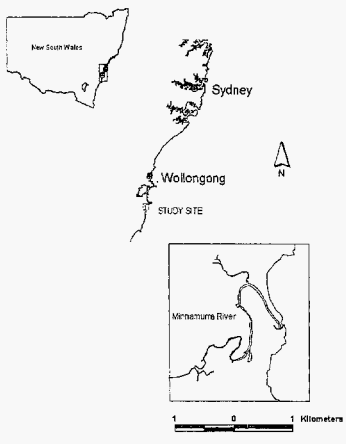

Figure 2.1. Study site location in NSW, Australia.

[1] School of Geosciences, University of Wollongong (laurie_chisholm@uow.edu.au)

2.1 Vegetation

The estuarine vegetation of the Minnamurra estuary has been described in a number of studies (Carne, 1991; Chafer, 1997). The vegetation in the muddy intertidal zone is composed of mangroves and saltmarsh (Figure 2.2). A swamp-oak forest composed of casuarina trees extends to the landward side of the mangrove and saltmarsh vegetation, outside the tidal range (Chafer, 1997). A littoral forest is found further inland, which has a patchy distribution. The widths of the mangrove, saltmarsh and swamp oak forest areas are usually smaller than 500 meters. Other cover types surrounding the estuary include: to the east, an extensive residential area, to the north a waste disposal depot and some artificial water bodies, and to the west, at higher elevations, an area composed of grasslands.

Two mangrove communities have been identified in the temperate mangroves of Australia (Saenger *et al.*, 1977). These are the *A. marina* low closed-forest and *A. marina* low woodland. The *A. marina* low closed-forest is a monospecific stand of *A. marina* trees that have a foliage cover of over 70 % and a height of less than 10 m. The *A. marina* woodland is composed of both *A. marina* trees and *A. corniculatum* shrubs. The term woodland corresponds to areas where the projective foliage cover of the upper stratum (*A. marina*) is very low (10-30 %) and the trees have a height of less than 10 m. A mid-stratum of both the shrub *A. corniculatum* and a 'dwarf' variation of *A. marina* become very extensive in this community. Similar to other temperate mangroves of New South Wales, the distribution of each community in the Minnamurra estuary is characterized by the formation of low closed-forests in the low intertidal zone, especially at the mouth of the estuary, while the low woodland develops to the landward side of the monospecific *Avicennia marina* forests (Carne, 1991).

Saltmarsh communities develop to the landward side of the mangroves, with the succulent *Sarcocornia quinqueflora* dominant in the low marsh area, while the grass *Sporobolus virginicus* and the rush *Juncus kraussii* dominate in the middle marsh areas. The reed *Phragmites australis* becomes dominant in less saline areas of the saltmarsh. Swamp-oak forests develop to the landward side of the mangrove and saltmarsh vegetation exclusively composed of the *Casuarina* spp. trees that grow extensively at higher elevations in Minnamurra.

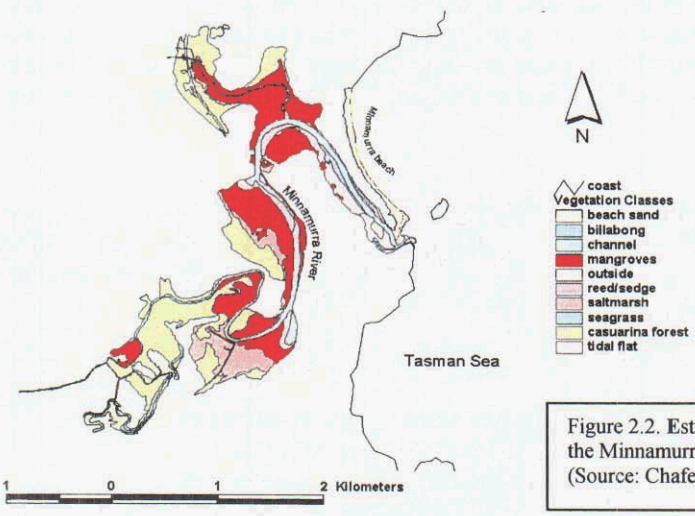

Figure 2.2. Estuarine vegetation of the Minnamurra River Estuary. (Source: Chafer, 1997)

3 Methods

3.1 Field data collection

Eleven plots of 90 m × 90 m each (3×3 pixels) were taped in the field: two of *Avicennia marina* low closed-forest, three of *A. marina* low woodland, five of the saltmarsh vegetation and two of the casuarina forest. The plots were made facing north in order to ensure that the largest number of pixels possible covered the plots. The tape and compass method was used to tape the plots. Each corner was marked using 1.5 m high stack marked with flagging tape. A Trimble ProXL GPS with TDCI data logger was used to obtain the coordinates of each corner. The points were verified to correspond to each corner by plotting these over a geo-referenced aerial photograph and deciding if

these coincided with each known point in the field. The coordinates of each corner were displayed in Arcview GIS and it was confirmed that the plots were rectangular and positioned in a south-north direction.

The information collected for mangroves included, for each plot, the projective foliage cover of the upper and mid-stratum, average height and the relative abundance of *A. marina* and *A. corniculatum*. The projective foliage cover was estimated using the gap-ratio method (McDonald *et al.*, 1984) and the relative abundance of each species was estimated using the line-intercept method. In the saltmarsh, the relative abundance of each species was measured for each plot. In the casuarina forest, the canopy closure and height of trees was sampled and an average calculated in order to determine the structural heterogeneity of the forest in each plot.

3.1.1 Structure and floristic of vegetation in each plot

The *A. marina* low closed-forest was composed of 100% *Avicennia marina* trees of an average height from 4 to 5.7 m in both plots. The projective foliage cover was approximately 50% in each plot and the gap between the crowns was 12 cm, while average crown diameter was from 250 to 1000 cm in each plot, indicating high canopy closure. The *A. marina* low woodland was composed of both A. marina and *A. corniculatum* species. In the low woodland vegetation, the relative abundance (aerial cover) of each species was over 50% for *A. corniculatum* and less than 30% for *A. marina*. The upper-stratum was dominated by isolated *A. marina* trees with a projective foliage cover of less than 10% and a mean gap between crowns of more than 7 m. The mid-stratum was dominated by *A. corniculatum* shrubs in all sites, with a projective foliage cover of approximately 40% in all sites. The saltmarsh vegetation was divided into low-marsh, dominated predominantly by the succulent herb *Sarcocornia quinqueflora* and the grass *Sporobolus virginicus*, and the mid/upper-stratum, dominated by *Junkus kraussii*, *Phragmites australis* and *Sporobolus virginicus*. The casuarina forest plots were composed of 100% *Casuarina* spp. trees, with both plots having the homogeneous forest formations.

3.2 Satellite hyperspectral imagery acquisition and characteristics

The EO-1 Hyperion image was acquired by USGS (United States Geological Survey)/EROS Data Center, Sioux Falls, South Dakota, USA, on 27 July 2002 at about 10:30 a.m. (local time). The Hyperion data consist of a data 'cube' represented by 242 spectral bands acquired over an array of 256 pixels (width). The number of lines (length) varies with the data acquisition event and the image is built up with the forward motion of the sensor (Jupp *et al.*, 2002). The image acquired over the study area was 7.7 km wide and 185 km long.

3.3 Pre-processing

3.3.1 Atmospheric and geometric correction

All pre-processing and analysis of the EO-1 Hyperion imagery was done using the image processing system ENVI® (Environment for Visualizing Images, Research Systems, Inc.). The EO-1 Hyperion image was atmospherically corrected in order to convert the data from at-sensor-radiance to apparent reflectance. The "coastal Waters and Ocean MODTRAN-4 Based ATmospheric correction" (c-Wombat-c) implemented in IDL/ENVI® was used. The c-WOMBAT-c applies a full MODTRAN-4 atmosphere parameterization and characterization to run the inversion from radiance to reflectance. The parameters correspond to very dry and clear atmospheric conditions without aerosol contents. An inspection of a false color composite agreed with these parameters since the image appeared very contrasted and without hazy effects. A spatial subset of 4 km wide by 5.7 km long was selected from the image to define the Minnamurra estuary study site, including the upland areas and coastal waters. The image was geometrically corrected using an image-to-image registration procedure using an ortho-rectified georeferenced aerial photograph of the area as reference. The image was registered to the Australian Map Grid 66 (AMG) coordinate system using 6 control points obtained from the photograph. A polynomial nearest-neighbor algorithm was applied. In this method, the pixel that has its center closer to the point located in the image is transferred to the corresponding display grid location (Richard and Jia, 1999). This technique does not alter pixel brightness values. The average RMS was 0.259 or within 1 pixel. Vegetation and cadastral vector files of the area were overlaid to observe the correspondence between the image and the geo-referenced files. After inspecting a number of points it was concluded that the registration was satisfactory.

3.3.2 Band selection

Of the 242 bands only 198 are calibrated to radiance while the rest are set to zero (Jupp *et al.*, 2002). The 198 bands were viewed through the animation tool in order to select noise-free bands for further processing. Bands

corresponding to water absorption features were very noisy containing no spatial information and were subsequently excluded from the data set. Streaking was apparent in some bands from both the VNIR and SWIR regions. Streaking is presented as vertical lines related to the along-track effects of push-broom systems (Jupp *et al.,* 2002) and are more apparent in low SNR (signal to noise ratio) bands. The streaking effect was pronounced in the SWIR region, specifically between 2000 nm and 2500 nm. De-streaking was initially attempted, however, the resulting images appeared worse than the originals. Consequently only bands 207 and 208 were retained from the 200-2500 nm region. All other bands deemed to have unacceptable noise or streaking were also removed. In total 105 bands were selected for further use.

3.4 Image analysis

3.4.1 Mixture Tuned Matched Filtering (MTMF)

The *Mixture Tuned Matched Filtering*™ (MTMF) is a technique that works by partially unmixing pixel spectra according to a user-defined endmember. In this procedure, the response of the reference endmember spectra is matched to the pixel spectra by maximizing the endmember response and masking the background unknown response (ENVI, 2001). The results indicate the degree to which the endmember was matched to the pixel spectra and the approximate sub-pixel response of the endmember (ENVI, 2001). An image is produced where bright pixels indicate high abundance of the endmember and therefore a high MF (matched filtering) score. An infeasibility result is also produced that represents the 'false positives' and assigns high infeasibility scores values to pixels erroneously matched to the endmember (see ENVI 2001 for details). This approach has been used to determine biochemical composition of leaves using data sets of leaf spectral response (Pinzon *et al.,* 1998) and species discrimination in saltmarsh vegetation (Zhang *et al.,* 1996) and the discrimination of a weed species (Parker Williams & Hunt Jr., 2002) using AVIRIS data. In this study, the technique was applied using each mangrove species as endmembers.

3.4.1.1 Data reduction and endmember selection for the mangrove species

Dimensionality reduction refers to the process by which the main components attributing to the spectral variance of the data set are identified. The aim is to reduce the information present in hyperspectral imagery so that it can be displayed in a minimized form without any alteration to the original data (Keshava & Mustard, 2002). The procedure used to achieve this was the Minimum Noise Fraction (MNF) implemented in ENVI®. The MNF transformation decomposes the data into the main components contributing most of the spectral variance and also accounts for the noise present in the data (Keshava & Mustard, 2002). The noise is first estimated resulting in a noise covariance matrix, which is then used to decorrelate and rescale the noise in the data. In the transformed data the noise has unit variance and no band-to-band correlation. A PCA is then applied to the noise-whitened data (ENVI, 2001). Two approaches were undertaken to find endmembers representative of each species. For the *A. marina* dominated low closed-forest community the endmember was selected from regions of interest (ROI) corresponding to the two plots for which field data indicated these were monospecific patches of *Avicennia marina.* For the low woodland community the endmembers were selected from the pixel cloud created with MNF bands 1, 8 and 9. The MNF band 9 showed that brighter pixels corresponded to Site 1 where *Aegiceras corniculatum* was dominant in terms of ground cover and projective foliage cover.

3.4.1.2 MTMF of the mangrove species and display

The MF score band and the infeasibility band were used to create a 2-dimensional scatter plot in order to select pixels that matched well with the reference endmember. Pixels of low infeasibility and MF score higher than approximately 0.25 were highlighted. These pixels corresponded to areas where the endmember was recorded as present at a sub-pixel level at a proportion according to the MF score (where 1 = 100 %). The maps were compared to the plots taped in the field for each community and to areas visited in the field that contained these communities. The MTMF results were assessed by correlating the ground-cover measurements taken for each site with the estimated cover of each species at the sub-pixel level. The Pearson correlation coefficient (r^2) was calculated to determine the correlation between the predicted and actual species ground cover. The correlation was applied to the *A. corniculatum* endmember only-the reason being that the *A. marina* endmember resulted in high MF scores and high infeasibility values for some of the low woodland areas making the data unsuitable for the comparisons between actual and predicted species cover.

3.4.2 Supervised classification- Spectral Angle Mapper (SAM)

In the spectral angle mapper (SAM) classification, pixels are considered vectors in n-dimensional space according to their DN values for each band, where the number of dimensions is equal to the number of bands (Kruse *et al.*, 1993).

SAM classifies pixels according to the angular distance between two vectors, the approach ignores vector lengths and is therefore unaffected by illumination effects (Mustard and Sunshine, 1999). Vectors with small angles are considered spectrally similar during the classification and the user must define the minimum spectral angle threshold to which all angles are compared. In this case the angle was set to 0.1 radians for all classes.

Regions of interest (ROI) were created for each community according to the position of their respective plot taped in the field. Additional spectral classes were also created using the information obtained during the endmember selection and field knowledge. A false color composite (RGB:50,33,17) was used to define other spectral classes, with all classes subsequently plotted in 2-to 3-dimension scatter plots using the original image bands. The visible and near infrared bands were used as vegetation features were of greatest interest. Pixels that plotted at the extremities of the spectral clouds were deleted from the class. The maximum, minimum, mean and standard deviation signature of each class were also calculated. These were inspected to ensure that the spectral variance was normal for each class. Supervised classifications were run using the original classes created, which included all 6 communities described in previous sections, and the newly created classes.

3.4.2.1 Accuracy assessment

The accuracy of the resulting images was assessed by calculating confusion matrices that show the level of accuracy of each classified image (Congalton & Green, 1999). Producer's and user's accuracies were calculated for each class, as well as the errors of omission and commission, overall accuracy and kappa coefficients. For each class additional non-biased regions of interest (ROI) were selected and used to calculate the statistics. For the mangrove and saltmarsh classes the regions of interest were defined by field checking carried out on the 20 and 25 November 2002. During field visits a Global Positioning System (GPS) was used to record the coordinates of the areas of interest. For the casuarina forest and littoral forest the ROIs were defined from maps already produced for the area by Chafer (1997) and Carne (1991) (not shown). For the other classes, defined from spectral analysis, false colour composites and scatter plots, the additional ROIs used for the accuracy assessment were defined from the false colour composite. The spectral signatures of these regions were inspected in order to ensure the pixels belonged to the relevant classes. The water classes, such as 'ocean' or 'river', were not included in the accuracy assessment. These classes were not correctly classified by SAM and it was determined that inclusion of the water classes would decrease the overall accuracy of the SAM classification.

4 Results

4.1.1 MTMF (Mixture Tuned Matched Filtering)

The mean spectral reflectance of the *A. marina* and *A. corniculatum* endmembers are shown in Figure 4.1. The spectral reflectance of the *A. marina* endmember is higher in the middle infrared than for the *A. corniculatum* endmember. Spectral reflectance for the *A. corniculatum* endmember is higher in the visible, from the green and red (559 nm to 661 nm) and in the left shoulder of the near infrared plateau from 750 nm to 1100 nm. Both endmembers have high absorbance in the chlorophyll band at approximately 675 nm. Figure 4.2 shows the scatter plot of the MNF bands 1, 8 and 9 and the pixels of *A. corniculatum* endmember that plotted to one of the corners.

The distribution of the *A. marina* endmember is shown in Figure 4.3. Pixels that resulted in low infeasibility values and high MF scores ranging from 0.35 to 1.35 are painted green. Colored pixels on the image represent areas where the *A. marina* endmember has been identified as present. The distribution of the *A. marina* endmember corresponds to Sites 4 and 5 (shown with an arrow) and other areas of the low-intertidal zone closer to the mouth of the estuary (circled) that have been visited and confirmed as being dominated by *A. marina* trees or shrubs. High MF scores and infeasibility values were recorded for some low woodland pixels. These areas were not highlighted since the MF scores are in reality 'false positives' (Boardman, 1998; ENVI, 2001) and do not match correctly with the *A. marina* endmember. The distribution of the *A. corniculatum* endmember is shown in Figure 4.4. The sub-pixel abundance for this species agrees with the distribution of field sites corresponding to the low woodland community. The distribution also extends to the upstream sections, over the low-intertidal zone. Correlation analysis between the actual and predicted ground cover of *A. corniculatum* indicated a high correlation between the predicted and actual abundance of the species (r^2=0.879).

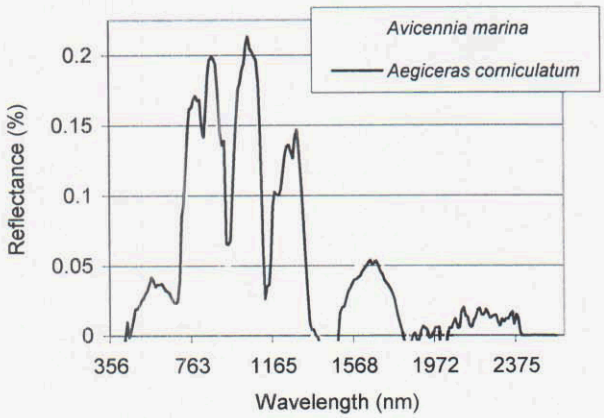

Figure 4.1. Spectral reflectance of the endmembers used in the MTMF of the two mangrove species; *Avicennia marina* (white) and *Aegiceras corniculatum* (black), obtained from the EO-1 Hyperion image subset of the Minnamurra estuary.

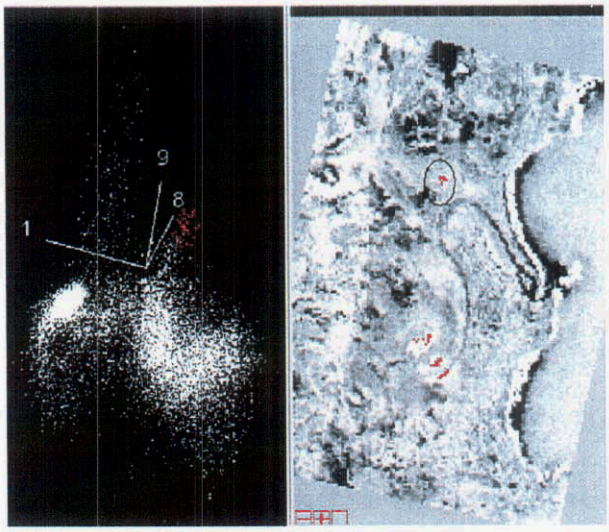

Figure 4.2. Scatter plot of MNF bands 1, 8 and 9 obtained from the EO-1 Hyperion image subset of the Minnamurra estuary (left) and the image subset of the area (right). Position of *Aegiceras corniculatum* endmember in the scatter plot (red pixels) and its spatial distribution in the area (red). *A. corniculatum* pixels corresponding to one of the plots (circled).

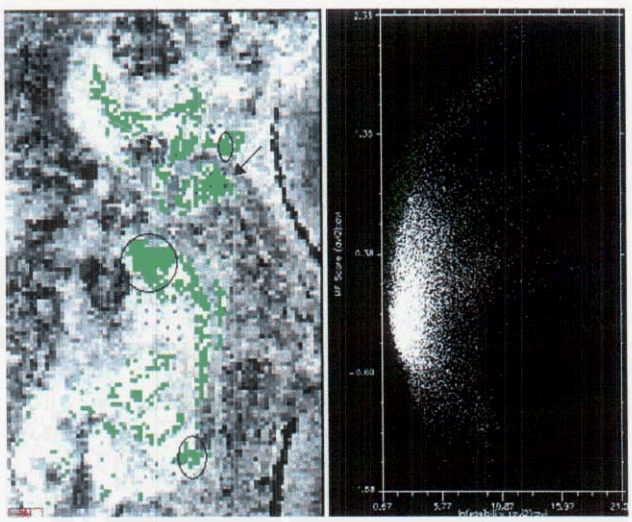

Figure 4.3. Distribution of the *Avicennia marina* endmember (green) obtained from the MTMF applied to the EO-1 Hyperion subset of the Minnamurra estuary (left). The image shows the coordinates of all sites (blue dots), low closed-forest (white and black arrow), and areas confirmed to be composed of *A. marina* (circled). Corresponding pixels in the scatter plot (right), showing high MF (matched filtering) scores and low infeasibility values (green).

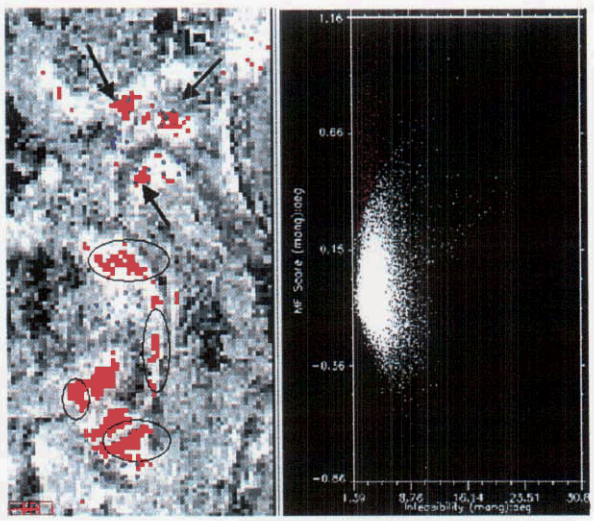

Figure 4.4. Distribution of the *Aegiceras corniculatum* endmember (red) obtained from the MTMF applied to the EO-1 Hyperion subset of the Minnamurra estuary (left). Shows: coordinates of all sites (blue dots), low woodland plots (arrows), and areas confirmed to be composed of *A. corniculatum* (circled). Corresponding pixels in the scatter plot (right), showing high MF (matched filtering) scores and low infeasibility values (red).

4.1.2 Supervised classifications (SAM)

The resulting map from the supervised classification agreed with the distribution of land-cover types at the landscape scale. Major cover classes, such as the urban areas, grasslands and littoral forests, were mapped in accordance to their distribution. In addition, the intertidal vegetation was discriminated well from the rest of the vegetation in the area. Figure 4.5a shows the distribution maps produced for the aggregated saltmarsh and mangrove

classes using the SAM classification and the already created map for the area. Table 4.1 shows the confusion matrix created with the mangrove and saltmarsh classes aggregated.

Table 4.1. Confusion matrix for the distribution map corresponding to Fig 4.5a, produced with the SAM applied to the EO-1 Hyperion subset of the Minnamurra estuary. All aggregated classes.

Overall accuracy = 76.74 % Kappa Coefficient = 0.73											
	Ground Truth (pixels)										
Class	bare ground	dry grass	mangroves	casuarina forest	saltmarsh	littoral forest	urban	green grass	Total	User's (%)	Commission (%)
unclassified	16	2	93	78	27	25	13	2	256		
bare ground	**87**		2				2	1	92	94.57	5.43
dry grass	1	**86**						2	89	96.63	3.37
mangroves			**257**	11	6	1			275	**93.45**	6.55
casuarina forest			20	**113**	2	10			145	**77.93**	22.07
saltmarsh			1	2	**38**				41	**92.68**	7.32
littoral forest			3	5		**90**			98	91.84	8.16
urban	16		4	4	17	1	**301**	1	344	87.5	12.5
green grass		2		1		12		**292**	307	95.11	4.89
Total	120	90	380	214	90	139	316	298	1647		
Producer's (%)	72.5	95.56	**67.63**	**52.8**	**42.22**	64.75	95.25	97.99			
Errors of Omission (%)	27.5	4.44	32.37	47.2	57.78	35.25	4.75	2.01			
Unclassified (%)	13.33	2.22	24.47	36.45	30	17.99	4.11	0.67	15.54		

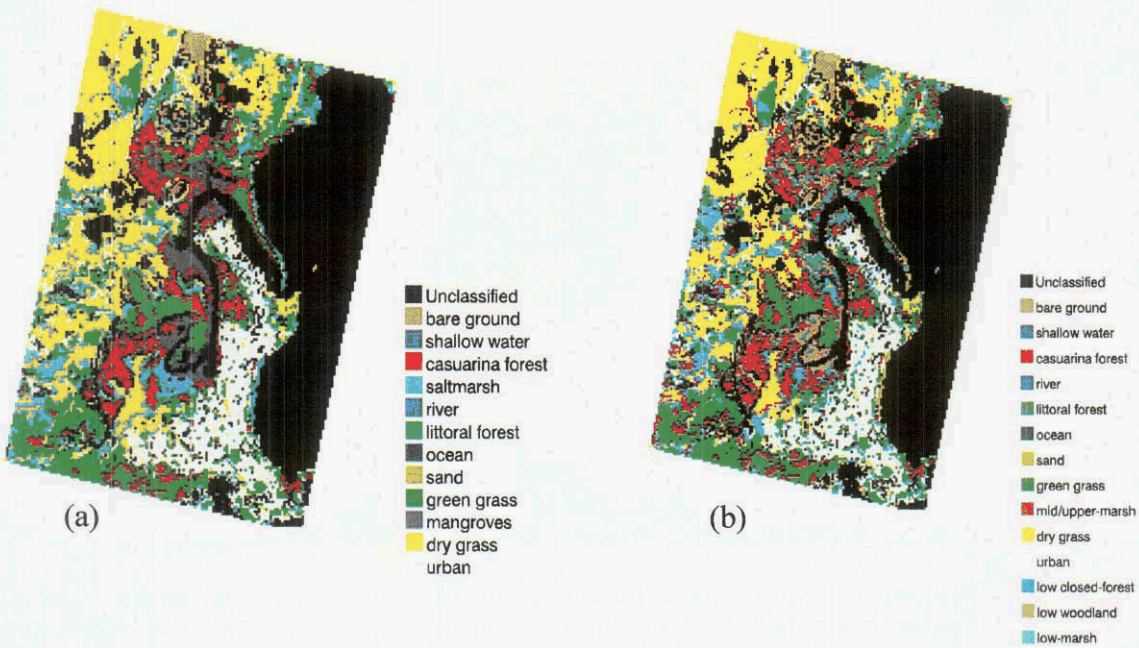

Figure 4.5. Distribution maps resulting from a SAM classification applied to the EO-1 Hyperion image subset of the Minnamurra River Estuary, NSW. (**a**) aggregated mangrove and saltmarsh classes (**b**) not aggregated mangrove and saltmarsh classes. Each image represents an area of 4 km by 5.7 km.

The confusion matrix corresponding to Figure 4.5b (Table 4.2) shows the mangrove class and casuarina forest class were accurately discriminated with producer's accuracies of 62.47 % and 67.29%, respectively. The saltmarsh class recorded lower levels of producer's accuracy of 42.22%. The user's accuracies were higher, approximately 90 % for all three wetland vegetation classes, however, the saltmarsh vegetation was erroneously mapped at high elevations as it was confused with the upland grasses and urban areas. The distribution maps produced by the SAM of the two mangrove classes are shown in Figure 4.5b. The distribution of low closed-forests is restricted to the mouth of the estuary and to the low-intertidal zone, while the distribution of low woodlands is more extensive in the low-intertidal zone upstream and in the upper intertidal zone downstream. The producer's accuracy for the low closed-

forest and the low woodland classes were 57.69 % and 56.67 %, respectively. The confusion occurs mainly between the two mangrove classes (Table 4.2). For example, some pixels corresponding to the low closed-forests were classified as low woodland, while some pixels known to contain mainly *A. corniculatum* shrubs were classified as low closed-forest (Table 4.2). The classifier produced good results, especially considering that around 10 % of the pixels in both classes remained unclassified.

Table 4.2. Confusion matrix corresponding to Figure 4.5b obtained for the SAM classification. Showing the discrimination of the two mangrove communities, low-marsh, mid/upper-marsh and casuarina forest.

	Overall Accuracy=66.39 % Kappa Coefficient = 0.61												
	Ground Truth (pixels)												
Class	bare ground	dry grass	low-closed forest	low woodland	low-marsh	mid/upper-marsh	green grass	urban	littoral forest	casuarina forest	Total	User's (%)	Commission (%)
unclassified	50	3	16	11	3	0	3	18	2	2	108		
bare ground	**33**										33	100	0
dry grass	9	**80**						8			97	82.47	17.53
low-closed forest			**60**	44	1	1				40	146	**41.1**	**58.9**
low woodland			24	**85**					3	17	129	**65.89**	**34.11**
low-marsh	2				**4**	26	27	16			75	**5.33**	**94.67**
mid/upper marsh		5			3	**19**	3			1	31	**61.29**	**38.71**
green grass						2	**237**	24	14	20	297	**79.8**	**20.2**
urban	5	2						**250**		1	258	96.9	3.1
littoral forest							6		**85**	10	101	84.16	15.84
casuarina forest			4	10	1		22		35	**123**	195	**63.08**	**36.92**
Total	99	90	104	150	12	48	298	316	139	214	1470		
Producer's accuracy (%)	33.33	88.89	**57.69**	**56.67**	**33.33**	**39.58**	79.53	79.11	61.15	**57.48**			
Errors of Omission (%)	66.67	11.11	**42.31**	**43.33**	**66.67**	**60.42**	20.47	20.89	38.85	**42.52**			
Unclassified (%)	50.51	3.33	**15.38**	**7.33**	**25**	**0**	1.01	5.7	1.44	**0.93**	7.35		

5 Conclusion

The MNF transformation applied to the Hyperion imagery showed that MNF band 9 corresponded with the distribution of *A. corniculatum*, especially in areas of high cover. The MTMF results obtained by using the *A. corniculatum* endmember agreed strongly with the distribution of this species. Its presence was recorded in the three plots and in other areas visited and confirmed (Fig. 4.4). The correlation analysis resulted in high positive correlation between the predicted cover of the *A. corniculatum* endmember and the actual cover measured in the field (r^2=0.879). Similarly the distribution obtained for the *A. marina* endmember showed that the distribution agreed with the two low closed-forest plots and other areas in the low-intertidal zone around the mouth of the estuary (Fig. 4.3), where this species has a high cover and forms extensive monospecific stands.

In mangrove forests, correlations have been found between the projective foliage cover (and leaf area index (LAI)) and the red and near infrared canopy reflectance (Jensen *et al.* 1991; Ramsey & Jensen, 1996; Green *et al.*, 1997), where increases in foliage cover result in increases of near infrared reflectance. However, no correlations have been established between species cover and any of the broad bands used by the most common satellite-borne sensors (Jensen *et al.*, 1991; Ramsey & Jensen, 1996). Previous studies have established that mangrove species could not be discriminated with broad-band satellite sensors because of the low spectral and spatial resolutions (Green *et al.*, 1996; 1998). Therefore, zonation has been mapped according to the structure of the vegetation in each zone (Blasco *et al.*, 1998; Rasolofoharinoro *et al.*, 1998) and the reflectance in the red and near infrared bands. The present study indicates that the improved spectral resolution of Hyperion, which allows for the application of more sophisticated methods of image analysis such as the MTMF, results in a good discrimination of the two mangrove species assessed in this study, despite the apparently low SNR (1:100) of the sensor (Kruse *et al.*, 2001) and 30 m pixels.

6 References

Blasco, F., Saenger, P. & Janodet, E. 1996. Mangroves as indicators of coastal change. *Catena* 27, 167–178.

Blasco, F., Gauquelin, T., Rasolofoharinoro, M., Denis, J., Aizpuru, M. & Caldairou V. 1998. Recent advances in mangrove studies using remote sensing data. *Marine and Freshwater Research* 49, 287–296.

Boardman, J.W. 1998. Leveraging the high dimensionality of AVIRIS data for improved sub-pixel target unmixing and rejection of false positives: Mixture Tuned Matched Filtering. *Summaries of the Seventh JPL Airborne Geoscience Workshop, JPL Publication 97-1* (pp. 55–56) Pasadena, CA: NASA Jet Propulsion Laboratory.

Carne, J. 1991. Landform vegetation relationships in the Minnamurra estuary, NSW, Monograph Series, No. 6, Department of Geography and Oceanography, University College, Australian Defense Force Academy, Canberra.

Chafer, C.J. 1997. *Biodiversity of Wetlands in the Illawarra Catchment: An inventory.* Illawarra Management Committee, Wollongong.

Clark, R.N. 1999. Spectroscopy of rocks and minerals, and principles of spectroscopy. *In* Andrew N.R. ed. *Remote Sensing for the Earth Sciences: Manual of Remote Sensing, 3 ed., Vol. 3* pp 3–58. John Wiley & Sons, Inc.

Congalton, R.G. & Green K. 1999. *Assessing the Accuracy of Remotely Sensed Data: Principles and Practices.* Lewis Publishers, Washington D.C.

Curran, P. J. 1994. Imaging spectrometry. *Progress in Physical Geography* 18: 247–266.

Dehaan, R.L. & Taylor G.R. 2002. Field-derived spectra of salinized soils and vegetation as indicators of irrigation-induced soil salinization. *Remote Sensing of Environment* 80, 406–417.

ENVI. 2001. ENVI (Environment for Visualizing Images) User's Guide: Images to Information. Research Systems, Inc., Boulder CO.

Environment Australia 2001. *A Directory of Important Wetlands in Australia.* 3rd Edition. Environment Australia, Canberra.

Finlayson, C.M., Davison N.C., Spiers A.G. & Stevenson N.J. 1999. Global wetland inventory-current status and future priorities. *Marine and Freshwater Research* 50, 717–727.

Green, E.P., Mumby P.J., Edwards A.J., Clark C.D. & Ellis A.C. 1997. Estimating leaf area index of mangroves from satellite data. *Aquatic Botany* 58, 11–19.

Green, E.P., Clark C.D., Mumby P.J., Edwards A.J. & Ellis A. 1998. Remote sensing techniques for mangrove mapping. *International Journal of Remote Sensing* 19, 935–956.

Gross, M.F., Hardinsky M.A. & Klemas V. 1989. Applications to coastal wetlands vegetation. *In* Asrar G. ed. *Theory and Application of Optical Remote Sensing*, pp. 474–490. John Wiley and Sons, New York.

Holmgren, P. & Thuresson T. 1998. Satellite remote sensing for forestry planning-a review. *Scandinavian Journal of Forest Research* 13, 90–110.

Jensen, J.R., Lin H., Yang X., Ramsey III E., Davis B. A & Thoemke C.W. 1991. The measurement of mangrove characteristics in Southwest Florida using SPOT multispectral data. *Geocarto International- A Multidisciplinary Journal of Remote Sensing* 6, 13–21.

Jupp, D.L.B., Datt B., Lovell J., Campbell S. & King E. 2002. *Discussions around Hyperion data: background notes for the Hyperion data users workshop.* CSIRO Office of Space Science & Applications, Earth Observation Center, Canberra. (unpublished).

Keshava, N. & Mustard J.F. 2002. Spectral unmixing. *IEEE Signal Processing Magazine* 19, 44–57.

Klemas, V.V. 2001. Remote sensing of landscape-level coastal environmental indicators. *Environmental Management* 27 (1), 47–57.

Kruse, F.A., Lefkoff A.B. & Dietz J.B. 1993. The Spectral Image Processing System (SIPS)- Interactive visualization and analysis of imager spectrometer data. *Remote Sensing of Environment* 44, 145–163.

Kruse, F.A., Boardman J.W. & Huntington J.H. 2001. Progress report: geologic validation of EO-1 Hyperion using AVIRIS. *Proceedings of the Tenth JPL Airborne Geoscience Workshop, JPL Publication 02-1.* http://popo.jpl.nasa.gov/docs/workshops/01_docs/2001Kruse_web.pdf

Küchler, A.W. 1988. Basic considerations: The nature of vegetation. *In* Küchler A.W. & Zonneveld I.S. eds. *Vegetation mapping* pp. 13–23. Klewer Academic Publishers, Dordrecht.

Lewis, M.M. 1999. *Discriminating Arid Vegetation Composition with Multispectral and High Spectral Resolution Imagery.* PhD thesis, University of New South Wales (unpublished).

McDonald, R.C., Isbell R.F., Speight J.G., Walker J. & Hopkins M.S. 1984. *Australian Soil and Land Survey: Field Handbook.* Inkata Press, Melbourne.

Muller, E. 1997. Mapping Riparian Vegetation along rivers: old concepts and new methods. *Aquatic Biology* 58: 411–437.

Mumby, P. J., Green, E. P., Edwards, A. J. Clark, C. D. 1999. The cost-effectiveness of remote sensing for tropical coastal resources assessment and management, *Journal of Environmental Management* 55: 157–166.

Mustard, J.F. & Sunshine J.M. 1999. Spectral analysis for Earth science: investigations using remote sensing data. *In* Andrew N.R. ed. *Remote Sensing for the Earth Sciences: Manual of Remote Sensing, 3 ed., Vol. 3* pp 251–306. John Wiley & Sons, Inc.

Parker Williams A. & Hunt Jr. E.R. 2002. Estimation of leafy spurge cover from hyperspectral imagery using mixture tuned matched filtering. *Remote Sensing of Environment* 82, 446–456.

Phinn S., Hess L. & Finalyson C. M. 1999. An assessment of the usefulness of remote sensing for coastal wetland inventory and monitoring in Australia. *In* Finlayson C.M. & Spiers A.G. eds. *Techniques for enhanced wetland inventory and monitoring.* Supervising Scientist Environment Australia, Canberra.

Pinzon J. E., Ustin S.L., Castaneda C.M. & Smith M.O. 1998. Investigation of leaf biochemistry by Hierarchical Foreground/Background Analysis. *IEEE Transactions on Geoscience and Remote Sensing* 36, 1913–1927.

Ramsey III E.W. & Jensen J.R. 1996. Remote sensing of mangrove wetlands: relating canopy spectra to site-specific data. *Photogrammetric Engineering and Remote Sensing* 62, 939-948.

Rasolofoharinoro M., Blasco F., Bellan M.F., Aizpuru M., Gauquelin T. & Denis J. 1998. A remote sensing based methodology for mangrove studies in Madagascar. *International Journal of Remote Sensing* 19, 1873–1886.

Richard J.A. & Jia X. 1999. *Remote Sensing Digital Image Analysis: An Introduction.* 3rd Edition. Springer, Berlin.

Rougharden J., Running S.W. & Matson P.A. 1991. What does remote sensing do for ecology? *Ecology* 72, 1918–1922.

Saenger P., Specht M.M., Specht R.L. & Chapman, V.J. 1977. Mangal and coastal salt-marsh communities in Australasia. *In* VJ Chapman ed. *Wet Coastal Ecosystems* pp.293–345. Elsevier, Amsterdam.

Serrano L., Penuelas J. & Ustin S.L. 2002. Remote sensing of nitrogen and lignin in Mediterranean vegetation from AVIRIS data: Decomposing biochemical from structural signals. *Remote Sensing of Environment* 81, 355–364.

Ustin S.L., Wessman C.A., Curtiss B., Kasischke E., Way J. & Vanderbilt V.C. 1991. Opportunities for using the EOS imaging spectrometers and synthetic aperture Radar in ecological models. *Ecology* 72, 1934–1945.

Vane G. & Goetz A.F.H. 1993. Terrestrial imaging spectrometry: current status, future trends. *Remote Sensing of Environment* 44, 117–126.

Zhang M., Pinzon J., Ustin S.L. & Rejmankova E. 1996. Differentiating salt marsh species using Foreground/Background analysis. *Proceedings of the ERIM Second International Airborne Remote Sensing Conference and Exhibition*, San Francisco. 1, 83–91.

ENDMEMBER SELECTION FOR MULTIPLE ENDMEMBER SPECTRAL MIXTURE ANALYSIS

Philip E. Dennison[1] and Dar A. Roberts[1]

1. Introduction

Spectral mixture analysis (SMA) models image spectra as the linear combination of endmembers (Adams et al., 1993). By utilizing an invariable set of endmembers, SMA does not account for the absence of one of the endmembers or spectral variation within "pure" materials. Multiple endmember spectral mixture analysis (MESMA) addresses these issues by allowing endmembers to vary on a per pixel basis (Roberts et al., 1998). MESMA has been applied in a variety of environments for vegetation and snow mapping. Roberts et al. (1997; 1998; 2003) and Dennison et al. (2000) used MESMA to map vegetation species and land cover type in Southern California chaparral. Painter et al. (1998; 2003) mapped snow grain size in the Sierra Nevada of California using MESMA. MESMA has also been used to map vegetation in semi-arid environments (Okin et al., 2001).

2. Background

Since the number of possible materials in an image can be very large, and since MESMA permits multiple endmembers for each material, an appropriate spectral library can contain hundreds of spectra. A large number of potential endmembers decreases computation efficiency and increases the complexity of the model output, so a parsimonious spectral library is desirable. Several methods of endmember selection for MESMA have been proposed. Painter et al. (1998) and Okin et al. (2001) used a limited number of reference spectra or *a priori* knowledge to select endmembers for their analyses. Roberts et al. (1997) devised a hierarchical endmember selection rule that used specialist endmembers to unmix a scene and then used generalist endmembers to model the remaining unmodeled or poorly modeled spectra. Roberts et al. (1998) selected endmembers to maximize the area mapped and minimize the overlap between models using a solution to the maximal covering problem (Church and Revelle, 1974). This paper presents the application of a new technique for selecting endmembers for MESMA using the endmembers that best model the spectra within their own class. The endmember with the minimum average root mean square error (RMSE) within a class is selected as the most representative endmember for the class.

Each spectrum in a spectral library can be modeled by any other spectrum within the library and shade using a two endmember model. Each of these models has a goodness of fit as measured by the RMSE. Endmember average RMSE (EAR) is the average RMSE for an endmember modeling the library spectra within its own material class. EAR is calculated as:

$$EAR_{A_i,B} = \frac{\sum_{j=1}^{n} RMSE_{A_i,B_j}}{n} \quad (1)$$

where A is the endmember class, A_i is the endmember, B is the modeled spectra class, and n is the number of modeled spectra in class B. For example, a "soil" class within a spectral library could contain 8 spectra. EAR can be calculated for the spectrum "soil3" as the average RMSE of "soil3" and a shade endmember modeling all the spectra within the soil class. EAR measures the actual model performance of an endmember for modeling spectra within its class. The spectrum with the lowest EAR best models the class, and is thus most representative of the class.

3. Methods

High altitude AVIRIS data were acquired on 5 dates over the Santa Barbara front range, including the city of Santa Barbara, California and the south-facing slope of the Santa Ynez Mountains. Six land cover classes were identified as dominant at a scale of 20 meters within the study area, including 5 vegetation classes (*Adenostoma fasciculatum*, *Arctostaphylos spp.*, *Ceanothus megacarpus*, *Quercus agrifolia*, and mixed introduced grasses) and an urban class. 65 reference polygons for the vegetation classes were identified using field inspection and hard copy 1 meter resolution United States Geological Survey digital orthophotos in June, 2002. Ten urban reference polygons were identified from the digital orthophotos in January, 2003. Polygons were required to be at least 50% dominated by one of the six land cover classes and be at least 40 meters by 40 meters in size, so that at least one pixel was contained entirely within the polygon.

AVIRIS data were acquired between 1998 and 2001, in the months of May, June and September (Table 1). All dates were processed to apparent surface reflectance using a modified version of the MODTRAN radiative transfer model (Green et al., 1993) and calibrated using the field-measured reflectance of a sand target. The data were

registered to an orthorectified SPOT mosaic resampled to 20 meters. Since the date is not a reliable indicator of vegetation water stress due to the variable nature of precipitation in Southern California, a simple soil water balance model was used to rank the relative moisture status of the 5 AVIRIS dates. Precipitation measured at the El Estero Water Treatment Plant in Santa Barbara was compared to reference evapotranspiration (ET_0) measured at a California Irrigation Management Information System (CIMIS) station approximately 4 kilometers to the northwest of the treatment plant. Soil water balance was set to zero for the full dry season preceding each date. Soil water balance was determined by cumulatively summing the daily ET_0 subtracted from the daily precipitation. Runoff and soil infiltration were not included in the model. The beginning of the dry season was determined to be the date on which the water balance reached zero after the last significant precipitation (> 3mm). Positive and negative soil water balance are referenced from this date (Table 1).

Image spectra from pixels entirely inside the reference polygons were extracted from the 5 registered AVIRIS reflectance images. 988 spectra from 59 polygons at least 75% dominated by a single land cover class were included in a separate spectral library for each date (Table 2). For each date, the library of 988 image spectra was unmixed by each of its component spectra and photogrammetric shade using MESMA. The non-shade endmember fraction was constrained to less than 106%, based on optimal constraints from Halligan (2002). For best-fit models with non-shade endmember fractions in excess of 106%, RMSE was calculated using the maximum non-shade endmember fraction of 106%. Permitting higher non-shade endmember fractions allows dark endmembers to have low EAR values that are not representative of their ability to model the spectra within their class. EAR was calculated for each endmember by averaging the RMSE for modeled spectra within the same land cover class. Endmembers with the minimum EAR within their class for each date were selected for mapping the AVIRIS images. Each AVIRIS image was modeled using 6 two endmember models corresponding to the 6 minimum EAR endmembers for each date. Non-shade endmember fractions were constrained to between -6% and 106%. Residuals were not allowed to exceed 2.5% reflectance for more than 7 contiguous bands and RMSE was constrained to below 2.5% reflectance (Roberts et al., 1998).

4. Results

The selected minimum EAR endmembers displayed significant spectral changes through the AVIRIS time series (Figure 1). Solar zenith was smaller for the 1998 and 2001 images (Table 1), and brightness effects due to lighting geometry were evident in the selected spectra of all of the land cover classes. All of the vegetation endmembers selected from the positive water balance images possessed a distinct red edge and chlorophyll absorption. Grassland endmembers exhibited the greatest changes in spectral shape due to the complete senescence of the grasslands. The red edge and shortwave infrared absorption features of the grassland endmember selected from the 1998 image were greatly reduced in the 2001 and 2002 endmembers, and were largely absent from the 1999 and 2000 endmembers (Figure 1d). A red edge was apparent in all of the selected urban spectra (Figure 1e), indicating subpixel scale vegetation was present in the urban environment. The presence of the red edge in both positive and negative soil water balance images indicates this vegetation was irrigated. The most interesting spectral changes occurred in *A. fasciculatum* and *Arctostaphylos* (Figure 1a,b). As soil water balance decreased, the presence of non-photosynthetic vegetation became more pronounced in the spectra of these land cover classes. Positive water balance spectra in these two land cover classes showed pronounced chlorophyll absorption and little ligno-cellulose absorption, while negative water balance spectra showed increased ligno-cellulose absorption and decreased chlorophyll absorption. This trend was less distinct in the selected *C. megacarpus* and *Q. agrifolia* spectra (Figure 1c,e).

Large areas corresponding to mixed residential and riparian areas were unmodeled by the 2 endmember models in all 5 AVIRIS images (Figure 2). Neither class was spectrally similar to the selected endmembers from the 6 land cover classes, and the high heterogeneity of residential neighborhoods made them difficult to model with only two endmembers. Both images with positive soil water balance (Figure 2a,b) were well mapped. *C. megacarpus* dominates the south-facing slope of the Santa Ynez Mountains, with bands of *A. fasciculatum* on rockier soils and *Q. agrifolia* on more mesic slopes and valley bottoms. *Arctostaphylos spp.* was properly limited to higher altitude rocky soils. Grassland was poorly modeled in the 1998 image, most likely due to varying degrees of grassland senescence. Three of the vegetation classes in the images with negative soil water balance were poorly modeled: *A. fasciculatum, Arctostaphylos spp.,* and *C. megacarpus* (Figure 2c,d,e). *Arctostaphylos spp.* and *A. fasciculatum* were overmodeled in all three images, while *C. megacarpus* was undermodeled. *Q. agrifolia* was overmodeled in the 2002 image, but was adequately modeled in the 1999 and 2000 images. Urban and grassland classes were well modeled in all the images with negative soil water balance.

5. Discussion

The accuracy of the modeled images was assessed using the entire set of 75 reference polygons. Land cover class accuracy was assessed by grouping all of the modeled image spectra within a reference polygon and selecting the most frequently modeled land cover class as the dominant class for the polygon. Unmodeled image spectra and polygons with equally dominant land cover classes were excluded from the accuracy assessment. Overall accuracy, kappa coefficient, and kappa variance were calculated for each date (Table 3) (Cohen, 1960; Congalton, 1991). The 2001 modeled image had the highest accuracy (0.90) and kappa coefficient (0.87) of the five AVIRIS dates. The 1998 modeled image also possessed overall accuracy and kappa coefficients over 0.80. Kappa and kappa variance were used to calculate a Z-statistic for each pair of dates to determine whether the kappa coefficients for each date were significantly different (Congalton, 1991). The kappa values of the two positive water balance images were found to be significantly better than the kappa values for two of the three negative water balance images, at the 95% confidence level. All three negative soil water balance images suffered from low accuracy. This is directly the result of *C. megacarpus* and *A. fasciculatum* polygons being modeled by *A. fasciculatum* and *Arctostaphylos* endmembers, as is apparent in Figure 2. The confusion matrix for the 2000 image highlights the confusion between these three vegetation classes (Table 4).

As the soil water balance decreases, the amount of senesced and dead material in a stand of vegetation increases. Even if the dominant species is not prone to senescence or dieback, subdominant components (grasses, *Artemisia californica, Salvia spp.*) of the stand may be. The vegetation classes modeled in the AVIRIS images become less distinct under drought conditions due to varying amounts of non-photosynthetic vegetation (NPV). The selected *C. megacarpus* endmembers model fewer *C. megacarpus* polygons in the negative water balance images than in the positive water balance images. *C. megacarpus* polygons with a higher fraction of NPV are modeled by the *A. fasciculatum* and *Arctostaphylos* endmembers, which displayed spectral features characteristic of increased NPV. Similarly, greener *A. fasciculatum* spectra were better modeled by *C. megacarpus* endmembers than by *A. fasciculatum* endmembers.

6. Conclusions

Endmember average RMSE was used to select the most representative image endmembers of six land cover classes from five AVIRIS images with varying soil moisture availability. Confusion between endmembers increased as soil water balance changed from positive to negative, reducing the accuracy of the modeled negative water balance images. Considering that many areas of all five AVIRIS images were unmodeled, a single two endmember model for each land cover class is not adequate for comprehensive mapping. Using multiple 2 endmember models for each class or adding 3 endmember models will reduce the number of unmodeled spectra. The use of additional models may also diminish confusion between *A. fasciculatum, Arctostaphylos,* and *C. megacarpus*. Endmembers with varying amounts of NPV could be selected for each species, allowing more accurate mapping in the negative water balance images. Even with an expanded set of endmembers, it is likely that wet season images with positive water balances will still be modeled with higher accuracies. This has implications for mapping vegetation using broadband sensor data, which will also be sensitive to seasonal spectral variability.

7. References

Adams, J.B., Smith, M.O., and Gillespie, A.R., 1993. Imaging Spectroscopy: Interpretation Based on Spectral Mixture Analysis. In: C.M. Pieters, and P.A.J. Englert (Eds.), *Remote geochemical analysis : elemental and mineralogical composition.* Press Syndicate of University of Cambridge, Cambridge, England, pp. 145-166.

Church, R. and Revelle, C., 1974. The maximal covering location problem. *Papers of the Regional Science Association,* 32:101-118.

Cohen, J., 1960. A coefficient of agreement for nominal scales. *Educational and Psychological Measurement,* 20:37-46.

Congalton, R., 1991. A review of assessment the accuracy of classifications of remotely sensed data. *Remote Sensing of Environment,* 37:35-46.

Dennison, P., Roberts, D., and Regelbrugge, J., 2000. Characterizing chaparral fuels using combined hyperspectral and synthetic aperture radar. *Proceedings of the Ninth JPL Airborne Earth Science Workshop.* Jet Propulsion Laboratory, Pasadena, California, pp. 119-124.

Green, R., Conel, J., and Roberts, D., 1993. Estimation of aerosol optical depth and additional atmospheric parameters for the calculation of apparent surface reflectance from radiance as measured by the Airborne Visible-Infrared Imaging Spectrometer (AVIRIS). *Summaries of the Fourth Annual JPL Airborne Geosciences Workshop,* Jet Propulsion Laboratory, Pasadena, California, pp. 73-76.

Halligan, K.Q., 2002. Multiple endmember spectral mixture analysis of vegetation in the northeast corner of Yellowstone national park. Master's Thesis, University of California Santa Barbara.

Okin, G.S., Roberts, D.A., Murray, B., and Okin, W.J., 2001. Practical limits on hyperspectral vegetation discrimination in arid and semiarid environments. *Remote Sensing of Environment,* 77:212-225.

Painter, T.H., Roberts, D.A., Green, R.O., and Dozier, J., 1998. The effect of grain size on spectral mixture analysis of snow-covered area from AVIRIS data. *Remote Sensing of Environment,* 65:320-332.

Painter, T. H., J. Dozier, D. A. Roberts, R. E. Davis, and R. O. Green, 2003. Retrieval of subpixel snow-covered area and grain size from imaging spectrometer data. In press, *Remote Sensing of Environment.*

Roberts, D.A., Dennison P.E., Gardner, M., Hetzel, Y.L., Ustin, S.L., and Lee, C., 2003. Evaluation of the potential of Hyperion for fire danger assessment by comparison to the Airborne Visible Infrared Imaging Spectrometer. In press, *IEEE Transactions on Geoscience and Remote Sensing.*

Roberts, D.A., Gardner, M., Church, R., Ustin, S.L., and Green, R.O., 1997. Optimum strategies for mapping vegetation using multiple endmember spectral mixture models. *Imaging Spectrometry III,* SPIE Optical Engineering Press, Bellingham, Washington, pp. 108-119.

Roberts, D.A., Gardner, M., Church, R., Ustin, S., Scheer, G., and Green, R.O., 1998. Mapping chaparral in the Santa Monica Mountains using multiple endmember spectral mixture models. *Remote Sensing of Environment,* 65:267-279.

Table 1. Dates of AVIRIS data, ordered by soil water balance.

AVIRIS Dates	Solar Zenith	Soil Water Bal. (cm)
May 30, 1998	12.5°	+66.2
June 14, 2001	11.2°	+12.5
May 5, 2002	19.7°	-18.4
Sept. 16, 2000	37.0°	-37.9
Sept. 11, 1999	32.9°	-64.0

Table 2. Spectral library constituents from each land cover class.

Class	# of spectra
A. fasciculatum	76
Arctostaphylos spp.	111
C. megacarpus	398
grassland	117
Q. agrifolia	107
urban	179
total	988

Table 3. Accuracy, kappa, and kappa variance for each AVIRIS date.

Year	Accuracy	Kappa	Kappa Var.
1998	0.85	0.81	0.0034
2001	0.90	0.87	0.0021
2002	0.63	0.56	0.0054
2000	0.68	0.62	0.0046
1999	0.79	0.74	0.0037

Table 4. Polygon dominant land cover class confusion matrix for the modeled 2000 AVIRIS image, including user's and producer's accuracies.

		Reference Dominant						
		A. fasc.	*Arcto.*	*C. mega*	grass	*Q. agri.*	urban	user's
Image Dominant	*A. fasc.*	5	1	5	0	0	0	0.45
	Arcto.	4	6	9	0	0	0	0.32
	C. mega.	2	0	9	0	0	0	0.82
	grass	0	0	0	10	0	0	1.00
	Q. agri.	0	0	1	0	8	0	0.89
	urban	0	0	0	0	0	9	1.00
	producer's	0.45	0.86	0.38	1.00	1.00	1.00	

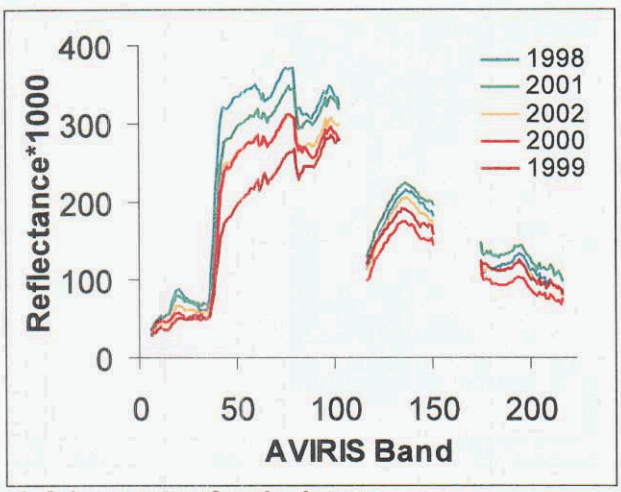

a) *Adenostoma fasciculatum*

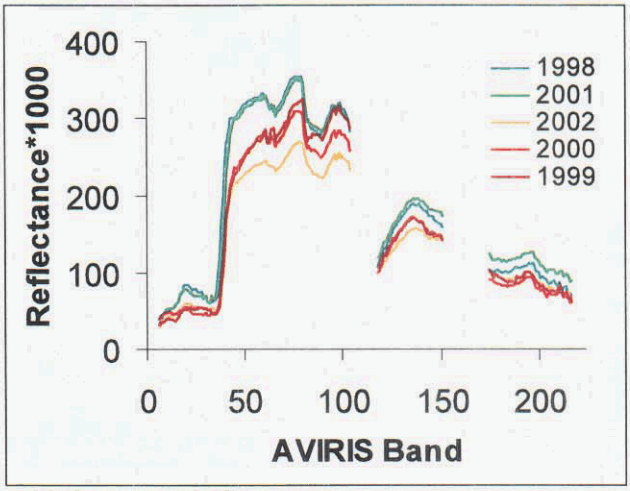

b) *Arctostaphylos spp.*

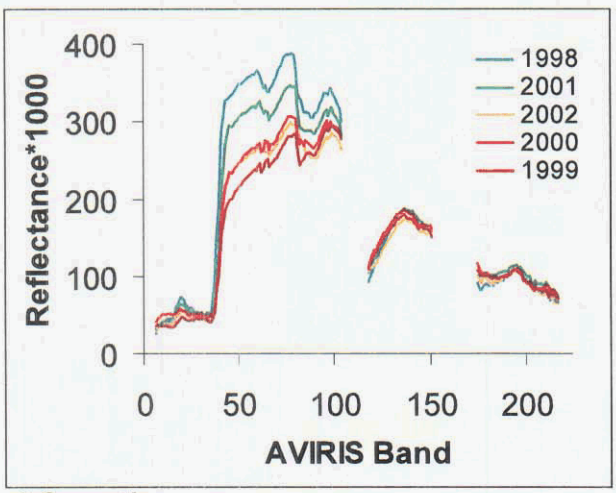

c) *Ceanothus megacarpus*

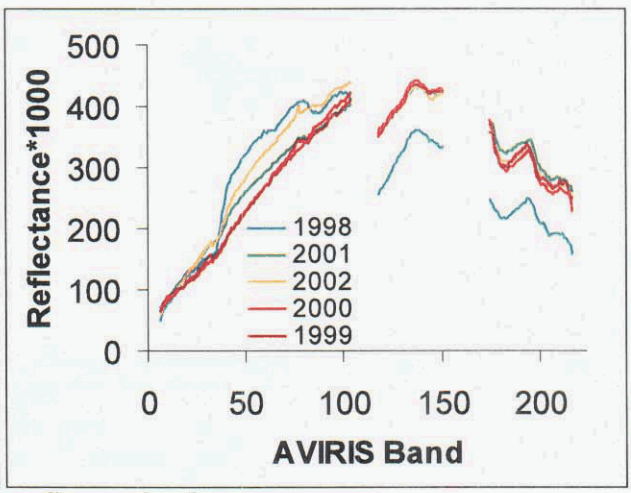

d) grassland

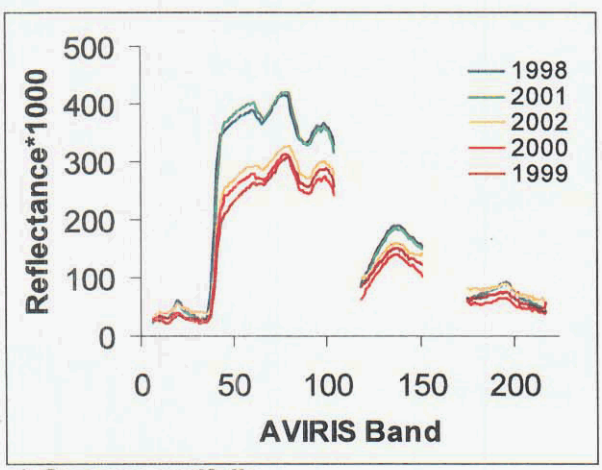

e) *Quercus agrifolia*

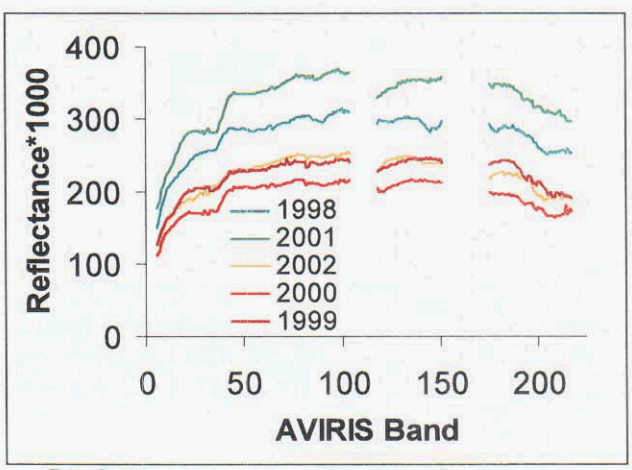

f) urban

Figure 1. Selected minimum EAR endmembers for each land cover class, by year.

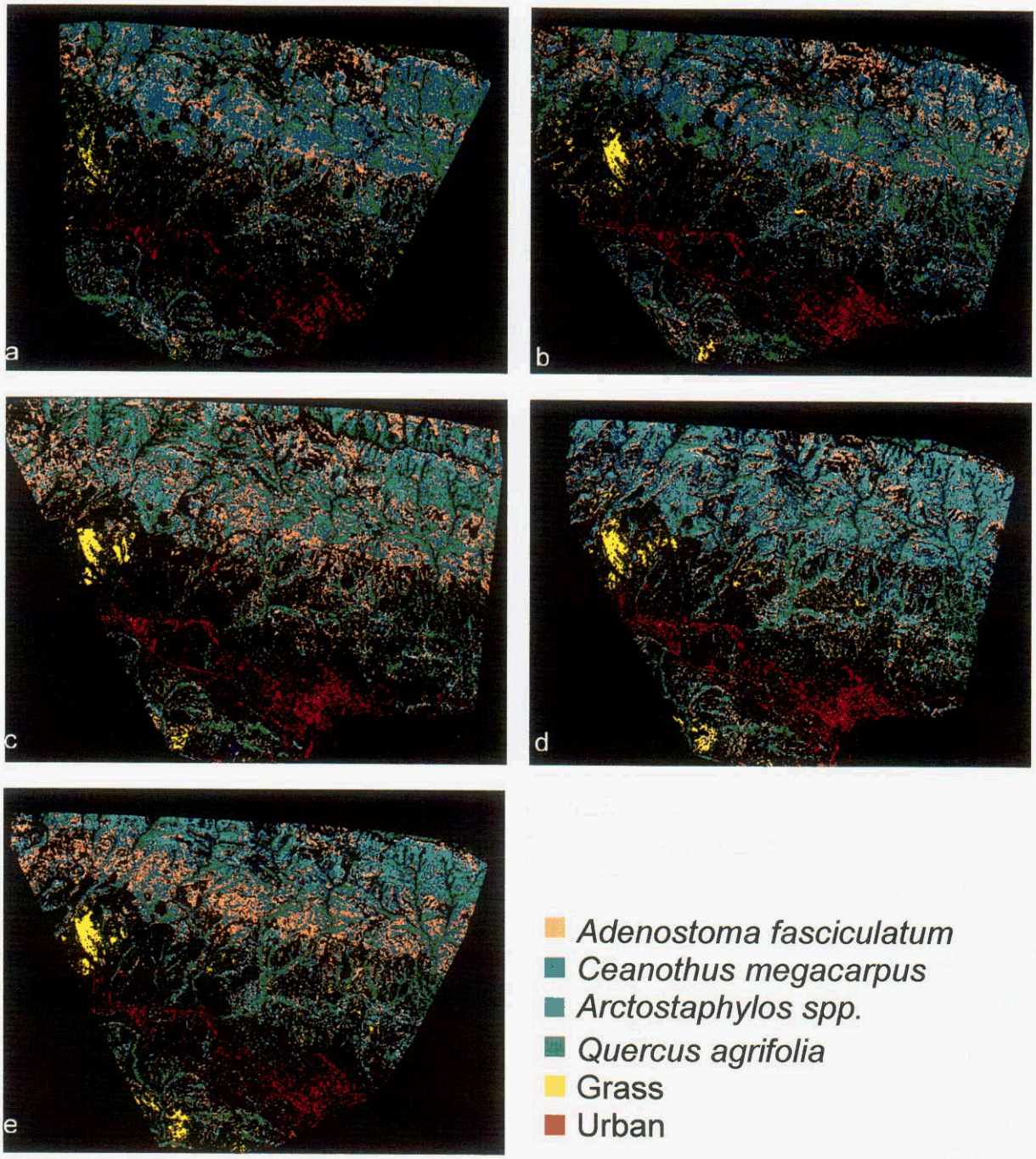

Figure 2. AVIRIS images of the Santa Barbara front range modeled using the minimum EAR endmembers for each date. Image letters correspond to the following dates: a) May 30, 1998; b) June 14, 2001; c) May 5, 2002; d) Sept. 16, 2000; and e) Sept. 11, 1999. Black areas are unmodeled.

Using AVIRIS Data to Map and Characterize Subaerially and Subaqueously Erupted BasalticVolcanic Tephras: The Challenge of Mapping Low-Albedo Materials

William H. Farrand[1]

1.0 Introduction

Increases in the signal-to-noise ratio (SNR) in AVIRIS has enabled the mapping and characterization of low albedo materials. Low albedo materials of interest include certain soils, man-made materials (asphalt, certain building materials, tires, etc.), and basaltic lava flows and ashes. Early in its history, the response of the AVIRIS sensor was not sensitive enough so that these low albedo materials could be reliably mapped. However, as indicated by Green and Pavri (2002) the noise equivalent delta radiance (NEdL) of AVIRIS in the 2001 flight season was below 0.010 in all but the shortest wavelength channels. This is approximately a ten-fold improvement from the 1989 flight season when NEdL was closer to 0.1 (Green et al., 1990). In the current investigation, AVIRIS data from the 2002 flight season collected over the Pavant Butte tuff cone, Tabernacle Hill tuff ring, and an associated lava flow in the Black Rock Desert of west central Utah were examined to determine how well these generally low albedo volcanic lavas and tephras could be discriminated from background materials. The Pavant Butte tuff cone was examined by the author in an earlier study with a 1989 AVIRIS dataset (Farrand and Singer, 1991).

2.0 Field Area

Figure 1 shows the location of the Pavant Butte area and the outline of the portion of the AVIRIS flightline that was examined. Tabernacle Hill and Pavant Butte are examples of, respectively, a tuff ring and a tuff cone. Such landforms are part of a continuum of volcanic landforms that are produced when magmas erupt in the presence of water. They represent different amounts of water present at the vent at the time of eruption. Tuff cones are produced from high water/magma ratios representative of eruption into standing water and tuff rings result from a lower water/magma ratio (Wohletz and Sheridan, 1983). Pavant Butte was erupted into Pleistocene Lake Bonneville in west-central Utah between 16,000 and 15,300 years ago (Oviatt and Nash, 1989). It consists of a partial cone that is composed of massively bedded ashes which are highly palagonitized and cemented into tuff. These palagonite tuff beds lie atop fresh to poorly palagonitized ash and tuff beds. The ash beds lie atop lacustrine sediments. Ash and cinders from the Pavant Butte eruption are prominent as a component of the soils surrounding the tuff cones. The AVIRIS scene analyzed in this study also contains a number of ephemeral lakes or playas some of which were apparently wet at the time of the overflight. South of Pavant Butte lies the younger, moderately palagonitized Tabernacle Hill tuff ring. Tabernacle Hill lies atop a weathered basalt flow. The age of the Tabernacle Hill eruptions is between 14,500 and 14,300 years ago (Oviatt and Nash, 1989). Between Pavant Butte and Tabernacle Hill lies a more recent, relatively fresh, low albedo basalt flow.

[1] Farr View Consulting, Thornton, Colorado and Space Science Institute, Boulder, Colorado, E-mail: farrand@ricochet.com

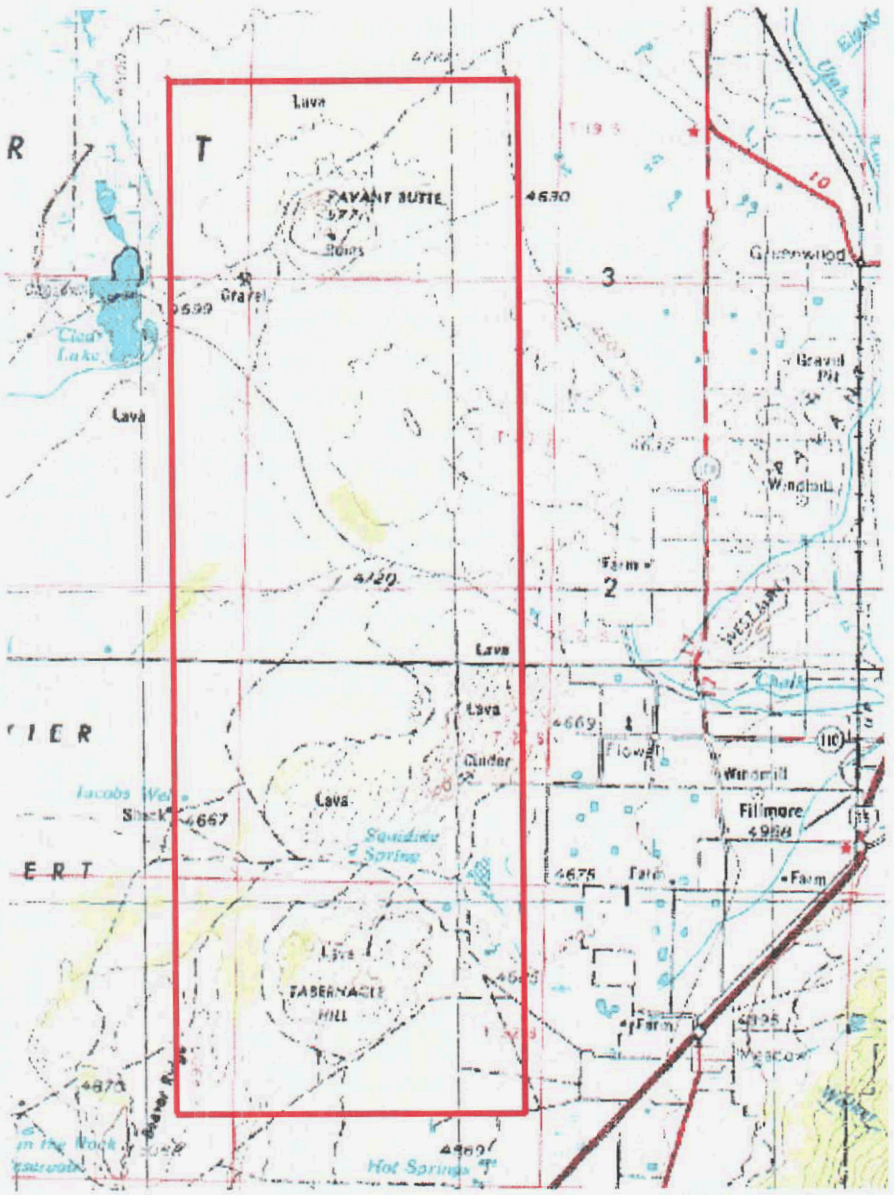

Figure 1. Portion of topographic map of the Pavant Butte area. The subsection of the AVIRIS flightline discussed here is outlined.

3.0 Materials of Interest

Reflectance spectra of hydrovolcanic tephras from Pavant Butte and the fresh basalt flow, extracted from the AVIRIS scene, are presented in Figure 2. The reflectance of the Tabernacle hill tuffs is approximately the same as that of the poorly palagonitized tuff shown in Figure 2. The well palagonitized tuff is distinguished by a distinct Fe^{3+} crystal field band just shortwards of 1 μm, deep water absorption features, and a small sheet silicate vibrational overtone at 2.3 μm. In the poorly palagonitized material, the "1 μm" feature is caused by both Fe^{3+} in the palagonite and Fe^{2+} in the unpalagonitized glass. Water absorption features are weak to absent. The highly palagonitized tuff is relatively bright while the poorly palagonitized tuff is characterized by relatively low reflectance values, on the order of 20%. The relatively unaltered ash has reflectance values below 10%. More detail on the spectroscopic characteristics of Pavant Butte tephras is provided in Farrand and Singer (1992).

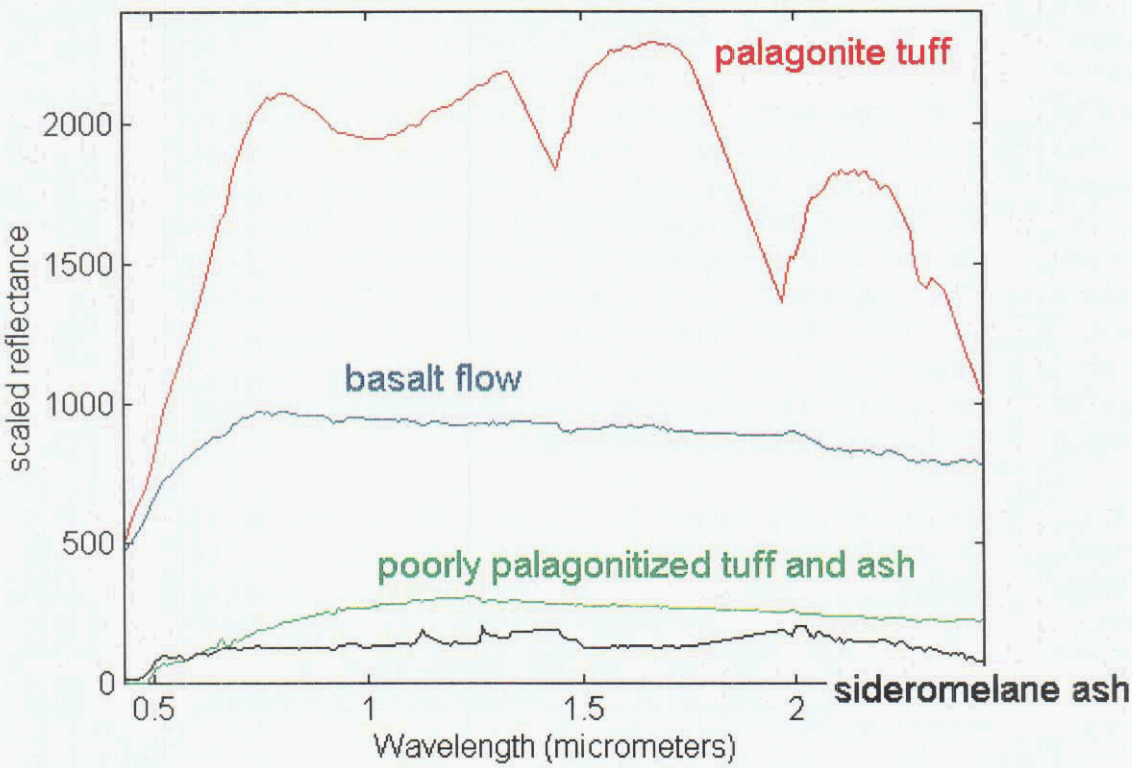

Figure 2. Reflectance spectra of hydrovolcanic tephras from Pavant Butte and fresh basalt flow as extracted from the AVIRIS data. Spectra have been scaled by a factor of 5000. Note that even the low reflectance sideromelane (basaltic glass) ash has discernable spectral shape.

The surrounding lacustrine sediments include several clay minerals as well as the evaporite mineral gypsum. There are aeolian sediments which to the naked eye appear reddish and whose reflectance spectra indicate the presence of iron and a weak 2.2 mm band indicative of a dioctahedral clay phase. The recent basaltic lava flow in the central part of the scene has low reflectance values. In addition to the volcanic materials and aeolian and lacustrine sediments, some circularly irrigated agricultural fields are also present in the scence near Tabernacle Hill and the recent lava flow.

4.0 Data

The hyperspectral data examined here were collected on October 8, 2002 by NASA's Airborne Visible/Infrared Imaging Spectrometer (AVIRIS). The data, as supplied by the AVIRIS data lab, were provided in a geometrically corrected format (Boardman, 1999). In order to eliminate null pixels at the borders of the scene that were introduced by the geometric correction, the data were spatially subsampled to a 688 by 2048 subsection. It is this spatial coverage that is outlined in Figure 1 and shown in the color composites of Figure 4. The data were corrected to surface reflectance by means of the HATCH atmospheric correction software (Qu et al., 2000). Spectral "polishing" of the data was achieved through application of the EFFORT software (Boardman, 1998) resident in ENVI.

5.0 Results

Selection of an initial set of image endmembers was achieved by applying the "standard" ENVI processing steps of Minimum Noise Fraction (MNF) transformation, Pixel Purity Index pixel selection, and n-Dimensional visualization (RSI, 2002). This initial set of image endmembers was used as input to the linear spectral mixture analysis (SMA) routine contained in ENVI. SMA was run iteratively in order to obtain additional endmembers indicated in the root mean square (RMS) error image (Adams et al., 1993). The final set of image endmember spectra is shown in Figure 3. The endmember materials include the highly palagonitized tuff of Pavant Butte, vegetation, oxidized cinders associated with the fresh basalt flow and several playa endmembers. A surface class that is notably absent from this set of endmembers is the basalt flow itself. The flow is one of the most obvious components of the scene upon visual inspection of a simple color composite (such as Figure 4a). However, it is a low albedo material and in running SMA on standard reflectance or radiance data, materials which are higher in albedo will be preferentially selected as required image endmembers.

In order to remove the effects of albedo, a hyperspherical directional cosine (HSDC) transformation (Pouch and Campagna, 1990) was applied to the data. Color composites of HSDC transformed data produced color contrasts much more vivid than composites of the non-transformed data. In Figure 4, a three band color composite of the original AVIRIS data is shown along with a composite of the same bands of the HSDC transformed data. In the color composite of the HSDC transformed data, low albedo materials such as the basalt flow and

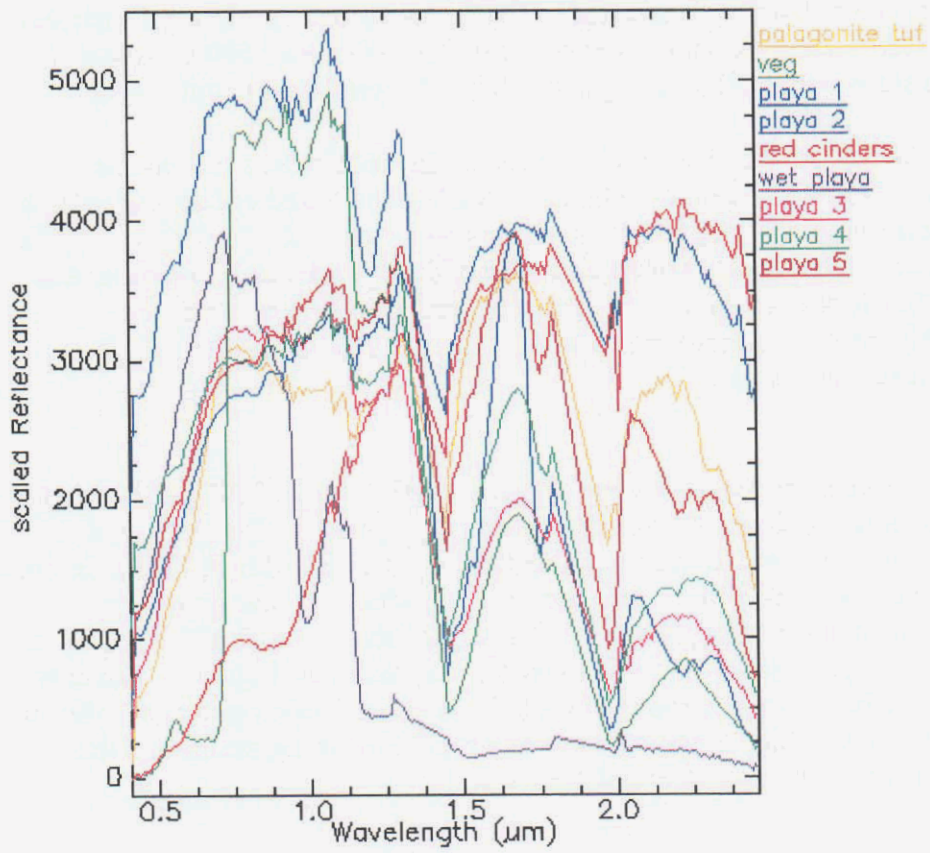

Figure 3. Image endmember spectra derived from iterative spectral mixture analysis of non-albedo normalized AVIRIS data for the Pavant Butte area.

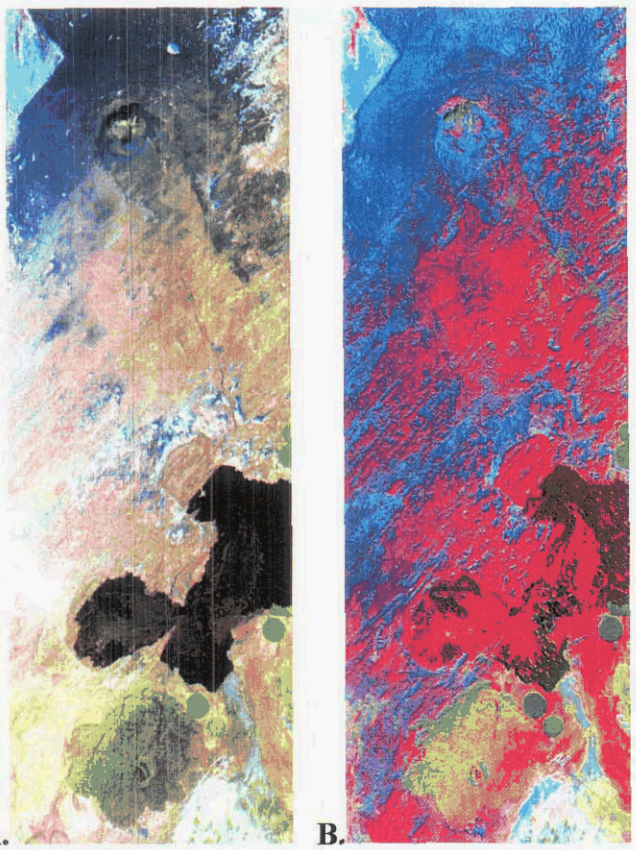

Figure 4. A. Composite of 1.7 μm (red), 0.8 μm (green), and 0.45 μm (blue) bands for the subsection of AVIRIS data discussed here. **B**. Composite of those same channels in data transformed by the HSDC transformation

exposures of the unaltered Pavant Butte ash show up as red. Iterative SMA was applied to the HSDC-transformed data and an endmember required by this analysis was the basalt flow. The resulting fraction image of the basalt endmember also displays higher contrast against the background than when the same pixels are averaged to produce a comparable image endmember set and run against the original/non-albedo normalized data (Figure 5).

Application of the HSDC transformation also helped to improve the mapping of the low albedo ashes associated with Pavant Butte and Tabernacle Hill. Fraction images of the relative abundance of the highly palagonitized tuff and the poorly palagonitized tephras associated with Pavant Butte and Tabernacle Hill were produced via application of constrained energy minimization (CEM) (Farrand and Harsanyi, 1997) and foreground / background analysis (FBA) (Smith et al., 1994). The highest fractions (fractions greater than 0.4) from these fraction images were thresholded and these results are presented in Figure 6. While the ability to map out the highly palagonitized tuff of Pavant Butte was demonstrated in a previous study with relatively low SNR 1989 AVIRIS data (Farrand and Singer, 1991), the lower albedo tephras could not be uniquely mapped out with that data set and the ability to do so in this study is attributed to the increase in instrumental SNR.

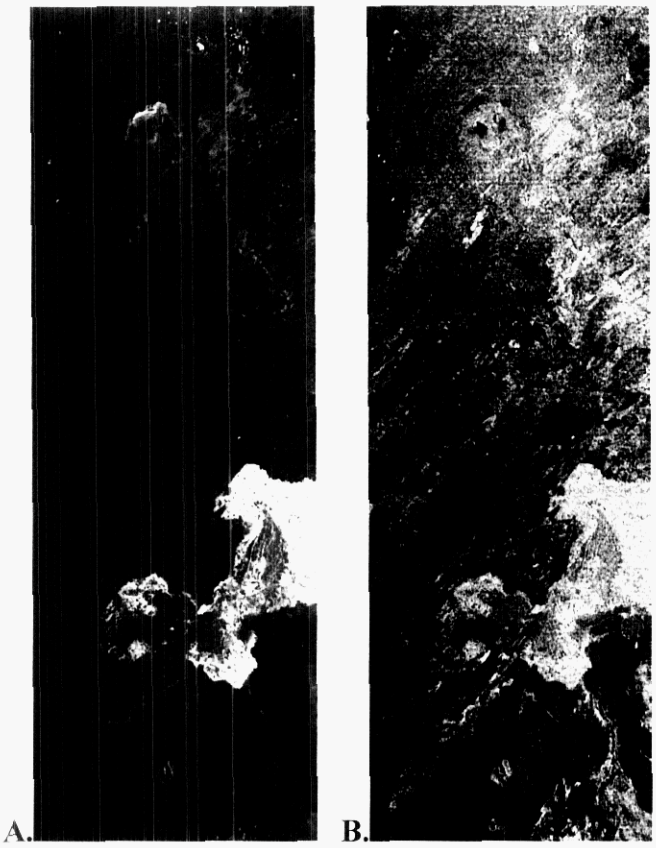

Figure 5. A. Fraction image for basalt flow image endmember as derived and run against the HSDC transformed data. **B**. Basalt fraction image as derived and run against non-albedo normalized data.

While the influence of albedo on SMA is profound, it should be noted that other processing techniques can be more insensitive to the effects of albedo. A spectral feature fitting approach such as is implemented in ENVI and which is a critical component of the USGS Tetracorder (Clark et al., 2003) software requires that the data have the continuum removed. Such a continuum removal is a *de facto* albedo normalization. The Spectral Angle Mapper technique (Kruse et al., 1993) is also insensitive to albedo differences.

6.0 Conclusions

The ability to map low albedo materials in AVIRIS data was demonstrated in this study. The materials of interest in this investigation were volcanic lava flows and tephras of the Black Rock Desert of west central Utah. It was demonstrated that image endmember spectra selected by iterative SMA are skewed towards high albedo materials. Hence, even a major low albedo component in the scene, such as the basalt flow in the Pavant Butte scene, that is readily apparent to the observer in color composites is not a required endmember in iterative SMA of non-albedo normalized data. Forcing the issue, and including such a low albedo endmember in SMA of the non-albedo normalized data, results in a fraction image in which there is low contrast between the target endmember and the background (Figure 5). A better representation of what materials in the scene are truly spectrally unique is obtained by conducting iterative SMA on albedo normalized data. In this study, the HSDC transformation (Pouch and Campagna, 1990) was used to remove albedo differences. Running SMA, or a related technique such as FBA, on the albedo normalized data also serves to increase the contrast between target and background in the the resulting fraction image.

By using the high SNR 2002 AVIRIS data and the HSDC transformation, it was demonstrated that even the low albedo, relatively spectrally featureless poorly palagonitized tephras associated with tuff rings and portions of tuff cones could be uniquely mapped. These materials could not be uniquely identified in an earlier study that was conducted using 1989 flight season AVIRIS data (Farrand and Singer, 1991).

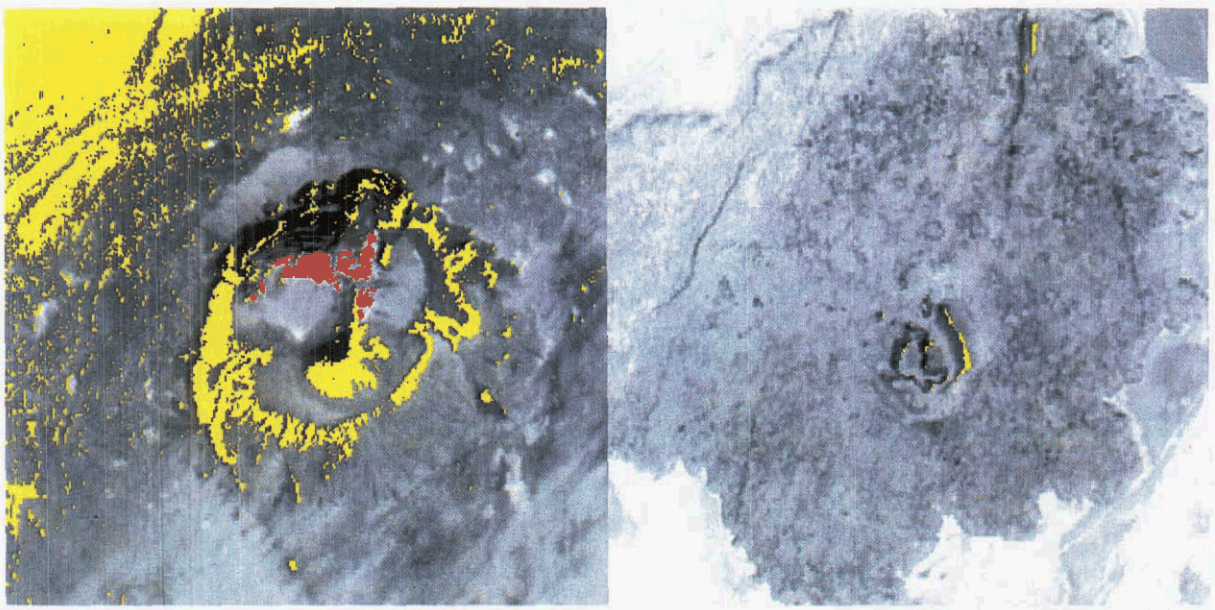

Figure 6. 1.7 μm band with overlay of highest (> 0.4) fractions of highly palagonitized tuff (red) and poorly palagonitized tuff and ash (yellow) over Pavant Butte (left) and Tabernacle Hill (right). Note the absence of highly palagonitized tuff at Tabernacle Hill.

7.0 Acknowledgements

Thanks to the AVIRIS team for the collection and pre-processing of the Pavant Butte AVIRIS data. Thanks to Dr. A.F.H. Goetz and Eric Johnson of the Center for Study of Earth from Space at the University of Colorado for assistance in running HATCH on the AVIRIS data. This work was supported in part by NASA grant NAG5-10577.

8.0 References

Adams, J.B., M.O. Smith, and A.R. Gillespie, 1993, Imaging spectroscopy: Interpretation based on spectral mixture analysis. In *Remote Geochemical Analysis: Elemental and Mineralogical Composition*, edited by C.M. Pieters and P.A.J. Englert (New York: Cambridge University Press), pp. 145-166.

Boardman, J.W., 1999, Precision geocoding of low altitude AVIRIS data: Lessons learned in 1998. *Proc. 8th JPL Airborne Earth Science Workshop*, (R.O. Green, Ed.), JPL Pub. 99-17, Jet Propulsion Laboratory, Pasadena, California, pp.63-68.

Boardman, J.W., 1998, Post-ATREM polishing of AVIRIS apparent reflectance data using EFFORT: A lesson in accuracy versus precision. *Proc. 7th JPL Airborne Earth Science Workshop*, (R.O. Green, ed.), JPL Publication 97-21, Vol. 1, Jet Propulsion Laboratory, Pasadena, California, pp 53.

Clark, R.N. et al. (7 others), 2003, Imaging spectroscopy: Earth and planetary remote sensing with the USGS Tetracorder and expert systems. *J. Geophys. Res.* (in press), http://speclab.cr.usgs.gov/PAPERS/tetracorder.

Farrand, W.H. and J.C. Harsanyi, 1997, Mapping the distribution of mine tailings in the Coeur d'Alene River Valley, Idaho through the use of a Constrained Energy Minimization technique. *Rem. Sens. of Env.* **59**, 64-76.

Farrand, W.H. and R.B. Singer, 1992, Alteration of hydrovolcanic basaltic ash: Observations with visible and near-infrared spectrometry. *J. Geophys. Res.* **97**, 17,393-17,408.

Farrand, W.H. and R.B. Singer, 1991, Spectral analysis and mapping of palagonite tuffs of Pavant Butte, Millard County, Utah. *Geophys. Res. Letters* **18**, 2237-2240.

Green, R.O. and B. Pavri, 2002, AVIRIS in-flight calibration experiment results for 2001, *Proc. 11th JPL Airborne Earth Science Workshop*, (R.O. Green, Ed.), JPL Pub. 03-4, Jet Propulsion Laboratory, Pasadena, California, pp. 125-137.

Green, R.O., J.E. Conel, V. Carrere, C.J. Bruegge, J.S. Margolis, M. Rast, and G. Hoover, 1990, Determination of the in-flight spectral and radiometric characteristics of AVIRIS, *Proc. Second Airborne Visible/Infrared Imaging Spectrometer (AVIRIS) Workshop*, (R.O. Green, Ed.), JPL Pub. 90-54, Jet Propulsion Laboratory, Pasadena, California, pp. 15-34.

Kruse, F.A., A.B. Lefkoff, J.W. Boardman, K.B. Heidebrecht, A.T. Shapiro, P.J. Barloon, and A.F.H. Goetz, 1993, The Spectral Image Processing System (SIPS)- Interactive visualization and analysis of imaging spectrometer data. *Remote Sens. Env.*, **44**, 145-164.

Oviatt, C.G. and W.P. Nash, 1989, Late Pleistocene basaltic ash and volcanic eruptions in the Bonneville basin, *Utah. Geol. Soc. America Bull.*, **101**, 292-303.

Pouch, G.W. and D.J. Campagna, 1990, Hyperspherical direction cosine transformation for separation of spectral and illumination information in digital scanner data. *Photogram. Eng. And Remote Sens.*, **56**, 475-479.

Qu, Z. A.F.H. Goetz, and K.B. Heidebrecht, 2000, High-accuracy atmosphere correction for hyperspectral data (HATCH), *Proc. 9th JPL Airborne Earth Science Workshop*, (R.O. Green, Ed.), JPL Pub. 00-18, Jet Propulsion Laboratory, Pasadena, California, pp. 373-380.

RSI, 2002, ENVI version 3.5 User's Guide.

Smith, M.O. et al., 1994, A new approach to determining spectral abundances of mixtures in multispectral images. *Proc. IEEE Geosci. Remote Sens. Symp., IGARSS '94.*

Wohletz K.H. and M.F. Sheridan, 1983, Hydrovolcanic explosions II. Evolution of basaltic tuff rings and tuff cones. *Am. J. Sci.*, **283**, 385-413.

Unsupervised Change Detection for Hyperspectral Images

Michael Frank[1] and Mort Canty[2]

1. Introduction

Change detection is a central task in the field of remote sensing. Detection of anthropogenic or natural impacts on landcover is essential for many environmental studies. On the regional to global scale, only multitemporal remote sensing is capable of monitoring landcover changes caused by short-term phenomena such as fire hazards and seasonal vegetation change, or long-term phenomena such as urban development and desertification in a practical way. A variety of change detection techniques has been developed for multispectral satellite and airborne imagery, including arithmetic operations, methods of principle component analysis as well as post-classification comparison and multitemporal classification [Singh, 1989], [Roberts et al., 1998a], [Yuan et al., 1998]. Spectral change detection techniques rely on the principle that a difference exists in the spectral response of a pixel on two dates if the biophysical material within the instantaneous field of view (IFOV) has changed between these dates [Jensen, 1996]. Hyperspectral change detection has many advantages over multispectral data in detecting and discriminating surface properties because it provides a continuous spectrum across a range in wavelengths [Green et al., 1998]. Nevertheless, only few attempts have been made for change detection based on hyperspectral images [Wiemker et al., 1997]. Until recently, the main limiting factor on the employment of hyperspectral sensors in change detection studies has been inadequate multitemporal coverage [Garcia and Ustin, 2001]. But with the launch of the hyperspectral sensor Hyperion [EO1, 2000] and the growing number of hyperspectral airborne sensors, more of these images may be available soon, and with them a greater need for hyperspectral change detection methods. Past investigations mainly focused on the use of hyperspectral change detection for vegetation. Garcia (2001) [Garcia and Ustin, 2001] and Roberts (1999) [Roberts et al., 1997] use spectral mixture analysis to identify changes between soil, green vegetation (GV) and non-photosynthetic vegetation (NPV). But this involves time-consuming pre-processing and endmember selection to extract the amount and kind of changes depending on the selected classes. Other researchers used vegetation indices for change purposes [Chen et al., 1998], [Gamon and Qiu, 1999]. But all of these methods only considered specific changes. None of these methods accounts for general purpose monitoring, which is often needed to interpret the different changes in a global context. For example, changes in vegetation may often be due to anthropogenic influences. However, as multitemporal hyperspectral coverage increases even in those areas where no or little ground truth data is available the need for robust unsupervised change detection methods will be more evident than before.

The purpose of this study is to detect seasonal vegetation dynamics in the Santa Monica Mountains using an unsupervised hyperspectral change detection approach. Seasonal vegetation dynamics in arid and semi-arid areas are largely regulated by the availability of water. But climatic shifts and anthropogenic influences may also have a major impact on seasonal fluctuations. Therefore it is important to understand how these properties interact to predict long-term environmental consequences of climate and land use changes on ecosystem function and sustainability [Ustin et al., 1998]. However, detecting vegetation dynamics in the absence of land cover change is more challenging then standard land cover analyses because of the subtle community response [Garcia and Ustin, 2001]. Therefore we investigate the usefulness of a relatively new unsupervised change detection procedure for hyperspectral images. The so-called multivariate alteration detection (MAD) technique proposed by Nielsen and Conradsen (1998) [Nielsen et al., 1998]. In past studies this method has been successfully applied to multispectral images [Canty and Niemeyer, 2002], [Niemeyer et al., 1999], [Nielsen, 1996]. Here it was used to highlight seasonal changes in bitemporal Airborne Visible/ Infrared Imaging Spectrometer (AVIRIS) images from the Santa Monica Mountains (California). We applied the algorithm to selected bands as well as to all bands to test the usefulness of this method. The MAD bands were then examined to identify the quantity and the quality of changes. The results were compared with a derivative-based green vegetation index (DGVI) proposed by Chen and Elvidge (1998) [Chen et al., 1998] and a spectral mixture analysis (SMA) [Ustin et al., 1993] to provide a basis for comparison with other studies.

[1] *Geographisches Institut der Rheinischen Friedrich-Wilhelms Universität, Bonn, Germany* **(uzs5or@uni-bonn.de)**
[2] *Forschungszentrum Jülich GmbH, Germany* **(m.canty@fz-juelich.de)**

2. Methods

2.1 Study Site

The study site was located in the Santa Monica Mountains (California, USA). The range extends 70 km westward from the City of Los Angeles to Ventura, along the Pacific coast. Elevation ranges from sea level to about 900 m. This region is characterized by a Mediterranean climate, having cool, wet winters and hot, dry summers. The mean annual precipitation is 600 mm per year mainly falling between December and April. Temperatures exceed 35°C in the summer but seldom drop below 10°C in the winter. The rough, discontinuous, mountainous terrain is mostly dominated by chaparral vegetation communities, including drought-senescent "soft" chaparral (coastal sage scrub) and evergreen "hard" chaparral [Barbour and Major, 1990]. Hard chaparral (dominated by *Ceanothus spp.* and *Adenostoma fasciculatum*) is mainly distributed at higher elevations on the interior side of the range. Soft chaparral (dominated by *Salvia* and *Eriogonum spp.* and *Artesemia californica*) is more common in the coastal area at lower elevation but does also occur in isolated patches at higher elevation on outcrops of shallow or fine textured soils [Holland and Keil, 1967]. However, vegetation patterns are complicated by the complex spatial distribution of chaparral species due to steep topographic gradients, variable fire histories, a complex landownership and different soil types [Roberts et al., 1998b].

2.2 AVIRIS Data

AVIRIS collects spectra in the wavelength range from 390 to 2500 nm in 224 bands with a nominal spectral response of 10 nm [Green et al., 1998]. The sensor is mounted on an ER-2 aircraft, flying at an elevation of approximately 20 km resulting in an IFOV of 20 m on the ground. A typical AVIRIS scene consists of 614 * 512 pixel (~ 11 km * 8 km).

Bitemporal AVIRIS data sets were acquired over the Santa Monica Mountains on 23 October 1996 and on 7 April 1997. The data presented here were obtained from flight-lines *f970407t01p02, run 06, scene 04* and *f961023t01p02 run 04, scene 05 and 06,* centered over Point Dume, California (34 °5`N, 118 °40`W). The images from 1996 were acquired 3 days after the Calabasas fire at the end of the dry Mediterranean summer, whereas the 1997 image represents a period of spring growth.

2.3 Preprocessing

Atmospheric correction was done using the MODTRAN 3 radiative transfer code to process the AVIRIS radiance data to reflectance. To retrieve apparent surface reflectance a method proposed by Green et al. [Green et al., 1993], Roberts et al. [Roberts et al., 1997] was applied on the MODTRAN corrected images. This model accounts for a spatially variable atmosphere, such as found over mountainous terrain. The images from fall 1996 were then mosaicked to cover the scene from spring 1997.

A tedious task associated with change detection is the registration of the images involved, in particular the setting of ground control points (GCPs). Registration errors will tend to reduce the accuracy of any digital change detection effort. It is essential that registration accuracies should be on the order of half a pixel or less, to avoid false change signals as much as possible. A typical problem of hyperspectral imagery recorded with airborne line scanners is that normal registration techniques like polynominal fitting yield accuracies of some pixels at best. This displacement is caused by the varying flight tracks of the aircraft (in contrast to satellites) and the usually large swath angles of airborne scanners which allow for oblique viewing angles. Therefore, imagery from airborne scanners in general requires locally adaptive transformation functions [Wiemker et al., 1997]. For the image-to-image registration, the scene from 1997 was used as base image and a thin plate spline model (TPS) was applied to compute the warping transformation [Geomatics, 1997]. This model computes, in addition to a global transformation, local interpolation functions between the GCPs. To ensure an accurate change detection registration, 400 GCPs were manually digitized. 150 GCPs were selected as check points to compute the root mean square error (RMS) of the transformation. The overall accuracy of the registration was about 0.41 pixels.

In order to preserve the spectral characteristics of the data as much as possible resampling was done using the nearest neighbor method. For further processing, 165 AVIRIS bands were selected and a sea mask was applied to the co-registered AVIRIS images.

2.4 Multivariate Alteration Detection (MAD)

The MAD procedure is an application of a classical statistical transformation referred to as canonical correlation and will briefly be described here. In general, hyperspectral imagery for monitoring purposes is recorded

by multitemporal overflights over the same land area. We represent hyperspectral pixel intensities measured at two different times by random vectors X and Y:

$$X = \begin{pmatrix} X_1 \\ \vdots \\ X_N \end{pmatrix}, \qquad Y = \begin{pmatrix} Y_1 \\ \vdots \\ Y_N \end{pmatrix} \tag{1}$$

N being the number of spectral components, then we search for a linear transformation

$$u = a^T X = a_1 X_1 + \cdots a_N X_N, \tag{2}$$

$$v = b^T Y = b_1 Y_1 + \cdots b_N Y_N, \tag{3}$$

where the coefficients a_i and b_i $(i = 1... N)$ are as yet unspecified. In order to detect the changes between the two images, we calculate the difference $U - V$. As an advantage of this procedure all the information is combined into a single image, and one is free to choose the coefficients a_i and b_i in a suitable way. The MAD procedure determines these coefficients so that the positive correlation between U and V is minimised [Nielsen, 1994].

In fact, we search for a linear transformation such that the difference between the transformed vectors has maximum variance:

$$\mathrm{var}(u - v) = \mathrm{var}\left(a^T X - b^T Y\right) \rightarrow \text{Maximum} \tag{4}$$

subject to the constraint

$$\mathrm{var}(u) = \mathrm{var}(v) = 1 \tag{5}$$

Under these constraints we have:

$$\mathrm{var}(u - v) = \mathrm{var}(u) + \mathrm{var}(u) - 2\,\mathrm{cov}(u, v) = 2(1 - corr(u, v)). \tag{6}$$

Therefore, we seek vectors a und b, which minimizes the positive correlation $corr(u, v)$. Mathematically this involves the solution of a generalized eigenvalue problem [Anderson, 1984]. The MAD transformation is then described as:

$$\begin{pmatrix} X \\ Y \end{pmatrix} \rightarrow \cdots \begin{pmatrix} a_1^T - b_1^T \\ \vdots \\ a_N^T - b_N^T \end{pmatrix} \tag{7}$$

where a_i and b_i are the defining coefficients from a standard canonical correlation analysis. X and Y are vectors with mean zero.

As a result we obtain as many MAD bands as input channels, whereby the last MAD component has maximum spread in its pixel intensities and, ideally, maximum change information. The second-to-last component has maximum variance subject to the condition that the pixel intensities are statistically uncorrelated with those in the first component, etc. Figure 1 shows a scatterplot of MAD1 vs. MAD2 for two AVIRIS scenes. The components are seen to be uncorrelated and approximately Gaussian. Assuming that different kinds of changes will generally be

uncorrelated with one another, these changes will be distributed among different MAD components. Noise will be concentrated in lower order components [Canty et al., 2001].

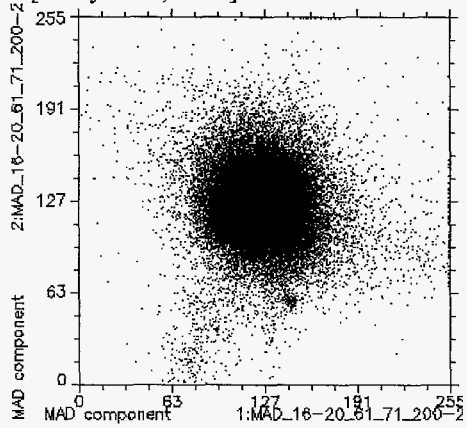

Figure 1: Scatterplot MAD1 vs. MAD2.

The MAD procedure is invariant to linear scaling. Therefore, it is insensitive to, for example, differences in gain and offset settings in a measuring device, and to the application of radiometric and atmospheric correction schemes that are linear in the digital numbers (DN) of each image band [Nielsen, 1999]. The MAD method can also be applied on any spatial and/or spectral subset of the full data set to focus the analysis in any desired manner. For specific applications, certain wavelength bands may be selected, whereby for general purpose monitoring, all spectral bands can be taken into account (see equation 2 and 3).

The resulting MADs can qualitatively be interpreted by

- ***visual interpretation***
- ***magnitude and direction of the changes***
- ***correlation with the original AVIRIS bands***

Furthermore the MAD method can be computed completely automatically because the calculation of the transformation is solely determined by the statistical properties (spectral dispersion matrices) of the original image data [Canty et al., 2001].

For cases where many spectral bands are to be used, pre-processing via the MNF (minimum noise fraction) transformation and/or post-processing by means of a MAF (minimum/maximum autocorrelation factor) transformation could be useful [Nielsen et al., 1998].

3. Results and Discussion

In unsupervised change detection studies, where little or no ground truth data are available, it is very useful to get a rough estimation of the expected changes. Besides visual interpretation this can be done by using some fundamental image statistics. Therefore the mean and the standard deviations of both images were computed for every band and compared with one another to provide insight into the type of process that may have produced the changes (Figure 2).

In Figure 2(b) the AVIRIS scene of October shows higher spectral variations in the NIR/SWIR. In addition, the mean signature of the AVIRIS scene of April (Figure 2(a)) shows a more pronounced red edge, chlorophyll and water absorption as well as lower mean values in the NIR and SWIR compared with the scene from October. On the basis of visual examination and due to the fact that both scenes are mainly covered with vegetation the signatures in the figure could be interpreted as a subsequent drying of the vegetation from April to October with an increasing amount of NPV and Soil at the expense of GV.

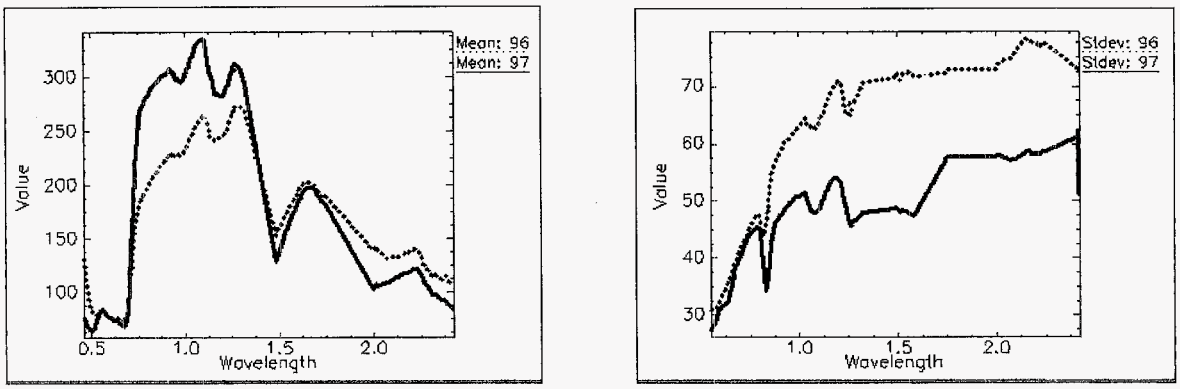

(a) mean **(b)** standard deviations

Figure 2: Mean **(a)** and standard deviations **(b)** from April 1997 (thick line) and October 1996 (dotted line) calculated over all AVIRIS bands.

The MAD method was applied to the co-registered images using:

(i) ***vegetation specific bands***

(ii) ***MNF bands***

(i) Wavelength regions from 673-702 nm (chlorophyll absorption), 770-818 nm (rededge shoulder), 1173-1211 nm (plant water absorption), 2088-2138 nm (ligno-cellulose absorption) and 2288-2338 nm (ligno- cellulose absorption) were selected as input channels for the MAD method in order to enhance these phenological changes as much as possible. The AVIRIS scene from April was selected as the base image in the MAD transformation. In order to detect the subtle vegetation dynamics we applied manual thresholding with 1.5 Standard deviations from the mean for the discrimination of change and no-change pixels. The MAD components are linearly stretched from mean minus and plus three standard deviations. The results of the MAD transformation (first 6 components) are shown in Figure 3. Maximum change areas are shown as white (positive changes) and black (negative changes) pixels. Gray areas indicate no change. Correlations between the change areas of the MADs and the original AVIRIS data (wavelength regions) are shown in Table 1.

Table 1: Correlation matrix of the MAD components with the original AVIRIS bands.

Date and wavelength region	MAD 1	MAD 2	MAD 3	MAD 4	MAD 5	MAD 6
April 7th (673-702 nm)	0.19	0.10	0.02	0.06	-0.08	0.00
April 7th (770-818 nm)	0.25	0.19	-0.07	0.09	-0.06	0.03
April 7th (1173-1211 nm)	0.15	-0.16	0.02	0.05	-0.09	-0.05
April 7th (2088-2138 nm)	0.16	-0.02	0.16	0.18	-0.00	-0.05
April 7th (2288-2338 nm)	0.11	-0.02	0.16	-0.19	0.02	-0.12
October 23rd (673-702 nm)	-0.11	0.10	-0.09	0.06	0.03	-0.04
October 23rd (770-818 nm)	-0.15	-0.21	-0.02	-0.08	0.04	-0.09
October 23rd (1173-1211 nm)	-0.25	0.19	-0.08	0.05	0.03	-0.07
October 23rd (2088-2138 nm)	-0.22	0.08	-0.28	0.16	0.08	0.01
October 23rd (2288-2338 nm)	-0.24	0.08	-0.22	0.28	0.09	-0.05

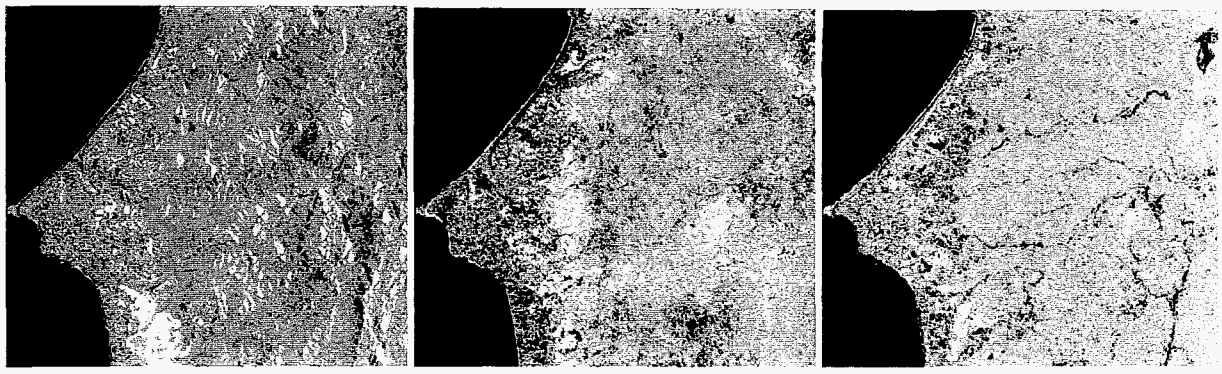

(a) MAD 1 **(b)** MAD 2 **(c)** MAD 3

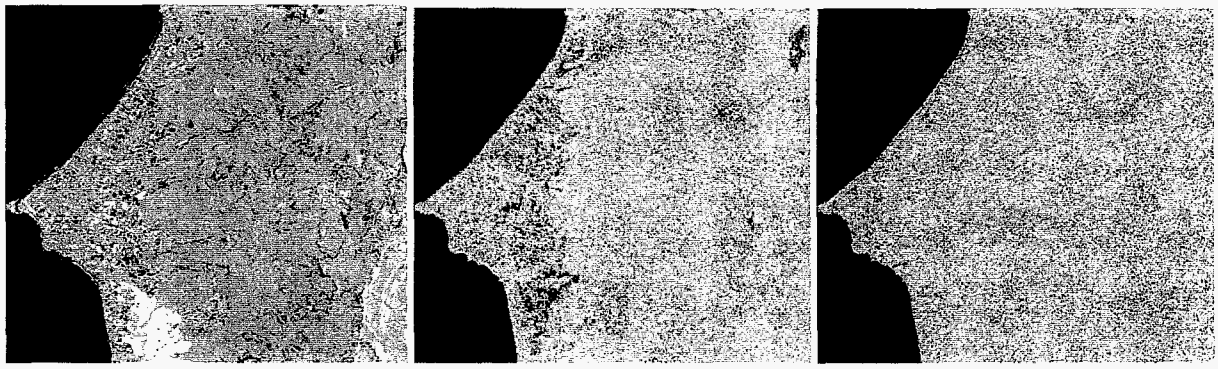

(d) MAD 4 **(e)** MAD 5 **(f)** MAD 6

Figure 3: MAD components 1 to 6 **(a-f)**.

As mentioned above, MAD1 shows the largest changes. The correlation of MAD1 shows a weighted mean of all channels with positive correlation in the October image and negative correlation in the April image. Therefore MAD1 is probably an indicator of shadow-induced changes. Actually, if we consider MAD1 (Figure 3(a)) * we can identify positive and negative changes mainly located in east-west valleys, which are strongly effected by intense shadowing. Positive changes at the Calabasas fire site (at the lower middle site of the image) are due to post-fire vegetation re-growth from October to April. In MAD2 we expect smaller changes that are furthermore uncorrelated to MAD1. Therefore more subtle changes, such as changes in phenology, are expected to occur in MAD2 and lower order MAD components. In fact MAD2 correlates with bands in the NIR and Red and could therefore be sensitive to changes in GV. Figure 3(b) shows high positive changes at the coastal region and in some isolated patches in the interior. These changes are consistent with the distribution of the soft chaparral communities. Soft chaparral is drought-deciduous and exhibits pronounced seasonal changes. Because seasonal vegetation dynamics in Mediterranean-climate ecosystems are mainly driven by the effect of water, most of the changes in the chaparral communities were basically due to loosing green leaves. Negative changes represent seasonal dynamics in hard chaparral communities. Most hard chaparral species are evergreen and undergo little seasonal senecense.

MAD3 and MAD4 have highest correlation in the SWIR regions and are presumably change indicators of NPV and/or soil. In general the change-enhanced data of MAD3 (Figure 3(c)) and MAD4 (Figure 3(d)) show small areas of changes in the soft chaparral areas. However, because of the larger changes at the Calabasas fire site, MAD4 seems to be more likely to represent changes in soil. Linear changes in MAD3 and MAD4 are probably due to poor registration of roads. MAD5 (Figure 3(e)) and MAD6 (Figure 3(f)) are uncorrelated with all bands in both years and show scanner noise.

Changes in the urbanized area apparent in all MAD components are probably due to registration errors, irrigation or seasonal planting of different flowers or plants. The golf course at the upper right shows high changes in some MAD components induced by irrigation and soil moisture. The changes at the coastline are caused by waves

* In this article all images are rotated 90 degrees clockwise.

and tides. Different changes at the Calabasas fire site best seen in (Figure 4(a)) are presumably due to the successive stages of post-fire vegetation re-growth.

In comparison to the SMA (not shown) we see a general agreement between the MAD components and the fraction images (GV, NPV, soil and shadow) of the SMA.

(ii) In order to concentrate and to visualize all spectral change information in one composite image the MAD transformation was performed based on a MNF transformation [Green et al., 1988] calculated from 165 AVIRIS bands. We used the first 10 MNF Bands describing 90% of the variance of the image data. Figure 4(a) shows the RGB image of MAD/MNF components two, three and four with the same decision threshold (MAD/MNF1 as an indicator of shadow induced changes was rejected).

To provide a basis for comparison with other methods a DGVI difference image (Figure 4(b)) with the same decision threshold as applied on the MAD transformation was computed [Chen et al., 1998]. In the MAD/MNF composite we can see more changes than in the DGVI difference image, especially in the housing estate areas, the Calabasas fire site and at the golf course.

In addition, a change probability based on a MAD transformation calculated from all 165 AVIRIS bands was performed. It was calculated using the sum of standardized, squared MADs [Canty et al., 2003] (see equation 8):

$$\sum_{i=1}^{N}\left(\frac{MAD_i}{\sigma MAD_i}\right)^2 \tag{8}$$

The resulting image (Figure 5) is approximately chi-square distributed with six degrees of freedom describing a change probability of 95%.

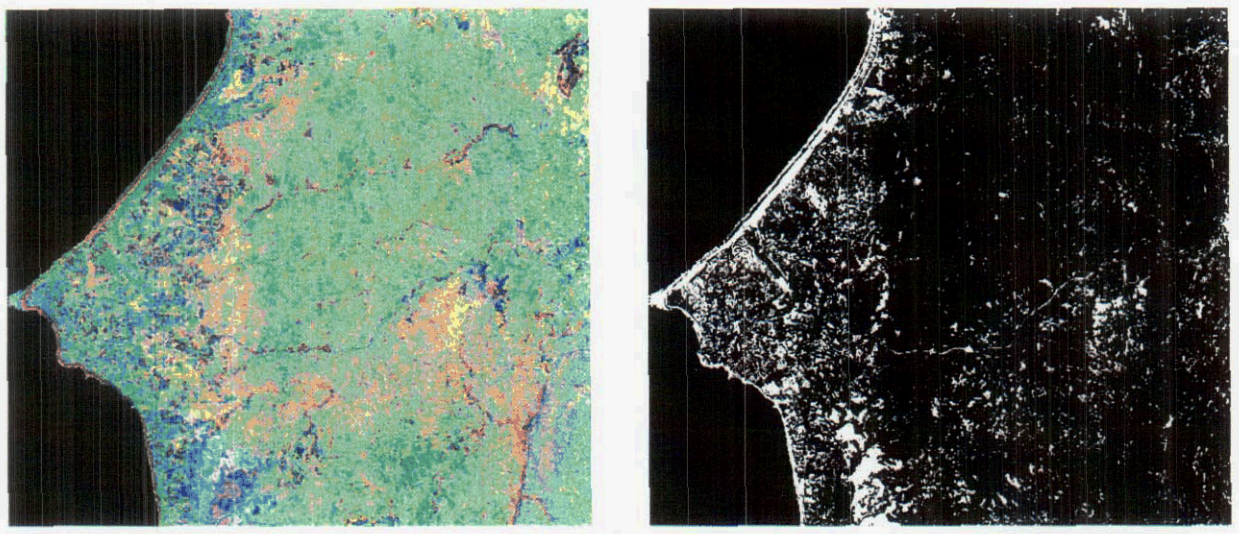

a) MAD/MNF RGB composite image with R=*MAD/MNF2*, G=*MAD/MNF3*, B=*MAD/MNF4*

(b) DGVI change mask

Figure 4: Comparison between MAD/MNF and DGVI.

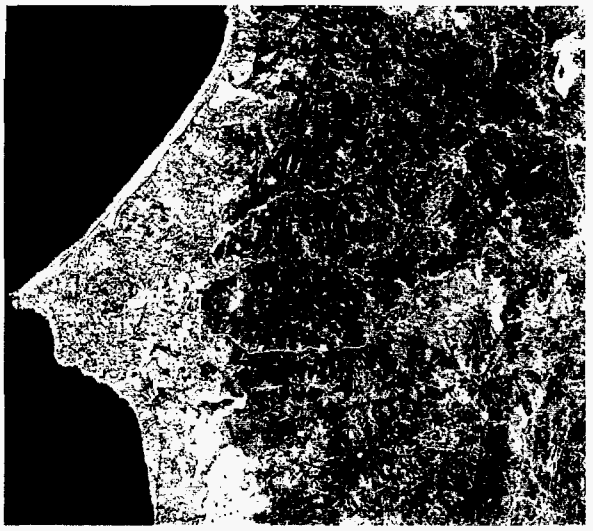

Figure 5: MAD change probability. White areas represent changes with a probability of 95%.

4. Conclusion

The applicability of the MAD method to hyperspectral, bitemporal, unsupervised change detection studies was demonstrated and an interpretation approach based on the correlation matrix was given. The MAD transformation was applied on bitemporal AVIRIS images of the Santa Monica Mountains to detect seasonal changes. The method was performed on selected bands, MNF bands as well as to all bands. The main changes observed are due to contrasting seasonal patterns of chaparral communities. Large change areas are located within soft chaparral communities and at the Calabasas fire site. The lowest changes occurred in areas covered with hard chaparral. In addition changes that can be related to registration errors, irrigation practices, shadow formation and other anthropogenic influences were also shown by the MAD method. As expected subtle vegetation changes occurred in the lower order MAD components whereas large changes like shadow formation are more apparent in the first MAD components.

We found the MAD transformation to be a good unsupervised change detection method for hyperspectral images. It can be applied on any spatial and/or spectral subset of the full data set and sorts different changes into different images. The MAD transformation is also comparable to other methods based upon DGVI or SMA. MAD tends to be robust against varying recording conditions at the time of the data acquisition and can be run completely automatically. But as for all change detection techniques a good registration accuracy is needed. On the other hand, interpretation of the MAD components is difficult when many spectral bands are used, so data reduction is sometimes necessary as a pre- and/or post-processing step. In general, the MAD transformation seems to be suitable for all kinds of change detection applications.

Acknowledgements

The Authors would like to thank Dar Roberts, Phil Dennison and Martin Herold from UCSB, Santa Barbara, for their provision of the atmospherically corrected images and for helpful suggestions. We also would like to thank Allan Nielsen (Technical University of Denmark, Lyngby) and Gunter Menz (University of Bonn) for helpful discussions.

References

[EO1, 2000]. Hyperion on EO-1. URL: *http://eo1. gsfc. nasa. gov.*

[Anderson, 1984] Anderson, T. W. (1984). An Introduction to Multivariate Statistical Analysis. New York. Wiley, New York, 2nd edition edition.

[Barbour and Major, 1990] Barbour, M. G. and Major, J. (1990). Terrestrial vegetation of California. Special publication No. 9. California Native Plant Society Press, University of California, Davis.

[Canty and Niemeyer, 2002] Canty, M. and Niemeyer, I. (2002). Analysis of digital satellite imagery. In Jasani, B. and Stein, G., editors, Commercial Satellite Imagery. A tactic in nuclear weapon deterrence, pages 67–78. Springer, Berlin Heidelberg.

[Canty et al., 2001] Canty, M., Niemeyer, I., Truong, B., et al. (2001). Change detection with multispectral satellite imagery: Application to nuclear verification. Proceedings of the International Symposium on Spectral Sensing Research, Quebec City. ISSSR.

[Canty et al., 2003] Canty, M., Nielsen, A. A., and Schmidt, M. (2003). Automatic radiometric normalization of multitemporal multispectral imagery. Remote Sensing of Environment, page in press.

[Chen et al., 1998] Chen, Z., Elvidge, C. D., and Groeneveld, D. P. (1998). Monitoring seasonal dynamics of arid land vegetation using AVIRIS data. Remote Sensing of Environment, 65(2): 255–266.

[Gamon and Qiu, 1999] Gamon, J. A. and Qiu, H. (1999). Ecological applications of remote sensing at multiple scales. In Pugnaire, F. I. and Valladares, F., editors, Handbook of functional plant ecology, chapter 23, pages 805–846. Marcel Dekker, New York.

[Garcia and Ustin, 2001] Garcia, M. and Ustin, S. L. (2001). Detection of interannual vegetation responses to climatic variability using AVIRIS data in a coastal savanna in California. IEEE Transactions on Geoscience and Remote Sensing, 39(7): 1480–1490.

[Geomatics, 1997] Geomatics, PCI. (1997). GCP Works User Manual. PCI Geomatics.

[Green et al., 1988] Green, A. A. et al. (1988). A transformation for ordering multispectral data in terms of image quality with implications for noise removal. IEEE Transactions on Geoscience and Remote Sensing, 26: 65–74.

[Green et al., 1993] Green, R. O., Conel, J. E., and Roberts, D. A. (1993). Estimation of aerosol optical depth and additional atmospheric parameters for the calculation of apparent reflectance from radiance measured by the airborne visible/ infrared imaging spectrometer (AVIRIS). Summaries of the Fourth JPL Geoscience Airborne Workshop, Wahington D. C., pages 73–76.

[Green et al., 1998] Green, R. O. et al. (1998). Imaging spectroscopy and the airborne visible/ infrared imaging spectrometer (AVIRIS). Remote Sensing of Environment, 65: 227–248.

[Holland and Keil, 1967] Holland, V. L. and Keil, D. J. (1967). California vegetation. California Polytechnic State University, San Luis Obispo.

[Jensen, 1996] Jensen, J. R. (1996). Introductory Digital Image Processing. Prentice Hall, New Jersey.

[Nielsen, 1994] Nielsen, A. A. (1994). Analysis of regularly and irregularly sampled spatial, multivariate, and multi-temporal data. PhD thesis, Informatics and Mathematical Modelling, Technical University of Denmark, Richard Petersens Plads, Building 321, DK-2800 Kongens Lyngby, Denmark.

[Nielsen, 1996] Nielsen, A. A. (1996). Change detection in multi-spectral, bi-temporal spatial data using orthogonal transformations. 8th Australasian Remote Sensing Conference, Canberra, Australia.

[Nielsen, 1999] Nielsen, A. A. (1999). Multi-channel remote sensing data and orthogonal transformations for change detection. In Kanellopoulos, I., Wilkinson, G., and Moons, T., editors, Machine Vision and Advanced Image Processing in Remote Sensing, pages 37–48. Springer, Berlin.

[Nielsen et al., 1998] Nielsen, A. A., Conradsen, K., and Simpson, J. J. (1998). Multivariate alteration detection (MAD) and MAF postprocessing in multispectral, bitemporal image data: New approaches to change detection studies. Remote Sensing of Environment, 64(1): 1–19.

[Niemeyer et al., 1999] Niemeyer, I., Canty, M., and Klaus, D. (1999). Unsupervised change detection techniques using multispectral satellite images. IEEE International Geoscience and Remote Sensing Symposium, Hamburg. IGARSS.

[Roberts et al., 1998a] Roberts, D. A., Batista, G., Pereira, J. L., et al. (1998a). Change identification using multitemporal spectral mixture analysis: Applications in eastern Amazonia. In Elvidge, C. D. and Lunetta, R., editors, Remote Sensing Change Detection: Environmental Monitoring Applications and Methods, chapter 9, pages 137–161. Ann Arbor Press.

[Roberts et al., 1998b] Roberts, D. A., Gardener, M., Church, R., et al. (1998b): Mapping chaparral in the Santa Monica Mountains using multiple endmember spectral mixture models. Remote Sensing of Environment, 65: 267–279.

[Roberts et al., 1997] Roberts, D. A., Green, R. O., and Adams, J. B. (1997). Temporal and spatial patterns in vegetation and atmospheric properties from AVIRIS. Remote Sensing of Environment, 62: 223–240.

[Singh, 1989] Singh, A. (1989). Digital change-detection techniques using remotly-sensed data. International Journal of Remote Sensing, 10(6): 989–1003.

[Ustin et al., 1998] Ustin, S. L., Roberts, D., and Hart, Q. J. (1998). Seasonal vegetation patterns in a California coastal savanna derived from advanced visible/infrared imaging spectrometer AVIRIS data. In Elvidge, C. D. and Lunetta, R., editors, Remote Sensing Change Detection: Environmental Monitoring Applications and Methods, chapter 10, pages 163–176. Ann Arbor Press.

[Ustin et al., 1993] Ustin, S. L., Smith, M., and Adams, J. B. (1993). Remote sensing of ecological processes: a strategy for developing ecological models using spectral mixture analysis. In Ehlringer, J. and Fields, C., editors, Scaling Physiological Processes: Leaf to Globe, chapter 19, pages 339–357. Academic Press, San Diego, Kalifornien.

[Wiemker et al., 1997] Wiemker, R., Speck, A., Kulbach, D., et al. (1997). Unsupervised robust change detection on multispectral imagery using spectral and spatial features. Proceedings of the Third International Airborne Remote Sensing Conference and Exhibition, 1 (Copenhagen): 640–647.

[Yuan et al., 1998] Yuan, D., Elvidge, C., and Lunetta, R. (1998). Survey of multispectral methods for land cover change analysis. In Elvidge, C. D. and Lunetta, R., editors, Remote Sensing Change Detection: Environmental Monitoring Applications and Methods, chapter 2, pages 21–39. Ann Arbor Press.

RELATIVE PERFORMANCE OF HATCH AND THREE OTHER TECHNIQUES FOR ATMOSPHERIC CORRECTION OF HYPERION AND AVIRIS DATA

Alexander F. H. Goetz,[1,2] Bruce Kindel,[1] Mario Ferri,[3] and Ethan Gutmann[1,2]

1.0 Introduction

The analysis of hyperspectral image data requires either the application of a radiative transfer model to correct radiance data from the sensor to reflectance or the simultaneous acquisition of surface spectral reflectance data to obtain correction factors for the solar irradiance and atmospheric transmission and scattering. The transmission, and in some cases the scattering, is highly location dependent because the major absorber is water vapor, a poorly mixed gas. Therefore, radiative transfer modeling is required to extend point measurements to the rest of the image.

Several models have been developed for atmospheric correction and four of them, ATREM (Gao et al., 1993), HATCH (Qu et al., 2003), ACORN (Miller, 2002) and FLAASH (Matthew et al., 2000) have gained prominence. The latter two are commercially available. In this paper we describe the results of using model and measured reflectances propagated to the top of the atmosphere using MODTRAN4 (Adler-Golden et al., 1999) and retrieved using the above models for different precipitable water vapor values. In addition, we have applied the models to AVIRIS and Hyperion data in order to compare the average reflectances obtained with each model, and compared the results for the derivation of spectral reflectance under a variety of precipitable water vapor conditions.

2.0 Approach

The methods used here are an extension of those described by Goetz et al. (2003). In order to eliminate the variables of sensor response and signal-noise ratio, and the uncertainties in ground reflectance in the comparison of models, the above-the-atmosphere radiance for several total precipitable water vapor values was modeled using MODTRAN4 (Adler-Golden et al., 1999). The modeled at-sensor radiance was entered into the four atmospheric correction models and the surface reflectance retrieved. MODTRAN4 was used to retrieve the modeled radiance to assure the validity of the at-sensor radiance values. A spectrum consisting of 50% reflectance values over the wavelength range 0.4-2.5 μm was input to MODTRAN4 for precipitable water vapor values of 0.5, 1.5, 2.5 and 4.5 cm. This artificial reflectance spectrum was created to emphasize the model differences since there were no slopes or absorption features normally associated with natural materials.

There are errors induced into the retrieval if the wavelength calibration of the sensor departs from that of the model. Reduction of at-sensor radiance to reflectance requires taking a ratio between the modeled and actual radiance that will accentuate wavelength calibration errors especially at the edges of atmospheric absorption bands (Qu et al., 2003). The differences between models as well as the calibration errors are the major contributors to the uncertainty in the retrieval of surface reflectance. The comparison of the ratio between two MODTRAN4 models, incorporating a wavelength shift in one of them, and the retrievals of the 50% spectrum discussed above make it possible to quantify the errors and their sources.

The individual models were applied to field spectra representing pure soil and pure vegetation cover at the four different precipitable water vapor amounts in order to examine the model behavior. This test was important because each model uses a different interpolation scheme and the results differ.

The models were also applied to AVIRIS and Hyperion images having varying average water vapor values. Water vapor images were created and compared. A mean reflectance spectrum was calculated for each entire image so that any sensor influences, such the signal-to-noise ratio, were minimized.

---

[1] Center for the Study of Earth from Space
[2] Department of Geological Sciences, University of Colorado, Boulder, Colorado, USA
[3] University of Naples, Italy

3.0 Results

3.1 Artifical Reflectance Spectra

Figure 1 shows the results of applying the ACORN, HATCH and FLAASH atmospheric corrections to retrieve the at-sensor radiance of a 50% reflectance target modeled using MODTRAN 4 (Adler-Golden et al., 1999). The differences are most notable at the edges of the water vapor absorption bands. There are no artifacts associated with inaccurate wavelength calibration, nor sensor signal-to-noise ratio characteristics. The departures from the 50% line correspond solely with differences between the atmospheric correction models and the MODTRAN 4 model. Retrieval of the reflectance from the at-sensor radiance using MODTRAN 4 produces the straight 50% line shown in Fig. 1. The differences among models become more pronounced as the water vapor amount is increased. At 4.5 cm precipitable water vapor the FLAASH model breaks down. This problem has been corrected in later versions of the program.

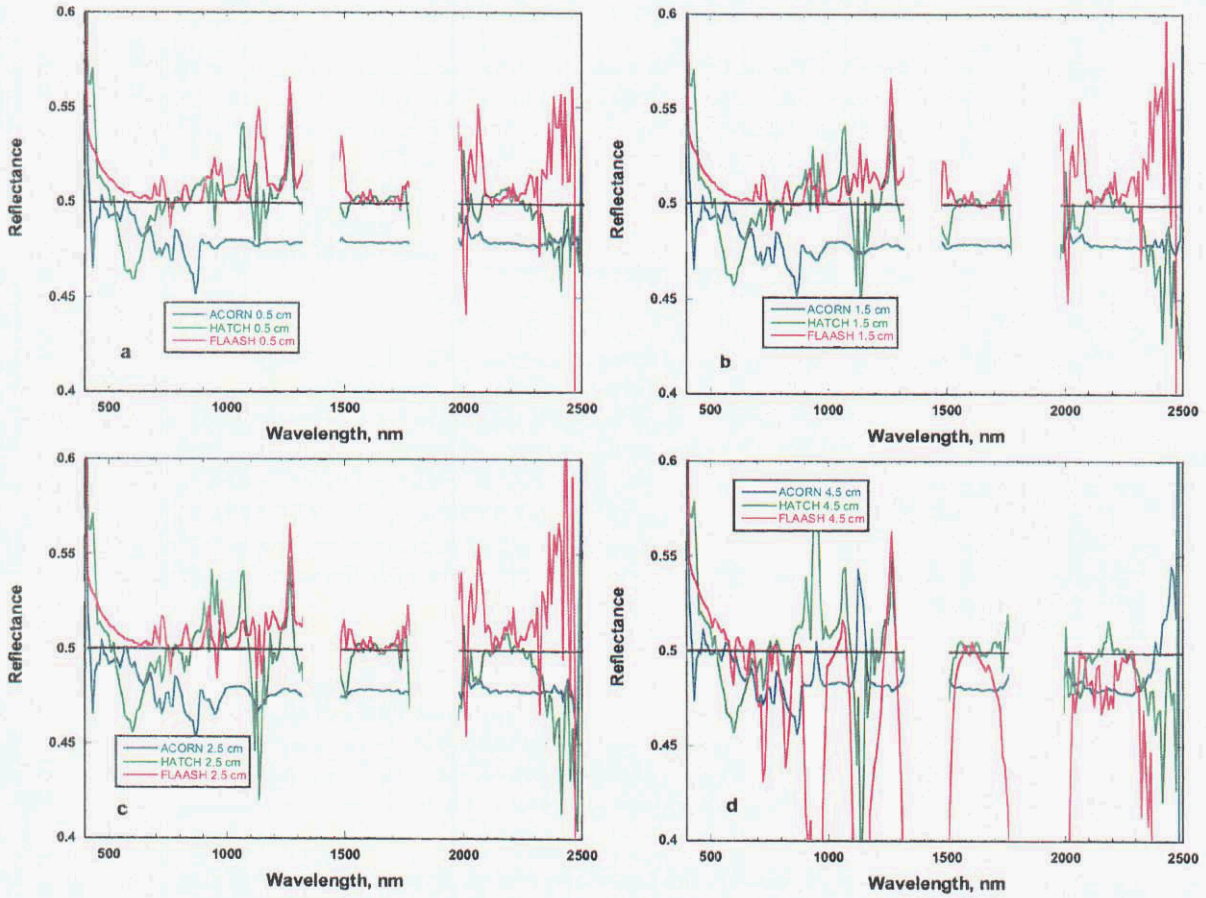

Figure 1. Model retrievals for varying total precipitable water vapor amounts. a) 0.5 cm; b) 1.5 cm; c) 2.5 cm; d) 4.5 cm. The gaps are associated with the saturated water vapor absorption features at 1380 and 1900 nm.

Sensor calibration errors lead to additional errors in the retrieval, particularly at the edges of sharp atmospheric or surface reflectance features. The errors are introduced through the process of ratioing the modeled at-sensor radiance with the measured radiance. Figure 2 shows the effects of wavelength calibration errors using a ratio of two MODTRAN 4 models convolved with the AVIRIS spectrometer point spread function and offset by 3 nm. The wavelength calibration error results in errors in reflectance of ± 20 % of the value at the edges of the sharp, unsaturated atmospheric absorption features caused by O_2, CO_2 and water vapor. Signal-to-noise ratio is important in the quality of the retrieved reflectance spectrum. Poor signal-to–noise ratio will produce artifacts at sharp absorption edges similar to those created by poor calibration shown in Fig. 2.

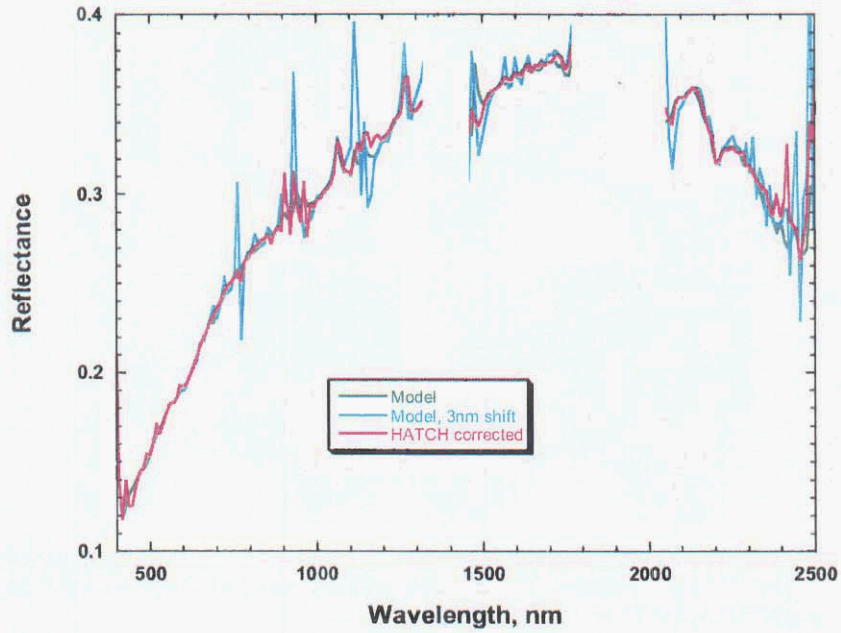

Figure 2. MODTRAN 4 model of sensor radiance from a soil surface that has been converted to reflectance using MODTRAN 4 (Model) and the same model but shifted to longer wavelengths by 3 nm. The results of the atmospheric model HATCH applied to the MODTRAN sensor radiance are shown in red.

3.2 Application to AVIRIS data

The atmospheric models were applied to AVIRIS images taken under different water vapor conditions. For comparison of the spatial quality of the water vapor effect removal, water vapor images were created. If the removal is complete, no surface albedo variability will be visible. In order to exclude the effect of sensor signal-to-noise ratio on the corrected reflectance, the entire reflectance image was averaged after the atmospheric correction was applied on a pixel-by pixel basis. Fig. 3 shows the water vapor images from the AVIRIS scene taken over Yerington, Nevada. The ATREM image (b) shows more albedo features and generally shows greater errors at high vapor values and in the presence of vegetation (Goetz et al., 2003). Fig. 4 shows the average reflectances as a result of the application of three atmospheric correction programs to correct the AVIRIS scene of Yerington, Nevada to.....???

Because the full scene is averaged, no sharp spectral reflectance features will be present. Any departure from a smooth reflectance curve is the result of an error in the model correction or an incorrect wavelength calibration. The HATCH algorithm automatically corrects for wavelength calibration errors up to ± 3 nm (Qu et al., 2003). There does not appear to be a significant wavelength calibration error because the reflectance errors at the edges of the sharp atmospheric absorption features are equivalent for each of the models.

An AVIRIS scene from Hawaii with a higher average water vapor content is shown in Figure 5.

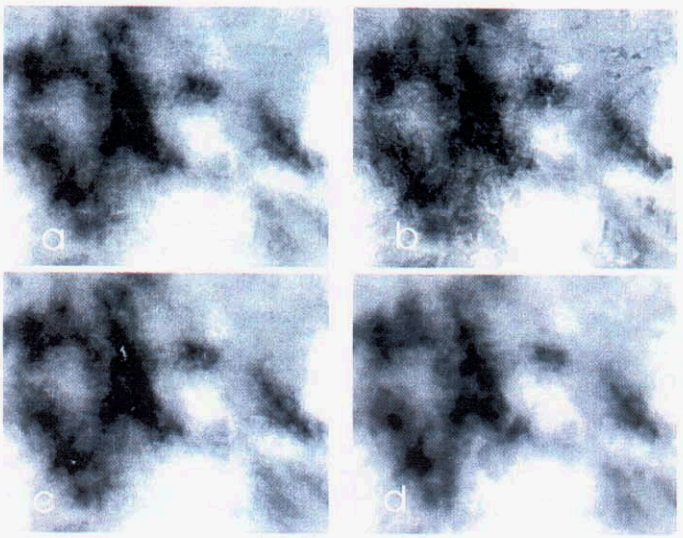

Figure 3. Water vapor images of Yerington, Nevada with average values of 0.69 cm precipitable water vapor. The models applied were a) ACORN; b) ATREM; c) FLAASH; d) HATCH

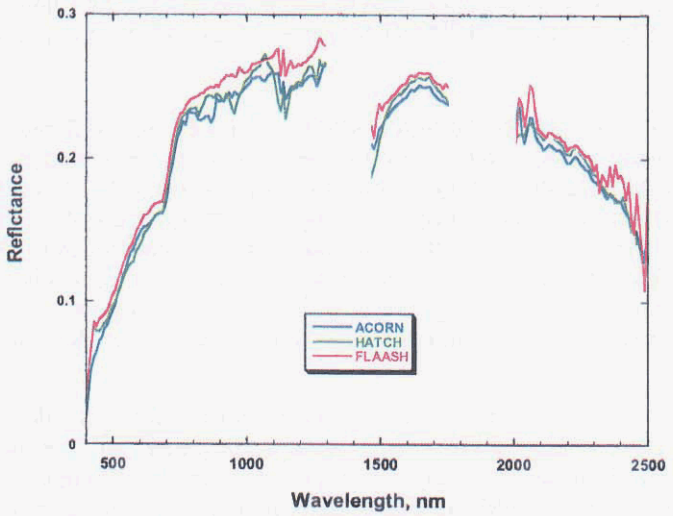

Figure 4. Reflectance derived from the Yerington scene using 3 different atmospheric correction models.

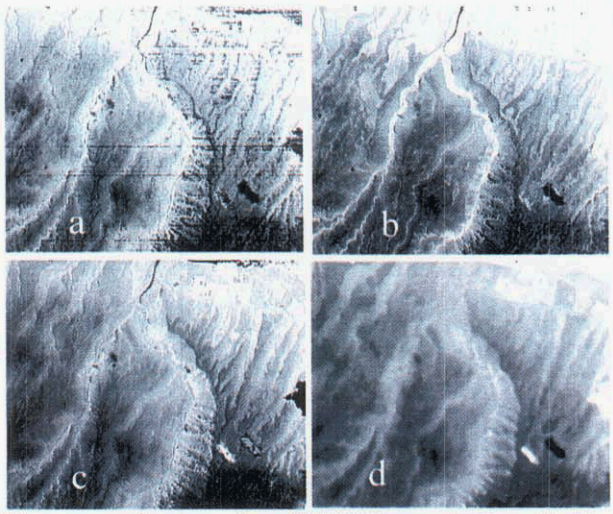

Figure 5. Water vapor images of an AVIRIS image in Hawaii. The average water vapor value is 2.21 cm. The models applied were a) ACORN; b) ATREM; c) FLAASH; d) HATCH

In this steep terrain the water vapor values are closely tied to the elevation giving the impression that the models are very sensitive to surface albedo. ATREM (b) looks the most different from the other three model images possibly reflecting higher sensitivity to vegetation cover differences. The whole-image reflectance retrievals are shown in Fig 6.

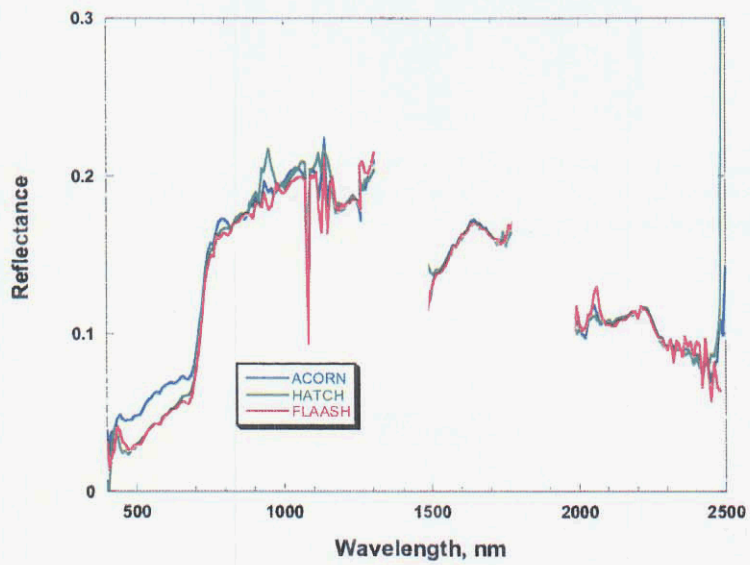

Figure 6. Reflectance averaged for the entire Hawaii scene for three correction models

The smoothest rendition of reflectance is given by ACORN but for an unknown reason the derived reflectance is considerably higher than from HATCH and FLAASH in the visible portion of the spectrum. FLAASH shows the greatest sensitivity to sharp atmospheric bands. HATCH exhibits a significant increase in reflectance around the 940 nm water vapor absorption band not shown by FLAASH or ACORN.

3.3 Application to Hyperion data

Hyperion (Pearlman et al., 2003) is a pushbroom imaging spectrometer that poses a different set of challenges for atmospheric correction. The 940 nm water vapor absorption, feature normally used to determine the column water vapor value for use in correcting the rest of the spectrum with the models, falls within the cross-over region between the two detector arrays. The signal-to-noise ratio is not high enough in this region to make an

accurate water vapor determination. As a result, the 1140 nm water vapor band is used. The difficulty here is that the calculation is more affected by the nearby deep 1200 liquid water feature in vegetation than the shallow 980 water feature near 940 nm (Goetz et al., 2003). An additional problem is the stability of the radiometric calibration and the inaccuracies in the pixel-to-pixel calibration precision leading to stripes in the images when they are enhanced by ratioing, principal components analysis or other means in which the least significant bits in the pixel values are utilized. Striping is also induced by atmospheric correction models because the small radiometric calibration errors are highlighted by ratioing the sensor radiance data with the modeled radiance. Additional artifacts are induced by sensor "smile" or the change in spectral calibration across the detector array. Smile is a characteristic of all pushbroom array systems and HATCH-2d was developed to compensate for smile by calculating the wavelength calibration for each column in the image (Qu et al., 2003). ACORN and FLAASH make use of only one wavelength calibration for each array.

Hyperion scenes having varying amounts of precipitable water vapor were processed using ACORN, HATCH-2d and FLAASH. Fig. 7 shows the water vapor images for a Hyperion scene of Yerington, Nevada. The average retrieved spectra are shown in Fig. 8.

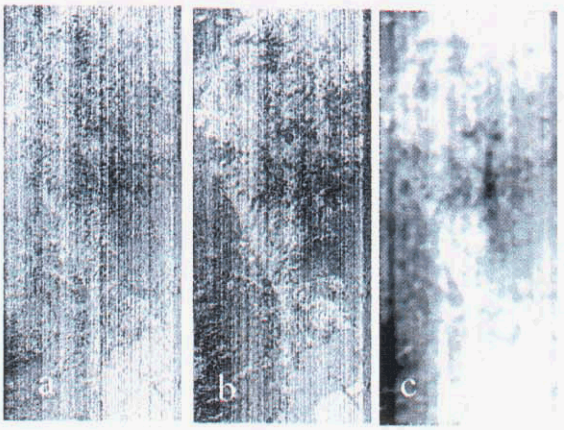

Figure 7. Water vapor images from the Hyperion scene of Yerington, Nevada. The models used were 1) ACORN; 2) FLAASH; 3) HATCH-2d. The average water vapor value is 1.26 cm.

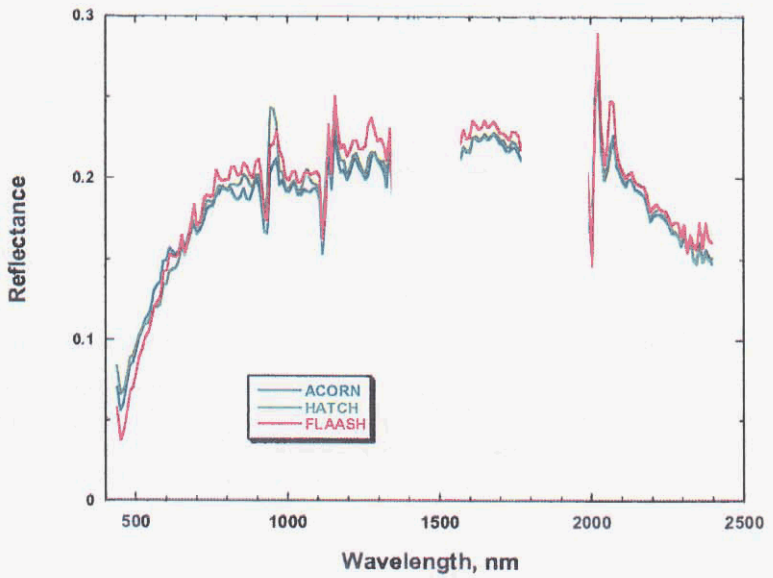

Figure 8. Reflectance spectra of the averaged Yerington, Nevada Hyperion scene.

The ragged look of the spectra is attributable to the column-to-column imprecision in radiometric calibration. In this plot the HATCH-2d column-by-column calibration was turned off. The smoothest rendition of reflectance appears to be from the ACORN model. All of the models show major departures from smooth behavior around 2050 nm, the position of two CO_2 absorption features. These features are most likely the result of wavelength calibration inaccuracies attributable to smile. In Fig. 9 the advantage of the HATCH-2d column-by-column calibration is demonstrated by switching the calibration option on. The 2050 nm CO_2 feature is significantly dampened as are some of the other water vapor band features.

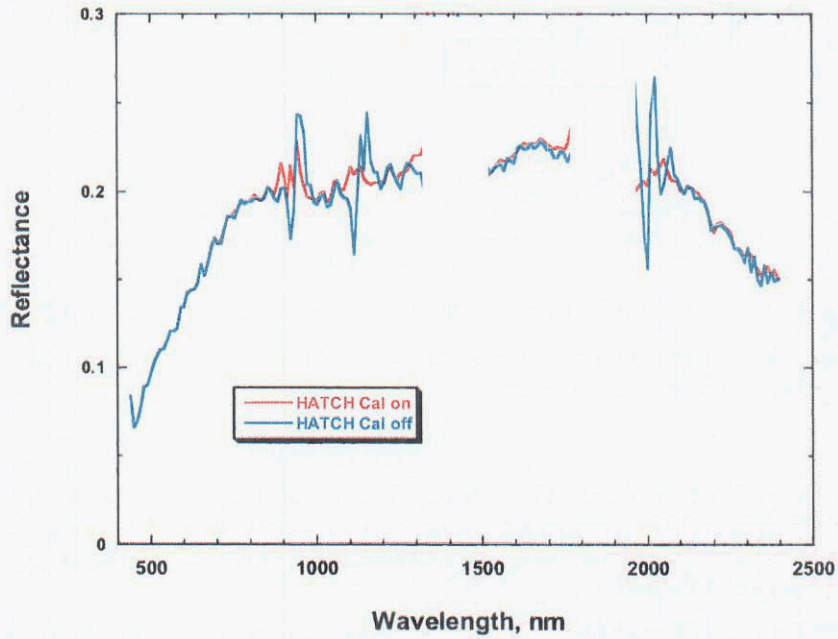

Figure 9. HATCH-2d derived reflectance of the Hyperion Yerington, Nevada scene. "HATCH Cal off" is the same curve "HATCH" shown in Fig. 8.

Figure 10 shows Table Mountain north of Boulder, Colorado. In this Hyperion scene the areas of dense vegetation were extracted and the reflectance values averaged after application of the models. Only HATCH-2d and ACORN results are shown in Fig 11.

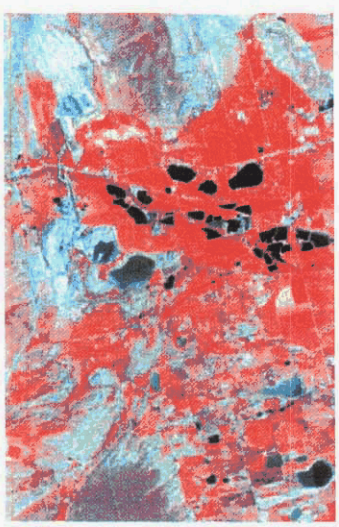

Figure 10. CIR composite of Table Mountain, Colorado. The average water vapor value was 2.6 cm.

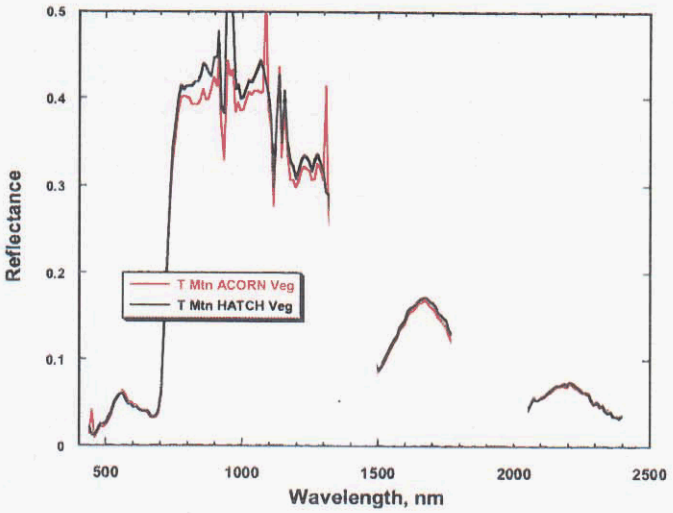

Figure 11. Average reflectances for the densely vegetated areas shown in Fig. 10.

HATCH-2d appears to provide a smoother result than ACORN in this case for the 900-1300 nm region. In the other regions the coincidence is almost perfect.

4.0 Conclusions

The results derived from artificial reflectance targets propagated through the atmosphere using MODTRAN 4 show that there are significant differences among the atmospheric correction models tested. The differences are equal to or greater than errors introduced by wavelength calibration or sensor noise. This result makes it impossible to know which model performs the best.

In retrievals from AVIRIS and Hyperion data there appears to be little to differentiate the models. In both cases the reflectances derived from scenes with higher water vapor contained more artifacts, or departures from a smooth reflectance curve.

Using HATCH-2d, with the column-by-column wavelength calibration enabled, appears to produce smoother reflectance spectra than when using an average spectral calibration for the entire array. The disadvantage is the increased computing time required.

5.0 References

Adler-Golden, S. M., M. W. Matthew, S. Bernstein, R. Y. Levine, A. Berk, S. C. Richtsmeier, P. K. Acharya, P. Anderson, J. W. Felde, J. Gardner, M. L. Hoke, L. S. Jeong, B. Pukall, A. J. Ratkowski, and H. K. Burke, H.K., 1999, Atmospheric correction for shortwave spectral imagery based on MODTRAN4, *Proceedings SPIE, Imaging Spectrometry V,* v. 3753, pp. 61–69.

Gao, B.-C., K.B. Heidebrecht, and A.F.H. Goetz, 1993, Derivation of Scaled Surface Reflectances from AVIRIS Data, *Remote Sens. Environ.*, vol. 44, 165–178.

Goetz, A.F.H., B.C. Kindel, M. Ferri, Z. Qu, 2003, HATCH: Results from simulated radiances, AVIRIS and Hyperion, *IEEE Transactions on Geoscience and Remote Sensing*, vol. 41, 1215–1222.

Matthew, M. W., S. M. Adler-Golden, A. Berk S. C. Richtsmeier, R. Y. Levin, L. S. Bernstein, P. K. Acharya, G. P. Anderson, G. W. Felde, M. P. Hoke, A. Ratkowski, H.-H. Burke, R. D. Kaiser, and D. P. Miller, 2000, Status of atmospheric correction using a MODTRAN4-based algorithm, *SPIE Proc. Algorithms for Multispectral, Hyperspectral, and Ultraspectral Imagery VI*, 4049:199–207.

Miller, C. J., 2002, Performance assessment of ACORN atmospheric correction algorithm, *Proceedings SPIE Algorithms and Technologies for Multispectral, Hyperspectral, and Ultraspectral Imagery VIII* ,v. 4725, pp. 438–449.

Pearlman, J.S., P. s. Barry, C.C. Segal, J. Shepanski, D. Beiso and S. l. Carman, 2003, Hyperion, a space-based imaging spectrometer, *IEEE Transactions on Geoscience and Remote Sensing*, vol. 41, 1160–1173.

Qu, Z., B.C. Kindel, A.F.H. Goetz, 2003, The High Accuracy Atmospheric Correction for Hyperspectral Data (HATCH) Model, *IEEE Transactions on Geoscience and Remote Sensing*, vol.41, 1223-1231.

FOREST INFORMATION PRODUCTS FROM AVIRIS AND HYPERION

David G. Goodenough,[1,2] Hao Chen,[1] Andrew Dyk,[1] Tian Han,[2] Sarah McDonald,[1,3]
Matthew Murdoch,[1] K. Olaf Niemann,[3] Jay Pearlman,[4] and Chris West[1]

1. Introduction

Hyperspectral remote sensing can provide forest information products for applications in forest inventory and forest chemistry. Forest inventory products include the ability to map forest species with high accuracy using the airborne AVIRIS sensor and the EO-1 satellite sensor Hyperion. Hyperion data were acquired in 2001 and 2002. Corresponding AVIRIS data were also acquired. Experiments were conducted to compare the accuracies of the data sets for mapping forest species. Bioindicators are also being developed for mapping nitrogen. Compression experiments were also conducted on Hyperion data to investigate the utility of compression in terms of classification accuracies for forest species. This paper reports on the Hyperion and AVIRIS analyses and the results of the compression experiments.

Ecosystem processes such as photosynthesis and nutrient cycling can be better understood by examining canopy biochemical content through analyzing chlorophyll, nitrogen, and lignin concentrations (Wessman, 1988). Detailed information derived from hyperspectral remote sensing data, such as chemicals present in the forest canopy, can be used to investigate indicators of forest health, known as bioindicators (Martin, *et al.*, 1998). Bioindicators can be used in forest management practices (Jacquemoud, 1996);(Adamus, 1995). Sources of stress in a forest ecosystem, such as nutrient deficiency, insect infestation and drought, may be examined using bioindicators that are detectable using remote sensing (Mohammed, 2000) and yet not visible to the human eye.

Various compression schemes have been suggested for acquisition, storage and distribution of hyperspectral remotely sensed data. Hyperspectral forestry applications that rely on the measurement of subtle variations in the spectral signature of the forest canopy can be affected by modification to the spectra induced by compression. As part of an experiment for the Canadian Space Agency (CSA), Hyperion data cubes acquired over the Greater Victoria Watershed District (GVWD) were compressed using the SAMVQ and HSOCVQ algorithms designed by CSA. Both the raw digital numbers (DN) and the radiance data were compressed using a compression ratio of 20:1 and were returned uncompressed. These data cubes were classified into forest species using the same supervised classification methodology used with the original data. Spectra and the classification accuracies from the compressed and uncompressed data were compared.

2. Data Collection

Under the NASA project Evaluation and Validation of EO-1 for Sustainable Development (EVEOSD), we have collected spaceborne and airborne hyperspectral remotely sensed imagery, as well as conducted extensive field reconnaissance, in the GVWD, located on Vancouver Island, British Columbia, Canada. Measurements of the foliar chemistry at this site have been collected over two years to correspond with image acquisitions. Both organic and inorganic chemistry measurements have been collected from this site.

Airborne Visible/Infrared Imaging Spectrometer (AVIRIS) data, acquired by NASA's ER-2 aircraft and EO-1 Hyperion data were used in this research. AVIRIS has the capability of capturing 224 contiguous spectral channels at approximately 10 nm intervals in the visible to near-infrared (400–2500 nm) portion of the electromagnetic spectrum (Green, 1998). The Hyperion sensor acquires 220 bands with a full-width half maximum of approximately 10 nm in the same wavelength regions as AVIRIS. The 20 m AVIRIS data were used in conjunction with 30 m EO-1 Hyperion data. Ground spectra, at 2.5 nm resolution, were collected using an Analytical Spectral Devices (ASD) at the time of image acquisition. Calibration sites consisted of a grassy field (bright target) and a deep-water lake (dark target). The ground spectra collected from the ASD were associated to corresponding AVIRIS and Hyperion data using Global Positioning Satellite (GPS) data collected along with the ground spectra.

[1]Pacific Forestry Centre, Natural Resources Canada, Victoria, British Columbia (dgoodeno@nrcan.gc.ca)
[2]Department of Computer Science, University of Victoria, Victoria, British Columbia
[3]Department of Geography, University of Victoria, Victoria, British Columbia
[4]Boeing Corporation, Seattle, Washington

3. Data Calibration

Data calibration was necessary for deriving species classification, for deriving forest chemistry, and for evaluating compression. Radiometric corrections of the Hyperion data were generated using the level 1B1 dataset from TRW, which was processed for smear correction, echo correction, background removal and bad pixel repair. Prior to further image processing, the data were corrected for destriping and desmiling as described by Han et al. (2002). The data were converted from radiance to reflectance using Environment for Visualizing Images (ENVI's) Fast Line-of-sight Atmospheric Analysis of Spectral Hypercubes (FLAASH) module based on MODTRAN4 radiation transfer code. Details of the geometric correction procedures are described in (Dyk, *et al.*, 2002). Geometric accuracies for the AVIRIS and Hyperion data were 10.1 m and 4.2 m, respectively. A force-fit function was created for each image using ground spectral data to calibrate reflectance values. The remotely sensed imagery, with the appropriate force-fit functions applied, were then used for forest classification and forest chemistry analysis.

4. Forest Classification

Species classification in the GVWD was performed using processed AVIRIS and Hyperion data. The Capital Regional District (CRD) provided a detailed forest cover GIS database to complement the chemical and field measurements made in EVEOSD for 54 plots. The forest cover layers were overlaid on 1 m orthophotos to delineate training areas for individual land cover types used in the classification. Forest and non-forest classes were selected based on definitions from the Canadian National Forest Inventory (NFI) photo plots (Dyk, 2001).

With the large number of bands in the hyperspectral data, a data reduction technique was necessary to achieve accurate estimates of the covariance matrices produced by the classification algorithms. The AVIRIS and Hyperion data were subsetted to 204 and 165 bands, respectively, to remove water absorption and low signal-to-noise bands. The data were then transformed using a Minimum Noise Fraction (MNF) method and reduced to a few channels. The AVIRIS data were reduced to twelve new channels, which were used in the classification. Due to the influence of smile in the Hyperion data, the first MNF channel was not used, leaving 11 channels for classification. The MNF channels from both sensors were run through a Maximum Likelihood Classification with a total of 17 classes defined. Overall classification accuracies (Table 1) for the AVIRIS data were 90.5% for the truth and 88.5% for the check or test data. Hyperion overall classification accuracies were 87.4% for truth and 81.6% for check data.

Table 1 - Detailed Classification Comparisons

	AVIRIS		Hyperion 1b (2-12)	
	Accuracy %		Accuracy %	
Class Label	Truth	Check	Truth	Check
Exposed land	100	87.5	100	100
Recent cuts<6 mo	99.2	100	100	97.3
Water	99.4	99.4	99.8	100.0
Shrub low	100	100	100	96.3
Old clear cuts	98.6	100	100	95.2
Farmer's field	100.0	97.6	100	100
Swamp	95.0	92.3	97.1	100
Red Alder	87.5	100	91.5	87.1
Hemlock 60% Dense	79.8	66.7	74.6	45.9
Hemlock 60% Open	93.0	78.8	91.1	52.2
Lodgepole Pine	88.0	89.7	87.7	79.6
Western Red Cedar 60%	88.2	N/A	83.3	N/A
DF Dense 60 yr	90.2	81.2	73.7	65.4
DF Dense 110 yr	71.8	73.3	79.9	73.6
DF Open 40 yr	90.3	75.0	70.8	63.9
DF Open 200+ yr	78.9	80.4	66.0	57.4
DF Sparse 40 yr	92.4	86.3	86.8	81.9
Overall accuracy	**90.5**	**88.5**	**87.4**	**81.6**

Results from the individual forest cover classification were aggregated and re-classified to produce a new set of forest cover percentages (Table 2). After aggregation, classification results for the sensors were 92.1% accuracy for AVIRIS and 90.0% accuracy for Hyperion. Image classification results are shown in Figure 1a-c. Classification results were verified with GIS reference data, field checks and ground plots.

Table 2 - Aggregated Classification Comparison

	AVIRIS	Hyp 1b (2-12)
Class Label	**Accuracy %**	**Accuracy %**
Exposed land	100	100
Water	99.4	99.8
Shrub low	99.4	100
Farmer's field	100	100
Swamp	94.5	97.1
Red Alder	89.4	91.5
Hemlock	88.8	83.0
Lodgepole Pine	89.4	87.7
Western Red Cedar	88.2	83.3
Douglas Fir	90.5	92.5
Overall accuracy with 70% of the training data	94.0	94.2
Accuracy with 30% of the test data	92.1	90.0

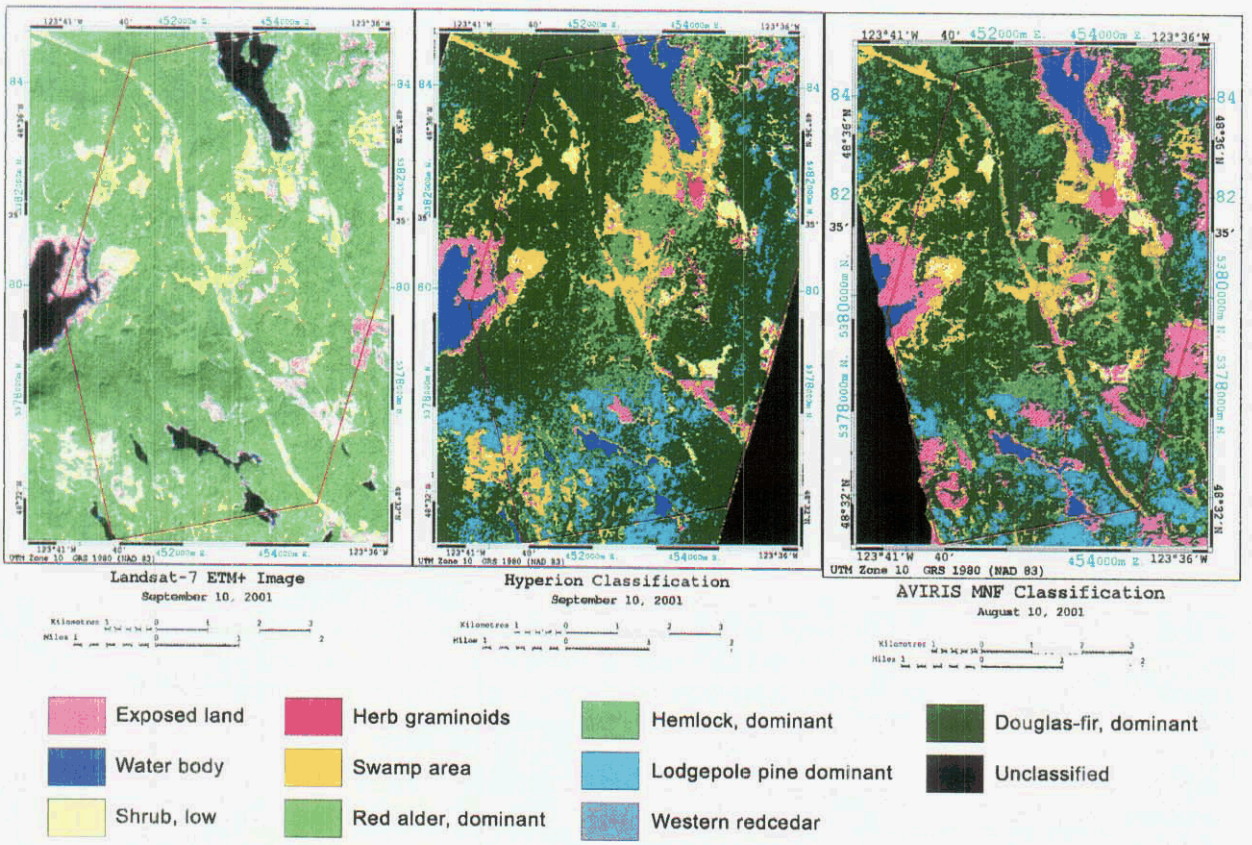

Figure 1a-c: Landsat-7 image (a) *left*, Hyperion classification (b) *middle* and AVIRIS classification (c) *right.*

5. Forest Chemistry and Bioindicators

Hyperspectral remote sensing provides a method of deriving forest chemistry. Canopy chemistry in the GVWD was examined using 20m AVIRIS data and compared with sampled chemistry measurements using multiple regression analysis. Canopy nitrogen content (N) was analyzed to derive a nitrogen distribution map of the study

site. In order to do so, the hyperspectral data were converted to absorbance and transformed to derivatives for use in regression analysis. Absorbance (A) was computed from reflectance (R) with the following equation (Smith, 2002):

$$A = \log_{10}(1/R)$$

Derivatives of reflectance were also computed. Derivatives provided a measure of the slope of the spectral curve at every point. The resulting derivative spectrum was comprised of peaks and valleys corresponding to inflection points in the original spectra. Statistical analysis was conducted using SAS statistical software. The most suitable regression model was determined using the diagnostic techniques available in SAS, such as the coefficient of determination (R^2), residual plots, and regression P values. It was found that the AVIRIS data were able to predict nitrogen content with a coefficient of determinate of 0.825 (Figure 2). A chemistry distribution map (Figure 3) was computed using the regression equation, which provided the distribution of nitrogen found in the GVWD forest canopy.

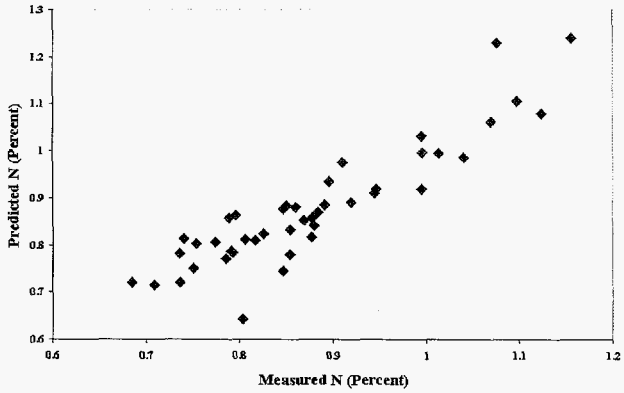

Figure 2: AVIRIS Predicted Nitrogen vs. measured nitrogen with r^2 of 0.825.

6. Compression

The accuracy of compression for storage and distribution of hyperspectral remote sensing data was examined. Hyperion data cubes acquired over the GVWD were compressed using the SAMVQ at a compression ratio of 20:1 as described in Goodenough et al. (2002), where three cubes were classified for forest species and results were compared. A level 1B Hyperion image acquired over the GVWD on September 10, 2001 was used for this research. Negative values and spikes were removed using a program called *rm_neg_spk* (RNS), designed by CSA, to create the second image cube used for comparison. The SAMVQ algorithm was applied by CSA at a ratio of 20:1 to the RNS data cube. This compressed cube was then uncompressed and used for species classification.

The three data cubes, the original, RNS and SAMVQ uncompressed, were then processed in preparation for classification. Negative values and stripes were removed from the original data cube using a BAD_PIXEL_CORR algorithm created by (Han *et al.*, 2002). Image bands containing zero values and VNIR/SWIR overlapping bands were removed to form spectra of 195 bands from the original 242 bands. A linear smile correction algorithm created by (Han *et al.*, 2002) was then applied to the image cube. The data cubes were geocorrected using methods described by (Dyk *et al.*, 2002). The data cubes were transformed using a forward MNF transformation (Goodenough, 2002); and the eigenchannels 2 to 12 were then used in the species classification as described previously. The first eigen channel was excluded as it contained a gradient due to smile. Seventeen classes were derived from ground truth data selected from a GIS database and high-resolution aerial photography. A supervised classification was performed using two thirds of the truth pixels for calibration and the remaining one third for validation.

Table 3 shows the difference in the classification accuracy between the three data cubes, the original, RNS and SAMVQ images. When examining the original data cube and the RNS data, no significant change (up to 1.1%) resulted. When comparing the difference between SAMVQ 20 and the RNS or original image, the non-aggregated classes decreased by 5.1% to 6.9% and the aggregated classes decreased by 2.1% to 6.8%.

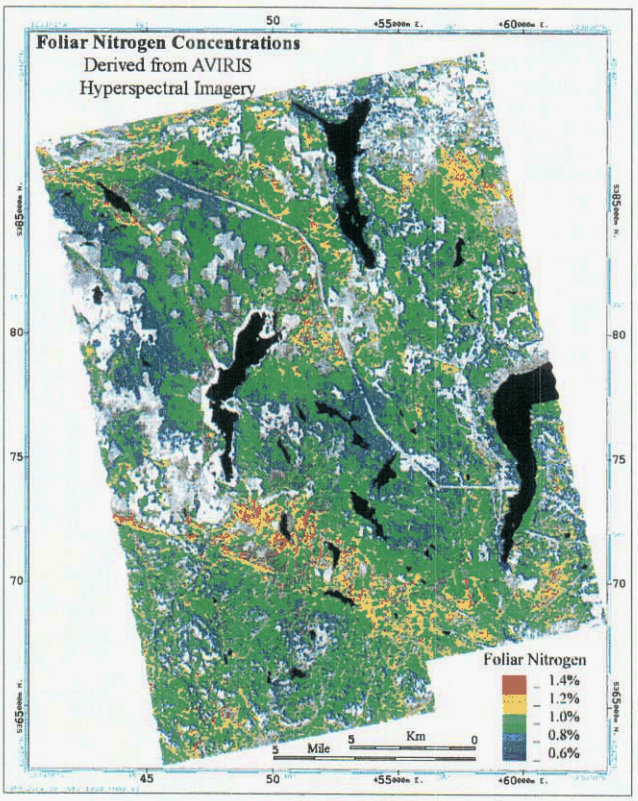

Figure 3: AVIRIS Nitrogen concentration map

Table 3: Classification Comparison and Differences of Original, RNS and SAMVQ 20:1.

Classification	Original		RNS		SAMVQ 20:1	
	Average	Overall	Average	Overall	Average	Overall
All Classes 1/3	**80.99%**	**81.61%**	**80.98%**	**81.11%**	**75.80%**	**74.95%**
All Classes 2/3	**88.37%**	**87.38%**	**88.47%**	**86.29%**	**81.58%**	**81.19%**
Aggregated 1/3	**89.24%**	**89.96%**	**89.54%**	**89.76%**	**87.19%**	**86.98%**
Aggregated 2/3	**93.50%**	**94.21%**	**93.96%**	**93.61%**	**87.49%**	**90.54%**
Difference	**RNS-Orig**		**SAMVQ-RNS**		**SAMVQ-Orig**	
	Average	Overall	Average	Overall	Average	Overall
All Classes 1/3	**-0.01%**	**-0.50%**	**-5.18%**	**-6.16%**	**-5.19%**	**-6.66%**
All Classes 2/3	**0.10%**	**-1.09%**	**-6.89%**	**-5.10%**	**-6.79%**	**-6.19%**
Aggregated 1/3	**0.30%**	**-0.20%**	**-2.35%**	**-2.78%**	**-2.05%**	**-2.98%**
Aggregated 2/3	**0.46%**	**-0.60%**	**-6.47%**	**-3.07%**	**-6.01%**	**-3.67%**

The difference between the non-aggregated confusion matrix of the SAMVQ and the original two thirds training data showed an increased confusion among forest species and densities (up to 19.43% difference). These differences show that the subtle changes made to the spectra are effecting the classifications at this finer level.

7. Conclusions

AVIRIS was an essential tool enabling us to demonstrate that we could recognize coastal forest species to operational accuracies. The overall correct classification accuracy for AVIRIS was 92.1% and for Hyperion was 90.0%. Initial results on nitrogen mapping are encouraging with reasonable agreement with field measurements of foliar chemistry. Compression does affect the results of even a simple supervised classification by reducing

accuracies from 2.1% to 6.8% for aggregated classes and from 5.1% to 6.9% for non-aggregated classes. At this time, it is not recommended that lossy compression be used for satellite downlinks from hyperspectral sensors. Such compression is very useful for creating browse images and allowing people to search large archives of hyperspectral data.

Table 4 : Classification confusion matrix difference (SAMVQ 20:1 – original)

Code	Name	Pixels	1	3	4	5	6	7	8	9	10	11	12	13	14	15	16	17	18
1	Exposed land	24	**0**	0	0	0	0	0	0	0	0	0	0	0	0	0	0	0	0
3	Recent cuts<6 mo	80	0	**0**	0	0	0	0	0	0	0	0	0	0	0	0	0	0	0
4	Water	414	0	0	**0.24**	0	0	0	-0.24	0	0	0	0	0	0	0	0	0	0
5	Shrub low	54	0	0	0	**0**	0	0	0	0	0	0	0	0	0	0	0	0	0
6	Old clear cuts	42	0	0	0	0	**0**	0	0	0	0	0	0	0	0	0	0	0	0
7	Herb Graminoids	46	0	0	0	0	0	**0**	0	0	0	0	0	0	0	0	0	0	0
8	Swamp	138	0	0	0	0	0	0	**-2.2**	1.48	0	0	-0.72	0	-0.72	0	0	2.2	-0.02
9	Red alder	59	0	0	0	0	0	0	3.41	**-11.8**	0.01	0	0	0	0	-1.69	1.7	1.7	6.8
10	Hemlock 60% Dense	67	0	0	0	0	0	0	0	3.01	**-8.93**	0.01	5.93	0	-1.49	8.91	-1.49	-4.48	-1.49
11	Hemlock 60% Open	45	0	0	0	0	0	0	0	0	4.4	**-13.31**	4.46	0	0	-0.02	0	4.48	0
12	Lodgepole pine	171	0	0	0	0	0	0	0	0	4.63	1.73	**-18.12**	0	2.92	0.05	2.36	6.43	0
13	Western redcedar 60%	12	0	0	0	0	0	0	16.7	0	0	0	0	**-16.63**	0	0	0	0.03	0
14	DF Dense 60 yr	95	0	0	0	0	0	0	0	0	-0.01	-1.05	1.04	0	**-2.08**	1.1	1.1	-3.12	3.13
15	DF Dense 110 yr	169	0	0	0	0	0	0	0	0.02	2.97	0.6	0.61	0	-0.58	**-7.08**	2.33	-0.58	1.82
16	DF Open 40 yr	72	0	0	0	0	0	0	0	-2.78	5.53	0	1.42	0	0.02	8.38	**-19.43**	2.73	4.12
17	DF Open 200+ yr	244	0	0	0	0	0	0	-0.41	0	-0.01	-0.42	-0.01	0	0.36	0.42	4.53	**-7.4**	2.82
18	DF Sparse 40 yr	288	0	0	0	0	0	0	3.1	1.76	0	0	0	0	3.49	-0.74	1.71	-0.71	**-8.71**

8. Acknowledgements

We acknowledge the cooperation of the Greater Victoria Watershed District staff and management. We are most grateful for financial support from Natural Resources Canada and the Canadian Space Agency (CSA). We thank Dr. Allan Hollinger and Dr. Shen-En Qian for their assistance in hyperspectral compression experiments. This research would not have been possible without the extensive efforts of NASA, the AVIRIS team, and Dr. Rob Green of JPL. We thank them deeply for their support and professionalism.

9. References

Adamus, P. R., 1995, "Bioindicators for Assessing Ecological Integrity of Prairie Wetlands," United States Environmental Protection Agency EPA/ 600/ R-96/ 082, September.

Dyk, A., 2001, "2001 National Forest Inventory Design Document Draft," Pacific Forestry Centre, Natural Resources Canada, Victoria, BC, Canada.

Dyk, A., D. G. Goodenough, A. S. Bhogal, J. Pearlman and J. Love, 2002, "Geometric Correction and Validation of Hyperion and ALI Data for EVEOSD," Proc. IGARSS 2002, Toronto, ON, Canada, vol. I, pp. 579--583.

Goodenough, D. G., A. S. Bhogal, A. Dyk, A. Hollinger, Z. Mah, K. O. Niemann, J. Pearlman, H. Chen, T. Han, J. Love, and S. McDonald, 2002, "Monitoring Forests with Hyperion and ALI," Proc. IGARSS 2002, Toronto, Ontario, Canada, vol. II, pp. 882–885.

Green, R., Eastwood, M., Sarture, C., Chrien, T., Aronsson, M., Chippendale, B., Faust, J., Pavir, B., Chovit, C., Solis, M., Olah, M., and O. Williams, 1998, "Imaging Spectroscopy and the Airborne Visible/Infrared Imaging Spectrometer (AVIRIS)," *Remote Sensing of Environment*, vol. 65, pp. 227–248.

Han, T., D. G. Goodenough, A. Dyk, J. Love and P. Cheng, 2002, "Detection and Correction of Abnormal Pixels in Hyperion Images," Proc. IGARSS 2002, Toronto, Ontario, Canada, vol. III, pp. 1327–1330.

Jacquemoud, S., Ustin, S., Verdebout, J., Schmuck, G., Andreoli, G. and B. Hosgood. 1996, "Estimating leaf biochemistry using the PROSPECT leaf optical properties model," *Remote Sensing of Environment*, vol. 56, pp. 194–202.

Martin, M. E., S. D. Newman, J. D. Aber and R. G. Congalton, 1998, "Determining Forest Species Composition Using High Spectral Resolution Remote Sensing Data," *Remote Sens. Environ.*, vol. 65, pp. 249–254.

Mohammed, G. H., Noland, T.L., Irving, D., Sampson, P.H., Zarco-Tejada, P.J., Miller, J.R., "Natural and Stress-Induced Effects on Leaf Spectral Reflectance in Ontario Species," Ontario Ministry of Natural Resources, Sault Ste. Marie Forest Research Report No. 156, 2000.

Smith, M. L., S. Ollinger, M. Martin, J. Aber, R. Hallett and C. Goodale, "Direct Estimation of Aboveground Forest Productivity Through Hyperspectral Remote Sensing of Canopy Nitrogen," *Ecological Applications*, vol. 12, pp. 1286–1302, 2002.

Wessman, C., Aber, J., Peterson, D. and J. Melillo, "Remote sensing of canopy chemistry and nitrogen cycling in temperate forest ecosystems," *Nature*, vol. 335, pp. 154–156, 1988.

APPLYING TAFKAA FOR ATMOSPHERIC CORRECTION OF AVIRIS OVER CORAL ECOSYSTEMS IN THE HAWAI'IAN ISLANDS

James A. Goodman,[1] Marcos J. Montes,[2] and Susan L. Ustin[1]

1. INTRODUCTION

Growing concern over the health of coastal ecosystems, particularly coral reefs, has produced increased interest in remote sensing as a tool for the management and monitoring of these valuable natural resources. Hyperspectral capabilities show promising results in this regard, but as yet remain somewhat hindered by the technical and physical issues concerning the intervening water layer. One such issue is the ability to atmospherically correct images over shallow aquatic areas, where complications arise due to varying effects from specular reflection, wind blown surface waves, and reflectance from the benthic substrate. Tafkaa, an atmospheric correction algorithm under development at the U.S. Naval Research Laboratory, addresses these variables and provides a viable approach to the atmospheric correction issue. Using imagery from the Advanced Visible InfraRed Imaging Spectrometer (AVIRIS) over two shallow coral ecosystems in the Hawai'ian Islands, French Frigate Shoals and Kane'ohe Bay, we first demonstrate how land-based atmospheric corrections can be limited in such an environment. We then discuss the input requirements and underlying algorithm concepts of Tafkaa and conclude with examples illustrating the improved performance of Tafkaa using the same AVIRIS images.

2. STUDY AREAS

Three AVIRIS flightlines from the 2000 Hawai'ian Islands acquisition were used in this analysis. All three were acquired from the high-altitude ER-2 platform at an altitude of 20 km, thereby producing a nominal pixel size of approximately 17 m. Two of the flightlines cover the southern portion of French Frigate Shoals (Fig. 1), which is a sizeable semi-circular atoll in the remote Northwestern Hawai'ian Islands extending nearly 34 km in width. The area contains a few small exposed sandy islets, but consists mostly of submerged coral reefs and other associated habitats. The two flightlines for this area, f000418t01p03_r01 and f000418t01p03_r02, are significant because they contain overlapping spatial coverage and exhibit substantial differences in specular reflection from the water surface. This overlapping region provides a valuable avenue for evaluating algorithm performance for the same area but under different illumination conditions. The third flightline, f000412t01p03_r08, covers Kane'ohe Bay on the northeast shore of O'ahu. Kane'ohe Bay is a partially enclosed embayment, extending approximately 4 km in width and 13 km in length along a northwest-to-southeast axis. The bay contains fringing reefs, sizeable patch reefs and an extensive protecting barrier reef. Habitat and water quality conditions vary within the bay and the reefs range from coral-dominated to algae-dominant systems. Differences in specular reflection are not as visually apparent in this flightline and thus serve to test algorithm performance under more consistent illumination conditions.

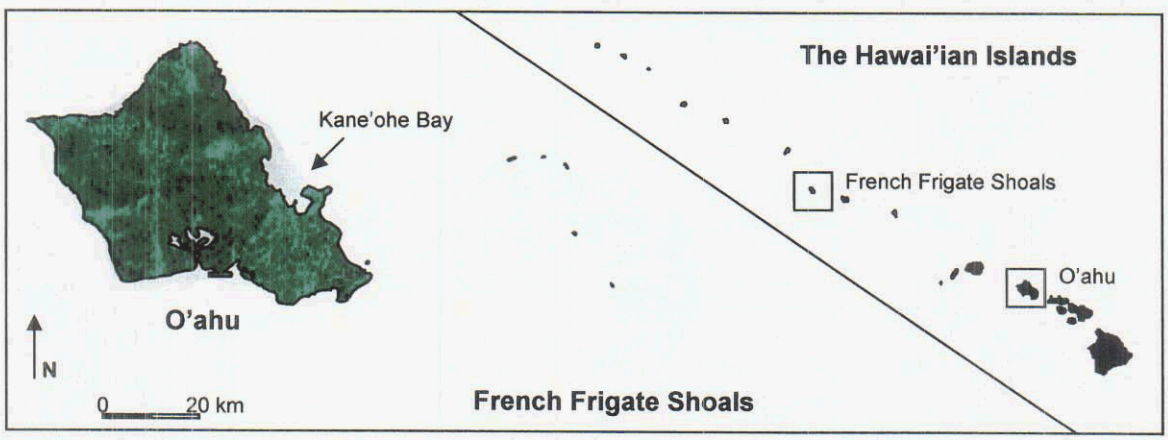

Figure 1. Study areas in the Hawai'ian Islands.

[1] Center for Spatial Technologies and Remote Sensing (CSTARS), Department of Land, Air and Water Resources, University of California, Davis (corresponding author: jagoodman@ucdavis.edu).
[2] Remote Sensing Division, Code 7232, Naval Research Laboratory, Washington, DC.

3. EXAMPLE CORRECTION LIMITATIONS

The Atmospheric CORrection Now (ACORN) software package was selected to provide an example of the potential difficulties of using a land-based atmospheric correction algorithm over water. ACORN (Analytical Imaging and Geophysics, LLC) is a readily available commercial atmospheric correction package that is commonly used in terrestrial hyperspectral applications. Its use here is not intended to identify weaknesses in ACORN nor be critical of its use on other datasets, but merely to illustrate a situation where limitations in terrestrial algorithms become evident when applied to an aquatic system.

3.1 ACORN Methods

ACORN requires radiometrically calibrated radiance data as input and produces estimates of apparent reflectance based on MODTRAN radiative transfer calculations (AIG, 2001). Other inputs to the model include: a description of sensor characteristics for the wavelength position, full-width half-max, gain, and offset for each band; the average elevations of the sensor and the image; and scene specific information identifying the latitude, longitude, time and date of the image center. For application to the three AVIRIS flightlines considered here, the algorithm was run in Mode 1 (hyperspectral atmospheric correction of complete image) with a tropical atmospheric model, using the 940 and 1140 nm bands to derive water vapor, and allowing the model to estimate atmospheric visibility based on image characteristics. Options were also selected to reduce the effects of spectral mismatch and minimize the errors associated with the 1400 and 1900 nm water vapor bands and other smaller spectral artifacts.

3.2 ACORN Results

Reflectance outputs for two locations in French Frigate Shoals are illustrated in Fig. 2. The first area (2A) depicts results for a shallow location with significant reflectance from the benthic surface and the other area (2B) for a deep-water location with no influence from the bottom. The two lines in each graph illustrate output for the same geographic location as derived from the two separate overlapping images, thereby providing a direct comparison of model performance for the same area but under differing amounts of specular reflection. Keeping in mind that reflectance in longer wavelengths should approach zero due to the absorption properties of water, it is apparent in all situations that the resulting reflectance exhibits a shift to higher values. Other observations reveal that this shift is not spatially uniform throughout the image nor is it dependent on water depth. Furthermore, it is uncertain whether this shift is constant across all wavelengths for a given pixel or whether it is independent of wavelength. There is also an inconsistency in results between the two overlapping images, which is presumably a function of the significant differences in specular reflection. Results for two locations in Kane'ohe Bay, an image with far less visually apparent variation in specular reflection, are presented in Fig. 3. A similar shift in reflectance is again apparent. The presence of this shift along with the observed inconsistencies illustrates a limit in the quantitative application of land-based atmospheric correction algorithms over water.

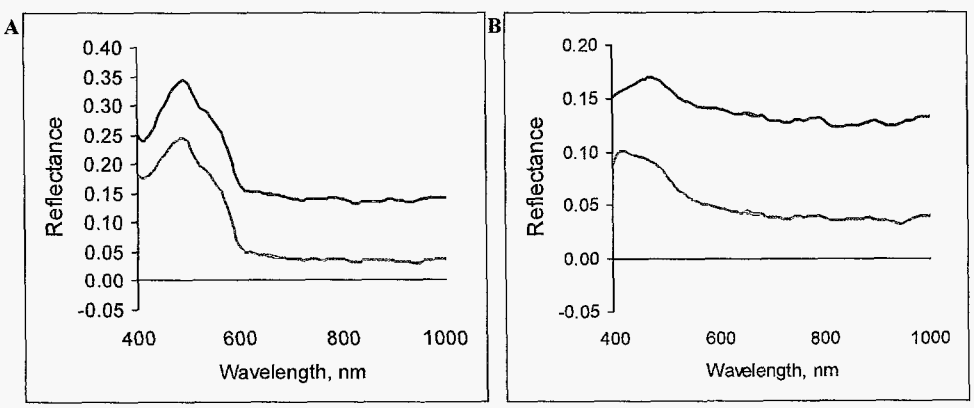

Figure 2. ACORN derived reflectance for French Frigate Shoals from two overlapping flightlines: (A) shallow area with strong bottom influence; and (B) deep water.

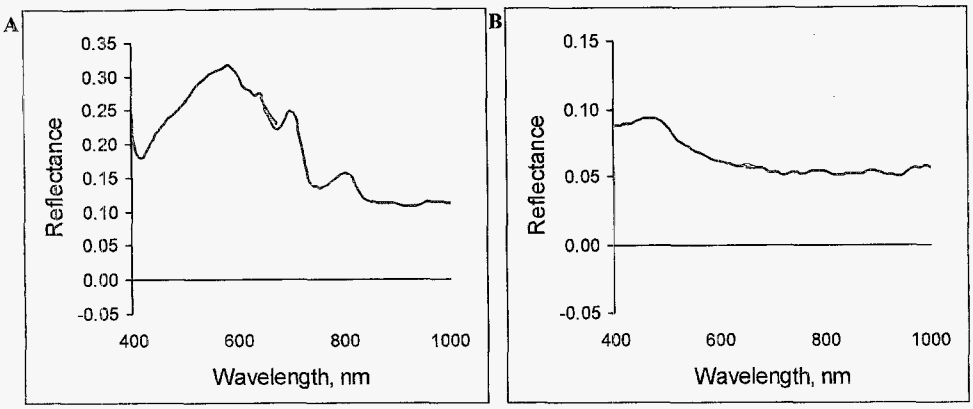

Figure 3. ACORN derived reflectance for Kane'ohe Bay: (A) shallow area with strong bottom influence; and (B) deep water.

4. TAFKAA

Tafkaa is an extensively modified version of the ATmospheric REMoval algorithm (ATREM; Gao and Davis, 1997; Gao et al., 1993) that has been specifically adapted to address the confounding variables associated with aquatic remote sensing applications (Gao et al., 2000; Montes et al., 2001, 2003a, 2003b). It uses information supplied in the input files and by the spectral characteristics of the input radiance data to generate atmospheric correction parameters from a series of lookup tables. Given input of radiometrically corrected at-sensor radiance data, Tafkaa provides output in the form of reflectance ($\rho = \pi L_w/E_d$), remote sensing reflectance (L_w/E_d), normalized water-leaving radiance ($[L_w]_N$), or observed reflectance (ρ_{obs}). Tafkaa also has an associated procedure called Mask that allows for masking of land and clouds. Presented below is an introduction to the Mask and Tafkaa algorithms, an overview of their input requirements, and a discussion of results as applied to the AVIRIS images of French Frigate Shoals and Kane'ohe Bay.

4.1 Mask

The Mask algorithm (undergoing development) provides a utility for identifying and masking land, cirrus clouds, and low altitude clouds. Tafkaa requires knowledge of which pixels are not aquatic because the underlying assumptions used for determining the appropriate aerosol model and optical depth over water do not apply to land or clouds. Thus, identification of land pixels allows Tafkaa to properly process land pixels using a different procedure. Additionally, independent identification of cirrus clouds may allow for correction of some of these pixels at a later date (Gao et al., 1998). Criteria for creating each of the three masks are based on values of observed reflectance, ρ_{obs}, as calculated from the input radiance data and approximations of extra-terrestrial solar irradiance. The land mask employs a user-defined threshold on either a single wavelength (also configurable) or on a normalized difference index, NDI. The cloud masks are both determined by user-defined thresholds on particular wavelengths, 1375 nm for cirrus clouds and 940 nm for low altitude clouds. A complete description of all configurable parameters can be found in the *Mask User's Guide*. Output is in BSQ image format, where bands in the image represent each of the resulting masks (0 is not masked and 100 is masked). The land mask selected for this analysis was the NDI option, $(\rho_{obs}(860nm)-\rho_{obs}(660nm))/(\rho_{obs}(860nm)+\rho_{obs}(660nm))$, with land assigned to pixels where NDI > 0.05. The cirrus cloud mask was identified by pixels where $\rho_{obs}(1375nm) > 0.0025$ and the low altitude cloud mask by pixels where $\rho_{obs}(940nm) > 0.1$. Example Mask output is presented in Fig. 4 for an area of Kane'ohe Bay centered on Moku O Lo'e (Coconut Island). Results reveal good agreement for the land areas of the land mask, but also appear to include areas of cloud as land. The cirrus and low altitude cloud masks show even less robust performance with these particular settings. Nevertheless, when used together the overall mask output does an acceptable job of leaving the aquatic areas unmasked while sufficiently masking land and clouds.

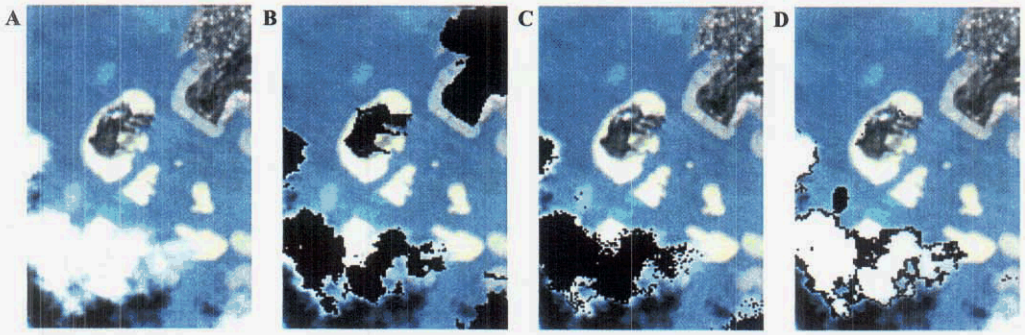

Figure 4. Mask output for Kane'ohe Bay with Moku O Lo'e (Coconut Island) shown at center: (A) unmasked RGB; (B) land mask; (C) cirrus cloud mask; and (D) low altitude cloud mask.

4.2 Atmospheric Correction

The underlying equation for Tafkaa considers total at-sensor radiance to be a function of path radiance, specular reflection from the water surface and reflected radiance from the water, which is a composite function of reflected radiance from the water column and bottom passing through the air-water interface. The algorithm interpolates correction parameters from lookup tables generated using a vector radiative transfer program and ultimately provides a pixel-by-pixel solution for the radiance reflected from the water. Input parameters include the sensor altitude, average ground elevation, wind speed, and level of atmospheric ozone (estimated using data from the TOMS sensor). A full description of these and other input parameters can be found in the frequently updated *Tafkaa User's Guide*. Tafkaa was run on the three AVIRIS flightlines with a tropical atmospheric model, all available gaseous absorption calculations (H_2O, CO_2, O_3, N_2O, CO, CH_4, O_2) and by excluding use of urban aerosols from the offered aerosol solutions. The model also allows the user to select bands from a set of options to signify wavelengths with no apparent water leaving radiance for determining aerosol computations (Fig. 5). Bands selected for French Frigate Shoals and Kane'ohe Bay included the 1040, 1240, 1640 and 2250 nm wavelengths. The most recent version of Tafkaa additionally includes a feature allowing for computations to explicitly account for pixel-by-pixel variations in view and illumination geometry (Montes et al., 2003a). Using this option proved to significantly enhance Tafkaa's ability to account for cross-track variations in specular reflection for the flightlines considered here. The additional input parameters for this option were the date, time and location of the center for every image line, as well as the AVIRIS cross-track pointing geometry.

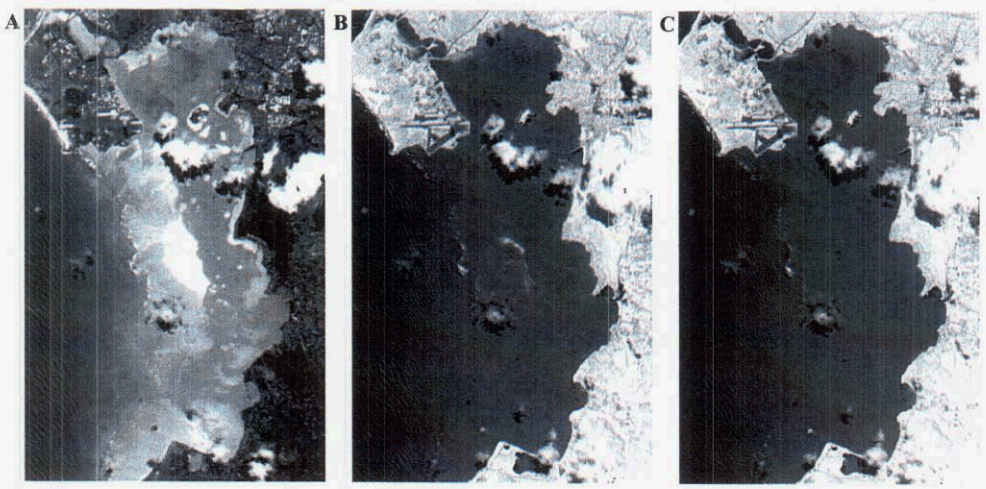

Figure 5. Observed radiance for three bands of radiometrically corrected AVIRIS data for Kane'ohe Bay: (A) 550 nm; (B) 860 nm; and (C) 1040 nm. Note that bottom is strongly visible at 550 nm, only slightly apparent at 860 nm, and no longer evident at 1040 nm.

4.3 Tafkaa Results

Reflectance results produced from Tafkaa are presented for the same areas as examined above and output is again presented in the form of reflectance. Fig. 6 illustrates results for French Frigate Shoals and Fig. 7 for Kane'ohe Bay. Unlike results from the land-based algorithm, reflectance values in the Tafkaa output appropriately tend towards zero at longer wavelengths, which holds true throughout each of the images. A certain amount of spectral mismatch is evident in the results (e.g., around the 940 nm water vapor absorption feature), but overall the generated values are reasonable. Although it is possible to analyze and even ameliorate the spectral mismatch (Gao et al., 2003), this ability has not yet been built into Tafkaa. Results for the same geographic areas from the two different flightlines in French Frigate Shoals (Fig. 6) are substantially more similar than those produced using the land-based algorithm (Fig. 2). Although this comparison is not perfect, the level of agreement between the two flightlines is encouraging considering the sizeable differences in specular reflection. Thus, analysis of spatial and temporal changes within and between flightlines can be performed with greater confidence that differences are a function of changing water and bottom conditions and not artifacts of the atmospheric correction routine. Overall, it is evident that there is still room for improvement, but improved results demonstrate that Tafkaa more successfully generates acceptable reflectance output for atmospheric correction over water and produces improved results over land-based algorithms.

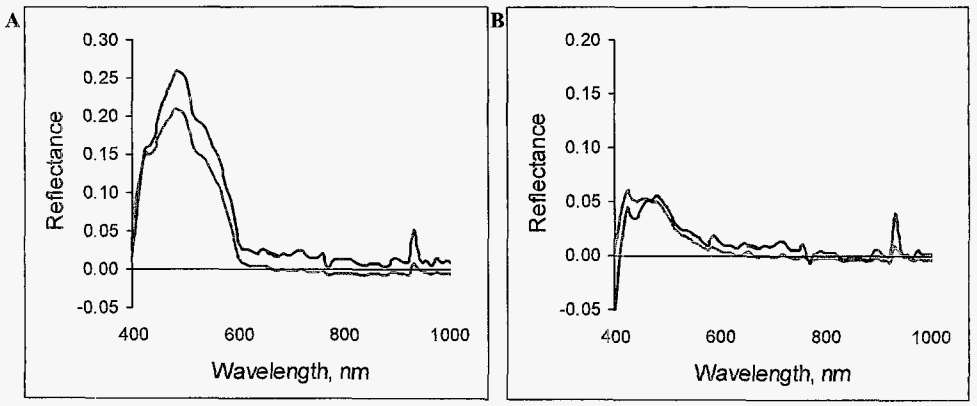

Figure 6. Tafkaa derived reflectance for French Frigate Shoals from two overlapping flightlines: (A) shallow area with strong bottom influence; and (B) deep water.

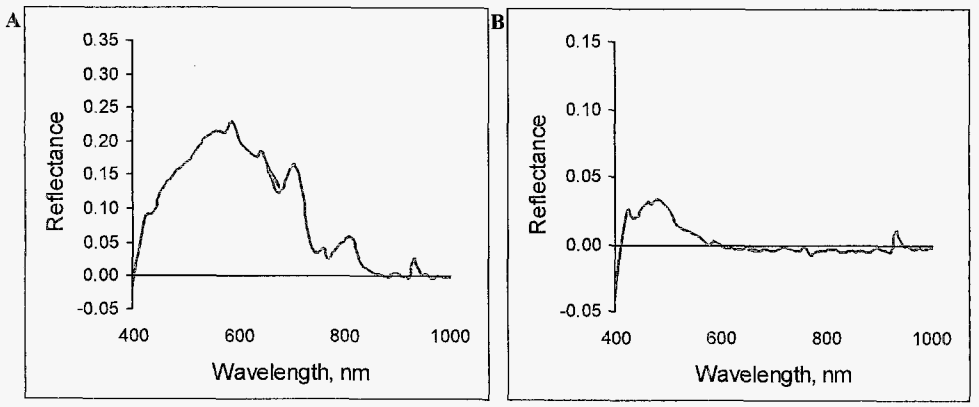

Figure 7. Tafkaa derived reflectance for Kane'ohe Bay: (A) shallow area with strong bottom influence; and (B) deep water.

5. CONCLUSION

Analysis of benthic habitats in shallow aquatic areas is complicated by the confounding effects of the overlying water column and the air-water interface. This means that in addition to atmospheric influences, at-sensor measurements over water are also a function of water properties, surface waves, water depth, bottom characteristics and illumination conditions. This presents a more challenging environment than typical atmospheric correction problems over land, and thus is not necessarily suitable for land-based correction algorithms. For instance, as shown in the examples above, there are situations where results from land-based algorithms can be inconsistent and of limited utility. In contrast, Tafkaa is designed to directly address the aquatic correction issues. The Tafkaa results illustrated above demonstrate physically realistic reflectance output and uniformity within and between images. This represents not only an improved atmospheric correction, but also a more appropriate foundation from which to next address issues of water column correction and spectral analysis of the benthic surface. Thus, improvements in the atmospheric correction will ultimately lead to advances in the evaluation of benthic habitats.

6. ACKOWLEDGEMENTS

This work was supported by NASA Headquarters under the Earth System Science Fellowship Grant NGT5-ESS/01-0000-0208. It is has been made possible by the Department of Land, Air and Water Resources and the Center for Spatial Technologies and Remote Sensing at the University of California, Davis. Additional support was also provided by the University of California Pacific Rim Research Program, the California Space Institute Graduate Student Fellowship Program, the Canon National Park Science Scholars Program and NASA's Jet Propulsion Laboratory. Furthermore, the authors would like to thank the Hawaiian Institute of Marine Biology for their assistance and Paul Sjordal for his untiring efforts in the field. Author MJM acknowledges support from the U.S. Office of Naval Research.

7. REFERENCES

Analytical Imaging and Geophysics, LLC (AIG), 2001, "ACORN User's Guide," Boulder, Colorado.

Gao, B.-C., K.H. Heidebrecht and A.F.H. Goetz, 1993, "Derivation of Scaled Surface Reflectance from AVIRIS Data," Remote Sens. Environ., vol. 44, pp. 165-178.

Gao, B.-C. and C.O. Davis, 1997, "Development of a Line-by-Line Based Atmospheric Removal Algorithm for Airborne and Spaceborne Imaging Spectrometers," in Imaging Spectrometry III (M.R. Descour and S.S. Shen, eds.), Proceedings of the SPIE Vol. 3118, pp. 132-141.

Gao, B.-C., Y.J. Kaufman, W. Han and W.J. Wiscombe, 1998, "Correction of Thin Cirrus Path Radiances in the 0.4-1.0 μm Spectral Region Using the Sensitive 1.375 μm Cirrus Detecting Channel," J. Geophys. Res., vol. 103, no. D24, pp. 32169-32176.

Gao, B.-C., M.J. Montes, Z. Ahmad and C.O. Davis, 2000, "Atmospheric Correction Algorithm for Hyperspectral Remote Sensing of Ocean Color from Space," Appl. Optics, vol. 39, no. 6, pp. 887-896.

Gao, B.-C., M.J. Montes and C.O. Davis, 2003, "Refinement of Wavelength Calibrations of Hyperspectral Imaging Data Using a Spectrum Matching Technique," Remote Sens. Environ., in press.

Montes, M.J., B.-C. Gao and C.O. Davis, 2001, "A New Algorithm for Atmospheric Correction of Hyperspectral Remote Sensing Data," in Geo-Spatial Image and Data Exploitation II (W.E. Roper, ed.), Proceedings of the SPIE Vol. 4383, pp. 23-30.

Montes, M.J., B.-C. Gao and C.O. Davis, 2003a, "Tafkaa Atmospheric Correction of Hyperspectral Data," in Imaging Spectrometry IX (S.S. Shen and P.E. Lewis, eds.), Proceedings of the SPIE Vol. 5159, in press.

Montes, M.J., C.O. Davis, B.-C. Gao and M. Moline, 2003b, "Analysis of AVIRIS Data from LEO-15 Using Tafkaa Atmospheric Correction," 12th AVIRIS/HYPERION Earth Science Workshop (R.O. Green, ed.), Jet Propulsion Laboratory, Pasadena, California, this volume.

MONITORING THE ON-ORBIT SPECTRAL CALIBRATION OF THE NEW MILLENNIUM EO-1 HYPERION IMAGING SPECTROMETER

Robert O. Green
Jet Propulsion Laboratory, California Institute of Technology, Pasadena, California

1. INTRODUCTION

Imaging spectrometers measure multiple contiguous spectral channels that are reported as spectra. These measurements are used to pose and answer science-research and application questions about the surface, based on the molecular absorption and constituent scattering signatures expressed in the spectra. Analysis of spectra measured of the Earth in the solar reflected portion of the electromagnetic spectrum from 400 to 2500 nm requires accurate and precise spectral calibration. The sensitivity of imaging spectrometer analyses to spectral calibration results from the fine spectral absorption features from the Earth's atmosphere imprinted on every spectrum (Green 1998). Figure 1 shows the modeled high-resolution upwelling radiance spectrum for a surface of constant 0.5 reflectance. The spectral response functions for a 10-nm imaging spectrometer and the convolved radiance spectrum are shown as well. In the presence of these strong atmospheric absorption features, errors in spectral calibration induce errors in reported radiances. Figure 2 shows the error in reported radiance resulting from spectral calibration errors of 1.0, 0.5, and 0.1 nm for a 10-nm imaging spectrometer. This sensitivity causes spectral calibration to be a critical parameter for analysis of imaging spectrometer measurements. This sensitivity has been used to investigate and derive the operational spectral calibration of imaging spectrometers instruments (Conel et al. 1988, Green et al, 1990, Goetz et al. 1995, Green 1995, Gao et al. 2002, Green and Pavri 2002).

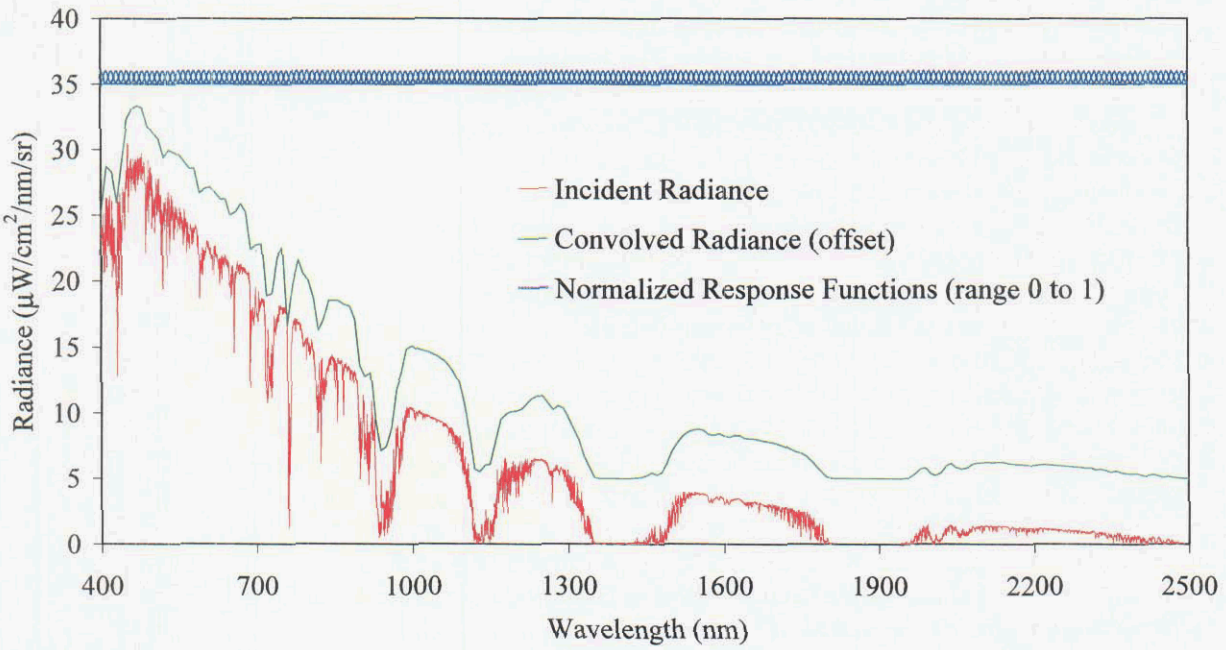

Figure 1. High-resolution total upwelling radiance spectrum for a 0.5-reflectance surface. Spectral response functions for a 10-nm imaging spectrometer and the resulting 10-nm convolved radiance spectrum are shown as well.

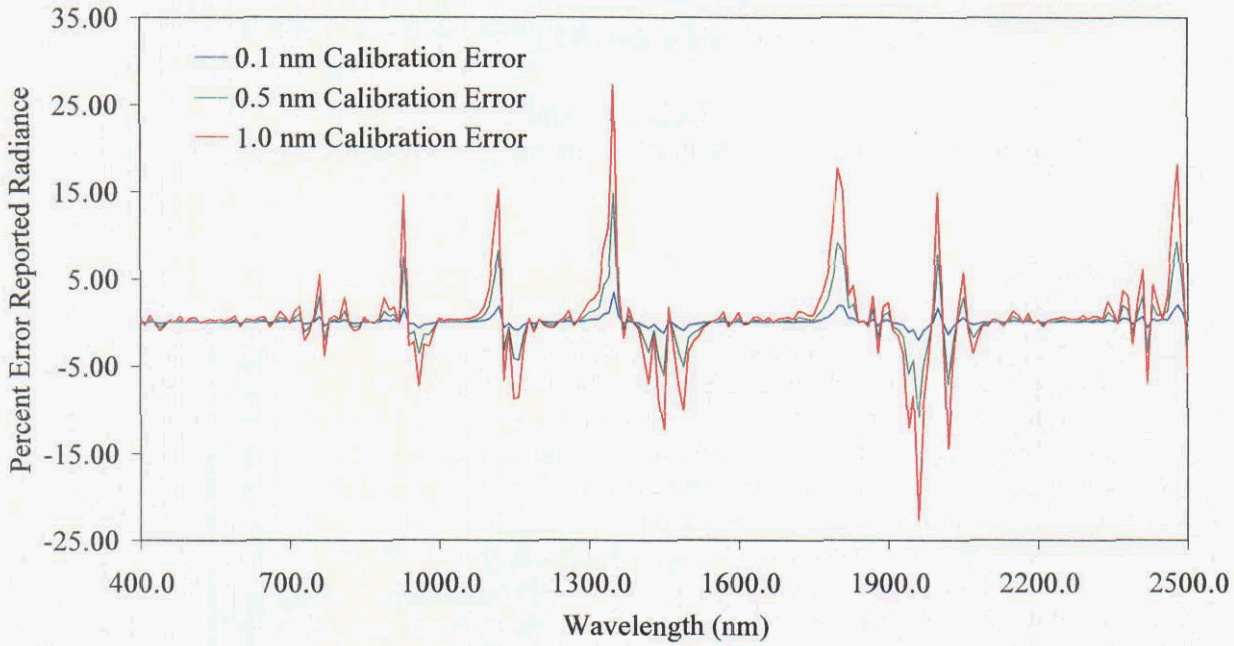

Figure 2. Errors in reported radiance resulting from errors in spectral calibration of 1.0, 0.5, and 0.1 nm.

Figure 3. A portion of the Hyperion image acquired of Salar de Arizaro, Argentina, on February 7, 2001.

The Hyperion imaging spectrometer (Folkman et al. 2000) was launched onboard the New Millennium EO-1 satellite on November 21, 2000. Hyperion is the first Earth-orbiting imaging spectrometer operating across a broad portion of the solar reflected spectrum with nominal spectral coverage from 400 to 2500 nm and 10-nm sampling and resolution. The Hyperion instrument was radiometrically and spectrally calibrated in the laboratory in the summer of 1999 (Barry 2001). To assess the on-orbit performance of Hyperion soon after launch, a series of experiments was orchestrated in the January and February summer illumination conditions of the Southern Hemisphere. For one of these experiments a Hyperion data set was acquired of the high-altitude dry salt lakebed of Salar de Arizaro on February 7, 2001. Salar de Arizaro is located at 24° south latitude and 67° west longitude with an elevation of 3700 m in the Andes of northwest Argentina. Figure 3 shows the Hyperion image acquired of Salar de Arizaro. Figure 4 shows the high uniform spectral reflectance for a calibration site on the surface of Salar de Arizaro. The large homogeneous high reflectance surface and thin low-water-vapor atmosphere provided an ideal target to assess and monitor the on-orbit spectral calibration of Hyperion. Additional Hyperion data sets were acquired on February 10, March 30, April 25, May 1, and December 11, 2002. This paper reports the approach, analyses and results of assessment and monitoring Hyperion on-orbit spectral calibration with data sets measured of the Salar de Arizaro, Argentina.

2. SPECTRAL CHARACTERISTICS OF PUSHBROOM IMAGING SPECTROMETERS

The design of the Hyperion imaging spectrometer is of the pushbroom form. With a pushbroom imaging spectrometer, the spectrum is dispersed onto an area

array detector such that each cross-track spatial element of the images is acquired by a different column in the detector array. For a uniform cross-track imaging spectrometer image, the dispersion of light into the spectrum must be identical in all cross-track elements on to the detector array. Factors in design, manufacture, alignment, and stability make development of a uniform pushbroom imaging spectrometer extremely challenging. Figure 5 depicts the goal of a uniform imaging spectrometer and two possible deviations from that goal resulting in a nonuniform imaging spectrometer.

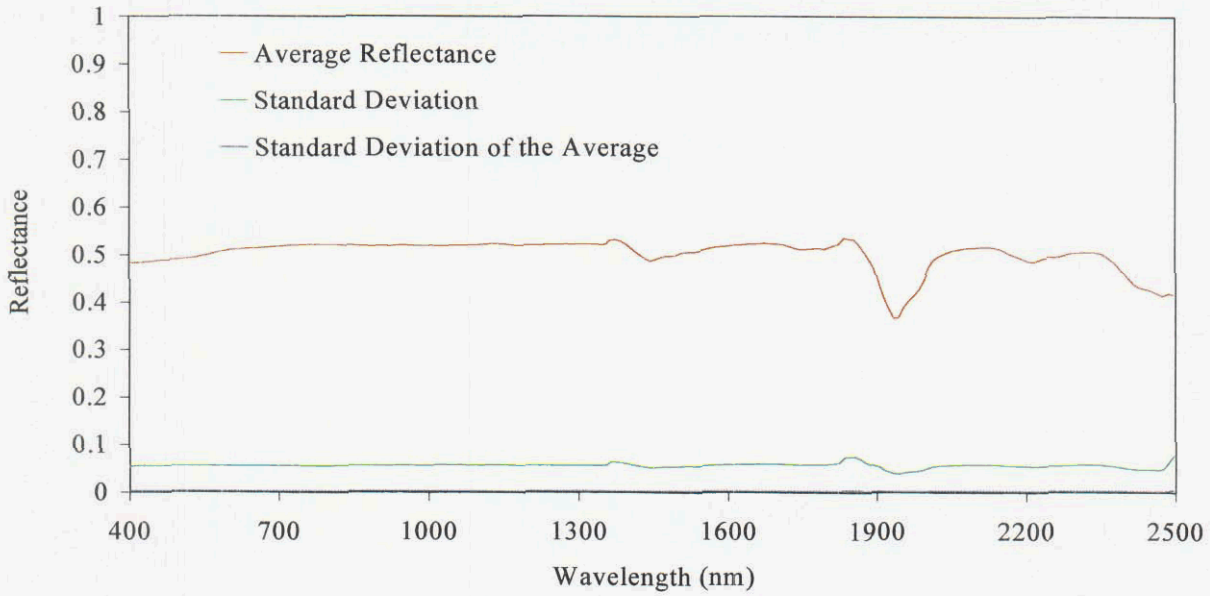

Figure 4. Measured spectral reflectance for a calibration target on the surface of Salar de Arizaro, Argentina.

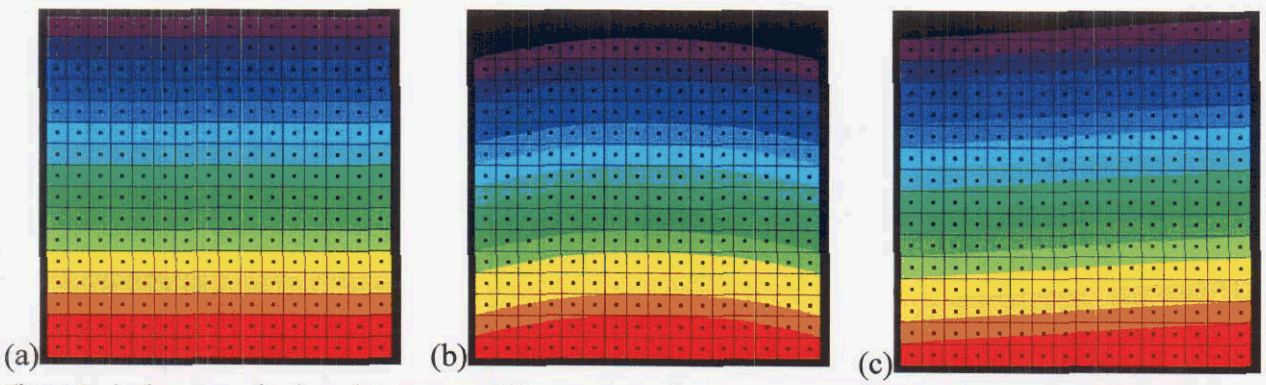

Figure 5. In these panels, the colors represent the spectrum, the squares represent the detectors, and the dots represent the spatial resolution field of view: (a) optimal imaging spectrometer design; spectral calibration is uniform across the full field of view, (b) nonuniform curved, and (c) tilted cross-track spectral calibration variation.

3. LABORATORY SPECTRAL CALIBRATION OF HYPERION

The Hyperion imaging spectrometer was spectrally calibrated in the laboratory (Barry 2001a). This spectral calibration resulted in a predicted spectral wavelength position and spectral response function full-width-at-half-maximum (FWHM) for each spectral channel and cross-track spectral sample. Figure 6 shows the laboratory spectral calibration for the spectral channel near 760 nm for each of the 256 cross-track spatial elements of Hyperion. Based on this laboratory calibration, the cross-track spectral calibration varies by as much as 3 nm in a tilted curve. A 3 nm variation corresponds to 30% of the 10-

nm FWHM of this spectral channel. Figure 7 shows the laboratory spectral calibration for the Hyperion spectral channel centered near 1145 nm. The cross-track variation is ~0.5 nm, which corresponds to 5% of the 10-nm FWHM of this spectral channel. The forms of spectral calibration cross-track variation in Hyperion are different in these two spectral regions because Hyperion uses two spectrometers to cover the full spectral range. The visible-near-infrared spectrometer (VNIR) covers the range from 430 to 900 nm, and the short-wavelength-infrared spectrometer (SWIR) covers the range from 900 to 2390 nm. Each of these two spectrometers have different design, manufacture, alignment, and stability properties. There is a corresponding cross-track spectral calibration for each spectral channel of Hyperion. These laboratory calibration results represent the best prediction of the on-orbit spectral calibration of the Hyperion imaging spectrometer.

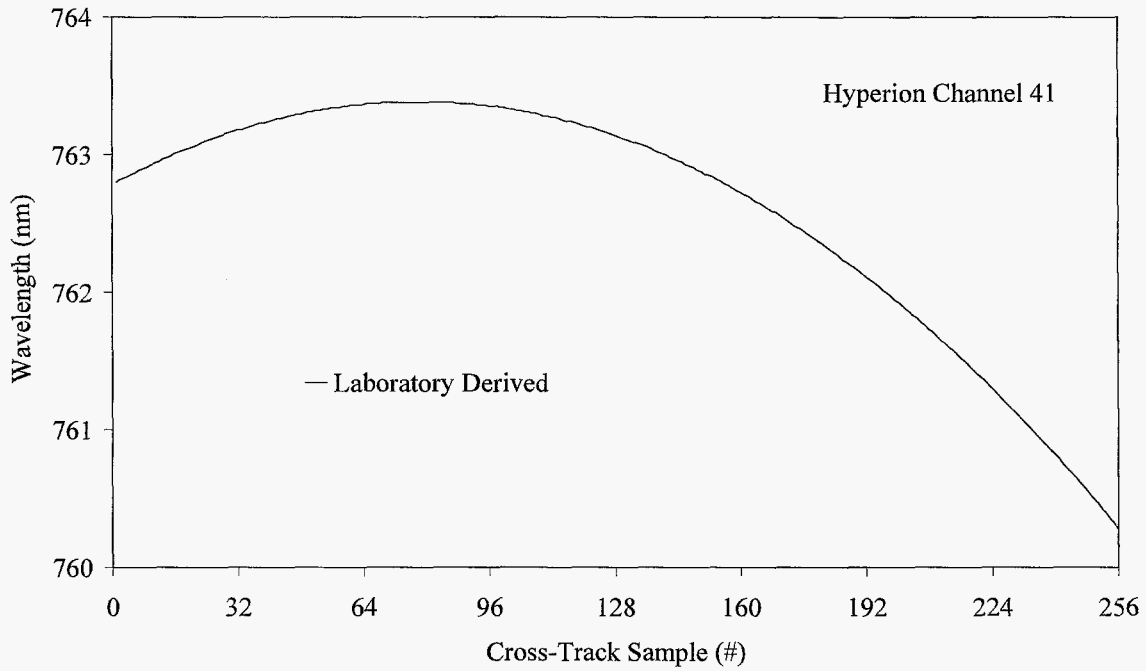

Figure 6. Laboratory-derived cross-track spectral calibration for the Hyperion spectral channel near 760 nm.

4. ON-ORBIT SPECTRAL CALIBRATION APPROACH

The approach used to assess the on-orbit spectral calibration of Hyperion relies on the strong narrow atmospheric absorption features present in the total upwelling spectral radiance incident at Hyperion. Figure 8 shows a full-spectral resolution MODTRAN radiative transfer code modeled spectrum for the Salar de Arizaro (Berk et al. 1989, Anderson et al. 1995 and 2000). Figure 9 shows a Hyperion spectrum from Salar de Arizaro for February 7, 2001. Shifts in spectral calibration were assessed by convolving the high-resolution MODTRAN radiance spectrum to the Hyperion laboratory calibration parameters and comparing the result to the Hyperion measured data over Salar de Arizaro. Errors in Hyperion spectral calibration become evident in spectral regions of strong atmospheric absorption, such as oxygen at 760 nm. Figure 10 shows the spectral agreement between the convolved MODTRAN spectrum and the measured Hyperion spectrum for the 760 nm spectral region using the Hyperion laboratory spectral calibration. The size and form of the disagreement between the two spectra indicate that an improvement on the laboratory spectral calibration is possible. Figure 11 shows the agreement between the convolved MODTRAN spectrum and the Hyperion spectrum with a 1.2-nm shift of the Hyperion laboratory spectral calibration. The agreement is improved with the 1.2-nm shift. This analysis approach was automated and applied to all the cross-track elements of Hyperion for the 760-nm oxygen atmospheric band spectral

region. Figure 13 shows the on-orbit derived spectral calibration for the 256 cross-track samples of Hyperion for the Salar de Arizaro measurements acquired on February 7, 2001. A similar analysis was performed for the carbon dioxide absorption band near 2000 nm. Figure 14 shows the on-orbit cross-track spectral calibration results for this spectral region derived through this approach.

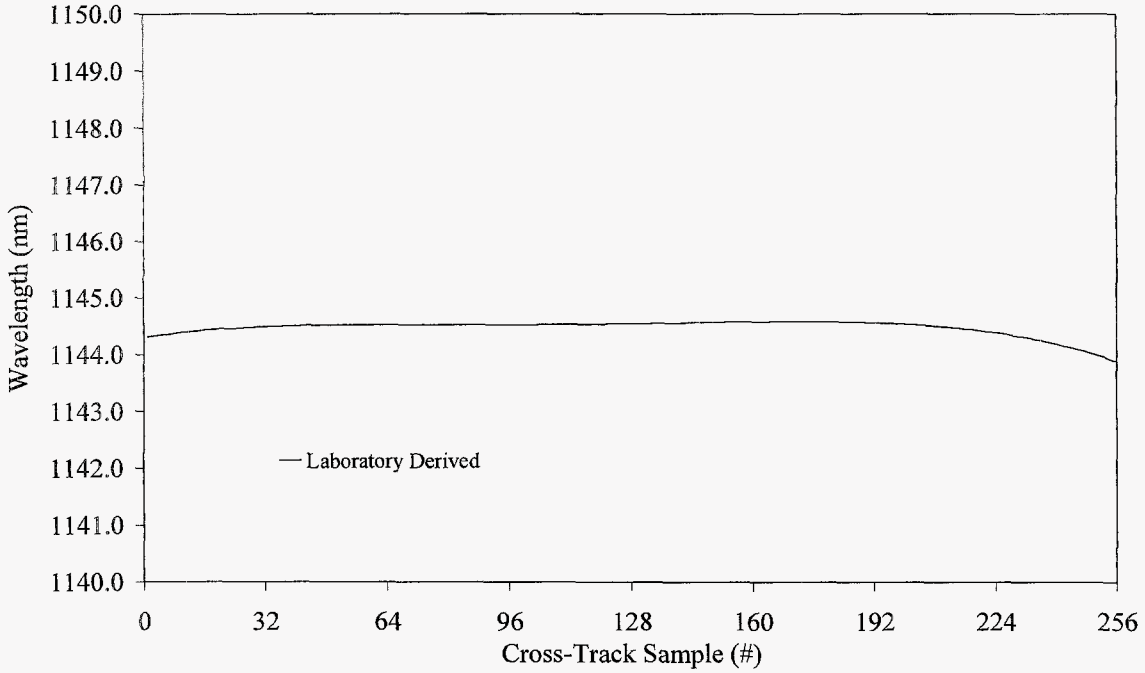

Figure 7. Laboratory-derived cross-track spectral calibration for the Hyperion spectral channel near 1140 nm.

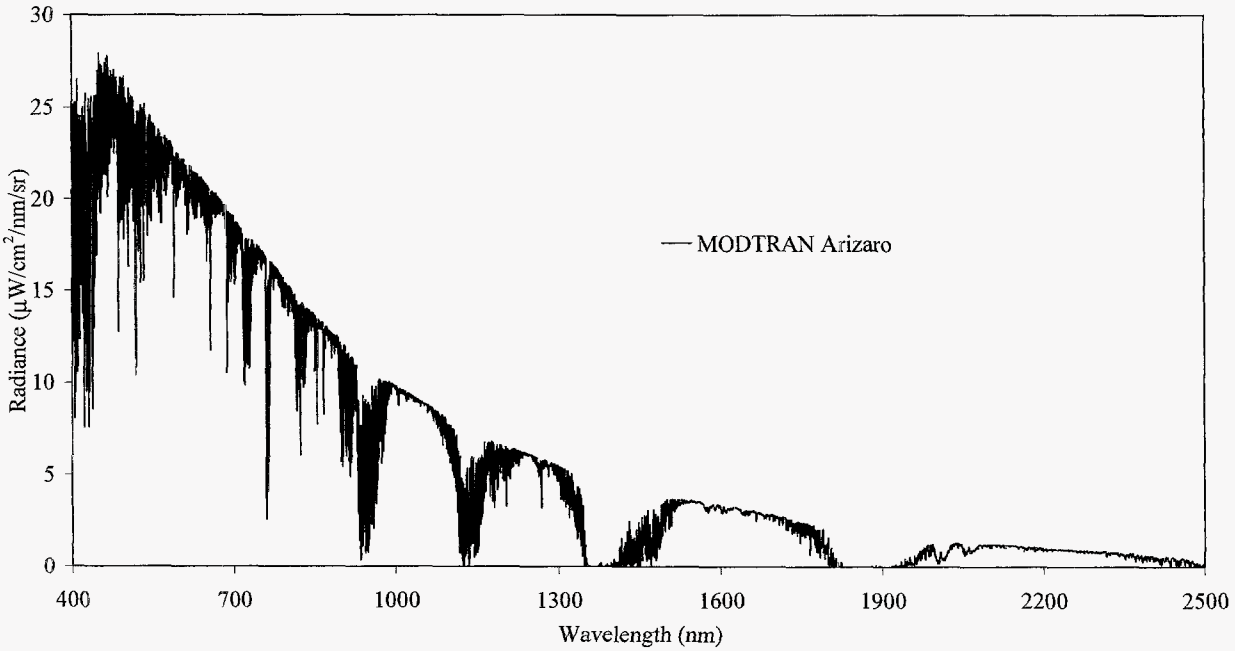

Figure 8. Full-spectral-resolution MODTRAN radiative transfer code modeled radiance spectrum for Hyperion for Salar de Arizaro on February 7, 2001.

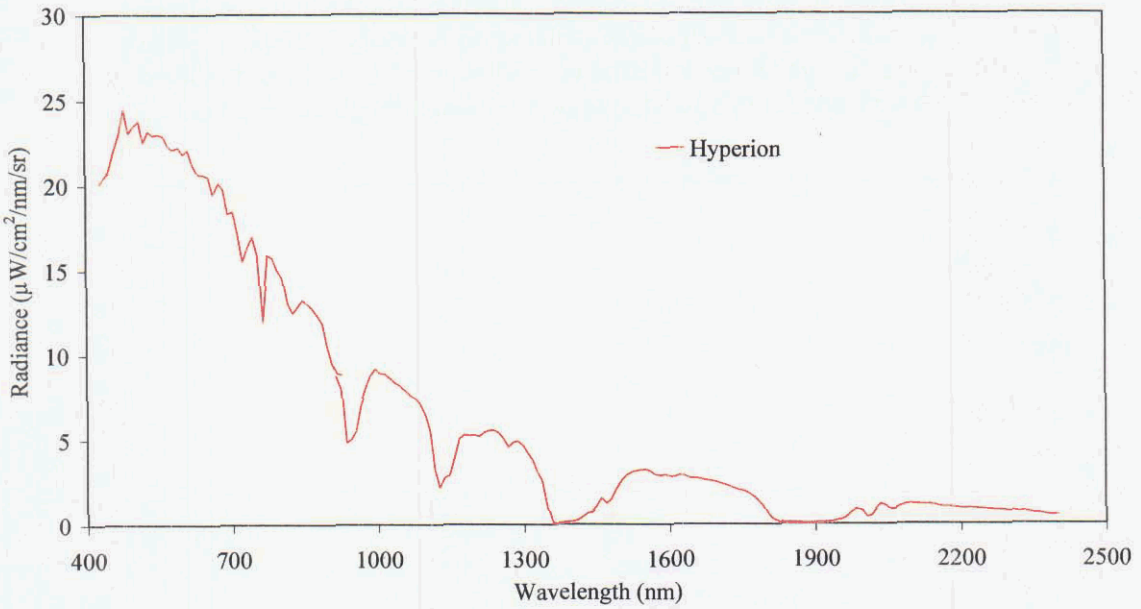

Figure 9. Hyperion spectrum from the Salar de Arizaro acquired on February 7, 2001.

Figure 10. Comparison of Hyperion-measured spectrum and MODTRAN modeled spectrum with no spectral shift in Hyperion laboratory spectral calibration. The residual disagreement in the spectral fit is significant.

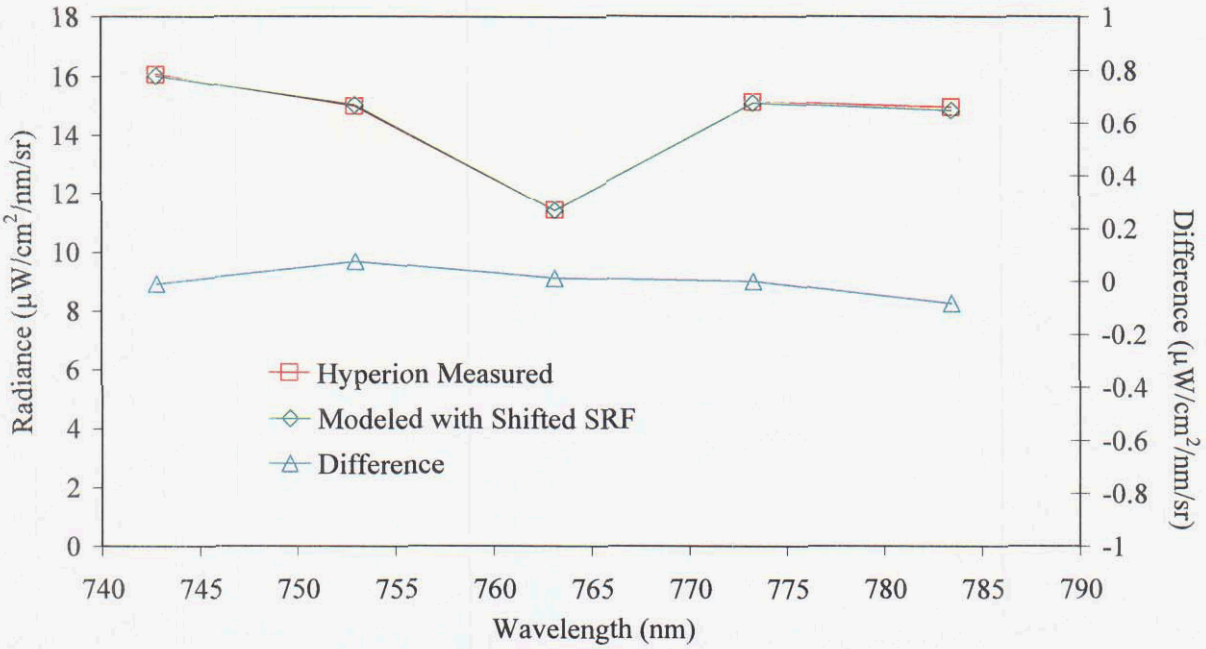

Figure 11. Comparison of Hyperion measured spectrum and MODTRAN spectrum with a 1.2-nm spectral shift in Hyperion laboratory spectral calibration. The spectral agreement is improved over the laboratory spectral calibration.

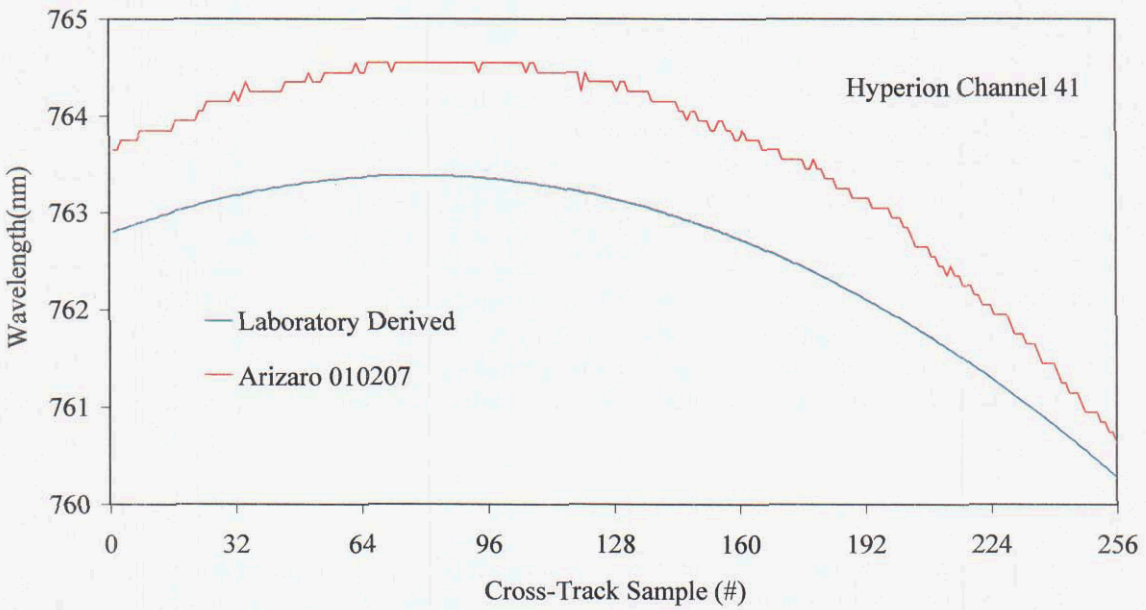

Figure 12. On-orbit derived cross-track spectral calibration for Hyperion in the 760-nm spectral region for the Salar de Arizaro data acquired on February 7, 2001.

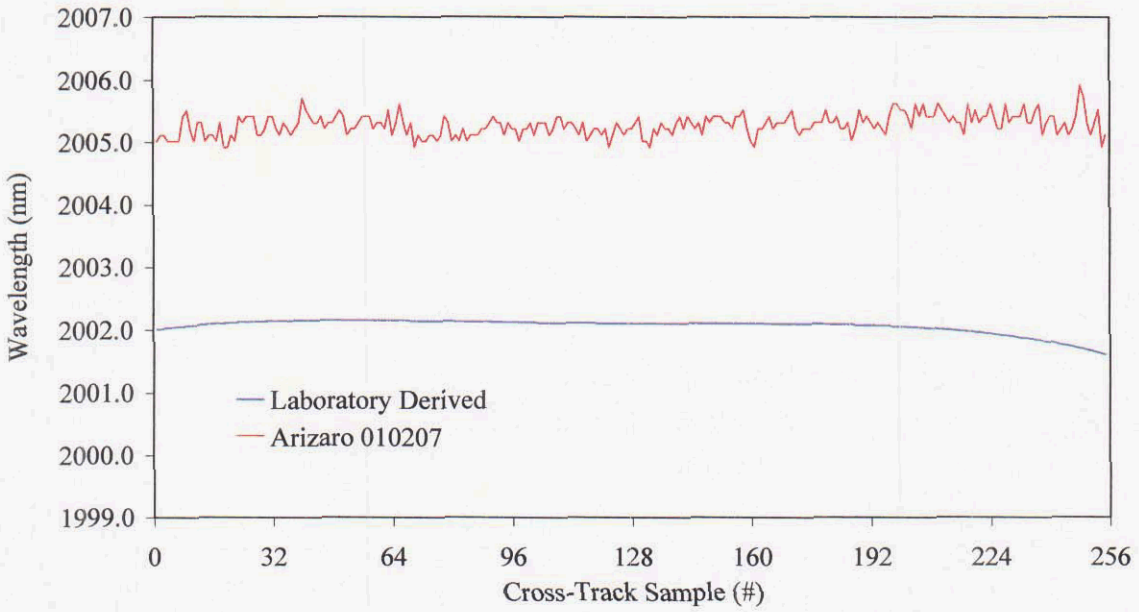

Figure 13. On-orbit derived cross-track spectral calibration for Hyperion in the 2000-nm spectral region for the Salar de Arizaro data acquired on February 7, 2001.

5. ON-ORBIT SPECTRAL CALIBRATION MONITORING RESULTS

In addition to the Hyperion data measured on February 7, 2001 at Salar de Arizaro measurements were acquired on February 10, March 30, April 25, May 1, and December 11, 2002. The on-orbit spectral calibration derivation algorithm was applied to these additional data sets. Figure 14 shows the on-orbit derived spectral calibration for the 760-nm spectral region for these additional dates. This spectral region is measured by the VNIR spectrometer of Hyperion. The on-orbit spectral calibration maintains a similar cross-track variation form and shows less than 0.5-nm shift among these data sets. The analysis was also repeated for the 2000-nm spectral region. The spectral region occurs in the Hyperion SWIR spectrometer. Figure 15 shows the spectral calibration variation among these data sets in the 2000-nm spectral region. With the exception of May 1, 2002, the spectral calibration showed similar excellent cross-track form and variation below 0.5 nm shift. The result for May 1, shows a 1.5-nm shift to shorter wavelengths. The source of this shift is currently unknown. Overall the derived on-orbit spectral calibration of Hyperion is shifted with respect to the laboratory spectral calibration, but with the exception of May 1, the derived on-orbit spectral calibration was stable among the Salar de Arizaro data sets examined.

6. CONCLUSION

Spectral calibration is required for pursuit of scientific research and application with imaging spectrometer data. Due to the ubiquitous, strong, narrow absorption features of the Earth's atmosphere, small errors in spectral calibration produce comparable or larger errors in the reported radiance. Fortunately this sensitivity to spectral calibration enables a spectral fitting approach to assess the spectral calibration of imaging spectrometers in the operational environment.

The Hyperion imaging spectrometer was launched on November 21, 2000. The laboratory spectral calibration of Hyperion predicted considerable curvature and tilt in the spectral calibration of VNIR spectrometer and minimal curvature and tilt in the spectral calibration of the SWIR spectrometer. Hyperion data sets were acquired at the high altitude high-reflectance dry salt lake of Salar de Arizaro starting on February 7, 2001. A spectral fitting approach was applied to derive the optimal on-orbit

spectral calibration of Hyperion for specific spectral regions of both the VNIR and SWIR spectrometers. In the VNIR spectrometer both cross-track spectral calibration curvature and tilt were derived of similar form to that of the laboratory spectral calibration. However, shifts in spectral calibration position of up to 2 nm with respect to the laboratory spectral calibration were determined. The on-orbit derived spectral calibration in the SWIR spectrometer had a similar form to the laboratory calibration, but with a shift of up to 3 nm in spectral position. These on-orbit derivations provide an assessment and basis for improving the on-orbit spectral calibration knowledge of Hyperion.

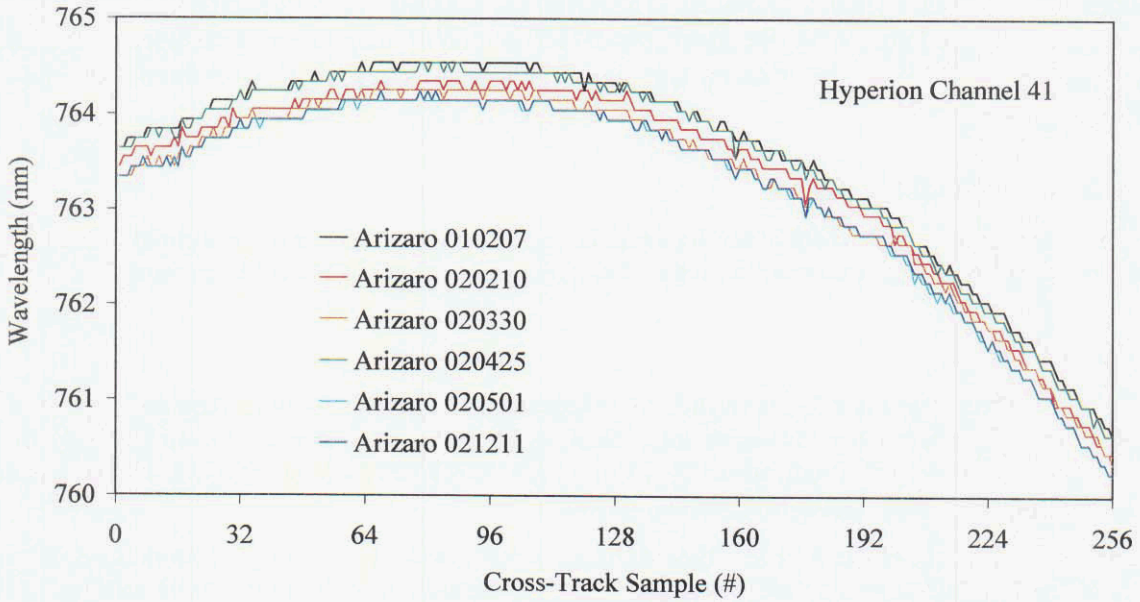

Figure 14. Derived on-orbit cross-track spectral calibration of Hyperion for the VNIR 760-nm spectral region at Salar de Arizaro, Argentina, for a range of dates.

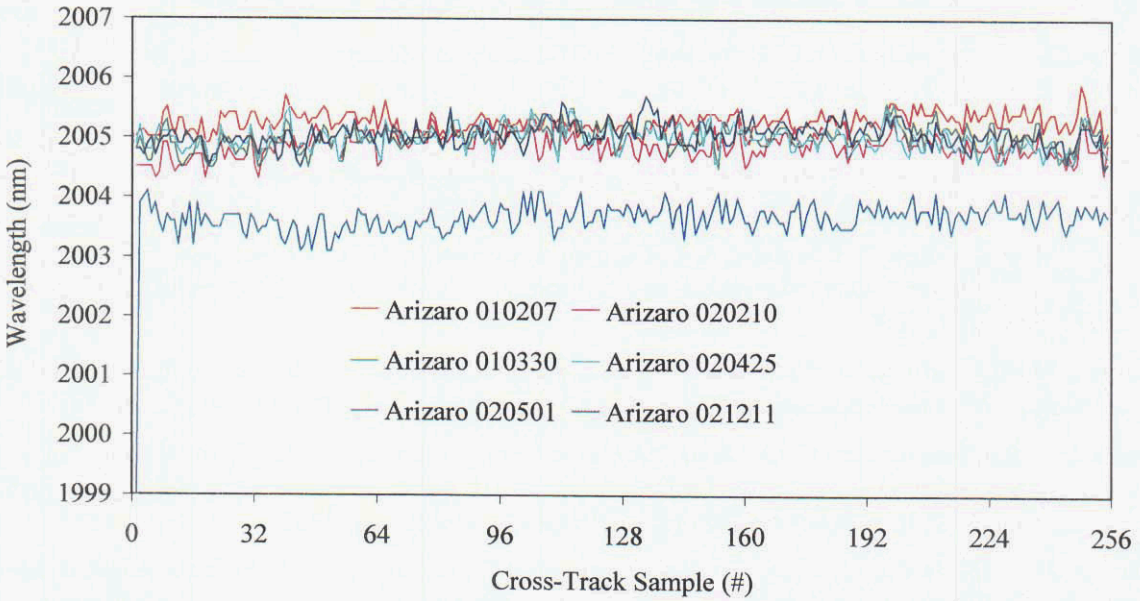

Figure 15. Derived on-orbit cross-track spectral calibration of Hyperion for the SWIR 2000-nm spectral region at Salar de Arizaro, Argentina, for a range of dates.

Hyperion data were acquired of the Salar de Arizaro dry salt lake on a number of dates during the period from February 7, 2001 to December 11, 2002. This range of data sets allowed assessment of the on-orbit spectral calibration stability of Hyperion. For the VNIR spectrometer in the 760-nm spectral region, Hyperion was shown to be stable, with variation of less than 0.5 nm. In the SWIR spectrometer the on-orbit spectral calibration was also stable to 0.5 nm, with the exception of May 1, 2002. Overall these analyses and results show a significant shift between the laboratory and on-orbit calibration of Hyperion and that on-orbit, the spectral calibration of Hyperion is stable.

As future imaging spectrometers are designed, manufactured, aligned, and operated, spectral calibration will remain of high importance. The technique used here for Hyperion provides an approach to derive, monitor and update the operation spectral calibration of imaging spectrometers. Nevertheless, it is of foremost importance that imaging spectrometers have excellent stability for these techniques to be optimally useful.

7. ACKNOWLEDGEMENTS

This research was carried out at the Jet Propulsion Laboratory, California Institute of Technology, Pasadena, California, under contract with the National Aeronautics and Space Administration.

8. REFERENCES

Anderson, G. P., J. Wang and J. Chetwynd, "An Update and Recent Validations Against Airborne High Resolution Interferometer Measurements," *Summaries of the Fifth Annual JPL Airborne Earth Science Workshop*, JPL Publication 95-1, Vol. 1, AVIRIS Workshop, pp. 5–8, 23, Jet Propulsion Laboratory, Pasadena, California., January 1995.

Anderson, G. P., M. L. Hoke, J. H. Chetwynd, Jr., A. J. Ratkowski, L. S. Jeong, A. Berk, L. S. Bernstein, S. M. Adler-Golden, et al., "MODTRAN4 Radiative Transfer modeling for remote sensing," *SPIE*, Vol. 4049, pp. 176–183, 2000.

Barry, P., C. Segal, S. Carman, "EO-1 Hyperion Science Data User's Guide, Level 1_A," TRW Space, Defence & Information Systems Publication, CAGE No. 11982, August 2001.

Berk, A., L. S. Berstein, and D. C. Robertson, "MODTRAN: A Moderate Resolution Model for LOWTRAN 7," Final report, GL-TR-0122, AFGL, Hanscomb AFB, Massachusetts, 42 pp., 1989,

Conel, J. E., Green, R. O., Alley, R. E.; Bruegge, C. J., Carrere, V., Margolis, J. S., Vane, G., Chrien, T. G., "In-flight radiometric calibration of the airborne visible/infrared imaging spectrometer (AVIRIS)," Proc. of the Orlando, Florida Meeting, Apr. 6–8, *SPIE*, Vol 924, p. 179–195, 1988.

Folkman, M. A., P., Lee, P. J. Jarecke, S. L. Carman, J. Pearlman, "EO-1/Hyperion hyperspectral imager design, development, characterization, and calibration," October 9–12, 2000, Sendai, Japan, *Proc. of SPIE*, Vol. 4151, 2000.

Folkman, M. A., Pearlman, J., Liao, L. B., Jarecke, P. J., "EO-1/Hyperion hyperspectral imager design, development, characterization, and calibration," *Proc. SPIE*, Vol. 4151, pp. 40–51, 2001.

Gao, B. C., M. J. Montes, and C. O. Davis, "A Curve Fitting Technique to Improve Wavelength Calibrations of Imaging Spectrometer Data," *Proc. 11th Airborne Earth Science Workshop*, JPL Publication 03-4, Jet Propulsion Laboratory, Pasadena, California, 2002.

Goetz, A. F. H., K. B. Heidebrecht, and T. G. Chrien, "High Accuracy In-Flight Wavelength Calibration of imaging Spectrometer Data," *Summaries of the Fifth Annual JPL Airborne Earth Science Workshop*, JPL Publication 95-1, Vol. 1, AVIRIS Workshop, pp. 5–8, 23, Jet Propulsion Laboratory, Pasadena, California., January 1995.

Green, R. O., J. E. Conel, V. Carrere, C. J. Bruegge, J. S. Margolis, M. Rast, and G. Hoover, "In-flight Validation and Calibration of the Spectral and Radiometric Characteristics of the Airborne Visible/Infrared Imaging Spectrometer (AVIRIS)," *Proc. SPIE Conference on Aerospace Sensing, Imaging Spectroscopy of the Terrestrial Environment*, Orlando, Florida, April 16–20, 1990.

Green, R. O., "Determination of the In-Flight Spectral Calibration of AVIRIS using Atmospheric Absorption Features," *Summaries of the Fifth Annual JPL Airborne Earth Science Workshop,* JPL Publication 95-1, Jet Propulsion Laboratory, Pasadena, California, Jan. 23–26, 1995.

Green R.O., "Spectral calibration requirement for Earth-looking imaging spectrometers in the solar-reflected spectrum," *Appl. Optics* 37: (4) pp. 683–690 Feb. 1, 1998.

Green, R. O., and B. Pavri "Hyperion On-Orbit Calibration Results from an AVIRIS Underflight in Argentina," *Proc. 11th Airborne Earth Science Workshop*, JPL Publication 03-4, Jet Propulsion Laboratory, Pasadena, California, 2002.

Inflight Calibration Experiment Results for AVIRIS on May 6, 2002 at Rogers Dry Lake, California

Robert O. Green and Betina Pavri
Jet Propulsion Laboratory, California Institute of Technology, Pasadena, California

1. INTRODUCTION

Calibration of any remote measurement is required in order to to (1) extract information directly from the measured spectral radiance, (2) compare measurements acquired at different times and from different regions, (3) compare measurements with measurements from other instruments, and (4) derive information from measurements using physically-based computer models.

The Airborne Visible/Infrared Imaging Spectrometer (AVIRIS) (Green 1998a) measures the spectral range from 370 to 2510 nm at ~10 nm sampling, and spectral response function. These spectra are measured as images with a 20 by 20-m spatial resolution and an 11-km swath with up to 1000-km image length from the NASA ER-2 aircraft flying at 20-km altitude. On the Twin Otter aircraft flying at 4-km altitude the spatial resolution is 4 by 4 m with a 2-km swath and up to 200-km image length. Each year AVIRIS is spectrally, radiometrically, and spatially calibrated in the laboratory (Chrien et al. 1990, 1995, 1996, 2000).

Laboratory calibration and characterization are essential, but not sufficient to ensure that measurements acquired in the operational airborne environment are calibrated. To assess and validate the calibration of AVIRIS in the flight environment, an inflight calibration validation experiment is orchestrated usually at the beginning, middle, and end of the flight season (Conel 1988; Green et al. 1990, 1992, 1993a, 1995, 1996, 1998b, 1999, 2000, 2001, 2002). For the inflight calibration experiment, AVIRIS measurements are acquired over an extended-area homogeneous-surface calibration target. At the time of the AVIRIS measurements, the surface reflectance and atmospheric conditions at the calibration target are measured. The surface reflectance and atmospheric conditions at the calibration target are measured. The surface and atmospheric measurements are used to constrain an atmospheric radiative transfer code and predict the upwelling spectral radiance arriving at AVIRIS. The quality of AVIRIS inflight calibration is assessed based on a comparison of the predicted incident upwelling spectral radiance and the AVIRIS-measured incident total upwelling spectral radiance. This paper reports the results of the principal AVIRIS inflight calibration experiment of 2002.

2. FIELD MEASUREMENTS

The primary inflight calibration experiment for AVIRIS in 2002 was orchestrated on a clear-sky day at Rogers Dry Lake, California on May 6, 2002. Rogers Dry Lake is located about 100 km north of Los Angeles, California, at 34.9° north latitude and 117.8° west longitude. Figure 1 shows an AVIRIS image of Rogers Dry Lake with the calibration target location indicated. The calibration target was designated on the surface as a visually homogeneous area of 200 by 40 meters of the dry lakebed surface. Large blue plastic demarcation tarpaulins were located 20 m beyond each end of the target. The elevation of the surface calibration target was 707 m.

At the calibration target, the surface spectral reflectance of the calibration target was measured in the period ±30 minutes of the AVIRIS airborne measurements with a portable field spectrometer (Analytical Spectral Devices Inc., Full Range Spectrometer). This field spectrometer measures the range from 350 to 2500 nm and reports the spectra at 1-nm spectral sampling. Spectra of both the calibration target and a reflectance standard (Spectralon, Labsphere Inc.) were acquired. The measurements were reduced to reflectance as ratios of the calibration target and reflectance standard measurements. The ratios were further corrected for the absolute spectral reflectance of the standard and the bidirectional reflectance distribution function for the solar zenith angle under which the measurements were acquired. Figure 2 shows the average reflectance of the calibration target, the standard deviation, and the standard deviation

of the mean (Taylor 1982) for these measurements. The standard deviation is less than 0.02 reflectance, and the standard deviation of the mean is less than 0.005 reflectance. The standard deviation of the mean indicates the accuracy to which the average reflectance of the calibration target is known. The average reflectance of the surface calibration target is required to predict the total upwelling spectral radiance incident at AVIRIS.

Adjacent to the calibration target on the surface of Rogers Dry Lake, atmospheric measurements were acquired with a 10-channel solar radiometer (University of Arizona, Reagan Instrument). This instrument measures the solar intensity in 10 spectral channels centered at 370, 400, 440, 520, 620, 670, 780, 870, 940, and 1030 nm. These measurements were acquired from sunrise through local solar noon. Figure 3 shows a plot of these measurements over time for the morning of May 6, 2002 AVIRIS inflight calibration experiment. Figure 4 shows a plot of the natural log of intensity versus airmass. Using the Langley method, the average total optical depth of the atmosphere at each spectral channel was calculated. With an absolute calibration of the solar radiometer, the instantaneous optical depths were calculated as well. The instantaneous derived optical depths for the May 6, 2002 AVIRIS inflight calibration experiment are shown in Figure 5. This solar radiometer measures a spectral channel centered at the 940 nm atmospheric water vapor absorption band. These data were used to calculate the instantaneous total column water vapor (Reagan 1987; Bruegge et al. 1992). A value of 9.27 mm precipitable water was derived for the time of the AVIRIS overflight.

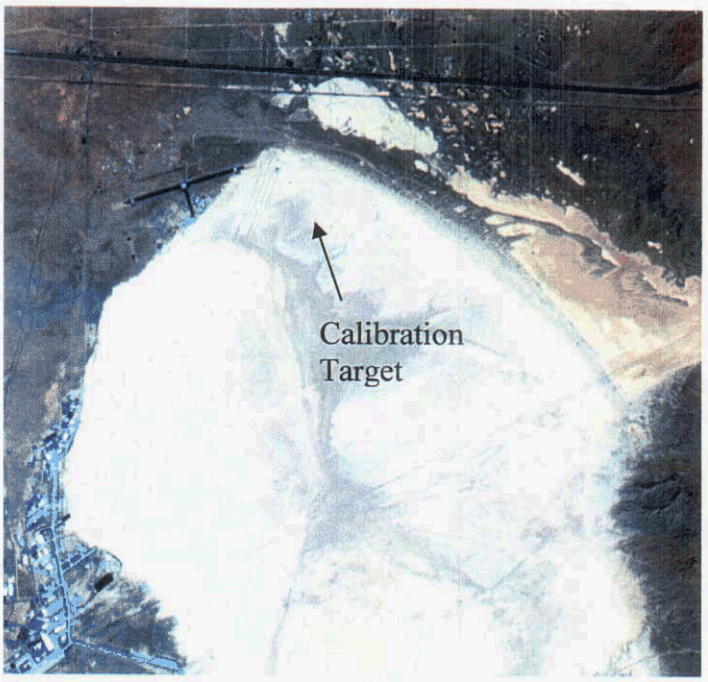

Figure 1. AVIRIS image of Rogers Dry Lake, California, with location of surface calibration target.

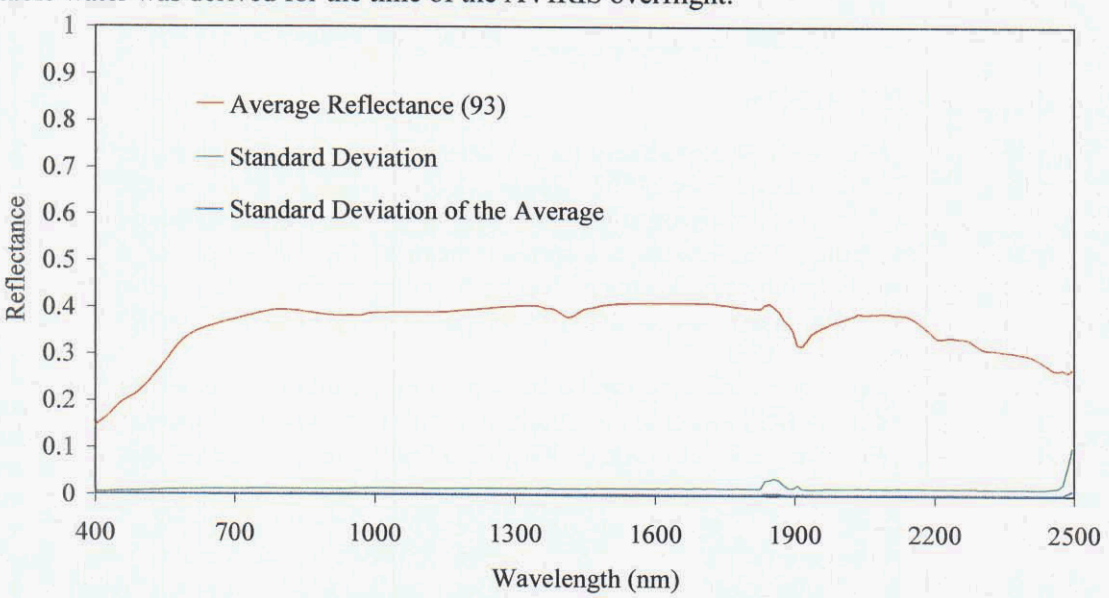

Figure 2. Spectral reflectance measurements of the calibration target on the surface of Rogers Dry Lake, California, on May 6, 2002.

Other properties of the atmosphere required for the inflight AVIRIS were the amounts of atmospheric carbon dioxide and ozone. Values for these constituents of the atmosphere were extracted from available global data sets. A value of 375 ppm was obtained for carbon dioxide Keeling and Whorf 2002). A value of 375 Dobson units was obtained for ozone in the Rogers Dry Lake, California, region on May 6, 2002. These parameters provide further constraint of the atmosphere for prediction of total upwelling spectral radiance incident at AVIRIS over the Rogers Dry Lake calibration target.

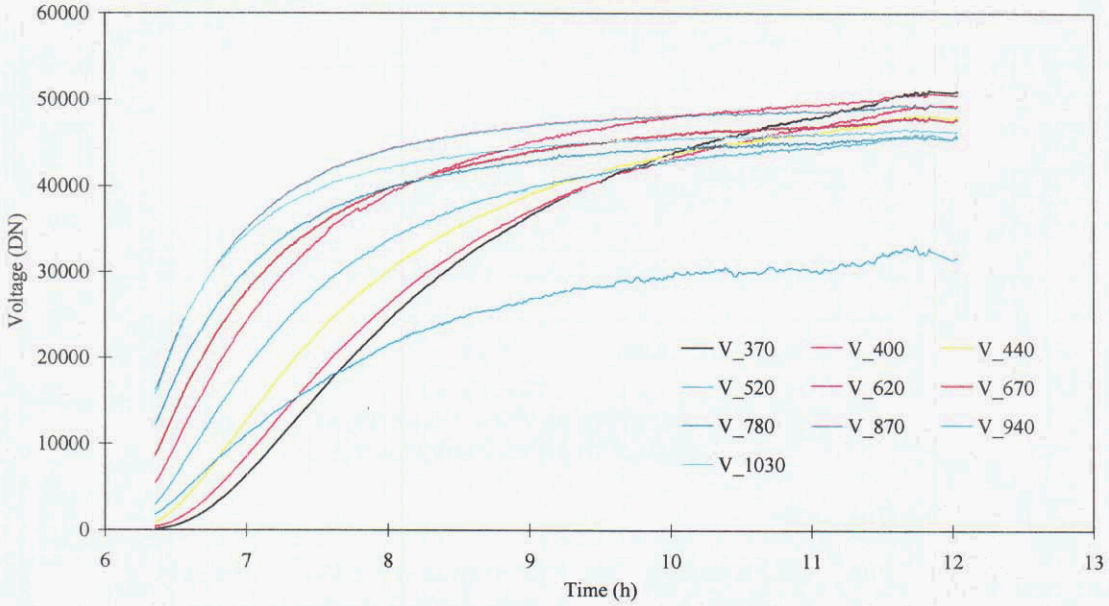

Figure 3. Solar radiometer measurements for the May 6, 2002 AVIRIS inflight calibration experiment.

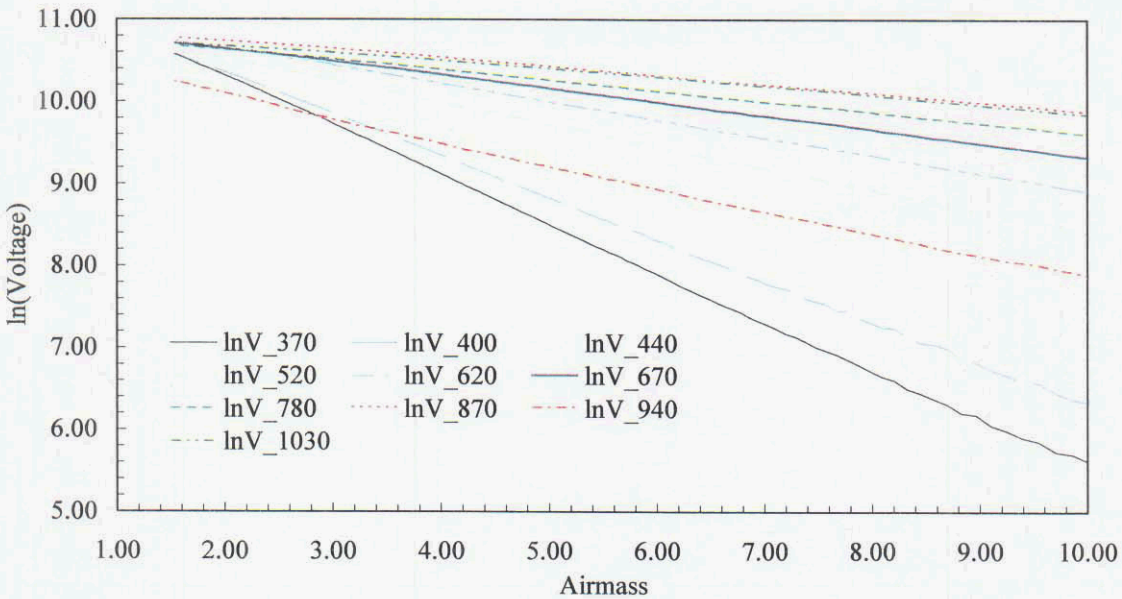

Figure 4. Langley plots of the solar radiometer measurements. The slope of each line gives the Langley optical depth of the atmosphere over the time of the measurements.

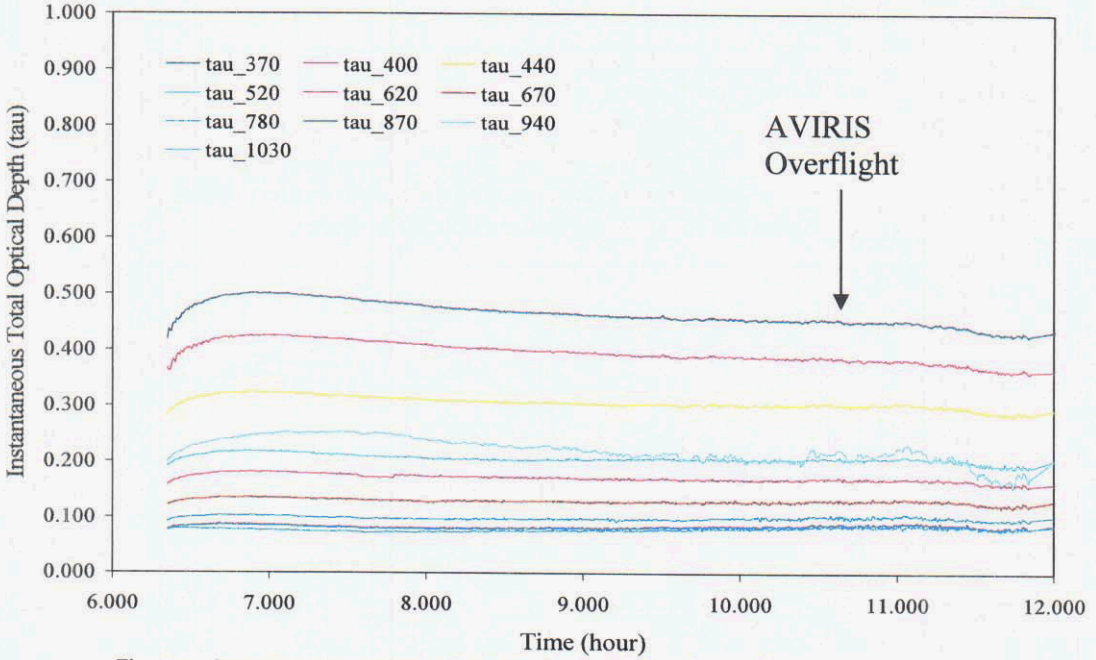

Figure 5. Instantaneous optical depths for May 6, 2002 at Rogers Dry Lake, California, with the time of the AVIRIS overflight indicated.

3. MODELED RADIANCE

To predict the total upwelling spectral radiance incident at AVIRIS over the calibration target at the time of the overflight, the surface and atmospheric measurements were used to constrain the MODTRAN radiative transfer code (Berk et al. 1989; Anderson et al. 1995). The mid-latitude summer atmospheric model was used and the visibility parameter adjusted until a good match was obtained between the measured total optical depths and the corresponding MODTRAN atmospheric model optical depths. Figure 6 shows the measured and MODTRAN optical depths for a visibility of 75 km. The MODTRAN

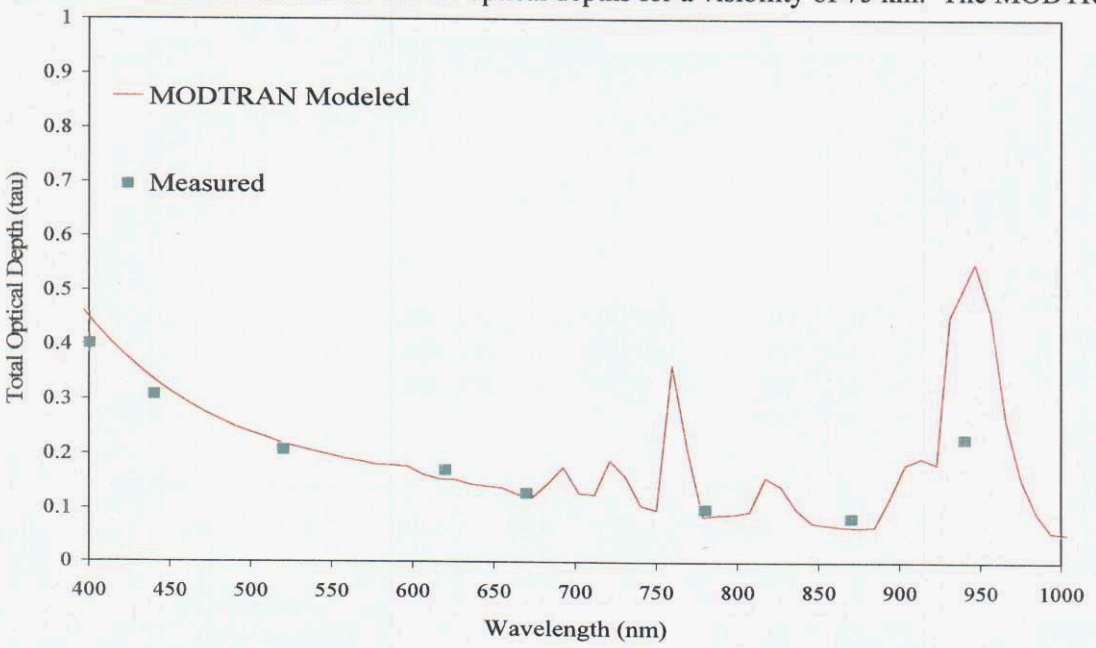

Figure 6. Comparison of the measured and MODTRAN model total optical depths for the AVIRIS inflight calibration experiment on May 6, 2002 at Rogers Dry Lake, California.

radiative transfer code was constrained for these optical depths as well as water vapor, ozone, carbon dioxide, and surface spectral reflectance and used to predict the radiance incident at AVIRIS over the calibration target at the time of the AVIRIS overflight. Figure 7 shows the predicted upwelling spectral radiance at full MODTRAN spectral resolution. In Figure 8, the predicted radiance was convolved to the AVIRIS spectral response functions. This spectrum of the predicted upwelling spectral radiance over the calibration target provides the basis to assess the radiometric calibration of AVIRIS in the operational flight environment.

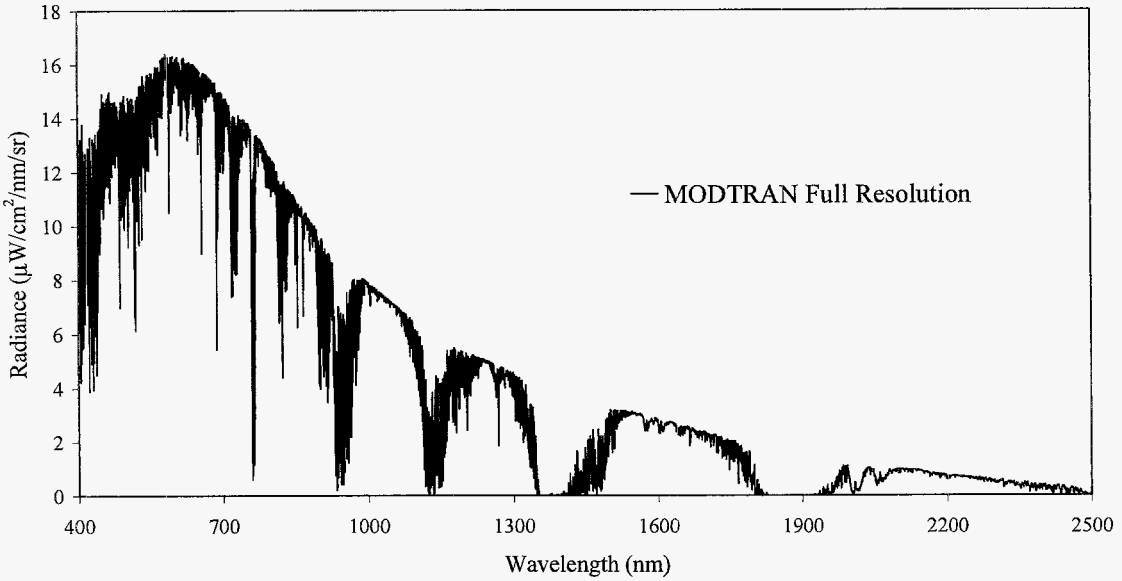

Figure 7. Predicted total upwelling spectral radiance for the calibration target at Rogers Dry Lake, California at the time of the AVIRIS overflight on May 6, 2002.

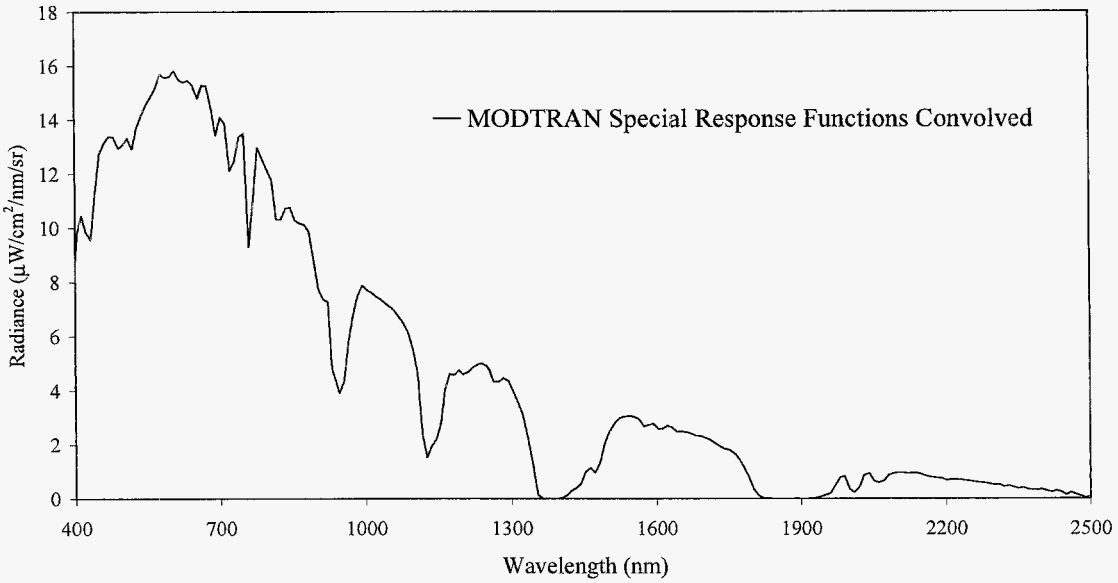

Figure 8. MODTRAN-predicted radiance incident at AVIRIS convolved to the AVIRIS spectral response functions.

4. AVIRIS MEASUREMENTS

AVIRIS measurements of the calibration target on the surface of Rogers Dry Lake, California, were acquired at 17:59 UTC on May 6, 2002. Figure 9 shows the location of the calibration target between the demarcation tarpaulins in a channel ratio of a subset of the AVIRIS image. The AVIRIS measurements for the 40 by 200-m area of the calibration target were extracted and averaged. Figure 10 shows the average total signal, end-of-scan-line dark signal, and total minus dark signal for the calibration target. These measured data were calibrated to spectral radiance with the laboratory-derived radiometric calibration coefficients and spectral calibration parameters shown in Figure 11. The ratio of the onboard calibrator signal between the time of laboratory calibration and acquisition of these data was used to compensate for changes between the laboratory and operational flight environment (Green 1993b). Figure 12 shows the AVIRIS-calibrated radiance for the Rogers Dry Lake, California, calibration target at 17:59 UTC on May 6, 2002.

Figure 9. A subset of the AVIRIS Rogers Dry Lake, California, image showing location of calibration target between demarcation tarpaulins on the surface.

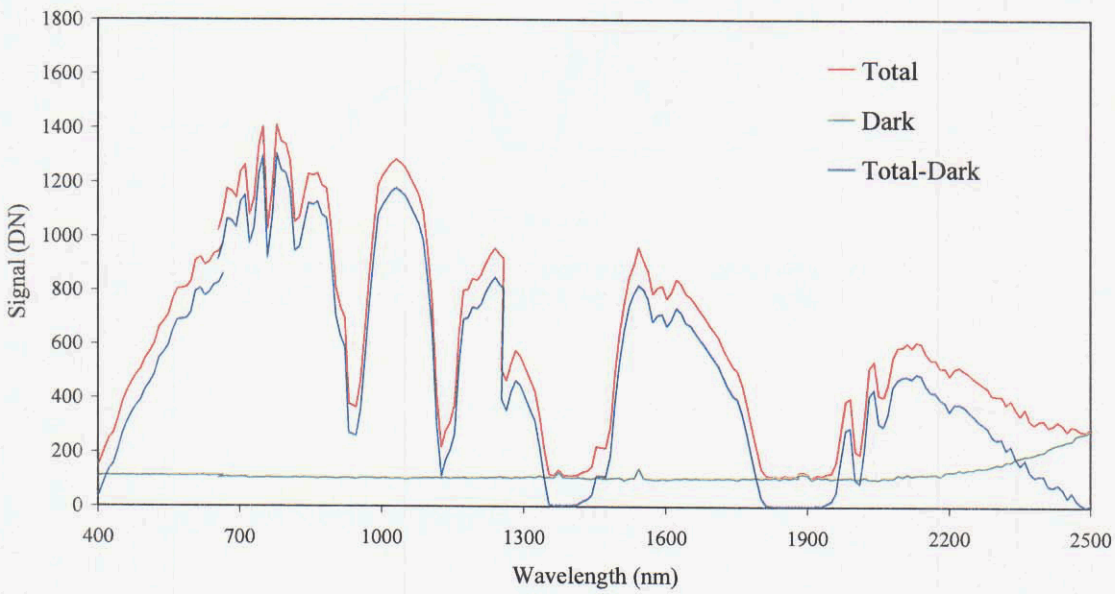

Figure 10. AVIRIS average total signal, end-of-scan-line dark signal, and total minus dark signal for the calibration target.

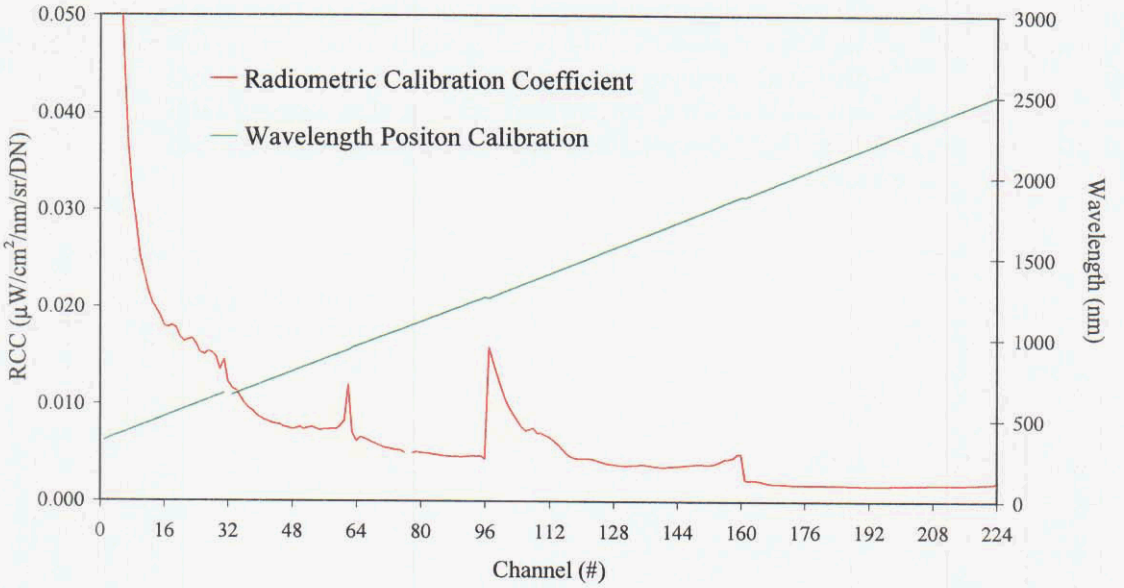

Figure 11. AVIRIS laboratory-derived radiometric calibration coefficients and spectral calibration parameters for the year 2002.

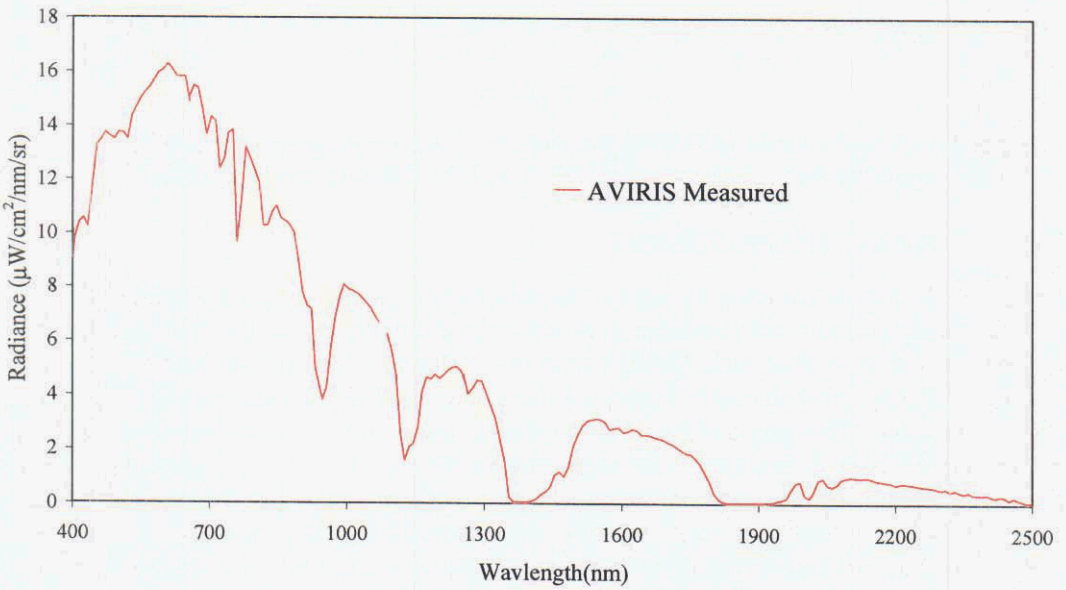

Figure 12. AVIRIS-calibrated radiance for the calibration target on the surface of Rogers Dry Lake, California, on May 6, 2002.

5. INFLIGHT RADIOMETRIC CALIBRATION VALIDATION

With the MODTRAN-predicted and AVIRIS-measured radiance for the calibration target, the accuracy of the AVIRIS calibration may be assessed in the flight environment. Figure 13 shows both the predicted and measured radiance for the Rogers Dry Lake, California, calibration target on May 6, 2002. The ratio of these two radiance spectra is also shown. The deviations of the ratio from 1.0 are attributed to several sources including (1) AVIRIS calibration standards, (2) AVIRIS stability, (3) the MODTRAN radiative transfer code, and (4) the atmosphere and solar parameters used by MODTRAN. Even with these residual uncertainties, the absolute average agreement between the MODTRAN-predicted and AVIRIS-measured radiance was greater than 96 percent, excluding the regions of strong water vapor

absorption at 1400 and 1900 nm. In these water vapor regions of the spectrum, the radiance was close to zero, and a valid comparison was not possible. The good agreement between the in situ measurement-constrained MODTRAN-predicted radiance and the AVIRIS-measured radiance for the calibration target shows that AVIRIS was well calibrated in the flight environment. The onboard calibrator data acquired before and after every AVIRIS flight line were used to maintain and monitor the calibration of AVIRIS over the full 2002 flight season.

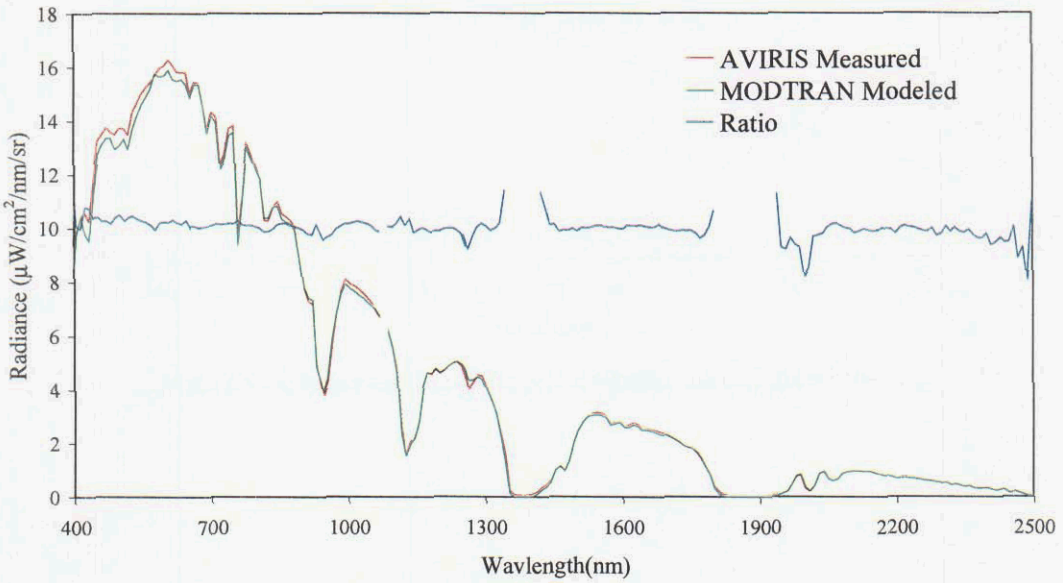

Figure 13. Comparison of the MODTRAN-predicted and AVIRIS-measured spectral radiance for the calibration target on the surface of Rogers Dry Lake, California, on May 6, 2002.

6. AVIRIS RADIOMETRIC PRECISION

In addition to AVIRIS radiometric accuracy, the radiometric precision was assessed in the flight environment. Dark signal radiometric precision is determined by calculating the standard deviation of dark signal measured at the end of each AVIRIS scan line. This provides an estimate of the dark signal noise for each AVIRIS spectral channel. Figure 14 shows this dark signal radiometric precision as noise equivalent delta radiance. This parameter was calculated as the product of radiometric calibration coefficients and the AVIRIS dark signal noise measured on May 6, 2002 in the flight environment.

Signal-to-noise ratio (SNR) is another common measure of instrument precision performance. The AVIRIS SNR was calculated from the high signal of the onboard calibrator measured for the Rogers Dry Lake, California, calibration target flight line. The dark signal noise contribution and the photon noise contribution based on an understanding of AVIRIS detector instrument throughput properties were used. Figure 15 shows the inflight SNR for AVIRIS at the AVIRIS reference radiance. The AVIRIS reference radiance was specified in the original AVIRIS proposals as the radiance from a 0.5-reflectance surface illuminated with a 23.5-degree solar zenith angle. The reference radiance is shown in Figure 16. The AVIRIS SNR continues to reach 1000 in the visible and near-infrared portion of the spectrum and reach 400 in the short wavelength infrared portion of the spectrum near 2200 nm.

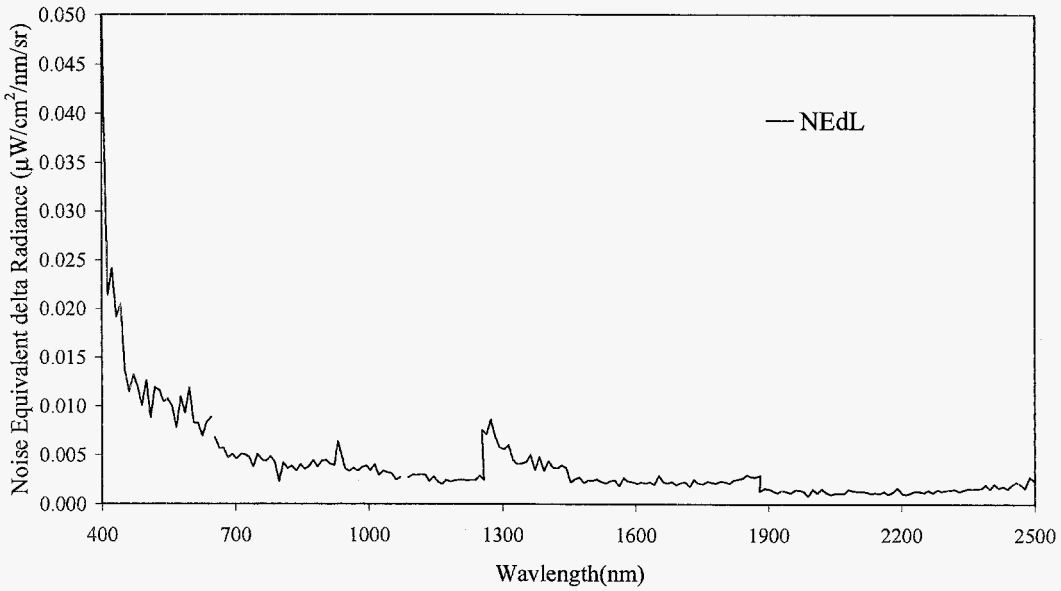

Figure 14. AVIRIS inflight radiometric precision for May 6, 2002 calculated from the end-of-scan-line dark signal measurements.

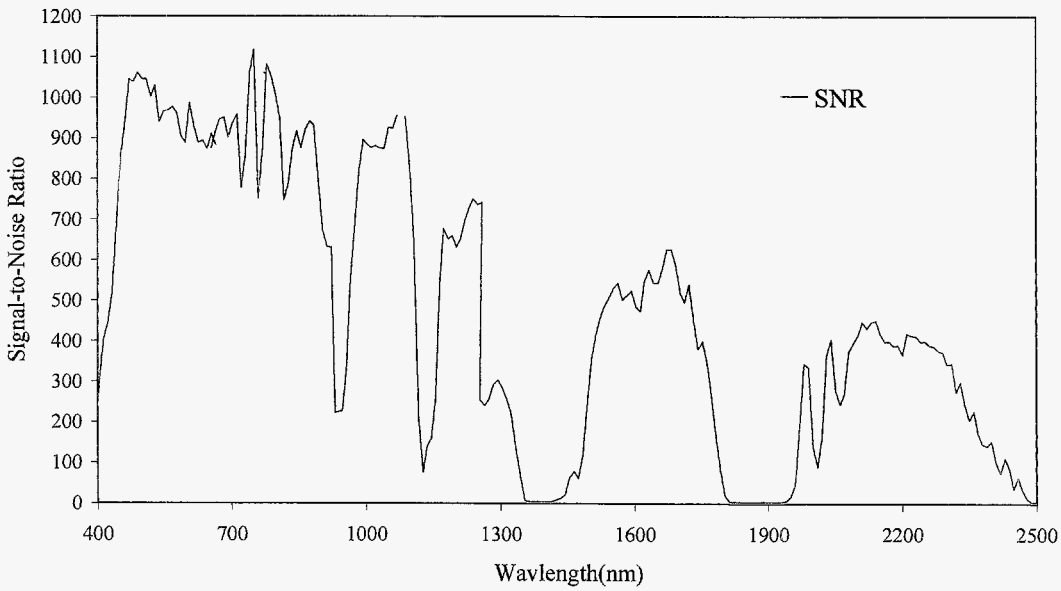

Figure 15. AVIRIS inflight signal-to-noise ratio for the AVIRIS reference radiance.

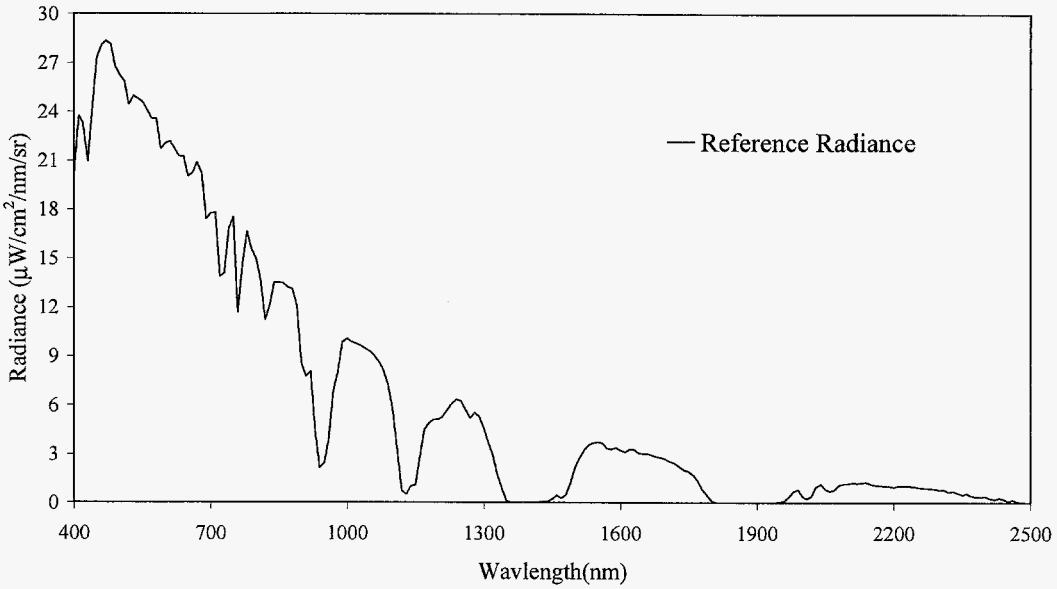

Figure 16. AVIRIS reference radiance as specified in the original AVIRIS proposal.

7. CONCLUSION

The principal AVIRIS inflight calibration experiment of the 2002 flight season was orchestrated at Rogers Dry Lake, California, on May 6, 2002. The experiment assessed the inflight radiometric calibration and precision of AVIRIS. A calibration target was designated on the surface of Rogers Dry Lake, where both surface and atmospheric measurements were acquired. These in situ measurements were used to constrain the MODTRAN radiative transfer code and predict the total upwelling spectral radiance incident at AVIRIS from the surface calibration target. The corresponding AVIRIS measured incident data for the calibration target were extracted and calibrated to upwelling spectral radiance based on the laboratory calibration coefficients and the onboard calibrator. A comparison of the MODTRAN predicted radiance showed good agreement with the AVIRIS-measured radiance for the Rogers Dry Lake calibration target. An average absolute agreement of better than 96% was obtained, excluding the strong water vapor absorption bands at 1400 and 1900 nm.

The inflight radiometric precision of AVIRIS was derived from the dark signal measurements acquired at the end of every scan line and the onboard calibrator high signal data. The inflight dark signal radiometric precision was reported as noise-equivalent-delta-radiance. The inflight SNR was calculated from the onboard calibrator high signal data and reported at the AVIRIS reference radiance. The AVIRIS SNR reaches 1000 in the visible and near-infrared portions of the spectrum and reaches 400 near 2200 nm in the short-wavelength infrared.

The results of this inflight calibration experiment show AVIRIS to be well calibrated and to possess high precision in the flight environment. Excellent radiometric calibration and high precision are required to pursue rigorous scientific research and applications with imaging spectroscopy measurements. Radiometric calibration of AVIRIS is expected to improve in 2004 with inclusion of an ultrastable onboard calibrator. The radiometric precision of AVIRIS is also expected to improve in 2004 with completion of the AVIRIS foreoptics refurbishment.

ACKNOWLEDGMENTS

This research was carried out at the Jet Propulsion Laboratory, California Institute of Technology, Pasadena, California, under contract with the National Aeronautics and Space Administration.

Reference herein to any specific commercial product, process, or service by trade name, trademark, manufacturer, or otherwise, does not constitute or imply its endorsement by the United States government or the Jet Propulsion Laboratory, California Institute of Technology.

REFERENCES

Anderson, G. P., J. Wang, and J. Chetwynd, "An Update and Recent Validations Against Airborne High Resolution Interferometer Measurements," *Summaries of the Fifth Annual JPL Airborne Earth Science Workshop*, JPL Publication 95-1, Vol. 1, AVIRIS Workshop, Jet Propulsion Laboratory, Pasadena, California, January 23, 1995.

Berk, A., L. S. Bernstein, and D.C. Robertson, "MODTRAN: A Moderate Resolution Model for LOWTRAN 7," Final report, GL-TR-0122, AFGL, Hanscomb AFB, Massachusetts, 42 pp. 1989.

Bruegge C. J., Conel J. E., Green R. O., Margolis J. S., Holm R. G, et. al., "Water vapor column abundance retrievals during fire," *Journal of Geophysical Research Atmospheres*, 97(D17) 18759–18768, 1992.

Chrien, T. G., R. O. Green, and M. Eastwood, "Laboratory spectral and radiometric calibration of the Airborne Visible/Infrared Imaging Spectrometer (AVIRIS)," SPIE Vol. 1298, *Imaging Spectroscopy of the Terrestrial Environment,* 1990.

Chrien, T. G., R. O. Green, C. Chovit, M. Eastwood, J. Faust; P. Hajek, H. Johnson, H.I. Novack, and C. Sarture, "New Calibration Techniques for the Airborne Visible/Infrared Imaging Spectrometer (AVIRIS), 1995," *Summaries of the Fifth Annual Airborne Earth Science Workshop*, JPL Publication 95-1, Jet Propulsion Laboratory, Pasadena, California, 1995.

Chrien, T. G., R. O. Green, C. J. Chovit, M.L. Eastwood, and C. M. Sarture, "Calibration of the Airborne Visible/Infrared Imaging Spectrometer in the Laboratory," *Summaries of the Sixth Annual Airborne Earth Science Workshop*, JPL Publication 96-4, Vol. 1, Jet Propulsion Laboratory, Pasadena, California, March 3–5, 1996.

Chrien, T. G., R. O. Green, D. Cohen, B. Pavri, J. Wall, and C. Sarture, "Predicted Accuracy and validation of the AVIRIS Radiometric Calibration Standard," *Proc. of the Ninth Airborne Earth Science Workshop*, JPL Publication 00-18, Jet Propulsion Laboratory, Pasadena, California, 2000.

Conel, J.E., R.O. Green, R.E. Alley, C.J. Bruegge, V. Carrere, J.S. Margolis, G. Vane, T.G. Chrien, P.N. Slater, S.F. Biggar, P.M. Teillet, R.D. Jackson and M.S. Moran, "In-Flight Radiometric Calibration of the Airborne Visible/Infrared Imaging Spectrometer (AVIRIS)," SPIE Vol. 924, *Recent advances in sensors, radiometry and data processing for remote sensing*, 1988.

Green, R. O., J. E. Conel, V. Carrere, C. J. Bruegge, J. S. Margolis, M. Rast, and G. Hoover, "In-flight Validation and Calibration of the Spectral and Radiometric Characteristics of the Airborne Visible/Infrared Imaging Spectrometer (AVIRIS)," *Proc. SPIE Conference on Aerospace Sensing, Imaging Spectroscopy of the Terrestrial Environment*, Orlando, Florida, 16–20 April 1990.

Green, R. O., J. E. Conel, C. J. Bruegge, J. S. Margolis, V. Carrere, G. Vane and G. Hoover, "In-flight Calibration of the Spectral and Radiometric Characteristics of AVIRIS in 1991," *Summaries of the Third Annual JPL Airborne Geoscience Workshop*, JPL Publication 92-14, Vol. 1, pp. 1–4, Jet Propulsion Laboratory, Pasadena, California, 1992.

Green, R. O., J. E. Conel, M. Helminger, J. van den Bosch, C. Chovit, and T. Chrien, "Inflight Calibration of AVIRIS in 1992 and 1993," *Summaries of the Fourth Annual JPL Airborne Geoscience Workshop*, JPL Publication 93-26, Vol. 1, Jet Propulsion Laboratory, Pasadena, California, Oct. 25, 1993a.

Green, Robert O., "Use of Data from the AVIRIS Onboard Calibrator," *Summaries of the Fourth Annual JPL Airborne Geoscience Workshop*, JPL Publication 93-26, Vol. 1, Jet Propulsion Laboratory, Pasadena, California, Oct. 25, 1993b.

Green, R. O., J. E. Conel, M. Helmlinger J. van den Bosch, P. Hajek, "In-Flight Radiometric Calibration of AVRIS in 1994," *Summaries of the Fifth Annual JPL Airborne Earth Science Workshop*, JPL Publication 95-1, Jet Propulsion Laboratory, Pasadena, California, Jan 23–26, 1995.

Green, R. O., Conel, J.E., Margolis, C. Chovit,; and J. Faust, "In-Flight Calibration and Validation of the Airborne Visible/Infrared Imaging Spectrometer (AVIRIS)," *Summaries of the Sixth Annual Airborne Earth Science Workshop*, JPL Publication 96-4, Vol. 1, Jet Propulsion Laboratory, Pasadena, California, March 3–5, 1996.

Green R. O., B. Pavri, J. Faust, O. Williams, and C. Chovit, "Inflight Validation of AVIRIS Calibration in 1996 and 1997," *Summaries of the Seventh Airborne Earth Science Workshop*, JPL Publication 97-21, Vol. 1, pp 193–205, Jet Propulsion Laboratory, Pasadena, California, 1998a.

Green, R.O., M.L. Eastwood, and C.M. Sarture, "Imaging spectroscopy and the Airborne Visible Infrared Imaging Spectrometer (AVIRIS)," *Remote Sens. Environ.* 65: (3) 227–248 SEP 1998b.

Green, R. O., B. Pavri, J. Faust, C. Chovit, and O. Williams, "AVIRIS In-Fight Radiometric Calibration Results for 1998," *Summaries of the Eighth Airborne Earth Science Workshop*, JPL Publication 99-17, Vol. 1, pp 161–175, Jet Propulsion Laboratory, 1999.

Green, R. O., B. Pavri, "AVIRIS Inflight Calibration Experiment, Measurements, Analyses and Results, Sensitivity Analysis and Intraflight Stablity," *Proc. of the Ninth Airborne Earth Science Workshop*, JPL Publication 00-18, pp 207–222, Jet Propulsion Laboratory, Pasadena, California, 2000.

Green, R. O., B. Pavri, "AVIRIS Inflight Calibration Experiment Measurements, Analyses and Results," *Proc. of the Tenth Airborne Earth Science Workshop*, JPL Publication 02-01, pp 205–219, Jet Propulsion Laboratory, Pasadena, California, 2001.

Green, R. O., and Betina Pavri "Inflight Calibration Experiment Results for 2001," *Proc. of the Eleventh Airborne Earth Science Workshop*, JPL Publication 03-4, pp. 125–137, Jet Propulsion Laboratory, Pasadena, California, 2002.

Keeling, C. D and T. P. Whorf, 2002, Atmospheric CO_2 concentrations (ppmv) derived from in-situ air samples collected at Mauna Loa Observatory, Hawaii, Scripps Institution of Oceanography, University of California, La Jolla, California, 92093-0244, http://cdiac.esd.ornl.gov/ftp/maunaloa-co2/maunaloa.co2

McPeters, R. D., 2001, EarthProbe/TOMS data set, NASA/GSFC TOMS Ozone Processing Team (OPT), Code 916, NASA Goddard Space Flight Center, Greenbelt, Maryland 20771, ftp://toms.gsfc.nasa.gov/pub/eptoms/images/global/y2002/et020506.gif

Reagan, J. A., K. Thome, B. Herman, and R. Gall, "Water Vapor Measurements in the 0.94 Micron Absorption Band: Calibration, Measurements and Data Applications," *Proc. IGARSS*, Ann Arbor, Michigan, 18–21 May 1987.

Taylor, J. R., *An Introduction to Error Analysis*, Oxford University Press, p. 270, 1982.

USING AVIRIS IN THE NASA BAA PROJECT TO EVALUATE THE IMPACT OF NATURAL ACID DRAINAGE ON COLORADO WATERSHEDS

Phoebe L. Hauff,[1] David W. Coulter, Douglas C. Peters, Matthew A. Sares,[2] Eric C. Prosh, Frederick B. Henderson III and David Bird

[1]Spectral International, Inc., pusa@rmi.net; [2]Colorado Geological Survey, Matt.Sares@state.co.us

1. INTRODUCTION

The Colorado Geological Survey and the co-authors of this paper were awarded one of 15 NASA Broad Agency Announcement (BAA) grants in 2001. The project focuses on the use of hyperspectral remote sensing to map acid-generating minerals that affect water quality within a watershed, and to identify the relative contributions of natural and anthropogenic sources to that drainage. A further objective is to define the most cost-effective remote sensing instrument configuration for this application.

The study area is located in the state of Colorado (Figure 1). Phase I of this project involves the Lake Creek watershed in central Colorado (a major tributary of the upper Arkansas River), which contains extensive, naturally exposed sulfide mineralization that is adversely impacting the water quality of Lake Creek. Phase II will map the upper Arkansas River, which is affected by mine drainage from the Leadville mining district. The two areas will then be compared.

There are two major sources (Red Mountain West and Red Mountain East) for the natural ARD (Acid Rock Drainage) in the study area (Neubert, 2000), and several minor ones, which have been identified through ASTER and AVIRIS imagery. These all lie within the Grizzly Peak Caldera (Oligocene) shown in Figure 1.

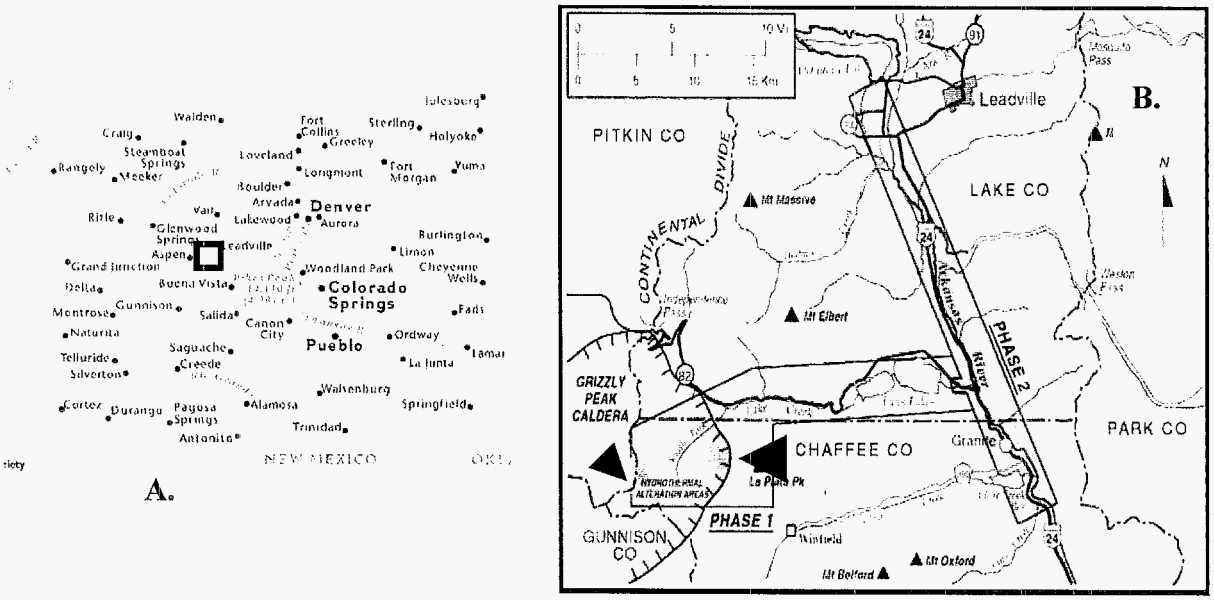

Figure 1 – [A] shows the general location map for the state of Colorado. The study area is located at the base of Mt. Elbert, near Twin Lakes Reservoir, about 20 miles south of the Leadville Mining District. It lies along the Independence Pass road to Aspen (Hwy.82). [B] shows the outlines of the Phase 1 and Phase 2 study areas. Phase 1 follows the Lake Creek watershed, starting with the Peekaboo Gulch drainage from one of the sulfide bodies (large arrow) into South Fork and into Lake Creek. It also includes Sayers Gulch drainage into South Fork from the second hydrothermal source (large arrow). Phase 2 follows the Arkansas River from the Leadville Mining District to south of Granite, and will evaluate mining impacts on water quality of the Arkansas in this area.

2. GEOLOGY

The Grizzly Peak Caldera is south of Independence Pass in the headwaters of Lake Creek (Fridrich et al., 1998). At about 39 Ma, prior to formation of the caldera, numerous rhyolitic stocks and dikes were emplaced in an arcuate zone of fractures that encircled and included the site of the future caldera. Circulation of hydrothermal fluids related to this pre-caldera magmatism caused widespread alteration and formed porphyry molybdenum/copper deposits and gold-bearing quartz-pyrite veins (Cruson, 1973; Fridrich and others, 1991; Neubert et al., in prep.).

The Grizzly Peak Caldera resulted from eruption of the rhyolitic Grizzly Peak Tuff between 37 and 32 Ma, into rocks largely Precambrian in age. During subsidence, an inner ring-fracture zone formed. Caldera resurgence caused by emplacement of a granodiorite laccolith resulted in a complexly faulted dome. Post-caldera, intermediate-composition dikes and small stocks later intruded the fault zones in the resurgent dome (Fridrich and others, 1991).

The dominant rock unit within the caldera is the Grizzly Peak tuff, a phenocryst-rich, lithic, lapilli ash-flow tuff that varies in composition from high- to low-silica rhyolite. Caldera collapse breccias (megabreccias), composed largely of Precambrian wall rock clasts, are prominent in the eastern part of the caldera (the "Red Mountain East" area). Numerous intermediate to felsic composition dikes and plutons related to the caldera appear within and on the margins of the caldera. Hydrothermal alteration is prominent in several areas within the caldera, most notably the Red Mountain West and Red Mountain East areas. While prospecting has occurred in those two Red Mountain areas, no significant mining activity has occurred on the eastern side of the Continental Divide (Neubert et al., in prep.).

A small, north-south trending, Tertiary quartz-latite porphyry stock on the western side of the Continental Divide on the southwestern flank of Red Mountain West (Figure 1B) is strongly hydrothermally altered and weathered. The stock contains quartz-molybdenite-pyrite stockwork veins in a quartz-sericite-pyrite matrix. This intrusive is the likely cause of the extensive alteration of the Red Mountain West area and source for sulfides (Neubert et al, in prep).

Acid-sulfate alteration, composed of the assemblage quartz-sericite-alunite-pyrophyllite, is known from Red Mountain West. Quartz-sericite alteration (QS) and quartz-sericite-pyrite-alteration (QSP) are the dominant alteration types present on the upper east slopes of Red Mountain.

A large area of hydrothermal alteration is exposed to the east of Sayres Gulch on Red Mountain East (Figure 1B), which lies along the eastern ring fracture of the Grizzly Peak caldera. The ring fracture is well marked by megabreccias and a ring dike. Based upon the localization of the hydrothermal alteration and its associated copper and molybdenum anomalies, the altered area probably overlies a shallow, felsic, post-caldera collapse, and porphyry intrusion, which was injected along the ring fracture (Cruson, 1973).

Bedrock in the lower southwestern slope of Red Mountain East, along the two southern tributaries to East Sayres Gulch, is composed of essentially unaltered, Precambrian, banded quartz-biotite gneiss. The gneiss locally contains quartz veins and pegmatites. The principal altered rocks at "Red Mountain East" also appear to be composed of Precambrian gneiss, but the intense alteration makes distinction of rock types difficult. Fragments of Precambrian gneiss form the large clasts in the Tertiary megabreccia. Quartz-sericite alteration (QS) forms the core of the Red Mountain East area. Local areas of quartz stockwork exist within the main quartz-sericite zone. These appear to be composed of nearly pure quartz from a mass of intersecting veinlets. Quartz-sericite-pyrite alteration (QSP) forms a semicircular zone around the north, east, and south sides of the principal quartz-sericite zone, and is also present in a separate zone on the southern end of the altered area. The main minerals are quartz, muscovite, illite, dickite, pyrophyllite and alunite. High kaolinite content, argillic alteration forms both the ridge top and the outermost alteration zone in much of the area. Propylitic alteration is the typical type of alteration present in the megabreccia unit on the northwest side of Red Mountain East. Chlorite is the dominant mineral in the zone of propylitic alteration. Muscovite/illite is the main gangue mineral found throught both hydrothermal areas and because of its high albedo will be prominent in the imagery (Neubert et al, in prep) .

Reconnaissance water quality data was collected in the area in 1994 (Sares, 1996 and 1999; Neubert, 2000) by the Colorado Geological Survey. During these investigations several springs on the east side of Red Mountain West exhibited extreme acidity with pH values ranging between 2.17 to 3.12. The pH of Peekaboo Gulch, the

receiving stream for these springs varied from 3.82, below the springs, to 4.40, approximately 1.5 miles downstream at its mouth with South Fork Lake Creek. The reconnaissance evaluations of spring water in the Red Mountain area confirmed the detrimental effect the hydrothermally altered rocks had on water quality in this area.

3. PROJECT DESCRIPTION

Phase 1 of the project focuses on areas that exhibit natural acid rock drainage, specifically, the South Fork of Lake Creek and its watershed, and Lake Creek downstream of the confluence with South Fork. The South Fork watershed contains two areas of hydrothermal alteration, Red Mountain West (Fig. 2) and Red Mountain East, which drain acidic, metal-laden water into Peekaboo Gulch, Sayres Gulch and smaller, unnamed tributaries. Metals and acidity derived from these areas affect water quality far downstream in Lake Creek. Before discharging to the Arkansas River, Lake Creek water moves through the Twin Lakes Reservoir, which stores trans-basin diversion water for the water supply of Colorado Springs. Water sampling will correlate stream water quality to mineral types identified in the alteration areas and downstream. Mineral types will be identified through hyperspectral remote sensing data and "ground-truth" spectral data collected in the field using hand-held spectrometers.

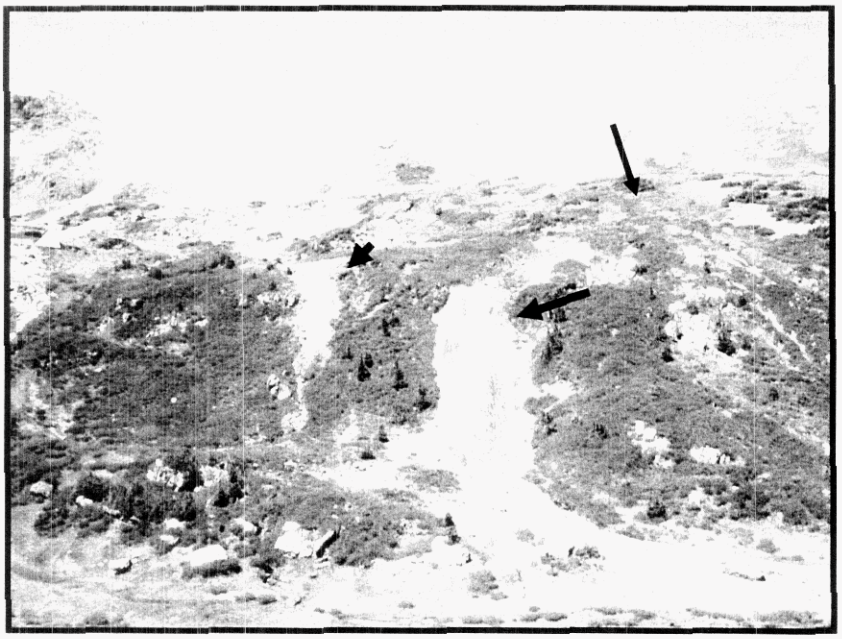

Figure 2 - Hydrothermally altered rocks of Red Mountain West in the heart of the Grizzly Peak Caldera. Springs here discharge very acidic (pH~2–5), metal-rich water. There are two types of activity. The iron sulfides are altering directly to iron sulfate minerals such as jarosite, schwertmannite, copiapite and melanterite. This is occurring at the spring sources (black arrows). Sulfur deficient, acid groundwater is also leaching the feldspars in the volcanic host rocks and creating a pH 5 effluent, highly aluminum enriched, that is discharged from a spring indicated by the white arrow. This results in major aluminum loading in the watershed.

Phase 2 will compare Lake Creek, primarily affected by natural acid rock drainage, with the upper Arkansas River, primarily affected by impacts from historic mining districts in the Leadville area. Much work has been done in identifying, characterizing, and remediating mining-induced contaminants in the Leadville area (USEPA, 2002). Phase 2 of the project will attempt to use hyperspectral remote sensing to identify sources of metals downstream from Leadville, such as mill tailings transported downstream and deposited in flood plains and point bars of the Arkansas River. Water quality will be analyzed and related to these types of metal sources along the main stem of the upper Arkansas River.

4. PROBLEMS & OBJECTIVES

A number of streams in eleven different headwater areas of Colorado have naturally high concentrations of metals and/or acidity, upstream of any significant human impacts. Rocks in these areas have been affected by intense hydrothermal alteration in the geologic past. It is hypothesized that by characterizing the iron and aluminum bearing minerals, through reflectance spectroscopy, that these areas can be mapped using hyperspectral remote sensing to identify the minerals and therefore delineate pH zones and transported metals.

The objectives are therefore to:

- Identify the spectrally active minerals in the watershed
- To correlate those minerals to stream pH water quality, source area and streambed precipitatesIdentify cost-efficient remote sensing technologies for identification of mineralogy
- Geochemically model controls of metal solubility and mobility
- Assess the ability of remote sensing to identify and discriminate natural vs. anthropogenic sources of contamination

The NASA grant will allow us to look at this area in greater detail and test the usefulness of current remote sensing technology for identification of natural and anthropogenic influences on the environment

5. APPROACH

The approach used in this project is similar to those developed in previous NASA funded investigations (Hauff et al., 1999a,b, 2000; Peters et al., 2000, 2001). Background information on the area is first collected. Field sample sites are chosen, GPS coordinates taken for each and surface samples collected from each site. These are analyzed with a field spectrometer for infrared active mineral signatures and portable XRF for metals content. For this project the iron and aluminum coatings on the rocks in the stream beds are of major interest. A special purpose, site specific database of spectral signatures and metal chemistry is compiled for the project.

Because the assessment and monitoring of water quality is the focus of this application, water quality data were collected at both high- and low-flow periods in the Lake Creek watershed. Data elements include dissolved and total recoverable metals, pH, conductivity, alkalinity, total mineral acidity, total acidity, sulfate, chloride, fluoride, nitrate/nitrite, and total suspended solids. A geochemical model of the entire watershed will be produced to predict seasonal flow and changes in pH, metal loading and mineralogy. It is anticipated that it will be possible to apply such a model to other similarly impacted watersheds, without the intense field work employed to develop the Lake Creek model.

The field data is then integrated with remotely sensed imagery. Several kinds of sensor data will be used during the project, as one of the objectives is to determine the optimum sensor configuration for the narrow, high mountain drainages. The NASA Stennis ART Toolkit (Zanoni, 2002) , with AVIRIS and SPECTIR high-resolution data sets will be used to simulate sensor configurations that are optimum for this application in other parts of Colorado and other mineralized and mined areas. The sensors used to collect the data vary in spatial resolution, spectral resolution, and operating cost. Obtaining data from a sensor on a satellite platform is less expensive than from an airborne platform, however, the spatial resolution is usually poorer. Table 1 summarizes the different sensors for this project.

Table 1 - SENSOR TYPES

Name	Description	Spectrum	Platform	Strengths
LANDSAT	Earth resources satellite	VNIR	Satellite	Regional view; low-cost
ASTER	Advanced Spaceborne Thermal Emission and Reflection Radiometer	VNIR & SWIR	Satellite	Monitoring potential; low-cost
IKONOS	Private-sector satellite	VNIR	Satellite	Spatial detail; low-cost
HYPERION	Hyperspectral Imager	VNIR & SWIR	Satellite	Spectral detail; moderate cost
AVIRIS (low-altitude)	Airborne Visible-Infrared Imaging Spectrometer	VNIR & SWIR	Airborne	Spatial & spectral detail
SPECTIR	Full range Hyperspectral imaging spectrometer	VNIR - SWIR	Airborne	High resolution spatial and spectral

6. WATER CHEMISTRY AND MINEROLOGY

6.1 IRON & ALUMINUM METALS DISTRIBUTION

The type and quantity of metals in the stream and within the precipitates coating the rocks is of major importance in determining water quality factors. Table 2 compiles an example of metal content from a very low (2.17) pH spring at the base of Red Mountain West.

Table 2 – Red Mountain West (from Sares, 1996).

Analyte	Multiple above aquatic life standards
Al	1,724x
Cd	42x
Cu	164x
Fe	100x
Mn	within standard
Pb	within standard
Ag	6x
Zn	21x
SO4	6x

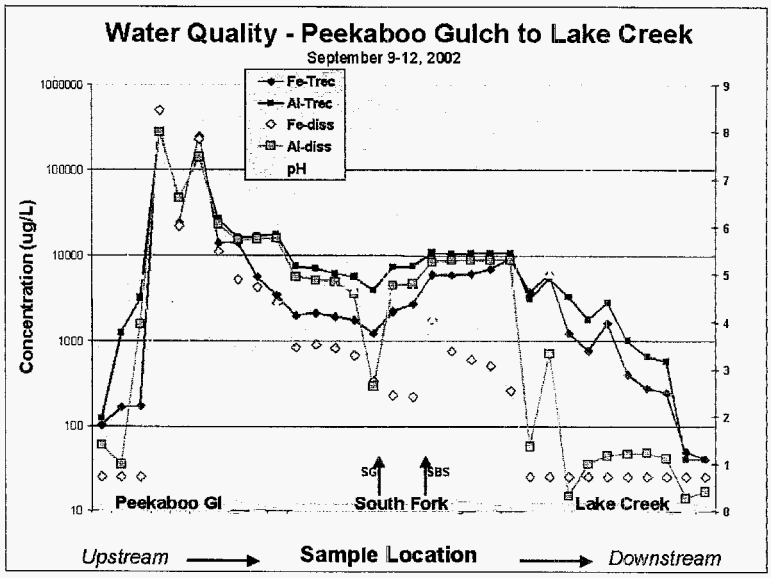

Figure 3-Graph showing water quality changes downstream of the Red Mountain West hydrothermally altered area. Extreme concentrations of iron and aluminum are shown in upper Peekaboo Gulch near the acid generating source rock. Metal concentrations generally decline downstream due to metals precipitating out of the water column onto the streambed and due to inflow of higher pH diluting water. Separation between the dissolved (diss) and total recoverable (trec) concentrations occurs as the Fe and Al ions moved out of the dissolved form into a suspended solid form. Acidic inflows from Sayres Gulch (SG) and Sayres Bowl Stream (SBS) show a temporary reversal in these downstream trends.

The values in the table show the presence of the listed elements in the spring, not in concentration, but in the multiple above the statewide water quality standards for aquatic life. For example, the concentration of aluminum is 1,724 times the aquatic life standard of 87 micrograms per liter. This spring is draining from the mineralized and altered areas on Red Mountain West. These rocks contain high volumes of aluminum bearing minerals such as feldspars, muscovite and illite. Aluminum poses a great danger to aquatic life. It can coat the gills of fish and suffocate them. New research is also showing that aluminum can be chemically toxic to fish in both acidic and neutral waters (Soucek et al., 2002) . No fish live in the upper parts of the watershed affected by natural acid rock drainage.

6.2 IRON MINERALS & pH CORRELATION

Over 80 ground truth data sets, which include seasonal water pH, water chemistry, mineral reflectance spectroscopy, and mineral XRF(X-ray Fluorescence), have been collected for correlation to the airborne and satellite sensor data. The main environmental remote sensing issues involve iron and aluminum oxyhydroxide phases that are created when the iron sulfides oxidize and generate acidic drainage, and the in-situ aluminum silicates that are chemically weathered by acidic ground waters. Iron and aluminum precipitates concentrate at the sources, collect metals, and are deposited throughout the drainages all the way down to Twin Lakes Reservoir.

The infrared-active iron minerals currently detected include: 1) the sulfates jarosite, schwertmannite, copiapite, and melanterite: 2) oxyhydroxides, maghemite, lepidocrocite, ferrihydrite, and goethite. The diagram below shows the pH zones at which the commonest of these minerals form. This model will be used to predict the minerals most likely to occur through the drainages within the changing pH zones.

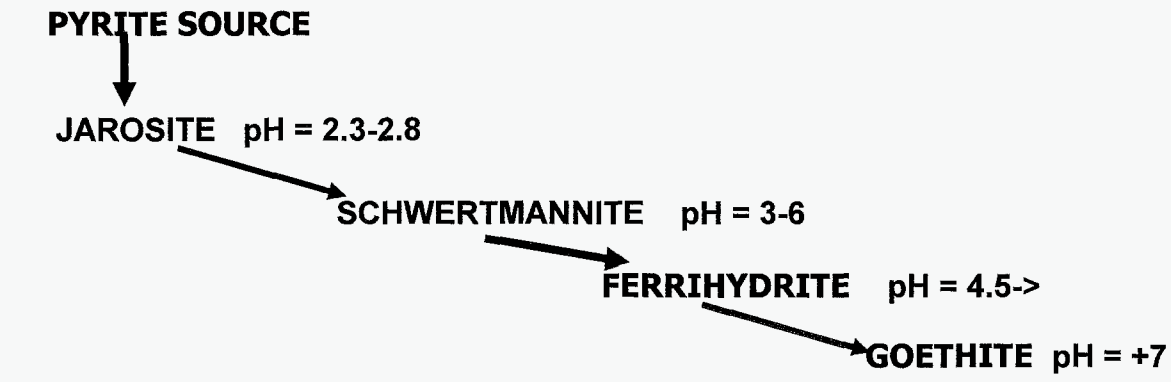

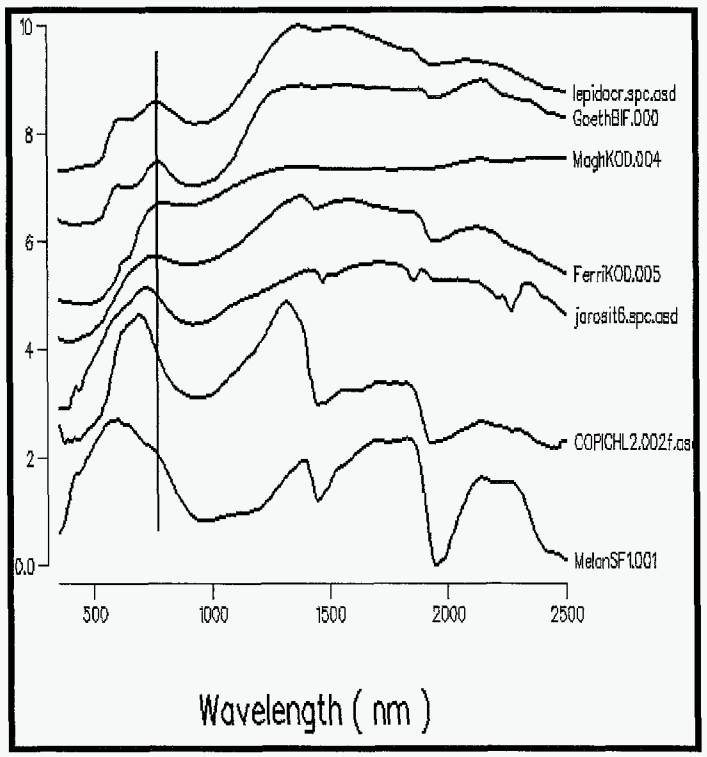

Figure 4 – This figure plots the iron oxyhydroxide and sulfate minerals observed to date in the Lake Creek drainage, and includes [A] lepidocrocite (γ-FeOOH), [B] goethite $Fe^{3+}O(OH)$, [C] maghemite (γ-Fe2O3), [D] ferrihydrite $Fe^{3+}{}_2O_3 \cdot 0.5(H_2O)$, [E] jarosite [KFe3(SO4)2(OH)6], [F] copiapite ($Fe^{2+}Fe^{3+}{}_4(SO_4)_6(OH)_2 \cdot 20(H_2O)$), and [G] melanterite ($Fe^{2+}(SO_4) \cdot 7(H_2O)$).

Please note that each of these minerals have diagnostic spectral profiles, especially in the visible through Near Infrared region (400-1000 nm). Although copiapite and melanterite have been identified in Peekaboo Gulch, they are not present in large enough amounts to be detectable from the air. The other issue is that nearly all of the spectra collected from the precipitates are mixtures of iron phases. Because the pH will change with stream flow, stability fields are constantly shifting as water levels fluctuate.

The ground data collected show a distinct zoning of iron minerals that correlates to pH. The iron sulfates jarosite, schwertmannite, melanterite and copiapite occur in Peekaboo Gulch, and all are low (2-4) pH. These mineral assemblages change, as the pH increases to the 4.0-4.99 range along the South Fork Drainage, to iron oxides, dominant of which is ferrihydrite. In the Lake Creek drainage, the water is diluted by neutral North Fork water and the pH values range from 6.93 to 7.75, with goethite and lepidocrocite the main iron minerals.

Table 3 summarizes the generalized mineralogy through the three drainages (Peekaboo – PG; South Fork-SF and Lake Creek-LC) under discussion. It can be seen how consistent the correlation of mineralogy to pH is. Location LC-1 has higher acidity as a function of inflow of lower pH waters from La Plata Creek and South Fork. Jarosite occurs along South Fork in selected areas below Site SF-7. At SF-7, a highly acid (pH=3) tributary drains into South Fork from the Red Mountain East sulfide source, causing jarosite precipitation within and below the mixing zones.

Table 3 – Comparison of Minerals against pH

Sample Site	Date	pH	Total Acid	Minerals
LC-01	9.10.02	5.02	23	goethite, maghemite, jarosite
LC-02	9.9.02	7.61	8	maghemite, goethite, lepidocrocite
LC-03	9.9.02	7.11	8.3	maghemite, goethite
LC-04	9.10.02	7.15	7	maghemite, goethite, lepidocrocite
LC-05	9.9.02	7.66	6	maghemite, goethite, lepidocrocite
LC-06	9.9.02	7.06	6.8	maghemite, goethite, lepidocrocite
LC-07	9.9.02	7.44	9	maghemite, goethite, lepidocrocite
LC_08				lepidocrocite, goethite
LC-09	9.9.02	7.75	9	lepidocrocite, goethite
LC-10	9.10.02	6.93	25.6	goethite
LC-11	9.9.02	7.01	1.11	lepidocrocite, goethite
SF-04	9.10.02	5.31	25	ferrihydrite
SF-05	9.10.02	4.57	40	ferrihydrite
SF-06	9.10.02	4.66	74	ferrihydrite
SF-07	9.10.02	4.07	73	ferrihydrite, jarosite
SF-08	9.10.02	4.16	72	ferrihydrite, jarosite
SF-09	9.10.02	4.45	*	ferrihydrite, jarosite
SF-10	9.10.02	4.28	65	ferrihydrite, jarosite
SF-11	9.10.02	6.5	16	maghemite, lepidocrocite, goethite
SF-12D	9.10.02	4.6	49	ferrihydrite, AlOH
SF-13	9.10.02	4.68	40	ferrihydrite, jarosite
SF-14	9.10.02	4.72	39	ferrihydrite
SF-15	9.10.02	4.68	33	ferrihydrite
SF-16	9.10.02	4.91	22	ferrihydrite
SF-17	9.10.02	4.32	69.1	ferrihydrite
PG-01	9.11.02	3.88	1050	melanterite, jarosite, copiapite
PG-02				copiapite. jarosite
PG-04	9.11.02	3.33	171.2	jarosite
PG-05	9.11.02	4.35	140.8	copiapite
PG-06	9.11.02	6.55	18	maghemite
PG-07	9.11.02	2.74	2300	jarosite, schwertmannite
PG-08	9.11.02	3.43	122	jarosite

pH values in Peekaboo Gulch change as a function of more neutral water sources (PG-6) above the main acid springs (PG-7, PG-1, PG-2).

7. HYPERSPECTRAL REMOTE SENSIING

7.1 INTEGRATION with ASTER and AVIRIS

ASTER satellite data are being evaluated in this project as a potential reconnaissance tool. The 30 meter SWIR range ASTER will have limitations in the narrow (3-5 meters), high mountain valleys. However, ASTER defines aluminum-bearing alteration minerals well. It can be used to outline areas of hydrothermal alteration and

can locate large concentrations of iron oxides (Figure 5, white arrow). It appears that ASTER can be used to vector towards drainages that potentially contain iron oxides and sulfates.

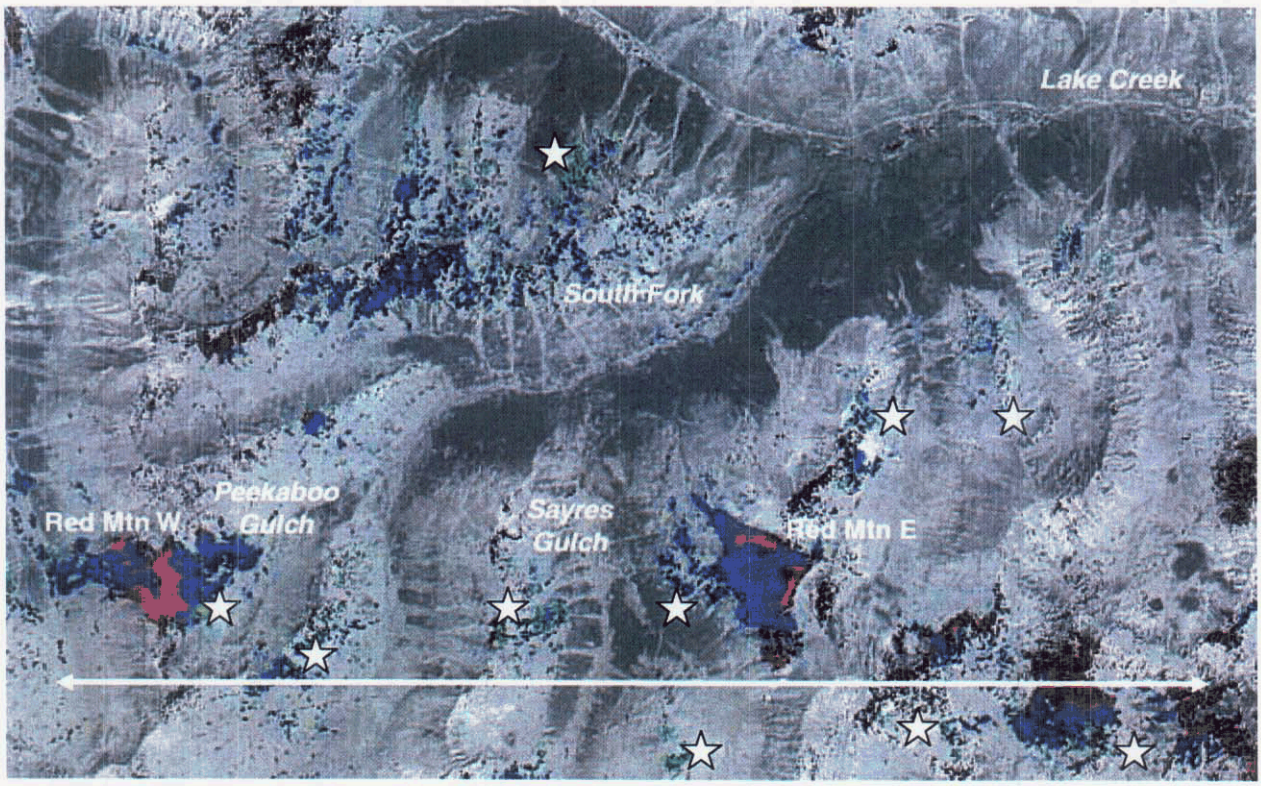

Figure 5 – Pixels from ASTER SWIR 30 meter alteration image are overlain on the 15 meter visible image. The white double arrow runs through the two main alteration systems at Red Mountain West and Red Mountain East. This image was processed for iron oxides, jarosite and muscovite/illite. Selected jarosite locations are marked with white stars. Some have been field verified. The image demonstrates that ASTER can be used as a first pass over an area to determine the presence of hydrothermal alteration and some secondary products. *This image was processed by David Coulter, Overhill Imaging and Cartography.*

7.2 AVIRIS IMAGE OF LAKE CREEK DELTA

7.2.1 CALIBRATION

Empirical line calibration spectra were collected from the broad, fairly homogeneous quartz-illite beach between the two reservoirs (Fig.6). The spectra were taken with an ASD FieldSpec Pro spectrometer. The calibration was checked with a pixel from the lake water.

The beach was considered a uniform flat field. A cross check was made using a deeper part of the lake where the spectrum should be flat. This calibration was used for the AVIRIS images

Low-altitude AVIRIS was flown in September, 2002, over both Phase 1 and Phase 2 areas. The data are now in the initial stages of calibration and processing. A segment of Flight Line LC-3 (Fig. 7B) is shown, covering the Twin Lakes Reservoir, lower Lake Creek, and the Lake Creek delta (Fig. 7A). The image was processed for the iron mineral goethite, which was identified at several sample sites (LC-7, 8, 9).

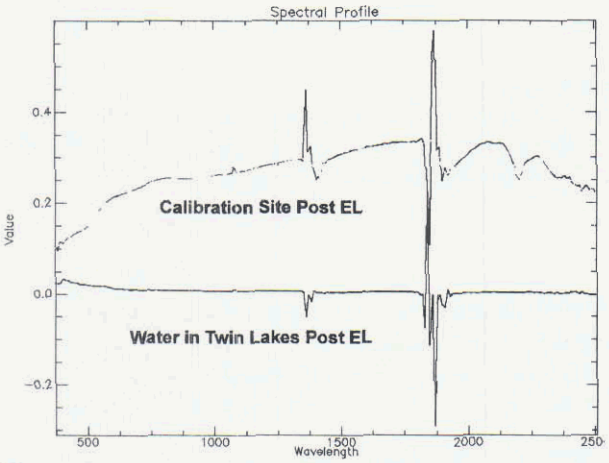

Figure 6 – Atmospheric calibration data.

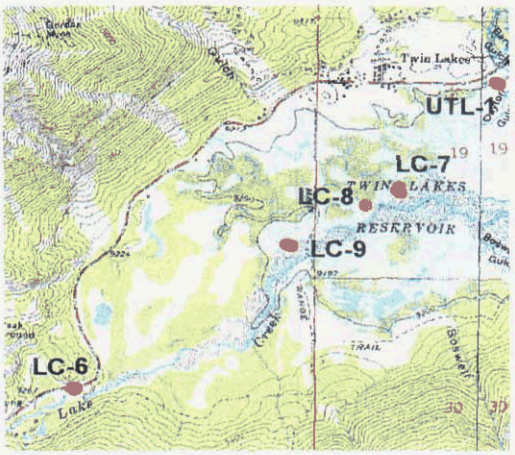

Figure 7A – Topographic map of AVIRIS image (below).

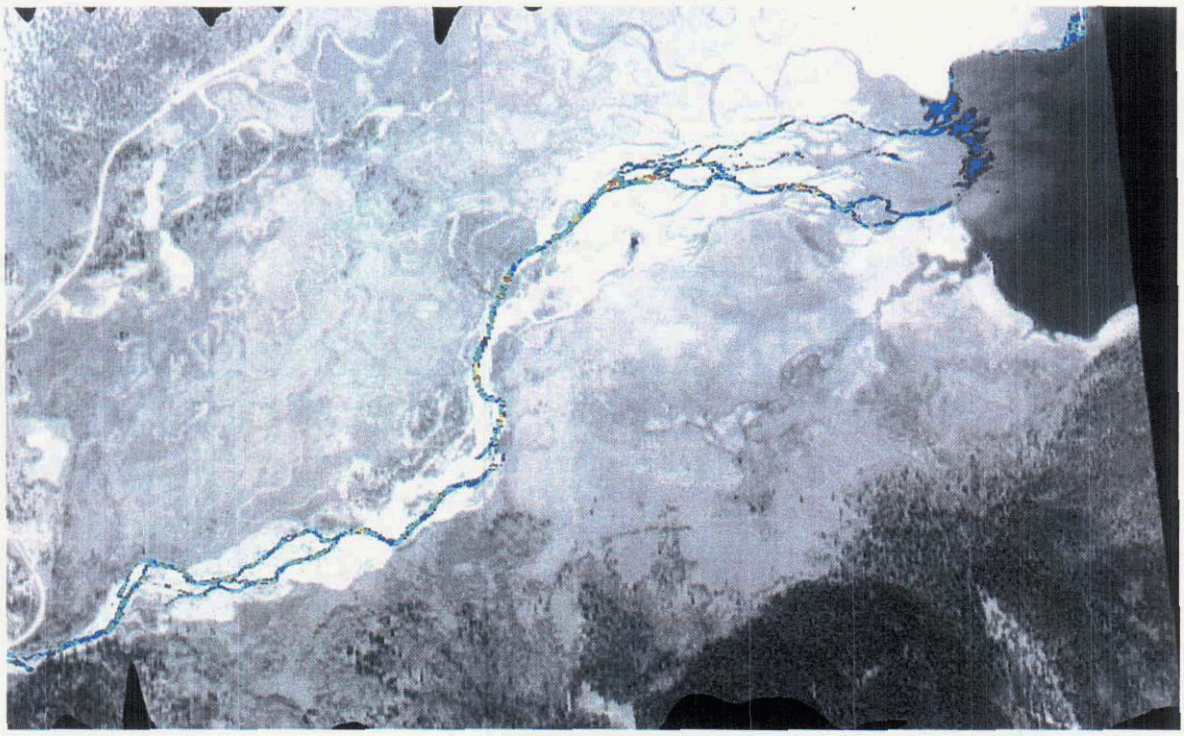

Figure 7B – Low-altitude AVIRIS classification image of the iron oxide mineral goethite. Distribution of goethite is directly along the banks of the main channel. Goethite indicates a neutral pH. Spatial resolution on the images is about 3 m. Image processed using SAM (Spectral Angle Mapper) algorithm. Displayed image is a rule image, with color progression of red-yellow-green-blue, with red = spectral angle of zero, or a perfect match of the image pixel to the reference.

8. DISCUSSION

Although this data contains the first stage results of the project, the correlations between the ground mineralogy and the pH zones are compelling and demonstrate the usefulness of reflectance spectroscopy to characterizing and monitoring this type of ARD. Initial imagery demonstrates that ASTER has the potential to be used in a reconnaissance mode over a watershed, indicating areas of iron oxide/sulfate minerals. AVIRIS low-altitude images with 1-3m pixel size will further target specific iron minerals and their distribution along stream banks, and even within the water itself.

9. ACKNOWLEDGEMENTS

The following list includes supporters of and participants in the project:
Colorado Mountain College, State Engineers Office, Colorado Division of Water Resources, U.S. Forest Service, U.S. Geological Survey, Lake County Conservation District, Upper Arkansas Water Conservancy District, Arkansas Valley Natural Damage Assessment Impact Response Team, Board of Chaffee County Commissioners, Western Governors Association.

10. REFERENCES

Cruson, M.G., 1973, Geology and ore deposits of the Grizzly Peak cauldron complex, Sawatch Range, Colorado: Colorado School of Mines, Ph.D thesis T 1538 (unpubl.), 181 p., 7 plates.

Fridrich, C.J., Smith, R.P. DeWitt, Ed, and McKee, E.H., 1991, Structural, eruptive, and intrusive evolution of the Grizzly Peak caldera, Sawatch Range, Colorado: Geological Society of America Bulletin, v. 103, no. 9 (September 1991), p. 1160-1177.

Fridrich, C.J., DeWitt, E., Bryant, B., Richard, S. and Smith, R.P., 1998, Geologic map of the Collegiate Peaks Wilderness Area and the Grizzly Peak Caldera, Sawatch Range, Central Colorado. U.S. Geol. Surv. Map MI I-2565 (1:50,000).

Hauff, P.L., N. Lindsay, D.C. Peters, G.A. Borstad, W. Peppin, L. Costick, and R. Glanzman, 1999a, Hyperspectral evaluation of mine waste and abandoned mine lands: NASA- and EPA-sponsored projects in Idaho, in R.O. Green, ed., Summaries of the Eighth JPL Airborne Earth Science Workshop, February 9-11, 1999: JPL Publication 99-17, p. 229-238.

Hauff, P.L., D.C. Peters, G.A. Borstad, W. Peppin, N. Lindsay, L. Costick, R. Neville, and R. Glanzman, 1999b Hyperspectral evaluation of mine waste and abandoned mine lands: NASA- and EPA-sponsored projects in Utah and Idaho, in Proceedings of the International Symposium on Spectral Sensing Research '99 Conference, October 31-November 4, 1999, Las Vegas, Nevada.

Hauff, P.L., D.C. Peters, G.A. Borstad, W.A. Peppin, E. Dillenbeck, L.G. Closs, and E.C. Prosh, 2000, Hyperspectral investigations of mine waste and abandoned mine lands – The Dragon calibration site case study, in Proceedings of the Ninth JPL AVIRIS Workshop, February 23-25, 2000, Pasadena, California: Jet Propulsion Laboratory.

Neubert, J.T., 2000, Naturally degraded surface waters associated with hydrothermally altered terrane in Colorado: Colorado Geological Survey Open-File Report 00-16, 153 p. [CD-ROM].

Peters, D.C., P.L. Hauff, G.A. Borstad, F.B. Henderson III, W.A. Peppin, E. Dillenbeck, E.C. Prosh, L.G. Closs, J.L. Thiros, D.W. Coulter, K. Lee, D.A. Robbins, and K.W. Wangerud, 2000, Mine and mill waste characterization using CASI/SFSI hyperspectral data: Utah abandoned mine lands study areas, in Proceedings of the 14th International Conference and Workshops on Applied Geologic Remote Sensing, November 6-8, 2000, Las Vegas, Nevada: Ann Arbor, Environmental Research Institute of Michigan, p. 54-61.

Peters, D.C., P.L. Hauff, W.A. Peppin, E.C. Prosh, G.A. Borstad, F.B. Henderson III, E.D. Dillenbeck, L.G. Closs, K. Lee, J.L. Thiros, D.W. Coulter, D.A. Robbins, and K.W. Wangerud, 2001, Waste identification and characterization for the International Smelter area using CASI/SFSI hyperspectral remote sensing data, *in* Tailings & Mine Waste '01: Rotterdam, Balkema.

Sares, M.A., 1996, The U.S. Forest Service abandoned mine land inventory in Colorado: Background, progress, and preliminary findings *in* Bell, R.S., and Cramer, M.H. (compilers), Symposium on the Application of Geophysics to Engineering and Environmental Problems, April 29-May 2, 1996: Keystone, Colorado, Environmental and Engineering Geophysical Society, p. 221-232.

Soucek, D. J., Cherry, D. S. and Zipper, C. E., 2002, Aluminum and iron dominated toxicity in neutral waters below an acid mine drainage discharge: Canadian Journal of Aquatic Science, v. 58, no. 12, pp. 2396-2404.

U.S. Environmental Protection Agency (USEPA), 2002, California Gulch, <http://www.epa.gov/region08/superfund/sites/co/calgulch.html> Accessed Sept. 10, 2002.

Zanoni, Vicki, 2002, Remote Sensing System Requirements Development: A Simulation-Based Approach, ASPRS 2002 Pecora Conference, abstracts. American Society of Photogrammetry and Remote Sensing.

USE OF EO-1 HYPERION DATA FOR INTER-SENSOR CALIBRATION OF VEGETATION INDICES

Alfredo Huete,[1] Tomoaki Miura,[1] HoJin Kim,[1] Hiroki Yoshioka[2]
[1]Department of Soil, Water and Environmental Science, University of Arizona, 85721 USA
ahuete@ag.arizona.edu; tomoaki@ag.arizona.edu; hjkim@ag.arizona.edu; yoshioka@urban.meijo-u.ac.jp
[2]Department of Urban Science, Meijo University, 4-3-3 Nijigaoka, Gifu, 509-0261 Japan

1. INTRODUCTION

Numerous satellite sensor systems useful in terrestrial Earth observation and monitoring have recently been launched and their derived products are increasingly being used in regional and global vegetation studies. The increasing availability of multiple sensors offer much opportunity for vegetation studies aimed at understanding the terrestrial carbon cycle, climate change, and land cover conversions. Potential applications include improved multi-resolution characterization of the surface (scaling); improved optical-geometric characterization of vegetation canopies; improved assessments of surface phenology and ecosystem seasonal dynamics; and improved maintenance of long-term, inter-annual, time series data records. The Landsat series of sensors represent one group of sensors that have produced a long-term, archived data set of the Earth's surface, at fine resolution and since 1972, capable of being processed into useful information for global change studies (Hall et al., 1991).

Spectral vegetation indices are one example of satellite-based products for mapping temporal and spatial variations in surface biophysical parameters. Vegetation index products from Advanced Very High Resolution Radiometer (AVHRR), SeaWiFS, SPOT-VEGETATION, Moderate Resolution Imaging Spectroradiometer (MODIS), Global Imager (GLI), Landsat, and other sensors are now or soon will be widely available for monitoring both seasonal and long-term ecosystem dynamics. Their combined use can greatly improve ecosystem spatial and temporal variability studies in two ways, (1) through inter-sensor synergies and (2) through multi-sensor data and product continuity records. Seasonal and inter-annual vegetation dynamics have been readily observed with moderate resolution satellite products, such as the 20-year NOAA-AVHRR normalized difference vegetation index (NDVI) time series record (Los, 1993: Roderick et al., 1996).

With the launch of new sensor systems, there is interest in maintaining data continuity and compatibility across the sensor-specific data sets. However, there will also exist compatibility problems among the various satellite data products due to differences in their sensor characteristics as well as algorithms used (Gao, 2000; Gitelson and Kaufman, 1998). Some of the multi-sensor differences, key to their synergy, may become limitations to data and product continuity. This includes the issue vegetation index (VI) continuity and compatibility among the various sensors, which must first be addressed. In shifting from an older sensor to a newer one, one can take advantage of 'state of the art' technology advancements (e.g., better sensor materials) and improved scientific knowledge (e.g., better spectral band configurations), however, there is the dilemma of maintaining data continuity across a time series data record while allowing for new and improved algorithms and data processing.

The "key" factors affecting continuity and compatibility of VI data sets computed from different sensors involve;

- sensor calibration and degradation
- differences in spatial resolutions and their associated point spread functions (PSF)
- co-registration and geolocation
- differences in spectral bandpass filters
- atmospheric correction methods (O_3, H_2O, aerosols)
- cloud masking methods and their efficiency
- compositing techniques and period

Narrow and broad-band vegetation indices were investigated by Elvidge et al. (1995). Miura et al. (2002) utilized Hyperion imagery along a Brazil transect and showed VI translation between sensors to be land cover, soil, and biomass dependent. Yoshioka et al. (2003) developed an algorithm for translating VI data among sensors utilizing a linear approximation of vegetation isolines and numerical simulations using leaf and canopy radiative transfer

models. They applied the algorithm to a Hyperion image and were able to significantly reduce the differences in NDVI data for a wide range of LAI conditions.

In this study we used EO-1 Hyperion imagery obtained over a set of biome types to generate broadband reflectance and VI values for various Earth observing satellite sensors. Multi-sensor comparisons and analyses of vegetation index products are made for the "Constellation" series of sensors that include Landsat-7 ETM+, EO-1, Terra-MODIS/ASTER, and the Multispectral Medium-Resolution Scanner (MMRS), as well as for additional fine and moderate resolution sensor systems. We focus on the spectral issues (filter response function, bandwidth, center wavelength) influencing the derived reflectance and vegetation index values and also address the various issues involved in multi-sensor synergy use, including translation, data continuity, and scaling. The objectives for this study were (1) to investigate the "spectral" continuity and compatibility of reflectances and VIs among the different sensors using Hyperion scenes over a range of land cover types, and (2) to investigate target dependencies (land cover, soil, etc.) on the translation coefficients among sensors.

2. STUDY SITES AND METHODS

There are many techniques that can be used to analyze multi-sensor differences in VI's, including the use of 'real' satellite sensor observations. The advantages of this approach are that the real data from which we wish to establish translation are used and this also encompasses all sources of uncertainty, including filter degradation and calibration drift. The disadvantages are the time intervals between different sensor 'looks' over the same target and the confusion created with possible variations resulting from sun angle and atmosphere differences. One must also be precise in co-registration of the two sensor data sets with additional uncertainties resulting from geolocation error. A more controlled approach is to utilize finer resolution sensor data and simulate the responses of coarser resolution sensor data sets. Hyperion hyperspectral data are thus ideal to simulate MODIS, SeaWiFS, AVHRR, and GLI pixels, the advantages being that only a single atmosphere and sun angle are involved and there are no spatial registration errors. The disadvantage is that the data is synthetic and the spectral response functions and modulation transfer function (MTF) need to be approximated.

We utilized Hyperion data over a 400–2500 nm wavelength range with nominal spectral resolution of 10 nm at 30 m ground resolution. The radiometrically calibrated level 1A images were first corrected for vertical destriping noise by using the average values of assumed homogeneous areas for subsequent pixel adjustment. The data were then spectrally convolved to the bandpasses of the sensors of interest and then processed to atmospherically-corrected reflectances and VI's. The variations in spectral bandpass properties encountered in this study are shown in Fig. 1. Some atmospheric simulations were also conducted with the "6S" radiative transfer code.

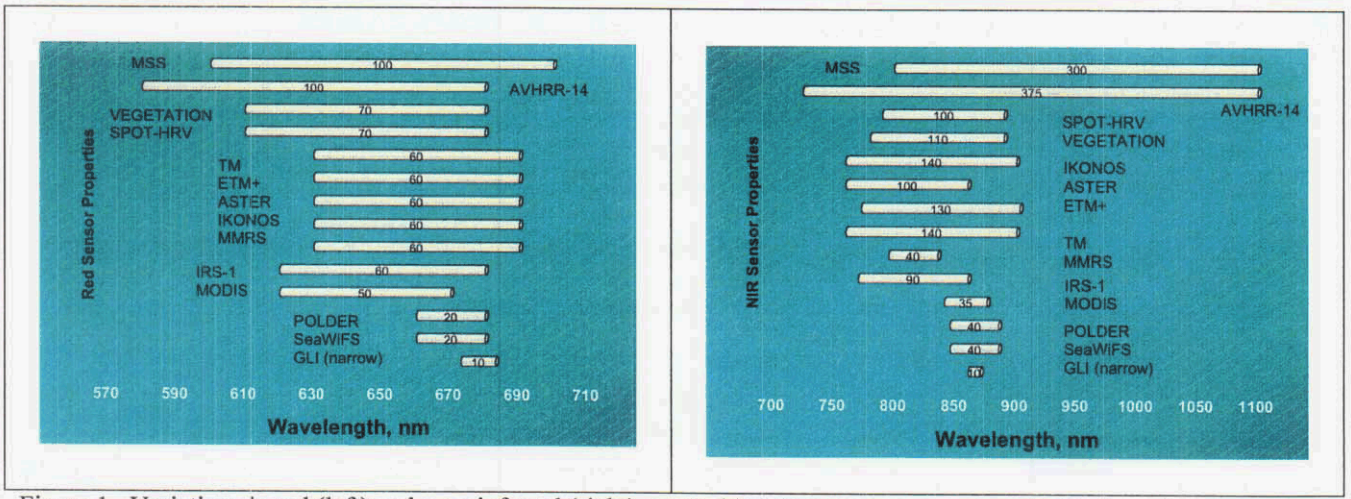

Figure 1. Variations in red (left) and near-infrared (right) spectral bandpasses among various Earth observing sensors used in vegetation studies.

Hyperion imagery over a range of international core land validation sites of varying land cover types and surface conditions were utilized in this study, including a Hyperion data over Maricopa Agriculture Center in Arizona, the

Mandalgovi steppe site in Mongolia, and the Harvard forest long-term ecologic research (LTER) site (Fig. 2). At each of the Hyperion sites, data were extracted from a 20 x 20 pixel area for further analyses.

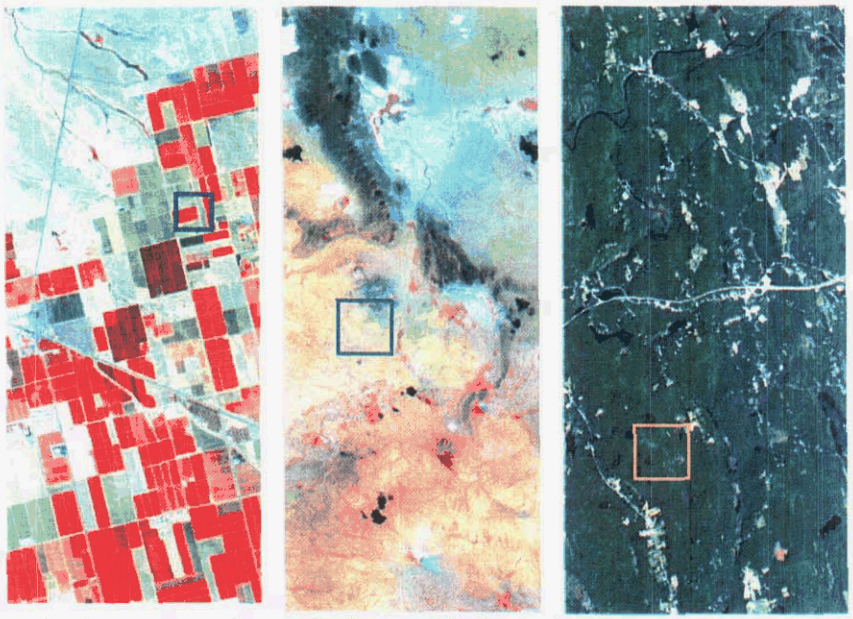

Figure 2. EO-1 Hyperion imagery over the study sites used in the evaluation of vegetation indices. Maricopa September 29, 2001 (left); Mandalgovi August 31, 2001 (middle); and Harvard forest September 5, 2001 (right).

3. RESULTS

The Hyperion bandpass-convolved results over the Harvard forest study area are shown in Fig. 3 for the MODIS, Landsat-7 ETM+, and NOAA-AVHRR 14 sensors under atmospherically corrected (surface) and uncorrected (top-of-atmosphere, TOA) conditions. There were much higher inter-sensor variations encountered with the TOA results, indicating the strong interactions of atmosphere and sensor bandpass on the resulting red, NIR, and NDVI data. The AVHRR varies the most from the other sensors with higher red reflectances and lower NIR and NDVI values. The surface NDVI values from the AVHRR are lower than the other 2 sensors due to the higher red reflectance response. The Maricopa Agriculture study site had a bi-modal range of surface conditions with bare soil and highly-vegetated crops present in the same scene (Fig. 4). The red reflectance results among the 3 sensors varied only slightly in both TOA and surface cases while the NIR results only varied in the uncorrected, TOA data with AVHRR yielding the lowest reflectances and MODIS the highest. This may be an atmosphere water vapor effect with the AVHRR bandpass the most vulnerable to water vapor while the MODIS NIR bandpass was designed to be free of water vapor contamination. The TOA- NDVI values followed the same pattern with AVHRR having the lowest values and MODIS the highest. By contrast, the surface-based NDVI values differed less significantly.

In the following graphs we analyze in more detail the inter-sensor spectral bandpass effects on the computed vegetation indices. The top portion of Fig. 5 shows that all bands are highly inter-correlated, as would be expected since they are measuring within the same portion of the spectrum. One can also note, however, that the inter-sensor relationships have significant slope and/ or intercept differences. The AVHRR and ASTER NIR reflectances, for example, deviate significantly from the 1:1 line (Fig. 5). In the lower portion of Fig. 5, we plotted the surface reflectance difference ($\rho_{sensorX} - \rho_{MODIS}$) to highlight these deviations. Using the MODIS reflectances as the reference (any sensor could be used for the reference case), we see that the differences associated with a different bandpass in the red and NIR region are dependent on the initial MODIS reflectance condition and that a second sensor's response could result in higher or lower values. In the case of the red bandpass, maximum deviations from the MODIS value occur at low and high reflectance conditions with deviations increasing as the MODIS surface reflectance departs from 0.15 in either direction (Fig. 5). In the case of the NIR reflectances, minimum variations occur at low MODIS reflectances (<0.33) with deviations becoming stronger as MODIS NIR reflectance increases in value. Another observation worth noting is that for any given MODIS reflectance values, there are varying

reflectance values for a second sensor, e.g., a MODIS reflectance value of 0.40 in the NIR yields numerous ASTER reflectances.

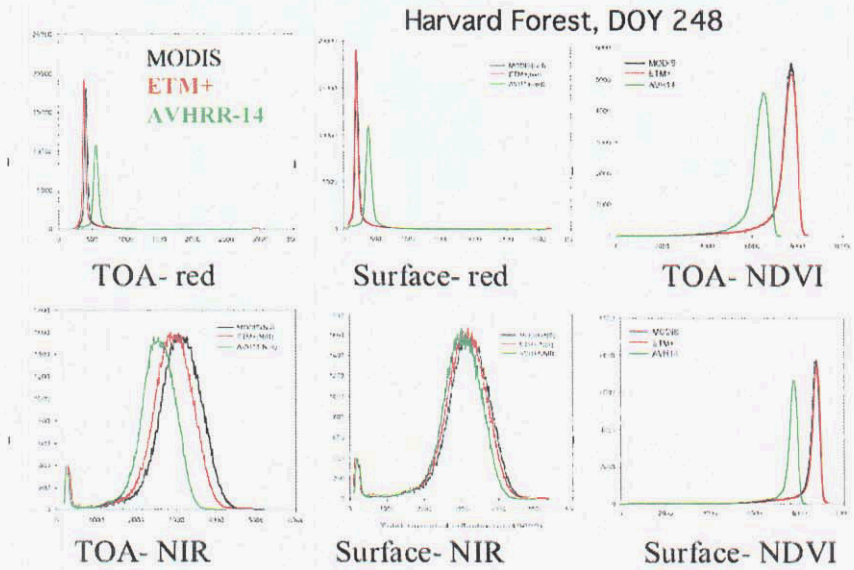

Figure 3. Histograms of red, NIR, and NDVI data over the Harvard forest study site for the 3 sensors, MODIS, Landsat-7 ETM+, and NOAA-AVHRR-14, and for TOA and atmospherically-corrected (surface) conditions.

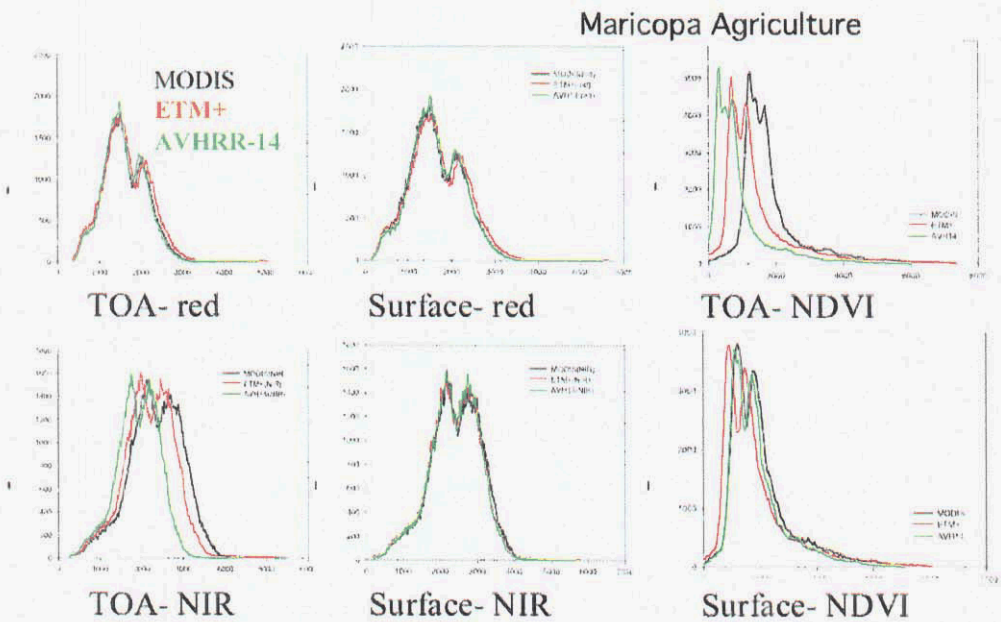

Figure 4. Histograms of red, NIR, and NDVI data over the Maricopa Agriculture Center study site for the 3 sensors, MODIS, Landsat-7 ETM+, and NOAA-AVHRR-14, and for TOA and atmospherically-corrected (surface) conditions.

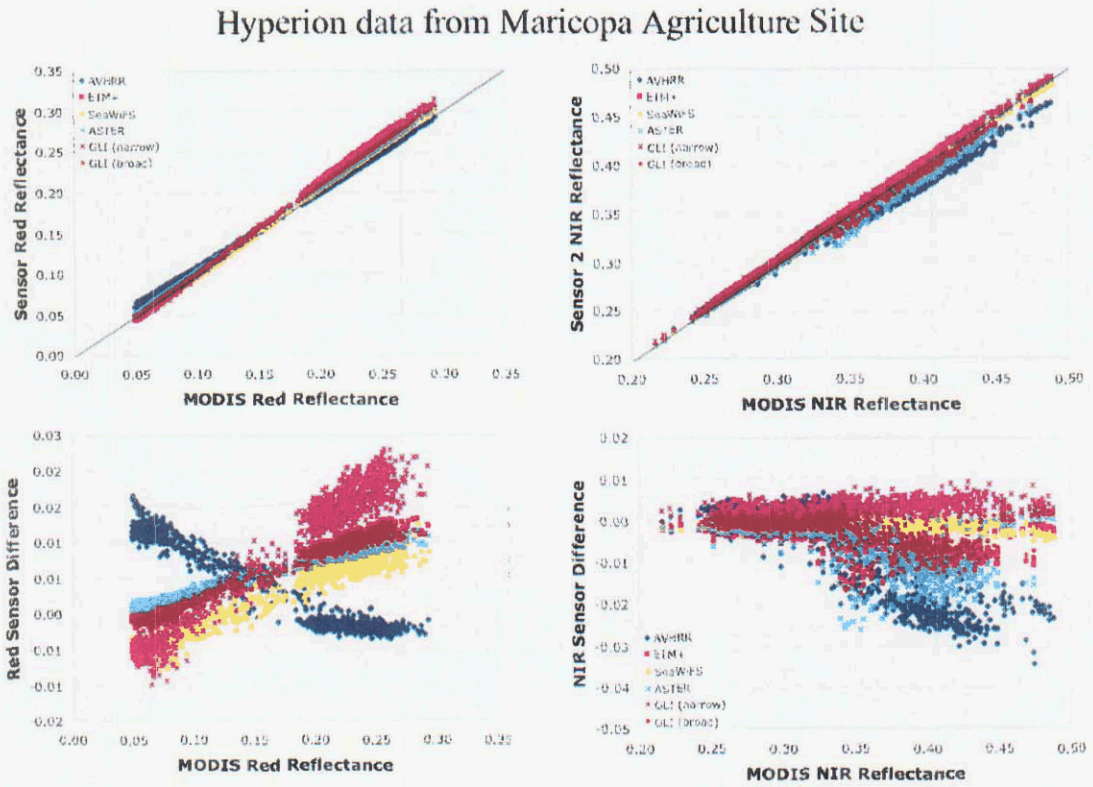

Figure 5. Hyperion-generated crossplots of inter-sensor band surface reflectances (top) and their differences using MODIS as a reference (bottom).

In Fig. 6, the corresponding VI values are plotted using the sensor differences to highlight the deviations. The NDVI comparisons behaved similar to the red bandpass comparisons in Fig. 5. Thus, the difference in NDVI between MODIS and AVHRR become greater at higher NDVI values, i.e., MODIS NDVI values are higher than AVHRR at higher biomass conditions (up to 0.07 NDVI units). In the right hand side of Fig. 6 we also compared a partially atmosphere corrected data set (only corrected for Rayleigh scattering and ozone absorption) and we found that atmosphere plays a bigger role in inter-sensor relationships than bandpass differences among sensors. However, in the case of the enhanced vegetation index (EVI) (Huete et al., 2002), atmosphere-induced variations are not so strong and bandpass variations among sensors become greater with higher MODIS EVI values (Fig. 6). There are not as many sensors available for comparisons given the need for a blue band for the EVI computation.

4. CONCLUSIONS AND DISCUSSION

We investigated continuity and compatibility of the broadband reflectances and VIs across various Earth observing sensors. EO-1 Hyperion data was used in different biome sites to synthetically generate multi-sensor reflectances and VI's, including the NDVI and EVI. Our analyses focused on the spectral issue (spectral characteristics of multiple sensors and their influences on the derived VI values). The sensors considered in this spectral syntheses were MODIS, AVHRR, SeaWiFS, VEGETATION, GLI, ASTER, and ETM+. The major findings were that:

- VI relationships among sensors were neither linear nor unique and were found to exhibit complex patterns and dependencies on spectral bandpasses.
- From the biophysical point of view, inter-sensor VI relationships varied with land cover types and surface characteristics. Thus, a prior knowledge of such ecosystem parameters as leaf area index (LAI), land cover type, and soil brightness are needed for exact translation.
- Atmospheric contaminations were found to increase the discrepancies and land cover dependencies of inter-sensor VI relationships, of which magnitudes depends both on level of atmospheric contaminations and on amount of vegetation density.

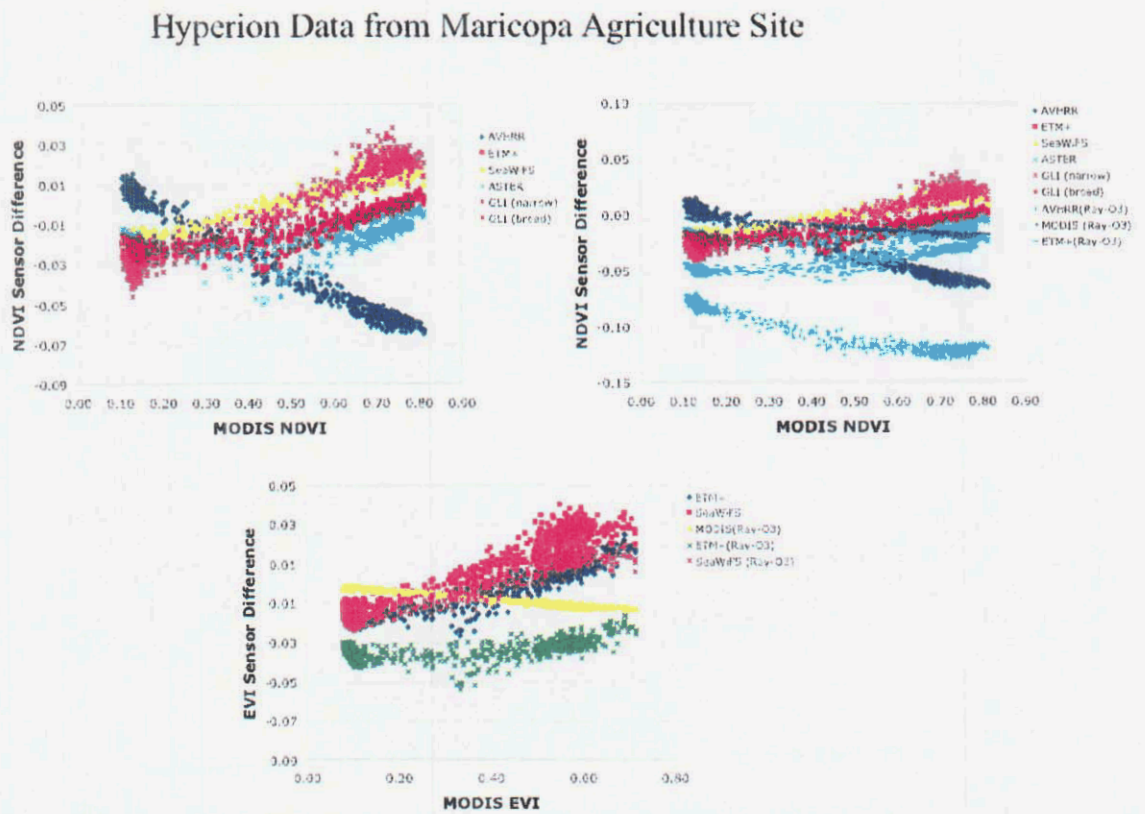

Figure 6. Hyperion generated crossplots of inter-sensor NDVI differences (top) and inter-sensor EVI differences (bottom) using MODIS as a reference.

Vegetation index relationships among sensors were found to exhibit complex patterns and dependencies based only on their spectral bandpasses. Thus, a reflectance or VI value from one sensor can yield multiple values in a second sensor. NDVI relationships among sensors varied with surface conditions, such as land cover type, biophysical parameter amounts, and possibly canopy background. The results shown here demonstrate that inter-sensor calibration and continuity of VI's are achievable but require biophysical and land cover characterization of surface conditions. We found that the atmosphere resistant VI's would provide improved multi-sensor translations, by reducing the effects of atmosphere on inter-sensor translation of VI's. Other factors that could affect the multi-sensor VI values to a greater extent include the cloud masking algorithm, BRDF-related effects, and the method of compositing, such as maximum value compositing (MVC), constrained view angle MVC (CV-MVC), minimum 'blue' compositing ('min. blue'), BRDF- based compositing, etc.

Multi-sensor comparisons with actual data from Landsat, EO-1, MODIS, AVHRR, and Terra are also needed to confirm some of the observations reported in this study. Such studies will become even more relevant in establishing a long term time series record involving the AVHRR time series record (1981-) with MODIS (2000-) and the next generation of the National Polar-orbiting Operational Environmental Satellite System (NPOESS).

ACKNOWLEDGMENTS

This work was supported by the NASA EO-1 grant NCC5-478 (A.R. Huete).

REFERENCES

Elvidge, C.E., and Chen, Z., 1995, "Comparison of broad-band and narrow-band red and near-infrared vegetation indices," *Remote Sensing of Environment*, 54:38–48.

Gao, B., 2000, "A practical method for simulating AVHRR-consistent NDVI data series using narrow MODIS channels in the 0.5–1.0 μm spectral range," *IEEE Transactions of Geoscience and Remote Sensing*, 38:1969–1975.

Gitelson, A.A., and Kaufman, Y.J., 1998, "MODIS NDVI optimization to fit the AVHRR data series-Spectral considerations," *Remote Sensing of Environment*, 66:343–350.

Hall, F.G., Strebel, D.E., Nickeson, J.E., and Goetz, S.J., 1991, "Radiometric rectification: toward a common radiometric response among multidate, multisensor images," *Remote Sensing of Environment*, 35:11–27.

Huete, A., Didan, K., Miura, T., and Rodriguez, E., 2002, "Overview of the radiometric and biophysical performance of the MODIS vegetation indices," *Remote Sensing of Environment,* 83:195–213.

Los, S., 1993, "Calibration adjustment of the NOAA AVHRR normalized difference vegetation index without recourse to component Channel 1 and 2 data," *International Journal of Remote Sensing*, 14:1907–1917.

Miura, T., Huete, A.R., Yoshioka, H., and Kim, H., 2002, "An application of airborne hyperspectral and EO-1 Hyperion data for inter-sensor calibration of vegetation indices for regional-scale monitoring," *Proceedings of the International Geoscience and Remote Sensing Symposium, IGARSS '02,* 6:3118–3120.

Roderick, M., Smith, R., and Lodwick, G., 1996, "Calibrating long-term AVHRR-derived NDVI imagery," *Remote Sensing of Environment*, 58:1–12.

Yoshioka, H., Miura, T., and Huete, A.R., 2003, An Isoline-based translation technique of spectral vegetation index using EO-1 Hyperion data, *IEEE Transactions of Geoscience and Remote Sensing,* 41.

HYPERSPECTRAL DETECTION OF FOREST FUEL ATTRIBUTES AS INPUT TO FARSITE FIRE MODEL IN THE FRONT RANGE OF COLORADO

Gensuo J. Jia, Ingrid C. Burke, and Sonia A. Hall[1]

1. INTRODUCTION

The increasingly severe forest fires in the western U.S. states in recent years (e.g., Colorado/Arizona/Oregon fires in 2002 and California/Oregon/Idaho fires in 2003) emphasized their power to modify the landscape and challenge the security of human life and economy in the urban-wildland interface. In the 2002 fire season alone approximately 3,000 structures were damaged or destroyed in some 71,200 forest fires that burned nearly 2.67 million ha (7.1 million acres) in the U.S. There is strong evidence that many current forests are denser and more vulnerable to catastrophic fires than they were historically (Covington et al., 1997, Kaufmann et al., 2000, Veblen et al., 2000). Those forest fires strongly influence the spatial distribution, variability and dynamics of plant communities (Romme 1982, Turner et al., 1997). In addition, forest fires have dramatic effects on ecosystem carbon storage (Houghton et al., 2000). Beyond the effects on the structure and carbon storage of forested landscapes, however, there are significant potential impacts to the growing human populations in the west, and particularly the Colorado Front Range, where three large fires since 1996 have devastated homes and municipal water supplies. These effects are evident in the high priority placed on fire research and management by the federal government, in programs such as the Joint Fire Science Program, a six-agency partnership authorized by Congress in 1997 to develop information and tools for managers and specialists who deal with wildland fuels issues, and by the newly designated $1.8 billion National Fire Plan. Therefore it is important to build our capacity to predict, with a reasonable degree of accuracy, the probability of fires occurring in time and space, in order to be able to appropriately minimize these risks with fuel treatments and prescribed fire. The probability and severity of fire are controlled by a series of factors, related to characteristics of the forest, to environmental conditions, and to the proximity and activities of humans. Among those, fuel attributes are critical and could be managed through mechanical thinning and prescribed burning.

Fire related forest characteristics vary across space, due to gradients in environmental and biological factors, including disturbance history (Romme 1982, Veblen et al., 2000, many others). These characteristics include species composition, stem biomass or volume, basal area, species composition, crown closure and understory biomass, all of which affect the probability of occurrence, spread and intensity of forest fires. Being able to quantify these characteristics, their potential development or change through time, and their spatial patterns is fundamental to decision-making. The existence of accurate fuel model and forest structure data could add important inputs and new strength to existing models of fire probability, fire behavior, and fire consequences (e.g., Perry 1998, Keane et al., 1996, Miller and Urban 2000), and allow policy-makers and managers to determine the best strategies for fire management.

Satellite and airborne remotely sensed imagery have been demonstrated to be useful for the description of spatial patterns of different forest ecosystem attributes (e.g., Wessman et al., 1988, Running et al., 1995, Roberts et al., 1998, Asner et al., 1998). The main advantages of using remote sensing are the spatial resolution and coverage, and the speed and relatively low cost with which these data are available. There is a fast-growing variety of remotely sensed data sources available. Their advantages only materialize and become implemented if and when research evaluates and validates the relationships between these data and actual, biologically relevant vegetation characteristics. Our objective is to evaluate

[1] Colorado State University, Fort Collins, Colorado 80523-1472, jiongjia@cnr.colostate.edu; indy@cnr.colostate.edu; sonia.hall@cnr.colostate.edu

the suitability of different remotely sensed data sets for the estimation of forest characteristics related to fire hazard, and their spatial patterns.

In the study, we tested various remote sensing and modeling efforts, including high altitude Airborne Visible and Infrared Imaging Spectrometer (AVIRIS) and Hyperion detection of fuel attributes, and LiDAR detection of forest vertical structure, in two test areas in the Colorado Front Range. We identified potential sources of remotely sensed imagery for estimating major fuel input variables for the FARSITE fire behavior model (Finney, 1998), and validated those spatial representations against field data. Based on those test analyses we generated maps of fuel classes and burn severity for fire assessment.

2. DATA AND METHODS

2.1 Field spectral and forestry measurements

The purpose of our fieldwork was to measure the spectral reflectance of all possible fuel related materials (endmembers) and to estimate fuel variables in the areas covered by remote sensing data, so as to validate remote sensing estimates. Vegetation types of concern in the montane zone of Colorado include ponderosa pine (*Pinus ponderosa*), Douglas-fir (*Pseudotsuga menziesii var. glauca*), mixed conifer (including ponderosa pine, lodgepole pine (*Pinus contorta*), and Douglas-fir), shrubland, grassland/woodland, aspen (*Populus tremuloides*), and riparian (cottonwood/willow). In summer 2002 and 2003, we conducted intensive field measurements of spectral reflectance and forest fuel loading/condition along 31 100m transects and 227 ground control points selected in the Pike National Forest and the Arapaho-Roosevelt National Forest, Colorado Front Range. Meanwhile, a large data set of 50 0.1-ha plots was available from USFS for a ponderosa pine landscape in the Pike National Forest (Kaufmann et al., 2000), and ready for analysis. Our measurements included complete overstory inventories, i.e., tree crown diameter, canopy cover, basal area, height, species, live or dead status, and burn severity (if any); modified-Whittaker understory data, i.e., percent cover by species, growth forms; and surface fuel inventory. We selected our sample sites randomly and covered various fuel conditions and burn severity classes in both NF. During the fieldwork, we also linked a Garmin V GPS unit to a laptop computer with ENVI software to instantly track and mark sample plots and transects on QuickBird (a spaceborne multispectral data with 2.8m pixel resolution, provided by DigitalGlobe Inc.) and AVIRIS images in term of species composition, canopy cover and burn severity. Later on we used those ground control points (GCP) to test spectral unmixing and to train classification algorithms based on AVIRIS, Hyperion and Landsat 7 data for estimating fuel variables over the study areas.

Along with forest transect and ground control points sampling, we collected field reflectance spectra of plant species and various fuel-related materials in the sample sites whenever weather condition were favorable, with a FieldSpec Pro spectroradiometer (Analytical Spectral Devices, Boulder, Colorado) over the 400-2500 nm wavelength region at 1 nm intervals. We made measurements on cloud-free days between 11:00 and 13:00 to minimize atmospheric effects and shade disturbance. The spectroradiometer was positioned approximately 1 meter from the sample surface at a 0° view zenith angle. With the 18° optics on the spectroradiometer, the diameter of the field of view at the sample was 28 cm. The sunlight and view angles were chosen to minimize shadowing and to emphasize the fundamental spectral properties of the plant and other materials. 9-15 spectra were acquired of each sample by moving the sensor over the objects to get the average spectra that are more comparable with the spectra of AVIRIS and Hyperion pixels. A white board panel was used to calibrate the spectroradiometer prior to measurement of each material. We calculated the average spectral curves for each endmember and established fuel spectral libraries in ENVI. We later used those field spectra as endmembers in AVIRIS-based spectral unmixing analysis.

2.2 Hyperspectral data acquisition and analysis

High-altitude AVIRIS radiance data (f021015t01) were acquired with the ER-2 plane by the Jet Propulsion Laboratory (JPL) on October 15, 2002 at 18:34 GMT (12:34 MT) over the Colorado Front Range, covering Hewlett Gulch-Bobcat Gulch (r12), West of Longmont-Boulder (r13), and South Platte (r14, r15, r16, r17, r18). The AVIRIS mission transected the short prairie grassland landscapes, urban/wildland interface, to the Ponderosa pine / Douglas-fir forest in the Front Range region, crossing Larimer, Boulder, Jefferson, Park, and Fremont Counties of Colorado. The flight approximately followed the Front Range from north to south. Flight f021015t01 had approximately 17.5 m spatial resolution, of 224 spectral bands, with 10 nm spectral resolution. There were patches of snow at high elevation, but the visibility was excellent, with a little haze over the southwest portion of r18. The data were then georectified in JPL based on on-board GPS records and USGS 10m Digital Elevation Model (DEM). Figure 1 shows the location of the flight lines. In the images, permanent vegetation is apparent as the ponderosa pine / Douglas- fir forest, conifer woodland, shrub and grassland. Due to the frequent wildfires in the region, fire scars and fire-disturbed landscapes of different ages are very commonly seen.

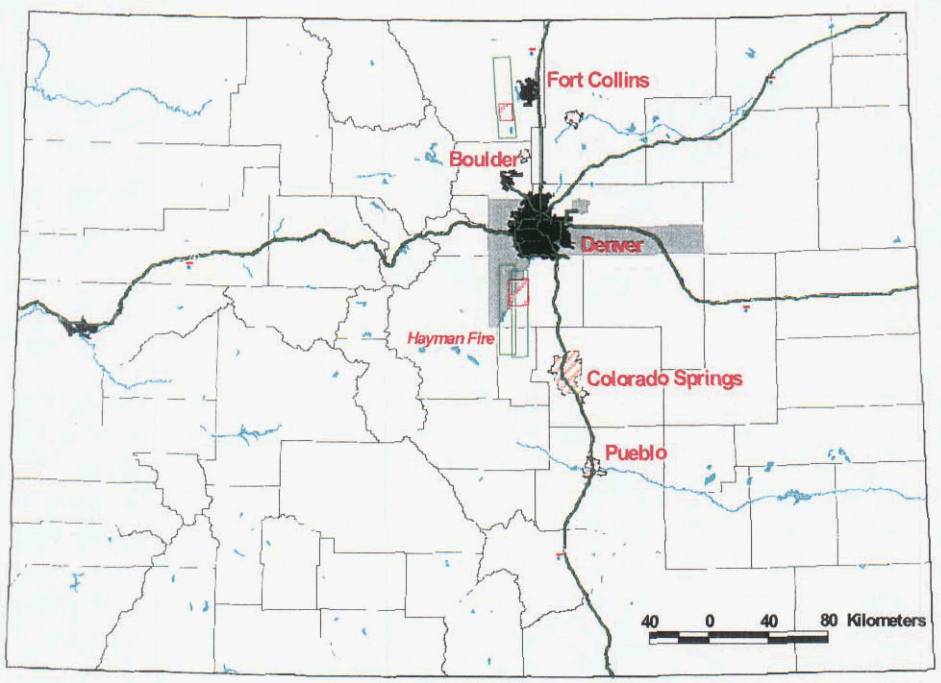

Figure 1 Location of the study areas and flight lines. The red polygons show the study areas, while the green polygons represent the AVIRIS flight lines used in this study. The approximate location of the Hayman fire is also shown on the map.

The original AVIRIS data sets were atmospherically corrected and converted to reflectance using the High-Accuracy ATmospheric Correction for Hyperspectral Data (HATCH) algorithm, evaluation version, developed by the Center for the Study of Earth from Space, University of Colorado at Boulder. Even after the calibration, atmospheric effects constantly existed in certain bands, i.e., band 1-5, 33-35, 107-113, 152-167, and 222-224. We spectrally subset the AVIRIS images by removing those bands, and finally had 190-band images ready for further analyses.

Hyperion data was acquired with a hyperspectral sensor on board NASA's EO-1 satellite on September 27, 2002. It has 220 bands (10 nm spectral resolution) with 30 m spatial resolution. The data

was radiometrically corrected in EROS Data Center and provided in radiation values. We atmospherically corrected and converted the radiation data to reflectance using the HATCH algorithm, and then georegistered it with a reference Landsat 7 image. To further eliminate atmospheric effects and to increase the signal-to-noise ratio, we excluded band 121-129 and 166-178 in further analyses.

In the hyperspectral unmixing analysis, we first calculated the minimum noise fraction (MNF) transformation of the original 190 AVIRIS bands, which resulted 40 MNF bands that contained 99% of the original spectral information. Then we checked each of the MNF for signal-to-noise ratio, and decided to use the first 13 bands for the spectral angle mapper (SAM) classification. We analyzed the pixel purity index (PPI) and matched PPI regions of interest with our spectral library to define known endmembers (classes). We combined those endmembers with the n-dimension visualizer spectra as input of classes for the SAM classification. As a post classification process, we compared the 32 undefined SAM classes to assorted reference data (e.g., QuickBird image, field plots and literature data) and then recoded them into broad classes of fuel types. According to USFS forest classification system, we created a map of fuel classes for the upper South Platte area. Using a similar approach, combined with QuickBird images, we classified forest canopy cover into five levels that meet the requirements of both the FARSITE model and USFS forest management.

Based on the spectral reflectance curves and burn severity inventory from our fieldwork, we analyzed burn severity on both AVIRIS and Hyperion images with linear unmixing of photosynthetic vegetation (PV) and non-photosynthetic vegetation (NVP) endmembers (Asner et al., 1998), and generated a three-level burn severity classification. We derived standard spectral reflectance curves from an AVIRIS image, a Hyperion image and from our field spectra and compared the reflectance features among them.

2.3 LiDAR analysis

Light Detection and Ranging (LiDAR) provides remotely sensed information describing the vertical structure of forests. Using LiDAR-derived metrics such as mean canopy height as input to predictive models, additional forest metrics such as timber volume and biomass can be estimated rapidly and frequently for individual holdings (Lefsky et al., 1999). In this study, 3Di/EagleScan's DATISII airborne discrete-return LiDAR system was flown over ponderosa pine dominated forests close to the Cheesman reservoir, Pike NF, in the fall of 2001. We derived 39 metrics from the raw LiDAR data, to synthesize the information on location and intensity of returned energy. These metrics were developed based on information from pre-existing LiDAR studies, both using discrete-return and waveform-digitizing LiDAR (e.g., Lefsky et al., 1999, Naesset, 2002). They include measures of mean canopy height, spatial variability in height, measures of canopy cover, biomass density, and height to live crown. We used these metrics as independent variables in a wide array of linear and non-linear models to predict a variety of stand structural variables on a per unit area basis, such as canopy bulk density, canopy base height, Lorey's height and basal area. Using an information-theoretic approach (Burnham and Anderson, 2002), we selected the best model to describe each stand structure variable. See Table 1 for summary of remote sensing data discussed above.

Table 1 Remote sensing data available for study

Remote Sensing Data Type	Date Acquired	Spectral Resolution	Spatial Resolution
AVIRIS (f021015t01)	10/15/2002	224 bands, 10 nm	17.5 m
EO-1 Hyperion	9/27/2002	220 bands, 10 nm	30 m
Landsat 7 TM	10/5/1999	8 bands	30 m, 15 m
LiDAR	11/2001	1 band	1-2 m
QuickBird	10/2/2002	5 bands	2.8 m, 0.7 m

3. RESULTS AND DISCUSSION

3.1 Fuel Spectra

Fuel models are integrated descriptions of typically fuel loading/condition based on fuel type, the amount of fuel, whether the fuel is alive or dead and on the time required for the fuel to come to moisture equilibrium with its environment (Finney 1998). Liquid water must be evaporated before a fuel can reach combustion temperatures. Live fuels require much more preheating than dead fuels. While traditional multi-spectral satellite data can measure biomass of live herbaceous and woody plant materials, it is less sensitive to dead plant materials and vegetation structure that are critical for characterizing fuel models and fire risk. Combining AVIRIS hyperspectral features and LiDAR backscatter metrics, with potential for detecting various materials and their spatial structures, is promising for efforts to overcome the lack of sensitivity of multi-spectral data.

The leaf-scale spectral reflectance of ponderosa pine and Douglas-fir, the two dominant conifer species in the region, are shown in Figure 2a. However, they do not completely match the spectra derived from AVIRIS (Figure 2b). Conifer species (Ponderosa pine and Douglas-fir) have very similar leaf scale spectral features. However, there is more different spectra at crown or stand scale, mainly due to their difference in canopy gap probability, crown shape and architecture. We failed to distinguish the two conifers using leaf spectra, but got relatively accurate results with crown scale ROIs. Linear spectral unmixing techniques proved to have the capacity to detect the proportion of conifer trees in a certain pixel or group of pixels, and therefore separate them from each other and from background vegetation.

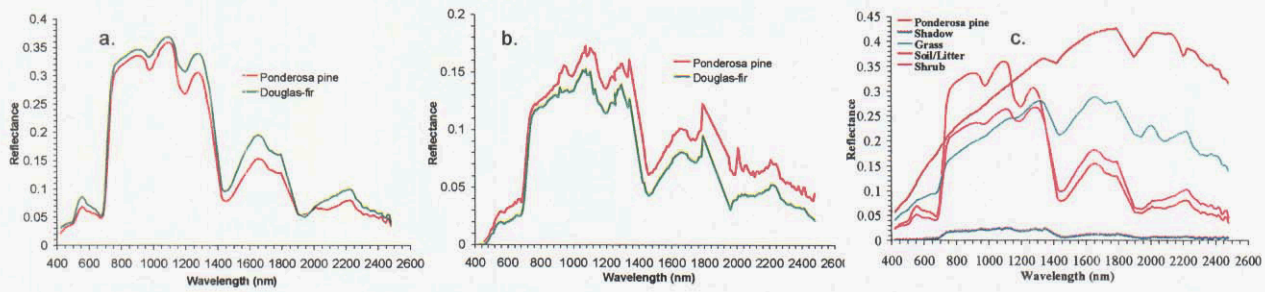

Figure 2 Spectral reflectance of dominant endmembers and spectral mixtures in the study area: a) Ponderosa pine and Douglas-fir at leaf scale, b) stand-scale ponderosa pine and Douglas-fir spectra derived from AVIRIS, c) field-measured endmember spectra for a ponderosa pine forest patch.

In a given AVIRIS pixel in our study area we distinguished at least five endmembers: ponderosa pine, shadow, grass, soil/litter, and shrub. Their field-measured spectra are shown in Figure 2c. Spectral mixture analysis cannot provide direct information about fuel condition underneath forest canopies (i.e. endmember of litter, grasses and shrub); however, it provides fraction cover of those components in a certain area and enables us to estimate live/dead fuels.

3.2 Fuel Mapping

We generated a map (see Fig. 3) of fuel attributes from AVIRIS spectral analysis procedures that includes 18 categories; they are five canopy cover classes for ponderosa pine forest and four canopy cover classes for Douglas-fir forest, three classes of burn severity, spruce/fir forest, aspen forest, shrubland, meadow/grassland, barren, and riparian. It was indicated in our AVIRIS derived fuel map that 13.2% of the study area has over 60% canopy cover with relatively high crown fuel loads. These are potentially

priority areas for fuel treatment plans. From this classification, we separated three data layers that are necessary for fuel condition and fire damage assessment, including fuel model, canopy cover, and burn severity. To generate a fuel model map, we evaluated the 18 classes of the fuel map against ground fuel measurements and literature, and then translated the classes into 5 customized fuel models.

We validated our remote sensing analyses with our field measurements and survey data from USFS fuel treatment units. It was shown that AVIRIS derived liquid water thickness and vegetation index were strongly and positively related to green leaf biomass and canopy cover respectively in conifer stands. There was 71.3% of agreement between AVIRIS-derived fuel classes and ground measurements. There was high accuracy in the interpretation of vegetation types, while most of the errors occurred with canopy cover estimates.

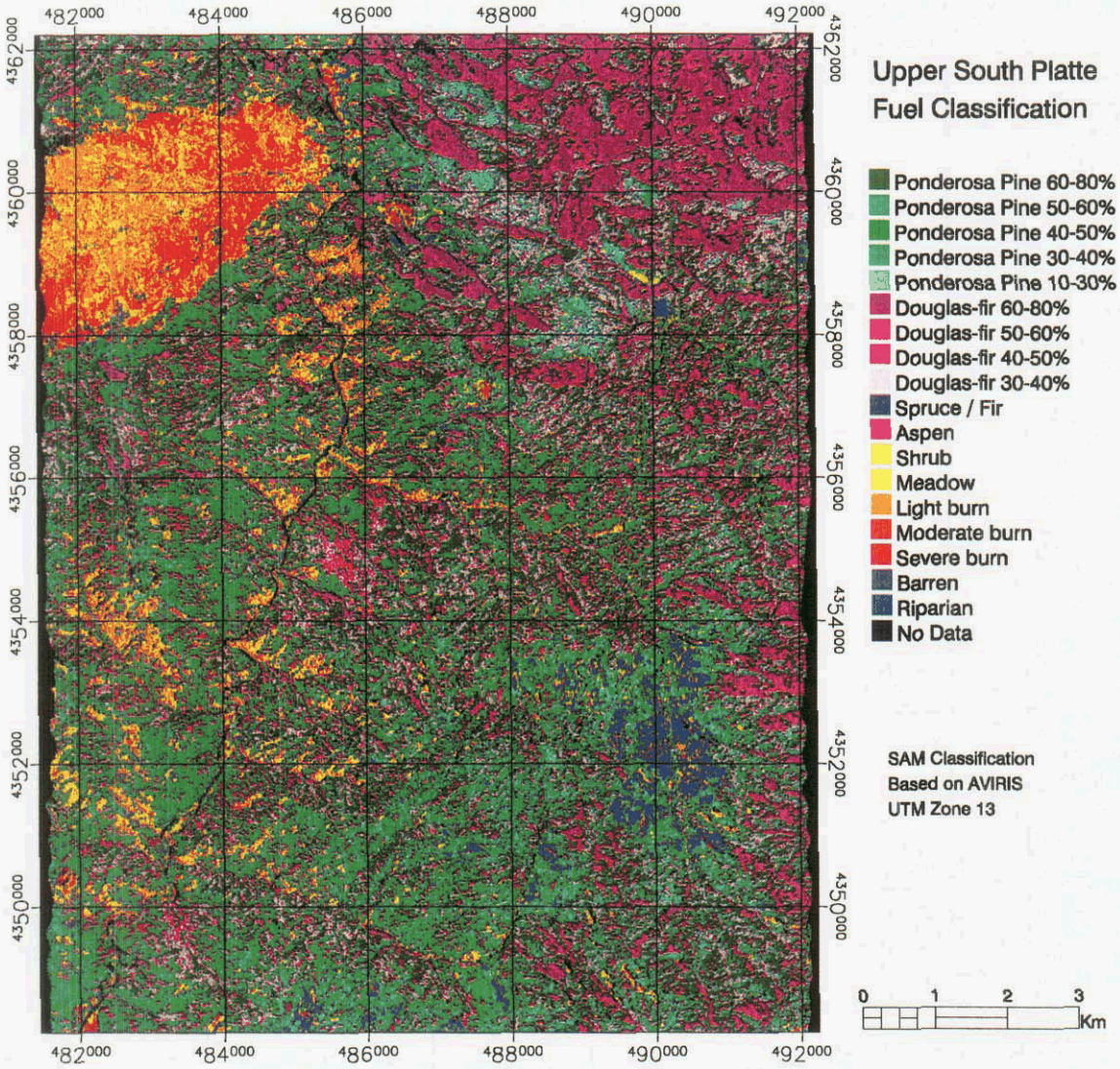

Figure 3 AVIRIS derived map of fuel classes in upper South Platte. The map was generated from SAM classification and was validated with ground fuel survey and spectral measurements.

3.3 Forest structure

Assessing forest fire potential requires accurate estimates of surface and canopy fuel characteristics. LiDAR's ability to capture stand structural information led us to estimate canopy variables that are critical for modeling fire behavior and variables that are directly related to the amount of combustible mass in a stand. Selected variables were: canopy bulk density, canopy base height, Lorey's height and basal area (see Fig. 4). Canopy bulk density is the density of canopy fuels that would be consumed in the flaming front of a fully active crown fire (Scott and Reinhardt, 2001). Canopy base height is the lowest height above the ground at which there is sufficient canopy fuel to propagate fire vertically through the canopy (Scott and Reinhardt, 2001). We used Lorey's height (basal-area weighed mean tree height) as a measure of stand height. All these variables are properties of the stand, not the individual tree.

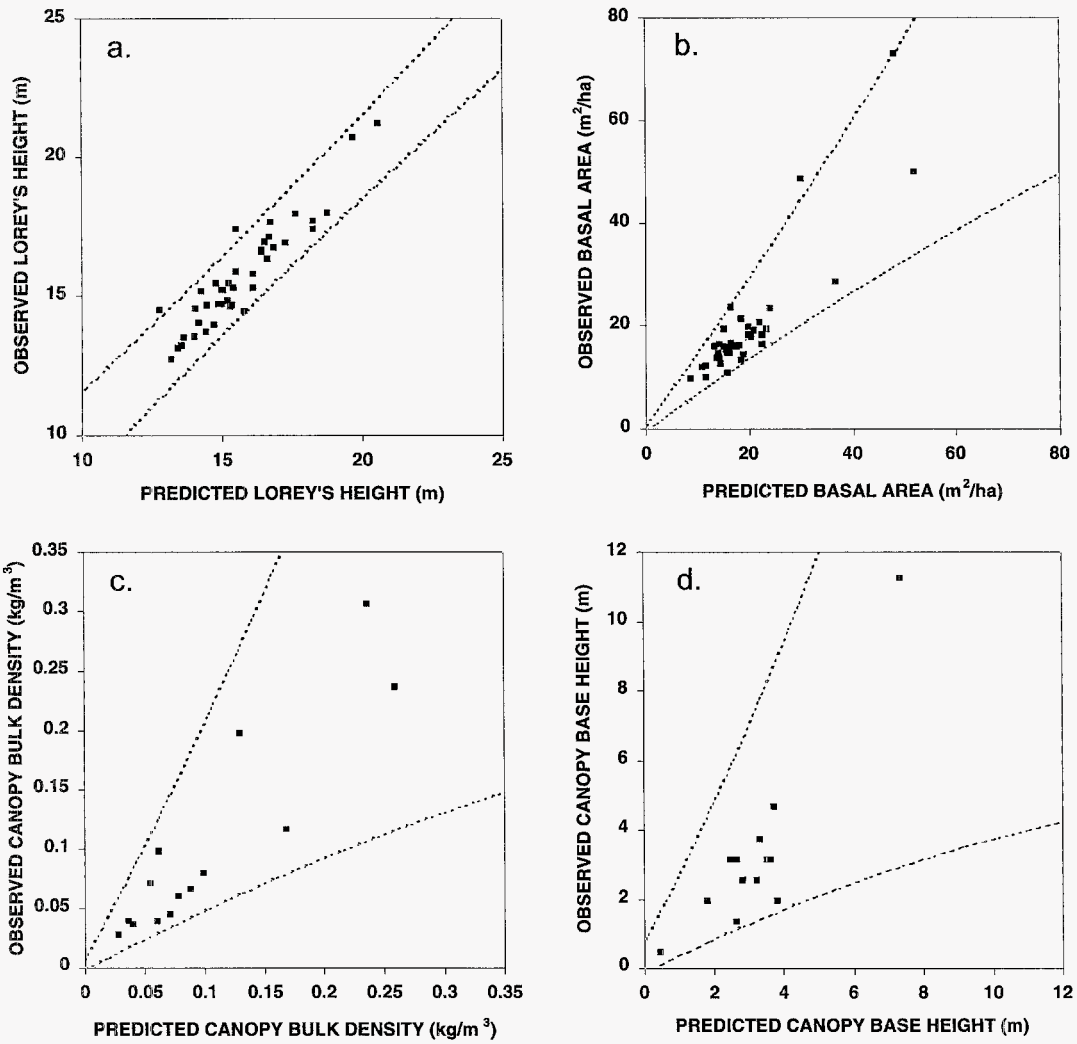

Figure 4 Observed values of forest structure attributes versus values predicted by the best regression model derived from LiDAR metrics. The solid gray line represents the 1:1 line, where observed = predicted. The dotted black lines are the limits of the 95% prediction intervals for the plotted model. a) Basal-area-weighed average height (Lorey's height, in meters) of sampled trees; b) Basal area (m^2/ha); c) Canopy bulk density (kg/m^3); d) Canopy base height (m).

We compared both linear and non-linear models with LiDAR metrics as predictors of each stand structure variables. Our results show high agreement between observed and predicted Lorey's height (Fig. 4a; r^2=0.87). Results for basal area and canopy bulk density were promising, especially for low values (Figs. 4b and 4c; r^2=0.79 and r^2=0.83, respectively). The lack of enough sites with large values for these two variables limits the generality of the relationships we found. Though we were able to explain 79.8% of the variability in canopy base height (Fig. 4d), this relationship was dominated by one particularly large value. Therefore, we conclude that there is evidence of LiDAR's capacity to provide estimates of canopy base height, but more research is needed to select a general model to do so.

Combined AVIRIS and LiDAR data can be used to map fuel type, fuel amount, fuel condition, and burn severity in forests of the Colorado Front Range. AVIRIS derived NDVI, equivalent liquid water thickness, cellulose absorption index and LiDAR backscatter metrics have demonstrated abilities for mapping fuel models, canopy cover and burn severity. Fuel properties derived from hyperspectral and LiDAR information will serve as valuable inputs for fire behavior modeling.

3.4 Burn Severity

Three levels of burn severity were clearly distinguished with the spectral reflectance derived from AVIRIS and Hyperion images, and visually separated on a RGB (band 4:3:2) QuickBird image. The higher the burn severity, the lower the fraction of live vegetation in pixels, and therefore, the less chlorophyll signature in spectral mixture. This can be clearly seen by comparing the spectra of PV and NPV endmembers. This is the basis for the burn severity classification and mapping with hyperspectral data. On this false-color infrared QuickBird image (Figure 5), live vegetation appears in bright red, while burned trees are in blue-green color. Single burned trees are also distinguished on the image.

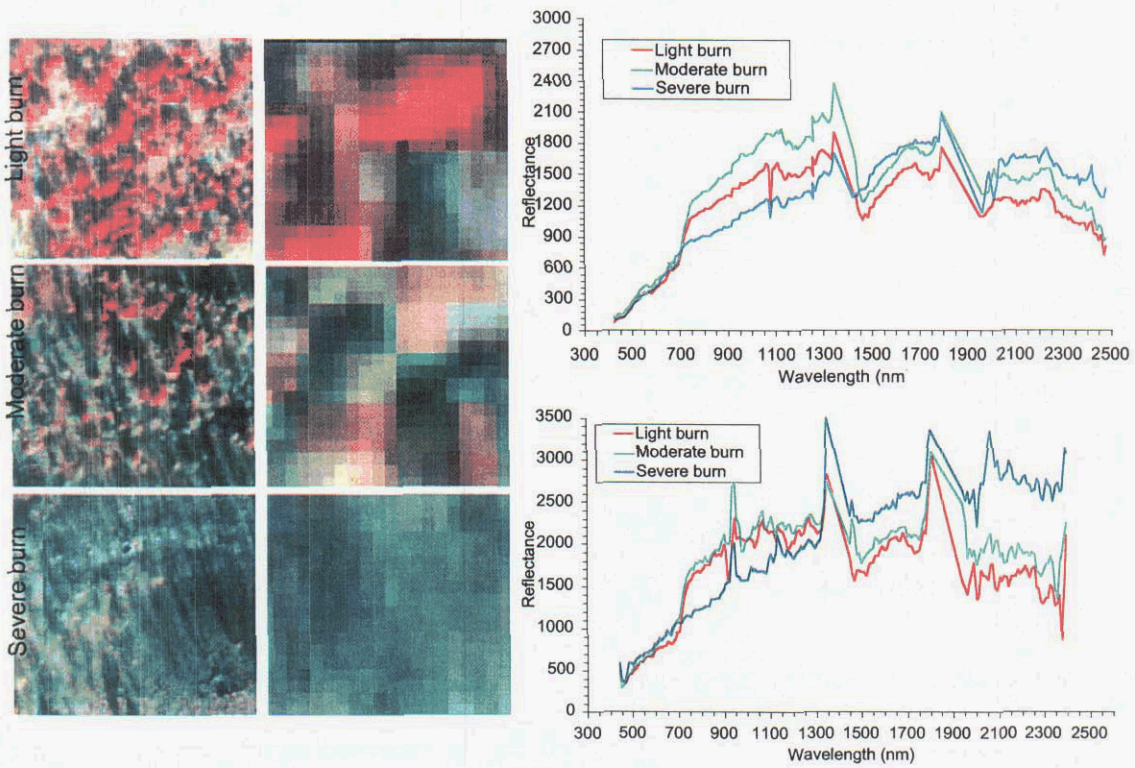

Figure 5 AVIRIS and Hyperion derived spectra reflectance of burned forest with different severity (right), and burn severity shown on QuickBird image (left)

4. FUTURE WORK

We have been examining the use of multi-sensor remote sensing imagery, including AVIRIS, Hyperion, ALI, ASTER, Landsat 7 and QuickBird image of the same area in upper South Platte, to develop a technique to identify fuel types based on their spectral differences in plant communities. We are hoping to reach a compromise between spectral resolution, spatial resolution, cost, and accuracy, and find the best data set for fuel loading estimates. Meanwhile, we are in a process to build relatively accurate data layers of fuel features for most of the Colorado Front Range based on the AVIRIS data collected in 2002 and 2003 and a scheduled ER-2 flight in 2004, combined with small areas of ASTER, ALI, Hyperion, and Landsat data.

Maps produced from our current hyperspectral analysis have been used to assess forest fuel condition and fire risk in both the Pike NF and the Arapaho-Roosevelt NF in the summer of 2003. That information has helped forest managers in their fuel treatment plans. In each case, operations were enhanced by the availability of information on fuels. Further comparative analysis between pre and post fuel treatment should assist forest managers to better evaluate the effect of their treatments and adjust the treatment plan while necessary.

As more AVIRIS data becomes available in coming years, additional information on forest fuel conditions should become discernible. This information will be incorporated into enhanced mapping techniques. With accurate fuels information in hand, fire managers should be able to make informed decisions about ongoing wildland fires and fuel treatments. These decisions will result in safer conditions for fire fighters and less damage during a fire.

As a part of the new forest management initiatives, the Arapahoe-Roosevelt and Pike National Forests have planned prescribe fire for several thousand hectares of Colorado Front Range forests since 2002. During the 2003-2004 year, we plan to interact with these National Forests and gain landscape coverage of the key variables for driving FARSITE for several prescribed burns. In the simulations, the remotely sensed input variables we derived from hyperspectral analysis will play a key role, and the accuracy of our remote sensing interpretation will be critical to the model result. After each fire, we will simulate the prescribed burns using relevant weather data and pre-fire fuel conditions, and we will compare our results to the observed fire behavior. This will provide us with important validation of our combined remote sensing-FARSITE simulation approach, and may feed back into modifications of either the input variable assessments, or the actual simulation approach.

5. ACKNOWLEDGEMENTS

This study is funded by National Aeronautics and Space administration (NASA)'s Application Program. We thank Dr. Barry Johnston of Pike National Forest for his assistance in fieldwork and map validation. We also thank Bruce Kindel, University of Colorado for his help in field spectral measurements.

6. REFERENCES

Asner, G.P., C.A. Wessman, and D.S. Schimel, 1998, "Heterogeneity of savanna canopy structure and function from imaging spectrometry and inverse modeling," *Ecological Applications* 8 (4): 1022-1036.

Burnham, K.P. and D.R. Anderson, 2002, "*Model selection and multimodel inference - A practical information-theoretic approach,*" Springer-Verlag, New York, New York, USA

Covington W.W., P.Z. Fule, M.M. Moore, S.C. Hart, T.E. Kolb, J.N. Mast, S.S. Sackett, and M.R. Wagner, 1997, "Restoring ecosystem health in ponderosa pine forests of the southwest," *Journal of Forestry* 95 (1): 23-29

Finney, M.A., 1998, *FARSITE: Fire Area Simulator- Model development and evaluation*, U. S. Forest Service Research Paper RMRS-RP-4.

Houghton R.A, J.L. Hackler, and K.T. Lawrence, 2000, "Changes in terrestrial carbon storage in the United States 2: The role of fire and fire management," *Global Ecology & Biogeography Letters* 9 (2): 145-170.

Kaufmann, M.R., L. Huckaby, and P. Gleason, 2000, "Ponderosa pine in the Colorado Front Range: long historical fire and tree recruitment intervals and a case for landscape heterogeneity," in *Proceedings from the Joint Fire Science Conference and Workshop*, pp. 153-160.

Keane R.E., K.C. Ryan, and S.W. Running, 1996, "Simulating effects of fire on northern Rocky Mountain landscapes with the ecological process model FIRE-BGC," *Tree Physiology* 16: 319-331.

Lefsky M.A., W.B. Cohen, S.A. Acker, G.G. Parker, T.A. Spies, and D. Harding, 1999, "Lidar remote sensing of the canopy structure and biophysical properties of Douglas-fir western hemlock forests," *Remote Sensing of Environment* 70 (3): 339-361

Miller C., and D.L. Urban, 2000, "Modeling the effects of fire management alternatives on Sierra Nevada mixed-conifer forests," *Ecological Applications* 10 (1): 85-94.

Naesset, E., 2002, "Predicting forest stand characteristics with airborne scanning laser using a practical two-stage procedure and field data," *Remote Sensing of Environment* 80: 88-99

Perry G.L.W., 1998, "Current approaches to modeling the spread of wildland fire: a review," *Progress in Physical Geography* 22 (2): 222-245.

Roberts, D.A., M. Gardner, R. Church, S. Ustin, G. Scheer, and R.O. Green, 1998, "Mapping chaparral in the Santa Monica Mountains using multiple endmember spectral mixture models," *Remote Sensing of Environment* 65 (3): 267-279.

Romme, W.H., 1982, "Fire and Landscape Diversity in Subalpine Forests of Yellowstone National Park," *Ecological Monographs* 52 (2): 199-221.

Running, S.W., T.R. Loveland, L.L. Pierce, R.R. Nemani, and E.R.Jr. Hunt, 1995, "A remote sensing based vegetation classification logic for global land cover analysis," *Remote Sensing of Environment* 51 (1): 39-48.

Scott, J.H. and E.D. Reinhardt, 2001, "*Assessing crown fire potential by linking models of surface and crown fire behavior*," U.S. Forest Service, Rocky Mountain Research Station Research Paper RMRS-RP-29

Turner, M.G., W.H. Romme, R.H. Gardner, and W.W. Hargrove, 1997, "Effects of fire size and pattern on early succession in Yellowstone National Park," *Ecological Monographs* 67 (4): 411–433.

Veblen T.T., T. Kitzberger, and J. Donnegan, 2000, "Climatic and human influences on fire regimes in ponderosa pine forests in the Colorado Front Range," *Ecological Applications* 10 (4): 1178-1195.

Wessman C.A., J.D. Aber, D.L. Peterson, and J.M. Melillo, 1988, "Remote sensing of canopy chemistry and nitrogen cycling in temperate forest ecosystems," *Nature* 335: 154-156

Mineral Mapping with AVIRIS and EO-1 Hyperion

Fred A. Kruse[1]

1.0 Introduction

Imaging Spectrometry data or Hyperspectral Imagery (HSI) acquired using airborne systems have been used in the geologic community since the early 1980's and represent a mature technology (Goetz et al., 1985; Kruse et al., 1999). The solar spectral range, 0.4 to 2.5 μm, provides abundant information about many important Earth-surface minerals (Clark et al., 1990). In particular, the 2.0 to 2.5 μm (SWIR) spectral range covers spectral features of hydroxyl-bearing minerals, sulfates, and carbonates common to many geologic units and hydrothermal alteration assemblages. Previous research has proven the ability of airborne and spaceborne hyperspectral systems to uniquely identify and map these and other minerals, even in sub-pixel abundances (Kruse and Lefkoff, 1993; Boardman and Kruse, 1994; Boardman et al., 1995; Kruse, et al., 1999). This paper describes a case history for a site in northern Death Valley, California and Nevada along with selected SNR calculations/results for other sites around the world. Various hyperspectral mineral mapping results for this site have previously been presented and published (Kruse, 1988; Kruse et al., 1993, 1999, 2001, 2002, 2003), however, this paper presents a condensed summary of key details for hyperspectral data from 2000 and 2001 and the results of accuracy assessment for satellite hyperspectral data compared to airborne hyperspectral data used as ground truth.

2.0 Comparison of Hyperion and AVIRIS Specifications

The launch of NASA's EO-1 Hyperion sensor in November 2000 marked the establishment of spaceborne hyperspectral mineral mapping capabilities. Hyperion is a satellite hyperspectral sensor covering the 0.4 to 2.5 μm spectral range with 242 spectral bands at approximately 10nm spectral resolution and 30m spatial resolution from a 705km orbit (Pearlman et al., 1999). Hyperion is a pushbroom instrument, capturing 256 spectra each with 242 spectral bands over a 7.5Km-wide swath perpendicular to the satellite motion. The system has two grating spectrometers; one visible/near infrared (VNIR) spectrometer (approximately 0.4 – 1.0 μm) and one short-wave infrared (SWIR)) spectrometer (approximately 0.9 – 2.5 μm). Data are calibrated to radiance using both pre-mission and on-orbit measurements. Key AVIRIS and Hyperion characteristics are compared in Table 1 and discussed further in Green et al., 2003.

The Airborne Visible/Infrared Imaging Spectrometer (AVIRIS) represents the current state of the art airborne hyperspectal system. AVIRIS, flown by NASA/Jet Propulsion Laboratory (JPL) is a 224-channel imaging spectrometer with approximately 10 nm spectral resolution covering the 0.4 – 2.5 μm spectral range (Green et al., 1999). The sensor is a whiskbroom system utilizing scanning foreoptics to acquire cross-track data. The IFOV is 1 milliradian. Four off-axis double-pass Schmidt spectrometers receive incoming illumination from the foreoptics using optical fibers. Four linear arrays, one for each spectrometer, provide high sensitivity in the 0.4 to 0.7 μm, 0.7 to 1.2 μm, 1.2 to 1.8 μm, and 1.8 to 2.5 μm regions respectively. AVIRIS is flown as a research instrument on the NASA ER-2 aircraft at an altitude of approximately 20 km, resulting in approximately 20-m pixels and a 10.5-km swath width. Since 1998, it has also been flown on a Twin Otter aircraft at low altitude, yielding 2 – 4m spatial resolution.

Table 1: AVIRIS/Hyperion Sensor Characteristics Comparison

HSI Sensor	Spectral Resolution	Spatial Resolution	Swath Width	SWIR SNR
AVIRIS-High Altitude	10 nm	20 m	12 km	~500:1
Hyperion	10 nm	30 m	7.5 km	~50:1

[1] Analytical Imaging and Geophysics LLC (AIG), Boulder, Colorado, USA, E-mail: kruse@aigllc.com

3.0 Methods

Analytical Imaging and Geophysics LLC (AIG) has developed methods for analysis of hyperspectral data that allow reproducible results with minimal subjective analysis (Kruse et al., 1996, 2001). These approaches are implemented and documented within the "Environment for Visualizing Images" (ENVI) software system originally developed by AIG scientists (now an Eastman Kodak/Research Systems Inc [RSI] commercial-off-the-shelf [COTS] product) (Research Systems Inc, 2001). They are also described in additional detail in Kruse et al. (2002, 2003). The hyperspectral analysis methodology includes 1) data pre-processing (area-array destriping as required), 2) correction of data to apparent reflectance using the atmospheric correction software ACORN (AIG, 2001), 3) linear transformation of the reflectance data using a Minimum Noise Fraction (MNF) transform to minimize noise and determine data dimensionality (Green et al., 1988; Boardman 1993), 4) location of the most spectrally pure pixels using the Pixel Purity Index (PPI) approach (Boardman et al. 1994, 1995), 5) extraction of endmemember spectra using n-dimensional scatter plotting (Boardman et al., 1995), 6) identification of endmember spectra using visual inspection, automated identification, and spectral library comparisons (Kruse and Lefkoff, 1993; Kruse et al., 1993) and 7) spatial mapping and abundance estimates for specific image endmembers using the Mixture-Tuned Matched Filtering (MTMF) method (Boardman, 1998). A key point of this methodology is the reduction of data in both the spectral and spatial dimensions to locate, characterize, and identify a few key spectra (endmembers) that can be used to explain the rest of the hyperspectral dataset. Once these endmembers are selected, then their location and abundances can be mapped from the linearly-transformed or original data. These methods derive the maximum information from the hyperspectral data themselves, minimizing the reliance on *a priori* or outside information.

4.0 Results – Northern Death Valley Site

The study area described here is located in northern Death Valley, at the extreme northern end of Death Valley National Park (Figure 1). The geology consists principally of a Jurassic-age intrusion exhibiting quart-sericite-pyrite hydrothermal alteration (Wrucke et al., 1984; Kruse, 1988). This site has been used as a test area for imaging spectrometers since 1983 (Kruse, 1988; Kruse et al., 1993, 1999). For the purposes of this study, AVIRIS data collected 9 June 2000 (f000609t01p03_r04) were compared to Hyperion data collected July 23 2001 (EO12001204_20AD20AC_r1_PF1_01.L1_A).

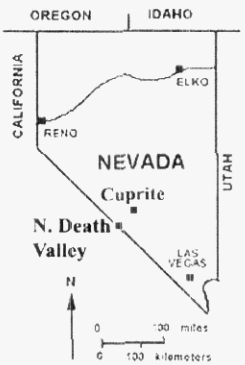

Figure 1: Location of the Northern Death Valley Site

A spectral subset of bands covering the short wave infrared (SWIR) spectral range (2.0 – 2.5 μm for AVIRIS and 2.0 – 2.4 μm for Hyperion) was selected and these bands were linearly transformed using the MNF transformation. A plot of eigenvalues versus MNF band number (not shown) shows a sharp falloff in eigenvalue magnitude between 1 and 20 for AVIRIS and between 1 and 10 for Hyperion. Because higher eigenvalues generally indicate higher information content, this indicates that the AVIRIS data contain significantly more information. The actual data dimensionality is usually determined by comparing both the eigenvalue plots and the MNF images for each dataset (Figures 2 and 3). In the case of AVIRIS, the MNF analysis indicates a dimensionality of approximately 20. The Hyperion data exhibits dimensionality of approximately 8.

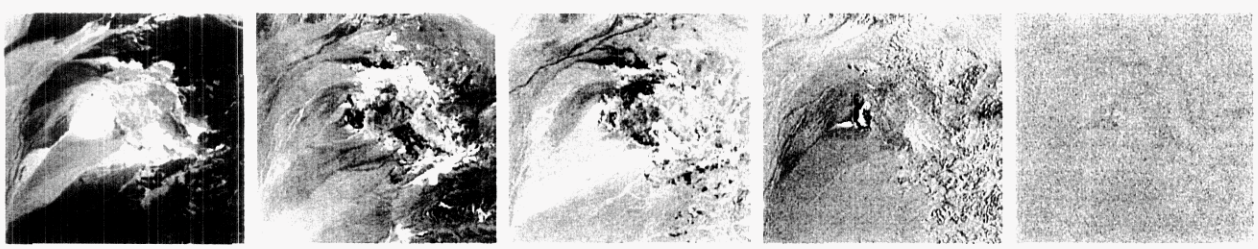

Figure 2. MNF images for the northern Death Valley AVIRIS SWIR data. Images from left to right, MNF band 1, MNF band 5, MNF band 8, MNF band 10, MNF band 20.

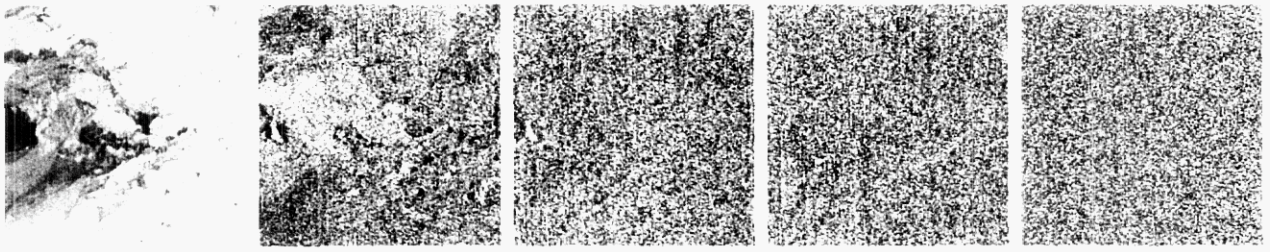

Figure 3. MNF images for the northern Death Valley Hyperion SWIR data. Images from left to right, MNF band 1, MNF band 5, MNF band 8, MNF band 10, MNF band 20.

The top MNF bands for each data set (20 for AVIRIS, 6 for Hyperion), which contain most of the spectral information (Green et al., 1988), were used to determine the most likely endmembers using the PPI procedure. These potential endmember spectra were loaded into an n-dimensional scatterplot and rotated in real time on the computer screen until "points" or extremities on the scatterplot were exposed (Boardman, 1993). These projections were "painted" using region-of-interest (ROI) definition procedures and then rotated again in 3 or more dimensions (3 or more MNF bands) to determine if their signatures were unique in the MNF data. Once a set of unique pixels were defined, then each separate projection on the scatterplot (corresponding to a pure endmember) was exported to a ROI in the image. Mean spectra were then extracted for each ROI from the apparent reflectance data to act as endmembers for spectral mapping (Figure 4). These endmembers were used for subsequent classification and other processing. Mixture-Tuned-Matched Filtering (MTMF), a spectral matching method (Boardman, 1998), was used to produce image-maps showing the distribution and abundance of selected minerals. (Note: MNF endmember spectra, not reflectance spectra are used in the MTMF). The results are generally presented as gray-scale images (not shown) with values from 0 to 1.0, which provide a means of estimating mineral abundance. Brighter pixels in the images represent higher mineral abundances. Results images for both AVIRIS and Hyperion were produced by correcting the Hyperion data to match the AVIRIS spatial scale and orientation as described above. Selected results were combined as color-coded images to show the distribution of the principal (spectrally predominant) minerals (Figures 5 and 6).

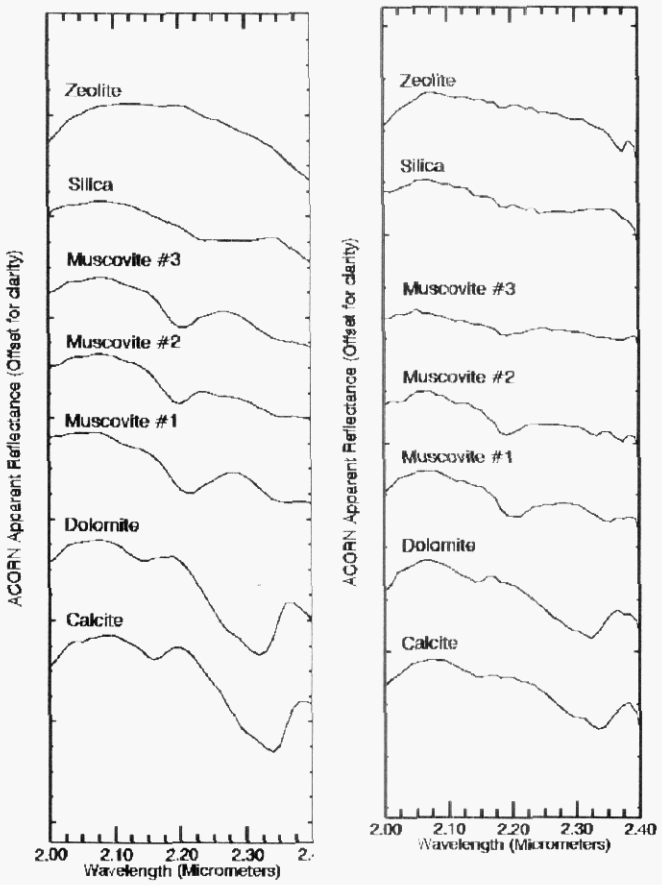

Figure 4: Comparison of selected AVIRIS endmember (mean) spectra (left) and Hyperion endmember (mean) spectra (right) for the northern Death Valley, California and Nevada site.

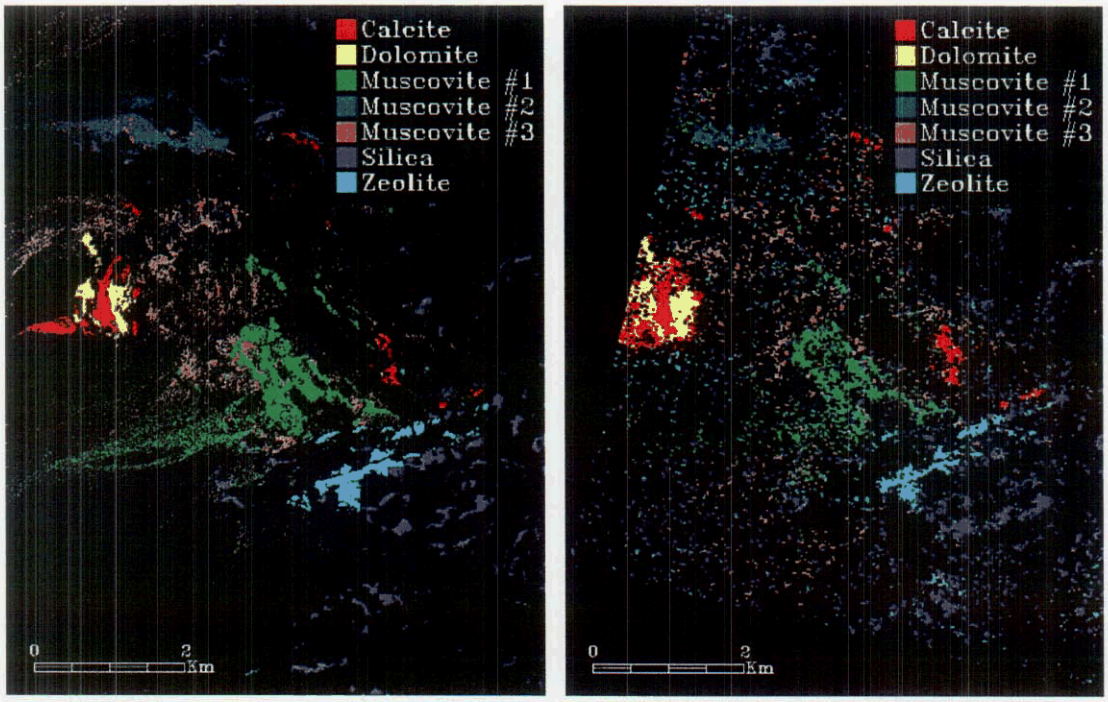

Figure 5: MTMF mineral maps for AVIRIS (left) and Hyperion (right) produced for the endmembers in Figure 4 for the northern Death Valley, California and Nevada site. Colored pixels show the spectrally predominant mineral at concentrations greater than 10%.

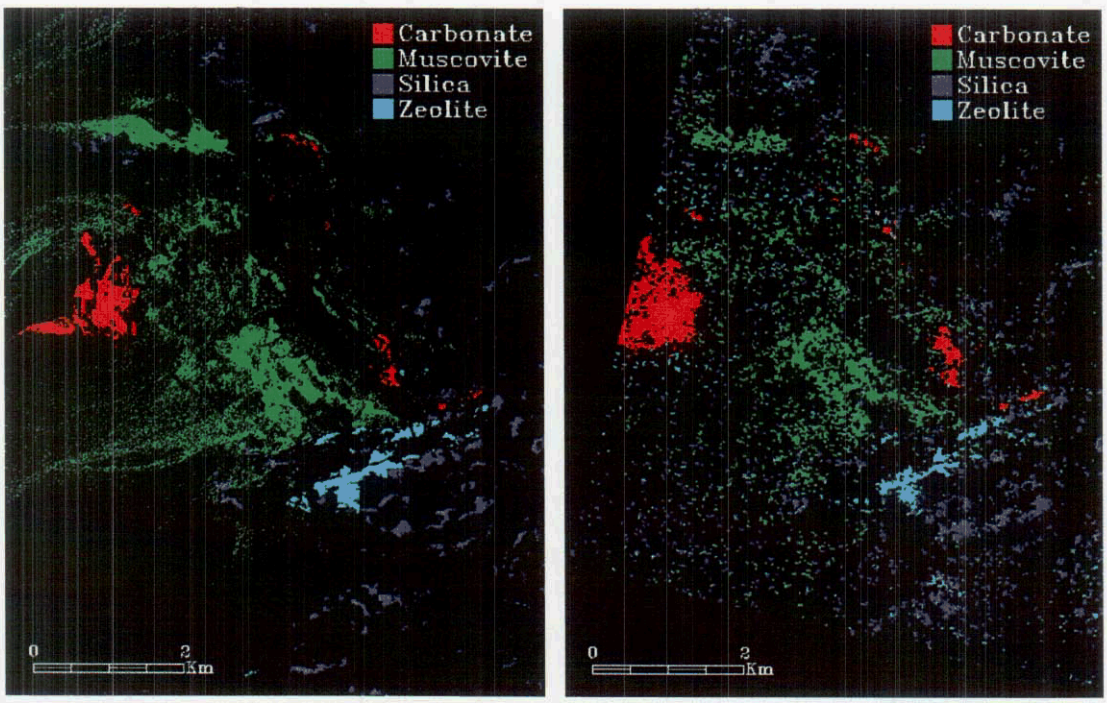

Figure 6: MTMF mineral maps for AVIRIS (left) and Hyperion (right) produced for a subset (combined) of the endmembers in Figure 4 for the northern Death Valley, California and Nevada site. Colored pixels show the spectrally predominant mineral group at concentrations greater than 10%.

Visual comparison of the detailed mapping results for the northern Death Valley site shows that Hyperion identifies similar minerals to AVIRIS and that there is generally good correspondence between the AVIRIS and Hyperion mapping. It is also possible to extract abundance information from both the AVIRIS and Hyperion data (Boardman and Kruse, 1994; Boardman et al., 1995, Kruse et al, 1999), but this is not illustrated here. Confusion matrix results comparing the AVIRIS and Hyperion mapping results, excluding the unclassified pixels show overall accuracy of approximately 76% for the Hyperion mapping as compared to AVIRIS, with a Kappa Coefficient of 0.71. Table 2 indicates that there is, however, considerable difficulty separating similar mineralogy. In this case, detecting and mapping the three muscovite varieties appears to be near the detection limit at the calculated 60:1 SNR of the Hyperion data. Grouping similar minerals together (calcite with dolomite, and combining the three muscovites) results in dramatic identification and mapping improvements (Figure 6, Table 3).

Table 2: Confusion Matrix comparing Hyperion northern Death Valley MTMF mineral mapping results to AVIRIS "Ground Truth" MTMF detailed mineral mapping results. Excludes unclassified pixels. Overall Accuracy is 76%. Kappa coefficient is 0.71

	AVIRIS Ground Truth (Percent)							
Hyperion Class	Calcite	Dolomite	Muscovite #1	Muscovite #2	Muscovite #3	Silica	Zeolite	Total
Calcite	**82.66**	16.75	0.00	0.31	1.11	0.46	0.21	11.46
Dolomite	15.73	**83.01**	0.00	0.00	0.00	0.09	0.10	9.74
Muscovite	0.10	0.00	**85.62**	15.04	41.13	1.37	0.00	33.07
Muscovite	0.00	0.00	2.11	**76.43**	11.49	0.09	0.00	8.62
Muscovite	0.10	0.00	8.33	4.50	**35.65**	2.46	0.72	10.14
Silica	0.20	0.24	3.81	3.72	6.36	**89.70**	6.00	14.76
Zeolite	1.21	0.00	0.13	0.00	4.26	5.83	**92.96**	12.21
Total	100.00	100.00	100.00	100.00	100.00	100.00	100.00	100.00

Table 3: Confusion Matrix comparing Hyperion northern Death Valley MTMF mapping results to AVIRIS "Ground Truth" MTMF basic (Combined Minerals) mapping results. Excludes unclassified pixels. Overall Accuracy is 94%. Kappa coefficient is 0.91.

	AVIRIS Ground Truth (Percent)				
Hyperion Class	Carbonate	Muscovite	Silica	Zeolite	Total
Carbonate	**99.01**	0.44	0.55	0.31	21.19
Muscovite	0.11	**93.23**	3.92	0.72	51.83
Silica	0.22	4.72	**89.70**	6.00	14.76
Zeolite	0.66	1.61	5.83	**92.96**	12.21
Total	100.00	100.00	100.00	100.00	100.00

5.0 SNR Comparisons – Effect on Mineral Mapping

The quality of digital remote sensing data is directly related to the level of system noise relative to signal strength. This is usually expressed as Signal-to-Noise Ratio (SNR), a dimensionless number that describes overall system radiometric performance (Collwell, 1983). System noise is tied to sensor design and takes into account factors such as detector performance/sensitivity, spatial/spectral resolution, and noise characteristics of the system electronics. Though the noise levels for a given sensor are generally fixed, for remote sensing data acquisition, the signal portion of the SNR is affected by other external factors such as solar zenith angle, atmospheric attenuation and scattering, and surface reflectance, which modify the signal available to the sensor (Collwell, 1983).

One common means for determining an approximate SNR for remote sensing data is to use a Mean/Standard Deviation method (Green et al., 1999, 2003). This approach requires definition of a spectrally homogeneous area, calculation of the average spectrum for that area, and determination of the spectrally distributed standard deviation for the average spectrum. SNR are normalized to 50% reflectance for comparison. SNR calculated using this method are representative of those that can be extracted directly from the data, however, SNR for bright targets may be underestimated because of homogeneity issues at higher SNR (increasing SNR may result in breakdown of apparently homogeneous areas into multiple materials and new homogeneous areas must be selected). Slightly higher SNR values could probably be obtained through direct analysis of the data dark current signal (Green et al., 1999), an "Instrument SNR", however, this isn't always possible. SNR calculated using the Mean/Standard Deviation method, an "Environmental SNR" are sensitive to acquisition conditions as mentioned above, and thus should be considered lower limits on performance.

Analysis of approximately 14 Hyperion scenes from around the world using the Mean/Standard Deviation SNR method shows that there is a strong relationship between the acquisition time of year (which controls the solar zenith angle) and the SNR of the Hyperion data (Kruse et al., 2001, 2003). Calculated SNR for Hyperion SWIR data are higher in the summer and lowest in the winter (Figure 7). This has a direct effect on spectral mineral mapping, with lower SWIR SNR resulting in extraction of less detail (Kruse et al., 2001, 2002, 2003). While Hyperion data with approximately 25:1 SNR allow basic mineral identification (no separation of within-species variability) more detail (additional endmembers) are detected and mapped using the higher SNR AVIRIS and Hyperion data (60:1 SNR) at the northern Death Valley site. This is also important for geologic/mineral mapping, because higher SNR allows separation of similar endmembers such as calcite from dolomite (Figure 4) and within-species variability such as kaolinite vs dickite (Figure 4). In the northern Death Valley case, the relatively high Hyperion SNR allows detection of 3 different mica endmembers with different aluminum substitution (Kruse et al., 1999). Previous investigations have indicated that SNR is critical for this determination (Kruse, 1988, Kruse et al., 2002).

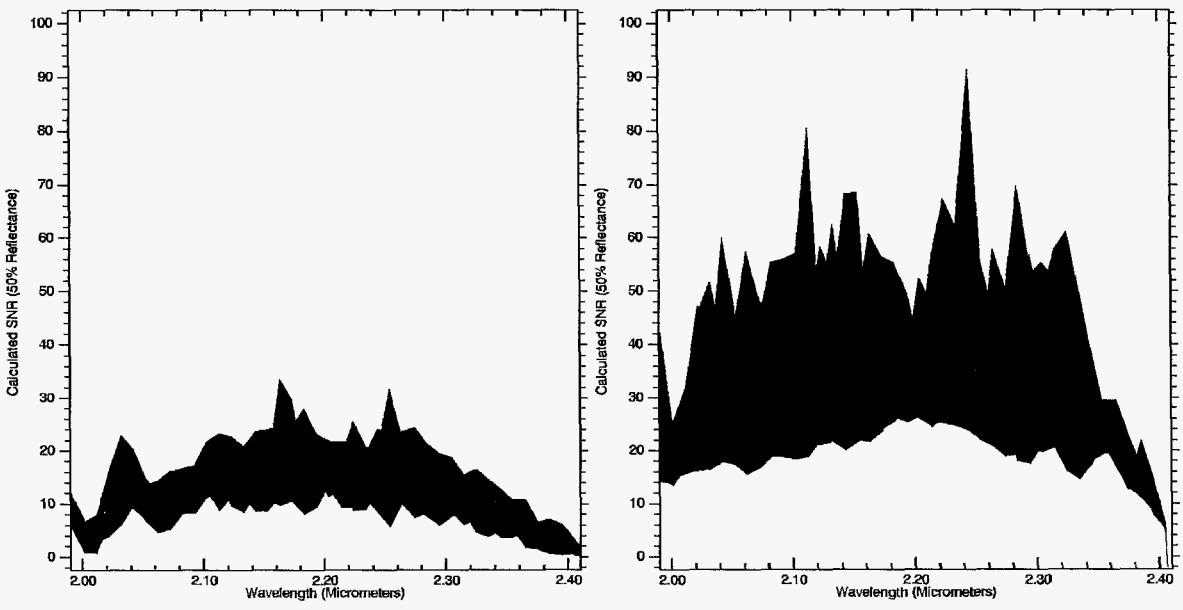

Figure 7: Comparison of Hyperion calculated SNR for "winter" data (left) and "summer" data (right). Filled areas indicate range of SNR for 14 Hyperion scenes.

6.0 Conclusions

Results at the northern Death Valley site establishes that data from the Hyperion SWIR spectrometer (2.0 – 2.4 μm) can be used to produce useful geologic (mineralogic) information. Comparison of Hyperion data to airborne hyperspectral data (AVIRIS) show that Hyperion provides the ability to remotely map basic surface mineralogy. Minerals mapped at this site include calcite, dolomite, muscovite (3 varieties), hydrothermal silica, and zeolites. These case histories demonstrate the analysis methodologies and level of information available from these Hyperion data. They also demonstrate the viability of Hyperion as a means of extending hyperspectral mineral mapping to areas not accessable to aircraft sensors.

AVIRIS data collected during July 2000 (northern Death Valley) served as the "ground truth" for this investigation. Comparison of Hyperion results for northern Death Valley (June 2001) to the known mineralogy derived from the AVIRIS data generally validate on-orbit mineral mapping and Hyperion performance. Standardized hyperspectral data processing methods applied to the Hyperion data lead to definition of specific key minerals, however, it is more difficult (than for AVIRIS) to extract the information because of the Hyperion data's lower SNR. The effect of this reduced response compared to AVIRIS is lower data dimensionality, thus fewer endmembers can be identified and mapped than with AVIRIS. Accuracy assessment and error analysis indicates that with Hyperion data that, in many cases, mineral identification is not possible where specific minerals are known to exist. In addition, Hyperion often confuses similar minerals that are separable using AVIRIS

The Hyperion data demonstrate the importance of high signal-to-noise performance for hyperspectral sensors. The northern Death Valley Hyperion scene was collected under optimum (summer – high solar zenith angle) conditions and exhibits SWIR SNR as high as approximately 60:1. These data allow detailed mineral mapping, including within-species variability, however, this capability is at the detection limit of current Hyperion SNR levels. Combining minerals to form a basic mineral map results in improved mapping with greater than 94% correspondence between AVIRIS and Hyperion at the northern Death Valley site. The level of mineralogic information available from the Hyperion data is directly tied to the SNR.

As a technology demonstration, Hyperion performs satisfactorily for mineral identification and mapping. Summer season Hyperion acquisitions with high SNR result in improved mapping capabilities. Improvements principally take the form of characterizing subtle distinctions such as determining the difference between calcite and dolomite and mapping within-species variability caused by molecular substitution (eg: aluminum substitution in micas). Unfortunately, Hyperion data collected under less than optimum conditions (winter season, dark targets) have marginal SWIR SNR and allow mapping of only the most basic mineral occurrences and mineral differences. This results in a recommendation that future HSI satellite sensors have significantly higher SNR performance specifications than Hyperion for the SWIR (at least 100:1 based on dark current measurements).

7.0 Acknowledgments

This research was partially funded by NASA under grant NCC5-495. Additional financial support was provided by Analytical Imaging and Geophysics LLC internal research and development funds. AVIRIS data were provided by JPL. ACORN is a trademark of ImSpec Associates, LLC. ENVI is a registered trademark of Research Systems Inc., Boulder, Colorado. Pixel Purity Index (PPI), n-Dimensional Visualizer, Spectral Analyst, and Mixture-Tuned Matched Filter (MTMF) are all trademarks of Research Systems Inc.

8.0 References

Analytical Imaging and Geophysics LLC (AIG), 2001, *ACORN User's Guide, Stand Alone Version: Analytical Imaging and Geophysics LLC*, 64 p.

Boardman, J. W., 1993, Automated spectral unmixing of AVIRIS data using convex geometry concepts: in *Summaries, Fourth JPL Airborne Geoscience Workshop, JPL Publication 93-26*, v. 1, p. 11-14.

Boardman J. W., and Kruse, F. A., 1994, Automated spectral analysis: A geologic example using AVIRIS data, north Grapevine Mountains, Nevada: in *Proceedings, Tenth Thematic Conference on Geologic Remote Sensing,* Environmental Research Institute of Michigan, Ann Arbor, MI, p. I-407 - I-418.

Boardman, J. W., Kruse, F. A., and Green, R. O., 1995, Mapping target signatures via partial unmixing of AVIRIS data: in *Summaries, Fifth JPL Airborne Earth Science Workshop, JPL Publication 95-1*, v. 1, p. 23-26.

Boardman, J. W., 1998, Leveraging the high dimensionality of AVIRIS data for improved sub-pixel target unmixing and rejection of false positives: mixture tuned matched filtering, in: *Summaries of the Seventh Annual JPL Airborne Geoscience Workshop*, Pasadena, CA, p. 55.

Clark, R. N., King, T. V. V., Klejwa, M., and Swayze, G. A., 1990, High spectral resolution spectroscopy of minerals: *Journal of Geophysical Research*, v. 95, no. B8, p. 12653-12680.

Collwell, R. N. (ed.), 1983, Manual of Remote Sensing, 2nd Edition, American Society of Photogrammetry and Remote Sensing (ASPRS), pp. 344-363, and pp. 1196.

Goetz, A. F. H., G. Vane, J. E. Solomon, and B. N. Rock, 1985. Imaging spectrometry for earth remote sensing, *Science*, v. 228, p. 1147 - 1153.

Green, A. A., Berman, M., Switzer, B., and Craig, M. D., 1988, A transformation for ordering multispectral data in terms of image quality with implications for noise removal: *IEEE Transactions on Geoscience and Remote Sensing*, v. 26, no. 1, p. 65 - 74.

Green, R. O., B. Pavri, J. Faust, and O. Williams, 1999, "AVIRIS radiometric laboratory calibration, inflight validation, and a focused sensitivity analysis in 1998," in *Proceedings of the 8th JPL Airborne Earth Science Workshop: Jet Propulsion Laboratory Publication 99-17*, p. 161 – 175.

Green, R. O., Chrien, T. G., and Pavri, B., 2003, "On-orbit Determination of the Radiometric and Spectral Calibration of Hyperion Using Ground, Atmospheric and AVIRIS Underflight Measurements," *TGARS Special Issue on EO-1* (in press).

Kruse, F. A., 1988, Use of Airborne Imaging Spectrometer data to map minerals associated with hydrothermally altered rocks in the northern Grapevine Mountains, Nevada and California: *Remote Sensing of Environment*, v. 24, no. 1, pp. 31-51.

Kruse, F. A., and Lefkoff, A. B., 1993, Knowledge-based geologic mapping with imaging spectrometers: *Remote Sensing Reviews*, Special Issue on NASA Innovative Research Program (IRP) results, v. 8, p. 3 - 28.

Kruse, F. A., Lefkoff, A. B., and Dietz, J. B., 1993, Expert System-Based Mineral Mapping in northern Death Valley, California/Nevada using the Airborne Visible/Infrared Imaging Spectrometer (AVIRIS): *Remote Sensing of Environment, Special issue on AVIRIS, May-June 1993*, v. 44, p. 309 - 336.

Kruse, F. A., Huntington, J. H., and Green, R. O, 1996, Results from the 1995 AVIRIS Geology Group Shoot: in *Proceedings, 2nd International Airborne Remote Sensing Conference and Exhibition*: Environmental Research Institute of Michigan (ERIM), Ann Arbor, v. I, p. I-211 - I-220.

Kruse, F. A., Boardman, J. W., and Huntington, J. F., 1999, Fifteen Years of Hyperspectral Data: northern Grapevine Mountains, Nevada: in Proceedings of the 8th JPL Airborne Earth Science Workshop: Jet Propulsion Laboratory Publication, *JPL Publication 99-17*, p. 247 - 258.

Kruse, F. A., Boardman, J. W., and Huntington, J. F., 2001, Progress Report: Geologic Validation of EO-1 Hyperion: in Proceedings of the 10th JPL Airborne Earth Science Workshop: Jet Propulsion Laboratory Publication 02-1, p. 253 – 265.

Kruse, F. A., Boardman, J. W., and Huntington, J. F., 2002, "Comparison of EO-1 Hyperion and Airborne Hyperspectral Remote Sensing Data for Geologic Applications," in *Proceedings, SPIE Aerospace Conference, 9-16 March 2002, Big Sky, Montana*, published on CD-ROM, IEEE Catalog Number 02TH8593C, Paper #6.0102, 12 p.

Kruse, F. A., Boardman, J. W., Huntington, J. F., Mason, P., and Quigley, M.A., 2003, Evaluation and Validation of EO-1 Hyperion for Geologic Mapping: in Special Issue, TGARSS, IEEE (in press)

Pearlman, J., Stephen Carman, Paul Lee, Lushalan Liao and Carol Segal, 1999, Hyperion Imaging Spectrometer on the New Millennium Program Earth Orbiter-1 System: In Proceedings, International Symposium on Spectral Sensing Research (ISSSR), Systems and Sensors for the New Millennium, published on CD-ROM, International Society for Photogrammetry and Remote Sensing (ISPRS).

Research Systems Inc (RSI), 2001, ENVI User's Guide, Research Systems Inc, 948 p.

Wrucke, C. T., Werschkey, R. S., Raines, G. L., Blakely, R. J., Hoover, D. B, and Miller, M. S., 1984, "Mineral resources and mineral resource potential of the Little Sand Spring Wilderness Study Area, Inyo County, California," U. S. Geological Survey Open File Report 84-557, 20 p.

PRELIMINARY RESULTS – HYPERSPECTRAL MAPPING OF CORAL REEF SYSTEMS USING EO-1 HYPERION, BUCK ISLAND, U.S. VIRGIN ISLANDS

Fred A. Kruse[1]
Analytical Imaging and Geophysics LLC
4450 Arapahoe Ave, Suite 100, Boulder, Colorado 80303 USA

1.0 Introduction

Hyperspectral imaging (HSI) data consisting of hundreds of spectral bands provide the unique ability to identify Earth surface materials based on their spectral properties (Goetz et al., 1985). While these data can be analyzed using multispectral image (MSI) analysis techniques, classical MSI methods do not take full advantage of the spectral dimensionality of these datasets. Geologists have been analyzing hyperspectral data since 1983 with excellent results (Goetz et al., 1985; Lang et al. 1987; Kruse, 1988; Crowley, 1993; Boardman and Kruse, 1994; Clark et al., 1996; Boardman and Huntington, 1996; Crowley and Zimbelman, 1996, Kruse et al., 1993a, 1999, 2001, 2002, 2003). Consequently, a broad range of hyperspectral-specific analysis techniques have been examined, refined, and put into operational practice (Kruse, 1988; Mazer et al., 1988; Clark et al., 1991; Clark and Swayze, 1995; Boardman et al., 1995; Boardman, 1998; Kruse et al., 1993a, 1993b, 1999). These methods utilize the unique capabilities of hyperspectral data to locate, map, and identify the materials present on the Earth's surface. This paper describes a successful geologic case history using an end-to-end approach with satellite-based (Hyperion) data, including data correction to apparent reflectance, use of a linear transformation to minimize noise and determine data dimensionality, location of the most spectrally pure pixels, extraction of endmember spectra, and spatial mapping of specific endmembers. Recently, AIG has begun utilizing this approach with hyperspectral data of the near-shore marine environment (Kruse et al., 1997; Richardson and Kruse, 2000). While ocean data are generally more complex, and some work has been done in applying HSI data to near-shore-marine problems (Dekker et al., 1992; Davis et al., 1993; Carder et al., 1993; Clark et al., 1997, Holasek et al, 1998; Holden and LeDrew, 1999; Holden et al., 1999; Hochberg and Atkinson, 2000), many of the concepts developed for geologic analysis are applicable to analysis of near-shore hyperspectral data. The Hyperion case history described here for Buck Island, St Croix, U.S. Virgin Islands utilizes the unique capabilities of hyperspectral data to locate, map, and identify components of the coral reef ecosystem, assessing hyperspectral data's capability with respect to established ground truth. Use of the "standard" methods provides a viable first look at reef composition and distribution. Application of additional water column corrections to the hyperspectral data prior to signature extraction results in mapping improvements and demonstrates the requirement for extraction of bottom reflectance signatures to avoid mapping water depth dependencies rather than bottom composition differences.

2.0 EO-1 Hyperion

The launch of NASA's EO-1 Hyperion sensor in November 2000 marked the establishment of spaceborne hyperspectral mapping capabilities. Hyperion is a satellite hyperspectral sensor covering the 0.4 to 2.5 μm spectral range with 242 spectral bands at approximately 10nm spectral resolution and 30m spatial resolution from a 705km orbit (Pearlman et al., 1999). Hyperion is a pushbroom instrument, capturing 256 spectra each with 242 spectral bands over a 7.5Km-wide swath perpendicular to the satellite motion along an up to 160km path length. The system has two grating spectrometers; one visible/near infrared (VNIR) spectrometer (approximately 0.4 – 1.0 μm) and one short-wave infrared (SWIR)) spectrometer (approximately 0.9 – 2.5 μm). Data are calibrated to radiance using both pre-mission and on-orbit measurements. Key Hyperion characteristics are discussed further in Green et al., 2003.

Hyperion data are available for purchase from the U. S. Geological Survey (see http://eo1.usgs.gov/). To date, over 5000 Hyperion scenes have been acquired for a variety of disciplines. The EO-1 Science Validation Team has evaluated and validated the instrument. Selected results have been presented at team meetings (see http://eo1.gsfc.nasa.gov/) and also published in various venues (Asner and Green, 2001; Hubbard and Crowley, 2001; Kruse et al., 2003; also see Ungar, 2003 for a summary along with associated papers). The instrument remains healthy and additional data can be requested for specific sites.

[1] Analytical Imaging and Geophysics LLC (AIG), Boulder, Colorado, USA, E-mail: kruse@aigllc.com

3.0 Analysis Methods

Analytical Imaging and Geophysics LLC (AIG) has evolved a "standardized" hyperspectral data analysis methodology (Figure 1) that has been tested for a variety of data (Boardman et al., 1995; Kruse et al., 1996; Kruse et al., 2001). These approaches are implemented and documented within the "Environment for Visualizing Images" (ENVI) software system originally developed by AIG scientists (now an Eastman Kodak/Research Systems Inc [RSI] commercial-off-the-shelf [COTS] product) (Research Systems Inc, 2001). They are also described in additional detail below. This is not the only way to analyze these data, but we have found that it provides a consistent way to extract spectral information from hyperspectral data without *a priori* knowledge or requiring ground observations. The analysis approach consists of the following steps:

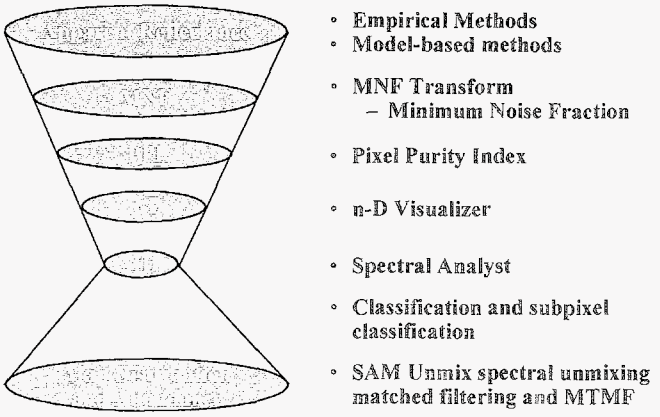

Figure 1: AIG Hyperspectral Analysis Scheme. Note the "hourglass" shape, which schematically represents the reduction of the hyperspectral data to just a few key spectra at the "neck" and then expansion back to spectral maps of the full dataset.

1. correction for atmospheric effects using an atmospheric model "ACORN" (AIG, 2001)
2. spectral compression, noise suppression, and dimensionality reduction using the Minimum Noise Fraction (MNF) transformation (Green et al., 1988; Boardman, 1993),
3. determination of endmembers using geometric methods (Pixel Purity Index – "PPI") (Boardman et al., 1995)
4. extraction of endmember spectra using n-dimensional scatter plotting (Boardman et al., 1995)
5. identification of endmember spectra using visual inspection, automated identification, and spectral library comparisons (Kruse and Lefkoff, 1993; Kruse et al., 1993a)
6. production of mineral maps using a variety of mapping methods. The "Spectral Angle Mapper" (SAM) produces maps of the spectrally predominant mineral for each pixel by comparing the angle between the image spectra and reference spectra in n-dimensional vector space (Kruse et al., 1993b). "Mixture-Tuned-Matched-Filtering" (MTMF) is basically a partial linear spectral unmixing procedure (Boardman, 1998).

3.1 ACORN Atmospheric Correction to Apparent Reflectance

One of the most critical steps in most imaging spectrometer data analysis strategies is to convert the data to reflectance, principally so that individual image spectra can be compared directly with laboratory or field data for identification and verification. Remote sensing measurements of the Earth's surface are strongly influenced by the atmosphere. Both scattering and absorption by gases and particulates affect the amount and wavelengths of light reaching the sensors. Absorption by atmospheric gases is dominated by water vapor with smaller contributions from carbon dioxide, ozone, and other gases (Gao and Goetz, 1990). Strong atmospheric water absorption bands make the atmosphere opaque in many regions (for example the 1.4 and 1.9 μm regions) and only small atmospheric windows are available for terrestrial remote sensing.

Ideally, imaging spectrometer data should be calibrated to absolute reflectance using onboard calibration. Onboard calibration, however, is difficult and typically not available. In its absence, one method that comes close to achieving this goal is a radiative transfer model-based technique ACORN (AIG, 2001). Currently used for correction of both airborne and satellite hyperspectral data, ACORN is a commercially-available, enhanced atmospheric model-based software that uses licensed MODTRAN4 technology. ACORN requires input of data parameters such as the acquisition date and time, the latitude and longitude of the scene, and the average elevation, along with atmospheric model parameters (AIG, 2001). The output of the procedure is high quality surface reflectance data produced without ground measurements. This method makes it possible to quantitatively derive physical parameters and analyze data from different regions and different times without *a priori* knowledge. It also makes possible comparison and analysis of imaging spectrometry data acquired by different instruments and comparison to field and laboratory spectral measurements or to spectra generated using theoretical models.

While ACORN works well over land and may form the starting point for atmospheric correction of near-shore-marine remote sensing data, unfortunately there are a number of other factors not taken into account by this model. These include corrections for sun glint and multiple scattering at the air/ocean interface and by the water

column itself (references here). Several researchers are working on improved model-based corrections that will account for these factors (references here). The results presented here using only ACORN demonstrate that considerable spectral mapping of corals is possible, however, even using the simple correction. We also present some mapping results with additional simple mathematical and model-based corrections, though we expect that refined/specialized models will improve the mapping results even further.

3.2 MNF Transformation

A "Minimum Noise Fraction" (MNF) Transform is used to reduce the number of spectral dimensions to be analyzed. The MNF transformation is a linear transformation related to principal components that orders the data according to signal-to-noise-ratio (Green et al., 1988). It can be used to determine the inherent dimensionality of the data, to segregate noise in the data, and to reduce the computational requirements for subsequent processing (Green et al., 1988; Boardman and Kruse, 1994). The MNF transformation can be used to partition the data space into two parts: one associated with large eigenvalues and coherent eigenimages, and a second with near-unity eigenvalues and noise-dominated images. By using only the coherent portions in subsequent processing, the noise is separated from the data, thus improving spectral processing results.

3.3 Pixel Purity Index (PPI)

Based on MNF results, the lower order MNF bands are usually set aside and the higher order bands selected for further processing. These are used in the "Pixel Purity Index" (PPI), processing designed to locate the most spectrally extreme (unique or different or "pure") pixels (Boardman et al., 1995). The most spectrally pure pixels typically correspond to mixing endmembers. The PPI is computed by repeatedly projecting n-dimensional scatterplots onto a random unit vector. The extreme pixels in each projection are recorded and the total number of times each pixel is marked as extreme is noted. A PPI image is created in which the digital number of each pixel corresponds to the number of times that pixel was recorded as extreme. A histogram of these images shows the distribution of "hits" by the PPI. A threshold is interactively selected using the histogram and used to select only the purest pixels in order to keep the number of pixels to be analyzed to a minimum. These pixels are used as input to an interactive visualization procedure for separation of specific endmembers.

3.4 n-Dimensional Visualization

Spectra can be thought of as points in an n-dimensional scatterplot, where n is the number of bands (Boardman, 1993; Boardman et al., 1995). The coordinates of the points in n-space consist of "n" values that are simply the spectral reflectance values in each band for a given pixel. The distribution of these points in n-space can be used to estimate the number of spectral endmembers and their pure spectral signatures, and provides an intuitive means to understand the spectral characteristics of materials. In two dimensions, if only two endmembers mix, then the mixed pixels will fall in a line in the histogram. The pure endmembers will fall at the two ends of the mixing line. If three endmembers mix, then the mixed pixels will fall inside a triangle, four inside a tetrahedron, and so on. Mixtures of endmembers "fill in" between the endmembers. All mixed spectra are "interior" to the pure endmembers, inside the simplex formed by the endmember vertices, because all the abundances are positive and sum to unity. This "convex set" of mixed pixels can be used to determine how many endmembers are present and to estimate their spectra.

In practice, the thresholded pixels from the MNF images are loaded into an n-dimensional scatterplot and rotated in real time on the computer screen until "points" or extremities on the scatterplot are exposed. These projections are "painted" using Region-of-Interest (ROI) definition procedures and then rotated again in 3 or more dimensions (3 or more bands) to determine if their signatures are unique in the MNF data. Once a set of unique pixels are defined, then each separate projection on the scatterplot (corresponding to a pure endmember) is exported to a ROI in the image. Mean spectra are then extracted for each ROI to act as endmembers for spectral mapping.

3.5 Spectral Identification

Spectral identification of the endmembers extracted using the n-dimensional scatterplotting is based on a combination of visual inspection of spectral plots and manual/automated comparison to spectral libraries (Clark et al., 1990, Kruse and Lefkoff, 1993, Kruse et al., 1993a). Spectra are visually examined to identify key spectral features locations, depths, and shapes, and these are compared against application-specific spectral libraries. Automated methods that compare overall spectral shape and specific features are also applied to determine candidate materials and to produce mathematical comparisons. Once names have been assigned to individual endmember spectra, then these can be passed forward to the spectral/spatial mapping algorithms.

3.6 Spectral Angle Mapper (SAM) Classification

The Spectral Angle Mapper (SAM) is an automated method for comparing image spectra to individual spectra (Boardman, unpublished data; Kruse et al., 1993b). The algorithm determines the similarity between two spectra by calculating the "spectral angle" between them, treating them as vectors in a space with dimensionality equal to the number of bands. Because this method uses only the vector "direction" of the spectra and not their vector "length", the method is insensitive to illumination. The result of the SAM classification is a color-coded image showing the best SAM match at each pixel. Additionally, rule images are calculated that show the actual angular distance (in radians) between each spectrum in the image and each reference or endmember spectrum. Darker pixels in the rule images represent smaller spectral angles and thus spectra that are more similar to the endmember spectra. For the purposes of display, the dark pixels are inverted, so that the best matches appear bright. These images present a good first cut of the spatial distribution of spectrally unique materials.

3.7 Mixture-Tuned-Matched Filtering (MTMF) Mapping

While the SAM algorithm does provide a means of identifying and spatially mapping materials, it only picks the best match to a given spectrum. Matched filtering (MF), based on well-known signal processing methodologies, maximizes the response of a known endmember and suppresses the response of the composite unknown background (Chen and Reed, 1987; Stocker et al., 1990; Yu et al., 1993; Harsanyi and Chang, 1994). MF also provides a rapid means of detecting specific minerals based on matches to specific library or image endmember spectra, again, however, it fails to consider spectral mixing. Matched filter results are presented as gray-scale images with values from 0 to 1.0, which provide a means of estimating relative degree of match to the reference spectrum (where 1.0 is a perfect match). Earth surfaces, however, are rarely composed of a single uniform material, thus it is usually necessary to consider mixture modeling to determine what materials cause a particular spectral "signature" in imaging spectrometer data. Mixture-Tuned-Matched-Filtering (MTMF) utilizes the MF theory above, but also includes a simple additive linear mixing model to estimate the abundances of the materials measured by the hyperspectral sensor (Boardman, 1998). Two dimensional scatterplotting of the MF score versus the MTMF Infeasibility score can be used to produce color-coded maps for materials occurring above specific abundance thresholds. Individual grayscale MF images can be used to show material abundances.

4.0 Geologic Example – N. Death Valley, California/Nevada

A site in northern Death Valley, California and Nevada, at the extreme northern end of Death Valley National Park was used to demonstrate and validate Hyperion data using existing geologic analysis methods (Kruse et al., 2001, 2002, 2003). The geology consists principally of a Jurassic-age intrusion exhibiting quart-sericite-pyrite hydrothermal alteration (Wrucke et al., 1984; Kruse, 1988). This site has been used as a test area for imaging spectrometers since 1983 (Kruse, 1988; Kruse et al., 1993a, 2003), thus considerable previous remote sensing information as well as ground truth exist for the area. Analysis results from this site serve to act as a guide to state-of-the-art processing of hyperspectral data for geologic applications.

Processing conducted on the northern Death Valley Hyperion data followed the standard AIG approach as described above: correction to apparent reflectance using "ACORN", spectral/spatial compression using the MNF transformation and PPI, determination of endmembers using geometric methods, spectral identification, and production of mineral maps using SAM and MTMF. A true color Hyperion image is shown for reference in Figure 2A. An endmember library (Figure 2B) defined using the n-dimensional visualization procedure was used with the Spectral Angle Mapper algorithm to produce a classified mineral map from reflectance-corrected Hyperion data (Figure 2C). This color-coded image presents the spectrally predominant mineral in each pixel as a distinct color. Mixture-Tuned Matched Filtering was also used to produce Hyperion mineral maps for the northern Death Valley site. Minerals identified using the Hyperion data by comparison to a spectral library and previously verified by X-Ray Diffraction include calcite, dolomite, muscovite (3 varieties), silica, and zeolite (Kruse, 1988, 2003). The Hyperion endmember library defined using the n-dimensional visualization procedure above was used in the unmixing process and abundance estimates were made for each mineral. These results can be presented in several ways. First, a set of gray-scale images stretched from 0 to 50% (black to white) provides a means of estimating relative mineral abundances. Selected results are shown in Figure 3A and 3B. Secondly, color composite images (not shown) can be used to highlight specific minerals and mineral assemblages. Pure colors in these images represent areas where the mineralogy is relatively pure. Mixed colors indicate spectral mixing, with the resultant colors indicating how much mixing is taking place and the relative contributions of each endmember. Finally, color-coded mineral maps can be formed by selecting the mineral with the highest abundance in each pixel (Figure 3C).

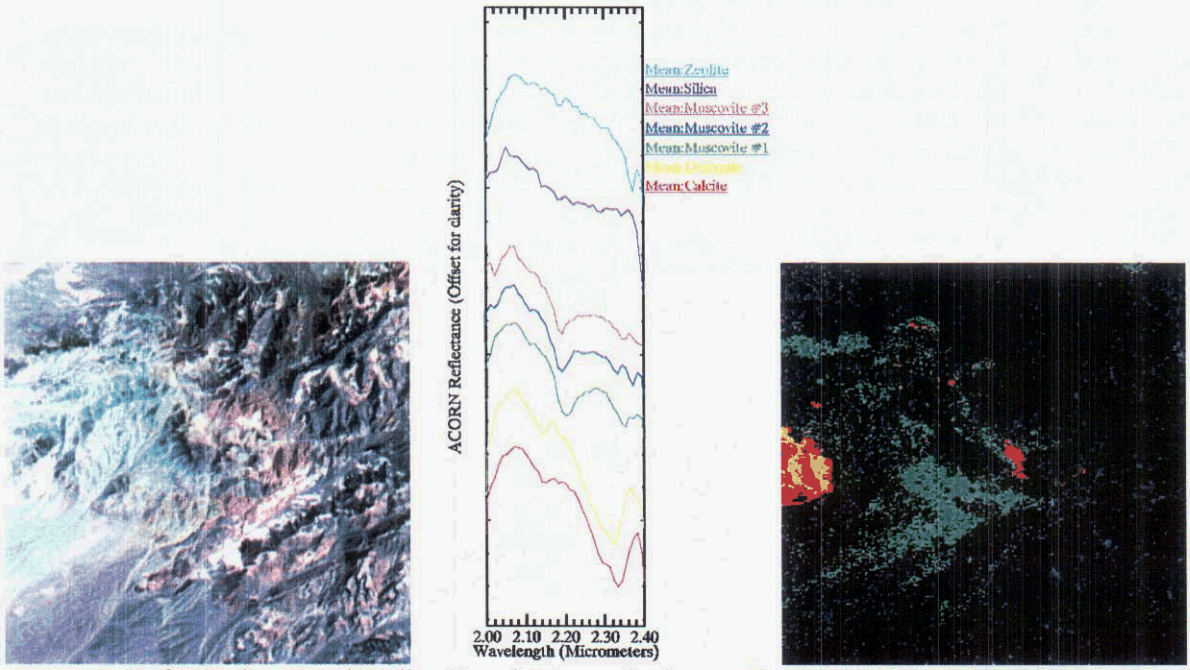

Figure 2: A. (Left) Northern Death Valley Hyperion true color image. B. (Center) Endmember spectra extracted using the n-dimensional scatterplotting approach. C. (Right) SAM results. The SAM image is color coded as follows: red=calcite, yellow=dolomite, green=muscovite#1, blue=muscovite#2, brown=muscovite#3, cyan=zeolite, purple=silica.

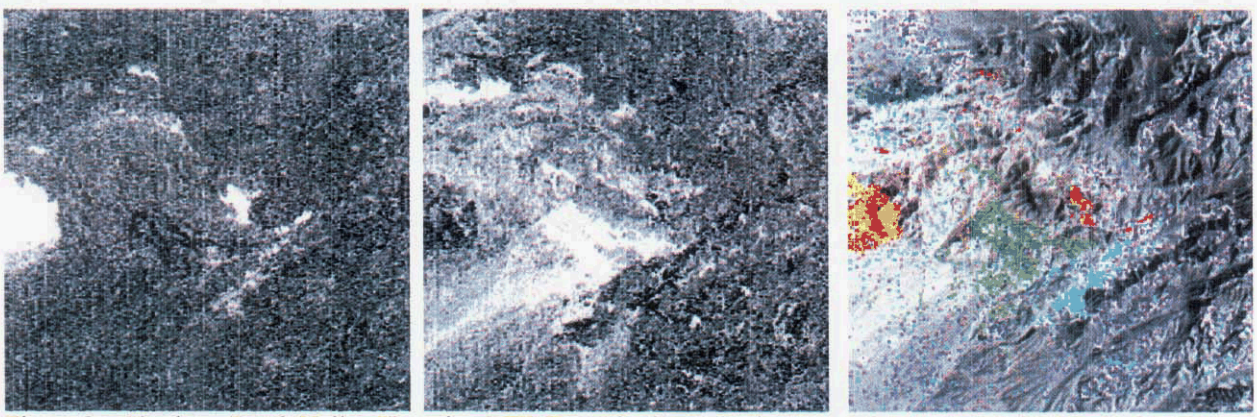

Figure 3: Northern Death Valley Hyperion MTMF results (MF score) presented as grayscale images (left and center). Brightness in grayscale images represents abundance, with brighter pixels corresponding to higher abundances. A. Left image is the calcite abundance image. B. Center image is the muscovite#1 abundance image. C. Combined MTMF mineral mapping results are shown on the right. Color-coded pixels representing specific minerals are overlain on Hyperion band 31 (0.66μm). Color coding is as follows: red=calcite, yellow=dolomite, green=muscovite#1, blue=muscovite#2, brown=muscovite#3, cyan=zeolite, purple=silica. Minerals were identified by comparison to a spectral library.

Figures 2 and 3 above demonstrate Hyperion's utility for mapping specific earth-surface materials (minerals) using AIG's standardized hyperspectral analysis methods. In this case, the data allow separation and identification of several very similar spectral signatures based on absorption features near 2.2 – 2.3 μm. Comparison to airborne hyperspectral data indicates that Hyperion performs with approximately 80-95% accuracy with respect to mineral maps produced using the same approach and verified utilizing field mapping and ground-based spectral measurements (Kruse et al., 2002, 2003). This provides the baseline against which to test hyperspectral mapping of the near-shore marine environment.

5.0 Application to Coral Reef Mapping

Extensive research has been conducted evaluating coral reefs and related marine environments. Recently, much attention and activity have been focused on coral reefs as dynamic ecosystems, and the common conclusion reached in these studies is that they are deteriorating world-wide (Dustan, 1977; Antonius, 1981; Dustan and Halas, 1987; Edmunds, 1991; Porter and Meier, 1992; Bischof, 1997; Bruckner and Bruckner, 1998; Cervino and Smith, 1997; Kuta and Richardson, 1996). Remote sensing technology has emerged as a tool for performing large-scale coral reef evaluations and monitoring. While multispectral, aircraft- and satellite-based observations have been available for some time (eg: Lyzenga, 1978, 1981; Biña et al., 1979; Jupp et al., 1985; Jupp, 1986; Kuchler et al., 1988; Bierwirth et al., 1993, Mumby et al., 1998a), only recently have reef-scale, long-duration studies been performed (Dunston and Halas, 1997). These examples illustrate the high potential of spectral remote sensing for coral reef mapping and monitoring, but also point out the requirements for higher spectral and spatial resolution. Hyperspectral data in particular offer high potential for characterizing and mapping coral reefs because of their capability to identify and map individual reef components based on their detailed spectral signatures (Clark et al., 1997, Holasek et al., 1998; Holden and LeDrew, 1999; Hochberg and Atkinson, 2000). Holden et al. (1999) show that a high spectral resolution *in situ* spectral library can be developed to differentiate between various coral types as well as bleached coral substrate. Hyperspectral remote sensing has also shown significant promise in distinguishing coral species and reef health. Holden and LeDrew (1998a) demonstrate differentiation between healthy and non-healthy corals based on their high resolution spectral signatures. Myers et al. (1999) describe how optical spectra can be used to differentiate between pigmented and bleached coral and between coral and macroalgae. Recent hyperspectral studies have demonstrated mapping of spectral differences attributable to bottom reflectance of corals and other substrates (Clark et al., 1997, 2000; Holasek et al., 1998; Andréfouët et al., 2003; Joyce and Phinn, 2003)

Most researchers also note, however, the significant effect of the water column on remotely sensed signals of coral reefs (Lyzenga, 1981; Maritorena et al., 1994; Mobley et al., 1993; Mumby et al., 1998b; Holden and LeDrew, 1998b, 2001, 2002). Several of the above works and other related publications demonstrate that the wavelength-specific nature of attenuation caused by the water should be removed using correction algorithms that are based on correction for depth and water optical attenuation and scattering, a correction to "remove the water" from the spectral signature (Dustan, 1985; Pratt et al., 1997; Mumby et al., 1998b; Holden et al., 1999; Holden and LeDrew 2002). Such a model would treat the coral reef as a Lambertian lower boundary at a specified depth and perform corrections for the ocean/atmosphere interface, marine aerosol conditions, and light attenuation by seawater. Several models exist (eg: Hydrolite), or are under development to perform such corrections, however, these are generally designed for analysis and modeling of single spectra not for full-image, per-pixel correction of hyperspectral data. Limited examples are available of the application of water column corrections to field or modeled spectra (Young et al., 1995; Clark et al., 2000; Holden and LeDrew, 2000, 2001, 2002; Kutser et al., 2003; Mobley et al., 2003) or directly to hyperspectral data (Gao et al., 2000; Goodman and Ustin, 2002; Goodman et al., 2003).

The research described here shows results from analysis of hyperspectral (Hyperion) data for a site in the U.S. Virgin Islands both with and without water column corrections applied on a per-pixel basis. The baseline analysis uses a "standard" atmospheric correction and analysis methods described above for geologic applications. Refinements of the analysis using a first cut empirical water column correction based on comparison of field and Hyperion spectra are also described, along with a application of a prototype per-pixel radiative transfer model-based water column correction.

5.1 Buck Island, USVI Site

Buck Island Reef National Monument, including and surrounding Buck Island approximately two miles off the north shore of St. Croix, was established in 1961. The island has white coral beaches and extends to an elevation of approximately 100m. An elkhorn barrier reef extends around approximately two thirds of the island. Benthic habitat mapping for an approximately 23 square km area around Buck Island, USVI was completed by NOAA and the National Park Service during 1999-2000 using conventional color aerial photography. (Kendall et al., 2001) and on-line at (http://www.csc.noaa.gov/crs/bhm/buck_is.html). This was part of a pilot project designed to test benthic mapping methods (see http://biogeo.nos.noaa.gov/benthicmap/caribbean/manual.shtml). Benthic habitats were visually interpreted on scanned orthorectified aerial photographs using a standardized classification scheme based on visual perception of color, tone, textures, and geographic context of features (Finkbeiner et al., 2001). Digital data are available from NOAA (http://biogeo.nos.noaa.gov/products/benthic/htm/data.htm).

A rasterized compilation of the NOAA mapping results produced for this study for the Buck Island site is shown in Figure 4. These results are used as the baseline to evaluate and validate Hyperion mapping for the Buck Island site. Additional supporting data available for the Buck Island site include bathymetric soundings (R. Warner, personal communication 2002) and Digital Elevation Models (DEM). The bathymetric data used in this study were obtained from NOAA as irregularly spaced X-Y-Z measurements with positions in Latitude/Longitude and soundings in meters. The data were gridded to a regular 30m pixel size to match the Hyperion data and projected to WGS84 map coordinates (Figure 5). The DEM data used were from standard USGS 7.5 minute (1:24,000 scale) quadrangles, mosaicked to cover the Buck Island site and merged with the bathymetry (Figure 5). The DEMs were also used to generate a "land" mask for use in the Hyperion processing.

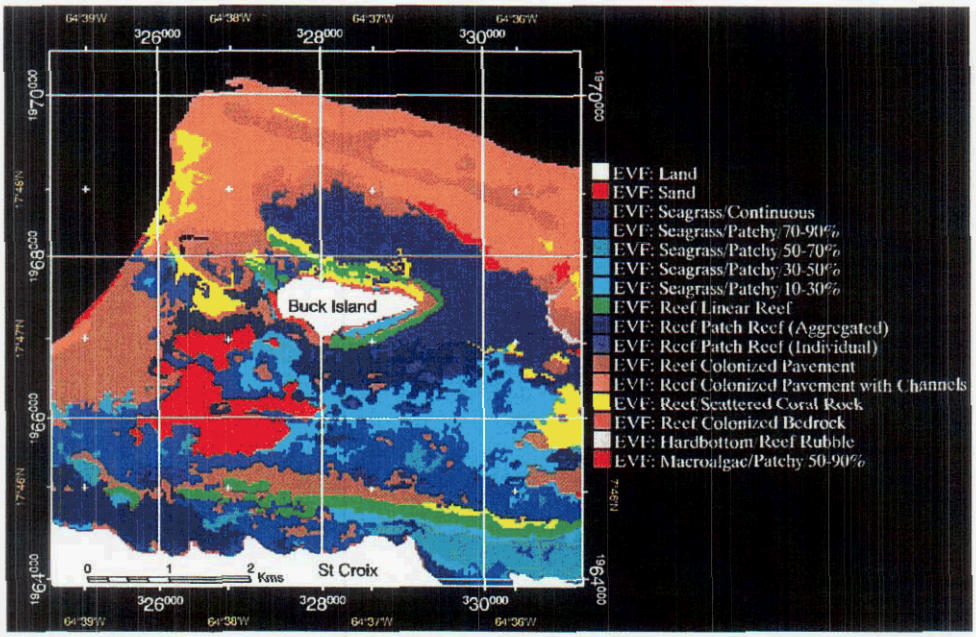

Figure 4: Compilation of NOAA Benthic Habitat Mapping results for Buck Island Reef National Monument, St. Croix, USVI (From NOAA digital data). Black areas represent unclassified pixels.

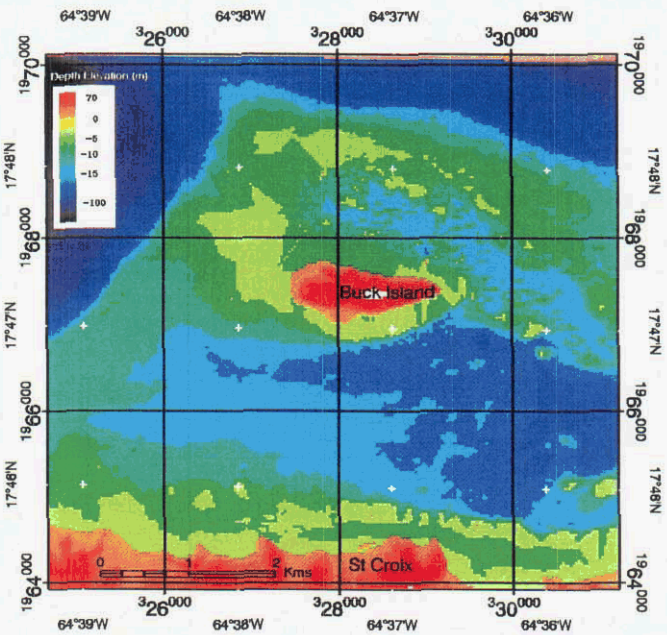

Figure 5: Combined NOAA bathymetry and USGS digital elevation for the Buck Island site.

5.2 Buck Island Hyperion – Standard Mapping Results

Hyperion data were acquired for a 7.5 x 165km strip crossing Buck Island Reef National Monument on 21 January 2002 as a target-of-opportunity (Scene ID: EO10030482002021111KP, Level 1B-1). While much of the data were cloud covered, the Buck Island area was essentially cloud-free. A small subset of Hyperion Data for the area surrounding Buck Island was cut out of the larger dataset for further processing (Figure 6).

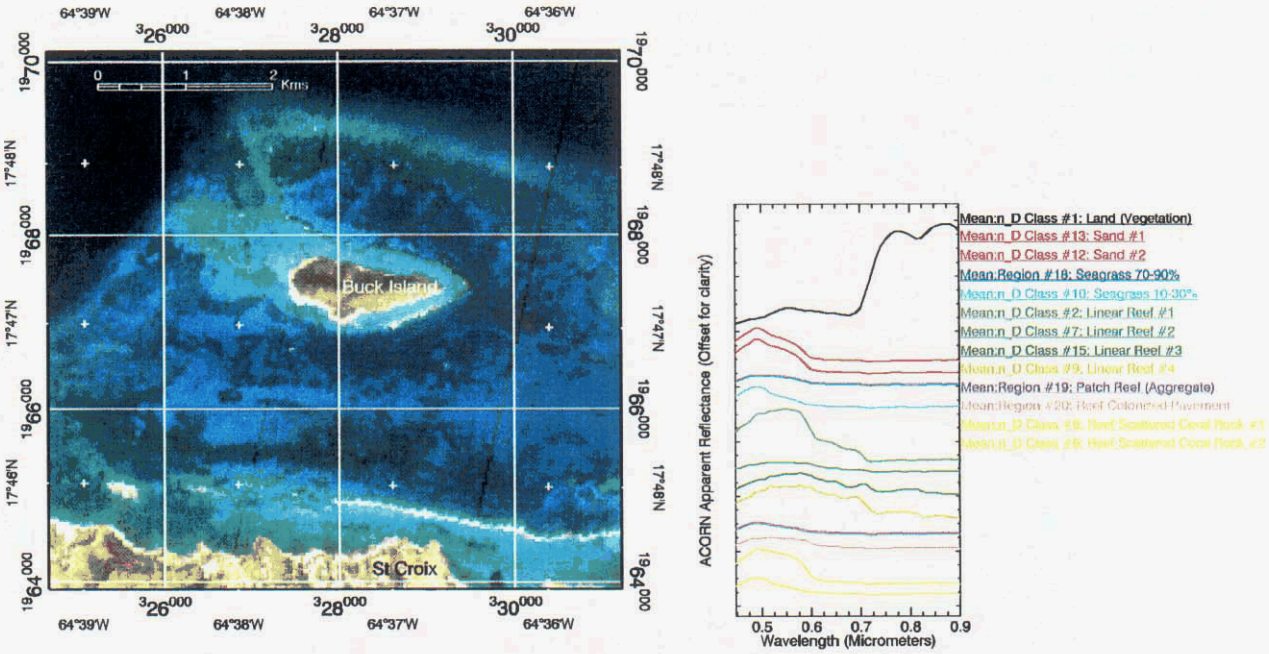

Figure 6: A (left). True color composite of Hyperion bands 31, 20, and 10 (0.66, 0.55, 0.45μm) (RGB) showing Buck Island and surrounding reefs. B (right). Selected Hyperion endmember spectra for Buck Island USVI.

As described for the geologic example above, the Hyperion data were used to extract representative spectral endmembers for mapping (Figure 6B). The data were corrected to apparent reflectance using ACORN (no water column correction was applied) and the corrected data were analyzed using the standardized geologic approach. The MNF procedure was used to reduce the spatial dimensionality of the data. The PPI procedure further reduced the dimensionality by selecting those spectra most likely to be pure endmembers. Figure 6B shows selected endmember spectra extracted from the data. "Best Fit" benthic habitat names and colors similar to those shown in Figure 4 were assigned to the spectra based on their locations and similarity to spatial patterns in NOAA mapping results (Figure 4). The "Land" spectrum in the plot is reversed to black for display purposes.

These spectra, representing the relatively "pure" occurrences of specific materials (at the Hyperion 30m spatial scale), were used to map the Buck Island site based on spectral signatures extracted directly from the Hyperion data. Figure 7 shows the combined results of SAM analysis using these endmembers on the Hyperion data. Again, "Best Fit" benthic habitat names assigned to the spectra above were used to define class names. Visual comparison of the SAM mapped classes in Figure 7 to the NOAA classes in Figure 4 illustrates some spatial correspondence between hyperspectral mapping results and "ground truth" as well as the detailed character of hyperspectral mapping of the near-shore environment based on spectral properties. It is apparent that some classes are mapped quite accurately. Other classes, however, are not well mapped using the hyperspectral data and there are some apparent correlations to depth that are not seen in the NOAA map. This points out drawbacks in the classification scheme as well as the hyperspectral method. The fact that the two approaches map different parameters is an important difference stemming from human observation of spectral/spatial associations on the aerial photographs versus the automatic hyperspectral mapping of bottom composition based solely on spectral properties in the Hyperion data. For example, a "Patch Reef" environment is an interpreted combination of corals and sand in the aerial photographs, whereas the hyperspectral data individually and separately map the coral and sand units at the 30m Hyperion pixel scale.

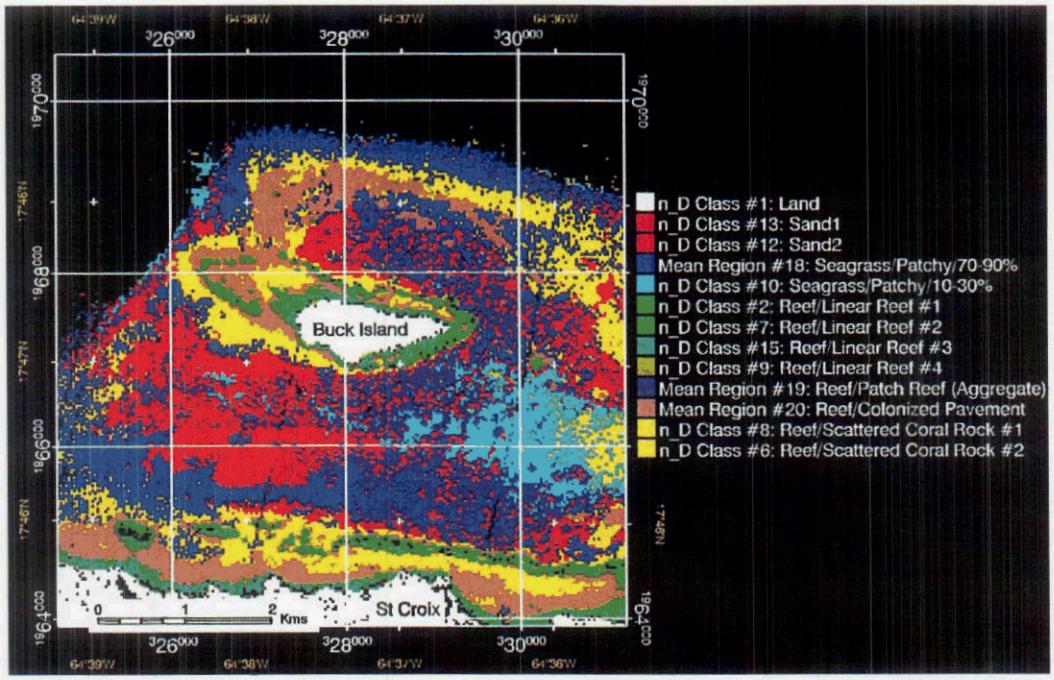

Figure 7. Spectral Angle Mapper (SAM) Hyperion analysis results using endmember spectra shown in Figure 6B. "Best Fit" benthic habitat names and colors similar to those shown in Figure 4 were assigned based on similarity to spatial patterns in NOAA mapping results (Figure 4). Black areas represent unclassified and/or hardbottom/uncolonized pavement. Note apparent depth dependence of some units when compared to bathymetry shown in Figure 5. Also note that not all classes mapped by NOAA were identified in the HSI data.

Figure 8 further shows the capabilities of the hyperspectral data to map and quantify individual ecosystem components. The MTMF procedure was used on the ACORN-corrected (non-water-column corrected) Hyperion data with the same set of endmembers shown in Figure 6 to map the distribution and abundance of specific components. The individual distribution of a "sand" unit, a "Seagrass – Patchy 10-30%" and one of the coral units is shown.

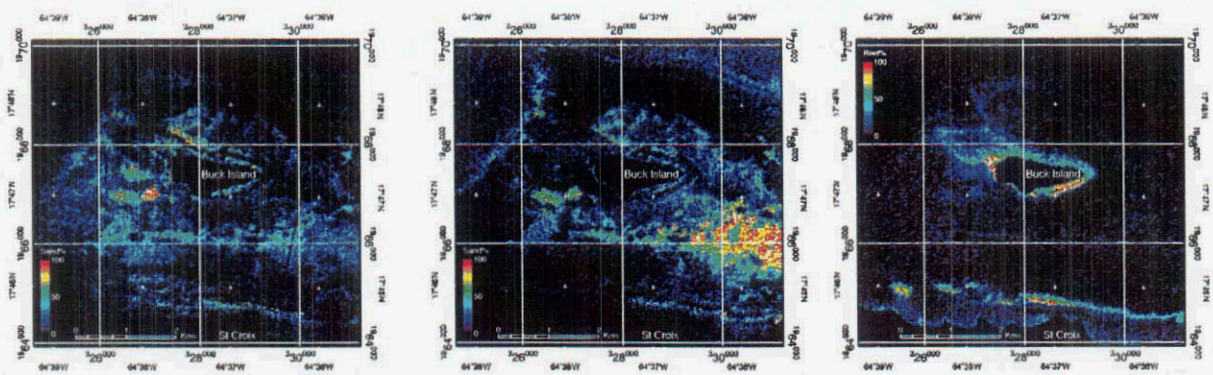

Figure 8. MTMF (MF Score) results for the "Sand #1", "Seagrass – Patchy 10-30%", and "Linear Reef #1" classes showing calculated abundances as color-coded images with 0-100% coded from black to white. A. Left image is "Sand #1", B. center image is "Seagrass Patchy 10-30%", C. right image is "Linear Reef #1" abundance.

5.3 Empirical Water Column Correction Hyperion Results

While the results using the standard atmospheric correction and hyperspectral analysis methods as above were moderately successful, it is clear that further corrections for the water column are required to allow improved and

quantitative mapping of coral reef ecosystems. One method that has shown promise is a simplistic empirical correction described by Goodman and Ustin (2002). This approach uses measured bottom spectra and their corresponding surface-leaving reflectance spectra measured by a hyperspectral instrument at various depths along with bathymetry to estimate correction coefficients for the hyperspectral data. Goodman and Ustin (2002) demonstrated both the linear case where:

$$R_{EST}(\lambda)=(R_{HSI}(\lambda)*A(\lambda))+(Z*B(\lambda))+C(\lambda)$$

And two non-linear (exponential) correction functions where either:

$$R_{EST}(\lambda)=(R_{HSI}(\lambda)*A(\lambda))*(e^{(Z*B(\lambda)})$$

or

$$R_{EST}(\lambda)=C+(R_{HSI}(\lambda)*A(\lambda))*(e^{(Z*B(\lambda)}).$$

Where $R_{EST}(\lambda)$ is the estimated bottom reflectance with wavelength, $R_{HSI}(\lambda)$ is the hyperspectral surface leaving reflectance calculated using a standard atmospheric model, Z is the depth from bathymetric per-pixel measurements, and A, B, and C are estimated coefficients based on minimizing the error between multiple field measurements and their corresponding estimated HSI bottom reflectances. While accepted radiative transfer theory for water column effects dictates that the water column should behave exponentially in accordance with Beer's Law (Holden and LeDrew, 2001 give a good overview of water column optical properties), Goodman and Ustin (2002) concluded that at least for their case (Kaneohe, Hawaii) that the linear function performed substantially the same as the exponential function.

For the Buck Island example, we used bottom-measured field spectra of Buck Island sands provided by Holden and LeDrew (2001, 2002) (Figure 9A). ACORN-corrected Hyperion sand spectra (Figure 9B) were selected based on NOAA mapping (Figure 4) for areas at various depths determined from the per-pixel gridded NOAA bathymetry described above and shown in Figure 5. Minimization of both the linear and non-linear equations described above was attempted, and again, the linear model produced the smallest estimation errors. Figure 10A shows the estimated coefficients over the 0.45 – 0.68 μm range, while Figure 10B shows the corrected spectra for the various depths. Note that the estimates at wavelengths longer than about 0.64 μm have unacceptably high errors.

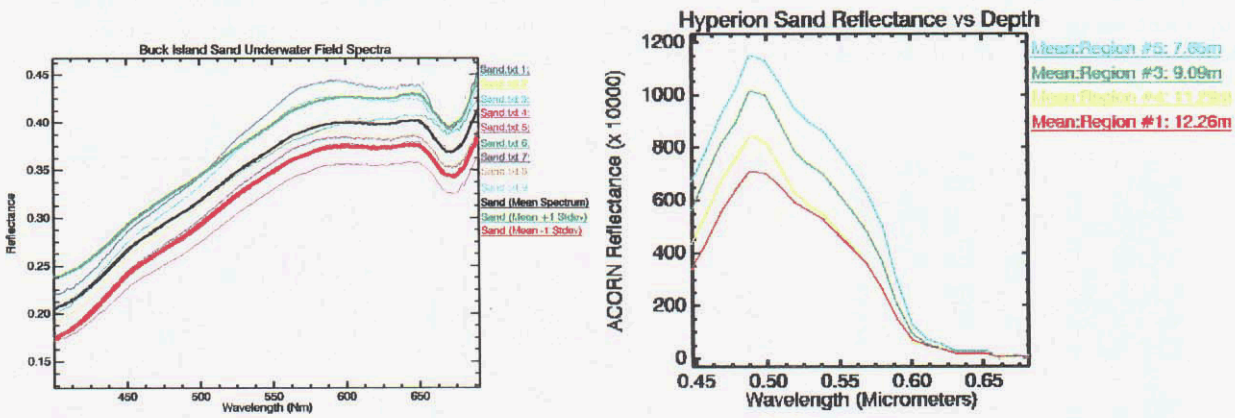

Figure 9: A. (Left) ASD Field sand spectra measured by Holden and LeDrew (2001). Average spectrum is black with one standard deviation below (red) and above (green). B. (Right) Hyperion "sand" surface-leaving reflectance spectra extracted from ACORN reflectance-corrected data for various depths.

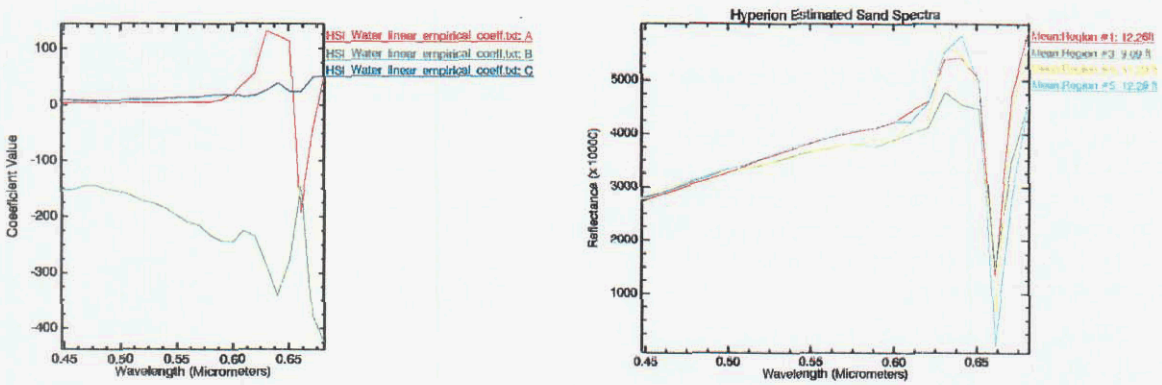

Figure 10: A. (Left) Empirical water-column correction linear coefficients. B. (Right) Figure 9B water-column corrected Hyperion "sand" bottom reflectance spectra for various depths.

Application of the linear equation and coefficients to the ACORN-corrected Hyperion data on a per-pixel basis results in a water-column-corrected (bottom reflectance) hyperspectral data cube. Display of a "true color" composite image shows the general effect of the correction (Figure 11A). It is easy to see that the sand areas are normalized to nearly the same appearance (cyan color), while the live coral areas appear green. Analysis of the full dataset using the AIG analysis methods (MNF, PPI, n-D Visualization, MTMF mapping) produces what appear to be improved material composition (sand and coral) and abundance images (Figures 11A and 11B), however, these don't necessarily correspond as well as the uncorrected (water-leaving reflectance) results to the NOAA benthic classes. In effect, the water-column correction has improved the compositional mapping by normalizing out depth effects. Specifically, what was mapped as a sand unit and a low abundance seagrass unit using the water-leaving reflectance are consolidated to one sand class by the empirical water column correction. Further examination of both results shows the correspondence of the uncorrected classes to depth differences shown in the bathymetry (Figure 5).

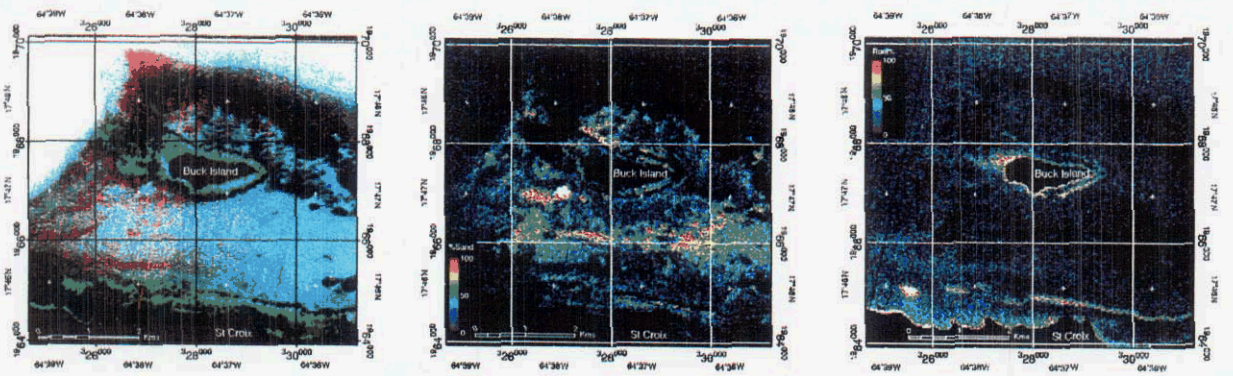

Figure 11: MTMF (MF Score) results calculated from the empirical-water-column-corrected Hyperion data for the "Sand" and "Linear Reef #1" classes showing calculated abundances as color-coded images with 0-100% coded from black to white. A. left image is water-column-corrected true color image, B. center image is water-column-corrected "Sand" abundance, C. right image is water-column-corrected "Linear Reef #1" abundance.

In summary, implementation of an accurate water column correction appears critical to bottom composition mapping using hyperspectral data. The empirical linear correction "works" to some extent and demonstrates the concept. What may apparently be sand mapped at different depths without the correction appears as one material after correction. While other classes of materials can be mapped, spectra for these materials, however, don't appear "reasonable" leading to the conclusion that a more advanced correction is required. The two exponential models were also evaluated, but produced poorer estimates than simple linear model.

5.4 Model-Based Water Column Correction Hyperion Results

Several radiative-transfer-based correction algorithms are under development for hyperspectral data (Gao et al., 2000; Acharya et al., 2002; Goodman and Ustin, 2003). The goal of these is generally to perform atmospheric correction, correct for air-sea interface effects, and to correct for the water column in support of hands-off (no *a priori* measurements required) littoral-zone quantitative remote sensing.

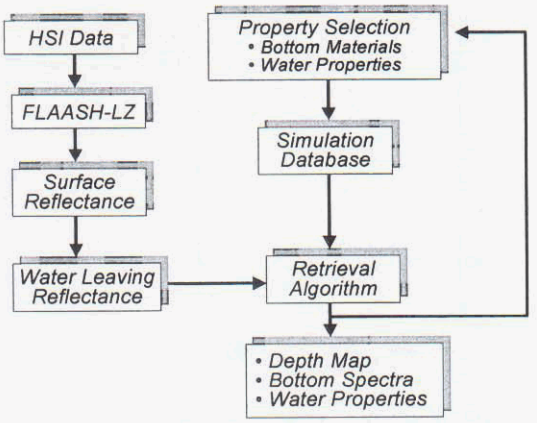

Figure 12: Flow chart for water and bottom property retrievals (From Acharya et al., 2002. Used with permission.)

The Acharya et al. (2002) correction (Figure 12) was applied to the Buck Island Hyperion data by Steve Adler-Golden of Spectral Science Inc. as a test case for this algorithm. The data were first atmospherically corrected to surface reflectance using "FLAASH-LZ", a littoral zone version of the Fast Line-of-sight Atmospheric Analysis of Spectral Hypercubes (FLAASH) atmospheric correction code (Matthew et al., 2000). Surface glint and foam components were derived using a spectral unmixing approach and removed by subtraction. This method then assumes uniform bottom characteristics and iteratively and simultaneously estimates water depth and bottom reflectance using a 3-D backward-propagation Direct Monte-Carlo Simulation (DSMC) radiative transport algorithm (Richtsmeier et al., 2001). The outputs are an estimated depth (bathymetry) image and a data cube of hyperspectral bottom reflectances (Acharya et al., 2002).

The Hyperion bottom reflectance data were analyzed following the previously described AIG analysis methods (MNF, PPI, n-D Visualization, MTMF mapping). This again produces a selection of endmember spectra, a bottom composition map, and abundance images for each endmember material (Figure 13). Results generated using this approach appear similar to those obtained using the empirically corrected Hyperion data (though somewhat noisier and less spatially coherent). Again, the sand unit and a low abundance seagrass unit mapped using the water-leaving reflectance are consolidated to one sand class by the model-based water column correction (Figures 13A and 13B). One noted problem, however, was that not all depth dependencies were removed, particularly at greater depths. This can be seen principally in the "sand" abundance map, which clearly still has depth dependencies when compared to the NOAA bathymetry (Figure 5). Also, comparison of the bathymetry map generated from the Hyperion data to the measured bathymetry reveals that the depth algorithm is only accurate at depths shallower than about 6m.

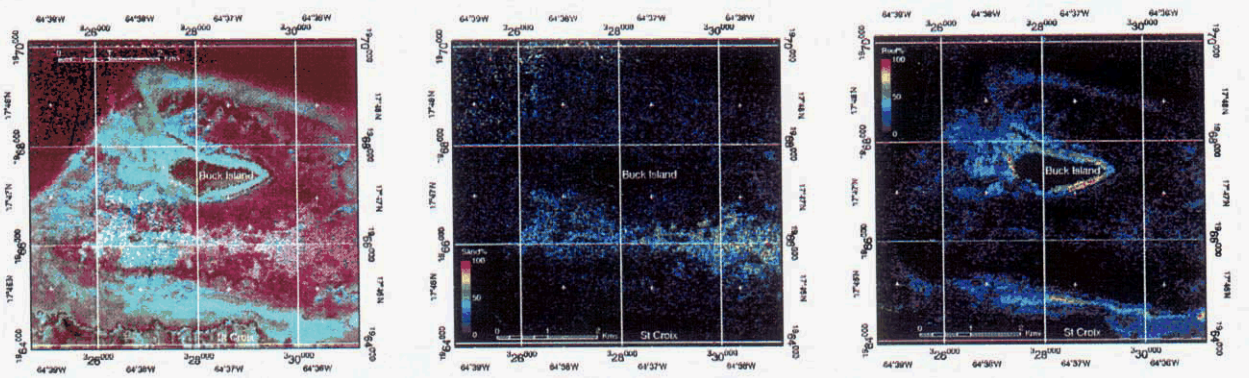

Figure 13: MTMF (MF Score) results calculated from the water-column-model-corrected Hyperion data for the "Sand" and "Linear Reef #1" classes showing calculated abundances as color-coded images with 0-100% coded from black to white. A. left image is water-column-corrected true color image, B. center image is water-column-corrected "Sand" abundance, C. right image is water-column-corrected "Linear Reef #1" abundance.

In summary, a prototype model-based method for atmospheric correction, removal of sea-surface effects, and water-column correction of hyperspectral data demonstrates that hands-off calculation of bottom reflectance may be

possible without supplemental field information. While demonstrating the potential, limitations imposed on the current model by incomplete knowledge of bottom reflectance properties result in unacceptably large errors of depth estimation and thus water depth corrections. Refinements to the method utilizing a simulation database of bottom reflectance properties are planned and may improve model performance (Achayara et al., 2002).

6.0 Discussion and Conclusions

This case study using Hyperion data to map coral ecosystems at Buck Island National Monument demonstrates the viability of methods originally developed for analysis of geologic targets for analysis of littoral-zone hyperspectral data. Standard processing of Hyperion data for the Buck Island site produces useful bottom composition information for benthic habitat mapping, however, limitations are apparent. Hyperion habitat maps are different from those produced using conventional methods. Hyperion produces detailed composition maps (including abundance), while classic benthic habitat maps rely on aggregation of diverse materials by analysts. While there is some correspondence of these basic Hyperion mapping results to published benthic habitat maps, depth dependencies are apparent. Spectral "ground truth" at Hyperion scales is required for verification of similarities/differences.

Use of a linear Empirical Water Column Correction improves mapping for some units. Materials with the same composition, but at different depths are consolidated after the water column correction. This approach, however, requires bathymetry and field spectra and thus is not applicable to areas without supporting ground information. Further study of empirical water column corrections is justified, but their reliance on in-situ measurements imposes significant limitations.

A prototype radiative transfer model-based correction for littoral zone hyperspectral data removes the requirements for supporting data by simultaneously calculating the bottom reflectance and bathymetry. Hyperion mapping results demonstrate that the corrected data can be used for successful extraction of bottom composition corrected for depth effects. The current assumption of bottom uniformity, however, imposes limitations on the approach and unacceptable errors in bathymetry estimation. Refinement of the algorithm is possible and in progress, but will require establishment of a simulation database of common bottom materials.

These analyses show that hyperspectral separation and mapping of distinct near-shore bottom characteristics is possible. The mapping results, however, are not exactly what scientist are used to receiving. Thus HSI data for mapping littoral scenes should be assessed not according to how well they can reproduce the conventional mapping process, but in terms of what additional information they can provide.

7.0 Acknowledgements

Development of the geologic case history for northern Death Valley was supported by NASA Grant NCC5-495. Hyperion data used for this research were obtained by NASA as a target of opportunity. Buck Island bathymetry were obtained by NOAA/NOS Hydrographic Surveys Division and provided by Rob Warner of the NOAA Center for Coastal Monitoring and Assessment (CCMA). Thanks to Heather Holden and Ellsworth LeDrew of the University of Waterloo for providing the Buck Island bottom reflectance spectra. James Goodman (UC Davis) deserves special thanks for his personal assistance in calculating the empirical water column coefficients for use on the Buck Island spectra and Hyperion data. Steve Adler-Golden (Spectral Science Inc) ran the Buck Island Hyperion data through the DSMC model-based correction.

8.0 References

Acharya, P. K., Adler-Golden, S., Berk, A., Bernstein, L. S., 2002, Bathymetry of the littoral zone using hyper-spectral images: In SPIE Conference Proceedings, Seattle, Washington, 8-11 July, v. 4816, paper 4816-20.

Analytical Imaging and Geophysics LLC (AIG), 2001, ACORN User's Guide, Stand Alone Version: Analytical Imaging and Geophysics LLC, 64 p.

Andréfouët, S., C. Payri, E. J. Hochberg, L. Mao Che, and M. J. Atkinson, 2003, Airborne hyperspectral detection of microbial mat pigmentation in Rangiroa atoll (French Polynesia): Limnology and Oceanography, Special Issue: Light in Shallow Waters, v. 48, no. 1 (Part 2), p. 426 – 430.

Antonius, A., 1981, Coral Reef pathology: a review: Proc 4th International Coral Reef Symposium, v. 2, p. 3-6.

Asner, G.P. and R.O. Green, 2001, Imaging spectroscopy measures desertification in the Southwest U.S. and Argentina. EOS Transactions, v. 80, p. 601-605.

Biña, R.T., Carpenter, K., Zacher, W., Jara, R. and Lim, J.B., 1979. Coral reef mapping using Landsat data, follow-up studies. In Proceedings of the International Symposium on Remote Sensing of Environment, v. 12, no. 3, p. 2051-2070.

Bierworth, P. N., T. Lee, and R. Burne, 1993, Shallow sea-floor reflectance and water depth derived by unmixing multispectral imagery: Photogrammetric Engineering and Remote Sensing, v. 59, no. 3, p. 331 – 338.

Bischof, B., 1997, Scientist launch survey of reef health: Science, v. 276, p. 1494.

Boardman, J. W., 1993, Automated spectral unmixing of AVIRIS data using convex geometry concepts: in Summaries, Fourth JPL Airborne Geoscience Workshop, JPL Publication 93-26, v. 1, p. 11 - 14.

Boardman J. W., and Kruse, F. A., 1994, Automated spectral analysis: A geologic example using AVIRIS data, north Grapevine Mountains, Nevada: in Proceedings, Tenth Thematic Conference on Geologic Remote Sensing, Environmental Research Institute of Michigan, Ann Arbor, MI, p. I-407 - I-418.

Boardman, J. W., Kruse, F. A., and Green, R. O., 1995, Mapping target signatures via partial unmixing of AVIRIS data: in Summaries, Fifth JPL Airborne Earth Science Workshop, JPL Publication 95-1, v. 1, p. 23-26.

Boardman, J. W., and J. H. Huntington, 1996. Mineral mapping with 1995 AVIRIS data: in Summaries of the 6th Annual JPL Airborne Earth Science Workshop, JPL Pub. 96-4, Vol. 1. AVIRIS Workshop, Jet Propulsion Laboratory, California Institute of Technology, Pasadena, Calif., p. 9-11.

Boardman, J. W., 1998, Leveraging the high dimensionality of AVIRIS data for improved sub-pixel target unmixing and rejection of false positives: mixture tuned matched filtering, in Summaries of the Seventh Annual JPL Airborne Geoscience Workshop, Pasadena, CA, p. 55.

Bruckner, A. W., and Bruckner, R. J., 1998, Emerging infections on reefs, Natural History, v. 106, p. 48.

Carder, K. L., Reinersman, P., Chen, R. F., Muller-Karger, F., Davis, C. O., and Hamilton M. K., 1993: AVIRIS calibration and application in coastal oceanic environments: Remote Sensing of Environment, v. 44, nos. 2-3, p. 205 - 216.

Cervino, J. M., and Smith, G., 1997, Corals in Peril, Ocean Realm v. 2, p. 33 – 34.

Chen, J. Y., and Reed, I. S., 1987, A detection algorithm for optical targets in clutter: IEEE Trans. on Aerosp. Electron. Syst., v. AES-23, no. 1.

Clark, C., H. Ripley, E. Green, A. Edwards, and P. Mumby, 1997, Mapping and measurement of tropical coastal environments with hyperspectral and high spatial resolution data: International Journal of Remote Sensing, v. 18, no. 2, p. 237 – 242.

Clark, C., P. Mumby, J. Chisholm, J. Jaubert, and S. Andrefouet, 2000, Spectral discrimination of coral mortality states following a severe bleaching event: International Journal of Remote Sensing, v. 21, no. 11, p. 2321 – 2327.

Clark, R. N., and Swayze, G. A., 1995, Mapping minerals, amorphous materials, environmental materials, vegetation, water, ice, and snow, and other materials: The USGS Tricorder Algorithm: in Summaries of the Fifth Annual JPL Airborne Earth Science Workshop, JPL Publication 95-1, p. 39 - 40.

Clark, R. N., King, T. V. V., Klejwa, M., and Swayze, G. A., 1990, High spectral resolution spectroscopy of minerals: Journal of Geophysical Research, v. 95, no. B8, p. 12653-12680.

Clark, R.N., G.A. Swayze, A. Gallagher, N. Gorelick, and F. Kruse, 1991, Mapping with Imaging Spectrometer Data Using the Complete Band Shape Least-Squares Algorithm Simultaneously Fit to Multiple Spectral Features from Multiple Materials, In Proceedings of the Third Airborne Visible/Infrared Imaging Spectrometer (AVIRIS) Workshop, JPL Publication 91-28, p. 2-3.

Clark, R. N., Swayze, G. A., Rowan, L. C., Livo, K.E., and Watson, K., 1996, Mapping surficial geology, vegetation communities, and environmental materials in our national parks: The USGS imaging spectroscopy integrated geology, ecosystems, and environmental mapping project: in Summaries of the 6th Annual JPL Airborne Earth Science Workshop, JPL Pub. 96-4, Vol. 1. AVIRIS Workshop, Jet Propulsion Laboratory, California Institute of Technology, Pasadena, Calif., p. 55-56.

Crowley, J. K., 1993 Mapping playa evaporite mineral with AVIRIS data: A first report from Death Valley, California: Remote Sensing of Environment, v. 44, nos. 2-3, p. 337 - 356.

Crowley, J. K., and Zimbelman, D. R., 1996, Mapping hydrothermally altered rock on Mount Rainier, Washington: Application of AVIRIS data to volcanic hazard assessments: in Summaries of the 6th Annual JPL Airborne Earth Science Workshop, JPL Pub. 96-4, Vol. 1. AVIRIS Workshop, Jet Propulsion Laboratory, California Institute of Technology, Pasadena, Calif., p.63-66.

Davis, C. O., Hamilton, M. Rhea, J. W. van den Bosch, J. Carder, K., and Steward, R., 1993, Spectral analysis of an AVIRIS image of San Pedro Channel: in Vane (ed), Imaging Spectrometry of the Terrestrial Environment: SPIE v. 1937, p. 64 - 76.

Dekker, A. G., Matlhus, T. J., Wijnen, M. M., and Seyham, E., 1992, The effect of spectral bandwidth and positioning on the spectral signature analysis of inland waters: Remote Sensing of Environment, v. 41, p. 211 – 225.

Dustan, P., 1985. The bio-optics of coral reefs. in: M.L. Reaks (ed.), The Ecology of Coral Reefs, NOAA Undersea Res. Pqm., Rockville, Md., NOAA, Symp. Ser. Undersea Res., v. 3, p. 1889-1917.

Dustan, P. 1977, Vitality of reef coral populations off Key Largo, Florida: Environmental Geology, v. 2, p. 51-58.

Dustan, P. and J.C. Halas. 1987. Changes in the reef-coral community of Carysfort Reef, Key Largo, Florida: 1974 to 1982. Coral Reefs, v. 6, p. 91-106.

Edmunds, P. J., 1991, Extent and effect of black band disease on a Caribbean reef: Coral Reefs, v. 10, p. 161 – 165.

Finkbeiner, M., Stevenson, B., and Seaman, R., 2001, Guidance for Benthic Habitat Mapping: An Aerial Photographic Approach, Technology Planning and Management Corporation, Charleston, SC. Available from: U.S. National Oceanic and Atmospheric Administration. Coastal Services Center. (NOAA/CSC/20117-PUB). Also on-line at http://www.csc.noaa.gov/crs/bhm/methods.html.

Gao B. and Goetz, A. F. H., 1990, Column atmospheric water vapor and vegetation liquid water retrievals from airborne imaging spectrometer data: Journal of Geophysical Research, v. 95, no. D4, p. 3549-3564.

Gao, B. C., M. J. Montes, Ahmad, Z., and C. O. Davis, 2000, Atmospheric correction algorithm for hyperspectral remote sensing of ocean color from space: Applied Optics, v. 39, no. 6, p. 887 – 896.

Goetz, A. F. H., Vane, G., Solomon, J. E., and Rock , B. N., 1985, Imaging spectrometry for earth remote sensing: Science, v. 228, p. 1147 - 1153.

Goodman, J. A., and S. L. Ustin, 2002, Hyperspectral image calibration in a coral reef environment: An empirical approach: In Proceedings IEEE International Geoscience and Remote Sensing Symposium (IGARSS'2002), 24 – 28 June 2002, Toronto, Canada, Published on CD ROM, ISBN: 0-7803-7537-8.

Goodman, J. A., M. Montes, and S. Ustin, 2003, Applying TAFKAA for atmospheric correction of AVIRIS over coral ecosystems in the Hawaiian islands: In proceedings 12th JPL Airborne Geoscience Workshop, 24 – 28 February 2003, Pasadena, CA, Jet Propulsion Laboratory Publication (in press).

Green, A. A., Berman, M., Switzer, B., and Craig, M. D., 1988, A transformation for ordering multispectral data in terms of image quality with implications for noise removal: IEEE Transactions on Geoscience and Remote Sensing, v. 26, no. 1, p. 65 - 74.

Green, R. O., Chrien, T. G., and Pavri, B., 2003, "On-orbit Determination of the Radiometric and Spectral Calibration of Hyperion Using Ground, Atmospheric and AVIRIS Underflight Measurements," IEEE TGARS Special Issue on EO-1 (in press).

Harsanyi, J. C., and Chang, C. I., 1994, Hyperspectral image classification and dimensionality reduction: An orthogonal subspace projection approach: IEEE Trans. Geosci. and Remote Sens., v. 32, p. 779-785.

Hochberg, E. J., and M.J. Atkinson, 2000, Spectral discrimination of coral reef benthic communities: Coral Reefs, v. 19, p. 164 – 171.

Holasek, R. F., Portigal, F. Even, D., Johnson, P, Segava, M., Susner, G., and Hill, C., 1998, Coral and substrate mapping in Kaneohe Bay, Oahu, Hawaii using the advanced airborne hyperspectral imaging system (AAHIS): In Proceedings of the Fifth International Conference on Remote Sensing for Marine and Coastal Environments, Orlando, FL, v.1, p. 177-186.

Holden, H., and LeDrew, E., 1998a, Spectral discrimination of healthy and non-healthy corals based on cluster analysis, principal components analysis, and derivative spectroscopy: Remote Sensing of Environment, v. 65, p. 217-224.

Holden, H., and LeDrew, E., 1998b, The scientific issues surrounding remote detection of submerged coral ecosystems: Progress in Physical Geography, v. 22, no. 2, p.190 – 221.

Holden, H., Kalbfleisch, W., Neman, C., and LeDrew, E., 1999, Hyperspectral identification of coral reef features: Proceedings of the Fourth International Airborne Remote Sensing Conference and Exhibition/ 21st Canadian Symposium on Remote Sensing, Ontario, Canada, p. I-129 – I-136.

Holden, H. and E. LeDrew, 1999, Hyperspectral identification of coral reef features: International Journal of Remote Sensing, v. 20, no. 13, p. 2545 – 2563.

Holden, H. and LeDrew, E., 2000, Accuracy assessment of hyperspectral classification of coral reef features based on first and second derivatives: Geocarto International, v. 15, no. 2, p 5-11.

Holden, H., and LeDrew, E., 2001, Effects of the water column on hyperspectral reflectance of submerged coral reef features: Bulletin of Marine Science, v. 69, no. 2, p. 685-699.

Holden, H., and LeDrew, E., 2002, Measuring and modeling water column effects on hyperspectral reflectance in a coral reef environment: Remote Sensing of Environment, v. 81, p. 300-308.

Hubbard, B. E. and Crowley, J. K., 2001, Alteration mineral mapping in the Central Andes using Hyperion, ALI and ASTER: Geological Society of America, Abstracts with Programs, v.33, no.6, p. A-319.

Joyce, Karen E., and Stuart R. Phinn, 2003, Hyperspectral analysis of chlorophyll content and photosynthetic capacity of coral reef substrates: Limnology and Oceanography, Special Issue: Light in Shallow Waters, v. 48, no 1 (Part 2), p. 489 –496.

Jupp, D.L.B., K. Mayo, D. Kuchler, S. Heggen, W. Kendall, B. Radke, and T. Ayling, 1985, Remote sensing for planning and managing the Great Barrier Reef of Australia: Photogrammetria, v. 40, p. 21-42.

Jupp, D.L.B., 1986, The application and potential of remote sensing in the Great Barrier Reef region. Great Barrier Reef Marine Park Authority Research Publication, Townsville, Australia, 56 p.

Kendall, M.S., M.E. Monacol, K.R. Buja, J.D. Christensen, C.R. Kruer, and M. Finkbeiner, R.A. Warner, 2001, (On-line). Methods Used to Map the Benthic Habitats of Puerto Rico and the U.S. Virgin Islands URL: http://biogeo.nos.noaa.gov/products/benthic. Also available on U.S. National Oceanic and Atmospheric Administration. National Ocean Service, National Centers for Coastal Ocean Science Biogeography Program. 2001. (CD-ROM). Benthic Habitats of Puerto Rico and the U.S. Virgin Islands. Silver Spring, MD: National Oceanic and Atmospheric Administration.

Kruse, F. A., 1988, Use of Airborne Imaging Spectrometer data to map minerals associated with hydrothermally altered rocks in the northern Grapevine Mountains, Nevada and California: Remote Sensing of Environment, V. 24, No. 1, p. 31-51.

Kruse, F. A., and Lefkoff, A. B., 1993, Knowledge-based geologic mapping with imaging spectrometers: Remote Sensing Reviews, Special Issue on NASA Innovative Research Program (IRP) results, v. 8, p. 3 - 28.

Kruse, F. A., Lefkoff, A. B., and Dietz, J. B., 1993a, Expert System-Based Mineral Mapping in northern Death Valley, California/Nevada using the Airborne Visible/Infrared Imaging Spectrometer (AVIRIS): Remote Sensing of Environment, Special issue on AVIRIS, May-June 1993, v. 44, p. 309 - 336.

Kruse, F. A., Lefkoff, A. B., Boardman, J. B., Heidebrecht, K. B., Shapiro, A. T., Barloon, P. J., and Goetz, A. F. H., 1993b, The Spectral Image Processing System (SIPS) - Interactive Visualization and Analysis of Imaging Spectrometer Data: Remote Sensing of Environment, Special issue on AVIRIS, May-June 1993, v. 44, p. 145 - 163.

Kruse, F. A., Huntington, J. H., and Green, R. O, 1996, Results from the 1995 AVIRIS Geology Group Shoot: in Proceedings, 2nd International Airborne Remote Sensing Conference and Exhibition: Environmental Research Institute of Michigan (ERIM), Ann Arbor, v. I, p. I-211 - I-220.

Kruse, F. A., Richardson, L.L., and Ambrosia, V. G., 1997, Techniques developed for geologic analysis of hyperspectral data applied to near-shore hyperspectral ocean data: In Proceedings, ERIM 4th International Conference, Remote Sensing for Marine and Coastal Environments: Environmental Research Institute of Michigan (ERIM), Ann Arbor, v. I, p. I-233 - I-246.

Kruse, F. A., Boardman, J. W., and Huntington, J. F., 1999, Fifteen Years of Hyperspectral Data: northern Grapevine Mountains, Nevada: in Proceedings of the 8th JPL Airborne Earth Science Workshop: Jet Propulsion Laboratory Publication, JPL Publication 99-17, p. 247 - 258.

Kruse, F. A., Boardman, J. W., and Huntington, J. F., 2001, Progress Report: Geologic Validation of EO-1 Hyperion: in Proceedings of the 10th JPL Airborne Earth Science Workshop: Jet Propulsion Laboratory Publication 02-1, p. 253 – 265.

Kruse, F. A., Boardman, J. W., and Huntington, J. F., 2002, "Comparison of EO-1 Hyperion and Airborne Hyperspectral Remote Sensing Data for Geologic Applications," in Proceedings, SPIE Aerospace Conference, 9-16 March 2002, *Big Sky, Montana*, published on CD-ROM, IEEE Catalog Number 02TH8593C, Paper #6.0102, 12 p.

Kruse, F. A., Boardman, J. W., Huntington, J. F., Mason, P., and Quigley, M.A., 2003, Evaluation and Validation of EO-1 Hyperion for Geologic Mapping: in Special Issue, TGARSS, IEEE (in press)

Kuchler, D.A., R.T. Biña, and D. van R. Claasen, 1988, Status of high-technology remote sensing for mapping and monitoring coral reef environments, Proc. 6th Int. Coral Reef Symp., Australia, v. 1, p. 97-101.

Kuta, K. G., and Richardson, L. L., 1996, Abundance and distribution of black band disease on coral reefs in the northern Florida Keys: Coral Reefs, v. 15, p. 219 – 223.

Kutser, T., Dekker, A. G., and Skirving, W., 2003, Modeling spectral discrimination of Great Barrier Reef benthic communities by remote sensing instruments: Limnology and Oceanography, Special Issue: Light in Shallow Waters, v. 48, no 1 (Part 2), p. 497 – 510.

Lang, H. R., Adams, S. L., Conel, J. E., McGuffie, B. A., Paylor, E. D., and Walker, R. E., 1987, Multispectral remote sensing as stratigraphic tool, Wind River Basin and Big Horn Basin areas, Wyoming: American Association of Petroleum Geologists Bulletin, v. 71, no. 4, p. 389-402.

Lyzenga, D. 1978. Passive remote sensing techniques for mapping water depth and bottom features. Applied Optics. V. 17, no. 3, p. 379-383.
Lyzenga, D. 1981. Remote sensing of bottom reflectance and water attenuation parameters in shallow water using aircraft and Landsat data. International Journal of Remote Sensing. V. 2, no. 1, p.71-82.
Maritorena, S., A. Morel, and B. Gentili. 1994. Diffuse reflectance of oceanic shallow waters: Influence of water depth and bottom albedo. Limnology and Oceanography, v. 39, p. 1689-1703.
Matthew, M. W., S. M. Adler-Golden, A. Berk, S. C. Richtsmeier, R. Y. Levine, L. S. Bernstein, P. K. Acharya, G. P. Anderson, G. W. Felde, M. P. Hoke, A. Ratkowski, H.-H. Burke, R. D. Kaiser and D. P. Miller, 2000, Status of atmospheric correction using a MODTRAN4-based algorithm: in SPIE Proceeding, Algorithms for Multispectral, Hyperspectral, and Ultraspectral Imagery VI, v. 4049.
Mazer, A. S.,Martin, M., Lee, M., and Solomon, J. E., 1988, Image processing software for imaging spectrometry data analysis: Remote Sensing of Environment, v. 24, no. 1, p. 201-210.
Mobley, C. D., B. Gentili, H. R. Gordon, Z. Jin, G. W. Katawar, A. Morel, P. Reinersman, K. Stamnes, and R. H. Stavn, 1993, Comparison of Numerical Models for Computing Underwater Light Fields: Applied Optics, v. 36, p. 7484 – 7504.
Mobley, Curtis D., Hao Zhang, and Kenneth J. Voss, 2003, Effects of optically shallow bottoms on upwelling radiances: Bidirectional reflectance distribution function effects: Limnology and Oceanography, Special Issue: Light in Shallow Waters, v. 48, no 1 (Part 2), p. 337 – 335.
Mumby, P.J., E.P Green, C.D. Clark, A.J. Edwards. 1998a. Digital analysis of multispectral airborne imagery of coral reefs. Coral Reefs, v. 17, p. 59-69.
Mumby P. J., C. Clark, E. Green, And A. Edwards, 1998b, Benefits of water column correction and contextual editing for mapping coral reefs: International Journal of Remote Sensing, v. 19, no. 1, p. 203-210.
Myers, M., J. Hardy, C. Mazel, and P. Dustan, 1999, Optical Spectra and pigmentation of Caribbean reef corals and macroalgae. Coral Reefs, v. 18, no. 2, p. 179-186.
Pearlman, J, Stephen Carman, Paul Lee, Lushalan Liao and Carol Segal, 1999, Hyperion Imaging Spectrometer on the New Millennium Program Earth Orbiter-1 System: In Proceedings, International Symposium on Spectral Sensing Research (ISSSR), Systems and Sensors for the New Millennium, published on CD-ROM, International Society for Photogrammetry and Remote Sensing (ISPRS).
Porter, J. W., and Meier, O. W., 1992, Quantification of loss and change in Floridian reef coral populations: American Zool, v. 23, p. 625 – 640.
Pratt, P., Carder, K. L., and Costello, D. K., 1997, Remote sensing reflectance algorithms developed to correct underwater coral imagery for the effects of optical thickness to assist in benthic classification: In proceedings, ERIM 4th International Conference, Remote Sensing for Marine and Coastal Environments: Environmental Research Institute of Michigan (ERIM), Ann Arbor, v. II, p. II-449.
Research Systems Inc (RSI), 2001, ENVI User's Guide, Research Systems Inc, 948 p.
Richardson, L. L., and Kruse, F. A., 2000, Use of AVIRIS Spectral Data to Discriminate Mixed Phytoplankton Communities, Seagrass Beds, and Benthic Algal Mats: in Proceedings of the 9th JPL Airborne Earth Science Workshop: Jet Propulsion Laboratory Publication.
Richtsmeier, S.C., A. Berk, L.S. Bernstein, and S.M. Adler-Golden, 2001, A 3-Dimensional Radiative-Transfer Hyperspectral Image Simulator For Algorithm Validation: in Proceedings of the International Symposium on Spectral Sensing Research, p. 537-545.
Wrucke, C. T., Werschkey, R. S., Raines, G. L., Blakely, R. J., Hoover, D. B, and Miller, M. S., 1984, "Mineral resources and mineral resource potential of the Little Sand Spring Wilderness Study Area, Inyo County, California," U. S. Geological Survey Open File Report 84-557, 20 p.
Stocker, A. D., Reed, I. S., and Yu, X., 1990, Multidimensional signal processing for electrooptical target detection, Proc, SPIE Int. Soc. Opt. Eng., v. 1305.
Ungar, S. G., 2003, Overview of the Hyperion Mission: in Proceedings of the 12th JPL Airborne Earth Science Workshop, 24-28 February 2003, Pasadena, CA: Jet Propulsion Laboratory Publication (in press).
Young, L. R., K.L. Carder, R. G. Stewart, and F. R. Chen, 1995, Comparison of measured and modeled bottom reflectance spectra on the southeastern shelf of the Florida Keys: in Proceedings SPIE, v 2480 (Imaging Spectrometry), p. 237 – 247.
Yu, X., Reed, I. S., and Stocker, A. D., 1993, Comparative performance analysis of adaptive multispectral detectors, IEEE Trans. on Signal Processing, v. 41, no. 8.

HYPERION STUDIES OF CROP STRESS IN MEXICO

David B. Lobell[1,2] and Gregory P. Asner[1,2]

1.0 INTRODUCTION

Satellite-based measurements of crop stress could provide much needed information for cropland management, especially in developing countries where other precision agriculture technologies are too expensive (Pierce and Nowak 1999; Robert 2002). For example, detection of areas that are nitrogen deficient or water stressed could guide fertilizer and water management decisions for all farmers within the swath of the satellite. Several approaches have been proposed to quantify canopy nutrient or water content based on spectral reflectance, most of which involve combinations of reflectance in the form of vegetation indices. While these indices are designed to maximize sensitivity to leaf chemistry, variations in other aspects of plant canopies may significantly impact remotely sensed reflectance. These confounding factors include variations in canopy structural properties (e.g., leaf area index, leaf angle distribution) as well as the extent of canopy cover, which determines the amount of exposed bare soil within a single pixel. In order to assess the utility of spectral indices for monitoring crop stress, it is therefore not only necessary to establish relationships at the leaf level, but also to test the relative importance of variations in other canopy attributes at the spatial scale of the remote sensing measurement. In this context, the relative importance of a given attribute will depend on (1) the sensitivity of the reflectance index to variation in the attribute and (2) the degree to which the attribute varies spatially and temporally.

In this study, we investigate the ability of spectral indices derived from data collected by the EO-1 Hyperion instrument to detect canopy stress in an agricultural region in Northwest Mexico. In particular, the objectives of this study were to: (1) determine the correlation between reflectance indices of canopy "structure" and "chemistry" within an agricultural landscape, and (2) quantify the extent to which information in chemical indices provide useful information for crop management. In essence, this equates to asking whether hyperspectral chemical reflectance indices provide any unique information on crop canopies, and, if so, whether this information is potentially useful for precision agriculture applications.

2.0 DATA AND METHODS

2.1 Site Description

The study was conducted in the Yaqui Valley, a region comprising roughly 225,000 ha of intensively fertilized and irrigated cropland on the west coast of Sonora, Mexico (Figure 1, after the references). A vast majority of this land is planted to wheat in November-December and harvested in April-May, with wheat yields among the highest in the world. Rising fertilizer prices, concerns about environmental pollution, and diminishing water supplies has increased the need for methods to improve nutrient and water use efficiencies of wheat production in this region. A particularly important time in the growing season is mid-January, when the first post-planting irrigation and fertilization is performed. At this time, detection of canopy nutrient or water stress could guide the timing and amount of water and fertilizer applications.

2.2 Data acquisition and processing

Hyperion data was acquired on January 14, 2002, one minute after an image was collected by the Landsat ETM+ sensor. The Hyperion image was roughly centered within the ETM+ image and covered a significant fraction of the irrigation district (see Figure 1). An additional ETM+ image acquired on March 16, 2002 was combined with the January image to estimate wheat yields using a previously validated methodology (Lobell, Asner et al. 2003). These yields were used to evaluate the eventual growth of fields observed by Hyperion in January, as described below.

Hyperion data were provided by the EROS Data Center (EDC) and processed to apparent surface reflectance using the ACORN 3 atmospheric correction model. A de-striping algorithm was then applied to correct for mis-calibration between cross track detectors. This algorithm determines the average noise in each column by summing all reflectance values by column and applying a Lee filter to the resulting 256 values. The column sums are divided by the filtered reflectance values to approximate the necessary gains for each column, which are then applied to the image. After this step, a cubic spline is fit to the water bands at 940 and 1140 nm in each pixel to reduce the effects of mis-calibration and modeling errors introduced by the atmospheric correction.

[1] Department of Global Ecology, Carnegie Institution of Washington, Stanford, California 94305
[2] Department of Geological and Environmental Science, Stanford University, Stanford, California 94305
(dlobell@globalecology.stanford.edu, gasner@globalecology.stanford.edu)

2.3 Reflectance Indices

Several indices drawn from the literature and shown in Table 1 were computed from the Hyperion data. The first two indices (NDVI and SR) are based on combinations of red and near infrared (NIR) reflectance that are known to capture variations in canopy structural attributes, such as canopy cover and leaf area index (LAI). The rest of the indices were designed to measure aspects of leaf chemistry, including contents of leaf pigments such as chlorophylls, carotenoids, and anthocyanin (PRI, SIPI, PSRI, R-Gratio); nitrogen (NDNI); and water (WI, NDWI, MSI, NDII). Many of these indices were defined by leaf-level studies and have not been widely tested at the canopy or landscape scales.

To determine the extent to which these indices provide unique information from each other in this agricultural landscape, Spearman's rank correlation coefficient (ρ_S) was computed for each combination of indices using all image pixels (n = 224,042). This non-parametric correlation was used to capture non-linear relationships between indices and to minimize sensitivity to extreme values. Two indices (PRI and WI) were judged to be too noisy using the Hyperion data and were therefore excluded from further analysis.

Table 1. Vegetation Indices Employed in this Study

Index	Index Name	Equation	Reference
SR	Simple Ratio	R800/R680	
NDVI	Normalized Difference Vegetation Index	(R800-R680)/(R800+R680)	
RG-Ratio	Red-Green Ratio	Σ(R600...R699)/ Σ(R500...R599)	Gamon and Surfus (1999)
SG	Sum-Green	ΣR500...R599)	
PRI	Photochemical Reflectance Index	(R531-R570)/(R531+R570)	Gamon et al. (1992)
PSRI	Plant Senescence Reflectance Index	(R680-R500)/R750	Merzlyak et al. (1999)
SIPI	Structure Insensitive Pigment Index	(R800-R445)/(R800-R680)	Peñuelas et al. (1995)
NDNI	Normalized Difference Nitrogen Index	[log(1/ R1510)-log(1/ R1680)]/ [log(1/ R1510)+log(1/ R1680)]	Serrano et al. (2002)
WI	Water band Index	R900/R970	Peñuelas et al. (1993)
NDWI	Normalized Difference Water Index	(R857-R1241)/(R857+R1241)	Gao (1996)
MSI	Moisture Stress Index	R1599/R819	Hunt and Rock (1989)
NDII	Normalized Difference Infrared Index	(R819-R1649)/(R819+R1649)	Hardinsky et al. (1983)

2.4 Quantile Mapping

There are several approaches to evaluating the utility of information in the chemical indices. One possibility is to define a suite of leaf chemistry variables of interest, measure these properties in various fields simultaneous to image acquisition, and then statistically test the ability of each index to predict each variable. In this study, we use an alternative approach that utilizes image data taken at a later point in the growing season. We refer to this procedure as quantile mapping (QM), which is illustrated in Figure 2 and can be described as follows:

1) To control for variations in canopy structure, which are shown to affect all indices (see below), we identify all pixels within a narrow range of NDVI values.
2) For these pixels, we compute the distribution of values for a selected index (e.g. RG-ratio), and identify all pixels falling below and above defined thresholds. In this case, we select pixels below the 25-percentile (group A) and above the 75-percentile (group B).

3) An image collected later in the season is used to define the eventual growth of each pixel. In this study, we used the yield estimates derived from Landsat ETM+, which rely on an image from March 16 (two months after the Hyperion image). By comparing the eventual yields of pixels in group A and group B, which possessed the same structural attributes (NDVI), we can evaluate whether the additional information in the selected index was predictive of canopy growth, and therefore indicative of canopy stress.
4) Steps (1)-(3) are repeated for each level of NDVI.

This procedure is called quantile mapping because pixels above and/or below a specified quantile are mapped and tracked through the growing season. To determine the sensitivity of this approach to sampling uncertainties, step (3) is repeated a large number of times (10,000), each time with random subsets of group A and B used in place of the entire groups. This provides a bootstrap estimate of sampling uncertainty (Efron and Gong 1983).

We see several advantages to this approach. First, it requires only image data and therefore can be used to test indices in any region where ground data is not available. Similarly, it can be used for retrospective studies of images acquired in previous years. Second, because it is based solely on image statistics, the entire process can be automated. For example, steps (1)-(2) effectively create maps of nutrient stress that can be quickly generated and potentially used for management applications. This is particularly important for agricultural applications, where quick turnaround times are essential. Third, the comparison of groups A and B is performed at various levels of NDVI, so that the effect of canopy structure on the information content of the selected index can be readily evaluated. For example, some aspects of leaf chemistry may only be retrievable at very high LAI (Asner 1998).

One drawback of this approach is that, because it relies on image statistics, it is only able to determine relative levels of stress within an image. For example, in cases where 50% of fields are stressed in reality, a procedure that selects only the top 25% will miss many fields. Alternatively, if only 5% of fields are stressed, then 20% will be falsely identified as stressed. However, by combining image statistics across several years, it should be possible to associate an absolute value with each quantile and therefore produce more robust measures of crop stress.

3.0 RESULTS AND DISCUSSION

Table 2 shows the correlation matrix for indices evaluated in this study. Given the high correlation of all indices with NDVI ($\rho_S > 0.9$, $p < 0.001$), it is clear that each index is highly impacted by variations in canopy cover and structure across the landscape. This is true even for indices designed to be "structure insensitive." Therefore, no single index should be considered as a measure of solely canopy chemistry. In general, high correlations between all indices indicated that no two indices provided independent measures of plant canopies. However, the fact that all correlations were less than unity implies that there is some information (or potentially noise) unique to each index.

Figure 3 illustrates the result of the QM procedure for several of the indices. Some indices appear to provide little information beyond NDVI, implying that the only differences between the two indices are due to sensor noise or some attribute that does not measurably affect plant growth. However, several indices exhibit the ability to predict future canopy growth, implying that they provide a useful measure of canopy stress.

The QM results clearly show that some indices, such as NDWI, provide information only at high values of NDVI. This is consistent with previous studies that showed the relationship between NDWI and canopy water content improved greatly when limiting the study to pixels with high canopy cover (Serrano, Ustin et al. 2000). Other indices, such as RG-ratio, appear to provide useful information on canopy chemistry across a wide range of canopy structure.

The difference between the upper and lower quartile provides a quantitative estimate, in terms of yield, of the potential value of using a given index for crop management. For example, if fields below the lower quartile of RG-ratio could be managed and raised to the level of the upper quartile, then a potential gain of roughly 0.5 ton ha^{-1} could be realized. Yield gains of this magnitude would represent a significant increase in farmer income and regional productivity.

Table 2. Spearman's Rank Correlation Coefficients for Vegetation Indices in Jan. 14, 2002 Hyperion Image.

	NDVI	SumGreen	SIPI	PSRI	NDNI	RG-Ratio	NDWI	MSI	NDII
SR	1	-0.85	-0.99	-0.99	-0.93	-0.98	0.9	-0.96	0.95
NDVI		-0.85	-0.99	-0.99	-0.93	-0.97	0.89	-0.96	0.95
SumGreen			0.83	0.85	0.79	0.85	-0.74	0.77	-0.77
SIPI				0.98	0.93	0.98	-0.89	0.95	-0.94
PSRI					0.93	0.99	-0.88	0.95	-0.94
NDNI						0.92	-0.83	0.91	-0.91
RG-Ratio							-0.87	0.92	-0.91
NDWI								-0.94	0.94
MSI									-0.99

4.0 SUMMARY

Reflectance indices derived from Hyperion data were highly correlated across an agricultural landscape, indicating that all indices were impacted by variations in canopy structure and bare soil extent. A procedure termed quantile mapping was developed to combine structural and chemical reflectance indices in an attempt to identify attributes of canopy chemistry associated with stress. Some chemical indices were successful in identifying stress, as judged by the ability to predict future growth estimated from late-season Landsat ETM+ imagery, while others were not. Of those successful in predicting future growth, R-G ratio was successful at various levels of NDVI (canopy structure and extent) while NDWI was useful only at high values of NDVI. Moreover, these indices depicted stress in different fields (not shown here), indicating that each index provides information on a unique aspect of canopy chemistry. Future work is needed to better quantify canopy stress from hyperspectral measurements, with careful attention to sources of reflectance variability other than canopy chemistry.

5.0 REFERENCES

Asner, G. P. (1998). "Biophysical and biochemical sources of variability in canopy reflectance." *Remote Sensing of Environment* **64**: 134-153.

Efron, B. and G. Gong (1983). "A Leisurely Look at the Bootstrap; the Jackknife; and Cross-Validation." *American Statistician* **37**(1): 36-48.

Gamon, J. and J. Surfus (1999). "Assessing leaf pigment content and activity with a reflectometer." *New Phytologist* **143**(1): 105-117.

Gamon, J., J. Peñuelas, and Field, C. (1992). "A narrow-waveband spectral index that tracks diurnal changes in photosynthetic efficiency." *Remote Sensing of Environment* **41**(1): 35-44.

Gao, B. C. (1996). "NDWI - A normalized difference water index for remote sensing of vegetation liquid water from space." *Remote Sensing of Environment* **58**(3): 257-266.

Hardinsky, M. A., V. Lemas, et al. (1983). "The influence of soil salinity, growth form, and leaf moisture on the spectral reflectance of Spartina alternifolia canopies." *Photogrammetric Engineering and Remote Sensing* **49**: 77-83.

Hunt, E. and B. Rock (1989). "Detection of changes in leaf water-content using near-infrared and middle-infrared reflectances." *Remote Sensing of Environment* **30**(1): 43-54.

Lobell, D. B., G. P. Asner, et al. (2003). "Remote sensing of regional crop production in the Yaqui Valley, Mexico: estimates and uncertainties." *Agriculture, Ecosystems, and Environment* **94**: 205-220.

Merzlyak, M., A. Gitelson, et al. (1999). "Non-destructive optical detection of pigment changes during leaf senescence and fruit ripening." *Physiologia Plantarum* **106**(1): 135-141.

Peñuelas, J., I. Filella, et al. (1993). "The Reflectance at the 950-970 Nm Region as an Indicator of Plant Water Status." *International Journal of Remote Sensing* **14**(10): 1887-1905.
Peñuelas, J., I. Filella, et al. (1995). "Assessment of Photosynthetic Radiation-Use Efficiency with Spectral Reflectance." *New Phytologist* **131**(3): 291-296.
Pierce, F. J. and P. Nowak (1999). "Aspects of precision agriculture." *Advances in Agronomy*, **67:** 1-85.
Robert, P. C. (2002). "Precision agriculture: A challenge for crop nutrition management." *Plant and Soil* **247**: 143-149.
Serrano, L., S. L. Ustin, et al. (2000). "Deriving water content of chaparral vegetation from AVIRIS data." *Remote Sensing of Environment* **74**(3): 570-581.

6.0 ACKNOWLEDGEMENTS

The authors are grateful to A. Warner, K. Heidebrecht, and I. Ortiz-Monasterio for assistance with data processing and helpful discussions. This work was supported by NSF Graduate Research Fellowship, NASA New Investigator Program grant NAG5-8709, NASA New Millenium Program grants NCC5-480 and NCC5-481, and the Packard Foundation.

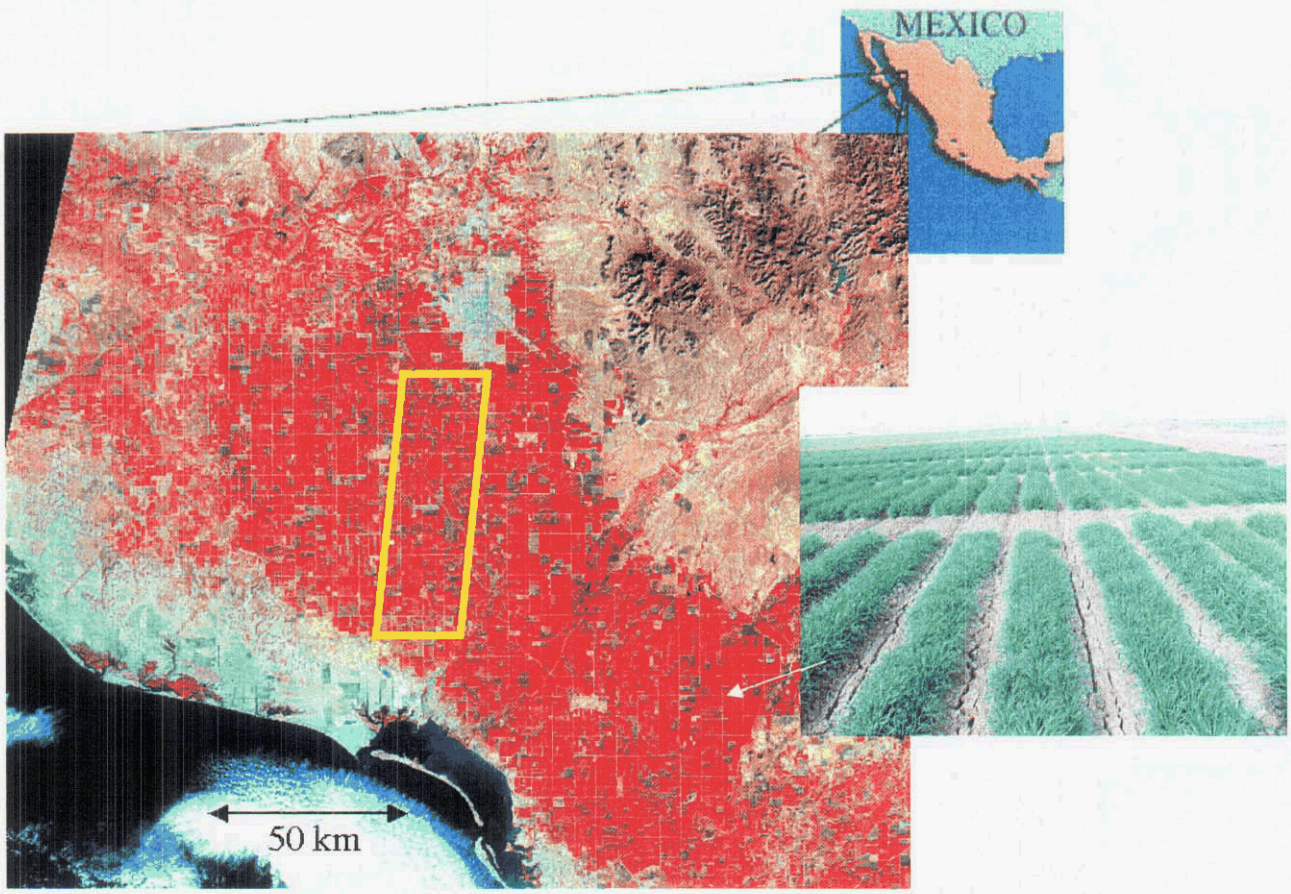

Figure 1. The Yaqui Valley study region. The satellite image is a color composite of Landsat ETM+ data (4-3-2) from January 14, 2002. The yellow box shows the swath of the Hyperion image used in this study, while the picture inset shows a typical wheat field at this time of year.

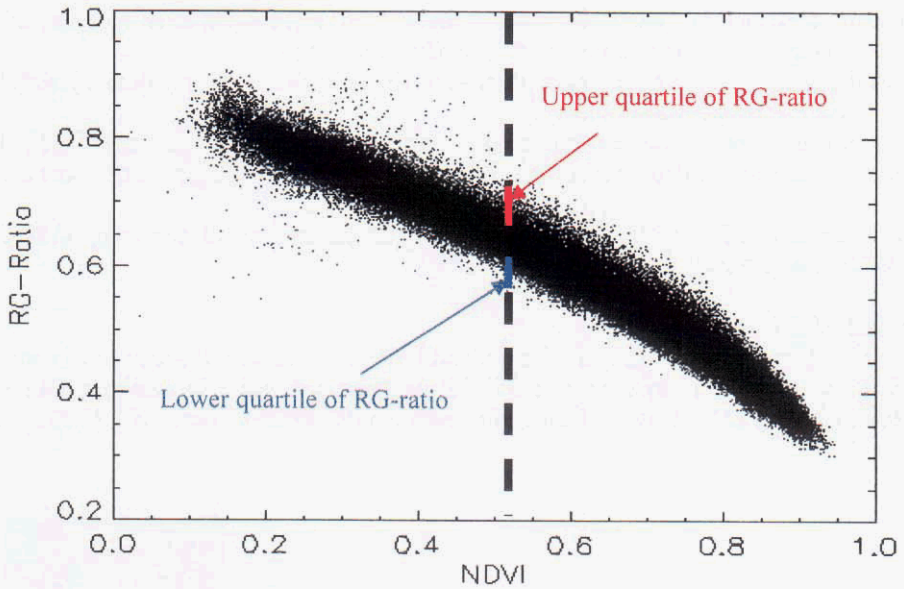

Figure 2. Schematic representation of the quantile mapping algorithm. At each value of NDVI, all pixels below and above prescribed quantiles of a selected reflectance index are identified and separated into two sets (high and low). The average states of these two sets later in the growing season, in this case as measured by Landsat-based yield estimates, are then compared to determine the ability of the given index to predict future growth, and thereby indicate stress.

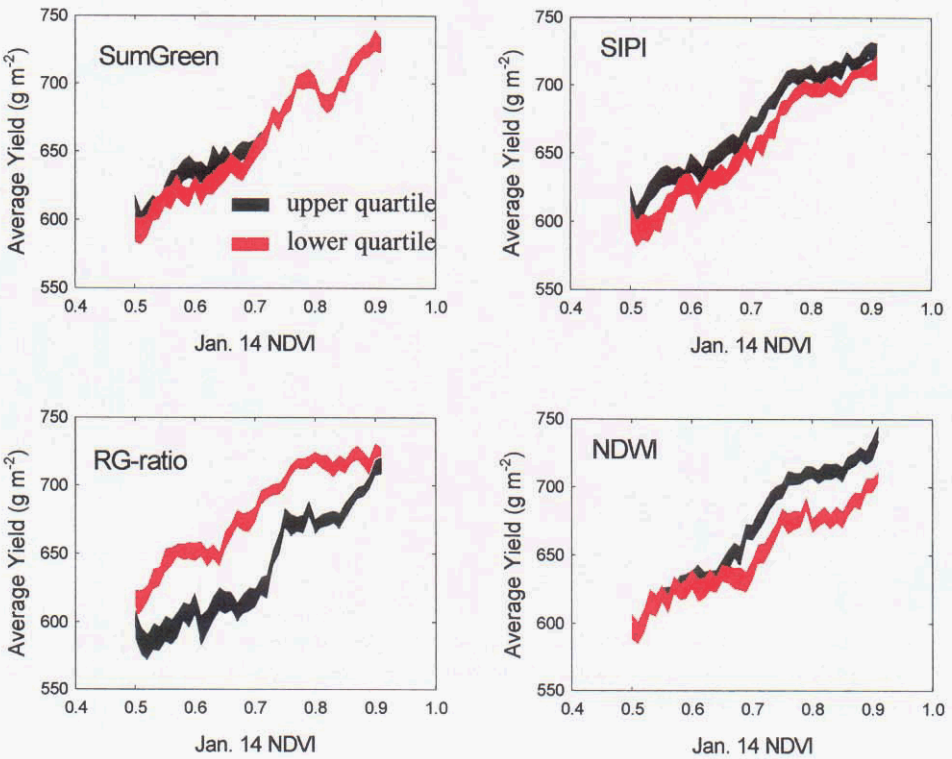

Figure 3. Average yield estimates for pixels in lower (red) and upper (black) quartiles of selected indices at each value of NDVI in Jan. 14 Hyperion image. Average yield is based on January and March Landsat images, and indicates the eventual growth of wheat. Width of line is a 95% confidence interval based on bootstrap estimates of uncertainty in average yield. Several indices appeared to offer little additional information beyond NDVI for predicting future growth (e.g. SumGreen and SIPI), while others were much more successful (RG-ratio and NDWI), with yield differences between the upper and lower quartile as high as 0.5 ton ha^{-1}.

MEASURING TRACE GASES IN PLUMES FROM HYPERSPECTRAL REMOTELY SENSED DATA

Rodolphe Marion,[1,2] Rémi Michel,[1] and Christian Faye[2]

1. INTRODUCTION

Characterizing surface and atmospheric properties from hyperspectral imaging spectrometry is of major importance in earth sciences. It has been successfully applied to geological, aquatic, ecological and atmospheric research (Curran, 1994) (Goetz, 1992).

Hyperspectral sensors (e.g., AVIRIS, HyMap, Hyperion) are passive earth-looking systems providing radiance images in the solar reflected portion of the electromagnetic radiation spectrum. Generally, they cover a spectral range included in the 400–2500 nm window with a few hundred contiguous bands about 10 nm wide. The nominal pixel size is about 20 m. Typical signal to noise ratios (SNR) are a few hundred. As an example, the AVIRIS spectral range is 400–2500 nm, the number of bands is 224, the spectral bands are about 10 nm wide, the spatial resolution is about 20 m, and the SNR is between 300 and 800 for the year 1995. The images depend on sun irradiance, atmospheric conditions, ground conditions, and on the system's transfer function in a complex way (scattering, absorption, reflection, averaging), leading to a strongly non-linear pixel equation (3). Fig. 1 shows a diagram of the hyperspectral observational geometry.

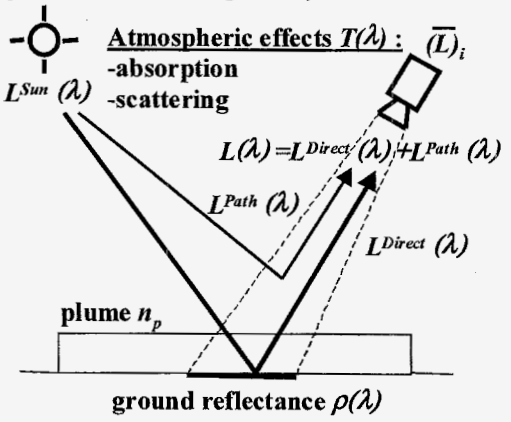

Figure 1. Hyperspectral data collection. Sun emitted electromagnetic wave $L^{Sun}(\lambda)$ interacts with atmospheric molecules and particles through absorption and scattering processes ($T(\lambda)$). At-sensor radiance $L(\lambda)$ is the sum of ground reflected radiance $L^{Direct}(\lambda)$ and backscattered atmospheric radiance $L^{Path}(\lambda)$. Radiance is band-averaged by the instrument, yielding measured signal $(\overline{L})_i$ for spectral channel i. This signal includes spectral features of effluent plume n_p.

One of the major issues of hyperspectral data processing is the joint retrieval of atmospheric gas concentrations and ground reflectance. It is essential not only for studying atmospheric properties but also for ground based applications requiring accurate atmospheric correction (Curran, 1994) (Goetz, 1992). Several techniques have already been proposed to measure the amount of a particular gas of interest (e.g., H_2O, CO_2, O_2, O_3) including : narrow/wide ratio, N/W (Frouin et al., 1990a) (Frouin et al., 1990b), continuum interpolated band ratio, CIBR (Green et al., 1989) (Bruegge et al., 1990) (Kaufman et al., 1992), atmospheric precorrected differential absorption technique, APDA (Borel et al., 1996) (Schläpfer et al., 1996a) (Schläpfer et al., 1998), linear regression ratio, LIRR (a variation of the CIBR introduced by Schläpfer et al., 1996b), and curve-fitting procedures (Gao et al., 1990). These methods typically yield the total water vapor content with an accuracy of about 7% rms from AVIRIS data. Accuracy may decline to more than several tens of a percent when the ground reflectance varies non-linearly with wavelength within gas absorption bands (Borel et al., 1996) (Schläpfer et al., 1998), or when other species than water are considered (Schläpfer et al., 1996b) (Green et al., 1996b) (De Jong et al., 1996). A more accurate estimation of gas amounts is generally required to investigate a wider range of phenomena including forest fires, volcanoes, and industrial pollution.

Hereafter, we first present those principles of imaging spectrometry useful for yielding the equation of the image. We then discuss the potential and the limitations of the existing methods, especially when the unknown surface reflectance varies non-linearly with wavelength within gas absorption bands. Afterwards, we propose an

[1] CEA-DIF-DASE-LDG-TSE, BP 12, 91680 Bruyères-le-Châtel Cedex, France (rodolphe.marion@cea.fr)
[2] ENSEA-ETIS, 6 avenue du Ponceau, 95014 Cergy-Pontoise Cedex, France

enhanced method, named Joint Reflectance and Gas Estimator, JRGE. It is dedicated to the measurement of trace gases within a plume corresponding to variations relative to a given standard atmosphere model. This method is based on a cubic smoothing spline-like surface reflectance estimator and non-linear radiative transfer calculations. Finally, JRGE is applied to simulated data as preliminary results. An aerosol-free atmosphere (Rayleigh atmosphere) and standard ground temperatures are assumed.

2. IMAGING SPECTROMETRY

From the viewing geometry schematically shown in Fig. 1, the monochromatic radiance at the input of a downward looking sensor can be written in a simplified form as (Esaias, 1986)

$$L(\lambda) = \rho(\lambda)L^{Sun}(\lambda)T(\lambda) + L^{Path}(\lambda) \tag{1}$$

where λ is the wavelength, $L(\lambda)$ is the radiance at the imaging spectrometer, $\rho(\lambda)$ is the surface reflectance, $L^{Sun}(\lambda)$ is the solar radiance above the atmosphere; $T(\lambda)$ is the total atmospheric transmittance, equal to the product of the atmospheric transmittance from the sun to the earth's surface and from the earth's surface to the sensor, according to the Beer-Bouguer-Lambert law (Liou, 1980); and $L^{Path}(\lambda)$ is the path-scattered radiance (i.e., the backscattered atmospheric radiance not reflected by the ground).

In the presence of a plume located just above the ground (typically in the first kilometer of the atmosphere) containing P gaseous species in addition to the standard atmospheric state, the at-sensor radiance becomes

$$L(\lambda, n_1, ..., n_P) = \rho(\lambda)L^{Sun}(\lambda)T(\lambda)\exp\left(-\eta\sum_{p=1}^{P} k_p(\lambda)n_p\right) + L^{Path}(\lambda, n_1, ..., n_P) \tag{2}$$

where $n_p, p = 1,...,P$, is the integrated density over the plume height of the pth species, η is a known geometrical parameter depending on the viewing angles (i.e., sun and sensor locations), $k_p(\lambda)$ is the known absorption coefficient (altitude-dependant) of the pth species, and $\exp\left(-\eta\sum_{p=1}^{P} k_p(\lambda)n_p\right)$ is the total plume transmittance. The path-scattered radiance L^{Path} is also a function of the unknown gas densities. The total atmospheric content in the pth species can be written $N_p = N_{0p} + n_p$ where N_{0p} represents the standard atmospheric density and n_p is the unknown excess due to the plume.

A hyperspectral sensor performs a band-averaging $(\overline{L})_i$ of the incoming radiance field $L(\lambda)$ at each channel i ($i = 1,...,N$, N is the total number of channels of the imaging system). This measure, corrupted by the additive noise b_i is then equal to

$$\begin{aligned} \left(\overline{L(n_1,...,n_P)}\right)_i &= \int_0^{\infty} L(\lambda, n_1, ..., n_P)H_i(\lambda)d\lambda + b_i \\ &= \left(\overline{\rho L^{Sun} T \exp\left(-\eta\sum_{p=1}^{P} k_p n_p\right)}\right)_i + \left(\overline{L^{Path}(n_1,...,n_P)}\right)_i + b_i \end{aligned} \tag{3}$$

where H_i is the normalized instrument's transfer function for channel i. The spectral atmospheric features are typically tenths narrower than the instrument channel width (e.g., H_2O absorption bands near 1 μm are about 10^{-3} nm wide and AVIRIS spectral channel width is about 10 nm). It is thus noteworthy that the multiplicative operator of monochromatic atmospheric terms in equation (3) does not commute with the instrument averaging operator.

According to the properties of surface reflectance spectra (see section 4.1) and by defining $A_0(\lambda) = L^{Sun}(\lambda)T(\lambda)$, the measured radiance of a pixel for channel i can be written

$$\left(\overline{L(n_1,...,n_P)}\right)_i = \rho_i\left(\overline{A_0\exp\left(-\eta\sum_{p=1}^{P} k_p n_p\right)}\right)_i + \left(\overline{L^{Path}(n_1,...,n_P)}\right)_i + b_i \tag{4}$$

where ρ_i is the mean ground reflectance over the channel i. Theoretically, L^{Path} depends on n_p, drastically increasing the complexity of the model. In our approach, we determine an excess of gases due to the plume and not the total atmospheric content so that L^{Path} can be considered independent of n_p. The measured radiance of a pixel for channel i can thus be written as

$$\left(\overline{L(n_1,...,n_P)}\right)_i = \rho_i \left(\overline{A_0 \exp\left(-\eta \sum_{p=1}^{P} k_p n_p \right)} \right)_i + \left(\overline{L^{Path}}\right)_i + b_i . \quad (5)$$

Hereafter, we propose a method to estimate the $n_p, p = 1,...,P$, from equation (5) for which the $\rho_i, i = 1,...,N$, are unknown, η and $k_p, p = 1,...,P$, are known, A_0 and L^{Path} are computed from a standard atmosphere model, and a noise model is available (see section 4.1).

3. POTENTIAL AND LIMITS OF CONVENTIONAL METHODS

Existing methods have extensively been applied to hyperspectral data, especially AVIRIS images, to retrieve the water vapor column (Green et al., 1989) and, with less accuracy, the ozone (Schläpfer et al., 1996b), oxygen (Green et al., 1996b), and carbon dioxide (De Jong et al., 1996) columns. For a comparison between these methods see e.g., (Carrère et al., 1993 for N/W and CIBR) and (Schläpfer et al., 1998 for CIBR and APDA). Ratioing and curve-fitting techniques are shown to suffer from limitations including (i) the assumed linear variations of the surface reflectance within gas absorption bands, (ii) the assumption of non-overlapping gas absorption bands, and (iii) the need for a high SNR at each side of the gas absorption bands. These limitations may yield a typical error far greater than 10% in H_2O column density retrieval over some ground materials (see (Borel et al., 1996) and (Schläpfer et al., 1998) for a validation of APDA over 379 reflectance spectra).

3.1 Effect of Non-linearity of the Reflectance ρ within Gas Absorption Bands

The reflectance spectrum of enstatite (sample IN-10B, particle size 45-125 µm) was chosen as a reference (from the Jet Propulsion Laboratory (JPL), Pasadena, CA, spectral library) because it is frequently encountered on the earth's surface and because of the high error of standard methods for this material. A radiance pixel was simulated using MODTRAN4 in the single scattering mode with the following entries: aerosol-free US 1976 Standard Atmosphere Model with an excess of water vapor equal to 3500 ppm in the first atmospheric kilometer (to simulate a vapor plume), solar zenith angle of 40 degrees, target at sea level, and nadir viewing sensor located above the atmosphere. Noise was added to the computed signal using the radiometric characteristics of the AVIRIS instrument for the year 1995 (see section 4.1). We used the 3-channel optimal APDA technique (reference channels: 875.25 nm / FWHM = 8.86 nm and 1000.13 nm / FWHM = 9.01 nm, measurement channel : 942.49 nm / FWHM = 8.95 nm) applied to the 940 nm water vapor absorption band (Fig. 2) (FWHM is the Full Width at Half-Maximum).

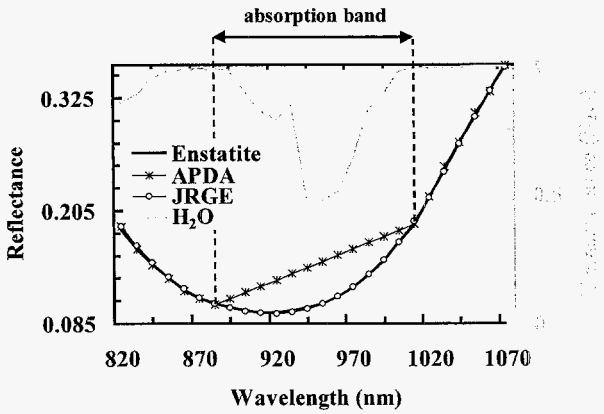

Figure 2. H_2O retrieval around 940 nm absorption band (grey line) over enstatite (black line). APDA linear interpolation (black stars) yields overestimation of reflectance and 41% overdetermined H_2O content. JRGE proposed method better fits parabolic enstatite shape (white circles) and reduces error on H_2O to 6% (see text for details).

Like other conventional methods, APDA first performs a linear interpolation of ρ within absorption bands. This assumption yields an overestimation of ρ reaching about 43% in the center of the 940 nm absorption band, leading to an estimated H_2O excess equal to 12,880 ppm instead of 3500 ppm. It corresponds to a relative error

in the first atmospheric layer equal to 268%. This error in the total atmospheric H_2O content is about 41%. This overdetermined value is due to the parabolic shape of enstatite near 940 nm. This example illustrates that the usual assumption of linear variations of ρ within absorption bands may yield large errors.

3.2 Effect of Overlapping Absorption Bands

Conventional methods use the assumption of separated gas absorption bands and estimate each n_p separately. However, absorption bands may overlap (Fig. 3) so that one may be in need for a more comprehensive method of retrieving simultaneously the n_p.

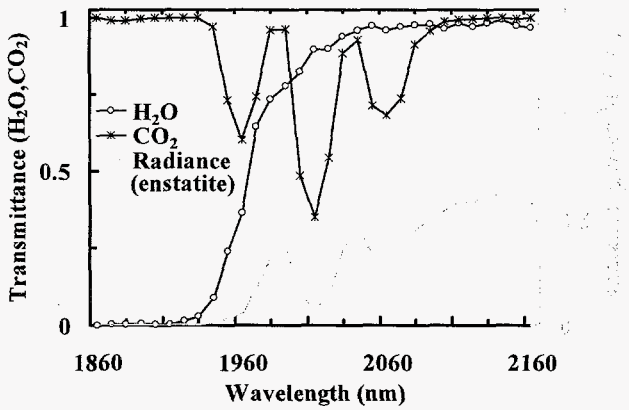

Figure 3. H_2O and CO_2 overlapping absorption bands near 2000 nm (white circles and black stars, respectively) yield a complex radiance pattern (grey line). Contrary to previous standard algorithms, JRGE addresses that point in a simultaneous gases retrieval procedure.

3.3 Effect of Noise

Conventional methods use a few reference channels located at each side of the absorption bands in order to interpolate the surface reflectance. The interpolation thus drastically depends on the noise in these reference channels. They do not benefit from the whole signal to minimize the influence of noise during the reflectance interpolation procedure. This point is generally negligible for H_2O retrieval but may be of high importance for CO_2 retrieval, with absorption bands located in low SNR spectral regions.

4. JRGE : THEORETICAL DEVELOPMENTS

In the following, we propose a method that overcomes the main drawbacks of the conventional methods listed above. It is based on a mathematical description of the physical characteristics of the signal. The developed algorithm is a two-step algorithm that first estimates the surface reflectance and then the densities of the plume gases.

4.1 Physical Constraints and Assumptions

We consider the following physical constraints and assumptions :

- From imaging spectrometry theory (Goetz, 1992), surface reflectance spectra generally do not include hyperfine absorption features. For current hyperspectral sensors (e.g., AVIRIS, HyMap, Hyperion), the surface reflectance can thus be considered as a spectrally smooth function of wavelength. This assumption allows (i) consideration of reflectance values at channel center in equation (4) and (ii) the construction of the proposed estimator.
- Estimates of the minimum and maximum values of n_p ($n_{p\min}$ and $n_{p\max}$, respectively) are available. As an example, the user may suggest that N_{0p} represents N_p with an accuracy of 20, 30, or 100%, or may give values depending on the studied phenomenon (e.g., forest fire, volcano, industrial plant). This requirement will allow the selection of the measurement (or absorption) channels (see section 4.2).
- A noise model is assumed to be available. The total noise on the measured radiance in channel i results from two independent noise contributions: (i) the inherent photon noise and (ii) the instrument's noise. The

total noise can be modeled by an additive gaussian white noise process b_i with zero mean and a standard deviation equal to σ_{bi}; the noises in the different channels are supposed to be statistically independent (Green et al., 1996a). The photon noise is estimated from the conversion factor of photons to signal, and the instrument's noise is defined as the standard deviation of the dark signal measured during the image acquisition ((Green et al., 1996a) and (Vane et al., 1987) for AVIRIS sensor specifications), so that an estimate of the noise standard deviation is available for each channel of each pixel. Typical SNR values are greater than 500 over much of the spectral range for 1995 AVIRIS data (between 300 and 800).

- The gases of interest are known and characterized by their absorption coefficient k_p, calculated from spectroscopic data obtained in (Rothman et al., 1998).
- The terms A_0 and L^{Path} are computed in standard atmospheric conditions using a line-by-line radiative transfer code before applying sensor averaging.

4.2 Channel Selection

The proposed method considers three types of channels (Fig. 4):

4.2.1 Measurement Channels

Measurement (or absorption) channels are the channels of the imaging system sensitive to variations in the amount of trace gases. First, an equivalent reflectance $\tilde{\rho}_i$ is computed from the data $\left(\overline{L(n_1,...,n_P)}\right)_i$ and equation (5) under the assumption of zero n_p (Fig. 4) :

$$\tilde{\rho}_i = \frac{\left(\overline{L(n_1,...,n_P)}\right)_i - \left(\overline{L^{Path}}\right)_i}{\left(\overline{A_0}\right)_i}. \tag{6}$$

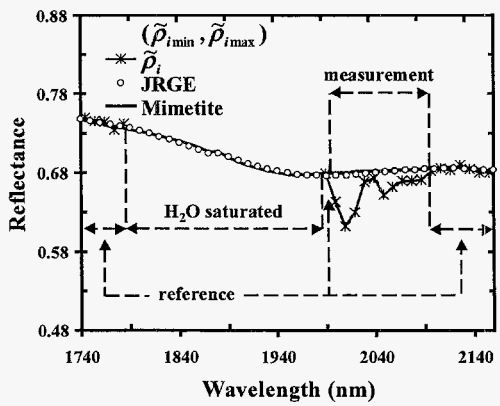

Figure 4. Spectral channels definition and selection. Standard atmospheric parameters and physical assumptions (see text for details) yield equivalent, minimum, and maximum estimates of reflectance from radiance signal (black stars and grey shape, respectively). $(\tilde{\rho}_{i\max} - \tilde{\rho}_{i\min})$ variations below noise define reference channels. Radiance below noise yields saturated channels. Gas-dependant channels are referred to as measurement channels. JRGE interpolation (white circles) constraints depend on channel type.

The associated standard deviation σ_i is related to the radiance standard deviation σ_{bi} by $\sigma_i = \sigma_{bi} / \left(\overline{A_0}\right)_i$. Similarly, the minimum and the maximum values of the reflectance ($\tilde{\rho}_{i\min}$ and $\tilde{\rho}_{i\max}$, respectively) are computed from the assumed variations $n_{p\min}$ and $n_{p\max}$ of n_p and equation (5)

$$\tilde{\rho}_{i\min} = \frac{\left(\overline{L(n_1,...,n_P)}\right)_i - \left(\overline{L^{Path}}\right)_i}{\left(\overline{A_0 \exp\left(-\eta \sum_{p=1}^{P} k_p n_{p\min}\right)}\right)_i}, \tag{7a}$$

$$\tilde{\rho}_{i\max} = \frac{\left(\overline{L(n_1,...,n_p)}\right)_i - \left(\overline{L^{Path}}\right)_i}{\left(A_0 \exp\left(-\eta \sum_{p=1}^{P} k_p n_{p\max}\right)\right)_i}, \tag{7b}$$

which represent the envelope of the possible values of the real reflectance (Fig. 4). The measurement channels are then defined to be those for which $\tilde{\rho}_{i\max} - \tilde{\rho}_{i\min} > \sigma_i$.

4.2.2 Saturated Channels

A channel is considered to be saturated if its radiance is below $3\sigma_{bi}$ (a factor of 3 is introduced in order to diminish the number of outliers). Within the 400-2500 nm spectral region, saturated channels are generally located near 1400 nm and 1900 nm, where H_2O strongly absorbs.

4.2.3 Reference Channels

The channels not selected as measurement or saturated channels are referred to as reference channels.

4.3 Surface Reflectance Estimator

This section describes the procedure used to estimate the surface reflectance from the radiance signal. In agreement with physical constraints and assumptions (see section 4.1), an estimator $\hat{\rho}_i$ of the surface reflectance in channel i is computed as

$$\hat{\rho}_i(\alpha) = \arg\min_{s\in\Omega}\left(\sum_{i=1}^{N} w_i(\tilde{\rho}_i - s(\lambda_i))^2 + \alpha \int_a^b s''(u)^2\, du\right) \tag{8}$$

where Ω=$\{ s : s \in C^2[a,b],\ s'' \in L^2[a,b]\}$, s'' denotes the second derivative of s, w_i are weighting coefficients, $\alpha > 0$ is a regularization parameter, and $[a,b]$ contains all the λ_i values. The first term in equation (8) controls the fidelity to the data and the second term controls the global smoothness of the estimator. $\hat{\rho}_i$ is called a smoothing spline estimator and is known to be a natural cubic spline with knots at the observation points $\lambda_1,...,\lambda_N$ (Reinsch, 1967) (DeBoor, 1978) (Wahba, 1975) (Kimeldorf et al., 1970) (Wahba, 1978). A cubic smoothing spline with knots in $\lambda_1,...,\lambda_N$ is a piecewise cubic polynomial $s(\lambda)$ where pieces join C^2-continuously at the points $\lambda_1,...,\lambda_N$, i.e., $s(\lambda)$ and satisfies the conditions :

- On each interval $[\lambda_{i-1},\lambda_i]$, $i = 1,...,N+1$, where $\lambda_0 = a$ and $\lambda_{N+1} = b$, $s(\lambda)$ is a polynomial of degree ≤ 3
- $s(\lambda)$ is C^2-continuous on $[a,b]$
- In addition, $s(\lambda)$ is called natural if it is linear on the end intervals $[a,\lambda_1]$ and $[\lambda_N,b]$

The weights w_i used to estimate the reflectance are given by:

- $w_i = 1/\sigma_i$ in the reference channels
- $w_i = 0$ in the measurement and saturated channels

The weights allow the noise on $\tilde{\rho}_i$ to be smoothed within the reference channels and to interpolate the reflectance elsewhere.

Equation (8) can be simplified if the natural cubic spline is represented with its value-second derivative form (Green et al., 1994). Let $\mathbf{S}$ denote the vector $[s(\lambda_1),...,s(\lambda_N)]^T$ (the superscript T is matrix transposition) and $\mathbf{U}$ the vector $[s''(\lambda_2),...,s''(\lambda_{N-1})]^T$ (by definition, a natural cubic spline has $s''(\lambda_1) = s''(\lambda_N) = 0$). Define $h_i = \lambda_{i+1} - \lambda_i$ for $i = 1,...,N-1$, and let $\mathbf{Q}$ be a tridiagonal matrix $N\times(N-2)$ in size with entries $q_{i,i} = 1/h_i$, $q_{i+1,i} = -(1/h_i + 1/h_{i+1})$, $q_{i+2,i} = 1/h_{i+1}$, and $\mathbf{R}$ a tridiagonal matrix $(N-2)\times(N-2)$ in size with entries $r_{i,i} = (h_i + h_{i+1})/3$, $r_{i,i+1} = r_{i+1,i} = h_i/6$. $\mathbf{S}$ and $\mathbf{U}$ specify a natural cubic spline if and only if the condition $\mathbf{Q}^T\mathbf{S} = \mathbf{R}\mathbf{U}$ is satisfied and then

$$\int_a^b s''(u)^2\, du = \mathbf{U}^T\mathbf{R}\mathbf{U}. \tag{9}$$

By substituting $\mathbf{U}$ by $\mathbf{R}^{-1}\mathbf{Q}^T\mathbf{S}$ in equation (9), equation (8) can be rewritten in matrix form as

$$\hat{\boldsymbol{\rho}}(\alpha) = \arg\min_{\mathbf{S}}((\tilde{\boldsymbol{\rho}} - \mathbf{S})^{\mathrm{T}} \mathbf{W}(\tilde{\boldsymbol{\rho}} - \mathbf{S}) + \alpha \mathbf{S}^{\mathrm{T}} \mathbf{Q} \mathbf{R}^{-1} \mathbf{Q}^{\mathrm{T}} \mathbf{S}) \tag{10}$$

where $\tilde{\boldsymbol{\rho}} = [\tilde{\rho}_1, ..., \tilde{\rho}_N]^{\mathrm{T}}$ and $\mathbf{W} = \mathrm{diag}[w_1, ..., w_N]$. Resolution of equation (10) yields

$$\hat{\boldsymbol{\rho}}(\alpha) = (\mathbf{W} + \alpha \mathbf{Q} \mathbf{R}^{-1} \mathbf{Q}^{\mathrm{T}})^{-1} \mathbf{W} \tilde{\boldsymbol{\rho}}. \tag{11}$$

By defining $\mathbf{A}_0 = \mathrm{diag}[\overline{(A_0)}_1, ..., \overline{(A_0)}_N]$, we can infer from equation (6) that $\tilde{\boldsymbol{\rho}} = \mathbf{A}_0^{-1}(\mathbf{L} - \mathbf{L}^{\mathrm{Path}})$ where $\mathbf{L} = [\overline{(L(n_1, ..., n_P))}_1, ..., \overline{(L(n_1, ..., n_P))}_N]^{\mathrm{T}}$ and $\mathbf{L}^{\mathrm{Path}} = [\overline{(L^{Path})}_1, ..., \overline{(L^{Path})}_N]^{\mathrm{T}}$. Then, by defining $\mathbf{B} = (\mathbf{W} + \alpha \mathbf{Q} \mathbf{R}^{-1} \mathbf{Q}^{\mathrm{T}})^{-1} \mathbf{W} \mathbf{A}_0^{-1}$, the surface reflectance estimator $\hat{\boldsymbol{\rho}}$ can be expressed as a function of the measured radiance and the path radiance by

$$\hat{\boldsymbol{\rho}}(\alpha) = \mathbf{B}(\mathbf{L} - \mathbf{L}^{\mathrm{Path}}). \tag{12}$$

We obtain a surface reflectance estimator for a given value of the smoothness parameter α.

α controls the tradeoff between the fidelity to the data and the global smoothness of the reflectance estimator. If it is too small, the model fits the noise and if it is too large then some of the original signal may be damped. In our study, the noise level σ_i is known and, therefore, the regularization parameter α can be determined using the discrepancy principle (Engl et al., 1996). A Newton's method is used to iteratively find the desired value of the parameter α.

4.4 Gas Concentrations Estimator

In this section, we compute simultaneously the estimates $\hat{n}_p$ of the P gases of interest as

$$(\hat{n}_p) = \arg\min_{n_p}(C(n_p)), \tag{13}$$

$$\text{with } C(n_p) = \sum_{i=1}^{N} w_{bi} \left(\overline{(L(n_1, ..., n_P))}_i - \hat{\rho}_i \left(\overline{A_0 \exp\left(-\eta \sum_{p=1}^{P} k_p n_p \right)} \right)_i - \overline{(L^{Path})}_i \right)^2,$$

where $w_{bi} = 1/\sigma_{bi}$ in the measurement channels and $w_{bi} = 0$ elsewhere. We use a Newton's method for minimization to solve equation (13) for the $P \times 1$ estimated vector $\hat{\mathbf{n}} = [\hat{n}_1, ..., \hat{n}_P]^{\mathrm{T}}$. Indeed, this method is particularly adapted because equation (13) is strongly non-linear towards the n_p and because the $P \times 1$ Jacobian and the $P \times P$ Hessian matrices (resp., $\mathbf{J}$ and $\mathbf{H}$) can be computed analytically. The $P \times 1$ vector of increments $\boldsymbol{\Delta}\mathbf{n}$ is given by

$$\boldsymbol{\Delta}\mathbf{n} = -\mathbf{H}^{-1}\mathbf{J} \tag{14}$$

where $\mathbf{J}$ and $\mathbf{H}$ are equal to

$$\mathbf{J} = \begin{bmatrix} \dfrac{\partial C}{\partial n_1} \\ \dfrac{\partial C}{\partial n_2} \\ \vdots \\ \dfrac{\partial C}{\partial n_P} \end{bmatrix}, \qquad \mathbf{H} = \begin{bmatrix} \dfrac{\partial^2 C}{\partial n_1^2} & \dfrac{\partial^2 C}{\partial n_1 \partial n_2} & \cdots & \dfrac{\partial^2 C}{\partial n_1 \partial n_P} \\ \dfrac{\partial^2 C}{\partial n_2 \partial n_1} & \dfrac{\partial^2 C}{\partial n_2^2} & \cdots & \dfrac{\partial^2 C}{\partial n_2 \partial n_P} \\ \vdots & \vdots & \cdots & \vdots \\ \dfrac{\partial^2 C}{\partial n_P \partial n_1} & \dfrac{\partial^2 C}{\partial n_P \partial n_2} & \cdots & \dfrac{\partial^2 C}{\partial n_P^2} \end{bmatrix}. \tag{15}$$

Starting with $\hat{\mathbf{n}} = \mathbf{0}$, the process is iterated until convergence is reached, which is when the added increment $\boldsymbol{\Delta}\mathbf{n}$ leads to variations in the concentrations of the gases lower than a specified tolerance. Note that in practice, only the measurement channels are retained in the calculation.

5. VALIDATION OF SIMULATED DATA

This section describes the preliminary results obtained with the proposed method. JRGE has been compared with APDA for water vapor retrieval. For this comparison, the JPL and the Johns Hopkins University (JHU), Baltimore, MD, spectral libraries were employed. These databases consist of measured reflectance spectra for 430 mineral samples (from JPL), to which we added 41 soil samples, 45 manmade samples, 4 vegetation samples, and 5 water samples (from JHU). Radiance spectra were simulated using MODTRAN4 in the following conditions : aerosol-free US 1976 Standard Atmosphere Model with an excess of water vapor equal to 3500 ppm in the first atmospheric kilometer (to simulate a vapor plume), solar zenith angle of 40 degrees, a target at sea level and a nadir-viewing sensor located above the atmosphere. Radiances were then averaged according to the AVIRIS instrument specifications for the year 1995 and related system noise was added to the computed signals. Retrieval of the water vapor content was performed both with the 3-channel optimal APDA technique (reference channels : 875.25 nm / FWHM = 8.86 nm and 1000.13 nm / FWHM = 9.01 nm, measurement channel : 942.49 nm / FWHM = 8.95 nm) and the proposed JRGE method. For comparison with APDA, which estimates the total gas column, we define the retrieval error $E(p)$ in the gaseous species p relatively to the total amount by

$$E(p) = \frac{n_p - \hat{n}_p}{N_{0p} + n_p}. \tag{16}$$

Results are reported in Table 1.

Table 1. Comparison between APDA and JRGE for water vapor retrieval. JRGE significantly reduces error in H_2O estimate for a set of widespread surface materials yielding APDA particularly large errors (Borel et al., 1996) (Schläpfer et al., 1998). JRGE enhancement factor is 2.5 for whole database (see text for details).

Material	APDA Error (%)	JRGE Error (%)
CUMMINGTONITE-IN-6A	-6.18	-0.12
ENSTATITE-IN-10B	-40.79	5.94
FAYALITE-NS-1A	-5.45	0.61
HEMATITE-FE2602	11.47	-2.92
MOLYBDENITE-S-11A	19.71	1.06
SIDERITE-COS2002	-31.81	4.45
TRIPHYLITE-P-4A	-42.13	-3.60
Database	APDA RMSE (%) : 7.10	JRGE RMSE (%) : 2.87

For the seven materials yielding the largest errors for APDA, the spectral shape of the reflectance within the 940 nm water vapor absorption band is fitted by the JRGE method (Fig. 2) with an accuracy of a few percent; the quality of the resulting determination of water vapor content is enhanced by a 8.4 average factor. For the whole database, the accuracy of JRGE for water vapor retrieval is 2.87%, yielding a 2.5 enhancement factor.

6. CONCLUSION

We have developed a comprehensive method to retrieve both ground reflectances and trace gas amounts from hyperspectral remotely sensed data. The method yields an enhancement factor equal to 2.5 in H_20 retrieval accuracy in comparison with conventional methods. The method can thus be also used to enhance existing atmospheric correction techniques for ground based applications (e.g., geology). Improved accuracy should allow the monitoring of numerous geophysical phenomena with relatively low gas emission.

7. REFERENCES

Borel, C. C. and D. Schläpfer (1996). Atmospheric Pre-Corrected Differential Absorption Techniques To Retrieve Columnar Water Vapor : Theory and Simulations. 6th Annual JPL Airborne Earth Science Workshop, Jet Propulsion Laboratory, Pasadena, CA.

Bruegge, C. J., J. E. Conel, J. S. Margolis, R. O. Green, G. Toon, V. Carrère, R. G. Holm and G. Hoover (1990). In-situ atmospheric water-vapor retrieval in support of AVIRIS validation. Imaging Spectroscopy of the Terrestrial Environment. Orlando, FL. **1298:** 150-163.

Carrère, V. and J. E. Conel (1993). "Recovery of Atmospheric Water Vapor Total Column Abundance from Imaging Spectrometer Data Around 940 nm - Sensitivity Analysis and Application to Airborne Visible/Infrared Imaging Spectrometer (AVIRIS) Data." Remote Sens. Environ. **44:** 179-204.

Curran, P. J. (1994). Imaging Spectrometry - Its Present and Future Rôle in Environmental Research. Imaging Spectrometry - a Tool for Environmental Observations. J. Hill and J. Mégier, ECSC, EEC, EAEC, Brussels and Luxembourg. Printed in The Netherlands: 1-23.

De Jong, S. M. and T. G. Chrien (1996). Mapping Volcanic Gas Emissions in the Mammoth Mountain Area using AVIRIS. 6th Annual JPL Airborne Earth Science Workshop, Jet Propulsion Laboratory, Pasadena, CA.

DeBoor, C. (1978). A practical guide to splines. New York.

Engl, H. W., M. Hanke and A. Neubaur (1996). Regularization of Inverse Problems, Kluwer Academic Publishers.

Esaias, W. (1986). Moderate resolution imaging spectrometer. Earth Observing System. NASA, Washington D.C. **IIb:** 49-53.

Frouin, R., P.-Y. Deschamps and P. Lecomte (1990a). "Determination from Space of Atmospheric Total Water Vapor Amounts by Differential Absorption near 940 nm : Theory and Airborne Verification." J. Appl. Meteorol. **29**: 448-460.

Frouin, R. and E. Middleton (1990b). A Differential Absorption Technique to Estimate Atmospheric Total Water Vapor Amounts. American Meteorological Society Symposium on the First ISLSCP Field Experiment (FIFE), Anaheim, CA.

Gao, B.-C. and A. F. H. Goetz (1990). Determination of total column water vapor in the atmosphere at high spatial resolution from AVIRIS data using spectral curve fitting and band ratioing techniques. Imaging Spectroscopy of the Terrestrial Environment. Orlando, FL. **1298:** 138-149.

Goetz, A. F. H. (1992). Imaging Spectrometry for Earth Remote Sensing. Imaging Spectroscopy : Fundamentals and Prospective Applications. F. Toselli and J. Bodechtel, ECSC, EEC, EAEC, Brussels and Luxembourg. Printed in The Netherlands: 1-19.

Green, P. J. and B. W. Silverman (1994). Nonparametric Regression and Generalized Linear Models. London.

Green, R. O., V. Carrère and J. E. Conel (1989). Measurement of Atmospheric Water Vapor using the Airborne Visible/Infrared Imaging Spectrometer. Image Processing '89, Sparks, NV, American Society for Photogrammetry and Remote Sensing.

Green, R. O., J. E. Conel, J. S. Margolis, C. Chovit and J. Faust (1996a). In-Flight Calibration and Validation of the Airborne Visible/Infrared Imaging Spectrometer (AVIRIS). 6th Annual JPL Airborne Earth Science Workshop, Jet Propulsion Laboratory, Pasadena, CA.

Green, R. O., D. A. Roberts and J. E. Conel (1996b). Characterization and Compensation of the Atmosphere for the Inversion of AVIRIS Calibrated Radiance to Apparent Surface Reflectance. 6th Annual JPL Airborne Earth Science Workshop, Jet Propulsion Laboratory, Pasadena, CA.

Kaufman, Y. J. and B.-C. Gao (1992). "Remote Sensing of Water Vapor in the Near IR from EOS/MODIS." IEEE Trans. Geosci. Remote Sensing **30**(5): 871-884.

Kimeldorf, G. and G. Wahba (1970). "A correspondence between Bayesian estimation on stochastic processes and smoothing by splines." Ann. Inst. Statist. Math. **41**: 495-502.

Liou, K.-N. (1980). An Introduction to Atmospheric Radiation, Academic Press, Inc.

Reinsch, C. H. (1967). "Smoothing by Spline Functions." Numer. Math. **10**: 177-183.

Rothman, L. S., C. P. Rinsland, A. Goldman, S. T. Massie, D. P. Edwards, J.-M. Flaud, A. Perrin, C. Camy-Peyret, V. Dana, J.-Y. Mandin, J. Schroeder, A. Mccan, R. R. Gamache, R. B. Wattson, K. Yoshino, K. V. Chance, K. W. Jucks, L. R. Brown, V. Nemtchinov and P. Varanasi (1998). "THE HITRAN MOLECULAR SPECTROSCOPIC DATABASE AND HAWKS (HITRAN ATMOSPHERIC WORKSTATION) : 1996 EDITION." J. Quant. Spectrosc. Radiat. Transfer **60**(5): 665-710.

Schläpfer, D., C. C. Borel, J. Keller and K. I. Itten (1996a). Atmospheric Pre-Corrected Differential Absorption Techniques to Retrieve Columnar Water Vapor : Application to AVIRIS 91/95 Data. 6th Annual JPL Airborne Earth Science Workshop, Jet Propulsion Laboratory, Pasadena, CA.

Schläpfer, D., C. C. Borel, J. Keller and K. I. Itten (1998). "Atmospheric Precorrected Differential Absorption Technique to Retrieve Columnar Water Vapor." Remote Sens. Environ. **65**: 353-366.

Schläpfer, D., J. Keller and K. I. Itten (1996b). Imaging Spectrometry of Tropospheric Ozone and Water Vapor, A. A. Balkema, Rotterdam.

Vane, G., W. M. Porter, H. T. Enmark, S. A. Macenka, M. P. Chrisp, T. G. Chrien, L. Steimle, G. C. Bailey, D. C. Miller, J. S. Bunn, R. E. Steinkraus, R. W. Hickok, J. H. Reimer, J. R. Heyada, S. C. Carpenter, W. T. S. Deich, M. Lee and E. A. Miller (1987). Airborne Visible/Infrared Imaging Spectrometer (AVIRIS) - A Description of the Sensor, Ground Data Processing Facility, Laboratory Calibration, and First Results.

Wahba, G. (1975). "Smoothing noisy data with spline functions." Numer. Math. **24**: 383-393.

Wahba, G. (1978). "Improper priors, spline smoothing, and the problem of guarding against model errors in regression." J. Roy. Statist. Soc. **40**(B).

ECOSYSTEM IMPACTS OF WOODY ENCROACHMENT IN TEXAS: A SPATIAL ANALYSIS USING AVIRIS

Roberta E. Martin,[1,2] Gregory P. Asner[2,3]

1. Introduction

Woody encroachment, the increase of woody plant density relative to herbaceous vegetation, has been documented in drylands of Texas as well as worldwide (Archer 1994, Harrington and Harman 1995, Moleele et al. 2002). Over-grazing, fire suppression and climate change are implicated in the shift from open grasslands to ecosystems now populated by trees and shrubs (Scholes and Archer 1997, Archer et al. 2001), such as *Prosopis glandulosa* var. glandulosa (honey mesquite) in north Texas (Teague et al. 1997, Ansley et al. 2001, Asner et al. 2003a). Several studies have examined changes in ecosystem properties accompanying woody vegetation encroachment in the Southwest U.S., with research focused on increases in plant and soil carbon (C) and nitrogen (N) stores (Hoffman and Jackson 2000, Asner et al. 2003a), isotopic shifts in these pools (Boutton 1999, Archer et al. 2001), and increases in N cycling rates (Rundel et al. 1982, Hibbard et al. 2001). However, little is known regarding the impact of woody encroachment on N trace gas emissions from dryland regions such as Texas.

NOx is produced in the soil during the processes of nitrification and denitrification (Firestone and Davidson 1989). The total N efflux from soils is most directly influenced by the internal cycling of N, which at a regional-scale, is controlled by the inputs and availability of N from vegetation via litterfall and subsequent decomposition (Robertson et al. 1989). Although plot-scale studies are critical to understanding controls over N oxide emissions, regionalization of the measurements is impeded by spatial variation in the factors contributing most to N cycling processes: soil properties (affecting soil moisture regimes and N stocks) and vegetation cover (affecting litter inputs and N uptake). While broad patterns in ecosystem structure and vegetation composition co-vary with general patterns of trace gas emissions (Matson 1997), there is no easily measured index of N availability that can be applied for regional-scale studies of N oxide fluxes.

Remote sensing is arguably the only approach available to develop a spatially-explicit understanding of ecosystem processes. More specifically, remotely detectable spatial patterns in the distal controls over soil N properties, such as vegetation cover, land use and soil type (Robertson et al. 1989), should be exploited for regional studies of N oxide emissions. The woody encroachment phenomenon provides an opportunity to test the strength of the relationship between N oxide emissions and those factors controlling the fluxes that can be remotely measured. If such linkages can be firmly established, and if the spatial pattern of distal controls is relevant, then the combination of field measurements and remote sensing offers to improve regional-scale N oxide estimates.

The paper presents the utility of linking field based sampling of soil NOx emissions with very high resolution remote sensing estimates of woody vegetation cover from the NASA AVIRIS, Airborne Visible-Infrared Imaging Spectrometer (Green et al. 1998, Asner and Green 2001) and automated spectral mixture analysis (Asner and Lobell 2000, Asner and Heidebrecht 2002) that provide a means to spatially extrapolate soil NOx emissions to the regional scale.

2. Study site.

The study site was located on the Waggoner Ranch in North Texas (33°50'N, 99°02'W; Figure 1). The region is temperate mixed –grass savanna with a mean annual temperature of 17 °C. Mean annual precipitation (640 mm) is bimodally distributed, with peaks in May and September. Topography of the region is gentle to moderately sloping (< 4%); elevation ranges from 355-370 m. Soils on lowland areas are fine, mixed thermic, Typic Paleustolls of the Tillman association, developed from Permian clay and shale parent material (SCS 1962). Upland soils are dominated by shallower Vernon series clay loams and intermittently exposed red-bed clays and shales. Vegetation is dominated by a mixture of native grasses (both C_3 and C_4) and a P. glandulosa (mesquite) overstory comprising > 95% of all woody cover and density (Hughes et al. 1999). While historical vegetation of the region was grassland and open savanna in the 1950s, in association with an increase in cattle grazing, the density of *P. glandulosa* increased to the point where brush management efforts were employed throughout the region (Fisher et al. 1959, Teague et al. 1997, Ansley et al. 2001). These efforts have continued to the present (Teague et al. 1997), producing

[1] Dept. of Geological Sciences, Univ. of Colorado, Boulder, CO, 80309; robin@globalecology.stanford.edu
[2] Dept. of Global Ecology, Carnegie Inst. of Washington, Stanford, CA 94305; greg@globalecology.stanford.edu
[3] Dept. of Geological and Environmental Sciences, Stanford Univ., Stanford. CA 94305

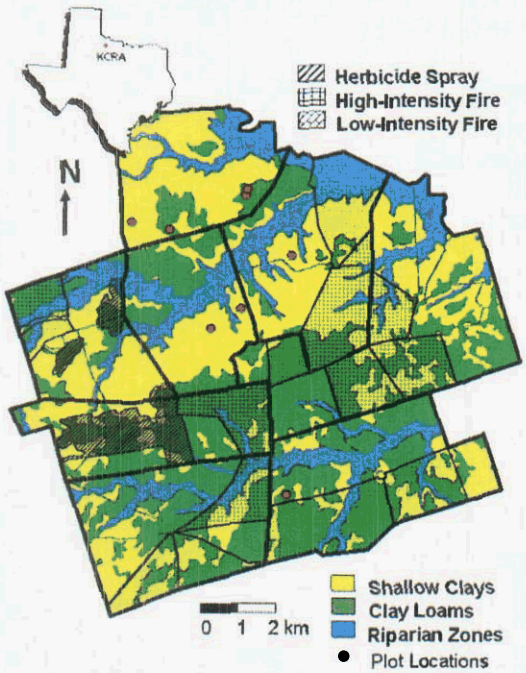

Figure 1. Pasture and soil map for Kite Camp Research Area (KCRA), Vernon, TX showing two dominant soil types and the riparian areas. Red circles mark locations where field measurements of soil NO fluxes were collected. Pastures experiencing prescribed fire and herbicide treatments prior to airborne imaging are hatched; non-hatched areas have no known brush management since at least the 1950s.

landscape mosaics of grassland, savanna (< 800 stems ha^{-1}) and woodland (up to 7,100 stems ha^{-1}) (Hughes et al. 1999).

3. Airborne Imaging Spectrometry.

Airborne imaging spectrometer data were collected on September 29, 2001 over a 140 km^2 region of Waggoner Ranch. The September time period afforded the greatest contrast between the woody *Prosopis* which were full and green and the herbaceous layer, which had senesced (Asner et al. 1998, Asner et al. 2003b). The NASA Airborne Visible and Infrared Imaging Spectrometer (AVIRIS) was flown onboard a Twin Otter aircraft at an altitude of 4000 m, providing image data with a 3.3 m spatial resolution. The data were geo-rectified using an onboard global positioning-inertial navigation system (GPS-INS) and a post-processing algorithm developed by (Boardman 1999). Eleven flightlines were then mosaicked using an algorithm developed by Asner et al. (2003b). AVIRIS data were then atmospherically corrected using the FLAASH algorithm (Matthew et al. 2000).

4. Spectral Mixture Analysis.

The spectral mixture model AutoMCU (Asner and Lobell 2000, Asner and Heidebrecht 2002) was used to calculate estimates of green photosynthetic vegetation (PV), senescent non-photosynthetic vegetation (NPV) and bare soil covers within each pixel, along with statistical uncertainty estimates for each cover type using an automated Monte Carlo uncertainty analysis. AutoMCU uses three endmember "bundles" of PV, NPV and soil, derived from an extensive endmember database for North American drylands (Asner et al. 1998, Asner et al. 2000), to decompose each image pixel using the following equation:

$$\rho_{pixel} = \Sigma[C_e * \rho_e] + \varepsilon = [C_{PV} * \rho_{PV} + C_{NPV} * \rho_{NPV} + C_{soil} * \rho_{soil}] \quad (1)$$

$$\Sigma C_e = 1.0 \quad (2)$$

where ρ is the reflectance factor, C is the cover fraction for each endmember, PV is photosynthetically active vegetation, NPV is non-photosynthetically active vegetation, and ε is the error term. Equation (2) constrains the sum of the fractions to one. On a pixel by pixel basis, the AVIRIS reflectance measurements were spectrally unmixed 50 times using PV, NPV and soil spectra randomly selected from each endmember bundle. The Monte Carlo approach was used to calculate both mean fractional cover values of PV, NPV and soil on a per-pixel basis, and to compute absolute errors in estimates of these cover types, reported as standard deviations. AVIRIS-derived estimates of PV were compared to field-based measurements of aboveground *Prosopis* canopy cover (from Asner et al. 2003a) to determine if this remotely sensed variable could be used to spatially extrapolate NO emissions across the region (Figure 2).

5. Field N Oxide Measurement and Extrapolation Incorporating AVIRIS predicted Woody Vegetation Cover

Soil NO flux measurements are documented in detail in Martin et al., (in press). Briefly, six field campaigns were conducted approximately bi-monthly from May 2000 to June 2001 on nine 60 x 60 m plots spanning a range of landscape units that have been previously characterized for soil texture, plant canopy cover, and standing biomass through remote sensing and ground-based measurements (Asner et al., 1998; Hughes et al., 1999). Fluxes were measured from six PVC chambers at each plot. Measurements were stratified at each site beneath tree canopies (n = 3) and in grass interspaces between canopies (n = 3).

Soil NO flux exhibited a strong linear relationship with *Prosopis* cover (Figure 3; Martin et al., in press). Based on this relationship, we extrapolated NO fluxes on a pixel by pixel basis as they related to the AVIRIS estimated *Prosopis* cover producing a spatially explicit map of NO flux. Error in the prediction of NO flux was calculated for each pixel as:

$$Total\ Spatial\ Error = \sqrt{(PV\ error)^2 + (NO\ error)}$$

where, PV error is the uncertainty in estimation of the PV cover fraction derived from Monte Carlo calculation in the spectral mixture analysis, and NO error is the standard error of NO relationship with *Prosopis* cover as:

$$NO\ error = \sigma^2 \left[1 + \frac{1}{n} + \frac{(x^* - \bar{x})^2}{S_{xx}} \right]$$

where σ^2 is the standard error in the regression estimate between field measurements of PV cover fraction and NO emissions, n is the number of samples in the image, x^* is the PV cover fraction of a given pixel, $\bar{x}$ is average PV cover measured in the field plots, and S_{xx} is the sum of squares of the error in the PV cover measured in the field plots.

6. Comparison of Regional Estimates

Estimates of NO emissions derived from the different calculation methods were compared: 1) simple averaging of all field data, 2) averaging of only the summer field measurements assuming NO is not produced during the months with low temperatures, 3) spatially extrapolating NO fluxes using a woody vegetation map derived from imaging spectrometer observations. The covariance was calculated for each estimate so that variation between methods could be assessed independent of sample size differences.

7. Results and Discussion

Soil nitrogen oxides are a broad indicator of the overall N balance of an ecosystem (Davidson et al. 2000). Regional studies of N oxide emissions from savanna soils

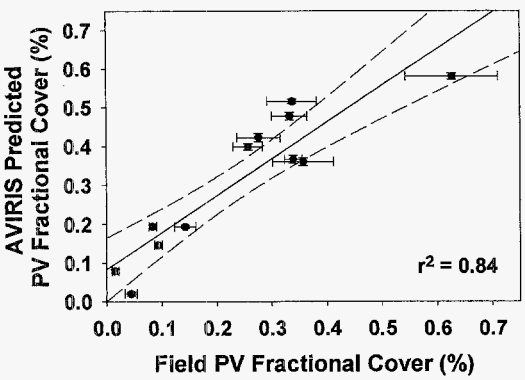

Figure 2. Relationship between woody *Prosopis* cover in georeferenced 60 x 60 m plots estimated from AVIRIS measurements collected in 2000 and field canopy measurements. Solid line shows the regression relationship used to adjust satellite estimates of PV cover (Estimated PV cover = 0.95 * Field PV Cover + 0.08). Dashed line depicts 95% confidence interval in the prediction of the regression. Vertical error bars indicate uncertainty in Monte Carlo analysis and co-location of AVIRIS pixels within field plots. Horizontal error bars indicate variability in belt-transect cover estimates within field plots (Asner et al. 2003a).

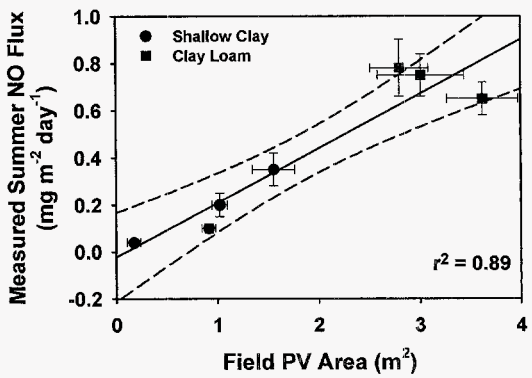

Figure 3. Relationship between NO flux and PV cover measured within field plots indicated in figure 1. Solid line show the regression relationship used to calculate NO emissions on a pixel by pixel basis as they relate to woody canopy cover across the region (NO flux = 0.23 * AG *Prosopis* cover – 0.02). Dashed line depicts 95% confidence interval in the prediction of the regression. Vertical error bars indicate standard error in NO field measurements. Horizontal error bars indicate variability in belt-transect cover estimates within field plots (Asner et al. 2003a).

are challenged by the great spatial and temporal heterogeneity in the processes regulating these emissions. Numerous studies report increases in woody plant cover in savanna ecosystems, most of which focus on classification and quantification of vegetation structure (Buffington and Herbel 1965, Harrington and Harman 1995, Ansley et al. 2001, Moleele et al. 2002, Asner et al. 2003a). Many plot-scale studies suggest that changes in canopy structure are translated to biogeochemical changes in the soil, specifically in the C and N stores (Archer et al. 2001, Asner et al. 2003b). N oxide emissions are subsequently related to N capital, which can be linked to plant cover and growth (Aber and Melillo 1991, Vitousek and Howarth 1991). This study aimed to capitalize on relationships between remotely sensed, spatially-distributed properties of vegetation and soil, and climatic controls (temperature and precipitation), to provide estimated regional variations in NO emissions from rangeland soils.

Spatial Patterns in Woody Cover

Prosopis glandulosa occurs on more than 20 million ha of rangeland in Texas, with documented increases over the past 100 y (Teague et al. 1997, Ansley et al. 2001, Asner et al. 2003a). The distribution and structure of *Prosopis* cover, and related biogeochemical properties, is a function of many of variables. Climate establishes the biogeographical setting, with seasonal temperature variations and limited rainfall promoting the co-evolution of woody communities and grasses. Accurate prediction of woody canopy cover is the key step to understanding the regional distribution of soil NO emissions as they respond to these controlling factors.

Fractional cover estimates of photosynthetic vegetation (PV), non-photosynthetic vegetation (NPV) and bare soil derived from AVIRIS reflectance measurements varied substantially across the study region (Figure 4). AVIRIS-derived fractional cover estimates of woody vegetation were well correlated to field measurements (r^2 = 0.84, p <0.01; Figure 2). Woody *Prosopis* cover (shades of red) was higher on the deeper clay loam soil than on the shallow clay soils, with values of 35 and 25%, respectively ($p < 0.001$, t-test). The areal extent of these two soil types was similar throughout the region, approximately 56 and 59 km^2 for shallow clay and clay loam, respectively, leading to an average regional woody cover of 30%. The standard deviation in predicted PV cover was low (0-9%). Averaged by soil type, the error was approximately 10% of the cover fraction for both soil types, indicating high confidence in the detection of woody plants within the AVIRIS pixels.

Remotely sensed NPV cover was slightly higher on clay loam than on shallow clay soils, with values of 57 and 51%, respectively. Areas of highest NPV cover (shades of green) were found on the upland clay loam soils, in the transition separating areas close to the riparian zones (in black) with high woody cover to the shallow clay areas with little cover (Figure 4). The standard deviation in predicting NPV was 0-10%, similar to that for PV. The bare soil fraction was higher on the shallow clay (42%) than on the clay loam soils (31%) ($p < 0.001$, t-test). The error in predicting the soil fraction was lower than that of PV or NPV (0-2%), indicating the clear detection of this land-surface component.

Using Landsat 7 ETM+ data at 30 x 30 m spatial resolution, Asner et al. (2003a) showed similar areal distributions of woody cover, but averages by soil type differed (48% and 33% on clay loam and shallow clay soils, respectively). They estimated a 23% increase in woody cover across the region over a 63 y period (1937 to 1999), and indicated a trend towards increasing spatial homogeneity of woody cover. The current analysis quantified similar heterogeneous distributions in woody cover in 1999.

The ~10% difference in woody fractional cover between the two studies is most likely do to

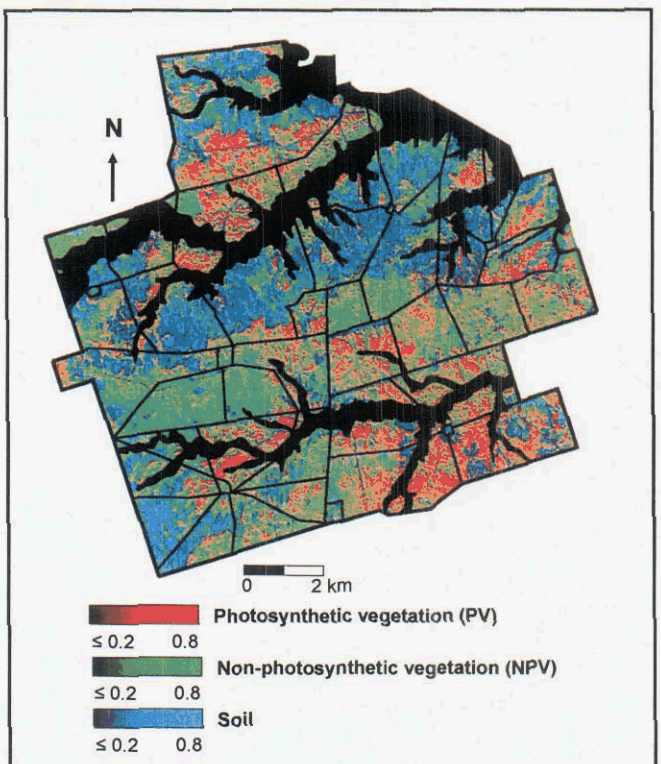

Figure 4. Regional mosaic of spectral unmixing results derived from AVIRIS measurements. Fractional surface cover of PV, NPV, and bare soil are shown in shades of red, green and blue respectively. Riparian areas have been removed. Fences enclosing pastures and the KCRA boundary are shown with black lines.

variation in plant phenology caused by interannual variation in precipitation. The September over-flights were chosen in both studies to maximize senescence of the herbaceous canopy, while the woody canopies remained fully green at the time of imaging. However, differences in the greenness of both woody and herbaceous vegetation occurred due to differences in precipitation during the preceding months in each study. On average, precipitation in the Waggoner Ranch region ranged from 400 to 900 mm over the last 10 y (NOAA, 2001). The 2001 season had extremely low rainfall (410 mm) and followed the summer drought of 2000 (no precipitation from July – September). In contrast, rainfall in 1999 during the Landsat study by Asner et al. (2003a) was average (620 mm). This suggests that our estimates of woody cover in this study are conservative, thus NO flux calculations incorporate woody vegetation cover may represent the lower limit for NO emissions in this region. Despite a difference in means, the slope and minimum value between field validation data and estimated woody cover were similar between the two studies (Figure 2; $p < 0.001$; t-test).

Spatial Variations in Soil NO Emissions

Due to the intensive amount of field work involved in the collection of soil trace gas flux data, a true random sampling over the entire area of a given biome is not feasible. In an attempt to characterize the spatial variability within a biome, measurements are often divided equally across soil type, vegetation cover or landscape position. The linkages between woody fractional cover and biogeochemical processes offers a way to capitalize on the power of remote sensing (in this case airborne imaging spectroscopy) to extend a limited number of plot-scale measurements to a regional area. If the distal controls that are remotely observable can be linked to N trace gas emissions, then greater confidence in the overall emissions estimates from the region can be achieved.

Our recent field study identified woody vegetation as the key spatial control over NO emissions following woody encroachment in North Texas (Martin et al. in press). A variety of NO emission rates associated with canopy cover types (woody versus herbaceous) have been documented in other studies. These range from small differences (~ 10%) in emissions measured under or away from mesquite canopies in southern New Mexico (Hartley and Schlesinger 2000) to a doubling in NO emissions following an increase in aboveground biomass and a doubling of total soil N from two savanna sites in South Africa (Levine et al. 1996, Parsons et al. 1996). Similarly, higher litter quality from an N-fixing legume contributed to increased N cycling and higher NO emissions in a Puerto Rican forest (Erickson et al. 2002).

Extrapolation of soil NO emissions using the photosynthetic vegetation (PV) cover, measured by AVIRIS and modeled by AutoMCU, highlighted a high degree of spatial variability across the study region with emissions ranging from 0 to 2.5 mg m^{-2} d^{-1} (Figure 5a). The extremes in predicted NO flux were then obvious, with lowest

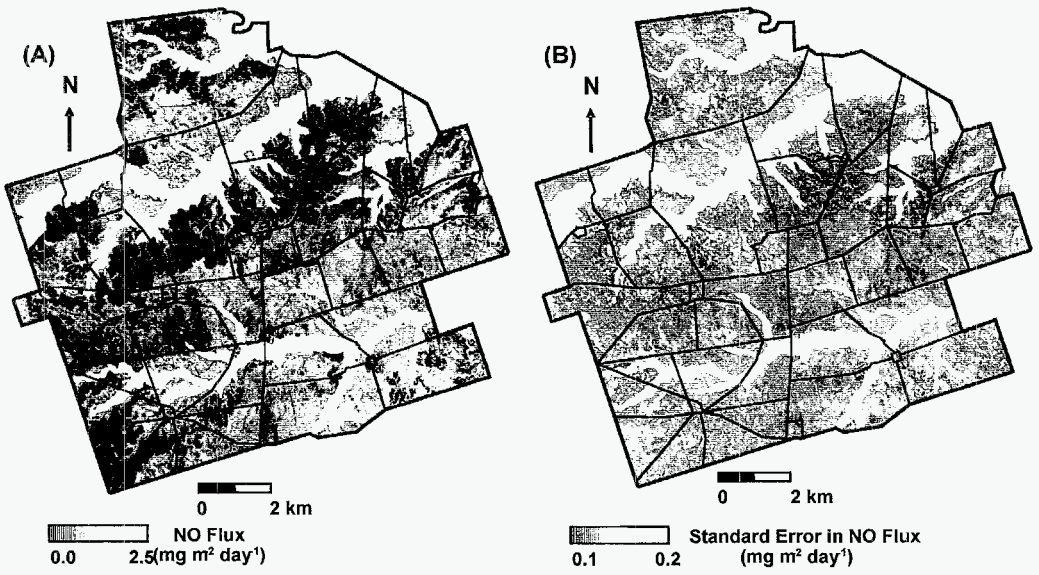

Figure 5. Regional map of NO emissions (A) and associated error (B). Brighter areas represent higher NO flux values. Riparian areas, indicated in white, were not included in the analysis. Fences enclosing pastures and the KCRA boundary are shown with black lines.

NO values in areas of high bare soil fractions (shades of blue, Figure 4) and highest values closer to the riparian zones containing dense canopies (black regions). The total error of NO flux estimates varied between 0.2 – 0.6 mg m^{-2} d^{-1}. Spatially, the error in estimation was higher at the extremes of woody cover values (Figure 5b).

Remote sensing highlighted the stratification of NO emissions by soil type, with higher emissions from clay loam than from shallow clays soils (5a). NO emissions measured in the field and averaged by soil type followed the same pattern (Table 1). Soil texture affects the production and emission of NO by influencing both N availability (plant growth and subsequent litter turnover) and soil porosity (emission path length and water-holding capacity; (Firestone and Davidson 1989, Robertson et al. 1989). In this system, NO emissions co-vary with vegetation change across soil type.

Evaluating regional NO emissions by soil type illustrates the benefit of incorporating remote sensing data in biogeochemical studies. On an area-integrated basis, the estimate for this region (120 km^2), based on stratification by soil type alone, estimated NO emissions by approximately 4 Mg NO-N y^{-1}. This value was nearly a third of the total annual flux calculated after accounting for the spatial variability of woody vegetation cover (14 Mg NO-N y^{-1}). The largest difference appeared in the estimation of emissions from shallow clay soils, producing a 260% difference when spatial variability was included (Table 1). In contrast, there was little change in the estimation of NO flux from clay loam soils. This difference in calculated NO emissions by soil type arises because the PV cover measured in the field plots located on shallow clay soil was lower (8%) than that of the entire region (25%). This difference would remain undetected without the aid of imaging spectroscopy data, which extended the estimation of vegetation fractional cover to the entire region.

8. Conclusions

Our study demonstrates the advantage of using remote sensing to characterize the spatial heterogeneity in ecosystem parameters at a scale (meters) commensurate with field-based measurements of these properties. Woody vegetation encroachment provided an opportunity to capitalize on detection of the remotely-sensible parameter of woody cover as it relates to belowground biogeochemical processes that determine N trace gas production. The first spatially-explicit estimates of NO flux were calculated based on *Prosopis* fractional cover derived from high resolution remote sensing estimates of fractional woody cover (< 4m) for a 120 km^2 region of North Texas.

Table 1. Estimated mean annual NO Flux for the entire region (120 km^2) and divided by soil type. Means and coefficient of variation are given.

	Total Area		Shallow Clay		Clay Loam	
Calculation Method	NO flux (mg m^{-2} y^{-1})	CV	NO flux (mg m^{-2} y^{-1})	CV	NO flux (mg m^{-2} y^{-1})	CV
1) all chamber measurements	89.8	1.4	42.6	1.6	137.1	1.3
2) summer chamber measurements (220 days)	86.1	1.0	38.8	1.2	133.9	0.9
3) AVIRIS vegetation map (220 days)	122.0	0.7	100.5	0.8	144.8	0.6

Differences in regional annual NO estimates calculated from traditional extrapolation methods with and without climate variability were compared to estimates calculated using spatially-explicit information on woody vegetation cover derived from remotely sensed data. Incorporating spatial variability nearly doubled the mean annual NO emissions over those estimated from field measurements alone, yielding an annual emission rate of 122 kg NO-N km^{-2} y^{-1} from the region. This emission rate is about half the total wet deposition rate (300-400 kg N km^{-2} y^{-1}; (NADP/NTN) and only a tenth of the estimated N fixed by *Prospis* in the region (600-3000 kg N km^{-2} y^{-1}; (Cleveland et al. 1999).

The spatially distributed nature of the data revealed discrepancies in total estimated NO emissions by soil type, due primarily to limited sampling on shallow clay soils. Spatially-explicit data also permitted the evaluation of the long-term effects of brush management on estimated NO emissions, an otherwise extremely labor intensive process. These data revealed that brush management may significantly decrease NO emissions once short-term variations due to the initial disturbance have dissipated.

9. Acknowledgements.

We thank J. Ansley, S. Archer, K. Heidebrecht, A. Mosier and A. Warner for their technical and logistical assistance. This study was supported by the NASA Earth System Science Fellowship Program (ESS/00-0000-

0188), NASA New Investigator Program (NIP) grant NAG5-8709, and NASA New Millenium Program (NMP) grant NCC5-480 and NCC5_481.

10. References.

Aber, J. D., and J. M. Melillo. 1991. Terrestrial Ecosystems. Saunders College Publishing, Philadephia.

Ansley, R. J., X. B. Wu, and B. A. Kramp. 2001. Observation: Long-term increases in mesquite canopy covering North Texas. Journal of Range Management **54**:171-176.

Archer, S. 1994. Woody plant encroachment into southwestern grasslands and savannas: rates, patterns, and proximate causes. Pages 13-68 *in* M. Vavra, W. A. Laycock, and R. D. Pieper, editors. Ecological Implications of Livestock Herbivory in the West. Society for Range Management, Denver.

Archer, S., T. W. Boutton, and K. A. Hibbard. 2001. Trees in grasslands: Biogeochemical consequences of woody plant expansion. *in* E.-D. Shultze, S. P. Harrison, M. Meimann, E. A. Holland, J. Lloyd, I. C. Prentice, and D. S. Schimel, editors. Global Biogeochemical Cycles in the Climate System. Academic Press, San Diego.

Asner, G. P., S. Archer, R. F. Hughes, R. J. Ansley, and C. A. Wessman. 2003a. Net changes in regional woody vegetation cover and carbon storage in Texas rangelands, 1937-1999. Global Change Biology **9**:1-20.

Asner, G. P., C. E. Borghi, and R. A. Ojeda. 2003b. Desertification in Central Argentina: Changes in ecosystem carbon and nitrogen from imaging spectrometry. Ecological Applications.

Asner, G. P., and R. O. Green. 2001. Imaging spectroscopy measures desertification in the Southwest U.S. and Argentina. EOS Transactions **82**:601-606.

Asner, G. P., and K. B. Heidebrecht. 2002. Spectral unmixing of vegetation, soil and dry carbon in arid regions: Comparing multi-spectral and hyperspectral observations. International Journal of Remote Sensing **23**:400-410.

Asner, G. P., and D. B. Lobell. 2000. A biogeophysical approach for automated SWIR unmixing of soils and vegetation. Remote Sensing of Environment **74**:99-112.

Asner, G. P., C. A. Wessman, C. A. Bateson, and J. L. Privette. 2000. Impact of tissue, canopy and landscape factors on reflectance variability in spectral mixture analysis. IEEE Transactions on Geoscience and Remote Sensing **38**:1083-1094.

Asner, G. P., C. A. Wessman, and D. S. Schimel. 1998. Heterogeneity of savanna canopy structure and function from imaging spectrometry and inverse modeling. Ecological Applications **8**:1022-1036.

Boardman, J. W. 1999. Precision geocoding of low altitude AVIRIS data: Lessons learned in 1998. *in* Eigth JPL Airborne Earth Science Workshop.

Boutton, T. W., S.R. Archer, A. J. Midwood. 1999. Stable isotopes in ecosystem science: Structure, function and dynamics of subtropical savanna. Rapid Communications in Mass Spectrometry **13**:1263-1277.

Buffington, L. C., and C. H. Herbel. 1965. Vegetational changes on a semiarid grassland range. Ecological Monographs **35**:139-164.

Cleveland, C. C., A. R. Townsend, D. S. Schimel, H. Fisher, R. W. Howarth, L. O. Hedin, S. S. Perakis, E. F. Latty, J. C. Von Fischer, A. Elseroad, and M. F. Wasson. 1999. Global patterns of terrestrial biological nitrogen (N_2) fixation in natural ecosystems. Global Biogeochemical Cycles **13**:623-645.

Davidson, E. A., M. K. Keller, H. E. Erickson, L. V. Verchot, and E. Veldkamp. 2000. Testing a conceptual model of soil emissions of nitrous and nitric oxides. Bioscience **50**:667-680.

Erickson, H. E., E. A. Davidson, and M. K. Keller. 2002. Former land-use and tree species affect nitrogen oxide emissions from a tropical dry forest. Oecologia **130**:297-308.

Firestone, M. K., and E. A. Davidson. 1989. Microbiological basis of NO and N2O production and consumption in soil. Pages 7-21 *in* M. O. Andrea and D. S. Schimel, editors. Exchange of Trace Gases Between Terrestrial Ecosystems and the Atmosphere. Wiley and Sons, New York.

Fisher, C. E., C. H. Meadors, R. Behrens, E. D. Robinson, P. T. Marion, and H. L. Morton. 1959. Control of mesquite on grazing lands. Texas Agricultural Experiment Station Bulletin **935**.

Green, R. O., M. L. Eastwood, C. M. Sarture, T. G. Chrien, M. Aronsson, B. J. Chippendale, J. A. Faust, B. E. Pavri, C. J. Chovit, M. S. Solis, M. R. Olah, and O. Williams. 1998. Imaging spectroscopy and the Airborne Visible Infrared Imaging Spectrometer (AVIRIS). Remote Sensing of Environment **65**:227-248.

Harrington, J. A., Jr., and J. R. Harman. 1995. Climate and vegetation in Central North America: Natural patterns and human alterations. Ecology Economy and Environment **5**:135-148.

Hartley, A. E., and W. H. Schlesinger. 2000. Environmental controls on nitric oxide emissions from northern Chihuahuan desert soils. Biogeochemistry **50**:279-300.

Hibbard, K. A., S. Archer, D. S. Schimel, and D. V. Valentine. 2001. Herbaceous biomass dynamics and net primary production accompanying woody plant encroachment in a subtropical savanna. Ecology **82**:1999-2001.

Hoffman, W. A., and R. B. Jackson. 2000. Vegetation-climate feedbacks in the conversion of tropical savanna to grassland. Journal of Climate **13**:1593-1602.

Hughes, R. F., J. B. Kauffman, and V. J. Jaramillo. 1999. Biomass, carbon, and nutrient dynamics of secondary forests in a humid tropical region of Mexico. Ecology **80**:1892-1907.

Levine, J. S., E. L. Winstead, D. A. B. Parsons, M. C. Scholes, R. J. Scholes, W. R. Cofer III, D. R. Cahoon Jr., and D. I. Sebacher. 1996. Biogenic soil emissions of nitric oxide (NO) and nitrous oxide (N_2O) from savannahs in South Africa: The impact of wetting and burning. Journal of Geophysical Research **101**:23689-23697.

Martin, R. E., G. P. Asner, A. R. Mosier, and R. J. Ansley. in press. Effects of Woody Encroachment on Soil Nitrogen Oxide Emissions in a Temperate Savanna. Ecological Applications.

Matson, P. 1997. NOx emission from soils and its consequences for the atmosphere: critical gaps and research directions for the future. Nutrient Cycling in Agroecosystems **48**:1-6.

Matthew, M. W., S. M. Adler-Golden, A. Berk, S. C. Richtsmeier, R. Y. Levin, L. S. Bernstein, P. K. Acharya, G. P. Anderson, G. W. Felde, M. P. Hoke, A. Ratkowski, H.-H. Burke, R. D. Kaiser, and D. P. Miller. 2000. Status of atmospheric correction using a MODTRAN4-based algorithm. Pages 199-207. *in* SPIE Proc. Algorithms for Multispectral, Hyperspectral, and Ultraspectral Imagery, VI.

Moleele, N. M., S. Ringrose, W. Matheson, and C. Vanderpost. 2002. More woody plants? the status of bush encroachment in Botswana's grazing areas. Journal of Environmental Management **64**:3-11.

NADP/NTN. National Atmospheric Deposition Program (NRSP-3)/ National Trends Network,. Natural Resource Ecology Laboratory, Colorado State University, Fort Collins, Colorado.

NOAA. 2001. Climatological data, 1970-2000, National Oceanic and Atmospheric Administration National Climatic Data Center.

Parsons, D. A. B., M. C. Scholes, R. J. Scholes, and J. S. Levine. 1996. Biogenic NO emissions from savanna soils as a function of fire regime, soil type, soil nitrogen, and water status. Journal of Geophysical Research **101**:23,683-623,688.

Robertson, G. P., M. O. Andreae, H. G. Bingemer, P. J. Crutzen, R. A. Delmas, J. H. Duyzer, I. Fung, R. C. Harriss, M. Kanakidou, M. K. Keller, J. M. Melillo, and G. A. Zavarzin. 1989. Group report, Trace gas exchange and the chemical and physical climate: Critical interactions. Pages 303-320 *in* M. O. Andreae and D. S. Schimel, editors. Exchange of Trace Gases Between Terrestrial Ecosystems and the Atmosphere. John Wiley and Sons, Chichester, England.

Rundel, P. W., E. T. Nelson, M. R. Sharifi, R. A. Virginia, W. M. Jarrell, D. H. Kohl, and G. B. Shearer. 1982. Seasonal dynamics of nitrogen cycling for a *Prosopis* woodland in the Sonoran Desert. Plant and Soil **67**:343-353.

Scholes, R. J., and S. R. Archer. 1997. Tree-grass interactions in savannas. Annual Review of Ecology and Systematics **28**:517-544.

SCS. 1962. Soil Survey of Wilbarger County, Texas. 18, United States Department of Agriculture\Soil Conservation Service, Fort Worth, TX.

Teague, R., R. Borchardt, J. Ansley, B. Pinchak, J. Cox, J. K. Fox, and J. McGrann. 1997. Sustainable management strategies for mesquite rangeland: the Waggnor Kite Project. Rangelands **19**:4-8.

Vitousek, P. M., and R. W. Howarth. 1991. Nitrogen limitation on land and in the sea: How can it occur? Biogeochemistry **13**:87-115.

ATMOSPHERIC CORRECTION OF SPECTRAL IMAGERY: EVALUATION OF THE FLAASH ALGORITHM WITH AVIRIS DATA

Michael W. Matthew,[1] Steven M. Adler-Golden, Alexander Berk,
Gerald Felde, Gail P. Anderson, David Gorodetsky, Scott Paswaters, and Margaret Shippert

1. INTRODUCTION

Visible to near infrared (NIR) hyperspectral imaging from aircraft or spacecraft is a highly valuable technology for remote sensing of the earth's surface because of its combination of good spatial and spectral resolution. Elimination of atmospheric effects caused by molecular and particulate scattering and absorption from the measurements is desired for many applications, such as when comparisons are to be made with data taken in the laboratory or under different atmospheric or viewing conditions. This process, which transforms the data from spectral radiance to spectral reflectance, is known as atmospheric correction, compensation, or removal.

A variety of methods and algorithms for atmospheric correction are available. The "empirical line method," consisting of a linear transformation derived from ground-truth spectra, remains a popular and accurate method where truth data exist. In other situations, a first-principles method is needed. ATREM, developed by Gao *et al.* (1996) using the 5S and, later, 6S radiation transport (RT) models (Vermote *et al.*, 1994), was for many years the industry-standard algorithm. Recently, more sophisticated algorithms have been developed, focusing primarily on land imagery. These algorithms, which incorporate more accurate RT models and improved methods for retrieving the atmospheric properties needed for the correction, include ATCOR (Richter, 1997), ACORN (Green, 2001), FLAASH (Matthew *et al.*, 2000; Adler-Golden *et al.*, 1998, 1999) and HATCH (Qu *et al.*, 2001).

In this paper we review the basic first-principles atmospheric correction methodology and present results from the latest version of FLAASH (Fast Line-of-sight Atmospheric Analysis of Spectral Hypercubes). FLAASH is an efficient correction code based on MODTRAN4 (Berk *et al.*, 1998) that has been developed collaboratively by Spectral Sciences, Inc. and the Air Force Research Laboratory; with assistance from the Spectral Information Technical Applications Center (SITAC); FLAASH is available in the Research Systems Inc. ENVI software package. We show some comparisons of ground truth spectra with FLAASH-processed AVIRIS data, including results obtained using different processing options, and with results from ACORN that derive from an older MODTRAN4 spectral database.

2. ATMOSPHERIC CORRECTION METHOD

2.1 Overview

First-principles atmospheric correction typically consists of three steps. The first is the retrieval of atmospheric parameters, most notably an aerosol description (the visibility or optical depth, and, if possible, an aerosol "type") and the column water amount. Since current methods allow aerosol retrieval over a very limited set of surface types (water and dark land pixels), typically only an average visibility is obtained for a scene. On the other hand, the spectral signature of water vapor is sufficiently distinct that the column amount may be retrieved on a pixel-by-pixel basis. The second step in the correction is the solution of the RT equation for the given aerosol and column water vapor and transformation to reflectance. Finally, an optional post-processing step called spectral polishing has been shown to remove many artifacts remaining from the correction process.

[1] Spectral Sciences, Inc. (matthew@spectral.com)

2.2 Radiance Equation

FLAASH uses the standard equation for spectral radiance at a sensor pixel, L*, in the solar wavelength range (neglecting thermal emission) from a flat Lambertian surface or its equivalent (Vermote *et al.*, 1994). Collecting constants reduces the equation to the form

$$L^* = A\rho/(1-\rho_e S) + B\rho_e/(1-\rho_e S) + L^*_a \quad (1)$$

Here ρ is the pixel surface reflectance, ρ_e is a surface reflectance averaged over the pixel and a surrounding region, S is the spherical albedo of the atmosphere, L^*_a is the radiance backscattered by the atmosphere, and A and B are coefficients that depend on atmospheric and geometric conditions but not on the surface. Each of these variables depends on the spectral channel; the wavelength index has been omitted for simplicity. The first term in Eq. (1) corresponds to radiance that is reflected from the surface and travels directly into the sensor. The second term corresponds to radiance from the surface that scattered by the atmosphere into the sensor, resulting in a spatial blending, or adjacency, effect.

In most other atmospheric correction codes (e.g., ACORN, HATCH, ATREM), ρ and ρ_e are replaced by a single variable, resulting in neglect of the adjacency effect. This approximation, which is a user option in FLAASH, is satisfactory for homogeneous surface areas and under high-visibility conditions, but is less successful under hazy conditions. The importance of the adjacency effect in a forested scene with a visibility of around 25 km is illustrated in Figure 5 of Adler-Golden *et al.* (1999), which shows FLAASH reflectance spectra of calibration panels retrieved with and without the adjacency correction. As another example, Figure 1 shows some spectra retrieved from an extremely hazy (~7 km visibility) AVIRIS image of rural N. Carolina taken on 7/22/93 as part of the Smoke, Clouds And Radiation (SCAR) experiment. Note that correction for the adjacency effect eliminates a chlorophyll residual in the soil spectra caused by strong scattering from the surrounding vegetation.

2.3 Radiation Transport Calculations

The atmospheric constants in Eq. (1) are calculated from an RT model, such as MODTRAN. These calculations usually represent the single most computationally intensive part of the atmospheric correction. For greatest efficiency, a look-up table (LUT) of these constants may be pre-calculated and interpolated as needed for the specific viewing geometry, atmospheric condition, and sensor channels of interest. A LUT for nadir viewing geometries is incorporated in ACORN. Other codes, including FLAASH, perform a custom RT calculation for the image at hand to permit coverage of a wider range of conditions (e.g., off-nadir viewing, all MODTRAN standard aerosol models).

When using MODTRAN, for the most accurate short-wave correction (which is needed over water, for example) the DISORT (Stamnes *et al.*, 1988) discrete ordinate multiple scattering option is superior to the computationally much faster Isaacs 2-stream method. Another option that can be selected in MODTRAN is the band model spectral resolution. Results at different resolutions are compared in Section 3.

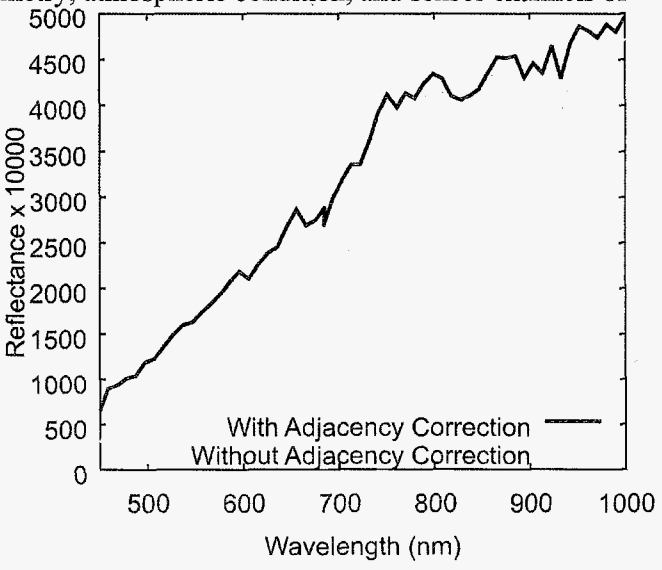

Figure 1. Comparison of light soil spectra retrieved by FLAASH from a very hazy 7/22/93 AVIRIS image of N. Carolina. The MODTRAN rural haze model was assumed.

2.4 Atmospheric Parameter Retrieval

The values of *A, B, S and* L^*_a in Eq. (1) depend on the viewing and solar angles and surface and sensor elevations, as well as on the atmospheric parameters of column water vapor, aerosol type, and visibility. A number of methods are available for retrieval of column water vapor and visibility. Perhaps the most accurate, but also the most computationally intensive, method for water vapor retrieval is a smoothness optimization approach, used in HATCH (Qu *et al.*, 2001). Other correction codes perform the retrieval from one or more water absorption features using a small number of in-band and out-of-band radiance values. FLAASH uses the combination of a radiance ratio and an out-of-band radiance to interrogate a MODTRAN4-generated 2-dimensional LUT for the column water vapor in each pixel. The water band typically used is at 1.13 μm, with the LUT for this spectral region generated on-the-fly. Several correction codes also provide a means to retrieve an approximate scene-average visibility (i.e., aerosol optical depth). In FLAASH this is done with a fast, adjacency-corrected implementation (Matthew *et al.*, 2000) of the 660 nm to 2200 nm reflectance ratio constraint for dark land pixels (2200 nm reflectance < ~0.1) found by Kaufman *et al.* (1997). Shadow and water are excluded from the dark pixel set by requiring that the ratio of 400-450 nm to 750-865 nm radiance is less than 1 (D. Miller and S. Sarlin, private communication).

2.5 Solution of the Radiance Equation

Once the atmosphere is adequately characterized and the Eq. (1) constants are derived, calculation of the image reflectance is straightforward using a method described in several papers (Richter, 1996; Vermote *et al.*, 1997). The method involves computing a spatially averaged radiance image L^*_e, from which the spatially averaged reflectance ρ_e is estimated using the relationship

$$L^*_e \approx (A+B)\rho_e/(1-\rho_e S) + L^*_a \quad (2)$$

The spatial averaging is performed using a point-spread function that describes the relative contributions to the pixel radiance from points on the ground at different distances from the direct line of sight. FLAASH approximates this function as a nearly exponential function of radial distance. Since clouds can be a severe contaminant in the spatial averaging process for the L^*_e calculation, FLAASH automatically identifies cloudy pixels (Matthew *et al.*, 2000) and replaces them with an average radiance.

As discussed elsewhere, up to an order of magnitude improvement in speed can be obtained by using an approximation in which the convolved reflectance and water vapor are averaged within pixel groups ("superpixels") and Eq. (1) is reduced to a simple linear form (Matthew *et al.*, 2000). This method, implemented with 4x4 superpixels, is the default in FLAASH, and is suitable for sensors that have a spatial resolution finer than the typical ~100 m distance of the adjacency point spread function.

2.6 Spectral Polishing

Spectral polishing refers to a spectral smoothing process that removes consistent artifacts in an atmospherically corrected hyperspectral image using only information from the image itself. The original, stand-alone algorithm, called EFFORT, was developed by Boardman (1998); others have been developed for particular atmospheric correction codes, including FLAASH (Adler-Golden *et al.*, 1999). The basic assumption behind polishing is that the scene contains some spectrally smooth pixels, such as road surfaces or bare soil that can be identified by a variance or similar measure. By comparing their raw reflectance spectra with a smoothed (low-pass filtered) spectrum, these pixels are used to develop a linear correction for the entire scene. The correction typically consists of a spectral gain or transmittance factor, and (in EFFORT) may also include a spectral offset. In FLAASH the smoothing is accomplished by taking a running average of N adjacent channels, where N is typically an odd number between 7 and 11.

The key to successful polishing is the selection of appropriate spectrally smooth pixels. They must not only be free of consistent, true spectral features, but also must be bright enough for derivation of a meaningful gain factor for all wavelengths. Vegetation pixels, although quite smooth overall, are unsuitable because of their sharp chlorophyll edge and darkness in the visible. As shown in the FLAASH

results of Figure 2, using a ratio test to exclude vegetation from the smooth pixel set eliminates a chlorophyll edge artifact in the polished spectra.

3. FLAASH RESULTS WITH AVIRIS DATA

In October 1998, a set of images were taken by the JPL AVIRIS instrument at the NASA Stennis Space Center in conjunction with a set of "ground truth" surface reflectance measurements. The sensor was at 3 km altitude, the sun was reasonably high (zenith angle of 48 deg), water vapor was moderate (1560 atm-cm according to a radiosonde measurement), and visibility was high. This data collection provides an excellent opportunity to evaluate the accuracy of FLAASH with a well-calibrated sensor covering the 0.4 – 2.5 μm range.

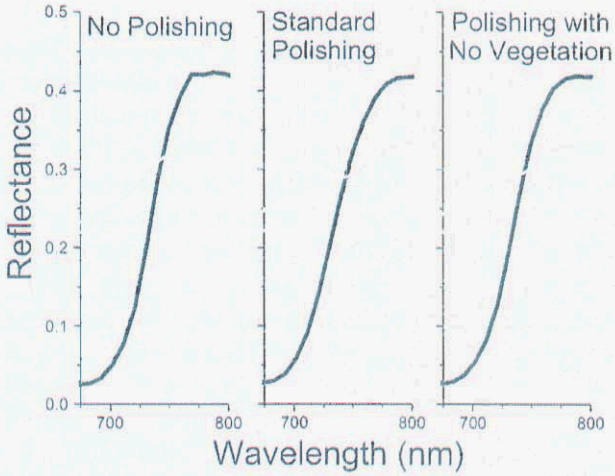

Figure 2. FLAASH retrieved spectra for soil (black curve) and vegetation (gray curve) in the chlorophyll edge region. At left, unpolished results; at center, with vegetation pixels included in the smooth set used to generate the polishing correction; and, at right, with vegetation pixels excluded from the smooth set.

Figure 3 compares near-"best" FLAASH results (1 cm^{-1} resolution with Isaacs multiple scattering and polishing) with ground truth spectra for four materials: a black panel, white panel, grass and soil. The wavelengths have been shifted by a few nm from the original spectrograph calibrations in order to optimize the results. The MODTRAN rural haze model was assumed; the retrieved visibility was around 70 km. Agreement between the two sets of spectra is good; the differences may reflect some combination of radiometric calibration error, atmospheric correction error, and effects caused by material non-uniformity and/or non-Lambertian reflectance. The FLAASH retrieved average water vapor of 1570 atm-cm (derived from the 1.13 μm band) is remarkably (perhaps fortuitously) close to the radiosonde measurement.

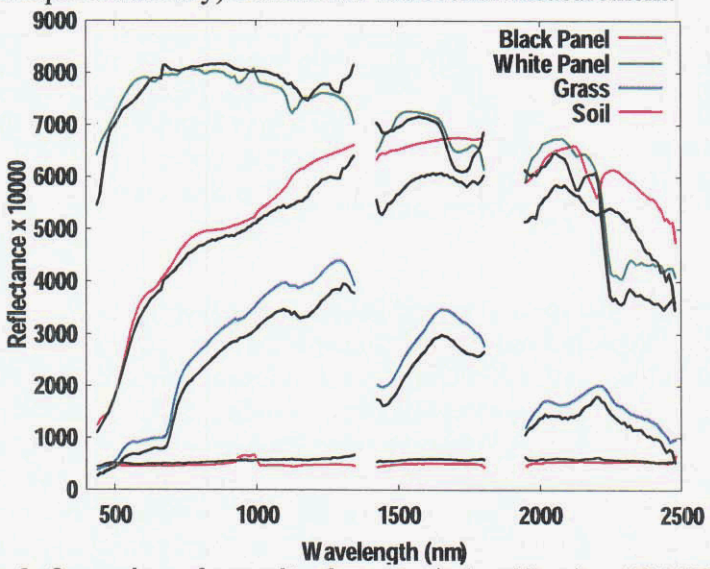

Figure 3. Comparison of ground truth spectra (colored lines) and FLAASH retrievals from AVIRIS data (black lines) at Stennis Space Center using 1 cm^{-1} band model parameters, shifted wavelengths and spectral polishing (N = 9).

Figure 4 compares unpolished spectra retrieved by FLAASH with different MODTRAN band model resolutions and with both the original and shifted wavelength sets. The shifted wavelengths yield a dramatic improvement in the unpolished spectra. The MODTRAN band model resolution has a smaller

effect. The 5 cm^{-1} results are very close to the 1 cm^{-1} results at all wavelengths. The 15 cm^{-1} results are close to the others at short wavelengths but are inferior at long wavelengths, where the resolution approaches the width of the instrument function. At all resolutions the polished results are similar to the 1 cm^{-1} spectra shown in Figure 3.

Figure 5 quantitatively compares the FLAASH results with the ground truth reflectance spectra via the Spectral Angle Mapper. The smaller the spectral angle, the closer is the agreement in spectral shape. In general, spectral polishing and wavelength optimization yield comparable and substantial improvements in accuracy, with the best results usually obtained by combining the two. The 1 cm^{-1} and 5 cm^{-1} results are very close and are virtually identical when polishing is used.

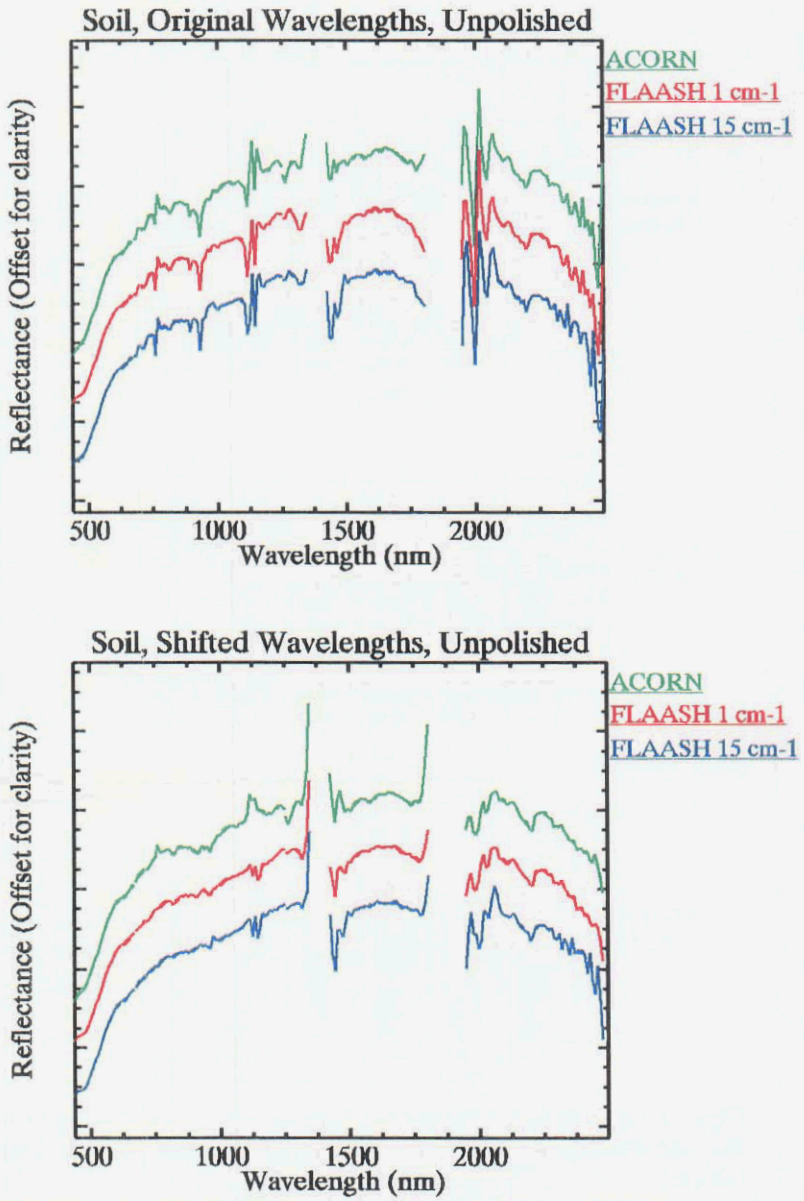

Figure 4. Comparisons of FLAASH retrieved spectra with different MODTRAN band model resolutions and wavelength calibrations. The ACORN calculations are from Version 3.12.

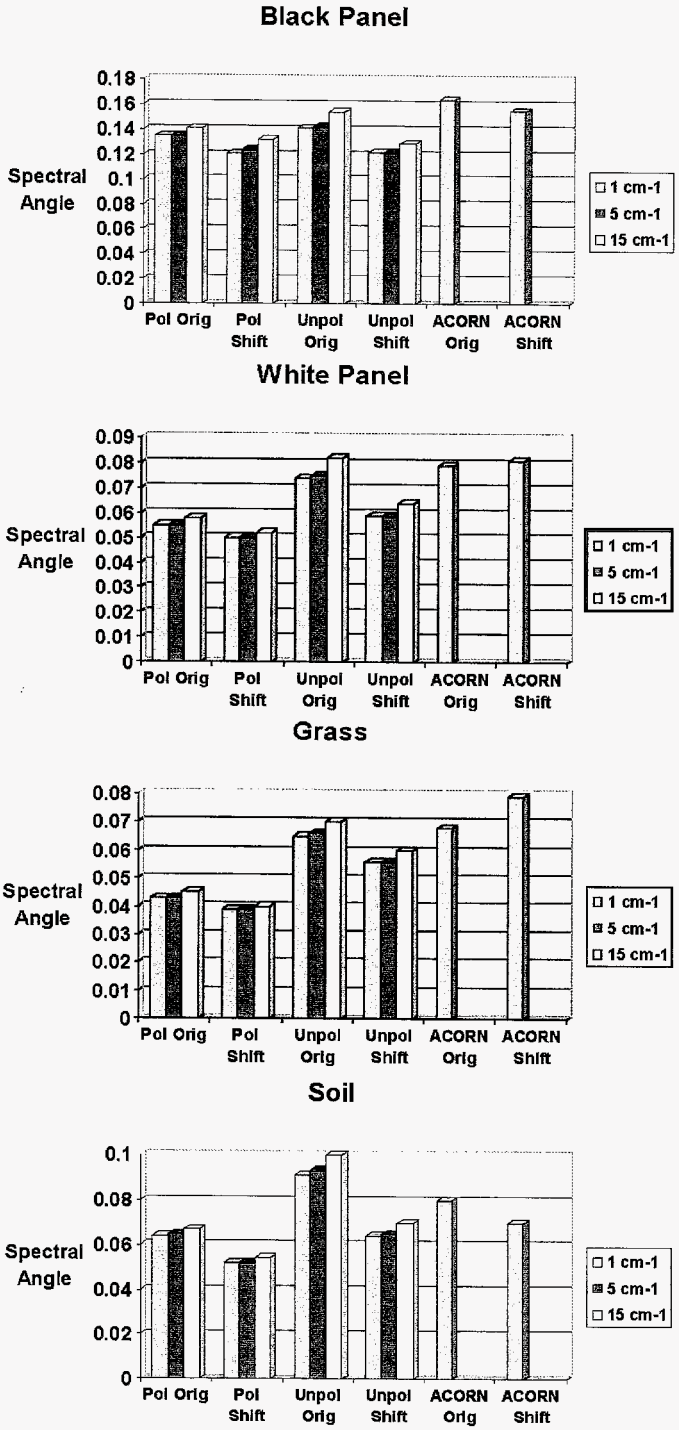

Figure 5. Spectral Angle Mapper comparison of ground truth spectra with atmospherically corrected spectra from the AVIRIS Stennis scene (angle in radians).

Also appearing in these comparisons are unpolished calculations from ACORN Version 3.12. Its LUT derives from older MODTRAN4 band model parameters that omitted collisional bands of O_2 and contained a 940 nm water band strength from HITRAN 1996 (Rothman *et al.*, 1998) that is around 12% too weak (Giver *et al.*, 2000). At long wavelengths the ACORN and FLAASH results are similar, but at

short wavelengths the effect of the improved spectral parameters in FLAASH's newer version of MODTRAN4 can be seen. Interestingly, the shifted wavelengths do not consistently improve the ACORN results, perhaps because they may exaggerate the water vapor overestimation that would result from the incorrect 940 nm band strength. We also tried ACORN's artifact removal algorithms, but the results turned out to be much less accurate and are not shown.

4. CONCLUSIONS

The FLAASH results presented here, together with previous work by a variety of investigators, confirm that a state-of-the-art atmospheric correction algorithm is capable of generating accurate surface reflectance spectra from hyperspectral imagery, at least under conditions of clear to moderate aerosol/haze, low to moderate water vapor, and nadir viewing from any altitude between the ground and the top of the atmosphere.

Many challenges remain, including developing real-time processing capability and achieving high accuracy under more stressing atmospheric and viewing conditions. In addition to the surface visibility, detailed aerosol/haze properties need to be retrieved for heavy aerosol conditions, for viewing at far off-nadir angles, and for achieving the accuracy needed for remote sensing of water bodies, including bathymetry and measurement of water composition and bottom properties. Knowledge of both the surface visibility and the single-scattering albedo is required for the simultaneous accurate correction of dark surfaces, which are sensitive to the backscatter term L^*_a, and of bright surfaces, which are sensitive to the transmittance factors in A and B. Possible uncertainty in the scattering phase function, which controls the ratio of forward to backward scattering, further complicates the analysis. A key test of aerosol and haze models is their ability to predict downwelling radiance. There have been reports of lower-than-expected diffuse downwelling radiance in clear skies (Kato *et al.*, 1999), which has been ascribed to aerosol "anomalous absorption;" however, both the observations and explanation remain controversial (Charlock *et al.*, 2001). Model refinements that address this issue should enable further improvements in atmospheric correction accuracy.

5. ACKNOWLEDGEMENTS

The work at Spectral Sciences, Inc. was supported by the U.S. Air Force Research Laboratory through the SBIR program under contract no. F19628-00-3010. The authors also acknowledge with thanks the contributions from many individuals, including David Miller and Paul Lewis (currently at NIMA) for FLAASH development and validation provided by SITAC, as well as P. K. Acharya, L. S. Bernstein and J. Gruninger (SSI), T. Cooley, M. L. Hoke, A. J. Ratkowski, J. H. Chetwynd, and J. A. Gardner (AFRL).

6. REFERENCES

Adler-Golden, S.M., A. Berk, L.S. Bernstein, S.C. Richtsmeier, P.K. Acharya, M.W. Matthew, G. P. Anderson, C.L. Allred, L.S. Jeong, and J.H. Chetwynd, "FLAASH, a MODTRAN4 Atmospheric Correction Package for Hyperspectral Data Retrievals and Simulations," *1998 AVIRIS Geoscience Workshop,* Jet Propulsion Laboratory, Pasadena, California, 1998.

Adler-Golden, S.M., M.W. Matthew, L.S. Bernstein, R.Y. Levine, A. Berk, S.C. Richtsmeier, P.K. Acharya, G.P. Anderson, G. Felde, J. Gardner, M. Hoke, L.S. Jeong, B. Pukall, J. Mello, A. Ratkowski and H.-H. Burke, "Atmospheric Correction for Short-wave Spectral Imagery based on MODTRAN4," *SPIE Proceeding, Imaging Spectrometry V*, **3753**, pp. 61–69, 1999.

Berk, A., L.S. Bernstein, G.P. Anderson, P.K. Acharya, D.C. Robertson, J.H. Chetwynd and S.M. Adler-Golden, "MODTRAN Cloud and Multiple Scattering Upgrades with Application to AVIRIS," *Remote Sensing Environment* **65**, 367, 1998.

Boardman, J.W., "Post-ATREM Polishing of AVIRIS Apparent Reflectance Data using EFFORT: a Lesson in Accuracy versus Precision," *1998 AVIRIS Geoscience Workshop,* Jet Propulsion Laboratory, Pasadena, California, 1998.

Charlock, T.P., F.G. Rose and D.A. Rutan, "Aerosols and the Residual Clear-Sky Insolation Discrepancy," *Eleventh ARM Science Team Meeting Proceedings,* Atlanta, Georgia, March 19–23, 2001

Gao, B.-C., K.B. Heidebrecht and A.F.H. Goetz, *Atmosphere Removal Program (ATREM) Version 2.0 Users Guide,* Center for the Study of Earth from Space/CIRES, University of Colorado, Boulder, Colorado, **26** 1996.

Giver, L.P., C. Chackerian, Jr., and P. Varanasi, "Visible-near infrared H_2O line intensity corrections for HITRAN-96," *J. Quant. Spectrosc. Radiat. Transfer,* **66**, pp. 101–105, 2000.

Green, R., "Atmospheric Correction Now (ACORN)," developed by ImSpec LLC, available from Analytical Imaging and Geophysics LLC, 2001.

Kato, K.S., T.P. Ackerman, E.G. Dutton, N. Laulainen, and N. Larson, "A comparison of modeled and measured surface shortwave irradiance for a molecular atmosphere," *J. Quant. Spectrosc. Radiat. Transfer.*, **61**, 493–502, 1999.

Kaufman, Y. J., D. Tanre, L. A. Remer, E. F. Vermote, A. Chu, and B. N. Holben, "Operational Remote Sensing of Tropospheric Aerosol over Land from EOS Moderate Imaging Spectroradiometer," *J. Geophys. Res.* **102**, 17051, 1997.

Matthew, M.W., S.M. Adler-Golden, A. Berk, S.C. Richtsmeier, R.Y. Levine, L.S. Bernstein, P.K. Acharya, G.P. Anderson, G.W. Felde, M.P. Hoke, A. Ratkowski, H.-H. Burke, R.D. Kaiser, and D.P. Miller, "Status of Atmospheric Correction Using a MODTRAN4-based Algorithm," *SPIE Proceeding, Algorithms for Multispectral, Hyperspectral, and Ultraspectral Imagery VI*, **4049**, pp. 199–207, 2000.

Qu, Z., B. Kindel and A.F.H. Goetz, "Aerosol Retrieval and Spectral Calibration of AVIRIS with HATCH," *2001 AVIRIS Geoscience Workshop,* Jet Propulsion Laboratory, Pasadena, California, 2001.

Richter, R., "Atmospheric Correction of DAIS Hyperspectral Image Data," *SPIE AEROSENSE '96 Conference,* Orlando, Florida, April 8–12, SPIE Proceedings, **2758**, 1996.

Richter, R., "Correction of atmospheric and topographic effects for high spatial resolution satellite imagery", Int. J. Remote Sensing 18:1099–1111, 1997.

Rothman, L.S., C.P. Rinsland, A. Goldman, S.T. Massie, D.P. Edwards, J.-M. Flaud, A. Perrin, C. Camy-Peyret, V. Dana, J.-Y. Mandin, J. Schroeder, A. McCann, R.R. Gamache, R.B. Wattson, K. Yoshino, K.V. Chance, K.W. Jucks, L.R. Brown, V. Nemtchinov and P. Varanasi, "The HITRAN Molecular Spectroscopic Database and HAWKS (HITRAN Atmospheric Workstation): 1996 Edition," *J. Quant. Spectrosc. Radiat. Transfer,* **60**, pp. 665–710, 1998.

Stamnes, K., S.C. Tsay, W.J. Wiscombe, and K. Jayaweera, "Numerically Stable Algorithm for Discrete-Ordinate-Method Radiative Transfer in Multiple Scattering and Emitting Layered Media," Applied Optics, **27**, 2502–2509, 1988.

Vermote, E.F., D. Tanre, J.L. Deuze, M. Herman and J.J. Morcrette, *Second Simulation of the Satellite Signal in the Solar Spectrum (6S),* 6S User Guide Version 6.0, NASA-GSFC, Greenbelt, Maryland, **134**, 1994.

Vermote, E.F., N. El Saleous, C.O. Justice, Y.J. Kaufman, J.L. Privette, L. Remer, J.C. Roger and D. Tanre, "Atmospheric Correction of Visible to Middle-Infrared EOS-MODIS Data Over Land Surfaces: Background, Operational Algorithm and Validation," *J. Geophys. Res.*, **102**, pp. 17131–17141, 1997.

DISCRIMINATION AND BIOPHYSICAL CHARACTERIZATION OF BRAZILIAN CERRADO PHYSIOGNOMIES WITH EO-1 HYPERSPECTRAL HYPERION

Tomoaki Miura,[1] Alfredo R. Huete,[2] Laerte G. Ferreira,[3] and Edson E. Sano[4]

1. Introduction

The savanna, typically found in the sub-tropics and seasonal tropics, are the dominant vegetation biome type in the southern hemisphere, covering approximately 45% of the South America. In Brazil, the savanna, locally known as "cerrado," is the most intensely stressed biome with both natural environmental pressures (e.g., the strong seasonality in weather, extreme soil nutrient impoverishment, and widespread fire occurrences) and rapid/aggressive land conversions (Skole et al., 1994; Ratter et al., 1997). Better characterization and discrimination of cerrado physiognomies are needed in order to improve understanding of cerrado dynamics and its impact on carbon storage, nutrient dynamics, and the prospect for sustainable land use in the Brazilian cerrado biome.

Satellite remote sensing have been known to be a useful tool for land cover and land use mapping (Rougharden et al., 1991; Hansen et al., 2000). However, attempts to discriminate and classify Brazilian cerrado using multi-spectral sensors (e.g., Landsat TM) and/or moderate resolution sensors (e.g., NOAA AVHRR NDVI) have often resulted in a limited success due partly to small contrasts depicted in their multi-band, spectral reflectance or vegetation index values among cerrado classes (Seyler et al., 2002; França and Setzer, 1998).

In this study, we aimed to improve discrimination as well as biophysical characterization of the Brazilian cerrado physiognomies with hyperspectral remote sensing. We used Hyperion, the first satellite-based hyperspectral imager, onboard the Earth Observing-1 (EO-1) platform.

2. Materials and Methods

Our study sites were located in the Brasilia National Park (BNP) in the northern Federal District, Brazil (S 15° 40', W 48° 02') (Figure 1). This preserved area contains several of the major "core" cerrado vegetation associations (physiognomies), including cerrado grassland (camp limpo), shrub cerrado (campo sujo), wooded cerrado (cerrado ralo), cerrado woodland (cerrado tipico), and gallery forest (mata de galeria) in the order of increasing arboreous cover (Ribeiro and Walter, 1998).

The first four major cerrado physiognomies described above were structurally characterized using ground transect surveys. At each site (physiognomy), landscape were vertically stratified into an arboreous (shrubs/trees) overstory layer and herbaceous understory layer dominated by grasses, in addition to a background soil/litter layer. Component cover fractions of each layer were then measured using a pin-point technique along a randomly-chosen 100-m transect. The landscape components considered in the measurements were: photosynthetic vegetation (PV), woody materials, and crown covers for the overstory; PV and standing litter for the understory; and soil and surface litter for the background surface layer.

[1] University of Arizona, Tucson, Arizona 85721, USA
(Currently at University of Hawaii at Manoa, Honolulu, Hawaii 96822, USA: tomoakim@hawaii.edu)
[2] University of Arizona, Tucson, Arizona 85721, USA
[3] Universidade Federal de Goiás, Goiânia – GO, Brazil
[4] EMBRAPA Cerrados, Planaltina – DF, Brazil

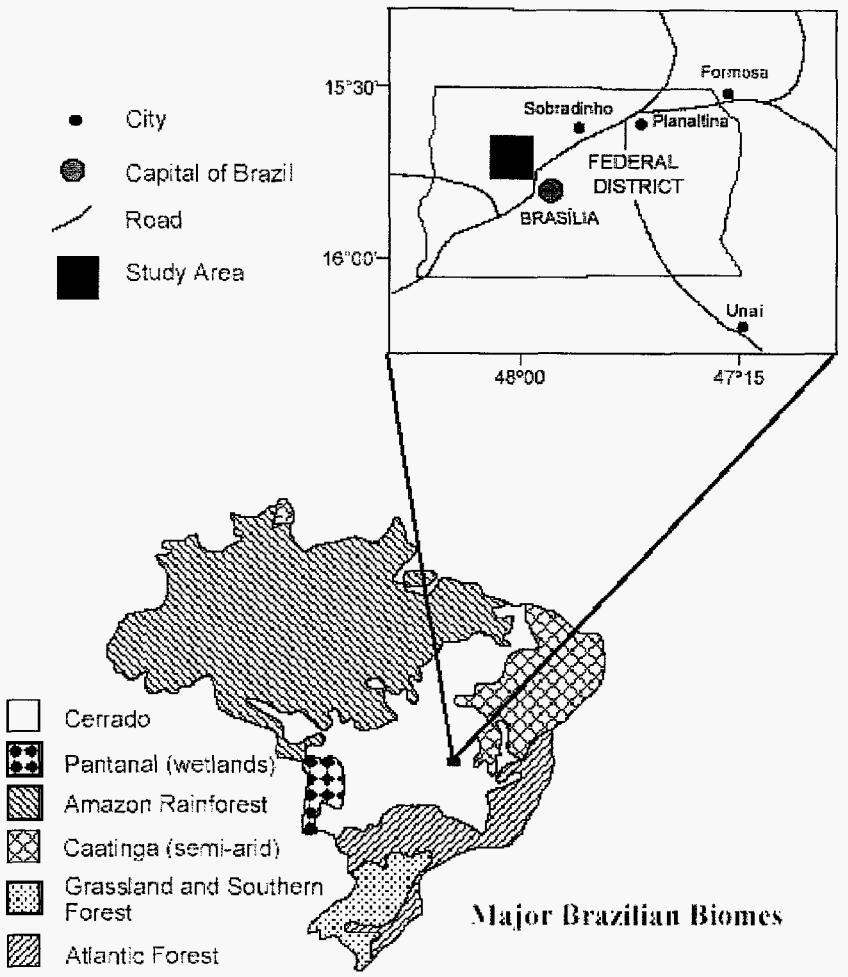

Figure 1. Location of the study area (Brasilia National Park).

Hyperspectral Hyperion data were acquired over the field sites on July 20, 2001 during the field measurement campaign. Hyperion collected full range spectral data (400-2400 nm) in 10-nm intervals (full-width at half maximum = 10 nm) at a 30-m ground spatial resolution. The data were preprocessed and radiometrically-calibrated into a Level 1A product at the TRW Hyperion data processing facility. The data were further processed to correct for several known artifacts in the Level 1A products and then converted to ground reflectances using a MODTRAN4-based atmospheric radiative transfer code (ACORN4, http://www.imspec.com/). The atmospherically-corrected Hyperion data were compared to airborne spectrometer (Analytical Spectral Devices, Inc., Boulder, Colorado) data collected at a large dry pasture field in the north of BNP near the Hyperion overpass time, but on the next day. An aircraft was flown "below the atmosphere" at 150 m AGL. The airborne data were calibrated to ground reflectances by taking a ratio to the readings made over a calibrated Spectralon white reference panel before and after the flight. The Hyperion and airborne spectrometer data were statistically similar, indicating good accounting of atmospheric constituents in the Hyperion correction.

Three optical measures of surface biophysical conditions which took a full advantage of hyperspectral remote sensing were employed and applied to the atmospherically-corrected Hyperion data. First, the 1st-order derivative-based green vegetation index with a baseline correction (1st_DGVI) which measures the amplitude of the red-edge feature and thus the amount of PV was computed as (Elvidge and Chen, 1995; Chen et al., 1998):

$$1st\_DGVI = \sum_{i=1}^{n} \left| \rho'(\lambda_i) - \rho_l'(\lambda_1) \right| \Delta\lambda_i , \quad [1]$$

where $\rho'(\lambda_i)$ is the 1st-order derivative reflectance (approximated by the reflectance difference) at the wavelength, λ_i, $\rho_l'(\lambda_1)$ is the local baseline value at the cut-on wavelength, λ_1. The cut-on and cut-off wavelengths were empirically determined to be ~640 nm and ~800 nm, respectively. Elvidge (1988) proposed the ligno-cellulose vegetation (absorption) index to map spatial variability of NPV using 1987 AVIRIS data, which was also applied and computed as the reflectance difference between 2200 nm and 2330 nm. Finally, we applied the shortwave infrared (SWIR) spectral unmixing to capture spatial variability of PV, NPV, and soils simultaneously in the Hyperion scene (Asner and Lobell, 2000). Details of these methods were provided in the corresponding references.

Pixels over the field sites were extracted from the atmospherically-corrected Hyperion image. GPS coordinates of the sites and low-altitude aerial photos were used to locate the sites in the image. In addition, another set of pixels were extracted over gallery forest, cultivated pasture, and lake water (Santa Maria Lake at the center of BNP) for comparisons.

3. Results

3-1. Field Measurements

Measured landscape component cover fractions of the four cerrado physiognomies as well as the field site locations are summarized in Table 1. The herbaceous layers were dominated by senescent tissues, while the shrub/tree layer were still green at the time of this field campaign. As used for the basis on many cerrado classification schemes (e.g., Ribeiro and Walter, 1998), the crown cover fractions increased from the cerrado grassland to cerrado woodland sites with a discrete increase between the shrub cerrado and wooded cerrado sites. There was a general increase (decrease) in the PV (NPV) cover fractions with an increase in the crown covers, except for the wooded cerrado site. Two of the four sites, the wooded cerrado and shrub cerrado sites, were dominated by the species that grow quickly after burnings and that remained green, which resulted in a larger green cover in the wooded cerrado site than the cerrado woodland site. Nearly no soils were exposed at any of the sites.

Table 1. Landscape component cover fractions of the cerrado physiognomies measured in the field sites

Site Name (Physiognomy)	Site Location (Lat./Lon.)	Crown (%)	Green (PV) (%)	NPV (%)	Soil (%)
Cerrado Grassland	N15°39'55"/ W48°01'52"	1	18	82	< 1
Shrub Cerrado	N15°35'20"/ W48°00'25"	3	23	76	< 1
Wooded Cerrado	N15°36'26"/ W48°01'47"	10	34	63	3
Cerrado Woodland	N15°43'58"/ W48°00'11"	13	30	69	< 1

3-2. Hyperion Reflectance Data

The Hyperion hyperspectral signatures clearly depicted the differences between pasture, gallery forest, and the other four cerrado physiognomies (Figure 2). Spectral signatures in the visible and near-infrared (NIR) regions for the cerrado physiognomies showed small differences, but with the red-NIR reflectance contrast corresponding well with green cover fractions (Figure 2, Table 1). The reflectance values at the shortwave-infrared (SWIR) region (1400 – 2500 nm) and the ligno-cellulose absorptions at 2090 nm and around 2330 nm wavelengths showed larger differences among the cerrado physiognomies (Figure 2). The cerrado physiognomies with less crown cover (and, thus, more NPV cover) showed higher SWIR reflectances and deeper ligno-cellulouse absorpotions (Table 1).

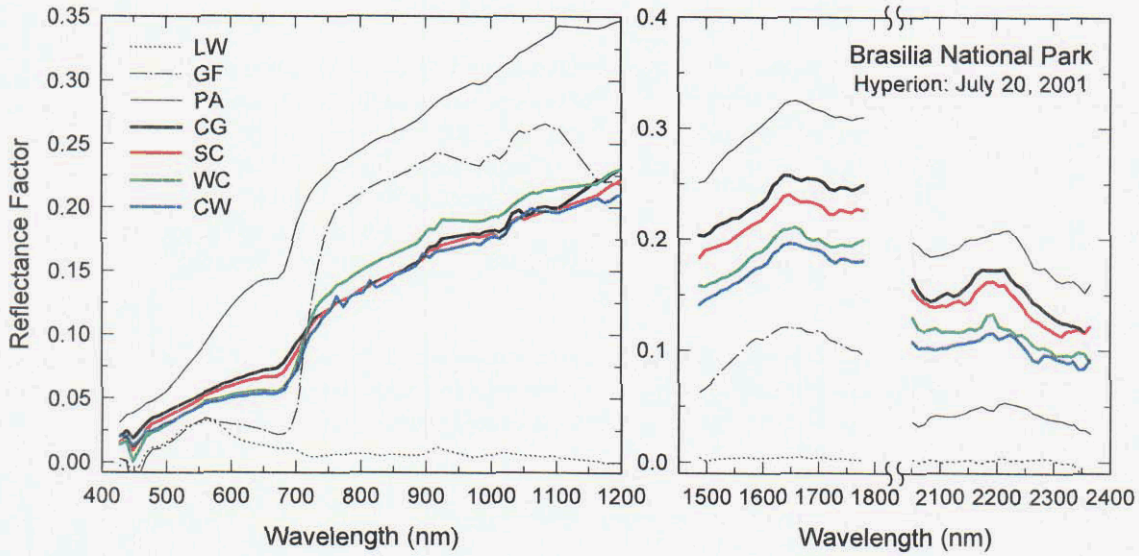

Figure 2. Mean Hyperion reflectance spectra for the four cerrado physiognomies: cerrado grassland (CG), shrub cerrado (SC), wooded cerrado (WC), and cerrado woodland (CW). Mean Hyperion spectra for lake water (LW), gallery forest (GF), and cultivated pasture field (PA) were also plotted for comparisons.

3-3. Correlative Analysis with Biophysical Data

In order to more quantitatively analyze these spectral signatures, we focused on two spectral regions that corresponded well to relative differences in physiognomies, namely, (1) the red-NIR transitional region (650-800 nm) and (2) the SWIR2 spectral region (2000-2400 nm), and performed a correlative comparison of the three optical measures described above with cover fractions.

In Figure 3, the 1st-DGVI values were plotted against the green cover fractions. The 1st-DGVI and green (PV) cover fractions correlated very well.

Similarly, the ligno-cellulose absorption index for 2330 nm was correlated well with the NPV cover fractions (Figure 4). The ligno-cellulose absorption index, however, had large standard deviations (Figure 4) due most likely to the low signal-to-noise ratios of the Hyperion sensor in this wavelength region (< 30:1).

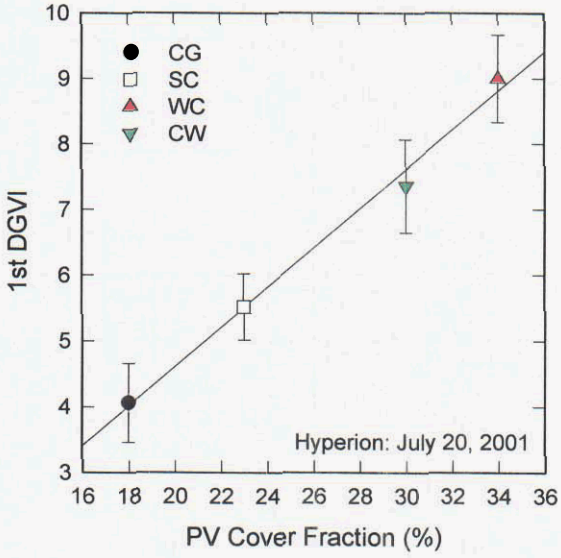

Figure 3. 1st-DGVI plotted against field estimates of PV cover fractions for cerrado physiognomies.

Finally, the SWIR unmixing results from the Hyperion image were compared to an existing vegetation map for BNP. The regional fractional estimates were consistent with the vegetation map (Figure 5). The largest values of green vegetation fractions corresponded well to the occurrences of gallery forest along stream lines. Similarly, relatively large values of green vegetation fractions corresponded spatially well with wooded cerrado and cerrado woodland, while cerrado grassland and shrub cerrado areas were consistent with large NPV fractions.

4. Conclusions and Discussions

In this study, we evaluated the utility of hyperspectral remote sensing in biophysical characterization and discrimination of cerrado physiognomies by taking an advantage of a newly available satellite-based imaging spectrometer, EO-1 Hyperion. The atmospherically-corrected hyperspectral reflectance of Hyperion clearly depicted such diagnostic absorption features of vegetation as the red edge, red-NIR transition, and ligno-cellulose absorptions. Likewise, these spectral features were found to be corresponding well with biophysical characteristics (i.e., landscape component cover fractions) of cerrado physiognomies. As the cerrado physiognomic classes are based on differences in the proportion of a grass understory and tree/shrub overstory layer, the cover component fractional estimates of green vegetation, NPV, and soil with the SWIR spectral unmixing resulted in not only biophysically characterizing, but also discriminating cerrado physiognomies. These preliminary analyses showed a great potential of hyperspectral remote sensing in biophysical characterization as well as discrimination of the land covers in the Brazilian cerrado.

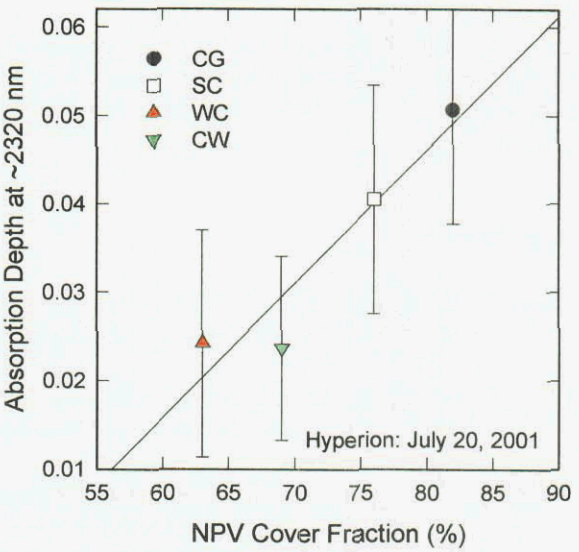

Figure 4. Ligno-cellulose absorption index plotted against field estimates of NPV cover fractions for cerrado physiognomies.

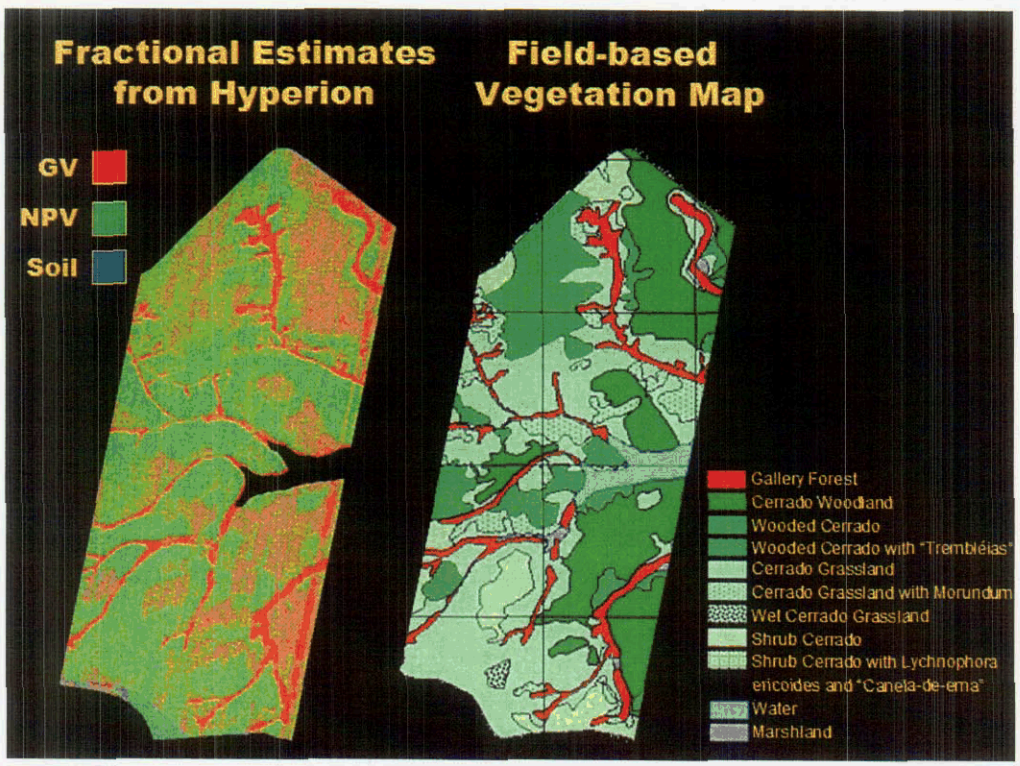

Figure 5. Color composite of green vegetation (red), total litter (green), and bare soil (blue) fractions in comparison to a field-based vegetation map (M. Ferreira, Universidade de Brasilia, personal communication).

Acknowledgement

The authors would like to thank personnel of EMBRAPA-Cerrado, University of Brasilia, and the LBA project office for their logistical support and assistance in the field data collections. This work was supported by a NASA MODIS contract NAS5-31364 (P.I., A. R. Huete) and NASA EO-1 grant NCC5-478 (P.I., A. R. Huete).

References

Asner, G. P. and Lobell, D. B. "A biogeophysical approach for automated SWIR unmixing of soils and vegetation." *Remote Sensing of Environment*, v. 74, p. 99-112, 2000.

Chen, Z., Elvidge, C. D., and Groeneveld, D. P. "Monitoring seasonal dynamics of arid land vegetation using AVIRIS data." *Remote Sensing of Environment*, v. 65, p. 255-266, 1998.

Elvidge, C. D. "Examination of the spectral features of vegetation in 1987 AVIRIS data." *Proceedings of the First AVIRIS Performance Evaluation Workshop*, Jet Propulsion Laboratory Publication 88-38, Pasadena, CA, USA, p. 97-101, 1988.

Elvidge, C. D. and Chen, Z. "Comparison of broad-band and narrow-band red and near-infrared vegetation indices." *Remote Sensing of Environment*, v. 54, p. 38-48, 1995.

França, H. and Setzer, A. W. "AVHRR temporal analysis of a savanna site in Brazil." Int. J. Remote Sensing, v. 19, no. 16, p. 3127-3140, 1998.

Hansen, M. C., DeFries, R. S., Townshend, J. R. G., and Sohlberg, R. "Global land cover classification at 1 km spatial resolution using a classification tree approach." *Int. J. Remote Sensing*, v. 21, no. 6&7, p. 1331-1364, 2000.

Ratter, J. A., Riberio, J. F., and Bridgewater, S. "The Brazilian cerrado vegetation and threats to its biodiversity." *Annals of Botany*, v. 80, p. 223-230, 1997.

Ribeiro, J. F. and Walter, T. M. B. "The major physiognomy in the Brazilian Cerrado region." Cerrado: Ambiente e Flora (ed. by Sano, S. M. and Almeida, S. P.), EMBRAPA-CPAC, Planaltina, DF, chap. 3, p. 169-188, 1998.

Rougharden, J., Running, S. W., and Matson, P. A. "What does remote sensing do for ecology?" *Ecology*, v. 72, p. 1918-1922, 1991.

Seyler, F., Chaplot, V., Muller, F., Cerri, C. E. P., Bernoux, M., Ballester, V., Feller, C., and Cerri, C. C. C. "Pasture mapping by classification of Landsat TM images: Analysis of the spectral behaviour of the pasture class in a real medium-scale environment: the case of the Piracicaba Catchment (12 400 km^2, Brazil)." Int. J. Remote Sensing, v. 23, no. 23, p. 4985-5004, 2002.

Skole, D. L., Chomentowiski, W. H., Salas, W. A., and Nobre, C. A. "Physical and human dimensions of deforestation in Amazonia." *Bioscience*, v. 44, p. 314-322, 1994.

ANALYSIS OF AVIRIS DATA FROM LEO-15 USING *TAFKAA* ATMOSPHERIC CORRECTION

Marcos J. Montes,* Bo-Cai Gao,† Curtiss O. Davis,‡ and Mark Moline§

1 INTRODUCTION

We previously developed an algorithm named Tafkaa for atmospheric correction of remote sensing ocean color data from aircraft and satellite platforms. The algorithm allows quick atmospheric correction of hyperspectral data using lookup tables generated with a modified version of Ahmad & Fraser's vector radiative transfer code. During the past few years we have extended the capabilities of the code. Current modifications include the ability to account for within scene variation in solar geometry (important for very long scenes) and view geometries (important for wide fields of view). Additionally, versions of Tafkaa have been made for a variety of multi-spectral sensors, including SeaWiFS and MODIS. In this proceeding we present some initial results of atmospheric correction of AVIRIS data from the 2001 July Hyperspectral Coastal Ocean Dynamics Experiment (HyCODE) at LEO-15.

2 BACKGROUND

Over the past two decades, atmospheric correction algorithms for application to case 1 waters (i.e., clear, deep ocean waters) have been developed by Howard Gordon's research group at the University of Miami, Florida. The complexity of these algorithms has increased greatly with time- from the early single scattering algorithm used for CZCS (Gordon, 1978) to the present more complete multiple scattering algorithm for SeaWiFS (Gordon & Wang, 1994). For the operational SeaWiFS algorithm, a simplified two-layer atmosphere system, i.e., aerosols being confined in the bottom boundary layer and atmospheric gaseous molecules being located in another layer above the aerosol layer, is assumed. An aerosol model and an aerosol optical depth are derived from channels located centered at 0.76 and 0.87 μm by assuming water-leaving radiances to be zero in that spectral range. A sophisticated lookup table procedure is used for the aerosol retrievals. The atmospheric path radiances in the visible are predicted based on the derived aerosol information. The difference between the measured radiances above the atmosphere-ocean system and the predicted path-radiance is the water-leaving radiance transmitted to the top of the atmosphere.

However, this approach does not work for some ocean environments. Over a bright sand bottom, a turbid coastal environment, or a coccolithophore bloom the water-leaving radiances in the 0.66-0.87 μm range are typically not close to zero. In the former case, reflectance by bright ocean bottoms in optically shallow water causes much more water-leaving radiance at these wavelengths than is measured in open oceans with similar water types. In the latter cases, this is due to scattering by suspended materials. Under these conditions, the channels in this spectral region have very limited use for the retrieval of information on atmospheric aerosols. The algorithms of Gordon (1997) and Fraser et al. (1997) derive aerosol information from channels in the 0.66-0.87 μm spectral range. These algorithms cannot be easily adapted for the retrieval of water-leaving radiances over coastal waters. In view of this situation, we have designed a different retrieving algorithm that can use channels in longer wavelengths, in addition to these channels, to derive aerosol information.

Since the liquid water absorption increases rapidly as a function of wavelength (Wieliczka et al., 1989), one can assume that the water-leaving radiance is zero at long enough wavelengths, even in turbid waters or over bright, shallow bottoms. In this case, one can use two or more of the atmospheric transmission window regions near 0.865, 1.04, 1.24, 1.64, and/or 2.25 μm in order to determine the aerosol type and optical depth. Our Tafkaa aerosol lookup tables include all of those wavelengths, in addition to several in the VNIR portion of the spectrum. The tables were calculated with Ahmad & Fraser's (1982) radiative transfer code that includes all orders of scattering, and components of polarization. The lower boundary condition is a rough ocean surface with capillary wave distribution as described by Cox & Munk (1954), as well as the effects of foam. The tables were calculated at 14 wavelengths and 3 wind speeds. There are 10 aerosol optical depths, 5 overall aerosol models, each of which has 5 size distributions (i.e., relative humidities). The geometrical grids have 9 solar zenith angles (θ_0), 17 view zenith angles (θ), and 17 relative azimuth angles ($\Delta\phi$). The calculations were output at 9 sensor altitudes, and all the calculations

* Remote Sensing Division, Code 7232, Naval Research Laboratory, Washington, D.C. 20375 (corresponding author: Marcos.Montes@NRL.Navy.mil)
† Remote Sensing Division, Code 7232, Naval Research Laboratory, Washington, D.C. 20375
‡ Remote Sensing Division, Code 7203, Naval Research Laboratory, Washington, D.C. 20375
§ Biological Science Dept., California Polytechnic State University, San Luis Obispo, California 93407.

assume a surface at sea-level. A thorough description of our algorithm may be found in Gao et al. (2000), and modifications are described in Montes et al. (2001) and Montes et al. (2003).

3 OVERVIEW OF THE LEO-15 SITE

The study site was the area in and around the Long-term Ecosystem Observatory in 15 m of water (i.e., LEO-15). This site is in the middle of the Middle-Atlantic Bight, off the coast of New Jersey, as shown in Fig. 1. The principal moorings are in about 15 m of water, and are about 22 km northeast of Atlantic City, New Jersey. The presence of the moorings and other underwater instrumentation led to LEO-15 becoming one of the diagnostic data sites used by the SIMBIOS project. Much of the of the area is very shallow, with depths of $z < 10$ m even a few kilometers offshore, as can be seen in Fig. 1b. The river outflow, tidal action, and the shallow water lead to the ubiquitous presence of suspended sediments throughout this area. Furthermore, high nutrient concentrations from river outflow and frequent episodic upwelling in the shallow system, allows for the rapid growth and accumulation of phytoplankton in this area.

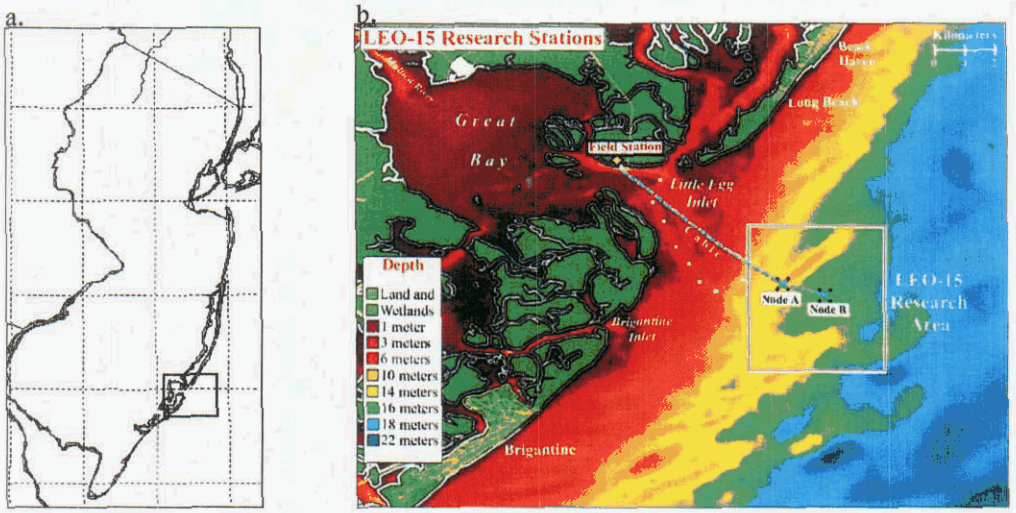

Figure 1. a.) A map of New Jersey, with an inset showing the approximate location of the map to the right. b.) A bathymetric map showing the location of the LEO-15 research area in relation to various geographic locations. (This image is courtesy of the Coastal Ocean Observation Lab, Institute of Marine and Coastal Sciences, Rutgers University.)

In July and August 2001, as a part of the HyCODE, a multi-institution collaboration measured ocean properties with a number of instruments deployed in the space, air, on the water's surface, and in the water in and around LEO-15. On July 31, 2001, hyperspectral and multispectral observations were obtained, as well as measurements from 5 research vessels and a number of in-situ autonomous systems. Imaging data at varying GSD was obtained from the multi-spectral sensors SeaWiFS and MODIS (~1 km GSD), as well as the hyperspectral instruments AVIRIS (~17 m GSD), PHILLS-2 (~9 m GSD), and PHILLS-1 (~2 m GSD). The various in-water and shipboard measurements provide us with the tools to perform closure experiments. In-water depth profiles of absorption and scattering allow us to compute forward models to compare with the water-leaving radiance measurements derived with Tafkaa, as well as allowing us to compare with shipboard measurements of remote-sensing reflectance.

The MODIS and SeaWiFS apparent reflectance images (Fig. 2) present a snapshot overview of the region around LEO-15 at ~16:24 and 18:00 GMT (i.e., about 40 minutes before and 55 minutes after local solar noon at the LEO-15 site), respectively. For this subsection of the MODIS image, geometries were $21.8° < \theta_0 < 23.8°$ and $33.3° < \theta < 42.3°$. Likewise, for the subsection of the SeaWiFS image, geometries were $23.4° < \theta_0 < 25.6°$ and $49.1° < \theta < 55.4°$. Both land (at the left) and clouds (lower right corner) have been masked in these images.

The July 31, 2001, AVIRIS apparent reflectance mosaic shown in Fig. 3 covers the entire region of Fig. 1b, but makes up only a small portion of the images in Fig. 2. The AVIRIS data consists of six runs during the local morning, i.e., from 13:47 GMT to 14:49 GMT (f010731t01p03_r0[2-7]). During that time, the solar zenith angle varied from 46.7° to 36.2°. For the mostly level flight of the ER-2, the AVIRIS images had the typical ~30° wide, nadir-oriented field of view. Figure 2 shows five of the six runs; run r03 evenly overlaps runs r02 & r04, and is omitted from the mosaic. The start and stop times, as well as the values for the solar zenith angle, solar azimuth angle, and heading at the center of the flight lines are listed in Table 1. The AVIRIS flight lines were planned to

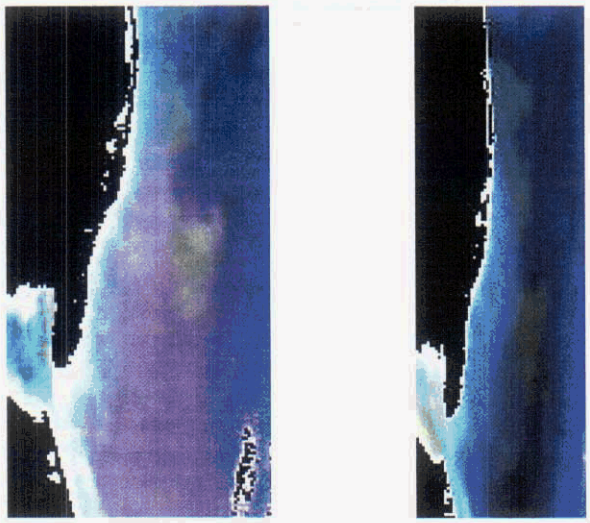

Figure 2: MODIS (left) and SeaWiFS (right) images of similar areas of the New Jersey coast around the LEO-15 site. Both images show observed reflectance, i.e., $\pi L_{obs}/(\mu_0 E_0)$ from 2001 July 31. The MODIS image (channels 13, 12, and 9) was obtained about 16:24 GMT, and the SeaWiFS image (channels 6, 5, and 2) was obtained about 18:00 GMT. Delaware Bay and Cape May, N.J., are easily recognized in the mid-lower left portion of each image. Neither image has been geometrically corrected.

overlap at the edges, to be mostly parallel, and to fly into or out of the sun to reduce the specular reflection of the direct solar beam from the ocean surface. Additional AVIRIS flights were obtained beginning 24 hours later on August 1, 2001 (f010801t01p03_r0[2-7]), along essentially the same flight paths. The August 1, 2001, data set has some offshore clouds in it, and was not studied for this paper. This area was also previously imaged in 1998 using AVIRIS (f980712t01p02_r03) along a flight line with very similar parameters to f010731t01p03_r03. A close examination of the AVIRIS mosaic shows that the features on the land do not quite overlap in neighboring runs. The georectification will be improved once we obtain the 10Hz navigation files for each of the flight lines, and will be necessary for some comparisons with data obtained from instruments in the ocean.

In comparison with Fig. 2, the MODIS and SeaWiFS images present a snapshot of the whole region, and allow for very uniform lighting conditions across the image since θ_0 and θ change very little across these sub-images, and even less over the smaller area spanned by the AVIRIS mosaics. In the AVIRIS mosaic one can easily see the lighting variations on the different runs, and even cross-track lighting variations within a run. On the other hand, the much smaller GSD of the AVIRIS image allows us to see many features in the coastal waters, estuaries, and bays that are not resolved in the MODIS and SeaWiFS images. The hyperspectral nature of AVIRIS allows researchers to determine aerosol parameters, as well as the promise of being able to derive in-water parameters such as bottom classification and bathymetry (Mobley et al. 2002; Lee et al. 2001), work that typically cannot be done with large-GSD multispectral imagers.

4 ATMOSPHERIC CORRECTION OF THE AVIRIS SCENES

We are in the process of correcting the AVIRIS scenes for atmospheric effects. For this work, we are using the latest version of Tafkaa, which allows for more exact corrections of solar and view geometry, as described in Montes et al. (2003). We assumed the pixel-to-pixel angular separation was 0.8715 milliradians, and that AVIRIS was mounted so that the center of the scan was nadir viewing. There are small deviations in roll and pitch that affect the pointing of the sensor (and therefore the view geometry); these have been ignored at this point. The solar zenith angle was computed for the center of each 614 sample line of data using the 1 Hz updated values of the latitude, longitude, and time, and assuming a flat surface, so the solar zenith angles change only every 12 lines, which is sufficient for a scene this size.

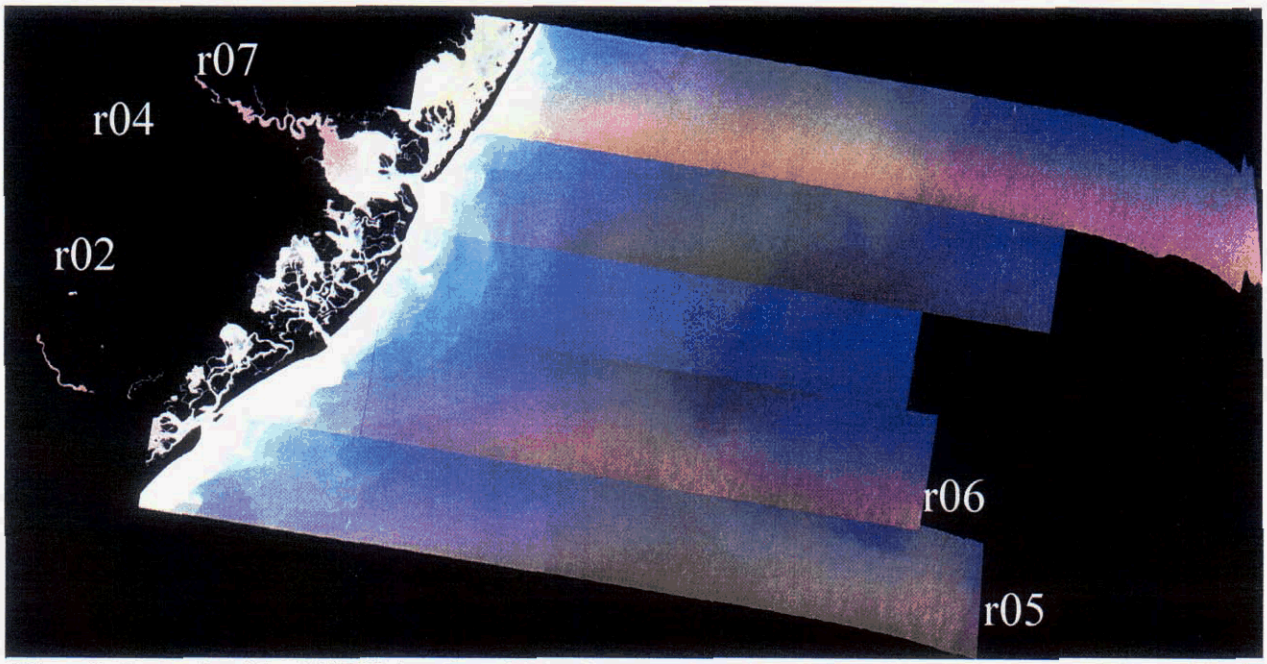

Figure 3. A mosaic of the AVIRIS data from 2001 July 31, excluding run r03 since it overlaps parts of runs r02 and r04. The times, headings, and solar geometry for each flight line are listed in Table.1. This RGB is made from apparent reflectance [$\rho_a = \pi L_{obs}/(\mu_0 E_0)$] maps at 664, 548, and 442 nm. The colors have been stretched to emphasize the features in the deep water. The georectification for this image used the AVIRIS provided *.igm files.

Table 1. The times and geometric information for the AVIRIS runs over the LEO-15 site on 2001 July 31. θ_0 is the mean solar zenith angle, ϕ_0 is the mean solar azimuth angle, and Θ_h is the mean heading for each run.

	GMT		Degrees		
Run	Start	End	θ_0	ϕ_0	Θ_h
r02	13:46:49	13:52:14	46.	102.7	100
r03	13:58:16	14:04:20	44.	105.3	280
r04	14:09:21	14:16:54	42.	107.7	99
r05	14:20:26	14:26:32	40.	109.8	279
r06	14:31:01	14:37:58	38.	112.5	100
r07	14:43:17	14:49:24	36.	116.3	279

As mentioned previously, we must assume that $L_w = 0$ for certain wavelengths in order to derive the aerosol parameters from the data. False-color RGB images constructed from combinations of the aforementioned channels can assist in the choice. Ideally, we choose 3 or 4 channels in which there is no variation in radiance that can be associated with in-water features, as well as being the bluest channels available (since the solar irradiance, and hence the measured signal, decreases as the radiance increases in the NIR and SWIR).

For this example, we show the results from run 4, scene 5 (f010731t01p03_r04_s05), a region associated with the fronts east-southeast of Great Bay in run 04 (see Figs. 1 & 3). The images both before and after atmospheric correction are shown in Fig. 4. The ER-2 was flying from the top of the image to the bottom of the image, and the sun was about 8° to the right of the plane (i.e., on the left side of the image). In both images, it is easy to see a wave

pattern due to swells, and it is more prevalent on the sunward side of the image. In this example, we use a version of Tafkaa that determines aerosol properties at each pixel, using the NIR/SWIR windows. The output image is on the left side of Fig. 4., output spectra from the labeled areas are shown in Fig. 5. The output image shows wave features that are more prominent than in the input scene. The reason for this is quite simple: the brighter swells are interpreted as being a different aerosol, usually one that is more optically thick. Subtracting this (wrong) aerosol from the observed spectrum give a result where because of the large swell pattern, much of the output spectrum is negative. In this case, the best approach is to either input the aerosol type from measurements made at the time of the overflight, or to determine the aerosol parameters from select pixels in clear water that avoids the swells. Either approach may be used with Tafkaa.

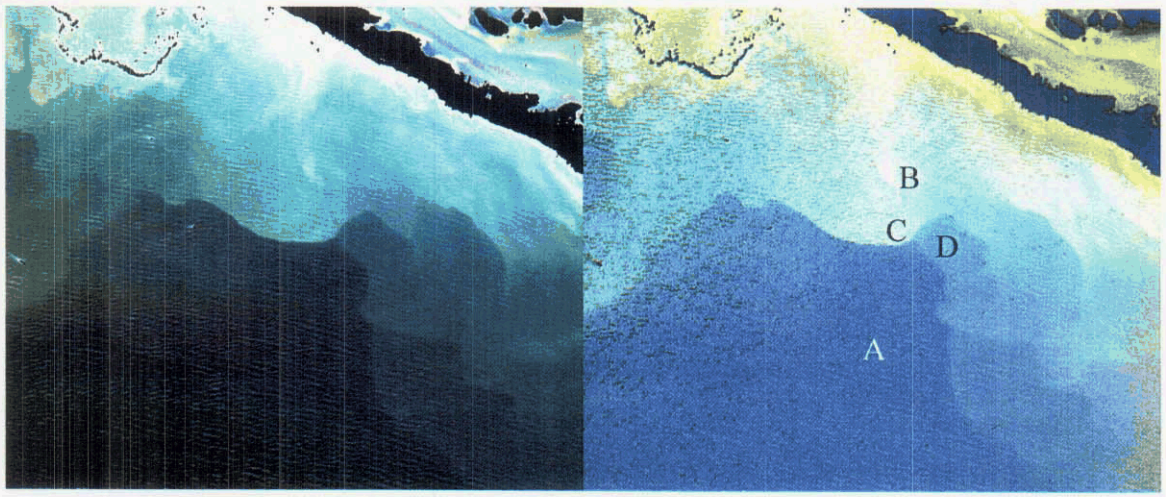

Figure 4. Apparent reflectance image of non-georectified run04, scene05 before atmospheric correction (left), and the same image after atmospheric correction (right). In both cases, the bands used to construct the RGB image are the same as in Fig. 2. The land has been masked in each image. Slopes of swells are obvious in both the uncorrected and corrected images, and are discussed in the text.

Having said that, there are many regions that return quite reasonable water-leaving reflectance (ρ_w) spectra, as shown in Fig. 5. The chlorophyll fluorescence peak is apparent at about 0.685 μm in all the spectra, indicating a high level of phytoplankton. The brightest spectrum (B) shows a small feature at about 0.810 μm that is due to a local minimum in the liquid water absorption spectrum and therefore indicates the presence of very shallow water or extremely high levels of suspended sediments in the top few meters of water.

5 DISCUSSION

Atmospheric correction of aquatic scenes is quite challenging since we must subtract most of the observed signal in order to obtain the water-leaving reflectance. Indeed, in the NIR/SWIR spectral regions we subtract *all* of the observed radiance since we assume the observed signal in this portion of the spectrum is entirely due to the atmosphere and specular reflection due to skylight. Stringent requirements for spectral and radiance calibration become very important in this environment. At such low light levels we see artifacts from the sensor, as well as artifacts in the method (i.e., improperly corrected swells). Research is ongoing in determining the best treatment of swells. Masking swells is an option, but might remove too many pixels from some scenes. Applying a uniform aerosol over the scene avoids selection of the wrong aerosols over swells, but it does not correctly account for the varying specular reflection over the swell's slopes.

6 ACKNOWLEDGEMENTS

The authors gratefully acknowledge the support of the U.S. Office of Naval Research for this research. M. Moline gratefully acknowledges the support of NASA (NAG5-8674).

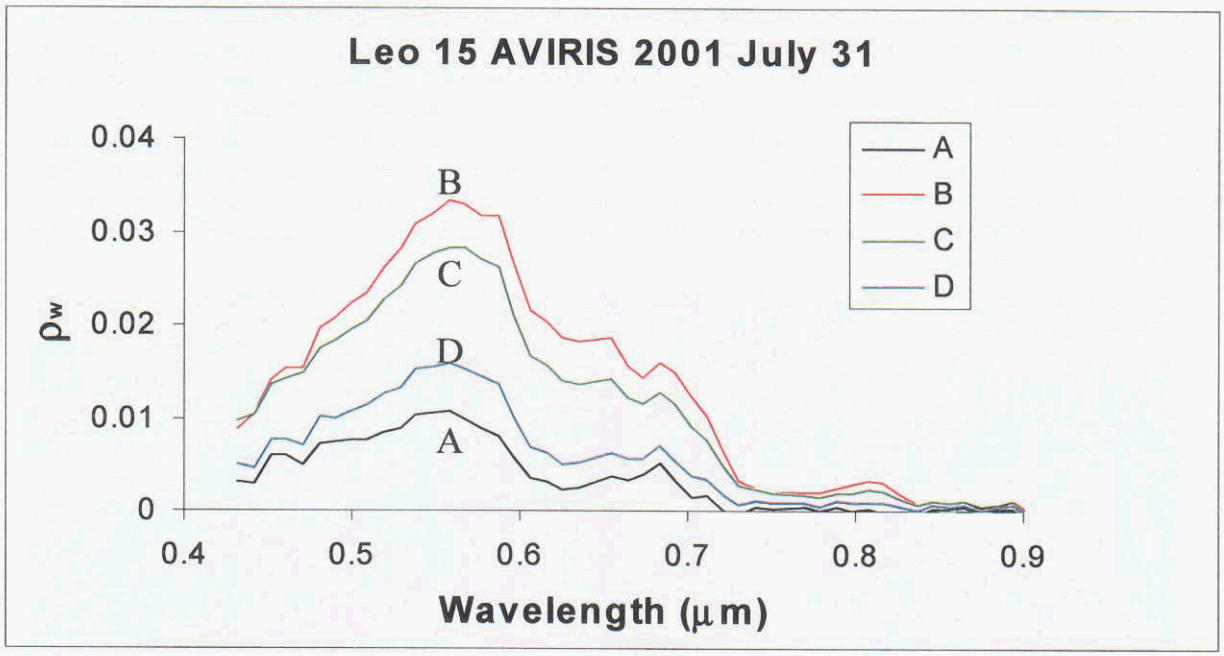

Figure 5. Atmospherically corrected water leaving reflectance (ρ_w) spectra from the labeled regions in Fig. 4.

7 REFERENCES

Ahmad, Z. and R. S. Fraser, 1982, "An iterative radiative transfer code for ocean-atmosphere systems," *J. Atmos. Sci.*, 39, 656-665.

Cox, C., and W. Munk, 1954, "Statistics of the sea surface derived from sun glitter," *J.Mar. Res.*, 14, 63-78.

Fraser, R. S., S. Matoo, E.-N. Yeh, and C. R. McClain, 1997, "Algorithm for atmospheric and glint corrections of satellite measurements," *J. Geophys. Res.*, 102, 17107-17118.

Gao, B.-C., M. J. Montes, Z. Ahmad, and C. O. Davis, 2000, "Atmospheric correction algorithm for hyperspectral remote sensing of ocean color from space", *Appl. Opt.*, 39, 887-896.

Gordon, H. R., 1978, "Removal of atmospheric effects from satellite imagery of the oceans," *Appl. Opt.*, 17, 1631-1636.

Gordon, H. R., 1997, "Atmospheric correction of ocean color imagery in the Earth Observing System era," *J. Geophys. Res.*, 102, 17081-17106.

Gordon, H. R. and M. Wang, 1994, "Retrieval of water leaving radiance and aerosol optical thickness over the oceans with SeaWiFS: A preliminary algorithm," *Appl. Opt.*, 33, 443-452.

Lee, Z., K. L. Carder, R. F. Chen, and T. G. Peacock, 2001, "Properties of the water column and bottom derived from Airborne Visible Infrared Imaging Spectrometer (AVIRIS) data," *J. Geophys. Res.*, 106, No. C6, 11639-11651.

Mobley, C. D., L. K. Sundman, C. O. Davis, M. J. Montes, W. P. Bissett, 2002, "A Look-Up-Table Approach to Inverting Remotely Sensed Ocean Color Data," on the *Ocean Optics XVI* compact disc.

Montes, M. J., B.-C. Gao, and C. O. Davis, 2001, "A new algorithm for atmospheric correction of hyperspectral remote sensing data," in *Geo-Spatial Image and Data Exploitation II*, W. E. Roper, ed., *Proc. SPIE*, 4383, 23-30.

Montes, M. J., B.-C. Gao, and C. O. Davis, 2003, "Tafkaa atmospheric correction of hyperspectral data," in *Imaging Spectrometry IX*, S. S. Shen and P. E. Lewis, eds., *Proc. SPIE*, 5159, in press.

Wieliczka, D. M., S.-S. Weng, and M. R. Querry, 1989, "Wedge shaped cell for highly absorbent liquids: Infrared optical constants of water", *Appl. Opt.*, 28, 1714-1719.

Methods for Detecting Anomalies in AVIRIS Imagery

Brian S. Penn
Mark W. Wolboldt
MASINT Resource Center
Boeing
1330 Inverness Drive, Ste. 330
Colorado Springs, Colorado 80910
Tel. (719) 572-8142
Email: Brian.S.Penn@Boeing.com

Introduction

At a very small scale the Earth's surface is heterogeneous, but the spatial resolution of current satellite and airborne sensors gives the appearance of homogeneity. This is an artifact of digital sensors that integrate the signal over well-defined instantaneous angular fields of view and spectral ranges. Because of limitations in spatial resolution, cursory examination of remotely-sensed imagery data leads to the conclusion there is a significant amount of redundant information, i.e., there are many similar pixels (picture elements) representing homogenous materials. Because so many pixels have similar spectra, finding anomalous pixels is a non-trivial problem.

Significant effort has been spent on classifying pixels in imagery. The goal of image classification is to group spectrally similar pixels together to the exclusion of anomalous pixels, i.e., separate the many from the few. Most classification methodologies do not easily lend themselves to the extraction of anomalous pixels. The reason for this is that these general classification algorithms address the relatively simple problem of analyzing the majority of the pixels. Nonetheless, it is useful to examine general classification approaches in the context of the method detailed here for anomaly detection.

The goal of anomaly detection is to find pixels that are significantly different from the majority of the pixels in an image, i.e., separate the few from the many. The definition of anomalous is rather arbitrary, but it can be expressed statistically, i.e., 2σ, or standard deviations, from the mean of a population with an assumed distribution, or merely as a proportion of the whole dataset, i.e., representing only $<<1$ % of the whole, etc.

Local anomaly detectors generally consider only the surrounding pixels to determine the nature of a pixel and are susceptible to noise, e.g., RX anomaly detection (Yu, Reed, and Stocker, 1993; Yu, et al., 1997). Global anomaly detectors evaluate each pixel in comparison to the entire image. The global approach generally alleviates problems associated with local variations in data values.

The purpose of this paper is to explore methods for finding anomalous pixels in AVIRIS imagery. Toward this end several approaches are described in detail beginning with the simplest and progressing to more complicated techniques. For completeness, a brief overview of finding anomalies using conventional supervised classification is also presented. Histograms are introduced first, followed by simple statistical measures, and concluding with the use of Self-Organizing Maps.

Location of Study Area

The Jet Propulsion Laboratory's Airborne Visible Infrared Imaging Spectrometer (AVIRIS) was flown over the Copper Flat (CF) porphyry copper deposit in the summer of 1998. The CF mine is 8 km NNE of the hamlet of Hillsboro in south-central New Mexico (Figure 1). The CF mine is in the Animas Hills and is part of the Hillsboro mining district of Western Sierra County, New Mexico. CF is one of the older Laramide porphyry-copper deposits in the Arizona-Sonora-New Mexico porphyry-copper belt (McLemore, et al., 1999). The Animas Hills consist of a horst block just west of the axis of the Rio Grande rift underlain by a circular body, nearly four miles in diameter, of andesite. Andesite is a fine-grained volcanic igneous rock extruded on the Earth's surface. The thickness of the andesite and circular shape suggest that the andesite is a remnant of a Cretaceous (144-65 million years ago) caldera or

collapsed volcano. A relatively small body of quartz monzonite intruded the andesite forming the entire CF deposit. Monzonite is a coarse-grained intrusive igneous rock. CF is predominately a low-grade hypogene (hydrothermal fluids carrying minerals up from below) deposit with thin veneer of supergene (meteoric water percolating from above) enrichment at the surface. The numerous latite dikes radiating from the CF quartz monzonite also show significant mineralization. The CF mine produced large quantities of gold, silver, and copper since the late 1800s.

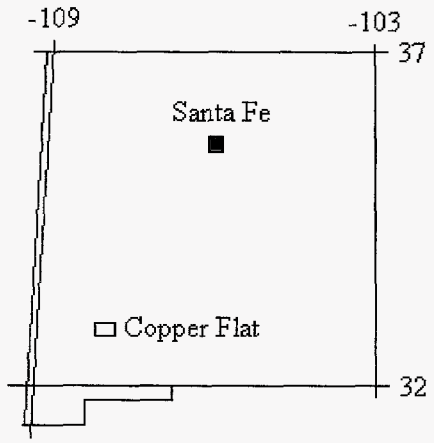

Figure 1 – Location of Copper Flat porphyry copper deposit in New Mexico.
The deposit is located 15 km west of the town of Truth or Consequences.

Gypsum ($CaSO_4 * 2(H_2O)$) is an anomalous mineral occurring only in close proximity to the pit filled with water at the center of the mine and along some of the streambeds in the Hillsboro district. Gypsum occurs as coatings of precipitate on the rocks surrounding the pit and comes from the pit waters. As such, gypsum was selected as the target to test the anomaly detection algorithms.

Finding Anomalies Using Supervised Classification Techniques

In general, supervised image classification is the process by which a classifier is presented with pixels of "known" contents that are used as a guide(s) for classifying other pixels in an image. The classifier function is "seeded" with *a priori* information about particular material types. The classification algorithm then determines which pixels are most like the "seed" pixel based on a similarity condition. Examples of supervised classification techniques include minimum distance, parallelepiped, mahalanobis distance and maximum likelihood. Set membership for these supervised classification techniques is based on Euclidian distance, standard deviation values, etc. A major assumption for these types of classifiers is that the data is linearly separable, i.e., the data is arranged such that a line (or plane or hyperplane) can be situated between different data classes.

Using *a priori* information for target identification is a useful but awkward method of finding anomalies because it is not based on set membership, but the logical negation of set membership. The premise of this approach is to classify every known spectrum and tag as anomalous any pixel that is not recognized.

Using a supervised classification approach to identify anomalies requires possessing a spectral library. Assuming the spectral library is well-populated, any pixel's spectral absorption features not found in the library are classified as anomalous. The U.S.G.S.'s Tetracorder operates in this manner. Tetracorder contains an extensive library of mineral spectra. If Tetracorder is unable to classify a pixel's spectrum, the classification is left blank. This pixel is then considered anomalous.

Unfortunately, this approach is has shortcomings. For example: if the number of material types within an image are not correctly identified prior to processing, then there can be a large numbers of pixels omitted because a class was not properly identified. The result is significant uncertainty in

determining whether a pixel is anomalous or merely incorrectly selected as a member of a larger group of pixels in the image. It is for this reason that unsupervised classification is more appropriate for anomaly detection.

Unsupervised Anomaly Detection

Global Histogram Technique

Histograms are graphs describing the frequency of occurrence for members of a dataset. In the context of imagery, a histogram graphs the digital number on the abscissa and the frequency on the ordinate axis. Histograms are a central concept in remote sensing because they enable image analysts to compress the information in an image into a simple format. One significant use for histograms is to enhance digital images through the use of various contrast stretches, i.e., linear, 2%, Gaussian, square root, etc. Often, as is the case with the linear and 2% stretches, the digital numbers (DNs) with the highest and lowest values are linearly translated to the largest and smallest radiometric values, i.e., for 8-bit data the lowest value is set to 0 and the highest value is translated to 255 with the remaining values linearly mapped between these two values.

For the purpose of anomaly detection, histograms are used in a slightly different manner. The two tails of the histogram are the extremes of the imagery DN population with the lower end representing the darkest pixels and the upper tail representing the brightest pixels. Pixels that repeatedly occur at the tails of histograms represent anomalies. A simple procedure is used to identify these pixels.

First a threshold is arbitrarily selected to mark a pixel as anomalous (< 2%). Next, a histogram for each band is generated and each pixel falling above or below a population threshold is recorded. The result is a two-dimensional array corresponding to the image with counts for high and low ends of the histogram. These images are then further constrained to show the highest number of counts for each tail of the histogram and a color-coded image is generated (Figure 2). In the CF imagery, there are known anomalous areas of gypsum near the mine pit. Figure 3 shows results of applying the histogram anomaly detection for the pit and surrounding pixels with an accompanying average spectra for surface materials adjacent to pit lake.

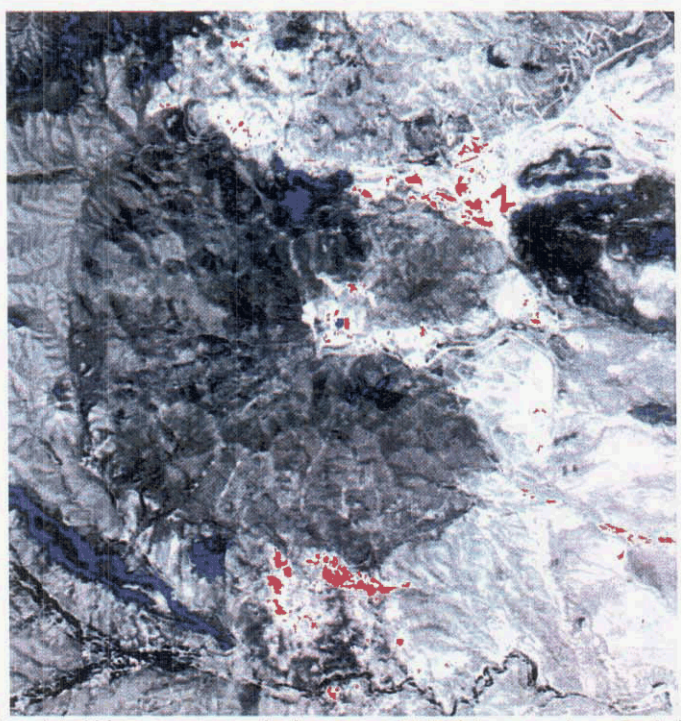

Figure 2 – Results of applying global histogram anomaly detector to AVIRIS imagery data. Red pixels are anomalously bright, blue pixels are anomalously dark. Water in the pit is blue, gypsum is found in pixels adjacent to pit lake.

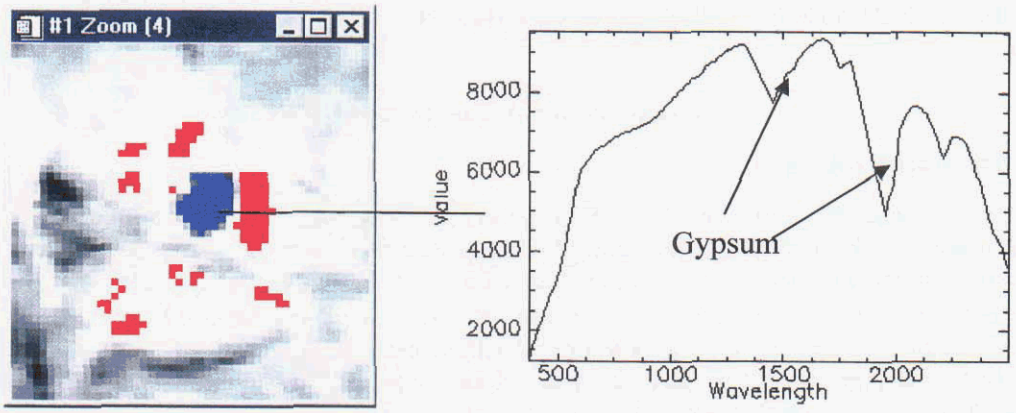

Figure 3 – Image of mine pit with average spectra for area of red pixels to the right of lake in middle. The absorption feature at 2208 nm results from overtones of the sulfate ion restrahlen bands at longer wavelengths. Other red pixels are anomalously bright, but contain no gypsum. Red pixels are anomalously bright, blue pixels are anomalously dark.

Simple Statistical Techniques

A common technique for finding anomalies in a dataset is to examine the data from the perspective of simple statistics. Most familiar statistical models are based on Gaussian or normal distribution, i.e., a bell-shaped curve. The assumptions for a normal distribution are: 1) most samples for any particular dataset are evenly distributed about the mean, or average, for a dataset with proportionately smaller numbers of members occurring progressively farther from the mean; and 2) the mode (greatest number of samples) and the mean for a dataset are the same. This is the basis for variance and standard deviation (σ) calculations. If the assumption of a normal distribution is not true, then basic statistical assumptions may not be valid. Nevertheless, the assumption is usually made that the data have a normal distribution and simple statistics such as variance and standard deviation are applicable. This appears to be a reasonable assumption for satellite and airborne images of the earth.

When working with standard deviation calculations it is necessary to know how much of the area under the curve (percentage of the sample population) is encompassed by various standard deviations. Values occurring $\pm 1\sigma$ from the mean include 68.3% of all the samples; $\pm 2\sigma$ and $\pm 3\sigma$ include 95.4 % and 99.7%; respectively. If an anomalous pixel is described as 1% of a population, then it should have a value that deviates more than $\pm 2\sigma$ from the mean.

Using this approach, the difference between pixels with values less than 2σ below the mean and those values greater than 2σ above the mean are separated. The result of applying this approach to imagery is shown in Figures 4 and 5.

Local Anomaly Detectors

Both the histogram and stand deviation techniques can be applied to an entire image. These approaches distinguish global anomalies, but some features can be globally typical yet locally anomalous. The way to address these types of anomalies is to constrain comparisons between each pixel and its surrounding neighborhood. The process of comparison is achieved by using the standard deviation criteria outlined above to the local environment around the pixel of concern. The results of this approach are shown in Figure 6. In general the larger anomalies were found by differing kernel sizes, but as expected anomalies are scale dependent. Also, the larger the kernel size, the greater the resulting anomalies are smoothed.

One of the reasons for color-coding the results in the previous examples is that there are anomalous bright and dark pixels. Another approach for comparing pixels is to treat spectra as vectors in n-space and use the Cauchy-Schwarz Inequality (1) to determine the angular distance between spectra. This approach has the additional benefit of ignoring differences in illumination

$$\cos\theta = \frac{\langle u, v \rangle}{\|u\| \, \|v\|} \tag{1}$$

Once again kernels of differing sizes are used to adjust compare to the center pixel. Figure 6 contains the results of this processing. Figures 6 and 7 show a significant decrease in the number of pixels considered anomalous with increasing kernel size.

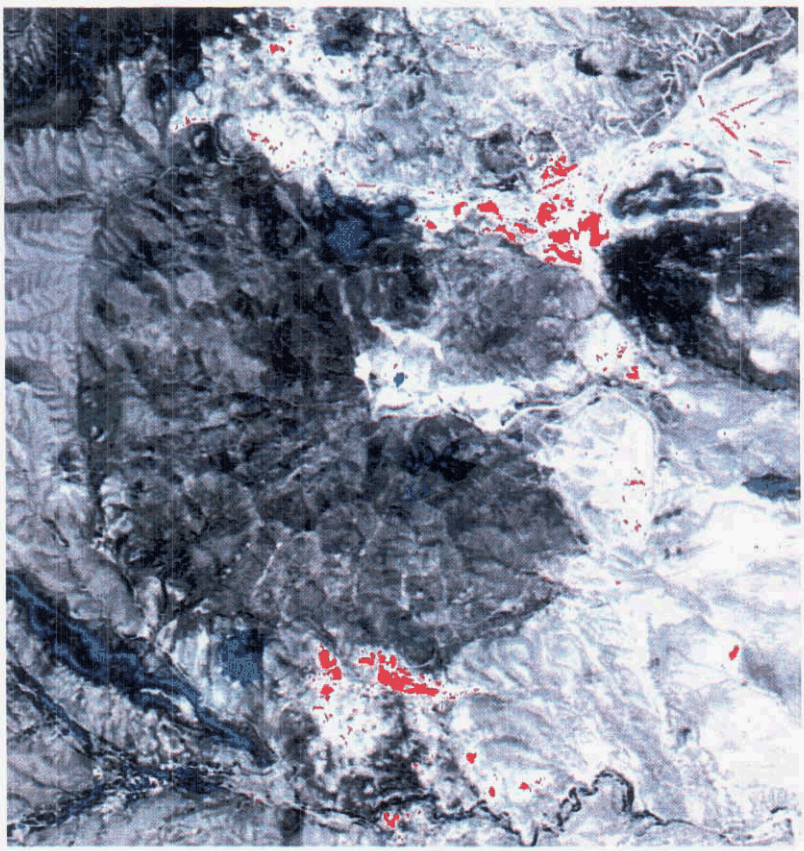

Figure 4 – Output results from standard deviation with threshold at 2.5 σ. Red pixels are those with values > 2.5 σ; blue pixels have values < -2.5 σ.

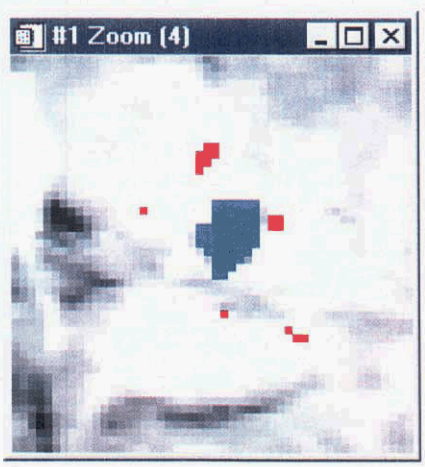

Figure 5 – Magnified image of mine pit lake (blue pixels) with surrounding red pixels.

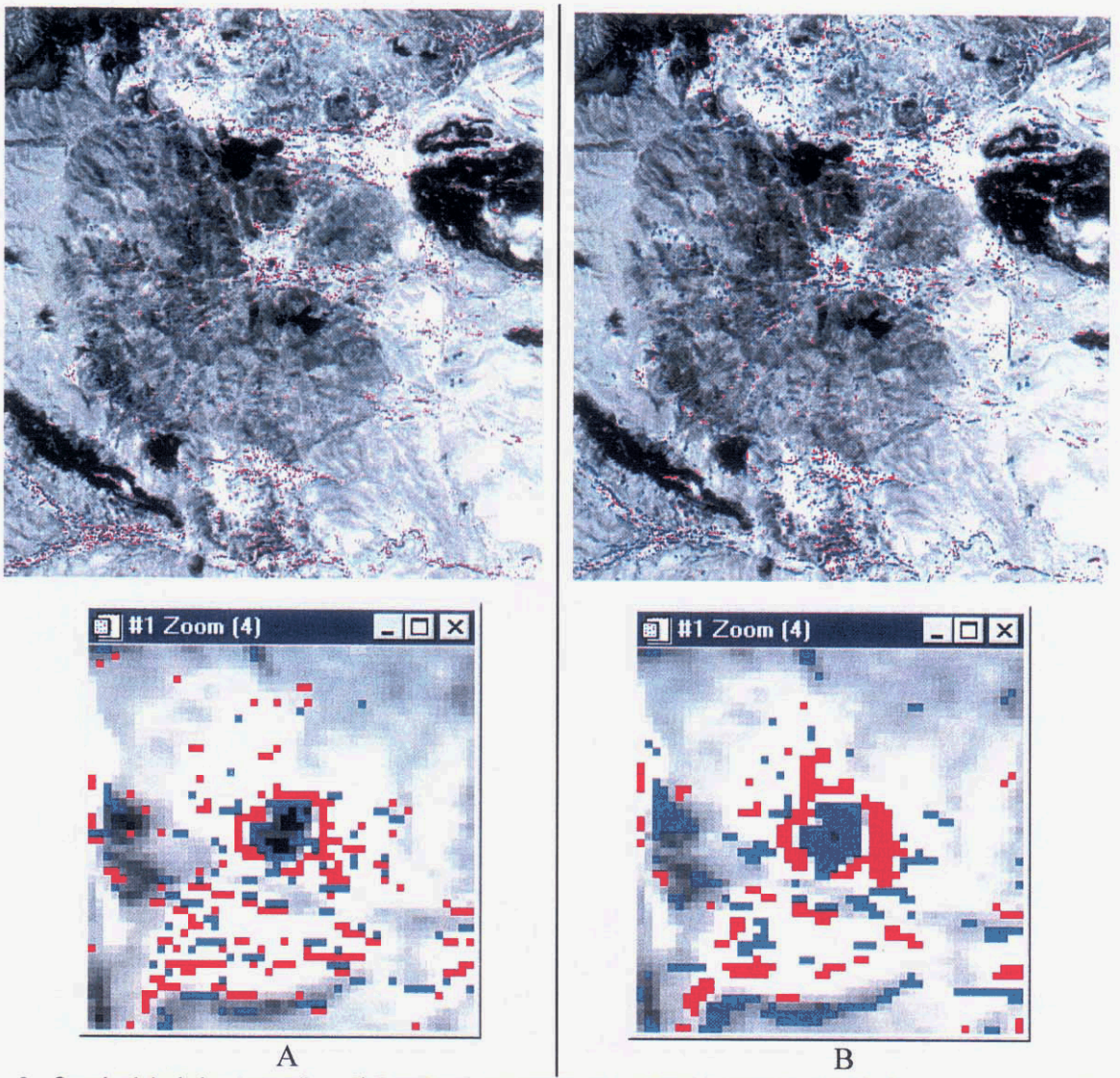

Figure 6 – Standard deviation anomalies. A) Results of performing local anomaly detection using 3x3 kernel with ±2.5σ; B) Results of performing local anomaly detection using 7x7 kernel with ±2.5σ. This approach involves looking at each band and accumulating standard deviation information. Another approach to local anomaly detection uses differences in spectral angle to compare adjacent pixels.

Clustering Techniques

The most common form of unsupervised classification utilizes clustering techniques. Clustering is a non-statistical method for grouping similar data. Clustering methods complement supervised classification. Most unsupervised classification techniques evaluate the entire image data set and assign each pixel to a cluster. There are generally no predetermined limits on the number of clusters. A benefit of this approach is the reduced likelihood of missing a coherent group in the classification process.

Two of the most common unsupervised classification methods are the Iterative Self-Organizing Data Analysis Technique (ISODATA) (Tou and Gonzalez, 1974) and K-Means. ISODATA iteratively evaluates imagery data based on spectral distance from predefined nodes. These nodes are treated as cluster centers and pixels are included in the clusters based on user specified thresholds defined primarily by Euclidian distance or standard deviation values. After each iteration, a new cluster mean is computed based on the actual spectral locations of pixels. These new means are used as the basis for the subsequent iterations. The process continues until change between cluster means falls below a set threshold value.

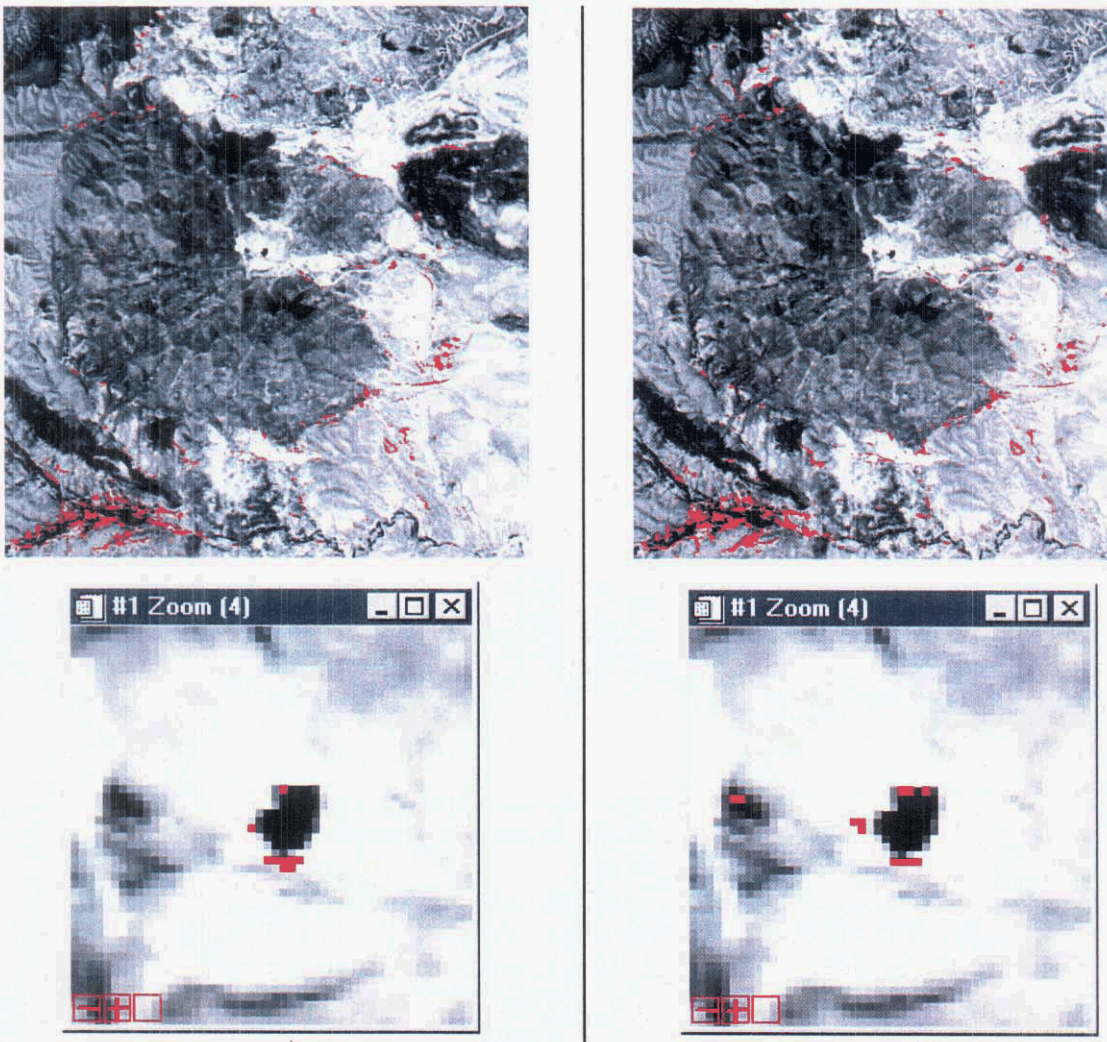

Figure 7 – Spectral angles used to compare pixel with surrounding neighbors. A) 3x3 kernel thresholded to 1%; B) 7x7 kernel thresholded to 1%. Pixels at the bottom of zoom images correspond to gypsum precipitates.

K-Means calculates initial class means evenly distributed throughout the data space. The process then assigns each pixel to the closest cluster. Once all the assignments are made, new cluster means are calculated, followed by the assignment of all pixels to the nearest cluster mean. This process is repeated until the number of user-defined changes fails to occur.

Another clustering technique based on neural networks is Kohonen Self-Organizing Maps (Kohonen, 1986). A Self-Organizing Map (SOM) is an array (1 or more dimensions) of nodes. Each node is composed of a unit vector pointing in a random direction in *n*-dimensional space. After in-band normalization, multi-dimensional data are presented to each of the individual nodes (Figure 8).

Using a "winner-take-all" learning strategy, the node whose vector most closely matches the input data is found. This winning vector incorporates, or adjusts, its vector coefficients (weights) to match the input data. As part of the learning strategy, vectors in the nodes nearest the winning node are modified to look less like the input vector. In this manner, each node in the SOM internally develops the ability to recognize vectors similar to itself. This technique is a form of self-organization, i.e., no external information is supplied to lead to a classification.

Two useful features of a SOM are its topology preserving capability and the automatic generation of probabilities for a dataset. Topology preserving means that the original relationships between the data

points remain intact after processing. This is the desired result when working with hyperspectral data because it maintains the spectral relationships between pixels. Secondly, as a SOM evaluates the data it spontaneously builds a statistical model, or probability distribution, of the dataset. SOMs perform this statistical modeling, even in cases when no closed-form analytic expression can describe the distribution (Caudill, 1988). The SOM approach is similar to ISODATA, but it operates in a much more flexible manner. Cluster centers move around dynamically to account for topological relations in the dataset. Output from the SOM is a series of spectra containing the mean spectra for each cluster group.

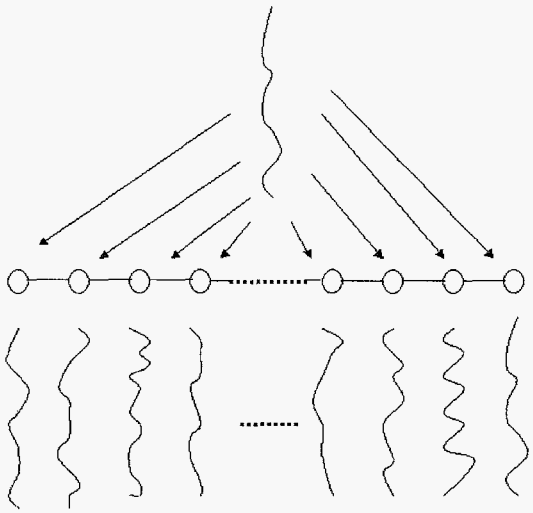

Figure 8 – Kohonen SOM presented with single spectrum input and the resulting spectra developed while processing various input spectra.

During SOM classification the cluster centers constantly adapt themselves to accommodate the spectra presented to them. The end result is a cluster center point representing an average spectrum for the spectra presented to the SOM for classification. The cluster centers are discretely located in *n*-space such that they can be projected into 2-d space (Figure 9). The actual data points lie on the *n*-plane at a distance from the cluster centers forming a cloud or convex hull (or zonatope enclosure) around the cluster centers. Those spectra closest to the cluster center are those that are most abundant while those located farthest away are the least abundant.

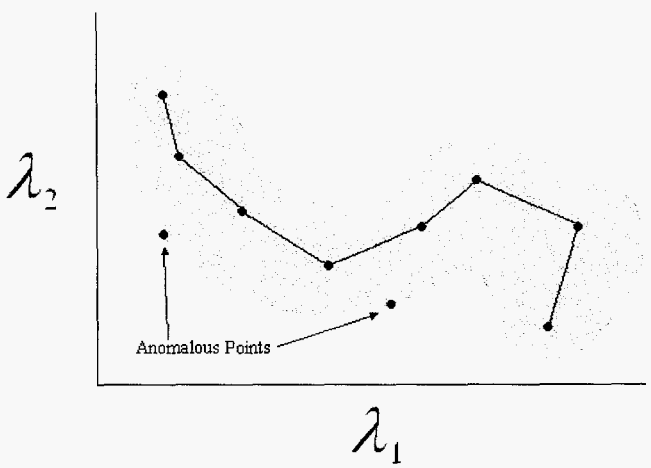

Figure 9 – SOM output for unknown dataset projected into wavelength axes λ_1 and λ_2. Data is arranged around the cluster points in a cloud. Anomalous points lie on the edge of the gray-shaded area indicating least amount of similarity to cluster points. Lines between cluster centers added for emphasis.

After the SOM is built, the spectra are again presented to the SOM for classification. A *2-d* map is generated with the distance from the nearest cluster center stored in the location for each pixel. A density slice of the *2-d* map is then created and those points farthest from a cluster center are identified. Those pixels with the largest values, i.e., greatest distance from a cluster center, are the anomalous pixels.

Data Compression via Minimum Noise Fraction

AVIRIS imagery contains a huge amount of data. A typical AVIRIS data cube contains 614 pixels, 512 lines, and 224 channels totaling slightly more than 170 Megabytes of data. This amount of data presents a significant computational challenge even to the fastest computer. It is possible to compress this amount of data into a manageable form by employing a Minimum Noise Fraction (MNF) transform (Boardman and Kruse, 1994). An MNF transform is a cascade of manipulations including a translation, rotation, scaling and another rotation (essentially an affine transform) of the data.

Stated another way, an MNF is a series of two cascading principal component (PC) transformations resulting in a change of basis for the vector space as defined by the number of bands for each pixel in an image. The high band-to-band correlation inherent in the original data is what makes the MNF so efficient. The net effect of the MNF transform is to compress the variation within the dataset from 224 bands down to 10-20 bands. Reducing the size of number of bands presented to a SOM for classification significantly increases its sped of operation. The results of applying a SOM to an MNF image to find anomalies is shown in Figure 10.

Alternate Hyperspectral Approaches for Anomaly Detection

The most widely known anomaly detection algorithm for hyperspectral data is RX (Reed and Yu, 1990; Yu, Reed, and Stocker, 1993; Yu et al., 1997). The RX algorithm is a variant of the algorithm for generating the Mahalanobis distance and is considered a local anomaly detector. Another way to view the RX algorithm is as the complement of a Principle Components Analysis (PCA), i.e., instead of performing a basis change to maximize the variance into major components emphasis is placed on the finding targets in the minor components. Since SOMs are applied to Minimum Noise Fraction (MNF) bands to generate statistical models, there are significant similarities between these techniques.

Discussion

For hyperspectral imagery, variations of unsupervised classification are possible because methods exist for extracting relevant end-members automatically from imagery based on spectral unmixing (Smith et al., 1985; Barnard and Casasent, 1989; Smith et al., 1990; Roberts et al., 1993; Settle and Drake, 1993; Foody and Cox, 1994; Van der Meer and de Jong, 2000; Penn, 2002). The basic assumption of spectral unmixing is the existence of "pure" pixels (end-members) from which all other pixels in an image can be derived by linearly combining the end-member pixels. While this statement is accurate to a first approximation, the uniqueness of end-member pixels is a function of the method of deriving end-members. Inasmuch as the uniqueness assumption is valid then, based on the method of identifying end-members, there is no guarantee that end-members are homogenous pixels for reasons cited previously. In all probability each end-member pixel is a combination of materials producing a relatively unique integrated signature at the particular resolution of the sensor.

Several tools exist for automatically finding end-members in hyperspectral imagery datasets including N-FINDR (Winter, 1999), ORASIS (Bowles et al., 1995), and Aspect-Sentinel and OSP (Harsanyi, 1993; Harsanyi and Chang, 1994). These programs generally transform the data into various *n*-spaces and fit a convex hull around the dataset. The apices of the hull are treated as the end-members from which all other spectra in the data volume are derived. The logical method for detecting anomalies using this approach is to determine which pixels appear not to fit within the hypervolume generated by the algorithms. These approaches, while automatic, can generate numerous false-alarms especially with the presence of anomalous pixels.

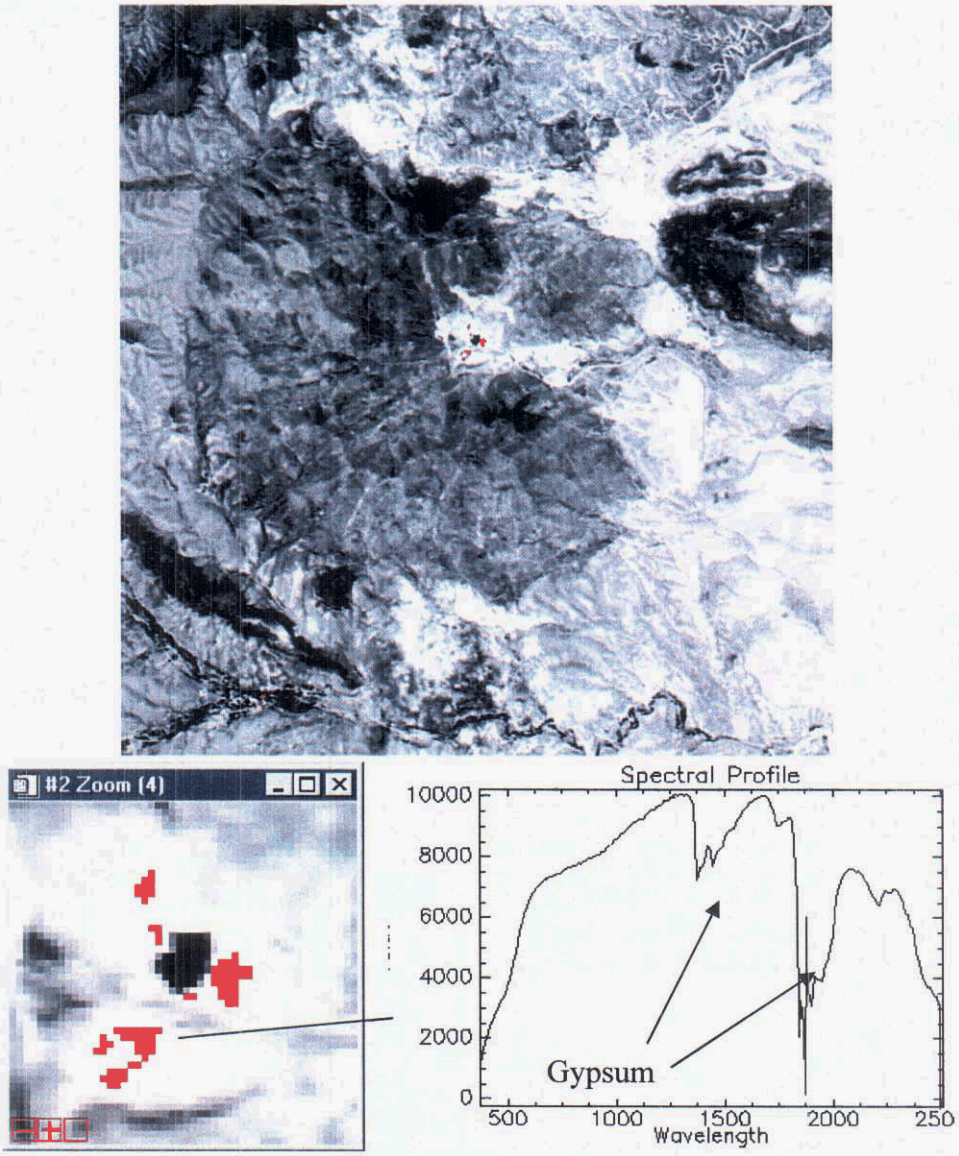

Figure 10 – Results of applying SOM to Copper Flat Imagery. The threshold is set to 0.01% of the output. The most anomalous pixels are found adjacent to the pit lake.

Validation of Anomalies

Once anomalies are detected their uniqueness can be validated using supervised classification methods. Two such methods include Constrained Energy Minimization (CEM) and Spectral Angle Mapper (SAM). This verification process is accomplished by providing proposed anomalous spectra to both CEM and SAM. This is necessary because both techniques require *a priori* information to find targets. An average spectrum from the identified anomalous pixels was provided to both algorithms. CEM and SAM then analyze the image to determine the presence of particular mineral spectra. Both of these approaches corroborate the effectiveness of using SOMs to find anomalous materials (Figure 11).

Conclusions

Several methods for anomaly detection including using Self-Organizing Maps (SOMs) were applied to the AVIRIS imagery of the Copper Flat porphyry copper deposit to extract anomalies. Copper Flat

was selected because it has been mapped extensively and there are several known anomalous occurrences of gypsum ($CaSO_4*2(H_2O)$) near the pit lake in the center of the mine.

The methods employed include both global and local methods of anomaly detection. These methods included using histograms and standard statistical approaches for global analysis. Local anomaly detection methods included standard deviation and spectral angle calculations to ascertain whether a pixel was anomalous compared to neighboring pixels. Each of these approaches was applied to atmospherically corrected data.

The final method used to look for anomalies involved a Self-Organizing Map (SOM). The results from the SOM were slightly more accurate with less clutter as compared to the other approaches. The improved accuracy may have resulted from applying the SOM to data that had a Minimum Noise Transform applied before processing.

The practical use of SOMs to detect anomalies is clearly demonstrated and has been verified by fieldwork. This technique is relatively simple and yields good results. The one drawback is that SOMs are not able to separate out different anomalies. A number of anomalous pixels found using SOMs did not contain any measurable gypsum instead they were dominated by other minerals. The best practical approach is to iteratively use SOMs to locate potential anomalies and use the resulting spectra to classify the image. In this manner the desired anomalies could be found and less desirable anomalies could be eliminated from the processing.

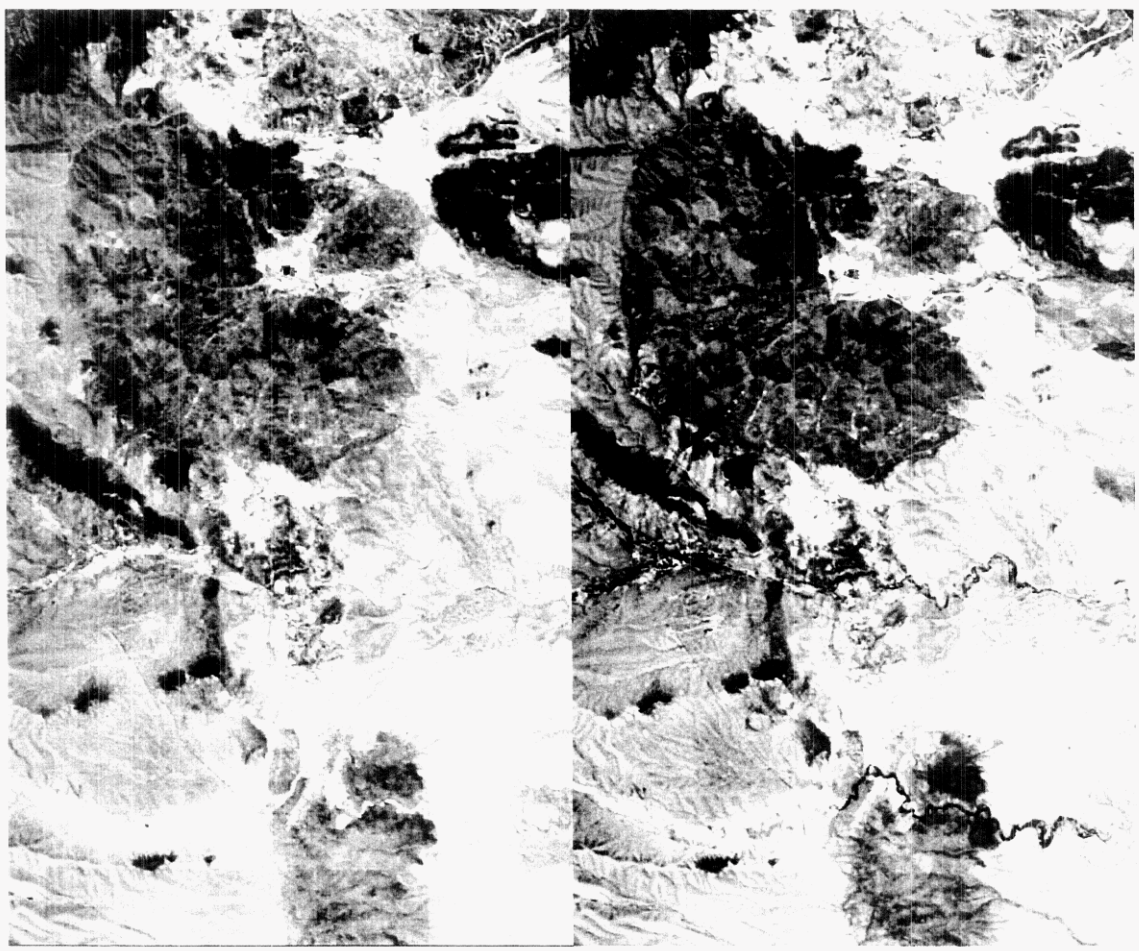

a b

Figure 11 – Results of applying spectral signatures of anomalous pixels using:
a) Constrained Energy Minimization (CEM) and b) Spectral Angle Mapper (SAM).

References

Barnard, E., and Casasent, D. P., 1989. Optical Neural Network for classifying imaging spectrometer data, Applied Optics 28(15), 3129-3133.

Boardman, J.W. and Kruse, F. A., 1994. Automated spectral analysis: a geological example using AVIRIS data, north Grapevine Mountains, Nevada inProceedings ERIM 10th Thematic Conference on Geologic Remote Sensing, Environmental Research Institute of Michigan, p. I407-I418.

Bowles, J. Palmadesso, P., Antoniades, J., Baumbeck, M., and Rickard, L.J. 1995. Useof Filter Vectors in Hyperspectral Data Analysis, Infrared Spaceborne RemoteSensing III, Scholl, M.S., and Anderson, B.F. (eds.), SPIE 2553, 148-157.

Caudill, M. 1988. Neural Networks Primer, Part IV, AI Expert, vol. 3(8), August 1988,61-67.

Foody, G.M., and Cox, D. P., 1994. Sub-pixel land cover composition estimation using a linear mixture model and fuzzy membership functions. International Journal of Remote Sensing 15(3), 619-631.

Harsanyi, J.C. (1993) Detection and Classification of Subpixel Spectral Signatures in Hyperspectral Image Sequences, Ph.D. Dissertation, University of Maryland, Baltimore County, 116 p.

Harsanyi, J.C. and Chang, C. 1994. Hyperspectral Image Classification and Dimensionality Reduction: An Orthogonal Subspace Projection Approach, IEEETransactions on Geoscience and Remote Sensing, vol. 32(4), 779-785.

Kohonen, T. 1986. Representation of Sensory Information in Self-Organizing Feature Maps and Relation of these Maps to Distributed Memory Networks, Proceedings of SPIE Advanced Institute on Hybrid and Optical Computing, vol. 634.

McLemore, V.T., Munroe, E.A., Heizler, M.T., and C. McKee. 1999. Geochemistry of the Copper Flat porphyry and associated deposits in the Hillsboro mining district, Sierra County, New Mexico, USA, Journal of Geochemical Exploration, vol. 67, 167-189.

Penn, B.S. 2002. Using Simulated Annealing to Obtain Optimal Linear End-member Mixtures of Hyperspectral Data," Computers & Geosciences, vol. 28(7), 809-817.

Reed, I.S. and Yu, X. 1990. Adaptive multiple-band CFAR detection of an optical pattern with unknown spectral distribution, IEEE Transactions on Acoustics, Speech and Signal Processing, vol. 38, 1760-17770.

Roberts, D.A., Smith, M.O., Adams, J.B., 1993. Green Vegetation, Nonphotosynthetic Vegetation, and Soils in AVIRIS Data. Remote Sensing of the Environment 44, 255-269.

Settle, J.J., and Drake, N.A., 1993. Linear mixing and the estimation of ground cover proportions, International Journal of Remote Sensing 14, 1159-1177.

Smith, M. O., Johnston, P.E., and Adams, J.B., 1985. Quantitative determination of mineral types and abundances from reflectance spectra using principal component analysis, Journal of Geophysical Research (90), 797-804.

Smith, M.O., Ustin, S.L., Adams, J.B., Gillespie, A.R., 1990. Vegetation in Deserts I: A Regional Measure of Abundance from Multispectral Images. Remote Sensing of the Environment 31, 1-26.

Tou, J.T., and Gonzalez, R.C. 1974. Pattern Recognition Principles, Reading, Massachusetts, Addison-Wesley Publishing Company, New York.

Van Der Meer, F., and De Jong, S.M., 2000. Improving the results of spectral unmixing of Landsat Thematic Mapper imagery by enhancing the orthogonality of end-members, International Journal of Remote Sensing (21:15), 2781-2797.

Winter, M. E. 1999. Fast Autonomous Spectral End-member Determination in Hyperspectral Data, 13th International Conference on Applied Geologic Remote Sensing, Vancouver, British Columbia, March 1-3, 1999, II-337-344.

Yu, X., Reed, I.S., and Stocker, A.D. 1993. Comparative performance analysis of adaptive multispectral detectors, IEEE Transactions on Signal Processing, vol. 41, 2639-2656.

Yu, X., Hoff, L.E., Reed, I.S., Chen, A.M., and Stotts, L.B. 1997. Automatic Target Detection and recognition in multispectral imagery: A unified ML detection and estimation approach, IEEE Transactions on Image Processing, vol. 6, 143-156.

THE USE 0F AVIRIS IMAGERY TO ASSESS CLAY MINERALOGY AND DEBRIS-FLOW POTENTIAL IN CATARACT CANYON, UTAH: A PRELIMINARY REPORT

Lawrence Rudd[1] and Erzsébet Merényi[2]

1.0 Introduction

Worldwide debris flows destroy property and take human lives every year (Costa, 1984). As a result of extensive property damage and loss of life there is a pressing need to go beyond just describing the nature and extent of debris flows as they occur. Most of the research into debris-flow initiation has centered on rainfall, slope angle, and existing debris-flow deposits (Costa and Wieczorek, 1987). The factor of source lithology has been recently addressed by studies in the sedimentary terranes of Grand Canyon (Webb et al., 1996; Griffiths et al., 1996) and on the Colorado Plateau as a whole.[3] On the Colorado Plateau shales dominated by kaolinite and illite clays are significantly more likely to be recent producers of debris-flows than are shales in which smectite clays dominate.[3]

Establishing the location of shales and colluvial deposits containing kaolinite and illite clays in sedimentary terranes on the Colorado Plateau is essential to predicting where debris flows are likely to occur. AVIRIS imagery can be used to distinguish between types of clay minerals (Chabrillat et al., 2001), providing the basis for surface-materials maps. The ultimate product of this study will be a model that can be used to estimate the debris-flow hazard in Cataract Canyon, Utah. This model will be based on GIS overlay analysis of debris-flow initiation factor maps, including surface-materials maps derived from AVIRIS data.

2.0 Debris-Flow Initiation

The mobility and transport competence of debris flows depends on a source of fine-grained material, particularly silt and clay, that serves as debris-flow matrix. In Grand Canyon this material is provided by the Hermit Shale, a terrestrial shale containing mostly (95%) illite and kaolinite clays (Griffiths et al, 1996). Kaolinite and illite-rich shales that have been identified as debris-flow source areas on the Colorado Plateau also have relatively high concentrations of exchangeable K^+ and Mg^{++} cations and low amounts (<15%) of Na^+ cations.[3] Smectite clays have the capacity to absorb large amounts of water. One possible mechanism by which smectite clays reduce the likelihood of debris-flow activity involves rapid absorption of water during initial wetting. Smectites that have absorbed water will swell and seal off underlying areas, effectively stabilizing colluvial deposits by preventing further water absorption.

When a debris flow occurs, sand and smaller-sized particles occupy interstitial spaces in the debris-flow slurry, increasing the density of the matrix and the buoyant forces that contribute to the suspension of larger particles (Beverage and Culbertson, 1964, Hampton, 1975, Rodine and Johnson, 1976). The clay constituents of Grand Canyon debris flows, which provide 2-5 % of the total particles, are 60-80 % illite and kaolinite by weight, reflecting the source materials of terrestrial shales and colluvial wedges (Griffiths et al., 1996). Debris flows are responsible for creating virtually all of the rapids in Grand Canyon (Webb et al., 1988). Debris flows that travel significant distances in Grand Canyon occur most often when the Hermit Shale, or its associated colluvial wedges, outcrop at a height of 100 m or more above the river (Griffiths et al., 1996). This association between the Hermit Shale and debris flows in Grand Canyon indicates that lithology is an important factor in identifying debris-flow source areas. Other factors identified by Griffiths et al. (1996) include drainage area, channel gradient, and aspect of drainages that produce debris flows.

The relationship between the presence of terrestrial shales and an increased probability of debris-flow occurrence that was established in Grand Canyon has been observed in several other canyons on the Colorado Plateau, notably Cataract Canyon (Fig. 1) and Desolation Canyon in Utah[4]. Conversely tributaries of the San Juan River generally do not produce debris flows because terrestrial shale units have been eroded from the top of the Monument Upwarp (Baars et al., 1991).

[1] Department of Geosciences, University of Arizona (lrudd@geo.arizona.edu)
[2] Electrical and Computer Engineering Department, Rice University (erzsebet@rice.edu)
[3] Rudd et al. (unpublished data) describe debris-flow initiation factors on the Colorado Plateau.
[4] Webb et al. (unpublished data) have studied debris-flow initiation factors in Colorado Plateau bedrock canyons.

3.0 Site Description

Ending more than two hundred miles north of the start of Grand Canyon, Cataract Canyon's rapids rival those of Grand Canyon in steepness and intensity (Belknap, 1996). Forming the sides of Cataract Canyon are late Paleozoic sedimentary rocks (Fig. 2). The oldest outcrops found in Cataract Canyon are evaporates of the Pennsylvanian Paradox formation. Gypsum outcrops of this formation appear initially at Spanish Bottom and become increasingly more visible along the Colorado River between Cross Canyon and Gypsum Canyon. As much as 400 feet of Paradox Formation gypsum is exposed in Cataract Canyon (Baars, 1987).

Approximately 1000 feet of interbedded limestone, shale, sandstone, and chert of the Honaker Trail Formation overlay the Paradox Formation at the start of Cataract Canyon (Belknap et al., 1996, Baars, 1987). The Pennsylvanian Honaker Trail Formation forms cliffs and steep slopes throughout Cataract Canyon (Fig. 3). These cliffs are often covered with aprons of colluvium, composed of debris from rocks closer to the canyon rim. These colluvial wedges provide source material for the short-runout debris-flows responsible for creating rapids throughout the Cataract Canyon.

The Permian system in Cataract Canyon starts with the complicated, interfingering Elephant Canyon Formation and Hailgaito Shale. These formations unconformably overlay the Honaker Trail Formation in Canyonlands and are composed of near-shore marine limestones, dolomite, shale and sandstone (Baars, 1987). Shales in both formations contain a high percentage of kaolinite and illite clays (Table 1) and are positioned at a sufficient elevation above the Colorado River to give debris-flows originating at this point sufficient gravitational potential energy to deliver large rapid-forming boulders to the river.

Table 1 Semi-quantitative mineralogy by weight percent of clays included in the clay-sized fraction of Cataract Canyon surface materials.

Sample Type	% Illite	% Kaolinite	% Montmorillonite	% Quartz	% Calcite	% Other
Shale - Honaker Trail Formation	14	15	55	2	3	11
Shale - Elephant Canyon Formation	51	10	0	20	12	7
Shale - Hailgaito Shale	35	50	0	7	2	6
Colluvium	24	48	0	6	1	21
Debris-flow matrix	21	30	5	9	16	19

The Cedar Mesa Sandstone of Permian age forms the capstone on the walls of Cataract Canyon. Cedar Mesa Sandstone is a generally light-colored, fine to very-fine grained quartz-rich sandstone generally believed to have been deposited in a near-shore marine environment (Baars, 2000). Outcrops of Cedar Mesa sandstone extend for five or more kilometers northwest and southeast of the Colorado River in the study area, creating an uneven surface of relatively uniform lithology. To the southeast of Cataract Canyon the Cedar Mesa Sandstone is fractured by northeast – southwest trending normal faults, creating the Grabens Fault Zone. The proximity of Cataract Canyon to a zone of fractured and slumping rocks such as the Grabens Fault Zone is believed to be instrumental in providing much of the rapid-forming debris (Baars, 1987) that has been transported to the river by debris flows.

Debris flows in Cataract Canyon reach the river in one of two ways. First is the occurrence of short-runout debris flows that develop in steep chutes cut into the Honaker Trail Formation and overlying Hailgaito Shale and Elephant Canyon Formation. Although these debris-flow chutes are relatively short and generally within the immediate confines of the canyon, they are nonetheless clearly caused by debris-flow activity and are the main source of the debris which is responsible for the formation of rapids in Cataract Canyon (Fig. 3). The role of debris flows in the creation of rapids in Cataract Canyon has been questioned (Baars, 1987). Direct observation of source regions for the material responsible for the creation of rapids in Cataract Canyon reveal that the majority of rapids in Cataract Canyon result from the transportation of debris relatively short distances from canyon walls to the Colorado River. Long runout debris-flows also occur in Cataract Canyon and are responsible for the formation of large debris fans and rapids at the mouths of larger tributaries (Fig 3), such as Range Canyon and Imperial Canyon.

4.0 Spectra of Surface Materials

AVIRIS data of Cataract Canyon was collected on November 9, 2001 (Fig. 1). This data consists of two approximately northeast-southwest trending flight lines composed of nine individual images. Samples of the major

clay-containing surface materials in Cataract Canyon were obtained in late-May of 2001. These samples were analyzed at Brown University's RELAB. Figure 4 shows the lab spectra plotted with spectra of montmorillonite, kaolinite, and illite from the U.S. Geological Survey's Spectral Library. An obvious feature on the spectra of the shale, colluvium and debris-flow matrix materials found in Cataract Canyon is the 1.9 μm water absorption band, which matches well in placement and depth with the water absorption band in the illite USGS Spectral Library sample. The characteristic double-absorption feature at 2.2 μm readily visible on the Spectral Library sample of kaolinite is difficult to see in the RELAB samples (Fig. 4).

The materials sampled in Cataract Canyon were dry and very friable. It was not possible to obtain these samples in one piece in order to maintain a surface that would accurately match the ground surface exposed during the AVIRIS flights. All shale, colluvium and debris-flow matrix samples obtained in Cataract Canyon and sent to RELAB were composed of clay, silt, fine sand, and a wide variety of sizes of clay aggregates. Handling and transporting these samples changed the nature of their surfaces considerably, which may also have had an effect on the usefulness of the lab spectra obtained from the samples.

The clay mineralogy of the surface materials samples taken in Cataract Canyon was determined by semi-quantitative x-ray diffraction at the U.S. Geological Survey in Denver, Colorado. The x-ray diffraction data (Table 1) shows that the samples' clay mineralogy is dominated by kaolinite and illite. Only the Honaker Trail Formation sample contains significant amounts of montmorillonite. Figure 4 shows that the sample spectra have some similarities with the spectra of illite and kaolinite at 1.9 and 2.2 μm. There is also a significant dip in the sample spectra between 2.3 and 2.4 μm, a possible indicator of chlorite. The dip in the 2.3 to 2.4 μm region is also shown in the kaolinite and illite spectra.

5.0 Atmospheric Correction

Atmospheric correction of the AVIRIS images both Cataract Canyon flightlines was performed using both ATREM and FLAASH. The results of the application of both atmospheric correction algorithms are shown for debris flows, colluvium and gypsum in Figure 5. The spectra produced by ATREM show extreme spikes and dips in the curves that make the spectra much more difficult to use and necessitate additional corrections. The FLAASH corrected data is much more readily used without additional manipulation and is easier to compare directly to lab spectra. The differences between the spectra of pixels analyzed using ATREM and those corrected using FLAASH were significant, making the choice of using the FLAASH corrected data obvious

6.0 Spectral Classification

Classification of the AVIRIS images to map the various clays of interest, is in progress. The class map will be one of the GIS layers that constitute the decision-making model for the assessment of landslide hazard. Training sites were chosen in the second AVIRIS image of the first flight line flown over Cataract Canyon. The average spectra for training sites containing gypsum, debris flows and colluvium (with kaolinite content), [shale of the Honaker Trail Formation (for montmorillonite content), and shale of the Elephant Canyon Formation (for illite representation)] are shown in Figure 6. In this figure the spectra are compared directly to USGS library spectra of similar materials. Gypsum associated with the Paradox Formation in Cataract Canyon compares very favorably to the library spectrum of gypsum. Both spectra show features due to OH stretching modes or H-O-H bending modes near 1.0, 1.2, 1.45, 1.55, 1.9 and 2.2 μm (Hunt et al., 1971) that are characteristic to gypsum. Debris-flow deposits and colluvium in Cataract Canyon display the double-absorption feature characteristic of kaolinite at 2.2 μm in the AVIRIS spectra. This feature is more pronounced in colluvium than in debris-flow matrix, consistent with the measurements shown in Table 1, and with the observation that the total clay content of most debris-flows is smaller, and the particle size distribution of debris-flow deposits is even more heterogeneous than that found in a typical colluvial wedge found in Cataract Canyon. For clay contents, the debris-flow and colluvium spectra are very similar to each other, a fact that supports the cause and effect link between these two types of surface materials. The failure of colluvial wedges in Cataract Canyon provides the raw material, including clay minerals, necessary for debris-flow initiation.

Debris-flow deposits and colluvium in Cataract Canyon tend to display the double-absorption feature characteristic of kaolinite at 2.2 μm and a chlorite signature between 2.3 and 2.4 μm. The fact that the kaolinite absorption feature is pronounced in colluvium is consistent with the mineralogy data in Table 1. This absorption feature is more pronounced in colluvium, perhaps because the total clay content of most debris-flows is small and

the particle size distribution of debris-flow deposits is even more heterogeneous than that found in a typical colluvial wedge found in Cataract Canyon.

7.0 Conclusions

The occurrence of debris-flow activity in Cataract Canyon is believed to have the same cause as debris-flow activity at Grand Canyon and elsewhere on the Colorado Plateau. In this physiographic province an abundance of clays rich in kaolinite and illite and lacking in smectite, high relief between the Colorado River and a shale-containing unit, and a river-corridor aspect that is aligned with the dominant storm track have been shown to increase the likelihood of debris-flow activity (Griffiths, 1996). The purpose of this study is the application of hyperspectral remote sensing technology to the assessment of surface material clay content in Cataract Canyon. To this end AVIRIS imagery of Cataract Canyon has been obtained, atmospherically corrected and preliminarily analyzed for patterns in the clay content of the surface materials.

At this stage the results of the study are promising. The spectra of training sites chosen for the image classification procedure have been found to compare favorably to library spectra of the minerals in the training sites. A goal of this study is the production of a map showing the composition of surface materials in Cataract Canyon based on the classification of both AVIRIS flight lines of this area. Areas containing kaolinte and illite clays will be considered to be at increased risk for debris-flow activity. The combination of a surface materials map and maps showing the relief and tributary-stream aspect of Cataract Canyon will provide the basis for a model of the debris-flow potential in this area.

8.0 Acknowledgements

Collection and analysis of data used in this study has been supported by the United States Geological Survey (Robert Webb, Project Director), the University of Arizona, and the NASA-funded project "Remote sensing for debris flooding hazard assessment in arid regions" (Vic Baker, Principal Investigator), grant number NAG-9293.

9.0 References Cited

Baars, D.L., 2000, The Colorado Plateau: A geologic history: Albuquerque, University of New Mexico Press, 254 p.

Baars, D.L., Stevenson, G., and Chesser, W.L., 1991, San Juan canyons: A river runner's guide and natural history of San Juan River canyons: Lawrence, Kansas, Canon Publishers, Ltd. 64 p.

Baars, D.L., 1987, Paleozoic rocks of Canyonlands country, *in* Campbell, J.A., ed., Geology of Cataract Canyon and Vicinity, A Field Symposium-Guidebook of the Four Corners Geological Society, Tenth Field Conference-May 14-17, 199 p.

Belknap, B., Belknap, B. and Evans, L.B., 1996, Canyonlands river guide: Denver, Eastwood Printing, 79 p.

Beverage, J.P., and Culbertson, J.K., 1964, Hyperconcentrations of suspended sediment: American Society of Civil Engineers, Journal of the Hydraulics Division, v. 90, p. 117-126.

Chabrillat, S., Goetz, A.F., Olsen, H.W. and Krosley, L., 2001, Field and imaging spectrometry for identification and mapping of expansive soils, *in* Van der Meer, F.D.and DeJong, S.M., eds., Imaging spectrometry: Basic principles and prospective applications: Dordrecht, Kluwer Academic Publishers, 403 p.

Costa, J.E., 1984, Physical geomorphology of debris flows, *in* Costa, J.E. and Fleisher, P.J., eds., Developments and applications of geomorphology: Berlin, Springer-Verlag Publishing, p. 268-317.

Costa, J.E., and Weiczorek, G.F., 1987, Debris flows/avalanches: Process, recognition and mitigation: Geological Society of America, Reviews in Engineering Geology, v. 7, 239 p.

Griffiths, P.G., Webb, R.H., and Melis, T.S., 1996, Initiation and frequency of debris flows in Grand Canyon, Arizona: U.S. Geological Survey Open-File report 96-491.

Hampton, M.A., 1975, Competence of fine-grained debris flows: Journal of Sedimentary Petrology, v. 45, no. 4, p. 834-844.

Hintze, L.F., 1988, Geologic History of Utah: Provo, Brigham Young University, 202 p.

Hunt, G.R., Salisbury, J.W., and Lenhoff, C.J., 1971, Visible and near-infrared spectra of minerals and rocks: IV, sulphides and sulphates, Modern geology, v. 3, p. 1-14.

Rodine, J.D., and Johnson, A.M., 1976, The ability of debris, heavily freighted with coarse clastic materials, to flow on gentle slopes: Sedimentology, v. 23, p. 213-234.

Webb, R.H., Pringle, P.T., Reneau, S.L., and Rink, G.R., 1988, Monument Creek debris flow, 1984 - Implications for formation of rapids on the Colorado River in Grand Canyon National Park, Arizona: U.S. Geological Survey Professional Paper 1492, 39 p.

Webb, R.H., Melis, T.S., Wise, T.W., and Elliott, J.G., 1996, "The Great Cataract," The effects of late Holocene debris flows on Lava Falls Rapid, Grand Canyon National Park, Arizona: U.S. Geological Survey Open-file Report 96-4.

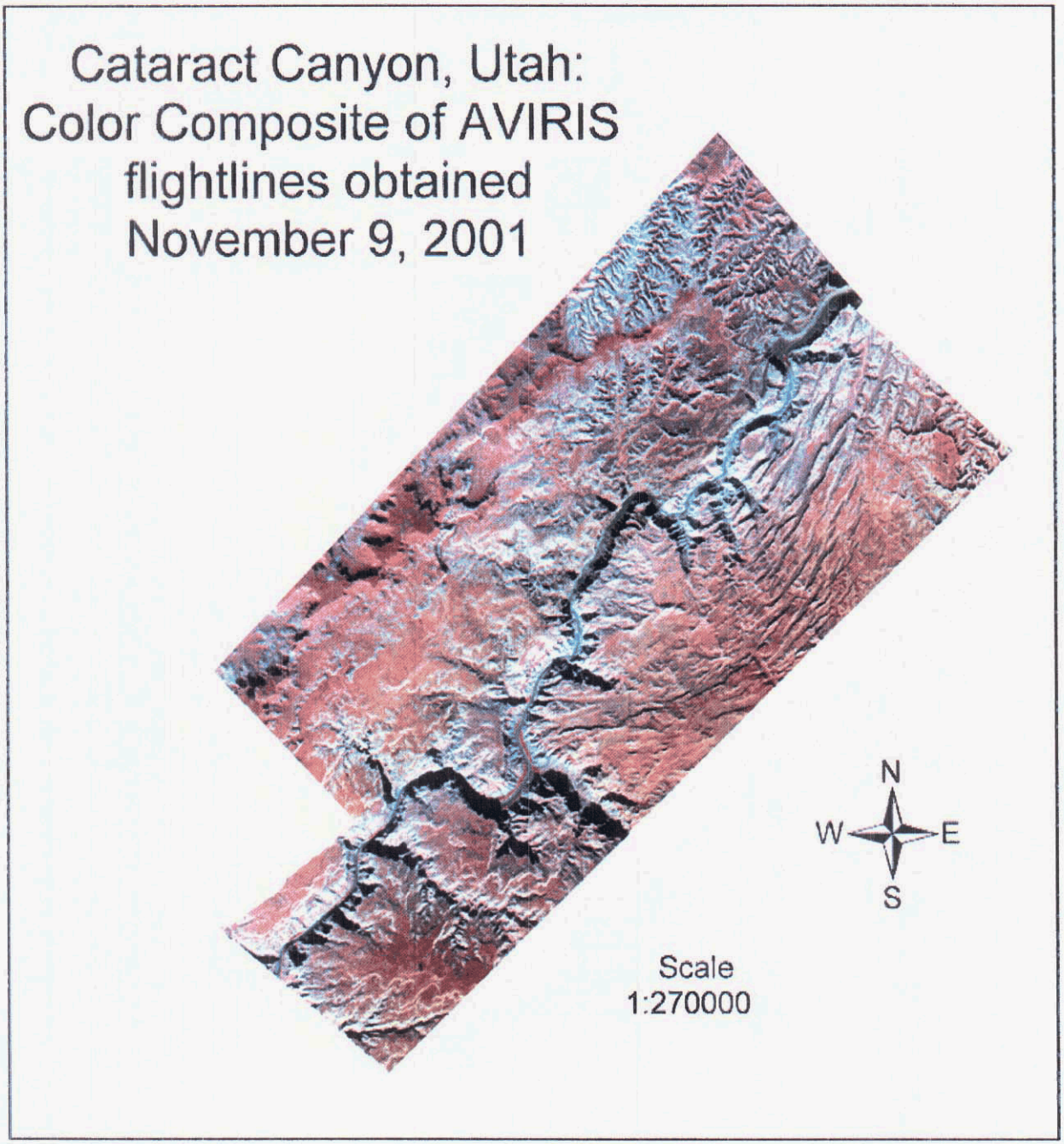

Figure 1 Color composite of the study area flight lines

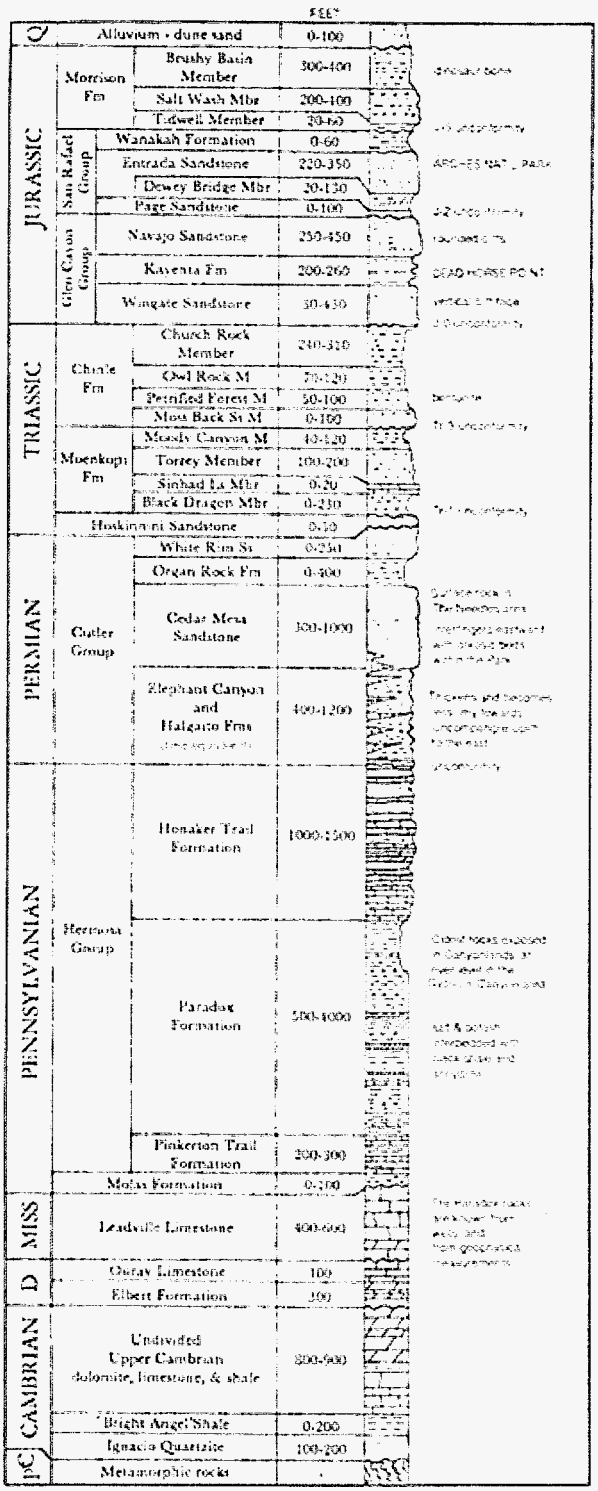

Figure 2 Stratigraphic section of the Canyonlands National Park area. Formations in Cataract Canyon extend from the Paradox Formation at river level to the Cedar Mesa Sandstone at the canyon rim (from Hintze, 1988).

Figure 3 View from the east across the Colorado River toward the mouth of Teapot (Calf) Canyon with Rapid 22 (Upper Big Drop) in the foreground. The Honaker Trail Formation is exposed at river level while the top one-third of the inner canyon consists of intertonguing Hailgaito Shale and Elephant Canyon Formation. Caprock is Cedar Mesa Sandstone. Note debris fan in Teapot Canyon and colluvial wedges at base of cliff downstream from rapid. (Photo Courtesy of Robert Webb)

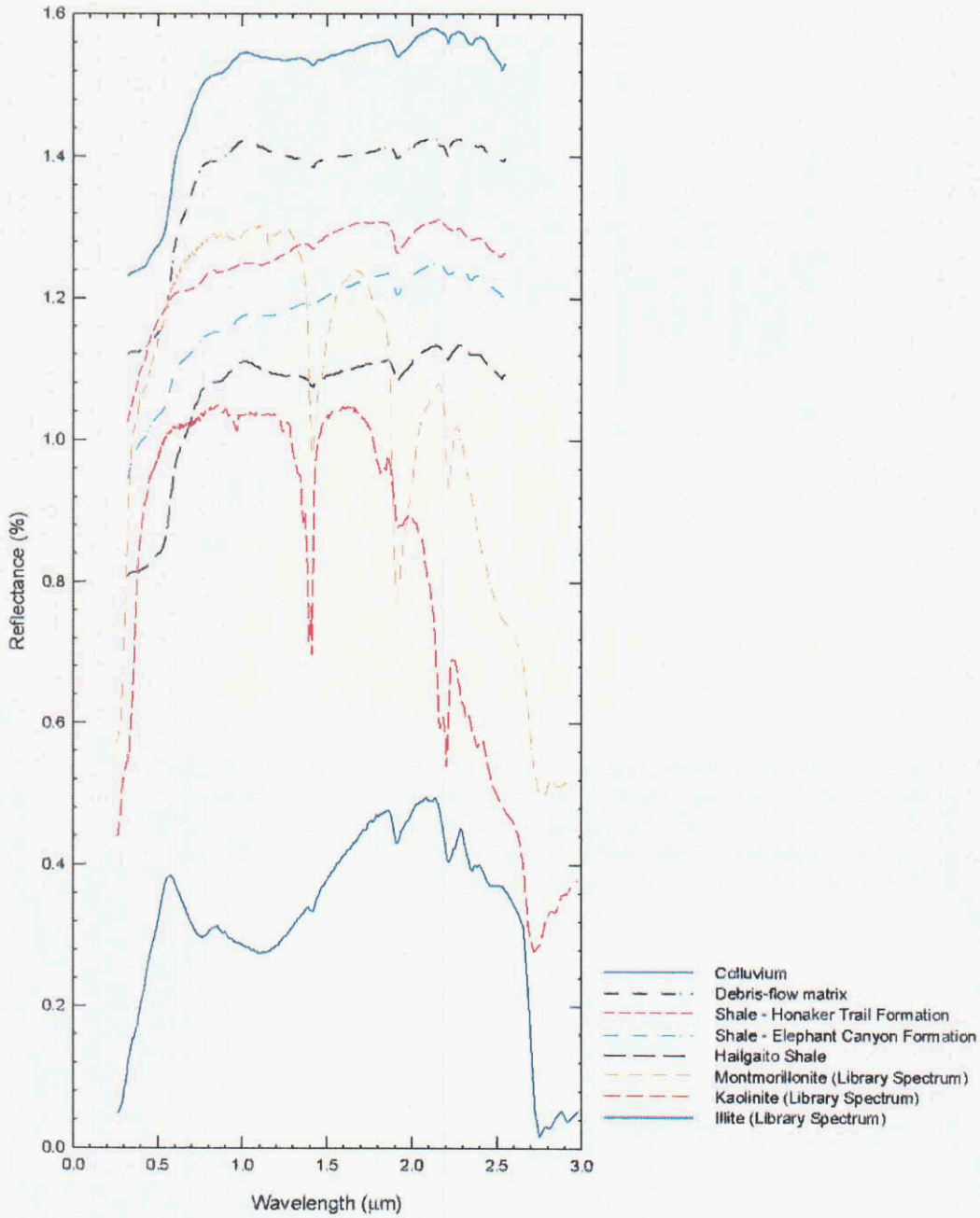

Figure 4 Comparison of Cataract Canyon surface material sample spectra as measured by RELAB and clay mineral spectra from the USGS spectral library. Spectra offset for clarity.

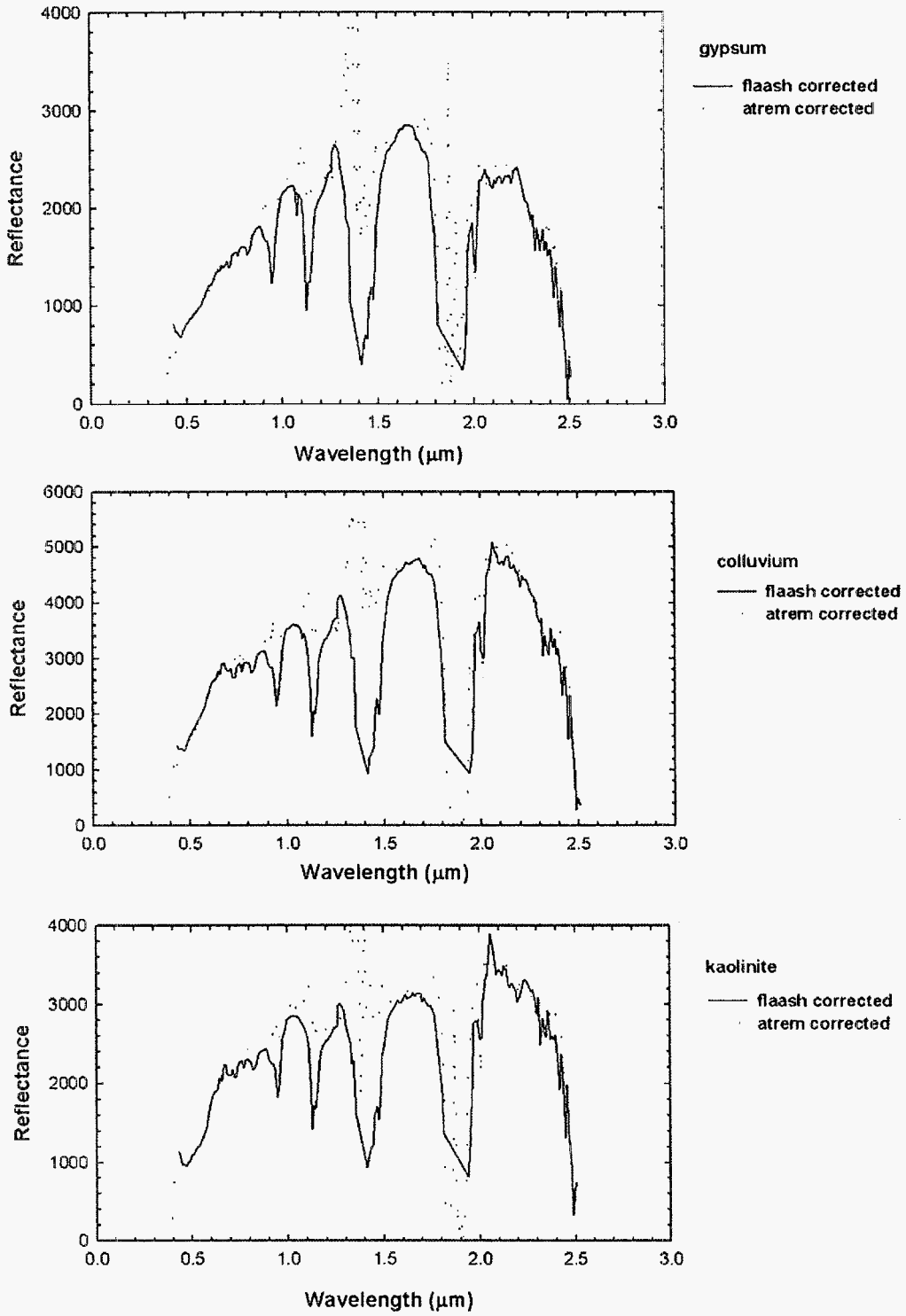

Figure 5 Representative AVIRIS spectra of classification training sites. Plots compare the results of FLAASH and ATREM atmospheric correction. The FLAASH correction is noticeably better.

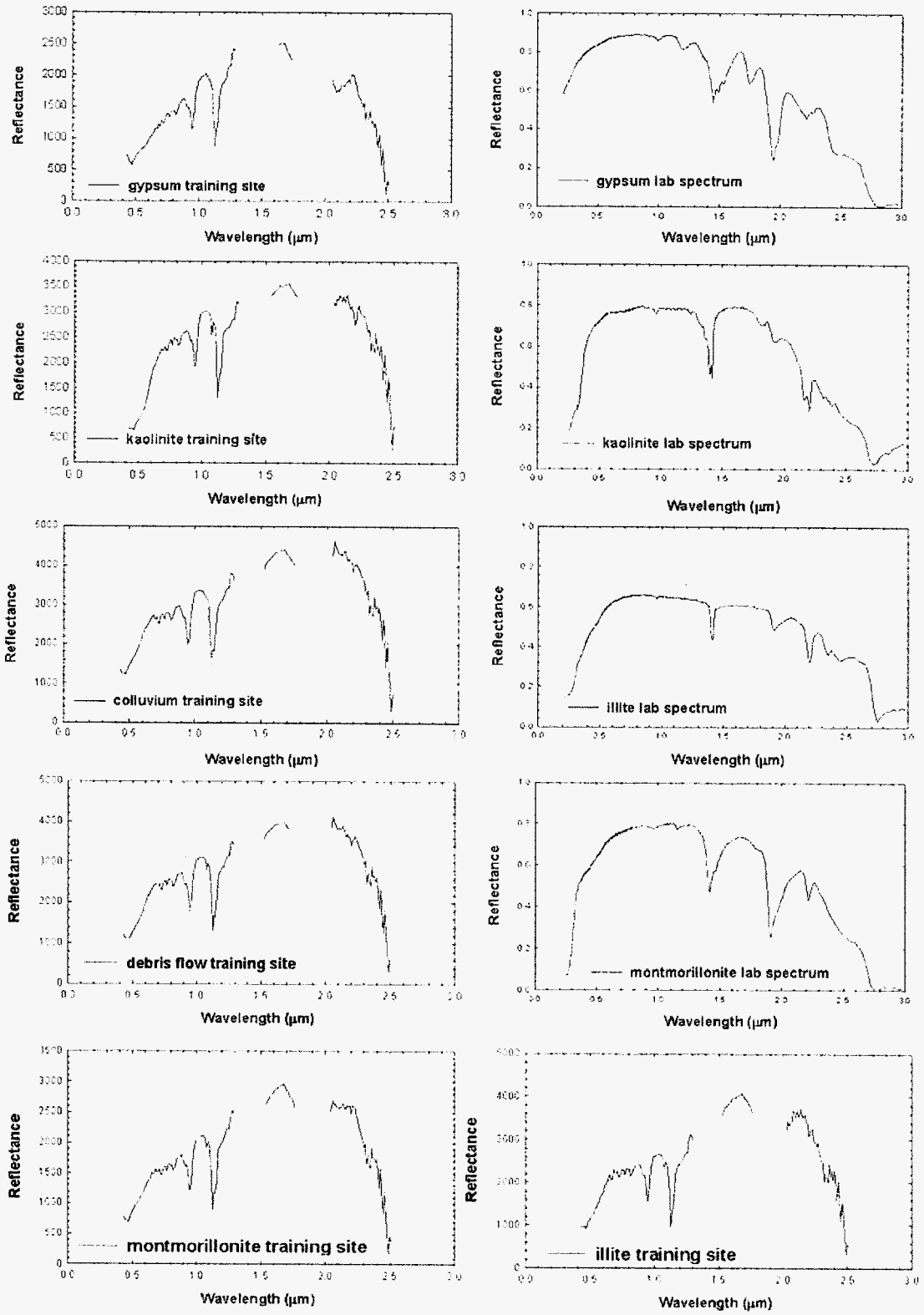

Figure 6 Spectra from preliminary classification training sites (AVIRIS data, shown in the first column and on the bottom of the second column) compared to USGS Spectral Library spectra (second column) for samples of gypsum, kaolinite, montmorillonite, illite, colluvium and debris-flow matrix.

A SUBPIXEL TARGET DETECTION TECHNIQUE BASED ON THE INVARIANCE APPROACH.

John R. Schott[1], Kyungsuk Lee, Rolando Raqueno, Gary Hoffmann, Glenn Healey[2]

[1]Rochester Institute of Technology (schott@cis.rit.edu)
[2]University of California at Irvine (ghealey@uci.edu)

1. Introduction and Summary

This paper introduces a method for detection of subpixel targets in image spectrometer data cubes. It is based on the premise that we know what the target is and can characterize it in terms of its reflectance spectrum $r(\lambda)$. Furthermore, we assume the target may exist at spatial scales such that it will present itself as a fraction of a pixel and that it may exist in a significant number of pixels (more specifically we can't assume that we can insure that a significant region of the scene does not contain any targets). We desire a data processing approach that can mitigate atmospheric and illumination effects such that atmospheric correction is not a required prerequisite for the method. The approach presented here involves defining a target spectral subspace that is common across the wide range of atmospheric illumination and viewing conditions that might exist in the scene (i.e., the target subspace is invariant to environmental changes within the scene). The target may be manifest at different locations within the subspace but is not expected to appear outside the subspace. We then introduce a method to characterize a background subspace using the same convex hull geometry used to define the target subspace (i.e., the target subspace and background subspace are defined in a common spectral space but ideally there is little or no overlap between the two subspaces). We then introduce a subpixel target detection algorithm that is based on how well each pixel spectrum can be described by either a set of background basis vectors or a combination of target and background basis vectors. The result is a subpixel target detection algorithm that only requires the target spectrum and a radiance image cube (i.e., an image spectrometer data set calibrated into sensor reaching radiance). The performance of the resulting algorithm is shown for both a HYDICE image and an AVIRIS image. These initial results demonstrate the potential of the approach showing very good background suppression (low false alarms) and a high degree of target detection.

2. Approach

This section presents an overview of the background theory on which this algorithm is based, as well as the advances needed to implement a subpixel version of the invariant algorithm.

2.1 The Invariant Approach

The subpixel algorithm developed here is built on the invariant method for fully resolved target detection described by Healey and Slater (1999). The invariant method is based on the assumption that an individual target may be manifest over a wide range of spectral values in an image due to illumination and atmospheric variation within a scene. However, even though a target may take on many spectral values the total range of those values is small compared to the entire scene spectral space. The goal of the invariant method is to define the subspace of the entire scene space that the target may occupy in terms of a relatively small set of basis vectors that span the target subspace. The range of possible target vectors can be generated by using the MODTRAN radiation propagation model (c.f. Berk et al., 1989) to predict the sensor reaching spectral radiance for the target reflectance vector. By changing the inputs to MODTRAN over a range of variables representing the range of atmospheric, illumination and viewing conditions that might occur under imaging conditions, a wide range of potential target spectral vectors can be generated. We can define a set of basis vectors that will predict these target vectors (i.e., span the spectral space they occupy) according to:

$$\mathbf{x}_i = \mathbf{T}\mathbf{a}_i + \boldsymbol{\varepsilon}_i = \sum_{j=1}^{N} \mathbf{t}_j a_{ij} + \boldsymbol{\varepsilon}_i \qquad (1)$$

where $\mathbf{x}_i$ is the i^{th} MODTRAN generated target vector for the sensor under study, produced by convolving the MODTRAN spectral radiance with the spectral response function of each of the k bands, $\mathbf{T}$ is a matrix made up of N target basis vectors $\mathbf{t}_j$, $\mathbf{t}_j$ is the j^{th} basis vector, $\mathbf{a}_i$ is a vector of N weights particular to the i^{th} target vector

and ε_i is the residual error. Healey and Slater (1999) used Singular Value Decomposition (SVD) to solve for the set of basis vectors that minimize the sum-squared error expressed as:

$$SSE = \sum_{i=1}^{C} (\mathbf{x}_i - \mathbf{T}\mathbf{a}_i)^2 \tag{2}$$

where C is the number of MODTRAN runs (17,920 for the Healey and Slater (1999) studies). Slater and Healey (1998) demonstrated that for a wide range of targets imaged by a 200+ band sensor (e.g. HYDICE or AVIRIS), the subspace spanned by variation in atmospheric and illumination variation could be spanned by a small number of basis vectors (typically 9 or less).

For any radiance vector $\mathbf{x}$ in the image we can solve for the basis vector weights $(\mathbf{a})$ according to:

$$\mathbf{a} = \mathbf{T}^{-1}\mathbf{x} = \mathbf{T}^{T}\mathbf{x} \tag{3}$$

Where we take advantage of the fact that the SVD derived basis vectors form an orthonormal set such that $\mathbf{T}^{-1} = \mathbf{T}^{T}$. Slater and Healey (1999) used the residual error from this process as a target detection metric for fully resolved targets according to:

$$\boldsymbol{\varepsilon} = \mathbf{x} - \mathbf{T}\mathbf{a} = \mathbf{x} - \mathbf{T}\left(\mathbf{T}^{T}\mathbf{x}\right) \tag{4}$$

Pixels with small magnitudes of $\boldsymbol{\varepsilon}$ (i.e., $\left(\boldsymbol{\varepsilon}^{T}\boldsymbol{\varepsilon}\right)^{\frac{1}{2}}$) are well fit by the model (i.e., they look like linear combinations of target basis vectors) and can be identified by thresholding an image expressed as the magnitude of the $\boldsymbol{\varepsilon}$ vectors from Equation 4. This method showed very promising results for fully resolved pixels, significantly out performing simpler approaches (e.g. the Spectral Angle Mapper (SAM) trained on sunlit targets) for targets in partial and full shadow. Regrettably, subpixel targets are not a good match to the model expressed in Equation 4 and an approach involving characterization of the background is required. This subpixel detection approach was the goal of Lee (2003) and is summarized below.

2.2 The Maximum Distance (MaxD) method for Basis Vector Selection

Lee 2003 suggests an alternative method to the SVD for basis vector selection that maintains the basis vectors in the native spectral space (i.e., the basis vectors all look like image spectral radiance vectors). This was motivated by the need to separate out target from background basis vectors as discussed in the next section (c.f. Section 2.3). The range of spectral values a target may assume in the image is again generated by using MODTRAN to predict the range of atmospheric, illumination and viewing conditions under which the target might be observed in a particular image. For this study only those conditions relevant to the particular image under analysis were included in the generation of possible target radiance values. The goal was to push the limits of how the target might appear in the particular image but not to exceed those bounds. This should generate a subspace large enough to contain the target but hopefully small enough to reduce false alarms. Typically 840 MODTRAN runs were used (compared to the 17,000 runs used by Slater and Healey (1998) to span the entire possible target subspace (e.g. all seasons, altitudes and water vapor, illumination and view angle ranges). The MODTRAN generated radiance vectors were then converted into discrete radiance vectors corresponding to the imaged radiance vectors for a particular imaging spectrometer by convolving the MODTRAN spectral radiance with the response fractions of the sensors k spectral bands. These target spectral vectors can be thought of as occupying some subspace in the scene spectral radiance domain (c.f. Figure 1). We seek a simplex that encloses these spectral vectors and postulate that such a simplex can be constructed from the extrema of the available data (note this is essentially the same conceptual problem as that of finding extrema or end members in an image cube). The largest magnitude vector $(\mathbf{v}_1)$ is one vertex of the simplex and we postulate that the smallest magnitude vector $(\mathbf{v}_2)$ is another candidate vertex. Note, that rigorously speaking, the smallest magnitude vector may not be a vertex of the simplex, however, empirical evidence suggests that real data form a cone in spectral space with the apex near the dark point or point of lowest magnitude (c.f. Ifarraguerri and Chang, 1999). Thus, we will tentatively use the darkest pixel $(\mathbf{v}_2)$ as a vertex of the simplex. If we assume the target subspace spans ℓ dimensions, a minimum of $\ell+1$ vertices are required to encompass the

subspace. Lee (2003) shows that the vertices of the $\ell+1$ element simplex will also be vertices of the ℓ element simplex formed by projecting all the data onto the subspace orthogonal to the difference vector between v_1 and v_2 (i.e., the projection that places v_1 on v_2) as shown in Figure 2. Furthermore, the point v_3 most distance from the point v_{12} (i.e., the point in the projected space jointly occupied by v_1 and v_2) in this new space must be a vertex of the simplex. By projecting the transformed data onto the subspace perpendicular to the difference vector between v_3 and v_{12}, the vertices of the simplex in ℓ dimensions will be vertices of an ℓ-1 element simplex in the new subspace. This process can continue until all the vertices of the subspace are located i.e., projected to a common point. This begs the question of determining how large (i.e., what is the dimension ℓ) is the target subspace. One way to determine the dimension is to use the SVD to estimate the dimension ℓ and then find $\ell+1$ vertices. Another approach is to find more than enough vertices and then use a method that eliminates any vertex that is a linear combination of earlier vertices (Lee, 2003 suggests using a stepwise linear regression (described by Gross and Schott, 1996) on the vector made from the mean of the target vectors to separate out excess vertices). It is important to remember that even though we select the latter vertices of the simplex in the projected spaces they are merely samples from the MODTRAN generated target set and once selected we can express the spectral vector in the image space units for use as the basis vector. At this point we have simply solved for a set of N target basis vectors in the native space and could solve the fully resolved target detection problem described in Equations 3 and 4. Note that in Equation 3 we would need to use the pseudo inverse of $\mathbf{T}$ (i.e., $\mathbf{T}\#$) not $\mathbf{T}^T$ since our native basis vectors do not form an orthonormal set. To solve the subpixel problem we still need to solve for a set of basis vectors to span the background subspace.

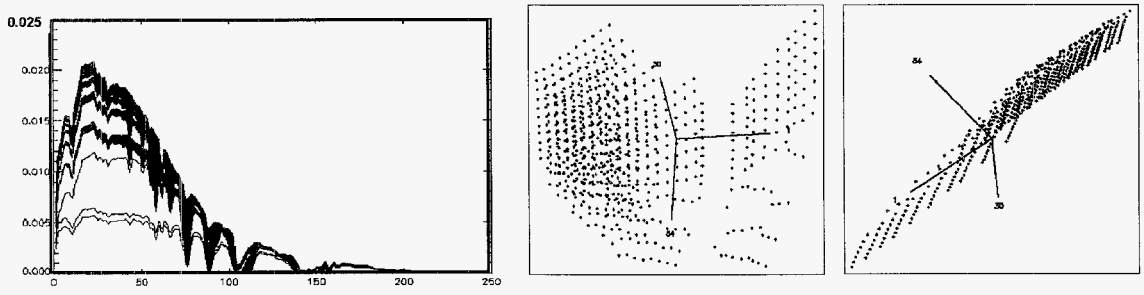

Figure 1. Illustration of potential target spectral radiance values: (a) plots of spectral radiance for the same reflectance spectrum viewed through different atmospheres, (b) a Plot of three bands of the data from figure a showing how the target radiance data is spread over the radiance space, (c) a plot of the same data as a and b illustrating that the subspace occupied by the target radiance values is actually a small subset of the entire spectral space.

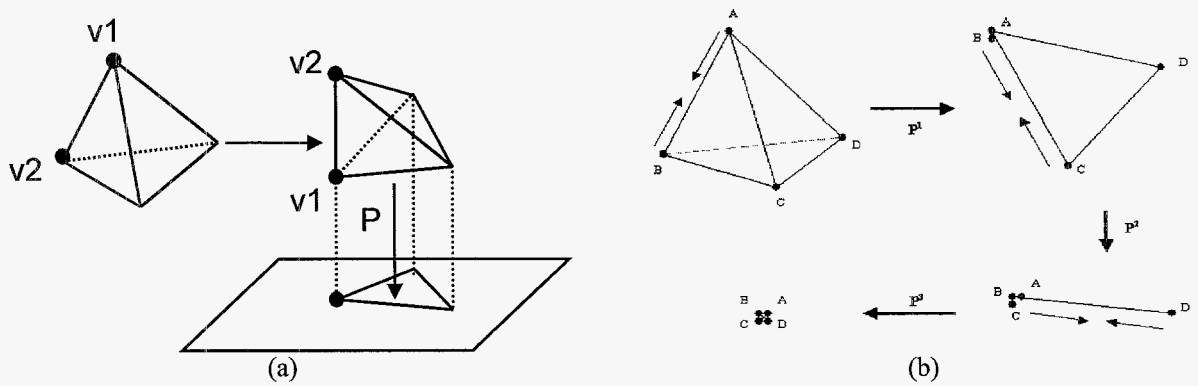

Figure 2. Illustration of (a) The preservation of vertices of a simplex through projection of a data set onto the difference in two vertices of a simplex and (b) the concept of maximum distance determination and sequential projection to find the vertices of a simplex spanning the data space.

2.3 Selection of Background Basis Vectors

The method for selection of background basis vectors is very similar to the method used to solve for target basis vectors. However, because the data set to be processed is so large (i.e., the entire image) the analysis is often more manageable if we first reduce the dimensionality of the data. First any bands that don't carry information of interest are removed (e.g., high noise or high atmospheric absorption). Second a transformation into a more information rich set of fewer bands is performed using an approach like the Minimum Noise Fraction (MNF) transform with higher order bands truncated (c.f. Green et al., 1998). This might reduce our data dimensionalities for an AVIRIS scene from 224 bands to 180 bands, by band rejection, and to 32 transformed bands using the MNF transform. If we run the MaxD algorithm described in Section 2.2 on the transformed image we could define a set of basis vectors that span the image space. However, there is a good chance that one or more of the basis vectors could be contaminated by the target signature. Since our goal will be to use these basis vectors to effectively suppress the background, having background basis vectors that include target characteristics would be counter productive. To overcome this limitation, we augment the image data set with the native target vectors generated in Section 2.2 after transforming them into the MNF space (in practice, it is often easier to also perform the target space MaxD calculations on data that has been transformed into the image MNF space to reduce data dimensionality). The output of this second MaxD process is a set of basis vectors that span the combined target-background space. As illustrated in Figure 3 any mixed target-background pixels should fall inside the convex hull described by these basis vectors and will not be identified by MaxD as a vertex. We then remove any target vertices from the vertices found by the MaxD of the combined image-target data set. This leaves us with a set of vertices that should only include background pixels and which should span the background subspace.

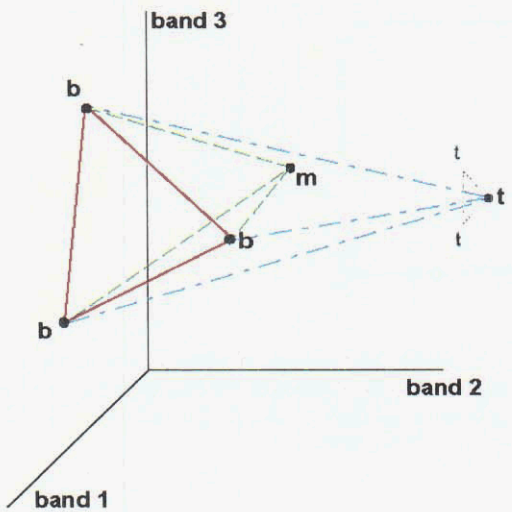

Figure 3. Simplex shapes before and after adding target basis vectors b illustrates a background vector, t a target vector, and m a mixed target-background vector.

2.4 Subpixel Target Detection Algorithm

The final detection algorithm uses a generalized likelihood ratio to compare how well a spectral vector (pixel) can be modeled as a linear combination of background basis vector to how well the spectral vector (pixel) can be modeled as a linear combination of target and background basis vectors. A simplified form of this can be express as:

$$L = \left(\frac{n_b^2}{n_T^2}\right)^{\frac{1}{2}} = \left(\frac{[\hat{\mathbf{x}} - \mathbf{B}\mathbf{b}]^2}{[\hat{\mathbf{x}} - \mathbf{M}\mathbf{c}]^2}\right) = \left[\frac{[\hat{\mathbf{x}} - \mathbf{B}[\mathbf{B}^{\#}\hat{\mathbf{x}}]]^2}{[\hat{\mathbf{x}} - \mathbf{M}[\mathbf{M}^{\#}\hat{\mathbf{x}}]]^2}\right]^{\frac{1}{2}} \tag{5}$$

where $\hat{\mathbf{x}}$ is the MNF transformed version of the pixel under test, $\mathbf{B}$ is the matrix made up of background basis vectors as columns, $\mathbf{b}$ is the vector of best fit weights obtained by modeling $\hat{\mathbf{x}}$ as a background, $\mathbf{B}^{\#}$ is the pseudo

inverse of **B** (i.e., $\mathbf{B}^{\#} = \left(\mathbf{B}^{\mathrm{T}}\mathbf{B}\right)^{-1}\mathbf{B}^{\mathrm{T}}$), **M** is the matrix made up of combining the target and background basis vectors as columns (i.e., the concatenation of **B** and **T**) and **c** is the vector of best fit weights obtained by modeling $\hat{\mathbf{x}}$ as a mixture of target and backgrounds. The numerator of Equation 5 will be small and the dominator large when the background model is a good fit and vice versa when the target-background model is a good fit. Thus a threshold on L that isolates large values can be used as a target detection mask.

3. Results

The MaxD method of selecting vertices to span the data subspace is essentially the same as the end member selection process. To test the method 50 SWIR bands of a reflectance corrected AVIRIS cuprite scene distributed with ENVI were analyzed with the ENVI PPI routine (c.f. Boardman et al., 1995) to select candidate end members, followed by a matched filter with a reflectance library to find final end members. These results were compared to the MaxD results. The results are shown in Figure 4. The slight differences are due to the fact that MaxD was totally scene derived and PPI was used with a matched filter applied to the reflectance library with the best-fit library value used as the final end member. The two methods show comparable performance, however, the MaxD processing is fully automated (PPI could be) and faster. One potential limitation of the MaxD approach is that some vertices may be extremes because of anomalies or noise in the data set. Meaningful extrema will generally have other points in close proximity. To avoid selecting isolated points the entire first set of vertices can be removed from the analysis and the MaxD repeated to generate a second set of vertices. For data with many anomalies this process could be repeated until sequential vertices are essentially the same. For the data sets we have studied we have never needed to go beyond a second pass. Figure 5 shows an example of how closely several first and second pass vertices compare (for non anomalous vertices). Note that slight changes in magnitude are not critical to this process and that the spectral shapes are very well reproduced (i.e., the correlation between the first and second pass spectra is very high).

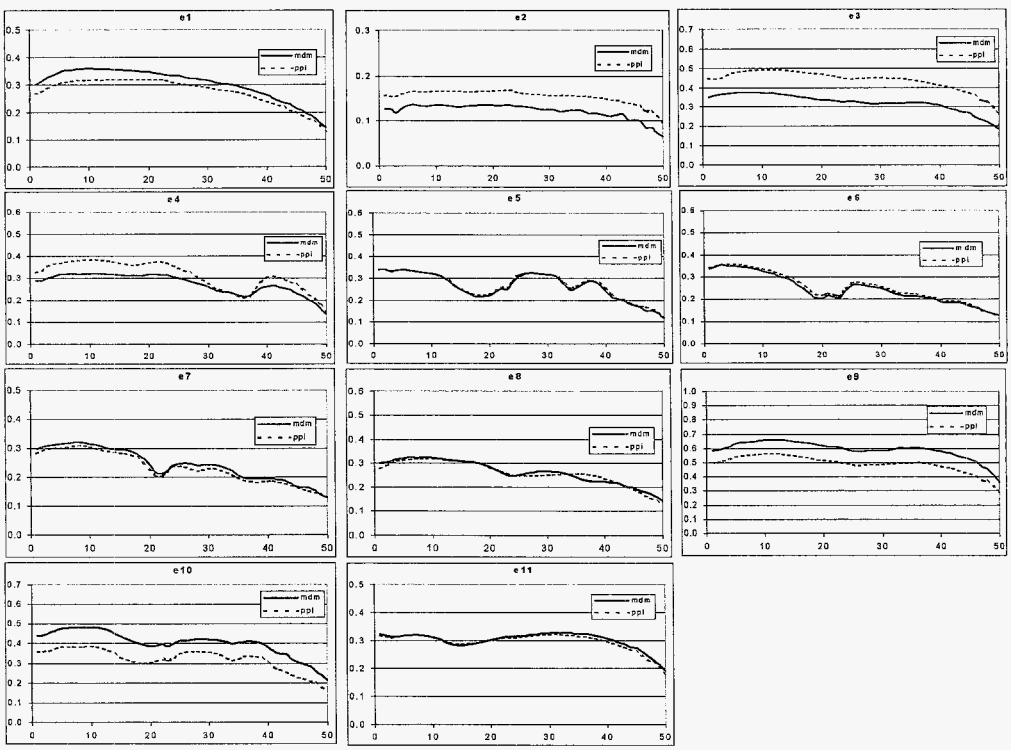

Figure 4. Comparison of vertices selected by MaxD of PPI and a matched filter on library spectra. The original data were 50 bands of an AVIRIS image of Cuprite, Nevada corrected for atmospheric effects.

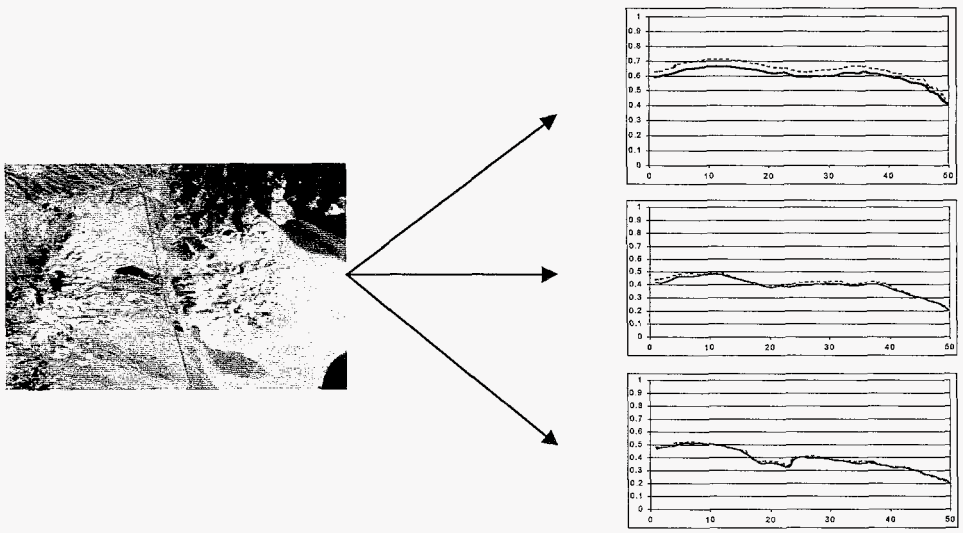

Figure 5: Comparison of first and second pass MaxD for non-noise pixels

The overall subpixel target detection was tested against three data sets of increasing complexity. The first test used synthetic data. Seven background spectra and one target spectrum from the USGS library were sampled into 224 AVIRIS like bands and 992 background and eight target background mixtures were produced using a uniform random number generator to produce fraction weights. The 8-target pixels had two pixels each of 25, 10, 5 and 1 % abundance. The reflectance spectra were converted to sensor reaching radiance using MODTRAN with one pixel at each target abundance propagated through a significantly different highly turbid atmosphere. Finally, noise was added to each radiance vector to simulate noise observed in an AVIRIS dark field image. The target and background subspaces were then generated using the methods described above and the GLR detection algorithm applied. The results shown in Figure 6 should show target pixels at locations 100, 150, 350, 400, 600, 650, 850 and 900. The second 5% pixel is missed due to the very turbid atmosphere and neither of the 1% pixels are detected. Note, there were no false alarms.

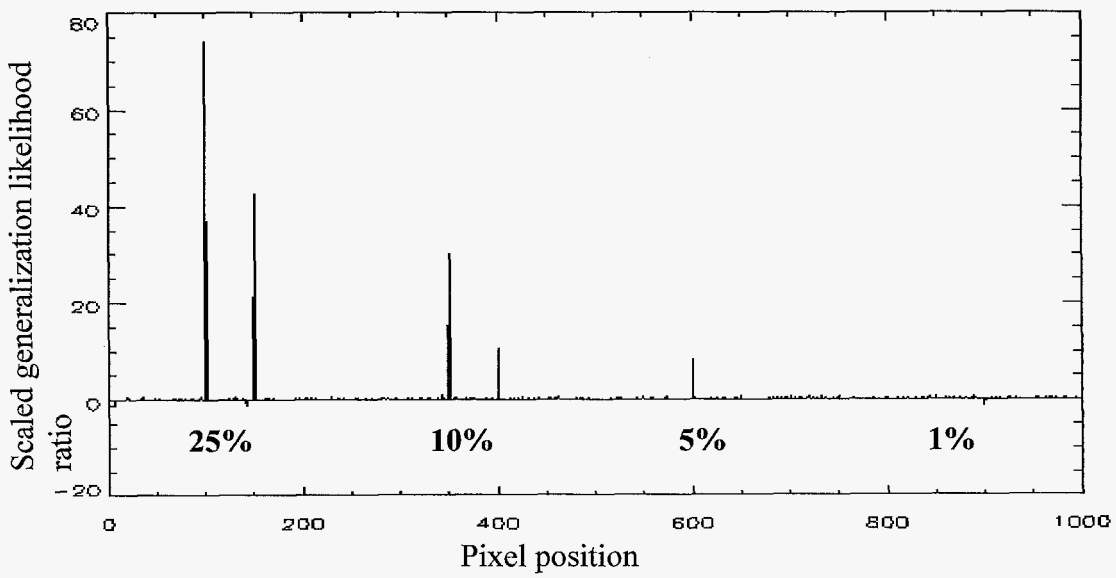

Figure 6: Detection result for the synthesized mixed pixel data set. Note the high level of background rejection.

A more rigorous test was applied to HYDICE imagery of the arm test site containing a number of target panels. The imagery was degraded to make the target panel of interest subpixel (cf. Figure 7). The results show complete success for the four-subpixel target pixels and no false alarms (cf. Figure 8). The ARM site was, however, not very stressing since the scene was not very cluttered and the target had a fairly high contrast.

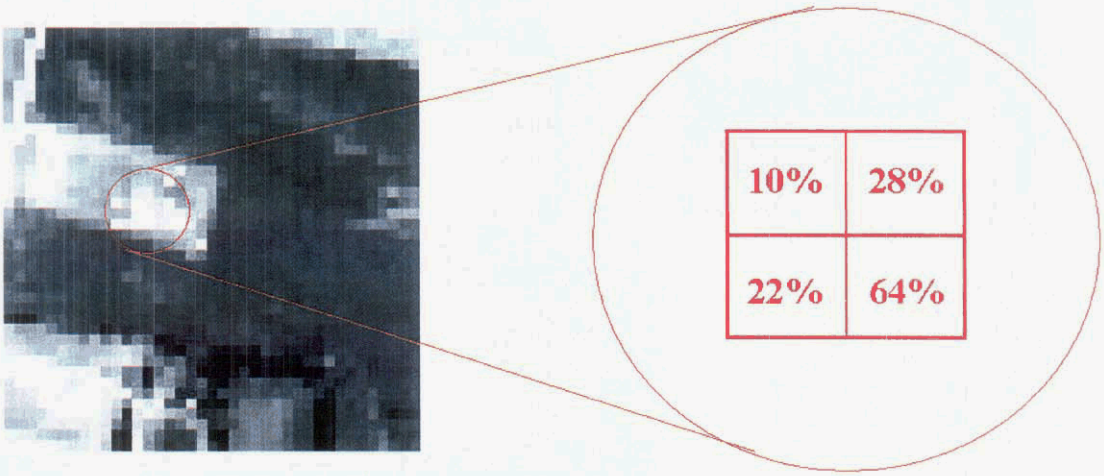

Figure 7: Original HYDICE image and target panel spectrum (top) and degraded image and fill factor estimates for the target panel (bottom).

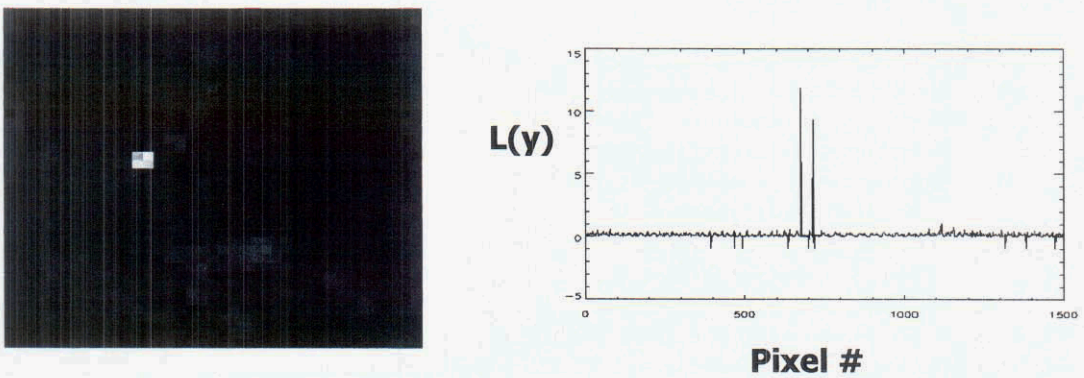

Figure 8: Detection image and scan profile of the detection metric for the HYDICE image in Figure 7.

Finally, an AVIRIS image of a cluttered urban area was used, with the target a reddish brown paint used for basketball courts (cf. Figure 9). The reflectance spectrum used was acquired for the single known target using a field spectrometer. The scene had a wide range of natural and man-made clutter including a mixture of commercial/warehouse and residential neighborhoods to add a wide range of spectral diversity. The results showed two target sites. High-resolution air photos were used to evaluate the detections as shown in Figure 9. The first site was the basketball court where the ground truth data were acquired approximately one year after the AVIRIS overpass. The second detection site was at a tennis court where the perimeter of the court appeared to be painted with the same paint used on the basketball court. Also shown in Figure 9 for reference is the approximate sample size for a nominal 20m AVIRIS pixel.

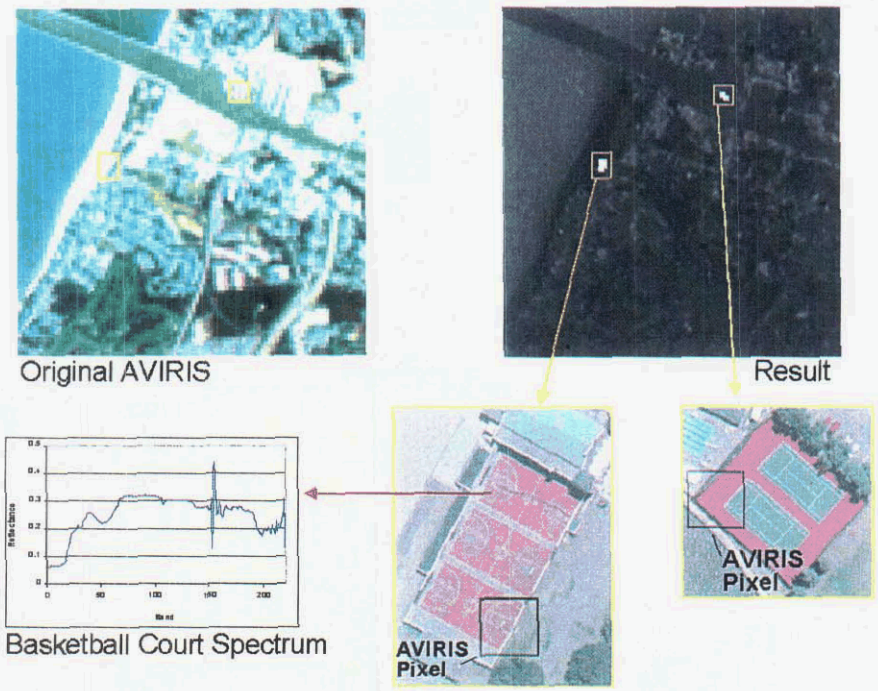

Figure 9: AVIRIS Results

4. Conclusions and Recommendations

The results shown in the previous section are quite encouraging. They indicate that the MaxD method shows potential as a simple, rapid and effective method for selection of native basis vectors. Note this is the same as an end member selection problem so that the MaxD approach could also be used for rapid selection of end members. Furthermore, the subpixel invariant method presented here shows good performance against an initial range of data sets with high detection rates and low false alarms over the range of targets and backgrounds tested. The method is particularly attractive because the only required inputs are a known target reflectance spectrum and an image cube expressed as spectral radiance. The effects of atmosphere and illumination are accounted for by the invariance process. From one perspective, this simplicity of inputs and the high level of automation of the process are significant advantages. On the other hand, the current implementation of this approach is limited to detection of targets whose reflectance spectrum can be defined in advance and to image sets that can be reasonably calibrated into spectral radiance. For the sensors used here (HYDICE and AVIRIS), the nominal sensor calibration data to convert counts to spectral radiance appeared adequate for the targets studied.

Future work in this area needs to address methods to more fully automate the process and to test the approach against a wider range of targets and backgrounds with a particular emphasis on low contrast targets and targets more directly influenced by the surround (e.g., partial shadow and tree shine). Ongoing work on this approach at RIT is concentrating on a more explicit treatment of noise in the algorithm to deal with sensors with significant noise levels. We are also investigating better ways to define the variability in the target space. This effort is focused on trying to define the full range of ways the target is likely to appear in the scene to improve target detection without generating too large a target space, which is likely to lead to false alarms. Finally, we are investigating methods to hybridize the original fully resolved invariant method and the subpixel method presented here to determine if higher performance can be achieved with a hybrid version.

5. References

Berk, A., Bernstein, L.S., & Robertson, D.C. (1989). "MODTRAN: a moderate resolution model for LOWTRAN 7," GL-TR-89-0122, Spectral Sciences Inc., Burlington, Massachusetts.

Boardman, J.W., Kruse, F.A., Green, R.O. (1995). "Mapping Target Signatures via Partial Unmixing of AVIRIS Data," *Summaries of the Fifth Annual JPL Airborne Earth Science Workshop*, Vol. 1, AVIRIS Workshop,JPL publication 95-1, Jet Propulsion Laboratory, Pasadena, California, pp. 23–26.

Green, A.A., Berman, M., Switzer, P., & Craig, D. (1998). "A transformation for ordering multispectral data in terms of image quality with implications for noise removal," *IEEE Transactions on Geoscience and Remote Sensing*, Vol. 26, No. 1, pp. 65–74.

Gross, H.N. and Schott, J.R., "Application of spatial resolution enhancement and spectral mixture analysis to hyperspectral images," *SPIE Optical Science, Engineering, and Instrumentation Annual Meeting*, Vol. 2821-4, pp. 30–41, Denver, Colorado, August 1996.

Healy, G. and Slater, D., "Models and Methods for Automated Material Identification in Hyperspectral Imagery Acquired under Unknown Illumination and Atmospheric Conditions," *IEEE Transactions on Geo Science and Remote Sensing*, Vol. 37 # 6, November 1999.

Ifarraguerri, A. and Chang, C-I, "Multispectral and Hyperspectral Image Analysis with Convex Cones," *IEEE Trans on Geoscience and Remote Sensing*, 37, pp. 756–770, 1999.

Lee, K., "A Subpixel Scale Target Detection Algorithm for Hyperspectral Imagery," Ph.D. Dissertation, Rochester Institute of Technology, Center for Imaging Science, 2003.

Slater, D. and Healey, G., "Analyzing the spectral dimensionality of outdoor visible and near infrared illumination functions," *Journal of Optical Society of America*, 15, pp. 2913–2920, 1998.

Volcanic CO_2 Abundance of Kilauea Plume Retrieved by Means of AVIRIS Data

C. Spinetti,[1,2] V. Carrere,[3] M.F. Buongiorno,[1] and D. Pieri[4]

[1]Istituto Nazionale di Geofisica e Vulcanologia, Rome, Italy
[2]Università degli Studi di Roma "La Sapienza," Rome, Italy
[3]Université du Littoral "Côte d'Opale," Calais, France
[4]Jet Propulsion Laboratory, California Institute of Technology, Pasadena, California

1. INTRODUCTION

Absorbing the electromagnetic radiation in several regions of the solar spectrum, CO_2 plays an important role in the Earth radiation budget since it produces the greenhouse effect. Many natural processes in the Earth's system add and remove carbon dioxide. Overall, measurements of atmospheric carbon dioxide at different sites around the world show an increased carbon dioxide concentration in the atmosphere. At Mauna Loa Observatory (Hawaii) the measured carbon dioxide increased from 315 to 365 ppm, in the period 1958–2000 [Keeling et al., 2001]. While at the large scale, the relationship between CO_2 increase and global warming is established [IPCC, 1996], at the local scale, many studies are still needed to understand regional and local sources of carbon dioxide, such as volcanoes. The volcanic areas are particularly rich in carbon dioxide; this is due to magma degassing in the summit craters region of active volcanoes, and to the presence of fractures and active faults [Giammanco et al., 1998]. Several studies estimate a global flux of volcanic CO_2 $(34 \pm 24)10^6$ tons/day from effusive volcanic emissions, such as the tropospheric volcanic plume (Table 1) [McClelland et al., 1989]. Plumes are a turbulent mixture of gases, solid particles and liquid droplets, emitted continuously at high temperature from summit craters, fumarolic fields or during eruptive episodes. Inside the plume, water vapour represents 70 – 90% of the volcanic gases. The main gaseous components are CO_2, SO_2, HCl, H_2, H_2S, HF, CO, N_2 and CH_4. Other plume components are volcanic ash, aqueous and acid droplets and solid sulphur-derived particles [Sparks et al., 1997]. Volcanic gases and aerosols are evidences of volcanic activity [Spinetti et al., 2003] and they have important climatic and environmental effects [Fiocco et al., 1994]. For example, Etna volcano is one of the world's major volcanic gas sources [Allard et al., 1991]. New studies on volcanic gaseous emissions have pointed out that a variation of the gas ratio CO_2/SO_2 is related to eruptive episodes [Caltabiano et al., 1994]. However, measurements and monitoring of volcanic carbon dioxide are difficult and often hazardous, due to the high background presence of atmospheric CO_2 and the inaccessibility of volcanic sites.

Hyperspectral remote sensing is a suitable technique to overcome the difficulties of ground measurement. It permits a rapid, comprehensive view of volcanic plumes and their evolution over time, detection of all gases with absorption molecular lines within the sensor's multispectral range and, in general, measurement of all the volatile components evolving from craters. The molecular and particle plume components scatter and absorb incident solar radiation. The integral of the radiation difference composes the signal measured by the remote spectrometer. The inversion technique consists of retrieving the plume component concentrations, hence decomposing the signal into the different contributions. The accuracy of remote sensing techniques depends primarily on the sensor capability and sensitivity.

Table 1. Volcanic CO_2 Emissions [McClelland et al., 1989]

Volcano	CO_2 (T/d)
Mt. Etna	11000–70000
Popocatepetl	6400–40000
Oldoinyo Lengai	7200
Augustine	6000
Mt. St. Helens	4800
Stromboli	3000
Kilauea	2800
White Island	2600
Erebus	1850
Redoubt	1800
Grimsvotn	360
Vulcano	270

2. KILAUEA VOLCANO–HAWAII

The Kilauea volcano system, called Hot Spot, has been active for 300,000–600,000 years, with no known prolonged periods of quiescence. Hot Spot means that magma penetrates the plate and rises up to the surface, leaving a string of volcanoes. The Hot Spot is merely an anomalous concentration of heat that is transferred constantly from the Earth's interior to the surface. Beginning in 1983, a series of short-lived lava fountains built the massive cinder and spatter cone named Pu'u 'O'o vent. This eruption of Kilauea is the most voluminous outpouring of lava in the volcano's east rift zone in the past five centuries.

Kilauea emits more than 700,000 tons of CO_2 each year, less than 0.01% of the yearly global contribution by human sources. For instance, this is about the same amount of CO_2 emitted by 132,000 sport utility vehicles [USGS, 2002].

3. DATA SET

An airborne study was performed on Kilauea volcano with the Airborne Visible Infrared Imaging Spectrometer (AVIRIS) at the end of April 2000.

Spring is the ideal time to acquire high-quality images because of the relatively low humidity in this tropical region [NOOA, 2000]. Several flights were performed in order to acquire different views of the site. On the day of acquisition over the Pu'u 'O'o vent, some clouds obscured the target and only one clear image of the degassing plume was acquired (Figure 1).

Weather conditions presented some clouds at the cone altitude during the morning. A temperature mean value of (13.8 ± 0.5) °C, a height relative humidity of 80% ± 5%, a pressure of (884 ± 3) hPa, a wind speed about 10 knot and wind direction of about 70 degree North were measured during the radiosounding at the cone altitude.

Ground-based measurements of different volcanic gases were performed at the same time as the AVIRIS flight. The USGS Volcano Observatory analysed gas samples of SO_2 and CO_2 using a Cospec Correlation Spectrometer and Li-Cor system [Gerlach et al., 1998]. In addition, instrumentation installed near the Pu'u 'O'o vent periodically measures the air quality with chemical sensors, as well as wind speed and direction. The data from this station are transmitted

to the observatory every 10 minutes, providing near-real-time data on degassing from the Pu'u 'O'o vent [Sutton et al., 1992].

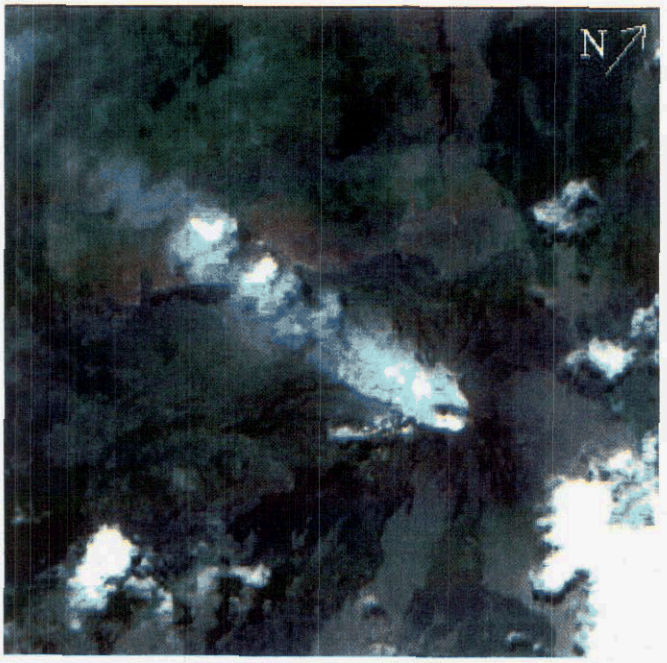

Figure 1. Pu'u 'O'o vent plume image acquired by AVIRIS 4/26/2000.

4. INVERSION TECHNIQUE

The hyperspectral sensor measures the solar irradiance reflected by the surface in its view angle, using contiguous bands at a high-spectral resolution. The algorithm was developed in the wavelength range from 1.9 to 2.1 μm, where the CO_2 molecules have absorption lines partially overlapped by the water vapour absorption lines. The near-2000-nm CO_2 absorption range has been selected because the AVIRIS spectra are more sensitive to different amounts of carbon dioxide than in the near-1600-nm CO_2 absorption range [Green, 2001].

The inversion algorithm to calculate volcanic CO_2 concentration is based on a differential absorption technique, which assumes that the absorption deep in the atmospheric spectrum curve is related to the volcanic CO_2 concentration in the column. Following the CIBR 'Continuum Interpolated Band Ratio' remote-sensing technique [Carrere and Conel, 1993] used to calculate water vapour columnar abundance, the CO_2 concentration is retrieved by solving the following equation:

$$CIBR = \exp\left(-\alpha \cdot [CO_2]^{\beta}\right) \tag{1}$$

Where:

- *CIBR* is given by the following ratio:

$$CIBR = \frac{L}{a \cdot L1 + b \cdot L2} \tag{2}$$

- L is the band interpolated radiance;

- a and b are the weighing coefficients ($a + b = 1$);
- L_1 and L_2 the continuum radiances.

- $[CO_2]$ is the CO_2 columnar abundance;
- α and β are parameters related to the model variables.

5. RESULT

In order to invert equation (1) on CO_2 concentration, α and β have been estimated. To this purpose, the MODTRAN radiative transfer code [Berk et al., 1989] was used to simulate the radiances acquired by the AVIRIS sensor in the Pu'u 'O'o vent image. In order to accurately represent the atmosphere and the measurement conditions, the input information for the model reflects the following conditions:

- atmospheric vertical profile (Pressure, Temperature, Humidity and Wind Speed), as measured at the Hilo site during the AVIRIS flight;
- atmospheric CO_2 concentration equal to 371.59 ppmv, as derived from in situ air samples collected at Mauna Loa Observatory [Keeling et al., 2001];
- surface reflectance equal to 0.1 for basaltic lava rock in the IR wavelength range, as derived from the USGS reflectance database;
- geometrical parameters, i.e., flight altitude, sensor view angle, volcano altitude;
- rescaling factors for carbon dioxide.

The radiance simulated at different CO_2 concentrations at AVIRIS spectral resolution is reported in Figure 2. The depth of the absorption bands is mathematically represented by the CIBR (2). Each CIBR corresponds a value of CO_2, as reported in Figure 3. The calibration curve follows equation (1) with parameter values of $\alpha = 3{,}71*10\text{-}3$ and $\beta = 0.804$, and a fit correlation of 95%.

Replacing the values of parameters α and β, equation (1) has been inverted in order to calculate the volcanic CO_2 abundance in the scene. The CIBR has been calculated using the radiance measured on each pixel by the AVIRIS sensor.

In Figure 4, the result of the inversion is reported. In the crater zone the value is a maximum reaching value of 350 ppmv of CO_2 concentration. Where the plume is dispersed in a large area, the CO_2 concentration is rather low. In the plume area over and near the crater zone, where the CO_2 concentration is expected to be much higher, the algorithm is not able to give reliable results. A possible explanation is the high emissivity of these zones partially overwhelming the CO_2 absorption. The contribution of the emissivity amount is probably due to either the hot ground in the crater area under the plume or the hot components of the plume coming out from crater, or a combination of both. This hypothesis explains why the low concentration of CO_2 is retrieved only in the central part of plume (ideally following the plume axis).

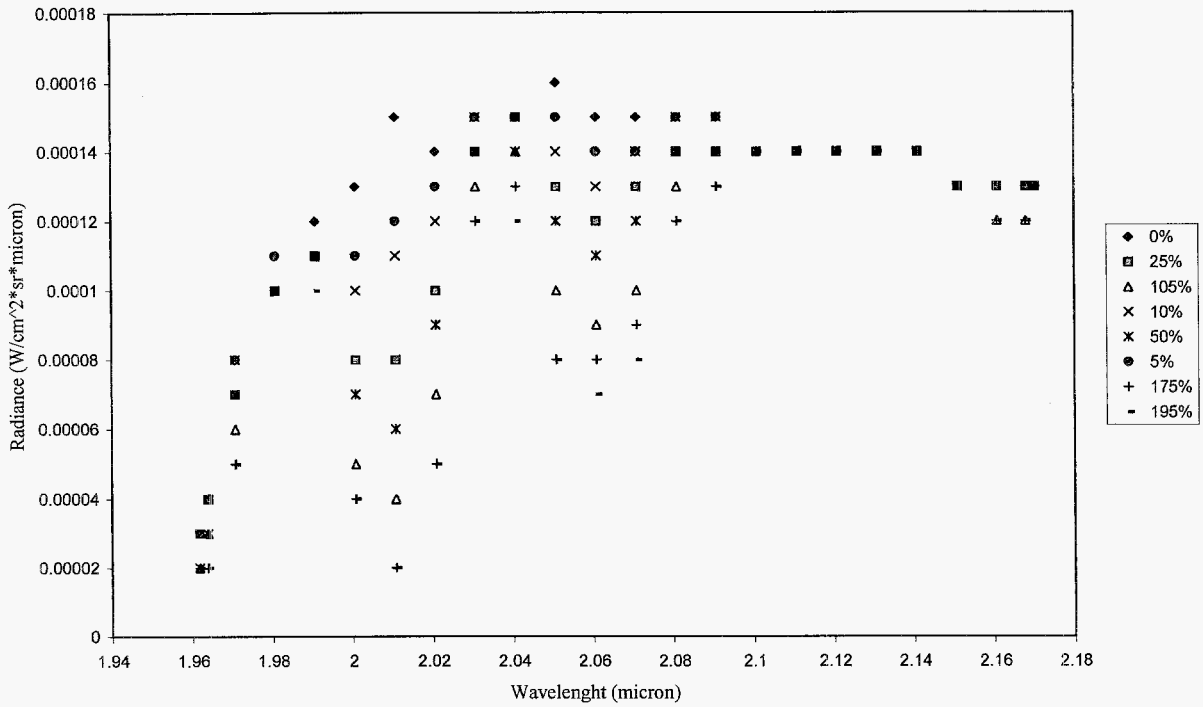

Figure 2. MODTRAN simulations at different carbon dioxide concentrations.

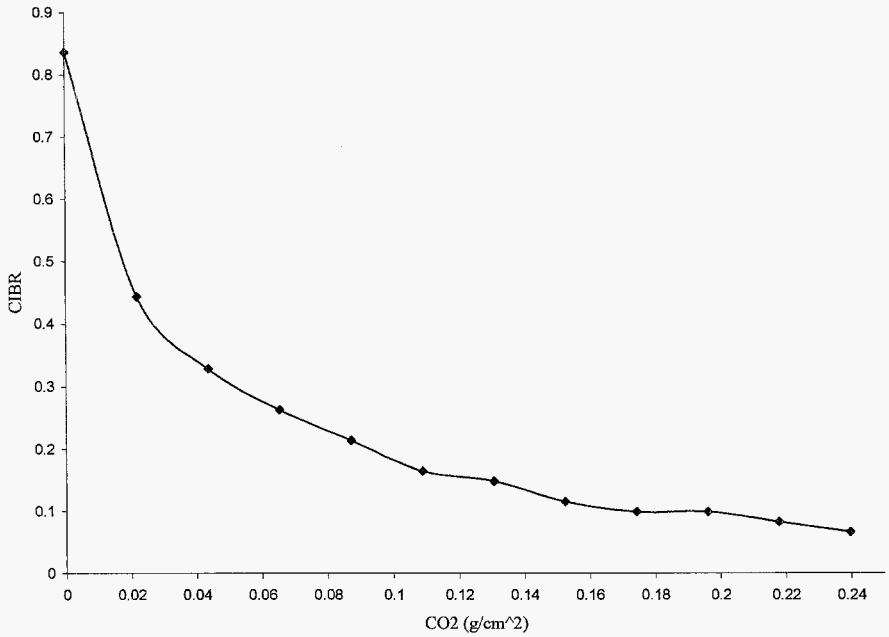

Figure 3. Calibration curve.

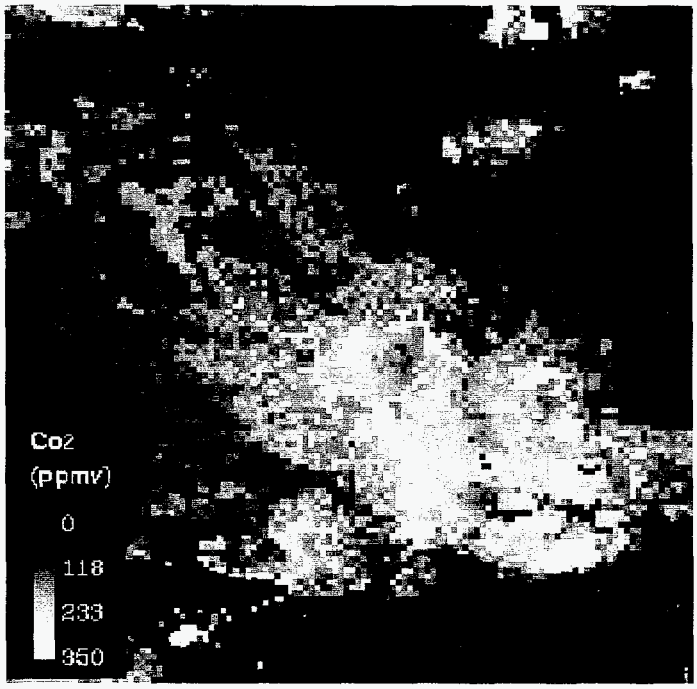

Figure 4. Volcanic plume carbon dioxide spatial distribution.

6. CONCLUSIONS

A remote-sensing technique based on a differential absorption technique has been developed in order to retrieve the tropospheric volcanic plume CO_2 abundance, using AVIRIS data acquired over the Kilauea volcano (Hawaii).

The atmospheric model MODTRAN has been tuned to the atmospheric carbon dioxide concentration measured at the ground during the AVIRIS measurements campaign.

This approach retrieves the volcanic CO_2 concentration in the Pu'u 'O'o vent plume area; the values retrieved are in agreement with ground-based measurements. Otherwise, the technique needs improvements in order to expand its validity to the entire plume area, and to retrieve the concentration of the plume in areas where the results are not reliable, probably caused by the high emissivity of these zones.

ACKNOWLEDGEMENTS

The work was carried out at University of Littoral. University of Rome "La Sapienza" Physic's Department funded the research project; we thank Prof. F. Melchiorri and the director of MNF Faculty Prof. F. Bossa. The work wills continues at INGV funded by GNV. Curtsey of Dr. A.J. Sutton the data for validation. We wish to thank particularly Prof. G. Fiocco for his helpful advice.

Part of this work was carried out at the Jet Propulsion Laboratory, California Institute of Technology, under a contract with the National Aeronautics and Space Administration.

REFERENCES

Allard, P., J. Carbonelle, D. Dajlevic, J. Le Bronec, P. Morel, M.C. Robe, J.M. Maurenas, R.F. Pierret, D. Martins, J.C. Sabroux, and P. Zettwoog, 1991. *Eruptive and diffuse emission of CO_2 from Mount Etna.* Nature, Vol.351, p.387.

Berk, A., L.S. Bernstein, and D.C. Robertson, 1989. *MODTRAN: a moderate resolution model for LOWTRAN 7.* GL-TR-89-0122, Final Report 12 May 1986- 11 April 1989.

Caltabiano, T., R. Romano, and G. Budetta, 1994. *$S0_2$ flux measurements at Mount Etna (Sicily).* Journal of Geophysical Research, Vol. 99, p. 12809.

Carrere, V. and J.E. Conel, 1993. *Recovery of Atmospheric Water vapour Total Column Abundance from Imaging Spectrometer data around 940nm – Sensitivity Analysis and Application to AVIRIS data.* Remote Sens. Environ. 44:179–204.

Fiocco, G., D.Fua', and G. Visconti, 1994. *The Mount Pinatubo Eruption Effects on the Atmosphere and Climate.* NATO ASI Series, Series 1: Global Environmental Change, Vol. 42.

Gerlach, T.M., K.A. McGee, A.J. Sutton, and T. Elias, 1998. *Rates of volcanic CO_2 degassing from airborne determinations of SO_2 emission rate and plume CO_2/SO_2: Test study at Pu'u'O'o cone, Kilauea volcano, Hawaii.* Geophysical Research Letters, Vol. 25, NO.14, pp. 2675–2678, July 15 1998.

Giammanco, S., S. Guerrieri, and M. Valenza, 1998. *Anomalous soil CO_2 degassing in relation to faults and eruptive fissures on Mt. Etna (Sicily, Italy).* Bull. Volcanol. 60: 252–259.

Green, R.O., M.L. Eastwood, C.M. Sarture, T.G. Chrien, M.Aronsson, B.J. Chippendale, J.A. Faust, and B. Parvi, 1998. *Imaging spectroscopy and the Airborne Visble/Imaging Spectrometer (AVIRIS).* Remote Sens. Environ. 65: (3) 227–248.

Green, R.O., 2001. *Measuring the Spectral Expression of Carbon Dioxide in the Solar Reflected Spectrum with AVIRIS.* AVIRIS Workshop, JPL/NASA, Pasadena, California. 2001. *July 6, 2002 URL* http://popo.jpl.nasa.gov/docs/workshops/01_docs/2001Green_co2_web.pdf.

IPPC Second Assessment: Climate Change 1995, Intergovernmental Panel on Climate Change. 1996.

Keeling, C.D. and T.P. Whorf, 2001. *Atmospheric CO_2 concentrations derived from in-situ air samples collected at Mauna Loa Observatory, Hawaii.* Sripps Institution of Oceanography (SIO), University of California, La Jolla, California USA 92093-0244.

McClelland, L., T. Simkin, M. Summers, E. Nielsen, and T.C. Stein, 1989. *Global volcanism 1975–1985.* Engelwood Cliffs, NJ: Prentice-Hall. 655 pp., 1989.

National Oceanic and Atmospheric Administration Climate, 2000. *Climate of 2000– April, U.S. National Analysis.* National Climatic Data Center, 15 May 2000.

Sparks, R.S.J., M.I. Bursik, S.N. Carey, J.S. Gilbert, L.S. Glaze, H. Sigurdsson, and A.W. Woods, 1997. *Volcanic plumes.* Wiley editor.

Spinetti, C., M.F. Buongiorno, V. Lombardo, and L. Merucci, 2003. *Aerosol optical thickness of Mt. Etna volcanic plume retrieved by means of the Airborne Multispectral Imaging Spectrometer MIVIS.* Annals of Geophysics Vol. 46 N.2.

Sutton, A.J., K.A. McGee, T.J. Casadevall, and B.J. Stokes, 1992. *Fundamental volcanic-gas-study techniques: an integrated approach to monitoring.* Ewert, J.W., and Swanson, D.A. (eds.), 1992.

USGS Hawaiian Volcano Observatory. 2002. *Kilauea - Perhaps the World's Most Active Volcano.* October 29, 2002 URL http://hvo.wr.usgs.gov/kilauea/.

USGS Digital Spectral Library. January 8, 2000 URL http://speclab.cr.usgs.gov/spectral-lib.html.

AVIRIS AND ARCHAEOLOGY IN SOUTHERN ARIZONA

Devin Alan White[1]

Introduction

Arizona is a state that is experiencing unprecedented growth in both its economy and its population. Cities like Phoenix and Tucson are expanding at exponential rates, converting open space to tract home communities and strip malls. Underneath both Phoenix and Tucson, and extending out far into the Sonoran Desert, are tens of thousands of archaeological sites associated with the prehistoric culture known as the Hohokam (Crown and Judge, 1991; Gumerman, 1991). While archaeologists do not like the fact that dozens of Hohokam sites are destroyed every day in the name of progress, we do take some small comfort in the federal legislation that mandates that we get to find, document, excavate, and report on those sites—thereby preserving some of Arizona's rich cultural heritage—before they are destroyed. The most expensive and time-consuming aspect of this work, known as Cultural Resource Management (CRM), is survey.

Most projects involve surveying a large piece of land on foot. Sites are recorded and ranked by perceived importance. The most important of these sites are either excavated (last resort) or avoided entirely (preferable), depending on the flexibility of the developer. If archaeological sites in southern Arizona were easily seen on the surface, as they generally are in other parts of the Southwest, survey would be relatively straightforward and inexpensive. However, Hohokam sites exhibit little to no surface expression that we can detect with the naked eye. The results of this dilemma have been disastrous. Construction crews find or destroy sites archaeologists missed and archaeologists sometimes end up digging in locations that yield no information.

The main contributing factors to the relative invisibility are dense vegetation cover and what archaeologists refer to as *site formation processes* (Schiffer, 1987). The Sonoran Desert, due to its complex geology and bimodal rainfall pattern, allows for a great degree of biotic diversity. The landscape is literally blanketed with vegetation ranging from sage brush to saguaro cacti to mesquite, greatly reducing site visibility from the ground or the air (Figure 1). Site formation processes, which are natural and cultural processes that affect an archaeological site once it has been abandoned by its prehistoric occupants, are perhaps the most devastating with respect to site visibility. The effects of natural processes such as erosion, weathering, sedimentation, and Aeolian deposition on an archaeological site over hundreds of years produce a fairly uniform result throughout the Sonoran Desert region: Sites are almost entirely invisible from the surface. Over time, sediments fill in all but the most prominent and large archaeological features until the ground surface appears completely flat (Figure 2). It is actually quite easy to walk over an entire Hohokam village and not know it is there, 30 cm beneath the surface (Figure 3).

Figure 1. Typical vegetation cover in the Sonoran Desert that results in low site visibility.

[1] University of Colorado, Boulder (devin.white@colorado.edu)

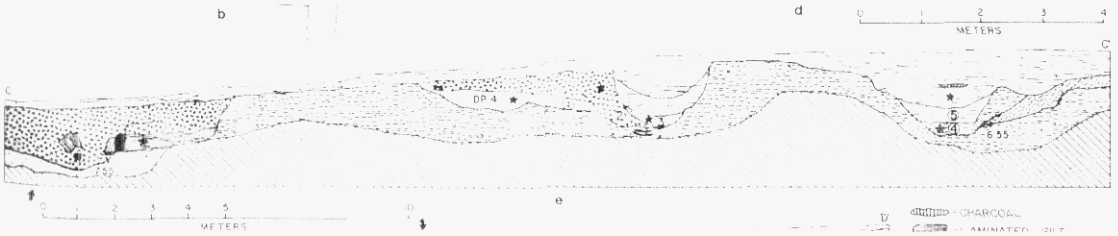

Figure 2. Typical stratigraphic profile from a Hohokam site. Archaeological features like canals (right of center) are often filled in with sediments until they are completely level with the modern ground surface, rendering them invisible to the naked eye and, potentially, remote sensing systems. (Haury, 1976)

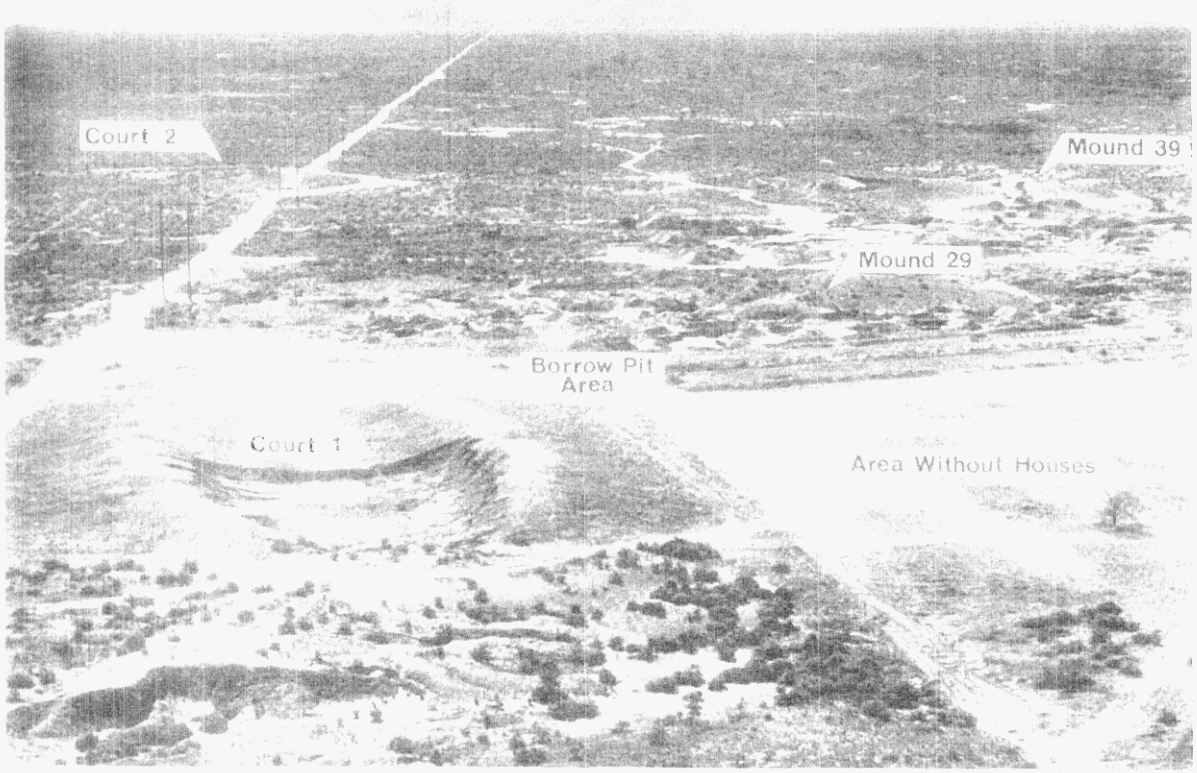

Figure 3. The Pre-Classic Hohokam site Snaketown, before excavation. Surface expression of archaeological features is minimal, even at a site as large and as important as this one. (Gladwin et al, 1938)

Spectral remote sensing holds a great deal of potential for archaeologists, especially now that advances in technology have moved spatial and spectral resolution into the range that is useful to us. The reasons that archaeologists working in southern Arizona have not embraced airborne and satellite remote sensing so far are that (1) the high spatial resolution systems (IKONOS) only cover the visible and near-Infrared portion of the spectrum, one in which sites are invisible, and (2) systems that cover more portions of the spectrum (Landsat) tend to do so only broadly and have large pixels (30 m or greater). While using thermal Infrared remains a possibility, it is still worthwhile to explore the utility of remote sensing that takes advantage of high spectral resolution, for it has not been tried before.

It is my belief that certain types of archaeological sites in southern Arizona may contain within them mixtures of materials that when seen as whole by a hyperspectral remote sensing system could be differentiated

from surrounding soils and rocks using a wide array of image processing techniques including the standardized "hourglass processing" regime available in ENVI. This study uses hyperspectral remote sensing data for southern Arizona obtained by AVIRIS, combined with ancillary data from the USGS and the Arizona State Historic Preservation Office (SHPO), in an effort to find a solution to the problem of site invisibility. After a thorough discussion of the methods used in analysis, the results of this study are presented. These results, as the reader will soon see, are indeed promising, but I must caution that they are only preliminary. Much additional research, including fieldwork, is required in order to validate the findings of this study and prove the utility of hyperspectral remote sensing for archaeological site detection in southern Arizona.

Methods

The first step in my analysis was finding the appropriate AVIRIS data. Candidate data sets had to (1) cover some part of southern Arizona, (2) contain within them areas that were not impacted by urban sprawl, and (3) contain within them regions where archaeological sites were known to exist. The coordinates for each candidate data set were plotted on a map and checked against known archaeological site locations, which was done via additional maps and personal communication with other archaeologists who work in the region. Out of the archived data sets examined, only one met all of the established criteria.

Each of the nine AVIRIS radiance-calibrated scenes were subjected to atmospheric correction and conversion to apparent reflectance using HATCH (Figure 4), a program still currently under development within the Center for the Study of Earth from Space (CSES) at the University of Colorado, Boulder. Several parameters within the HATCH input file had to be modified in order to ensure an accurate correction and conversion. Date, time of day, surface elevation, location (lat/long), visibility, and aircraft altitude all had to be changed to match local conditions at the time the data were acquired. HATCH was directed to use the Full Width Half Maximum (FWHM) file that accompanied the data and to weight the seventh water vapor band (0.86, 1.25). The Z-profile of each scene was examined and any bands that exhibited a high degree of noise, were overlapping, demonstrated severe over-correction by HATCH, or did not contain data were thrown out. Out of the 224 bands on the AVIRIS system, 58 bands (1-7, 32-35, 96, 105-117, 151-172, 213-224) were removed due to one or more of these problems. The remaining 166 bands were used extensively throughout the rest of this study.

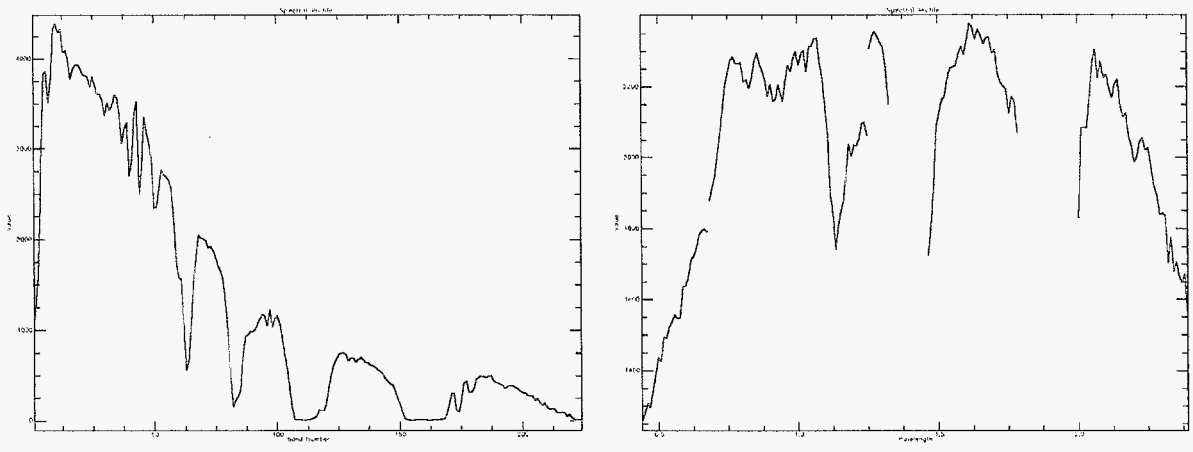

Figure 4. Example of atmospheric correction and conversion of radiance (left) to apparent reflectance (right) using HATCH.

The next step in my analysis was to obtain relevant ancillary data. 1:100,000 scale digital line graphs in Option Format were downloaded from the USGS WebGLIS server to aid in registering the AVIRIS scenes to a UTM map projection. Digital elevation models (DEMs)—accurate to within 30 meters—were downloaded to aid in data interpretation and presentation, as well as to increase the accuracy of the atmospheric correction carried out by HATCH. By far the most important ancillary data set needed for this study was a relational database that contained accurate locations for and information about known archaeological sites in the region. The State Historic Preservation Office for Arizona, in cooperation with Arizona State University and the University of Arizona, maintain just this kind of database (AZSITE). While AZSITE mainly functions as an archive to be used by Cultural

Resource Management firms and other government agencies, it can also be accessed by individual researchers who have the proper clearance. Getting access to this sensitive data was not easy and required the acceptance of a non-disclosure agreement with respect to accurate site locations if I ever decided to present the findings of this study in a public forum. In accordance with this agreement, I have gone to great lengths in this paper to avoid making any sort of reference to exactly where in southern Arizona these data derive from. However, all delineated sites presented in the images below are exactly where they should be, even though geographical references and scales are not present.

Once clearance to AZSITE was granted, I instructed the database administrator to search the extent of my entire AVIRIS flight line for known archaeological sites. When the total number began to exceed 3000, we both thought it wise to limit the search to the types of sites that would be of particular interest to me. A new search was conducted that only looked for sites that were prehistoric (before Spanish contact, containing no modern man-made materials) and exhibited some form of surface expression. I knew that sites with surface expression were rare (hence the need for this study), but if any existed within the study area I might be able to increase the success of my analyses due to the fact that reflected light only penetrates the upper few microns of the earth's surface. Buried archaeological sites would not do me much good. A list of candidate sites was compiled and the database administrator generated a geo-referenced ArcView shape file (UTM projection) that contained both their locations and site type. The importance of this shape file for my study cannot be overstated. Once the AVIRIS scenes were warped to a UTM map projection, this file could be accurately overlaid on each scene, thereby providing exact site locations within an image and allowing for comparison between known sites and predicted sites.

I next selected three adjoining scenes that covered an area of interest (Figure 5). This area was chosen for its "pristine" condition—where native vegetation and archaeological sites are still relatively intact. I took each scene (unwarped) and performed several standard "hourglass processing" analyses in ENVI (MNF, PPI, n-DV, Identification, MTMF, Mapping location and abundance) focusing on different parts of the spectrum (especially NIR and the 2-2.5 μm region). My thought was that archaeological sites might show up as an endmember in portions of the spectrum not detectable to the human eye, where differences in vegetation and soil composition show up more clearly. These initial analyses were focused on deriving archaeological site locations from the data themselves. Candidate Regions of Interest (ROIs) were made into masks, and the resulting images were warped to a UTM map projection using 20-30 Ground Control Points (GCPs). The warped masks were thresholded back into ROIs, now geo-referenced. The AZSITE shape file was overlaid on a warped version of each scene and the locations of the ROIs were compared to known site locations.

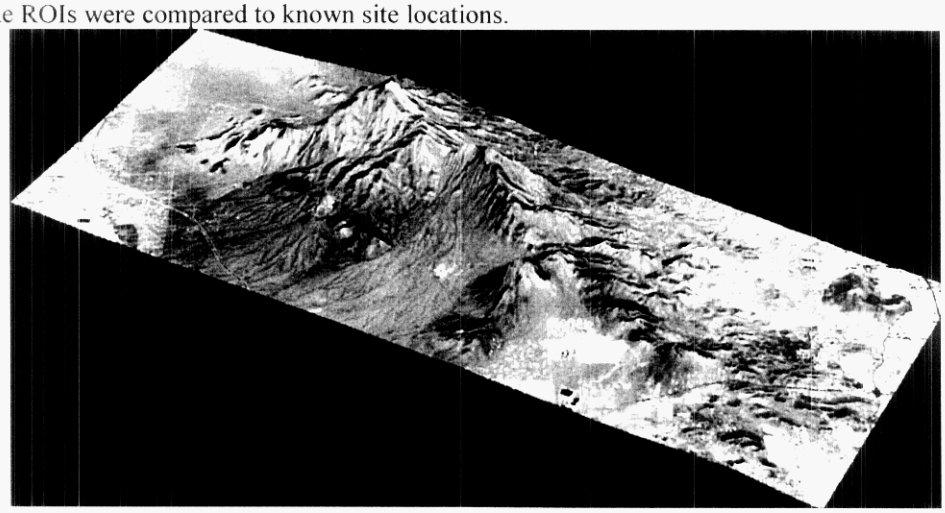

Figure 5. The three adjoining AVIRIS scenes draped on a DEM.

Unfortunately, standard hourglass processing techniques produced negative results. If archaeological sites are indeed endmembers, they are very subtle ones that are most likely overshadowed by endmembers associated with vegetation and mineralogy. Even setting the PPI iterations to maximum (32,767) failed to yield any pure pixels that matched with known site locations. Part of the problem extends from the fact that by focusing on only small portions of the spectrum the resulting data dimensionality is low (7-10 endmembers). In a last ditch effort to stick to standard processing techniques, I tried Maximum Noise Fraction (MNF) color composites and ratio images, as well as Spectral Angle Mapper (SAM) supervised classification (based on average spectra derived from sites within the park). Both of these methods produced disastrous results. Known archaeological sites were still invisible in the

MNF images and the SAM, set to a very narrow threshold, still classified the bulk of each image as an archaeological site.

I was initially very disheartened by the results of standard hyperspectral image processing. Instead of giving up, I decided to try something a little unusual. It is clear that archaeological sites are mixtures of several different materials, affected by the elements over hundreds of years, and hence they would never show up as pure pixels in a PPI image. But what if archaeological sites are *predictable mixtures*? That is, perhaps the mixtures of materials that compose sites are fairly constant in this region. As such, they could be classified as an coherent endmember, albeit one that hourglass processing would never find on its own. If average spectral profiles from known archaeological sites in the region were fed into a Mixture Tuned Matched Filter (MTMF), if it was given some direction, ENVI might be able to find archaeological sites because it would know what to look for.

In order to test the hypothesis that a directed MTMF should find archaeological sites, I chose one scene out of the three selected that I knew contained many archaeological sites of different types. The scene contains a mixture of urban sprawl and protected open space. As such, there are sites in the AZSITE database that still existed on the surface as well as some that were destroyed shortly after they were recorded and mapped. I also decided to increase the spectral range of the MNF rotation to include the entire spectrum. Since the "archaeological endmember," if it exists, is subtle, having more dimensions to work with will allow for a more accurate representation of that endmember. The MNF rotation produced 30 endmembers, which is not too surprising considering the mixture of man-made and natural materials in the scene.

The MNF image was then polynomially warped with Nearest Neighbor interpolation to a UTM projection using 20 GCPs. The AZSITE shape file was then placed on top of the image. The same shape file was opened in ArcView and the region covered by the scene was analyzed to glean site types for each delineated site. Ultimately, I focused on two site types for my analysis: pithouses and mounds. Each has surface expression and each would contain a human-induced mixture of various materials ranging from sediments to organics. I located three intact pithouses in the warped MNF image and turned each one into a member of a Region of Interest (Figure 6). A mean MNF spectra was then derived for this ROI. The same procedure was carried out for mounds, of which there was only one in the image, unfortunately. These two mean spectra (Figure 7), which I believed represented two distinct archaeological endmembers, were then fed into a MTMF analysis of the unwarped MNF image. The pixels that had the highest MF score and the lowest infeasibility for each site type were selected and turned into members of an ROI. Both ROIs were then converted to masks that were subsequently warped using the same methods applied to the MNF image. Each warped mask was then thresholded back to an ROI and overlaid on the warped MNF image, upon which was also overlaid the AZSITE shape file containing known sites for the area. MTMF-predicted site locations for each site type (pithouses and mounds) were then compared to the locations of the known sites (see Figure 8). The results of this analysis were both surprising and encouraging.

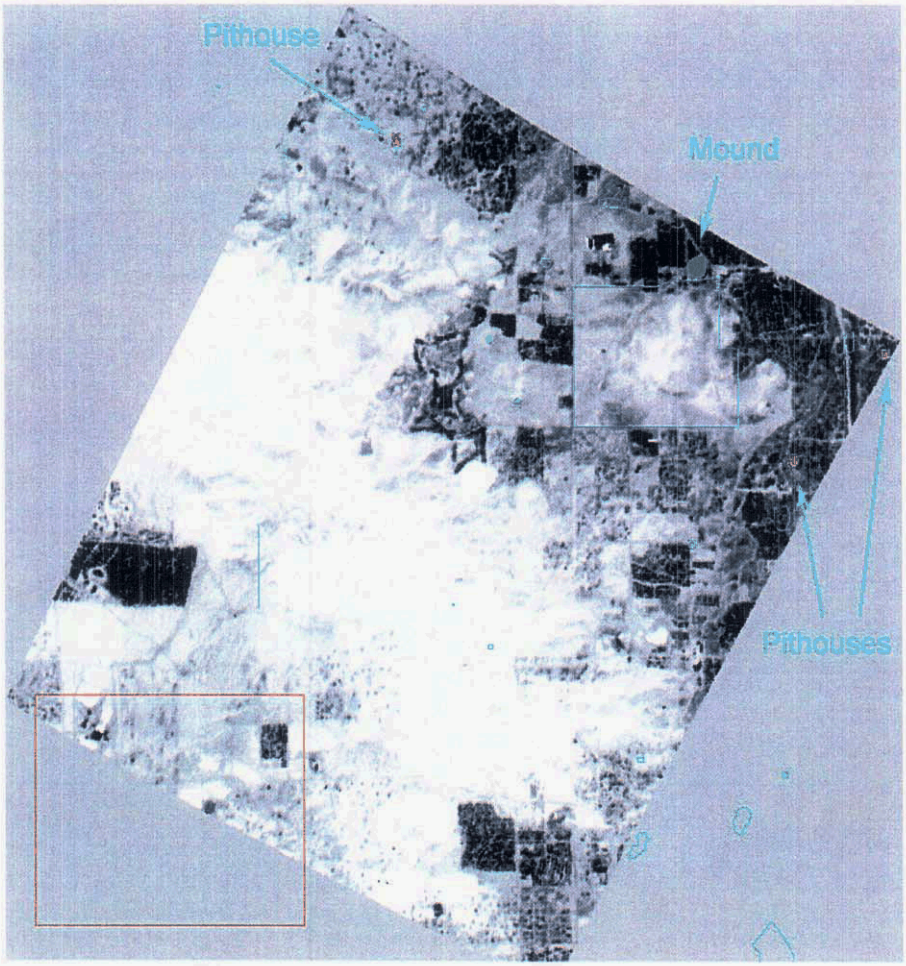

Figure 6. Warped MNF image with known sites delineated (teal). Red represents the ROI created for pithouses, Green the ROI created for mounds.

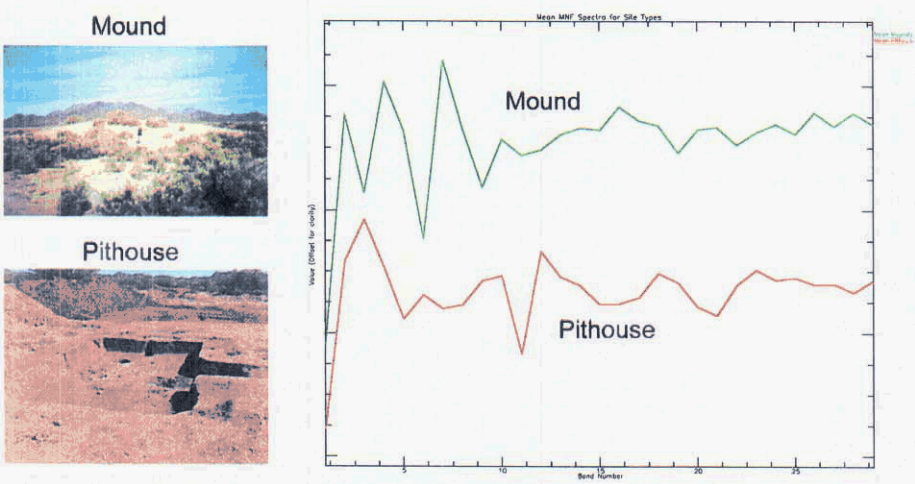

Figure 7. Examples of the two site types used in this study and their average MNF spectra as derived from the AVIRIS scene.

Figure 8. MTMF-predicted site locations (Red for pithouses, Green for mounds) compared to known site locations (Purple).

Results

The success of the directed Mixture Tuned Matched Filter analysis varied between the two site types. I was able to relocate all three pithouses used to create the average MNF spectrum for that site type (see Figure 8). Accuracy ranged from dead-on (center of bounded area in the AZSITE file) to within 70 meters. The MTMF also classified a handful of smaller rockpile sites as pithouses and pointed out a few additional locations for sites that are not included in the AZSITE file. This suggests that (1) perhaps the mixture of materials I attributed solely to pithouses might encompass a broader range of archaeological site types and (2) all of the archaeological sites contained within the scene are either not recorded in the AZSITE database or were missed in my search of the AZSITE database for sites that exhibited some form of surface expression. The MTMF missed the mound by approximately 140 meters. What is interesting to note, however, is that the AZSITE location for the mound contains within it three different modern roads. This suggests that the mound was either bulldozed to make way for the roads or the mapped location of the mound is inaccurate. If the mound was indeed bulldozed, the green pixels produced by the MTMF that show up near the mound might represent material from that mound that was relocated prior to road construction. If the mound itself is inaccurately mapped, the green pixels might represent the true mound. Ground truthing would greatly aid in clearing up this inconsistency. The green pixels that occur far away from the mound demonstrate one big problem with trying to locate mounds using an MTMF: Mounds are essentially large "bumps" composed of the surrounding soil. It is logical that other locations that are not mounds would look very similar, if not identical, to mounds if their soil composition was similar. These "stray" green pixels, though, occur very close to predicted pithouse sites or within other known sites. As with pithouses, perhaps the average MNF spectra for mounds encompasses more than just this one type of archaeological site.

One apparent problem with the MTMF analysis of this scene is the lack of predicted sites within the large semi-rectangular bounded area (Figure 8). While one green and one red pixel appear within the boundaries, the vast majority of it shows up site-free. At first this puzzled me greatly, since I knew that the area was full of sites. What is interesting is that the preserve contains sites that are fundamentally different (no pithouses) and much older than the ones I am looking for. A cultural tradition known as "Trincheras" built terraces and houses on the hill slopes contained within this area long before the Hohokam ever showed up in the region (Cordell, 1997). The Hohokam did not build their houses or mounds on slopes; instead they preferred flat areas (Haury, 1976; Crown and Judge, 1991; Gumerman, 1991). This type of cultural behavior could help explain why all of the MTMF-predicted pithouses and mounds occur only in the flat areas surrounding the hill, not on the hill itself. If predicted sites did show up on hill slopes, then I would have to completely rethink my methods. The fact the *none* showed up on hill slopes is indeed encouraging. If the AZSITE database was more accurate and delineated specific sites within the area, I might be able to create average MNF spectra for Trincheras sites—ones that are perhaps different than those associated with Hohokam sites—and look for more of them in the AVIRIS scenes.

An additional factor that may play a role in the apparent accuracy of this study is the amount of error introduced during the analysis phase. While great care was taken to use a large number of GCPs and to keep the RMS well below 0.500 when warping the AVIRIS scenes, MNF images, and masks, the warps were not perfect. It is quite possible that all of the warps are "off" by a few pixels. While nearest neighbor interpolation was used to preserve as much radiometric accuracy as possible, the technique is not perfect and some slight error was most likely introduced. On top of error introduced by the analyses I undertook, it is also quite possible that site locations recorded in AZSITE are not entirely accurate due to errors in field recording or data entry. Having said all of this, however, the results of the analysis presented here are still encouraging and further research is warranted to see if accuracy can be improved and if the techniques can be applied on a much broader scale than one AVIRIS scene.

Conclusions and Directions for Future Research

The initial results obtained using standard hyperspectral image processing techniques were not good. I believed that archaeological sites exhibited enough individuality as a coherent endmember that a Pixel Purity Index would detect them with no outside assistance. I was wrong. No matter what portion of the spectrum I focused on, no matter how high I set the iteration number, ENVI could not find the archaeological sites in my flight line on its own. Instead of throwing in the towel, I decided to rethink my methodology. If archaeological sites are indeed endmembers, they must be very subtle ones for ENVI to miss them. I went to known sites of different types and derived their average MNF spectra—now ENVI knew what to look for. A Mixture Tuned Matched Filter analysis focused on these average spectra produced some interesting results. While the accuracy could still be greatly improved through a further refining of techniques, the MTMF did a reasonable job of finding known sites once it was given some direction.

In what ways could the detection of archaeological sites using hyperspectral imagery be improved? What directions should future research take? There are two potential directions at the moment, both of which require fieldwork. The first would be to ground truth both the known site locations in the AVIRIS scene as well as the predicted ones from the MTMF analysis. This would very quickly establish which analytical steps, if any, introduced the most error. If the known sites are exactly where AZSITE says they are, then the image processing methods need to be refined. If the sites are where the MTMF analysis predicts them to be, including the additional ones not included in the database, then the techniques used here would be validated. The second would be to compile a spectral library for archaeological materials and site types in this region using lab and field spectrometers. This library could then be fed into an MTMF analysis or used in conjunction with continuum removal and Tetracorder to classify AVIRIS scenes within the flight line. The results of these analyses would hopefully be much more accurate than those presented above since ENVI would have examples of "pure" archaeological materials to work with.

On the whole, I believe that hyperspectral remote sensing holds great potential for archaeological site detection in southern Arizona. This study is the first of what I hope will be many more sophisticated uses of spectral remote sensing data in archaeology. If the techniques outlined above can be refined and their usefulness proven at larger and larger scales and across multiple AVIRIS flight lines, it could revolutionize how archaeologists conduct business in this part of the world once the technology becomes more widely available, affordable, and understood.

Works Cited

Cordell, L.S., 1997, Archaeology of the Southwest, Academic Press, New York.

Crown, P.L. and W.J. Judge, eds., 1991, Chaco & Hohokam: Prehistoric Regional Systems in the American Southwest, School of American Research Press, Santa Fe.

Gladwin, H.S., E.W. Haury, E.B. Sayles and N. Gladwin, 1938, Excavations at Snaketown: Material Culture, University of Arizona Press, Tucson.

Gumerman, G.J., ed., 1991, Exploring the Hohokam: Prehistoric Desert Peoples of the American Southwest, University of New Mexico Press, Albuquerque.

Haury, E.W., 1976, The Hohokam: Desert Farmers and Craftsmen, University of Arizona Press, Tucson.

Schiffer, M.B., 1987, Formation Processes of the Archaeological Record, University of Utah Press, Salt Lake City.

Estimating Surface Soil Moisture in Simulated AVIRIS Spectra

Michael L. Whiting,[1, 2] Lin Li,[2] and Susan L. Ustin[2]

[1]USDA – Natural Resources Conservation Service, Davis, California 95616-4165
[2]Center for Spatial Technologies and Remote Sensing, University of California
Davis, California 95616-8671

1.0 INTRODUCTION

Soil albedo is influenced by many physical and chemical constituents, with moisture being the most influential on the spectra general shape and albedo (Stoner and Baumgardner, 1981). Without moisture, the intrinsic or matrix reflectance of dissimilar soils varies widely due to differences in surface roughness, particle and aggregate sizes, mineral types, including salts, and organic matter contents. The influence of moisture on soil reflectance can be isolated by comparing similar soils in a study of the effects that small differences in moisture content have on reflectance. However, without prior knowledge of the soil physical and chemical constituents within every pixel, it is nearly impossible to accurately attribute the reflectance variability in an image to moisture or to differences in the physical and chemical constituents in the soil. The effect of moisture on the spectra must be eliminated to use hyperspectral imagery for determining minerals and organic matter abundances of bare agricultural soils. Accurate soil mineral and organic matter abundance maps from air- and space-borne imagery can improve GIS models for precision farming prescription, and managing irrigation and salinity. Better models of soil moisture and reflectance will also improve the selection of soil endmembers for spectral mixture analysis.

Previous investigations have used laboratory spectra that are continuous throughout the full range to estimate moisture based on water absorption bands. Unfortunately, light is absorbed by water in the atmosphere, preventing the use of many of these bands in image spectra. In laboratory studies, it is common to relate soil moisture to specific water absorption overtones at 1.1, 1.4, 1.9 μm (Liu et al., 2002; Lobell and Asner, 2002). For image spectra it is necessary to utilize the general shapes of the spectra, properly calibrated for the atmosphere, excluding the individual absorptions of the water overtones.

Consistent with previous investigators, we noted the loss of reflectance with increasing water content (Bowers and Hanks, 1965); our spectra showed the same decline of albedo in Figure 1. The shape of the continuum in the VIR and SWIR responds, in a large part, to the water fundamental absorption in the 2.8 μm region (Bishop, 1988). The fundamental absorption of water affects the soil spectrum by spreading the absorption with increasing water bulk content (Bishop et al., 1994). We observed that as the overall reflectance declined, the position of the maximum reflectance also shifted to shorter wavelengths.

Currently available field and airborne instruments with a SWIR range to 2500 nm are just short of this fundamental water absorption peak. Therefore, it is necessary to model the SWIR continuum to extrapolate beyond the wavelength range of the instruments. Fitting a mathematical curve and linear functions to the extrapolated continuum provides numerical measures of the absorption depth and area changes in the fundamental water absorption. The shifting of the maximum reflectance to shorter wavelengths lengthens the tail of the curve as the absorption deepens. This shape response is characteristic of the changes seen in an inverted Gaussian function. Mineral and vegetation absorptions have been commonly measured through parameterizing the absorption bands with Gaussian functions (Miller et al., 1990; Mustard, 1992; Sunshine and Pieters, 1993).

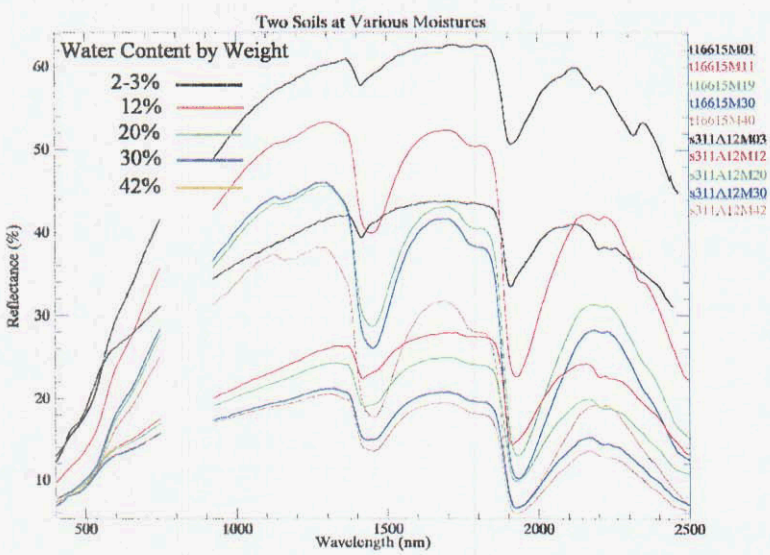

Figure 1. Distinctly different soils at similar moistures.

To demonstrate that water content can be estimated through its relationship

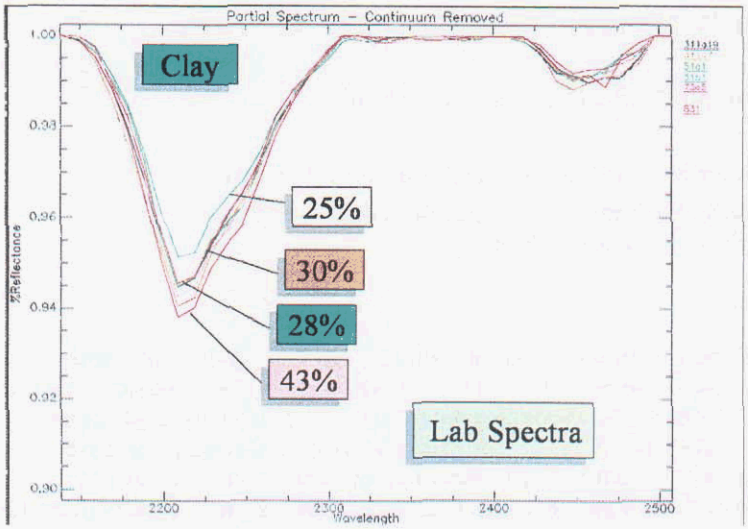

Figure 2. The absorption depth at 2200-nm is related to the clay contents.

to the fundamental absorption spread, laboratory soil spectra from a range Mediterranean soils and moisture contents were fitted to inverted Gaussian curves. The returned Gaussian parameters were regressed against the moisture contents of these soil samples. Several parameters from the Gaussian model were tested and demonstrated different levels of accuracy from 0.017 to 0.025 RMSE for estimating water content (g/g) (Whiting et al., in press).

Specific to the interest of this AVIRIS conference, determining whether AVIRIS has significant resolution for this modeling process is necessary before the process is applied to AVIRIS image. Eliminating the effect of soil water is essential to obtain accurate estimates of mineral and organic matter abundances. The first step in developing the correction for moisture effects is to accurately estimate moisture content. A large subset of these laboratory spectra were used to develop and validate the soil moisture Gaussian model (SMGM), degraded from 1-nm to 10-nm band widths, to simulate AVIRIS reflectance spectra. The regression of water content on these model parameters demonstrated even a slight improvement in estimating water content.

1.1 Effect of Moisture on Mineral Abundance Estimates

The depths of absorption near 2.2 μm increases corresponding to the increasing clay mineral contents when shown in the continuum removed spectra (Figure 2), obtained from similar soils in our study area. The shape of other absorption features has been associated with abundance, as in the derivatives of the 2.3 μm region in laboratory spectra data for carbonate abundance (Ben-Dor and Banin, 1990). The problem is that this contrast observed in the continuum is inconsistent with changes of water content, whether measured by the depth or shape.

As determined early on, the over-all reflectance of soil declines with increasing moisture (Figure 1). In contrast to increasing moisture absorption at 1.4 and 1.9 μm, mineral absorptions diminish, non-linearly, with increasing moistures as shown in continuum removed spectral from our study soils (Figure 3). Determining the correction for the spectra, and the mineral and organic matter absorptions, is part of our on-going research program.

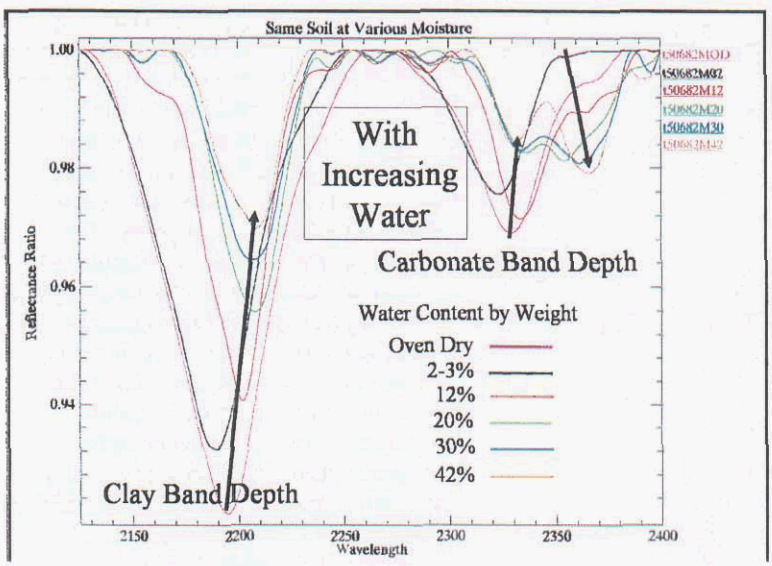

Figure 3. Absorption depth declines disproportionately to the amount of increasing water content, and decline in soil reflectance.

1.2 Physical and Mathematical Moisture Model

The decline in soil reflectance with increasing moisture follows a characteristic pattern, even among dissimilar soils. In Figure 1, the brighter soil from calcareous terraces in Spain and the darker soil from southern San Joaquin Valley, California basin rims, at the same moistures, appear to have very different continuum patterns. However, after the differences in intrinsic or matrix reflectance is eliminated by normalizing to the spectrum's maximum reflectance (Figure 4), the spectra from the same moistures show similar patterns, denoted by curved lines. Also,

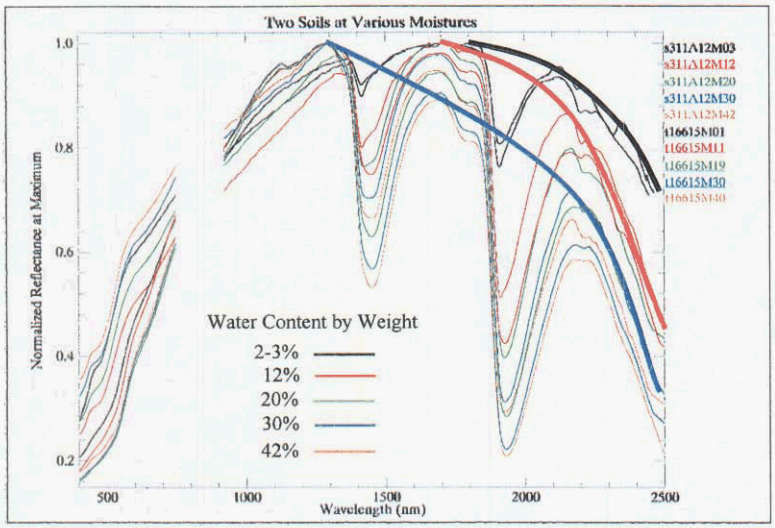

Figure 4. After spectra are normalized by maximum reflectance for each spectrum, the trend due to moisture becomes more apparent.

the maximum reflectance in the SWIR declines with increasing moisture content and the wavelength position of maximum shifts to shorter wavelengths, following the spread of the fundamental water absorption.

From the Beer-Lambert Law, we know that absorptions are log based, that is, absorbance is the negative log of reflectance. The difference from incident and reflectance light on soil (considered infinitely thick optically) is the portion absorbed. This apparent absorbance (Kortum, 1969) is equal to the product of a mineral's absorption coefficient and optical depth (Clark and Roush, 1984).

$$I = Io \exp(-ad) \text{ or } -ad = lnI - lnIo \quad (1)$$

where I is transmitted energy, Io, incident energy, *a,* absorption coefficient, and, *d* is the optical path length. While Hapke (1993) provides a number of techniques for converting reflectance to absorbance to reduce the effects of logarithmic compression, Yen et al. (1998) found the natural log the least unsatisfactory for linearizing reflectance data from laboratory measurements and transforming to apparent absorbance, defined by Kortum (1969) as the – ln(r). For the remainder of this discussion, the absorbed energy is described and modeled using the natural log of reflectance.

A common method of reduce complex shapes of absorptions to a few parameters is fitting the Gaussian Function (Miller et al., 1990; Sunshine and Pieters, 1993). The model has the advantages of parameterizing the absorption into three values: a) function center, b) its amplitude, and c) the distance to the inflection point. A fourth parameter can be derived, the area under the curve. After a series of trial and error, the position of the maximum reflectance was left unconstrained, which allowed the functional tail to shift with the spread of the fundamental water absorption. The spectra are normalized by dividing the reflectance at each band by this maximum reflectance (R_0). The center of function was constrained to 2.8μm (μ), the other parameters were determined through a least-squares fitting of the reflectance at each wavelength (λ_i), for the depth (R_d) or the amplitude of the Gaussian Function, and the distance to the inflection point (σ) in Equation (1).

$$g(\lambda) = R_0 - R_d * \exp\left\{\frac{-(\lambda_i - \mu)^2}{2\sigma^2}\right\} \quad (1) \qquad A = \int_{\lambda_0}^{\lambda_{max}} \frac{2\sigma^2 R_d}{-(\lambda_0 - \lambda)^2} \quad (2)$$

The area between the extrapolated Gaussian curve and its baseline was determined through integrating equation (1) from the maximum reflectance wavelength to the center of Gaussian curve, shown in Equation (2).

The continuum was found by defining the upper general shape of the spectrum through a convex hull algorithm. The hull boundary points, at wavelengths greater than the maximum reflectance, were used in an iterative least squares fitting algorithm to solve for the best Gaussian function for SWIR spectrum, returning both the Gaussian parameters and the minimum least squares fit errors (Figure 5). The root mean squared error (RMSE) of the fit was calculated using the least squares and the number of hull boundary points for each spectrum. IDL (Research Systems, Inc., Boulder, CO.) was used to program the functional fits and the error determinations. The Gaussian parameters and area were regressed against the gravimetric water contents to determine the moisture curve coefficients. The linear and non-linear regressions and statistical evaluations were conducted using S-Plus 2000 (Insightful Corporation, Seattle, Washington).

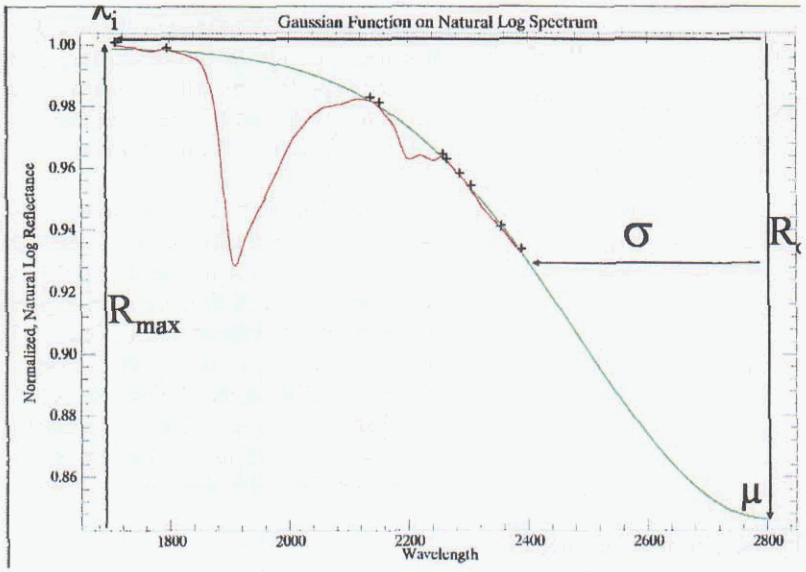

Figure 5. The Gaussian function fitting to a dry normalized soil spectrum.

2.0 STUDY METHOD

To evaluate the effectiveness of the Gaussian function to describe the response of the soil reflectance to moisture, the function was fitted to spectra from a variety of soils and a sequence moisture contents. The resulting Gaussian parameters were compared to a range of measured moistures, from oven dry to saturation.

2.1 Study Sites and Soil Sampling

Soils were from two distinctly different locations in Spain and California. The soils from Castilla-La Mancha, Spain, were collected from the calcareous uplifted Miocene calcareous and fill-cut terraces just south of the town of Tomelloso. These samples were stratified by their five landform surfaces, a) uplifted pedogenic carbonate terrace, b) internal drains on the upper terraces, c) and d) two lower level cut and fill alluvial terraces, and e) flood plain. In general, they are described as the upper fans or piedmont of "calizas y margas" (limestone and marls) mixed with "conglomerado arcilloso, coarzoso con gravas" (conglomerates of clays and gravels), (Martin et al., 1994). Sanchez et al. (1996) described the general types using the FAO soil classification system. Within the sampled area, the older surfaces of Petric Calcisols, limestone and marl with laminar calcareous crust, formed on alluvial fans, "developed from limestone and detritic materials of the upper Pliocene." In the younger alluvium and river wash, the soils are described as Haplic Calcisols, as calcisols lacking an argic B horizon and petrocalic horizon, "developed on detritic materials of alluvial bottom valleys." This map is general and designed for regional studies and planning.

The soils from the second region were formed on the basin rim of the Tulare Lake playa in the southern San Joaquin Valley, near the city of Lemoore, Kings County, California, United States. These samples were stratified by sodicity using (electro-conductivity, EC) and visible vegetation vigor or necrosis. The USDA Natural Resources Conservation Service described the soils as fine-loamy, mixed (calcareous), thermic Typic Torriorthents, and fine, montmorillonitic, thermic Typic Natrargrids using the USDA classification system (USDA, 1978). Their laboratory analysis described the mixed mineralogy of illite and montmorillonite clays.

Within the stratifications of both locations, one typical site was selected for modeling, where three samples were taken by transecting from west to east, at 10m apart. At a different location, more than a kilometer from the modeling site, an additional typical site was selected to collect one sample for validation.

These two regions provided soils with varying dry and moist colors, wide range of clay, and calcium carbonate and sodium chloride contents. Organic matter contents were similar, less than 2 % for both regions. Soils from the calcareous terraces in Tomelloso are bright due to adsorbed and free amorphous calcium carbonate. Pedogenic carbonate formations, from deep in the soil profile, have been exposed by erosion and surfaced by farm tillage practices. Carbonate aggregates, ranging in size from larger than gravels to finer than slit, are dispersed throughout the profiles. Younger cut-fill terraces and floodplains contained less carbonate and pedogenic gravels.

Soils in Lemoore differed in fine sand, silt and clay contents and in sodium chloride contents. The sodium contents promoted smooth surfaces through slaking of surface micropeds, and possibly influencing changes in the spectra (Courault et al., 1993). The Sodium Absorption Ratio (SAR) is the amount of sodium to the squared sum of calcium plus magnesium contents (Tanji, 1990) and ranged from 2.5 to 6.5 for Lemoore and 0.05 to 0.12 for Tomelloso. Though the mean for the basin high sodicity group is less than the minimum ratio of 15:1 for the sodic classification (SSSA, 1997), it is more than double the mean ratio of the low sodicity group, and one or two orders of magnitude greater than the Tomelloso region.

2.2 Collecting the Soil Spectra

In the laboratory, using a Cary 5E spectrophotometer (Varian Incorporated, San Jose, California) fitted with an external integrating sphere (Labsphere, Inc, North Sutton, New Hampshire) each moisture level of each samples was measured three times. The sample holders were mounted in the light-tight port at the base of the sphere. The instrument projected a collimated light onto the soil surface at nadir, with a constant reference double beam. The maximum relative reflectance was calculated from measurements of a white Spectralon panel (Labsphere, Inc, North Sutton, New Hampshire). The light from the spectrophotometer struck the targets in a fixed rectangle approximately 1 cm by 2.8 cm within the 3.5 cm diameter holder. To avoid any bias due to surface geometry, three measurements were made of the soil target. The holders were rotated approximately 60° before the consecutive spectral measurements.

After lightly hand grinding with a mortar and pestle, two replicate samples were packed into small clear plastic petri dish sample holders. Spectra were collected at the air dry, then oven dry states. The collection of spectra continued after each of eleven additions of water, at approximately 5% water content intervals. At the end, the soils were returned to the desiccators to air dry, then oven dried and spectra were collected with each moisture change. Of the possible 3600 combinations of soil replicates and moisture contents, 45 samples, by 2 soil replicates, and 3 spectral measurements with each of 15 moistures, there were 3,462 acceptable measurements, with 2,619 used for modeling and 843 for validation. Some samples had fewer measurements because they saturated earlier than the others and did not need all 11 water additions. Additional spectral were discarded when the second oven dry weight for the soil replicate did not return to within 0.1% of the first oven dry weight. Either the initial weight was in error or sample material was lost with handling.

3.0 RESULTS AND DISCUSSION

3.1 Fitting the Moisture Model to Laboratory Spectra

The Gaussian parameters were determined for each spectra from the sequence of moistures and soil replicated samples, and then evaluated against the measured water contents. Of the spectra, the number of hull boundary points for each spectrum ranged from 20 to 100, with the greater numbers being from the drier replicates due to greater curvature in the spectra. The maximum reflectance moved from between 1650 and1800 nm for the dry soils to near 1300 nm for moist soils. There was not a gradation of maximum reflectance positions due to the deep water absorption at 1400 nm. The fitted Gaussian returned parameters of depth, distance to inflection and area under the shortward portion of the curve.

For all soils and all moistures, the area of the curve was the best predictor of moisture content. While the functional depth and distance to the inflection point predicted the water content less accurately, analyzed together as the integration of the area, the performance was far superior. The prediction accuracy for all parameters decreased with increased moisture, and significantly worsened above 0.30 water content. The increase in moisture begins to saturate the soil samples, filling the small pores then the larger pores (Jury et al., 1991). The reflectance from the water becomes dominate, instead of the soil and water (Liu et al., 2002).

Since the area was far superior in predicting the water content, further analysis was conducted with this parameter. From the increasing variability exhibited in the predictions by the functional parameters, the linear model developed from the area was restricted to air dry to near field capacity, 0.02 to 0.32 gm/gm water content. Field capacity is defined as the water content that free draining soil holds against gravity after 24 hours (Jury et al., 1991). Most soils reach field capacity between 0.25 and 0.40 gm/gm water content (Brady and Weil, 1996). Our value of 0.32 gm/gm was derived from the sudden increase in variability for values above 0.32. The "restricted" model also eliminated spectra where the error in the Gaussian fit exceeded 0.0125 RMSE. The same variability was apparent in the validation set. The restricted validation set had no spectra fit exceeding the 0.0125 RMSE, within the moisture contents below 0.32.

The restricted soil moisture Gaussian model (SMGM) for these spectra was highly correlated to water content, though the regression coefficients were slightly different for the two locations. The result of the model for all soils and moistures was coefficient of correlation (r^2) = 0.89, and for the restricted model set was r^2 = 0.92, and with stratifications within the study sites the r^2 improved in most to 0.95. The model for Lemoore has a slightly higher r^2 than that of Tomelloso.

The Lemoore soils are much more consistent between samples in texture and aggregate size. The Tomelloso varied widely between the geomorphic surfaces. The correlation coefficients for the Tomelloso restricted model and validation sets improved substantially by stratifying by the geomorphic surface. When the model was applied to the

validation set for only Lemoore the results were very similar to the modeling set, with r^2 of 0.92 and RMS of 2.85 in water content percentage. The fit lines for the restricted models for the two regions are shown in Figure 6.

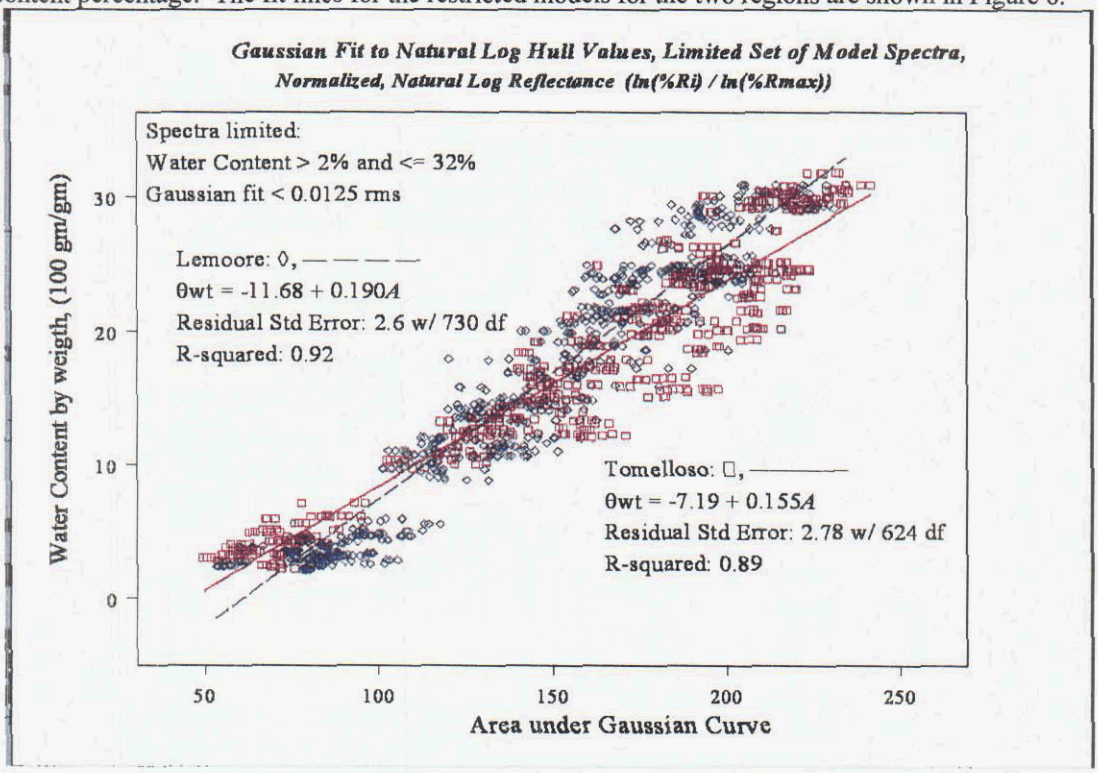

Figure 6. The linear fit of water content on the Gaussian area for Lemoore and Tomelloso soils.

3.2 Fitting the Model to Simulated AVIRIS Spectra

More relevant to this conference, we tested the effectiveness of this model at the 10-nm full width half maximum (FWHM) channels of AVIRIS data. The model and validation samples were selected to capture both saline-sodic and healthy vegetation responses determined from a pseudo-color infrared composite of a 1998 ER-2 AVIRIS image of the Sheely Farms, near Lemoore, California.

Resampling lab spectra has the advantage of studying the effects of spectral resolution without increasing the errors associated with incorrectly calibrated image data. The same lab spectrophotometer data between 400 nm and 2390 nm was interpolated to AVIRIS image band centers, which degraded the spectra from 1,990 1-nm bands to 189 nominal 10-nm bands. The resampling improved the smoothness of the spectra, though it reduced the range in the number hull boundary points from 20 to 100 in the full laboratory spectral to 5 to 20 in the simulated AVIRIS data. The fit to the Gaussian improved substantially with no error rate greater than 0.0125 RMS. With high moisture contents, the number of hull points for some spectra fell below 5, and the fitting with the Gaussian function would not converge. The number of hull points must be greater than the number of parameters in the function.

Table1. Comparison of laboratory and simulated AVIRIS spectra fitting and water content model prediction.

Comparison of RMS		
	Lab Spectral	AVIRIS-Sim
g(λ) to Hull Points	0.015	0.0125
R^2 – Limited Set	0.92	0.93
Area Fit to Water Content:		
Overall	3.7	4.4%
Limited Range	2.9%	2.9 %

The variability in the AVIRIS Gaussian parameters values was similar to the laboratory spectral data (Figure 7). While the amplitude of the function, again, was correlated to the water content, the area of Gaussian was a better predictor of the water content. In Table 1, the laboratory restricted model and the AVIRIS simulation model are basically the same, though there is a slight difference in the off-set coefficient, -1.68 to -11.81, and the same 0.19 coefficient for the area. The r^2 is virtually the same for both, 0.92 to 0.93, respectively.

When the model is applied to the validation spectral set, the accuracy of the model was similar to the model set for all moisture contents and is within RMS of 4.4 %-water

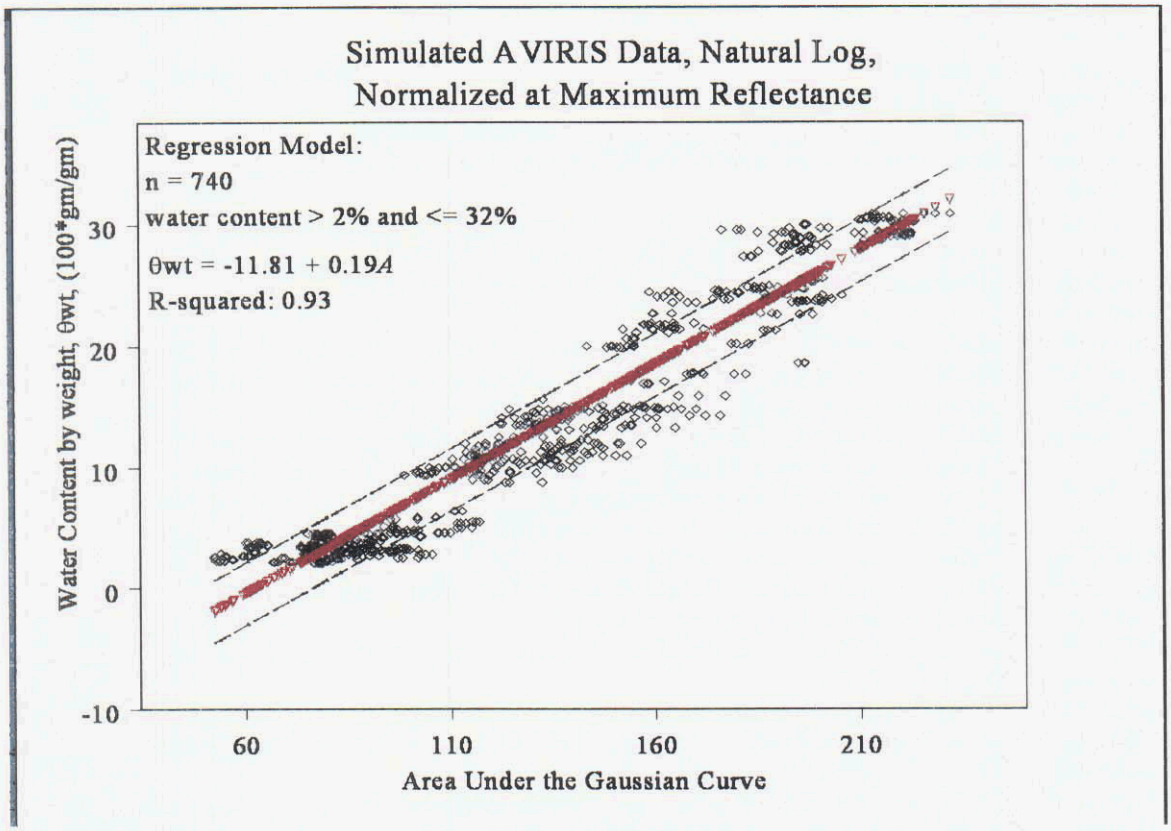

Figure 7. Similar linear fit of water content for the AVIRIS spectra simulation.

content. Again, the model is much improved within a restriction of the range of the water contents from 0.02 to 0.32 with the RMS falling to 2.84 %-water content.

4.0 CONCLUSIONS

The general shape of soil spectra SWIR region is related to water's fundamental absorption slightly beyond the spectral range of our field and imagery instruments. The fundamental absorption can be modeled with a Gaussian function on the hull boundary points of the continuum by extrapolating the SWIR continuum to the region of fundamental water absorption. The function and change of the SWIR general shape are sufficiently sensitive to the water content changes. Within the sandy loam to clay loam textures, in widely diverse Mediterranean soils from California and La Mancha, Spain, and common moisture ranges, the area under the curve has a linear relationship that can accurately estimate the surface moisture content within 3 %-water content (RMSE).

Specific to the application of this model for the retrieval of soil water content to imaging spectrometer data, the 10-nm FWHM of AVIRIS data appears to have sufficient detail to return the same accuracies. Smoothing, induced by the interpolation of resampling, did improve the fit accuracy slightly. At the higher moisture contents, some spectra had a reduced the number of hull boundary points, less than the needed number of the parameters, and fail to converge. Investigations are continuing on using the model of eliminate the effects of soil moisture to improve the estimates of other soil constituents in the soil spectra.

5.0 ACKNOWLEDGEMENTS

Contributions by JPL-NASA of ER-2 and Twin Otter flights with AVIRIS over the Sheely Farm in Lemoore are gratefully acknowledged. Also, the researchers wish to thank the USDA, Natural Resources Conservation Service for the staff time provided through an Interagency Personal Agreement with University of California, Davis. A portion of this study was funded by NASA EOS grant #NAG5-9360. The cooperation of Ted Sheely, of AzCal Farm Management, is greatly appreciated.

6.0 REFERENCES

Ben-Dor, E., and Banin, A. 1990. "Near-infrared reflectance analysis of carbonate concentration in soils," Applied Spectroscopy, vol. 44, no. 6, pp. 1064-1069.

Bishop, J. L. 1988. "The effects of water, octahedral cation substitution and exchangeable cation composition on the shortwave infrared reflectance spectrum of montmorillonite," M.S. Thesis, Stanford University, Stanford, California.

Bishop, J. L., Pieters, C. M., and Edwards, J. O. 1994. "Infrared spectroscopic analyses on the nature of water in montmorillonite," Clays and Clay Minerals, vol. 42, no. 6, pp. 702-716.

Bowers, S. A., and Hanks, R. J. 1965. "Reflection of radiant energy from soils," Soil Science, vol. 100, no. 2, pp. 130-138.

Brady, N. C., and Weil, R. R. 1996. *The Nature and Properties of Soils*, Prentice Hall, Upper Saddle River, NJ.

Clark, R. N., and Roush, T. L. 1984. "Reflectance spectroscopy: Quantitative analysis techniques for remote sensing applications," Journal of Geophysical Research, vol. 89, no. B7, pp. 6329-6340.

Courault, D., Bertuzzi, P., and Girard, M. C. 1993. "Monitoring surface changes of bare soils due to slaking using spectral measurements," Soil Science Society of America Journal, vol. 57, pp. 1595-1601.

Hapke, B. 1993. *Theory of Reflectance and Emittance Spectroscopy*, Cambridge Univ. Press, New York.

Jury, W. A., Gardner, W. R., and Gardner, W. H. 1991. *Soil Physics*, John Wiley & Sons, Inc., New York.

Kortum, G. 1969. *Reflectance Spectroscopy*, Springer-Verlag, New York.

Liu, W., Baret, F., Gu, X., Tong, Q., Zheng, L., and Zhang, B. 2002. "Relating soil surface moisture to reflectance," Remote Sensing of Environment, vol. 81, pp. 238-246.

Lobell, D. B., and Asner, G. P. 2002. "Moisture effects on soil reflectance," Soil Science Society of America Journal, vol. 66, pp. 722-727.

Martin, J. L. B., Saenz, M. C., Crues de Abia, J., Portillo, A., and Madurga, M. R. L. 1994. "Hidogeologia," *Desertificacion en Castilla-La Mancha, El Proyecto EFEDA*, F. M. Manas, ed., Universidad de Castilla-La Mancha, Albacete, Spain, pp. 71-96.

Miller, J. R., Hare, E. W., and Wu, J. 1990. "Quantitative characterization of the vegetation red edge reflectance 1. An inverted-Gaussian reflectance model," International Journal of Remote Sensing, vol. 11, no. 10, pp. 1755-1773.

Mustard, J. F. 1992. "Chemical analysis of actinolite from reflectance spectra," American Mineralogist, vol. 77, pp. 345-358.

Sanchez, J., Boluda, R., Morell, C., Colomer, J. C., Artigao, A., and Tebar, J. I. 1996. "2.1. Assessment of soil degradation in desertification threatened areas: a case study in Castilla-La Mancha (Spain)," *EFEDA-II. Final Report: Desertification processes in the Mediterranean Area and their interlinks with the global climate*, F. M. Manas, ed., Universidad de Castilla-La Mancha, Albacete, Spain, pp.19-53.

SSSA. 1997. *Glossary of Soil Science Terms*, Soil Science Society of America, Madison, WI.

Stoner, E. R., and Baumgardner, M. F. 1981. "Characteristic variations in reflectance of surface soils," Soil Science Society of America Journal, vol. 45, pp. 1161-1165.

Sunshine, J. M., and Pieters, C. M. 1993. "Estimating modal abundances from the spectra of natural and laboratory pyroxene mixtures using the modified Gaussian model," Journal of Geophysical Research-Planets, vol. 98, no. 5, pp. 9075-9087.

Tanji, K. K. 1990. *Agricultural Salinity Assessment and Management*, ASCE Manuals and Reports on Engineering Practice No. 71, American Society of Civil Engineers, New York, pp. 619.

USDA, NRCS. 1978. *Soil Survey Kings County, California*, USDA Soil Conservation Service in cooperation with University of California Agricultural Experimental Station, Hanford, CA.

Whiting, M. L., Li, L., and Ustin, S. L. in press. "Predicting Water Content Using Gaussian Model on Soil Spectra," Remote Sensing of Environment.

Yen, A., Murray, B., and Rossman, G. 1998. "Water content of the Martian soil: Laboratory simulations of reflectance spectra," Journal of Geophysical Research-Planets, vol. 103, no. E5, pp. 11125-11133.